

APR 1 1988

NAS 1.55:3026

NASA Conference Publication 3026

ORIGINAL
COMPLETED

mf-0830-H-10
330

Rotordynamic Instability Problems in High-Performance Turbomachinery 1988

*Proceedings of a workshop held at
Texas A&M University
College Station, Texas
May 16-18, 1988*

NASA

Rotordynamic Instability Problems in High-Performance Turbomachinery 1988

Proceedings of a workshop sponsored by
the Texas A&M University, College Station,
Texas, the U.S. Army Research Office, Durham,
North Carolina, the Aeropropulsion Laboratory,
Wright-Patterson Air Force Base, Ohio, and the
NASA Lewis Research Center, Cleveland, Ohio,
and held at Texas A&M University
College Station, Texas
May 16-18, 1988



National Aeronautics
and Space Administration

Scientific and Technical
Information Division

1989

BLANK PAGE

PREFACE

A review of the proceedings from the past workshops and the program for the current workshop shows a continued trend toward a more unified view of rotordynamics instability problems and several new developments from manufacturers in the design and manufacture of new machinery with enhanced stability characteristics. Test programs that were in existence two years ago continue to yield new reference data. Results from programs developed in the interim are also reported.

Without wishing to slight any authors, the following papers appear to be of particular interest:

(1) The papers by Schmied and Kanki et al. on new enhanced-stability, high-pressure compressor designs are of interest since they realize in hardware the lessons of research related to rotordynamic instability problems.

(2) The papers by Palazzolo et al. on piezoelectric pushers and by Nikolajsen et al. on electroviscous dampers and eddy-current bearings are of interest to the extent that new bearings and damper concepts and mechanisms are introduced.

(3) The paper by Iwatsubo et al. presents the first test results for annular liquid seals including the effect of fluid preswirl and separately identifying the direct and cross-coupled rotordynamic coefficients.

(4) The continued analytic/computational developments of Nordmann's group at Kaiserslautern continue to demonstrate the virtues of a marriage between CFD and classical perturbation approaches.

(5) The paper by Ohashi et al. is helpful in increasing our physical understanding of the mechanisms which yield destabilizing forces from impeller-diffuser interaction.

We are confident that you will find all of the papers on this proceedings to be of interest. Please read them and pick your own favorites.

This workshop was organized to continue addressing the general problem of rotordynamic instability by gathering those persons with immediate interest, experience, and knowledge of this subject for a discussion and review of both past stability problems and present research and development efforts. The intent of the workshop organizers and sponsors is that the workshop and this proceedings provide a continuing impetus for an understanding and resolution of these problems.

Chairmen:

Dara Childs and
John Vance
Turbomachinery Laboratory
Texas A&M University

Robert C. Hendricks
NASA Lewis Research Center

MAIN PAGE

CONTENTS

Page

Session I - Field Experiences

SOME FIELD EXPERIENCE IN SUBSYNCHRONOUS VIBRATION OF CENTRIFUGAL COMPRESSORS

Wang Xi-xuan, Gu Jin-chu, Shen Qin-gen, Hua Yong-li, and
Zhu Lan-sheng, Zhejiang University; and Du Yun-tian,
Zhengzhou Polytechnic Institute 1

ROTOR INSTABILITY DUE TO A GEAR COUPLING CONNECTED TO A BEARINGLESS SUN WHEEL OF A PLANETARY GEAR

E.T. Bühlmann, Sulzer Brothers, Ltd.; and A. Luzi, Swiss Locomotive
and Machine Works, Ltd. 19

SOME IN-FIELD EXPERIENCES OF NON-SYNCHRONOUS VIBRATIONS IN LARGE ROTATING MACHINERY

Giuseppe Colnago, CESI; and Claudio Frigeri, Andrea Vallini, and
Gian Antonio Zanetta, ENEL 41

Session II - Dampers

THE SPECTRAL ANALYSIS OF AN AERO-ENGINE ASSEMBLY INCORPORATING A SQUEEZE-FILM DAMPER

R. Holmes and M.M. Dede, University of Southampton 61

PIEZOELECTRIC PUSHERS FOR ACTIVE VIBRATION CONTROL OF ROTATING MACHINERY

A.B. Palazzolo, Texas A&M University; A.F. Kascak,
U.S. Army Aviation Research and Technology Activity - AVSCOM;
R.R. Lin, Texas A&M University; J. Montague, Sverdrup Technology;
and R.M. Alexander, Texas A&M University 87

CAVITATION EFFECTS ON THE PRESSURE DISTRIBUTION OF A SQUEEZE FILM DAMPER BEARING

Fouad Y. Zeidan and John M. Vance, Texas A&M University 111

AN ELECTROVISCOUS DAMPER

J.L. Nikolajsen and M.S. Hoque, Texas A&M University 133

Session III - Seals I

ANNULAR HONEYCOMB SEALS: TEST RESULTS FOR LEAKAGE AND ROTORDYNAMIC COEFFICIENTS; COMPARISONS TO LABYRINTH AND SMOOTH CONFIGURATIONS

Dara Childs, David Elrod, and Keith Hale, Texas A&M University 143

ROTORDYNAMIC COEFFICIENTS FOR LABYRINTH SEALS CALCULATED BY MEANS OF A FINITE DIFFERENCE TECHNIQUE

R. Nordmann and P. Weiser, University of Kaiserslautern 161

ROTORDYNAMIC COEFFICIENTS FOR STEPPED LABYRINTH GAS SEALS

Joseph K. Scharrer, Rockwell International, Rocketdyne Div. 177

**INFLUENCE OF DIFFERENT TYPES OF SEALS ON THE STABILITY BEHAVIOR
OF TURBOPUMPS**

W. Diewald and R. Nordmann, University of Kaiserslautern 197

Session IV - Seals II

**A 3-DIMENSIONAL FINITE-DIFFERENCE METHOD FOR CALCULATING THE DYNAMIC
COEFFICIENTS OF SEALS**

F.J. Dietzen and R. Nordmann, University of Kaiserslautern 211

**AN EXPERIMENTAL STUDY ON THE STATIC AND DYNAMIC CHARACTERISTICS OF PUMP
ANNULAR SEALS**

T. Iwatsubo, B.C. Sheng, and T. Matsumoto, Kobe University 229

**A SEAL TEST FACILITY FOR THE MEASUREMENT OF ISOTROPIC AND ANISOTROPIC
LINEAR ROTORDYNAMIC CHARACTERISTICS**

M.L. Adams and T. Yang, Case Western Reserve University;
and S.E. Pace, Electric Power Research Institute 253

**FINITE DIFFERENCE ANALYSIS OF ROTORDYNAMIC SEAL COEFFICIENTS FOR AN
ECCENTRIC SHAFT POSITION**

R. Nordmann and F.J. Dietzen, University of Kaiserslautern 269

Session V - Impeller Forces

**INFLUENCE OF IMPELLER AND DIFFUSER GEOMETRIES ON THE LATERAL FLUID
FORCES OF WHIRLING CENTRIFUGAL IMPELLER**

Hideo Ohashi, University of Tokyo; Akira Sakurai, Kobe Steel, Ltd.;
and Jiro Nishihama, Asahi Glass Co. 285

**A THEORETICAL STUDY OF FLUID FORCES ON A CENTRIFUGAL IMPELLER ROTATING
AND WHIRLING IN A VANED DIFFUSER**

Yoshinobu Tsujimoto, Osaka University; Allan J. Acosta,
California Institute of Technology; and Yoshiki Yoshida,
Mitsubishi Heavy Industry 307

INFLUENCE OF IMPELLER SHROUD FORCES ON TURBOPUMP ROTOR DYNAMICS

Jim P. Williams, Bell Helicopter Textron, Inc.; and Dara W. Childs,
Texas A&M University 323

Session VI - Bearings

MAGNETIC BEARING STIFFNESS CONTROL USING FREQUENCY BAND FILTERING

H. Ming Chen, Mechanical Technology Incorporated 341

**A MAGNETIC DAMPER FOR FIRST MODE VIBRATION REDUCTION IN MULTIMASS
FLEXIBLE ROTORS**

M.E.F. Kasarda, Rotor Bearing Dynamics, Inc.; and P.E. Allaire,
R.R. Humphris, and L.E. Barrett, University of Virginia 353

**INCORPORATING GENERAL RACE AND HOUSING FLEXIBILITY AND DEADBAND IN
ROLLING ELEMENT BEARING ANALYSIS**

R.R. Davis and C.S. Vallance, Aerojet TechSystems Company 373

EXPERIMENTAL VERIFICATION OF AN EDDY-CURRENT BEARING	
Jorgen L. Nikolajsen, Texas A&M University	389

Session VII - Compressor and Rotor Modeling

ROTOR DYNAMIC STABILITY PROBLEMS AND SOLUTIONS IN HIGH PRESSURE TURBOCOMPRESSORS	
J. Schmied, Sulzer Escher Wyss, Ltd.	395
ROLE OF CIRCUMFERENTIAL FLOW IN THE STABILITY OF FLUID-HANDLING MACHINE ROTORS	
D.E. Bently and A. Muszynska, Bently Rotor Dynamics Research Corporation	415
ENHANCED ROTOR MODELING TAILORED FOR RUB DYNAMIC STABILITY ANALYSIS AND SIMULATION	
R.R. Davis, Aerojet TechSystems Company	431
HIGH STABILITY DESIGN FOR NEW CENTRIFUGAL COMPRESSOR	
H. Kanki, K. Katayama, S. Morii, Y. Mouri, S. Umemura, U. Ozawa, and T. Oda, Mitsubishi Heavy Industries, Ltd.	445

SOME FIELD EXPERIENCE WITH SUBSYNCHRONOUS VIBRATION OF CENTRIFUGAL COMPRESSORS

Wang Xi-xuan, Gu Jin-chu,
Shen Qin-gen, Hua Yong-li, Zhu Lan-sheng
Zhejiang University, Hangzhou

Du Yun-tian
Zhengzhou Polytechnic Institute, Henan
People's Republic of China

A lot of large chemical fertilizer plants producing 1000 ton NH_3 /day and 1700 ton urea/day were constructed in the 1970's in China. During operation, subsynchronous vibration takes place occasionally in some of the large turbine-compressor sets and has resulted in heavy economic losses. In this paper, two cases of subsynchronous vibration are described.

(1) Self-excited vibration of the low-pressure (LP) cylinder of one kind of $\text{N}_2\text{-H}_2$ multistage compressor

(2) Forced subsynchronous vibration of the high-pressure (HP) cylinder of the CO_2 compressor

THE SELF-EXCITATION OF THE $\text{N}_2\text{-H}_2$ GAS COMPRESSOR

The general arrangement of the $\text{N}_2\text{-H}_2$ gas compressor is shown in figure 1, and the sketch of the rotor of the LP cylinder is shown in figure 2. The specifications of the LP compressor are given below:

Shaft power, kW	8300	
Max. speed, rpm	11230	
Weight of rotor, kg	500	
Length of rotor, mm	2050	
Span, mm	1635	
Diameter of main portion of the shaft, mm	150	
Diameter of journal, mm		
Driven end (DE)	114	
Nondriven end (NE)	104	
L/D of tilting pad bearing		
Driven end (DE)	0.4	
Nondriven end (NE)	0.41	
Length of oil ring seals, mm		
Outer	25.4	
Inner	23.8	
	1st SEC	2nd SEC
No. of impellers	5	4
Suction pressure, bar	26	
Discharge pressure, bar	54	94.5
Suction temperature, °C	40	
Discharge temperature, °C	139	121

Both the thrust and journal bearings are of the tilting pad type, and the journal bearings have 5 pads. The compressor is arranged with back-to-back impeller staging. The length of the interstage labyrinth seal with 38 teeth is about 120 mm and the clearance between the surface of the shaft and the tips of the teeth is about 0.3-0.4 mm.

In the early stage, the compressor set ran at about 10050 rpm for more than three years. Its normal operation at 90 percent of capacity lasted for about 100 days after the speed was raised to 10700-10750 rpm. But it was tripped off because of a sudden destructive vibration on one early morning in May 1982. All the bearings and labyrinth seals of the LP cylinder were destroyed. The machine could not be started up again without the replacement of these parts. But the operators could not find any evidence of anything unusual or of abrupt changes from the instrument panel, and there was no extraordinary signal on the recording charts before the violent vibration occurred. The same failure occurred once again on another morning one month later.

In order to make the machine more stable, several modifications made during overhaul were as follows:

- (1) Increasing the viscosity of the oil by using No. 30 turbine oil instead of No. 20 and choosing 45 °C as the oil inlet temperature
- (2) Decreasing the bearing L/D ratio to 0.39
- (3) Using the seal rings which have the largest clearance
- (4) Creating an equalizing pressure zone in the middle of the interstage labyrinth by turning off 6 teeth to a depth of 1/2 the tooth height
- (5) Making a full speed dynamic balancing for the rotor

After the overhaul, a violent vibration occurred again when the compressor was started and run to a speed of 10200 rpm, and later on start-up failed again and again for eight times. All the modification steps taken during the overhaul were eliminated, returning to the original condition. A new gear coupling was used to replace the old one, which had some wear on the surface of the teeth. The lubrication condition of the coupling was also improved. The geometric dimensions of the tilting pad bearings were carefully controlled according to the design requirements. All these steps, however, did not make any significant progress in stability.

According to the vibration spectrum analysis, it was found that there was an instability component with a frequency of 75 Hz, which is just over the 1st natural frequency of the rotor on rigid support. The frequency was unchangeable, staying at 75 Hz. In fact, the maximum wear of the labyrinth seals occurred in the middle of the casing, and the distribution of the abrasion wear along the axial line of the compressor answered to the 1st mode shape of vibration. This means that the vibration resulted from self-excitation.

In order to get a better understanding of the characteristics of the compressor, to search into the mechanism of the instability and to predict the

effectiveness of the proposed modifications, a stability analysis was performed.

A technique similar to that described by Lund (ref. 1) was used to solve the logarithmic decrement and the damped natural frequency of the system. Though the precision of the calculation may be limited because of the boundary conditions, such as the dynamic coefficients of the bearings and seals, the tendency indicated by the calculation is valuable.

The following system states were considered for stability analysis.

(1) Rotor-bearing system: in the calculation of this state, all the aerodynamic and hydrodynamic effects of seals were neglected. So there are no excitations from labyrinth or floating ring type oil film seals, etc. In the calculation, the internal friction and damping of the shaft material were also neglected.

The results are presented in figure 3-a. The abscissa of points at which the dotted line and the damped natural frequency lines intersect are critical speed values. The figures printed beside the points on the frequency lines are δ in the corresponding states.

As shown in figure 3-a, all the values of δ are greater than zero up to $n = 15000$ rpm. This means that if only the effect of the bearings is considered, the system will not lose its stability within its operation range. This conclusion tallies with the characteristics of tilting pad bearings.

(2) Rotor-bearing-seal system: The action of an oil ring seal on the rotor is something like that of a bearing though its effect is not immense.

By considering the effect of seal elements, the sign and value of δ obtained in the stability analysis was changed to -0.038 at a running speed of about 11000 rpm. Though the calculated instability threshold is somewhat greater than the practical value, the calculation indicates that, at least, the stability safety factor of this machine is small. The small excitations produced by the seal elements are great enough to cause instability. In order to find a solution, the effectiveness of several proposed modifications was also evaluated by the stability calculation method.

It was found that the following measures would significantly improve the stability of the rotor system:

(1) To enlarge the shaft diameter and/or shorten the bearing span, i.e., to increase the 1st critical speed of the rotor system

(2) To modify the parameters of the oil ring seals, especially that of the construction of the long middle labyrinth

(3) To use a flexible support squeeze film damper

It will take much time to adopt any of these modifications and the factory cannot be permitted to stop its production that long. Therefore effective, easily implemented measures, though temporary, were urgently sought.

According to the experience with these failures, we found that whenever the magnitude of the 75 Hz component grew, the machine ran unstably. If the magnitude of this component becomes greater than that of the main component, i.e., the running frequency component, catastrophic vibration can occur at any moment. The spectrums of different conditions are shown in figure 4.

This phenomenon was used to monitor the operation of the LP cylinder when the compressor was brought into operation with a reduced load of 80-85 percent after a thorough fixing of the whole system. Whenever the amplitude of the 75 Hz component grew and approached that of the running frequency component, the speed and load had to be reduced for a while until the peak disturbance exciting the LP cylinder rotor decreased to a safe limit.

The 75 Hz component can be monitored only by a real-time spectrum analyzer, so monitoring is not convenient. Because the figures of the shaft center orbit are closely related to the amplitude of the subsynchronous component and can be easily observed on an oscilloscope screen, a cheap oscilloscope, as a temporary measure, was installed in the field to monitor the condition of the LP cylinder.

The scheme of this installation is shown in figure 5. When the machine worked normally, the boundary line of the shaft center orbit was clear and stable. Otherwise the boundary line became indistinct and oscillatory, and the orbit became large as shown in figure 6. With the help of this method, production was preserved for more than one year before the final modification of the LP cylinder was performed.

THE FORCED SUBSYNCHRONOUS VIBRATION OF CO₂ COMPRESSORS

In China, centrifugal compressors have been generally used in urea production to compress CO₂ gas to a final pressure of 145 kg/cm². The main parameters of the most common machines are shown below:

Composition of gas	CO ₂ -94.5%	Air-4%	Others-1.5%
Relative humidity			100%
Av. mol. wt.			41.2% (40 °C)
Suction temperature, °C			<40
Suction pressure, kg/cm ²			0.96
Discharge temperature, °C			127
Discharge pressure, kg/cm ²			144

Type of rotor	Turbine	LP	HP
Normal speed, rpm	7200	7200	13900
1st crit. speed, rpm	4500	4200	8000
2nd crit. speed, rpm	9500	9200	17520

The schematic diagram of this compressor is shown in figure 7, and the sketch of the HP rotor is shown in figure 8. Most of the HP cylinders of this type of CO₂ compressor suffered from high vibration. Up to now, this serious vibration problem has not been solved completely. Many factories can only raise the alarm threshold to continue working. Even so, the HP rotors often work over the raised alarm threshold. This was the reason why we surveyed the vibration failure of this type of machine and collected the information about it.

There are nearly 20 similar HP rotors in Chinese urea synthesis factories. These rotors were manufactured according to the same detailed drawings and can be used interchangeably. The difference between them is only the dimension tolerances. Their performances, however, seemed to be similar but not quite the same.

We put forward some typical cases for analysis:

(1) A few of these machines work quite well. The peak-to-peak amplitudes of HP rotors measured by eddy current probes near the bearings are less than 30 μm . For example, in factory A, the vibration amplitudes of driven end (DE) and nondriven end (NE) HP rotors are less than 30 μm and 25 μm , respectively. Their vibration spectrums are shown in figure 9. The main vibration component is a synchronous component. The subsynchronous components are very small. Only the component at 180 Hz is slightly greater. The main component in the pressure pulsating spectrum of the discharge pipe is also at 180 Hz.

(2) In some factories, factory G for example, the vibration amplitudes of the HP rotors are at a high level ($>100 \mu\text{m}$). The spectrum is shown in figure 10. The synchronous component is leading. After full-speed dynamic balancing, the amplitude can be greatly reduced. So the vibration results from the loss of balancing accuracy.

(3) The amplitudes of many HP rotors are not very high, but the vibrations of the pipes are a serious problem. The vent pipes, drainage pipes, and instrument tubings connected to the discharge pipe were often broken by strong vibration during the early stage after the factories were put into operation, and this breakage was the main reason the compressor shut down. Strong vibration of the pipes may result from resonance of the pipes with one of the subsynchronous frequencies in the discharge gas stream. In factory B, the spectrum obtained during the measurement of the natural frequency of the pipes is shown in figure 11-a. The main component is at 115 Hz. The spectrum of the discharge gas pressure pulsating under normal conditions is shown in figure 11-b. The main component is at 190 Hz. The vibration spectrum of one pipe section is shown in figure 11-c. The main component is at 110 Hz. The amplitude of this pipe at that time is 12-18 μm . Under abnormal conditions, the spectrum of the discharge gas pressure pulsating is shown in figure 11-d. At that time, the main component is at 110 Hz, nearly equal to the natural frequency of that pipe section. So the amplitude increased suddenly to 330 μm as shown in figure 11-e. In the spectrum of the rotor at DE, the 115-Hz component, as shown in figure 11-f, appeared simultaneously. In some factories, the pipe vibrations were eliminated by varying the turn radius or support condition of the discharge pipes.

(4) In the start-up period of many of these machines, the subsynchronous components (mainly at 53, 120, and 180 Hz) were small if the speed was less than 3000 rpm, but they grew gradually with the speed. During the period of rising pressure, the amplitude of the synchronous component grew a little. At the moment when the pressure rose to 110 kg/cm^2 , the machines vibrated violently. For example, in factory C, the amplitude of DE rose from 25 to 37 μm , and not only the pipes, but also the foundation and floor vibrated so intensely that they generated a very loud noise. The vibration spectrums of the rotor and the pressure pulsating of the discharge pipe at that moment are

shown in figure 12-a and b, respectively. As compared with the spectrum at 145 kg/cm², there is a noteworthy subsynchronous component at 58.3 Hz. Its amplitude exceeds that of the synchronous component. At 145 kg/cm², the main component in figure 12-c and d is the synchronous one.

(5) During the operation of many rotors, instantaneous high amplitude vibration occasionally appeared. The total amplitude reached a maximum of 110 μ m. At that moment, accompanied by a low, deep sound of gas flow pulsation, the vibration of the foundation and floor deck increased greatly. The flow rate of the compressor dropped 10 percent. In a case of violent vibration, in factory C, the recorded process parameters were an HP rotor speed of 13400 rpm, a flow rate of 28000 Nm³/hr and a discharge pressure of 145 kg/cm².

The amplitude of the HP rotor was greater than 50 μ m. The foundation and floor deck vibrated severely. The spectrums in the normal and alarm states are shown in figure 12-c and figure 13, respectively. After making a comparison between these two spectrums, one may come to the conclusion that the violent vibration was caused by the 58.3-Hz subsynchronous component which grew remarkably and exceeded the synchronous component. The same condition occurred in other factories. It is considered that the vibrations are caused by rotating stall. Therefore, two methods have been used to increase the volume flow rate of the fourth stage of the HP cylinder:

(1) To increase the temperature of the fourth stage inlet gas

(2) To increase the circulation flow in the fourth stage by using a 4-to-4 bypass valve

These methods can decrease the vibration in some factories, and a comparison between amplitudes (μ m) gives the following:

	Factory E			Factory F		
With 4-to-4 bypass valve closed	96	94	81	68	53	31.7
With 4-to-4 bypass valve opened	43	31	20	40	34	31.7

The effectiveness of these methods shows that the above estimation is correct. Method (2) is rather simple but costs an extra 10 percent of energy. Method (1) has only limited effectiveness. A better solution was needed at that time.

After a thorough study, a newly designed rotor with adjusted impeller structure parameters was constructed by Shen-yang Blower Manufactory. In operation, its performance is satisfactory. Under design conditions, its total vibration amplitude can reach a very low level and the amplitudes of the subsynchronous components are very small. The normal spectrums of rotor and gas pressure are shown in figure 14-a and b. If the operation was not correct, the large subsynchronous component at 55 Hz certainly appeared and caused vibration. The abnormal spectrums are shown in figure 14-c and d. Subsynchronous components at 110 and 165 Hz can also be significant.

Some discussions and concluding remarks about the vibrations of CO₂ compressors are as follows:

(1) The high vibration of CO₂ HP rotors is due to the forced subsynchronous vibration caused by aerodynamic instability. Its characteristics are similar to those pointed out by reference 2. The amplitude is stable. The machine can run for a long time in a state of serious vibration.

(2) On some occasions, the amplitude of the HP rotor increases to 100 μm , but the compressor operation appears to be normal. Under other conditions, however, the amplitude of the HP rotor is only about 40 μm , yet the floor deck and the foundation vibrate severely. These phenomena depend upon whether the pipes are excited by the gas stream or not.

(3) The main subsynchronous components are about 60, 120, and 180 Hz. The component at 60 Hz (within the range of 57-64 Hz), which is 25 percent of the synchronous frequency, seems more powerful. According to reference 3, it may be considered that the vibration is caused by the rotating stall in the diffuser. As statistics (ref. 4) show, however, the vibration is closely related to the ratio of the relative inlet velocity W_1 to the relative outlet velocity W_2 of the impellers. When the HP rotor of a CO₂ compressor works with $(W_1/W_2) < 1.4$, it operates quite well, otherwise the vibration will be high. This means that the impeller parameters have a more important effect on the rotating stall than the static components even if the subsynchronous frequencies are as low as 25 percent of their own.

REFERENCES

1. Lund, J.W., "Stability and Damped Critical Speeds of a Flexible Rotor in Fluid-Film Bearings." J. of Eng'g for Industry, Vol. 26, No. 2, 1974, p. 509.
2. Smith, D.R., Wachel, J.C., "Experiences with Nonsynchronous Forced Vibration in Centrifugal Compressors," NASA CP-2238, 1984, p. 37.
3. Frigne, P., Braembussche, R. Van Den, "Comparative Study of Subsynchronous Rotating Flow Patterns in Centrifugal Compressors with Vaneless Diffusers," NASA CP-2250, p. 365.
4. Liu YUan-zhi "A Suggestion for Improving the Vibration in HP Cylinder of CO₂ Compressors," Selected Papers from the Annual Meetings of the Machinery and Pumps of Large Chemical Fertilizer Plants, p. 38-52.

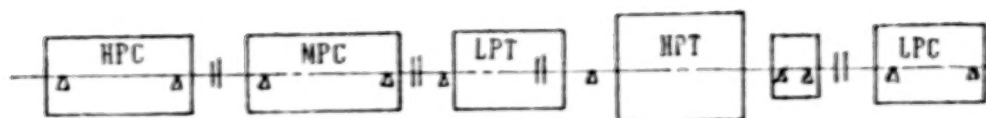


Fig. 1 General arrangement of the N₂-H₂ compressor set

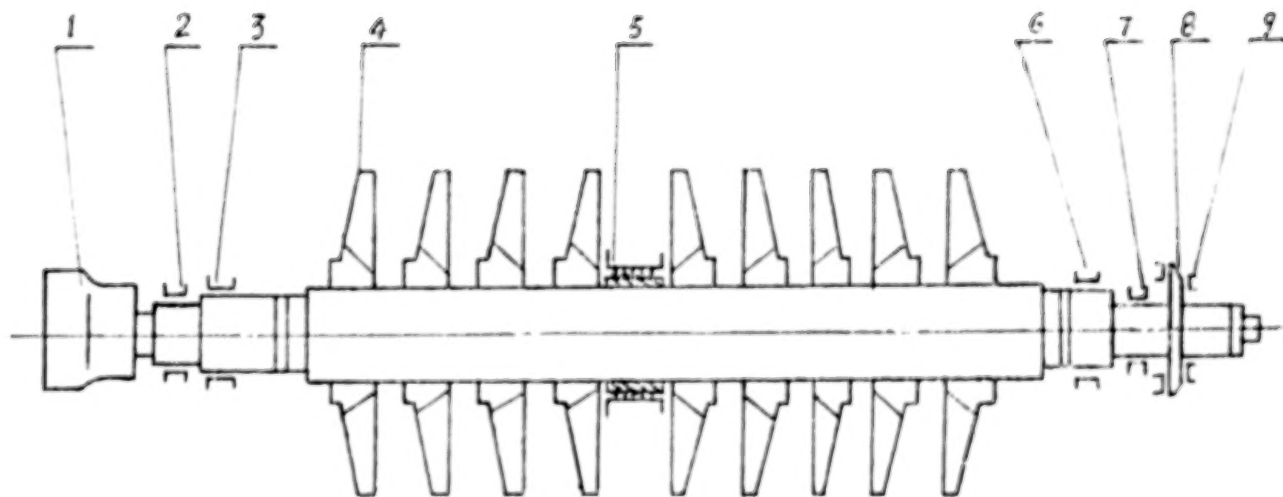


Fig. 2 Sketch of the low pressure rotor

- 1 gear coupling
- 2,7 bearing
- 3,6 oil ring seal
- 4 impeller
- 5 interstage seal
- 8 thrust disk
- 9 thrust pads

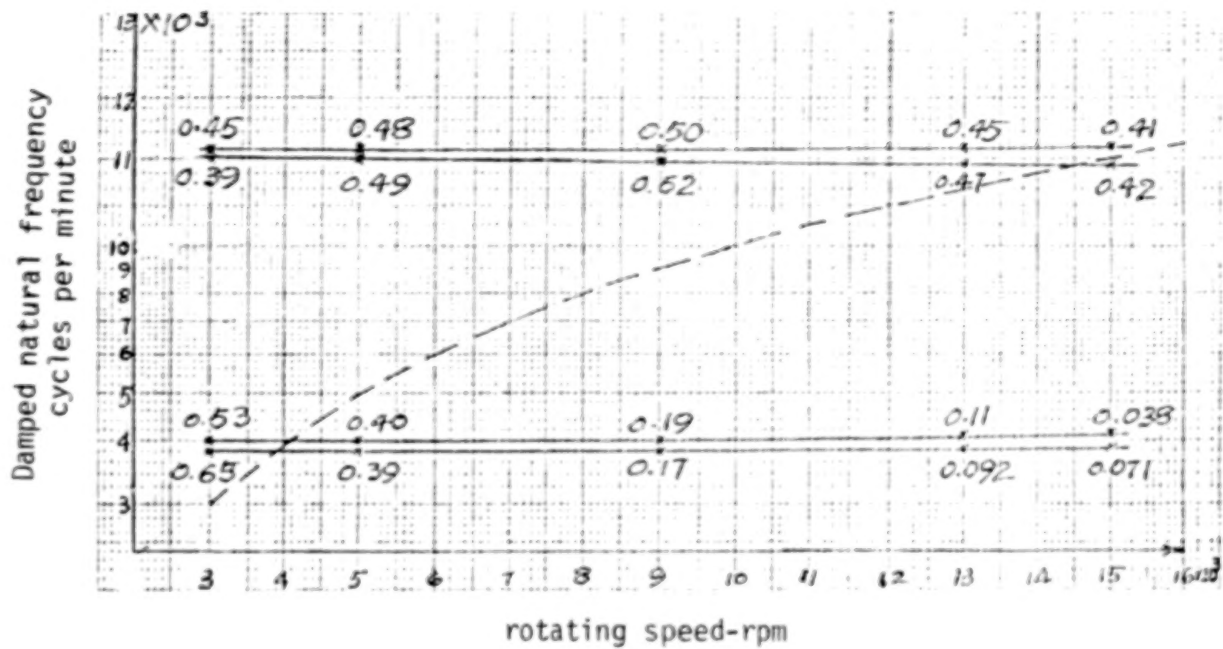


Fig. 3-a δ, ω versus rotating speed (rotor-bearing system)

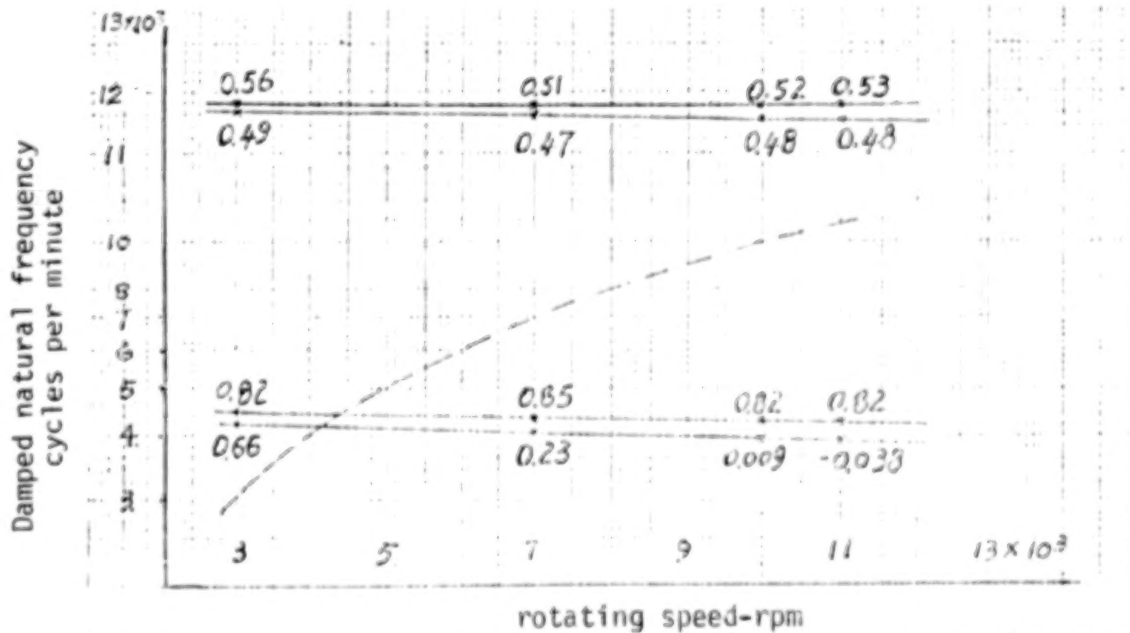


Fig. 3-b δ, ω versus rotating speed (rotor-bearing-seal system)

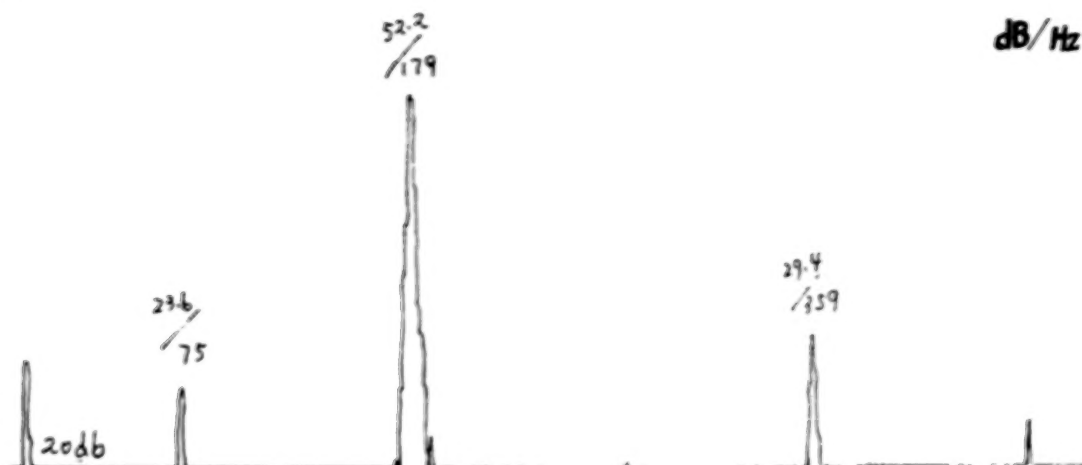


Fig. 4 - a

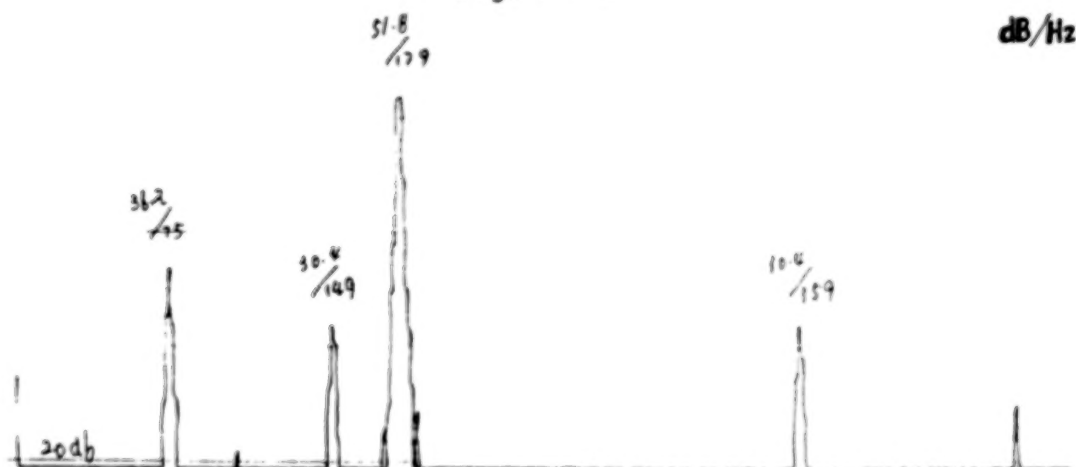


Fig. 4 - b

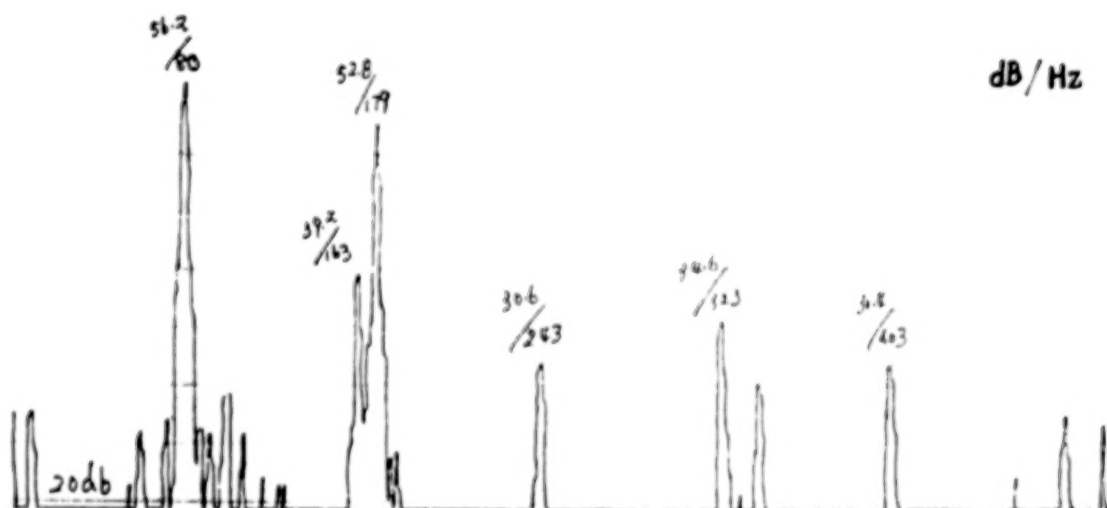


Fig. 4 - c

Fig. 4 Spectrum
 a - stable state
 b - transient state
 c - unstable state

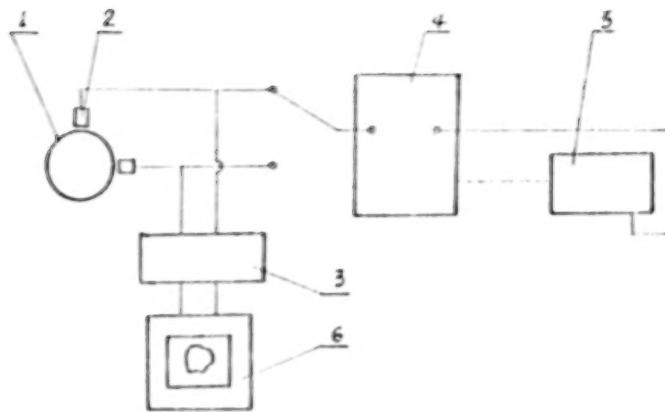


Fig. 5 Schematic diagram of orbit monitoring installation and spectrum

1 - shaft 2 - probe 3 - amplifier
4 - spectrum analyzer 5 - recorder 6 - oscillograph

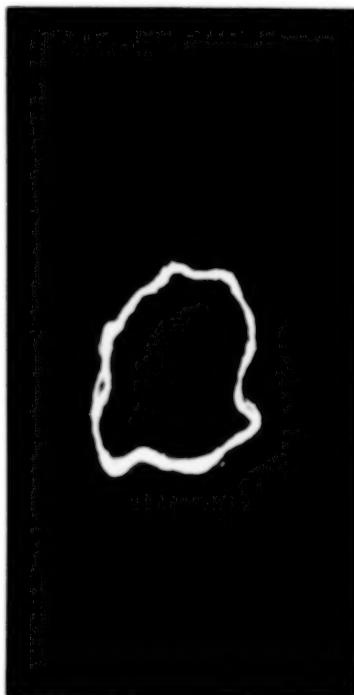


Fig. 6 - a



Fig. 6 - b

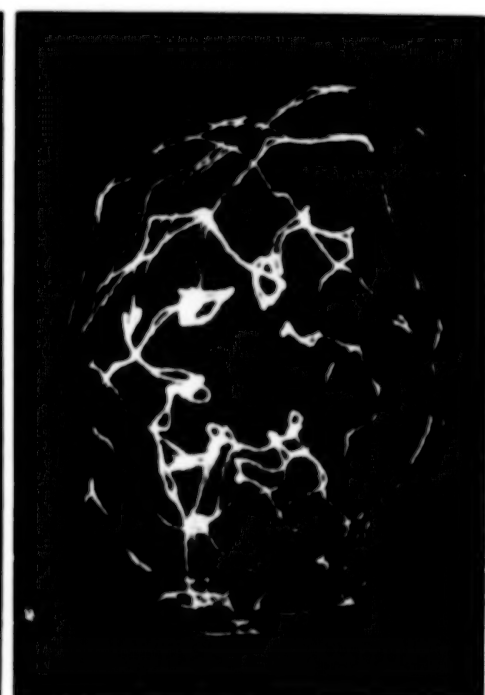


Fig. 6 - c

Fig. 6 Orbit of shaft centre
a - normal state
b - transient state
c - unstable state

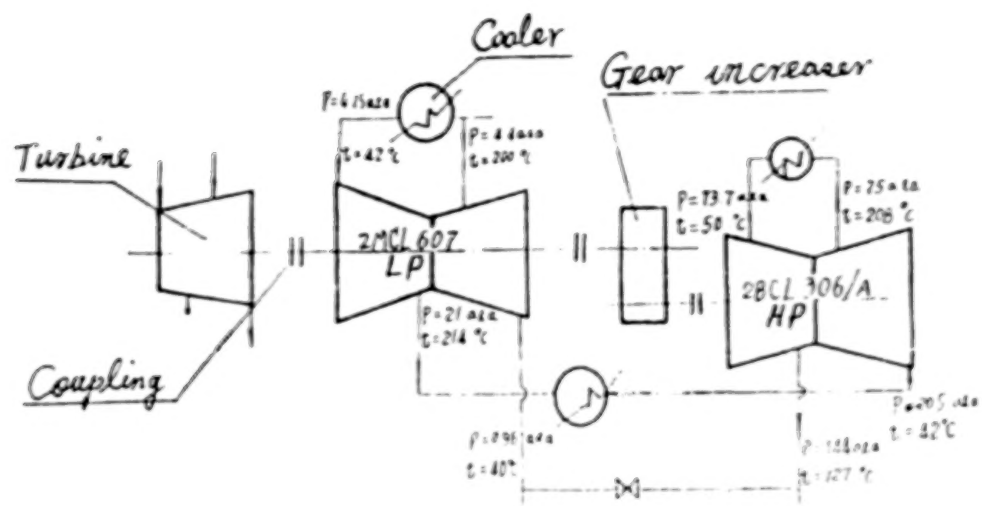


Fig. 7 Schematic diagram of CO₂ compressor

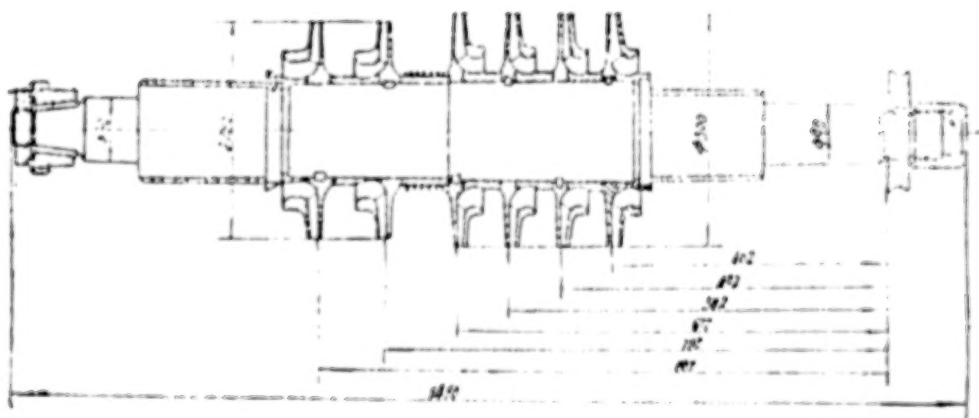


Fig. 8 Sketch of CO₂ high pressure rotor

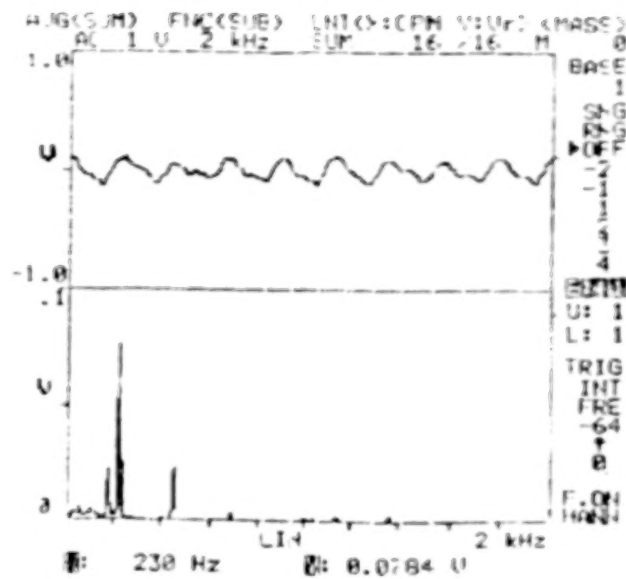


Fig. 9 - a

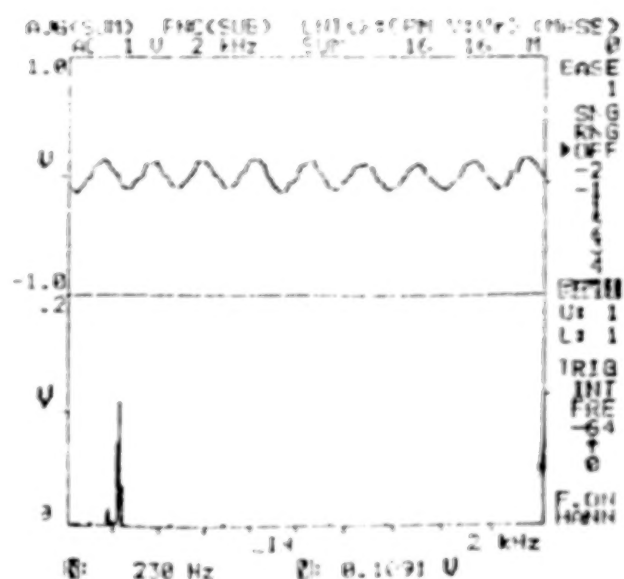


Fig. 9 - b

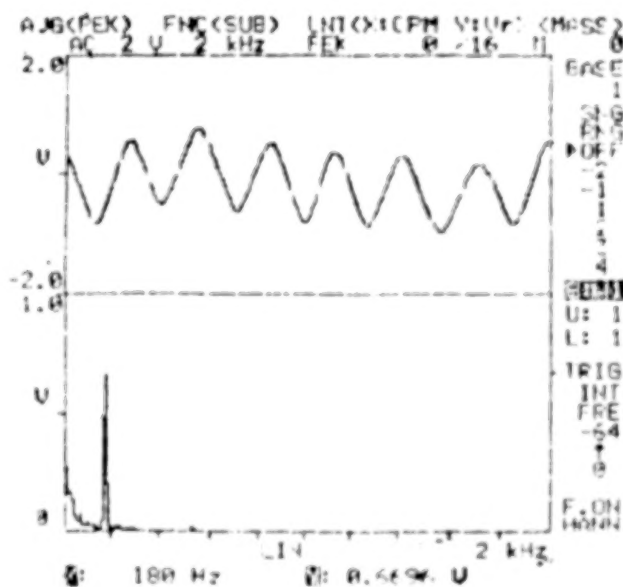


Fig. 9 - c

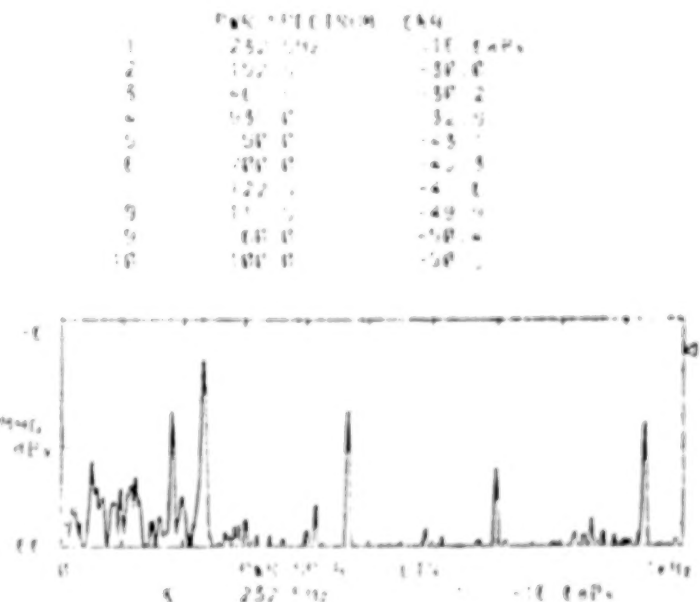


Fig. 10 Vibration spectrum - plant G

Vib. 9 Vibration spectrum - plant A

- a - DE
- b - NE
- c - gas pressure pulsating in outlet pipe

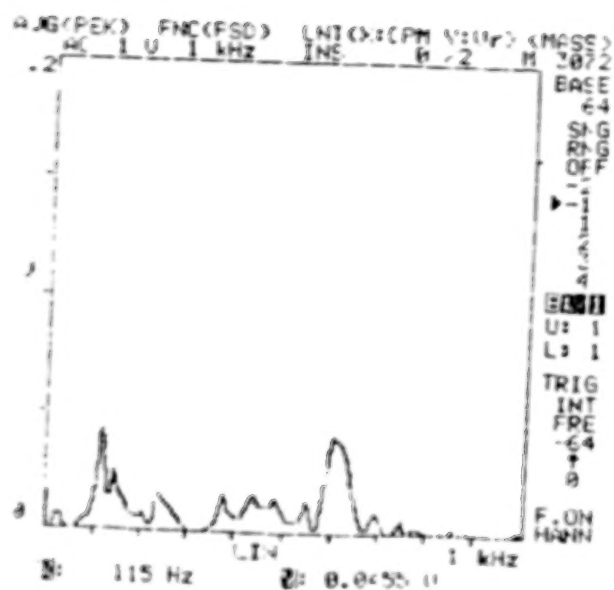


Fig. 11 - a

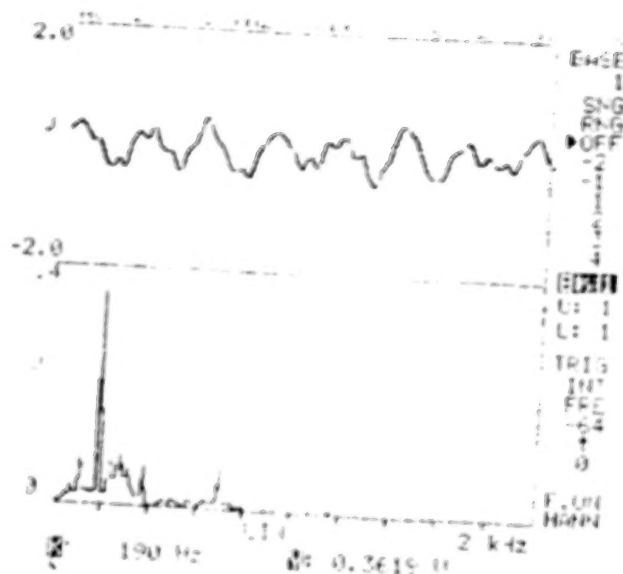


Fig. 11 - b

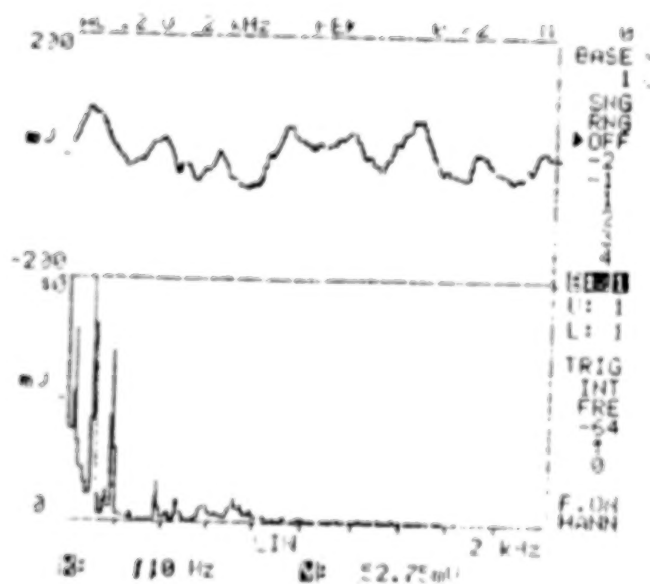


Fig 11 - c

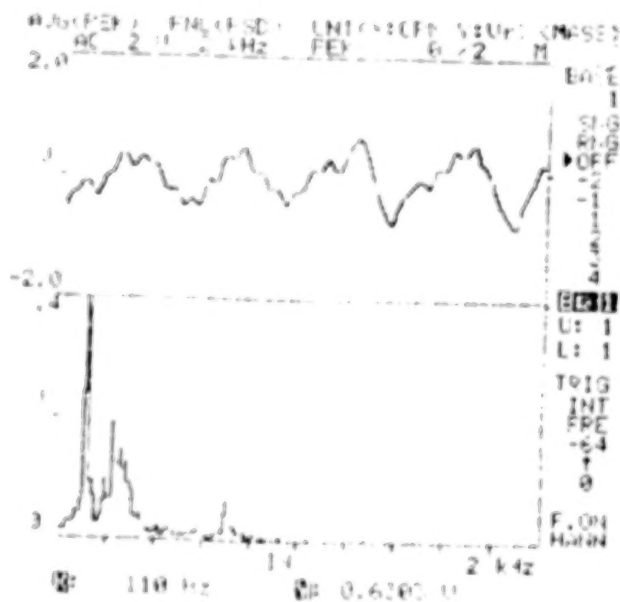


Fig 11 - d

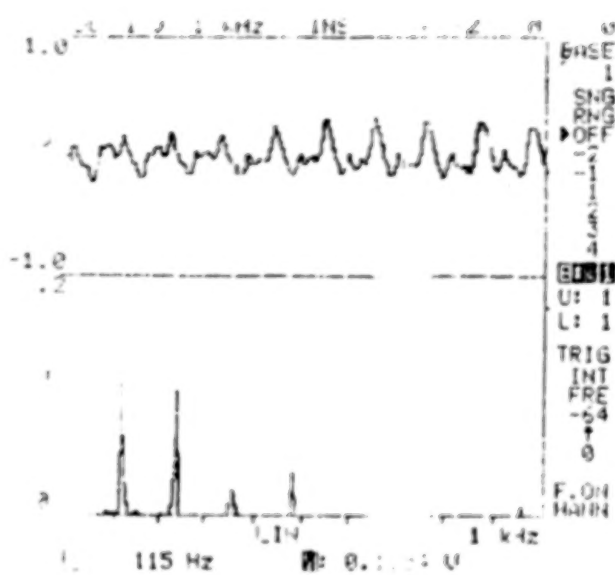


Fig. 11 - e

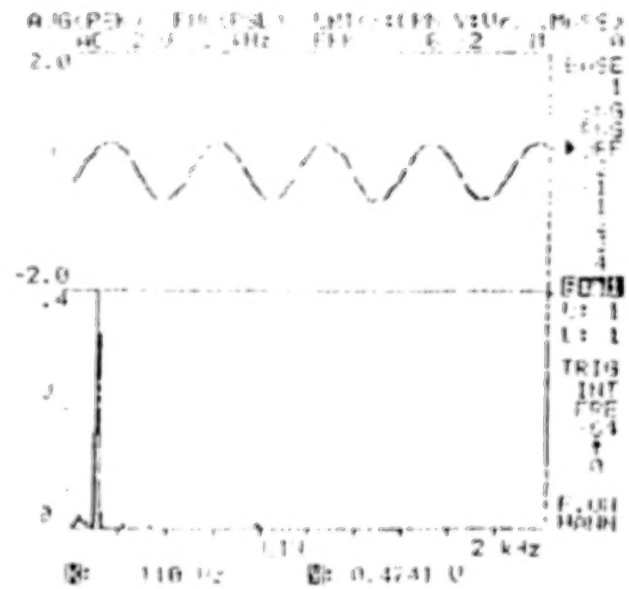


Fig. 11 - f

Fig. 11 Vibration Spectrum - plant B

- a - measurement of nature frequency of discharge pipe
- b - pressure signal under normal condition
- c - vibration of pipe under normal condition
- d - pressure signal under abnormal condition
- e - vibration of pipe under abnormal condition
- f - DE

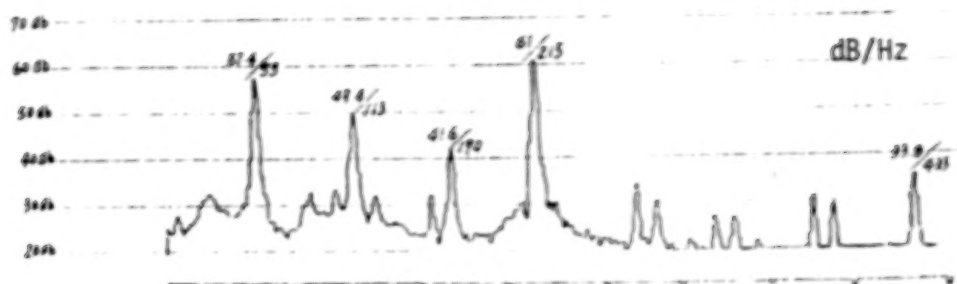


Fig. 12 - a

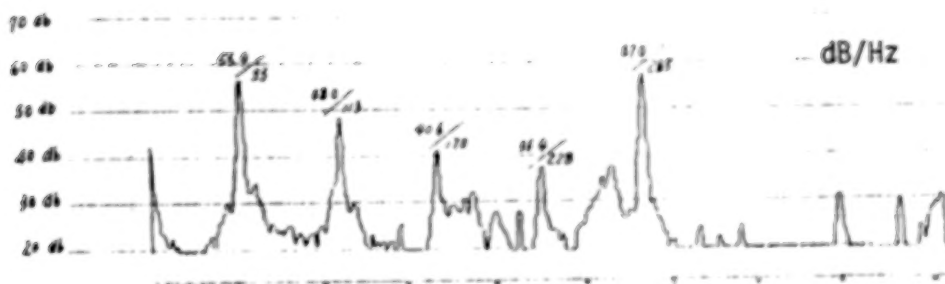


Fig. 12 - b

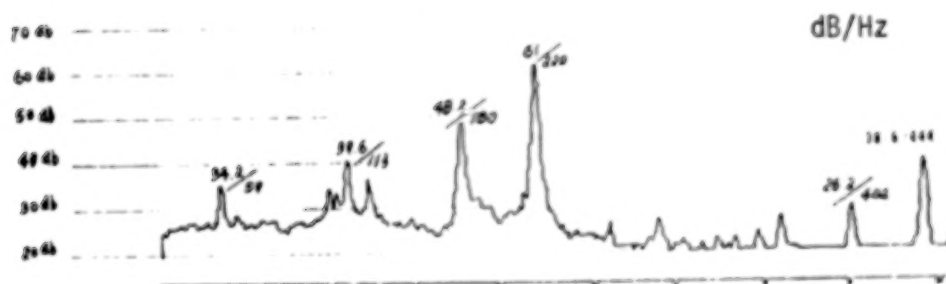


Fig. 12 - c

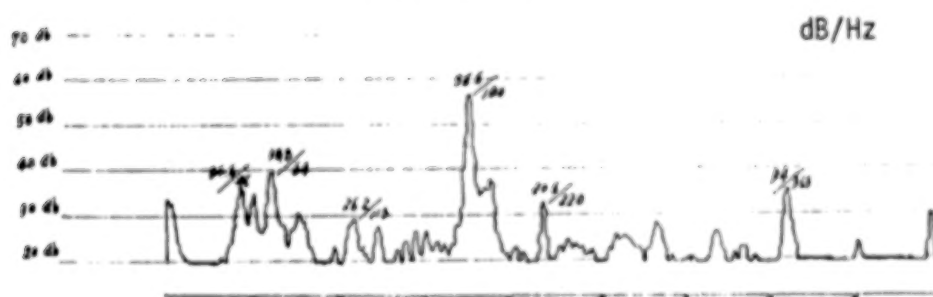


Fig. 12 - d

Fig. 12 Vibration Spectrum $\frac{1}{2}$ plant C

- a - DE. at 110kg/cm²
- b - gas pressure signal at 110kg/cm²
- c - DE. at 145 kg/cm²
- d - gas pressure signal at 145kg/cm²

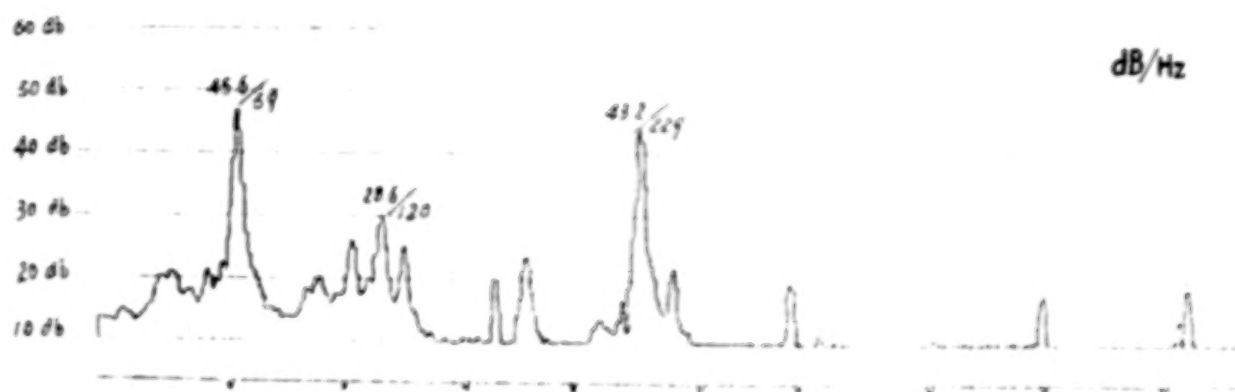


Fig. 13 Vibration Spectrum - plant C
DE at 145kg/cm² under violent vibration

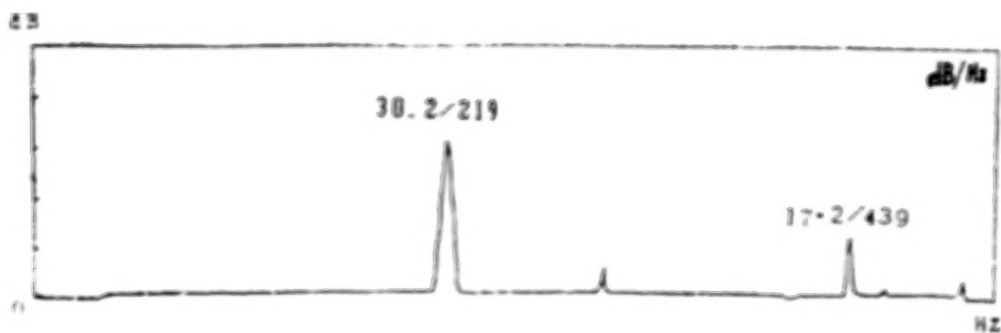


Fig. 14 - a

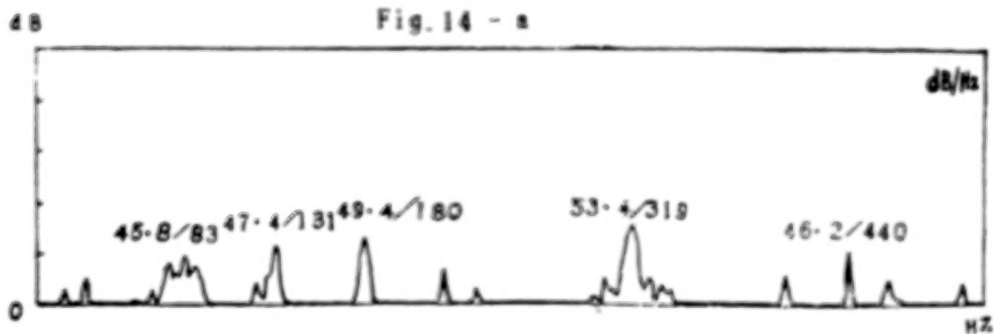


Fig. 14 - b

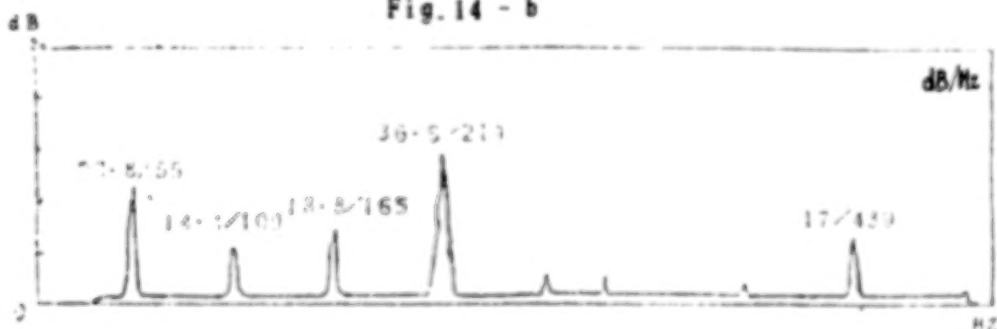


Fig. 14 - c

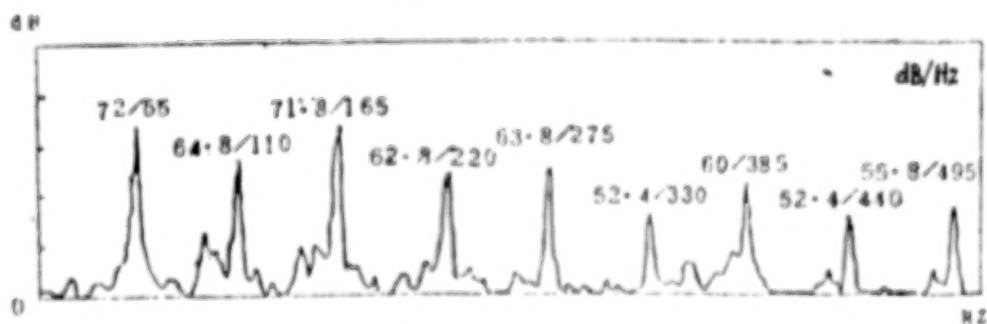


Fig. 14 - d

Fig. 14 Vibration Spectrum of newly designed CO₂ HP rotor
 a - DE, under normal operation condition
 b - gas pressure signal under normal condition
 c - DE, under incorrect operation condition
 d - gas pressure signal under incorrect operation condition

ROTOR INSTABILITY DUE TO A GEAR COUPLING CONNECTED TO A
BEARINGLESS SUN WHEEL OF A PLANETARY GEAR*

E.T. Bühlmann
Sulzer Brothers, Ltd.
Laboratory for Vibrations
and Acoustics KSFE-1512
CH-8401 Winterthur, Switzerland

A. Luzi
Swiss Locomotive and Machine Works, Ltd.
CH-8401 Winterthur, Switzerland

A 21 MW electric power generating unit comprises a gas turbine, a planetary gear, and a generator connected together by gear couplings. For simplicity of the design and high performance the pinion of the gear has no bearing. It is centered by the planet wheels only. The original design showed a strong instability and a natural frequency increasing with the load between 2 and 6.5 MW. In this operating range the natural frequency was below the operating speed of the gas turbine, $n_{PT} = 7729$ RPM. By shortening the pinion shaft and reduction of its moment of inertia the unstable natural frequency was shifted well above the operating speed. With that measure the unit now operates with stability in the entire load range.

INTRODUCTION

Any new machine design is characterized by the manufacturing cost and, for thermal machines, also by the overall efficiency. Therefore, the machines become more compact, with a tendency to smaller shaft size for the same power than in the past and a reduced number of machine elements.

These rules were considered in the design of an electric generating unit comprising a gas turbine, a planetary reduction gear and a generator (Fig. 1). The shafts are connected by gear couplings. The rated power of the set is 21 MW, the operating speed of the gas turbine $n_{PT} = 7729.4$ RPM, and of the generator $n_{GEN} = 1800$ RPM. The planetary gear has a gear ratio of 1:4.294. For simplicity of the design (fewer parts) and improved efficiency (fewer bearings) the sunwheel of the gear is centered by four planet wheels only, and not as is usual by a bearing. The pinion shaft is connected to the power turbine shaft by a gear coupling to accommodate transient and residual misalignment between both shafts (Fig. 2). The vibrations of the gear were monitored and recorded as well as the actual electrical power and the oil temperature of the axial bearing, etc.

* The publication of this paper was kindly supported by the Gas Turbine Division of the Sulzer Group Ltd.

During the commissioning period the unit was started and run up to full power at synchronous speed. A typical recording of the generated power, the gas temperature (T7) and the vibrations of the gear are shown in Fig. 3. In all these run-ups a steep increase of the vibration level on the gear was observed at a unit load range of 2 to 6.5 MW. From 2 to 4 MW the vibrations increased gradually, from as low as 2 mm/s (RMS) to a prohibitively high level of 11 mm/s. They remained at that high level in the range 4 - 6.5 MW and "fell" to a low level at approximately 6.5 MW load. During run-down similar recordings were obtained; the vibrations of the gear were mainly load dependent (Fig. 4).

MEASUREMENT OF THE VIBRATIONS

From the overall recordings (e.g., Figs. 3 and 4) a sound analysis of the problem was not possible. However, the gear with the coupling was expected to be the source of the excitation, as the maximum vibrations occurred at the gear box. Therefore additional probes (eddy current transducers) were installed at the gear and the gas turbine in order to observe the motion of the spacer of the coupling. The relative radial and axial displacements were recorded on tape and later analyzed by a 2 channel FFT analyzer. Figs. 5, 6 and 7 were generated from the recorded start Nr. 29. Fig. 5 shows the frequency spectrum of the "peak hold" amplitudes of the displacement of the sunwheel in an axial direction, while the power was increased from 2 to 7 MW. Several peaks at the rotational frequencies and their multiples were observed. Excitations at 1800, 3600, 5400, 7200 RPM are caused by the generator, at 7730 RPM caused by the gas turbine and the sunwheel and at 4680 RPM by the planets. These excitations remain constant during the increase of the load. As the speeds of these shafts remained unchanged during operation the rest of the peaks could not be explained by excitations of rotational speeds. Fig. 6 shows the frequency spectrum of the radial displacement of the coupling. It is essentially similar to Fig. 5; dominant peaks occurred at the same frequencies as explained above. In the frequency band $5100 \text{ RPM} < f < 7300 \text{ RPM}$ the peaks were high but not dependent on operating speeds of the unit. In Fig. 7 the predominant frequency is given as a function of the load. In start-up Nr. 30 the radial deflection of the coupling on the gear side was analyzed at constant load. The result is plotted as frequency spectra in Fig. 8. The dominant frequency and its amplitude increased with the load of the unit from 2 to 6.4 MW. At 6.4 MW it coincided with the operating speed of the turbine and at the same point the amplitude reduced to the value of that speed.

During start-up Nr. 30 the oil temperature of the axial bearings in the gear were also recorded. Fig. 9 shows the inlet temperature and the outlet temperatures of the axial bearings on the turbine and the generator side. The temperature on the generator side remained almost constant while on the turbine side the temperature remained constant up to 6.4 MW, above this load it increased gradually with the load. The friction forces became dominant and prevented spontaneous relative movements in the coupling. However, it decreased gradually over a long period of time at full load. It

seems the gear coupling does not allow for relative movements above 6.4 MW as the spacer is blocked. This fact is also demonstrated by the measurement of the axial movement of the pinion (see Fig. 9). The relaxation of the pinion took a long period of time.

From these diagrams one may conclude:

- In the load range 2 to 6.4 MW the unit shows unstable behaviour
- The natural frequency of the bending mode depends on the load of the shaft
- If the natural frequency is above the operating speed of the turbine the unit behaves in a stable manner
- The instability may be due to the undefined position of the spacer of the gear coupling. As there is no bearing for the pinion the angular deflection of the pinion is not prescribed and the spacer is free to move in both hubs.

THEORETICAL MODEL

Modelling

The measurements indicated an unstable lateral frequency on the pinion side of the gear. From the strong dependence on the load of such a natural frequency on the high vibrations of the gear a nonlinear spring stiffness in the gear was expected. Two different models were set-up:

- a) Model 1 is a single degree-of-freedom system shown in Fig. 10. The spring couple consists of the teeth of the pinion and planets. The stiffness of the gear depends on the Hertzian stress which is highly nonlinear, so that the stiffness increases with increasing load. The mass may be given by the pinion and the spacer so that

$$m = \frac{J_p}{r^2} + \alpha m_s$$

J_p = moment of inertia of the pinion

r^p = distance between center of spring couple and the center of the mass

m_s = mass of the spacer

α = coupling factor ≈ 0.5

Then the natural frequency may be estimated by

$$f_e = \frac{1}{2\pi} \sqrt{\frac{2a^2 k}{r_m^2}}$$

k = spring stiffness (constant at constant load)

a = half the length of the pinion gear

The natural frequencies are known by the measurement and the calculation. The spring stiffness is composed of the stiffnesses of, (a) gear contact between sunwheel-planets, (b) oil film between sunwheel-planets, (c) oil film between planet and planet shafts, (d) planet shaft, and (4) planet shaft bearings. The resultant flexibility (reciprocal value of stiffness) is given in Fig. 11.

b) Model 2 is a finite element model comprising the complete rotor of the gas turbine, gear coupling and pinion shaft. The following assumptions were made:

- the elastic rotor is undamped
- the radial bearings are damped
- the spacer of the gear coupling is hinged in its hubs. These assumptions may be valid at very low load, when the static friction force in the coupling is smaller than the restoring force in the hub.
- the pinion is fixed by a spring couple. The magnitude of the springs is estimated by model 1.
- the rotor behaves linearly at a set load and speed

The calculation of the natural frequencies and the mode shapes were calculated by the computer program MADYN designed for rotor dynamics.

RESULTS

The calculation of the natural frequencies and mode shapes were executed for loads $P = 2, 4$ and 6 MW. The natural frequencies are tabulated in Table 1. Most of them are hardly influenced by the stiffness of the gear. However, the natural frequency which is sensitive to changes at the gear compares well with the measured ones. The mode shapes of that frequency show maximum amplitudes at the coupling hub of pinion-coupling (Fig. 12). For completeness the reduced model 1 was also compared with the measurements taking into consideration the natural frequency and the spring stiffness of the spring couple. The effective mass may be estimated by

$$m = \frac{2a^2k}{(2\pi f_e)^2 r^2}$$

The values of the effective mass for different loads are also tabulated in Table 1. For each load case this mass remains almost constant.

DISCUSSION OF THE RESULTS

The measured and the calculated natural frequencies and mode shapes compare very well. The assumptions made are confirmed, such as

- the lateral natural frequency depends on the stiffness of the meshing gears and
- the connection spacer-pinion is hinged

Both of the models may be used for any further discussions and improvements of the design. The calculation revealed several natural frequencies below the rotating frequency of the turbine. However, apparently only one mode behaves unstably. The unstable mode shape shows a maximum deflection at the hub between pinion and spacer.

IMPROVEMENTS OF THE SET IN SITU

Method

The high vibrations measured at the gear box and the coupling were due to an instability in the rotor system. The unstable mode shape was excited subsynchronously in the gear coupling. In order to improve the system the natural frequency of that mode had to be shifted above the rotating frequency of the gas turbine, $f_{PT} = 128.8$ Hz. The operating load of the generating unit ranges from 2nd to 21 MW. Therefore, the measured frequency at 2 MW, $f_e = 86$ Hz, had to be lifted above 129 Hz. Several measures may be considered in a new design, e.g., at the gear box, a bearing for the pinion, which fixes the pinion and suppresses rotations around any axis perpendicular to the axis of the shaft, or a reduced distance between the gear box and gas turbine. However, such remedies were out of the question. To discuss other measures one may observe model 1 which estimates the unstable natural frequency

$$f_e = \frac{1}{2\pi} \frac{a}{r} \sqrt{\frac{2k}{m}}$$

This formula indicates the effect of the main parameters on the frequency. An increase of a and k and a reduction of r and m will increase the natural frequency. Changes on the gears, pinion and planets, would have necessitated a new gear box, thus a change of a and k was out of the question; therefore r and m had to be reduced substantially. This measure was then further investigated. Finally m was reduced by 2.5 % to $m = 86.5$ kg and r by 40 % to 179.5 mm.

The new design is shown in Fig. 13. A detailed calculation (model 2) estimates the natural frequency $f = 146$ Hz at 2 MW which is well above the operating speed of the rotor (see Table 1). Fig. 14 shows the sensitive mode shape of the improved system. The maximum displacement is still at the gear coupling.

RESULT OF THE IMPROVEMENT

The pinion of the gear was changed in situ based on the drawing shown in Fig. 13. In all of the later start-ups and run-downs the vibrations on the gear and the bearings of the gas turbine remained well below the limits (Fig. 15). The frequencies of excitation were all rotating speeds or their harmonics and constant in the entire load range of the unit from 2 MW to 21 MW. The unit now has stable behaviour. The unstable natural frequency is above the operating speed of the turbine.

CONTI-BARBARAN-NUMBER

Gear couplings are inherently unstable at low loads (Ref. 1) This is due to the radial clearances between the teeth. At low load the spacer is free to move as the contact (circumferential) force is smaller than the inertia (centrifugal) force. An indicator of the behaviour of the coupling is given by the Conti-Barbara-Number E (or Newtons number).

$$E \sim \frac{F_u}{F_c}$$
$$E = \frac{1.36 P}{M D^2 N^3}$$

where P = transmitted power in MW
M = mass of the spacer in kg = 105 kg
D = pitch circle diameter in m = 0.28 m
N = operating speed in RPM = 7729 RPM
 F_u = circumferential force in N
 F_c = centrifugal force in N

Experience shows if

$E > 10$	no problems may be expected
$5 < E < 10$	problems may be expected
$E < 5$	problems should be expected

However, these limits are very rough and do neither consider design and manufacturing quality of the teeth nor the alignment of the units. For the gear coupling of the above unit

$$E_o = .358 P$$

applies for the original design and

$$E_p = .417 P$$

applies for the improved design.

In the entire load range 2 to 21 MW, E is < 10 at, e.g. 2 MW $E_o = 0.7$ ($E_o = 0.8$). The instability occurs only if there exists a feedback^P mechanism as in the original design, which was the instable natural frequency below the operating speed of the turbine. The mode shape of that natural frequency has its maximum displacement at the gear coupling and therefore is easily excited by the gear coupling.

REFERENCES

1. O. Staedeli: "Toothed Couplings". MAAG Gear Wheel Company Ltd. Zürich, Switzerland
2. R. Fleiss, G. Pahl. Radial und Axialkräfte beim Betrieb von Zahnkupplungen. VDI-Bericht Nr. 299, 1977, pp. 153-159.
3. P.C. Renzo, S. Kaufmann, D.E. De Rocker. Gear Couplings. Trans. ASME J. of Eng. for Ind., August 1968, pp 467-474.
4. R.G. Kirk, R.B. Mondy, R.C. Murphy. Theory and Guidelines to Proper Coupling Design for Rotor Dynamics Considerations. Trans. ASME J. of Vib. Acoust., Stress and Reliability in Design Vol. 106, January 1984, pp. 129-138.
5. H. Möhle. Beurteilungsmassstäbe für hochtourige Zahnkupplungen. Konstruktion 17. 1965, Heft 2. pp. 61-66.
6. J.S. Sohre. Operating Problems with High Speed Turbomachinery Causes and Correction. Part I, ASME Paper, Petroleum Mech. Eng. Conf., Dallas Texas, September 23, 1968.
7. J.S. Sohre. Operating Problems with high Speed Turbomachinery Causes and Correction. Part II available from the author at cost, address One Lakeview Circle, Ware, Mass 01082.
8. Y.N. Chen. Vibrations in Centrifugal Pump Units Induced by External System. Pumpentagung Karlsruhe 73, 2.-4. October 1973 - Part I: Instability of the Rotor System due to Torsional-Lateral Vibrations Coupling.

Table 1: Calculated and measured natural frequencies (model 2) and the estimated spring stiffness and effective mass (model 1)

Number of Mode	Natural Frequency at Load P			
	2 MW	4 MW	6 MW	2 MW**
1	34.4 Hz	34 Hz	34 Hz	34 Hz
2	50 Hz	50 Hz	50 Hz	50 Hz
3	73 Hz	73 Hz	73 Hz	74 Hz
4	87* Hz	93 Hz	94 Hz	141 Hz
5	94 Hz	112 Hz*	119 Hz*	146 Hz**
6	104 Hz	139 Hz	136 Hz	160 Hz
Measured Dominant Frequency	86.2	112.5	120	
Spring Stiffness of the Couple N/m	$2.068 \cdot 10^8$	$3.47 \cdot 10^8$	$3.967 \cdot 10^8$	
Effective Mass	86.5	88.4	89.0	

* Natural frequency with a large deflection in the gear coupling

** Lowest natural frequency with large deflection in the gear coupling

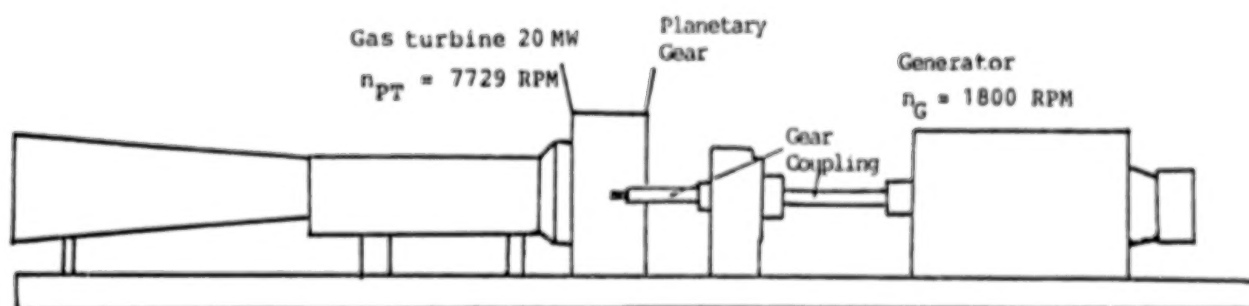


Fig. 1: Schematic of the 21 MW Electric Power Generating Unit.

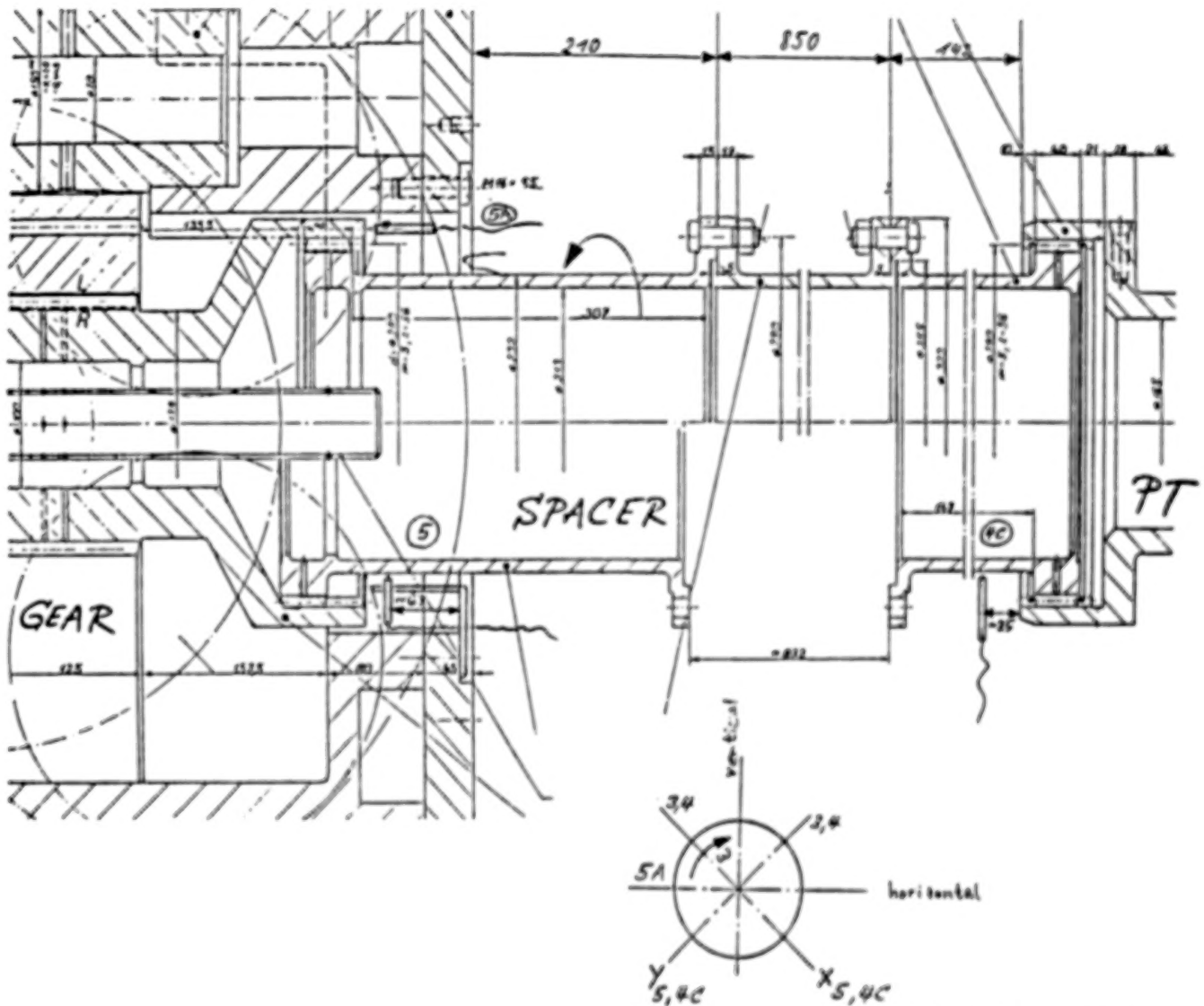


Fig. 2: Drawing of the Pinion and Gear Coupling and the Locations of the Additional Probes.

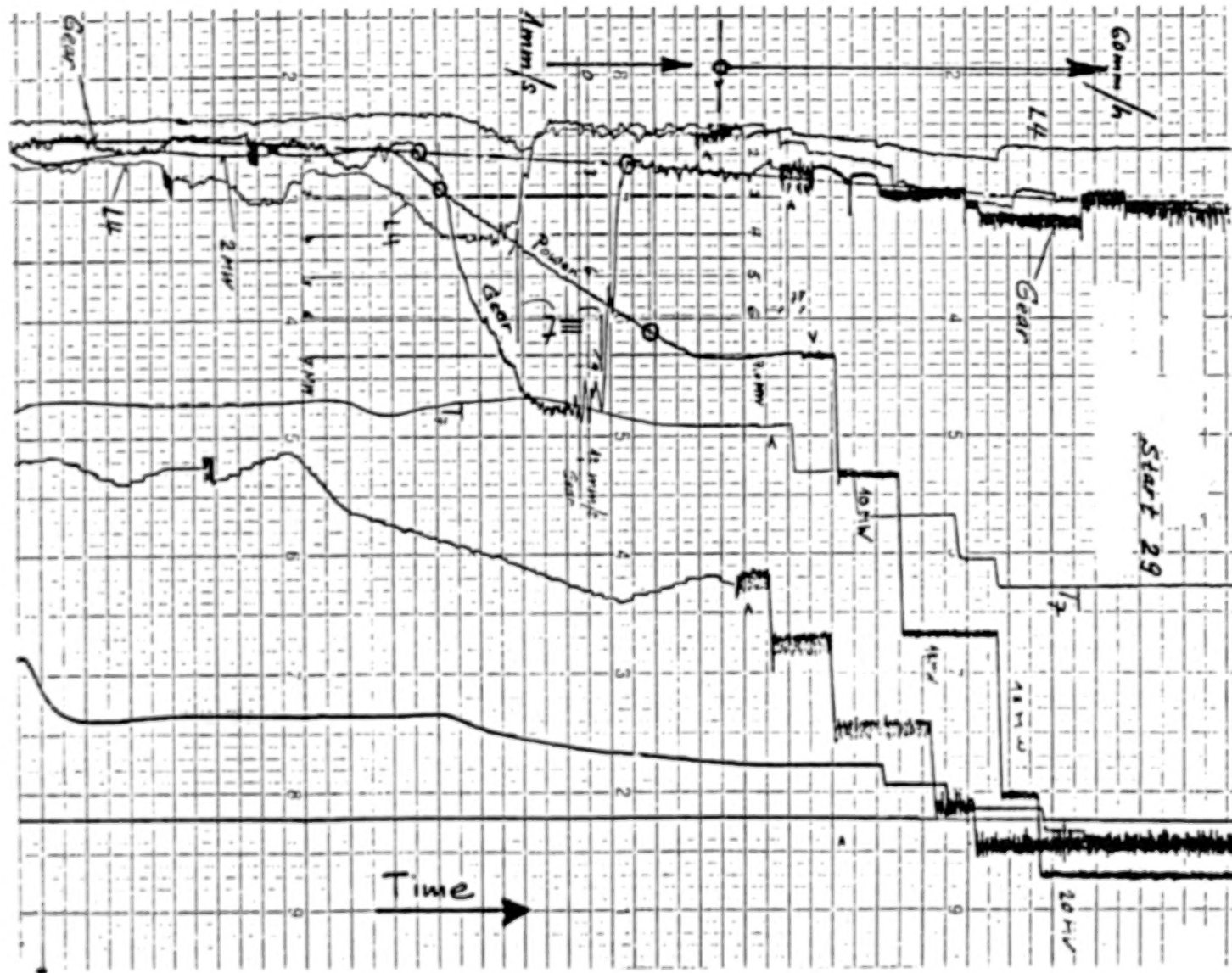


Fig. 3: Record of Start-up Nr. 29.

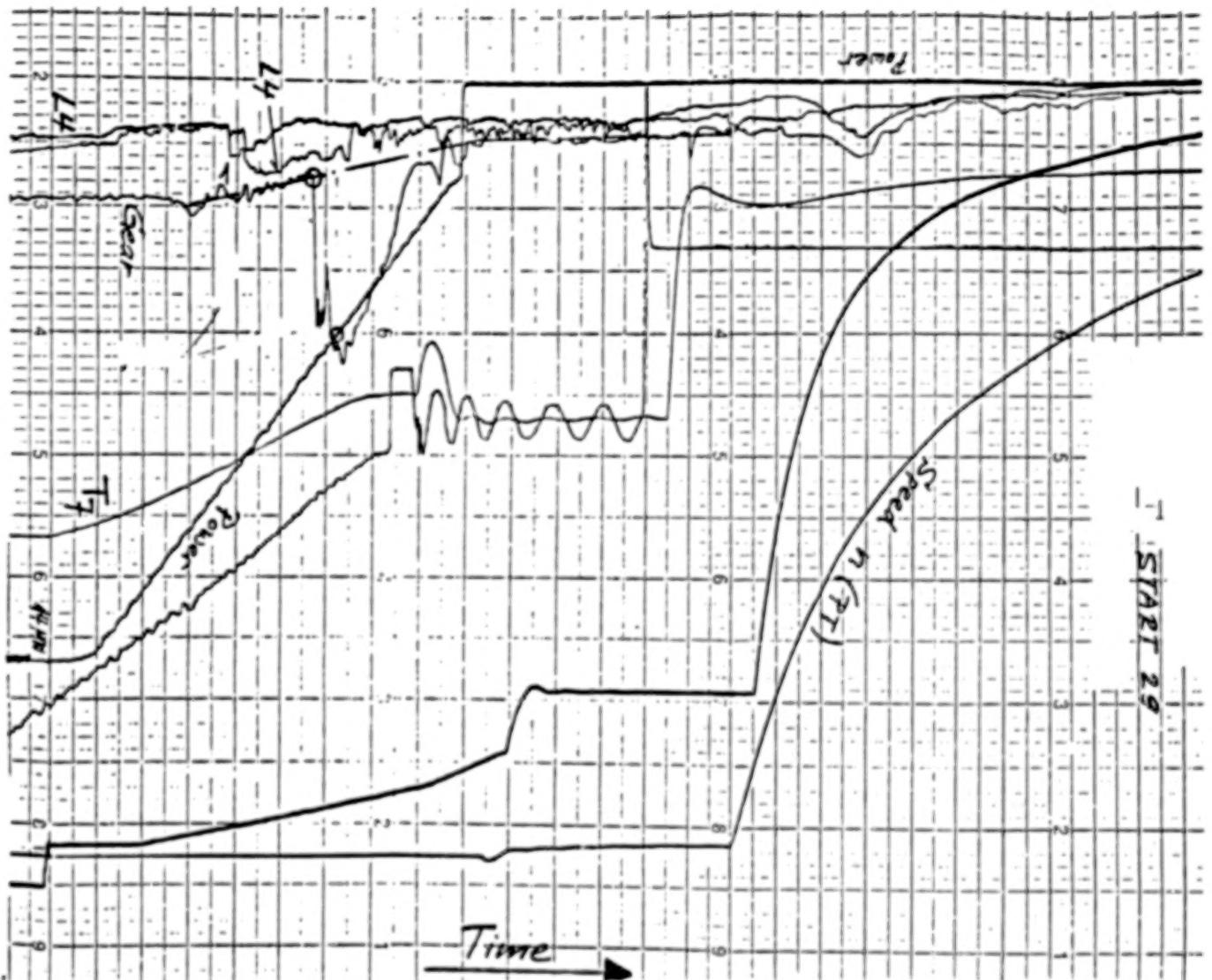


Fig. 4: Record of the Run-down Nr. 29.

BEST COPY AVAILABLE

Start#30 17.12.86
2-6.5 MW/Peak Hold/Dir. 5A

Sunwheel axial

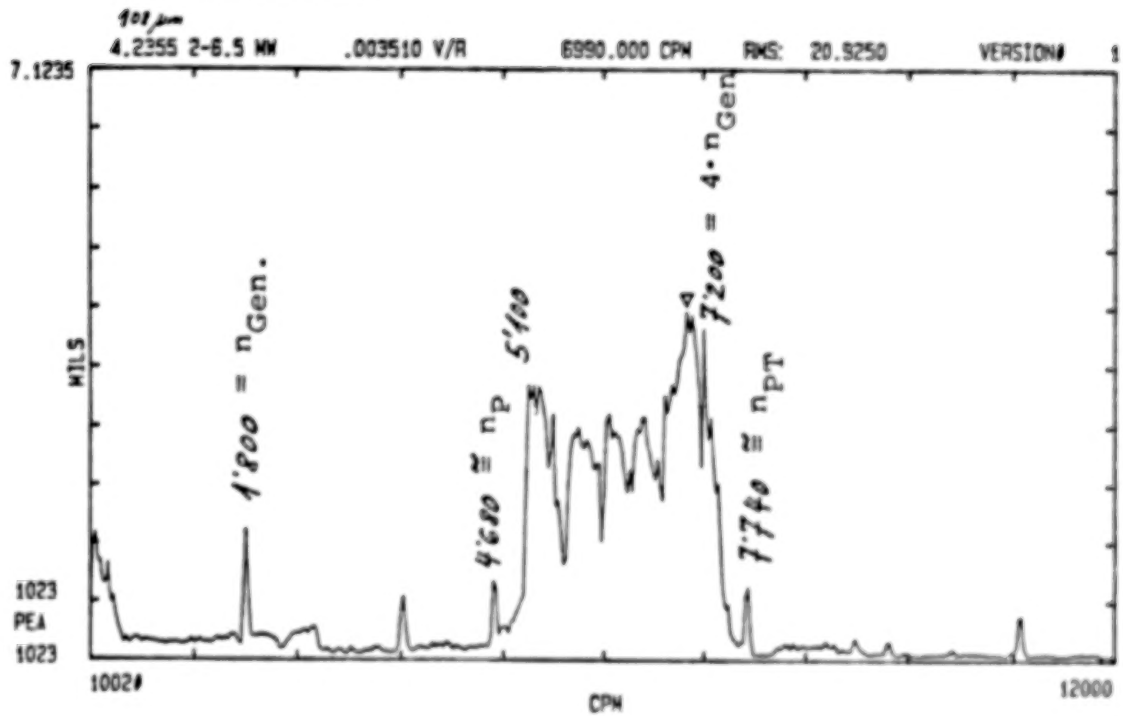


Fig. 5: Frequency Spectrum of "Peak Hold" Axial Displacement of the Pinion; Start-up Nr. 30; 2 + 6.5 MW.

Start#30 17.12.86
2-6.5 MW/Peak Hold/Dir. 5X

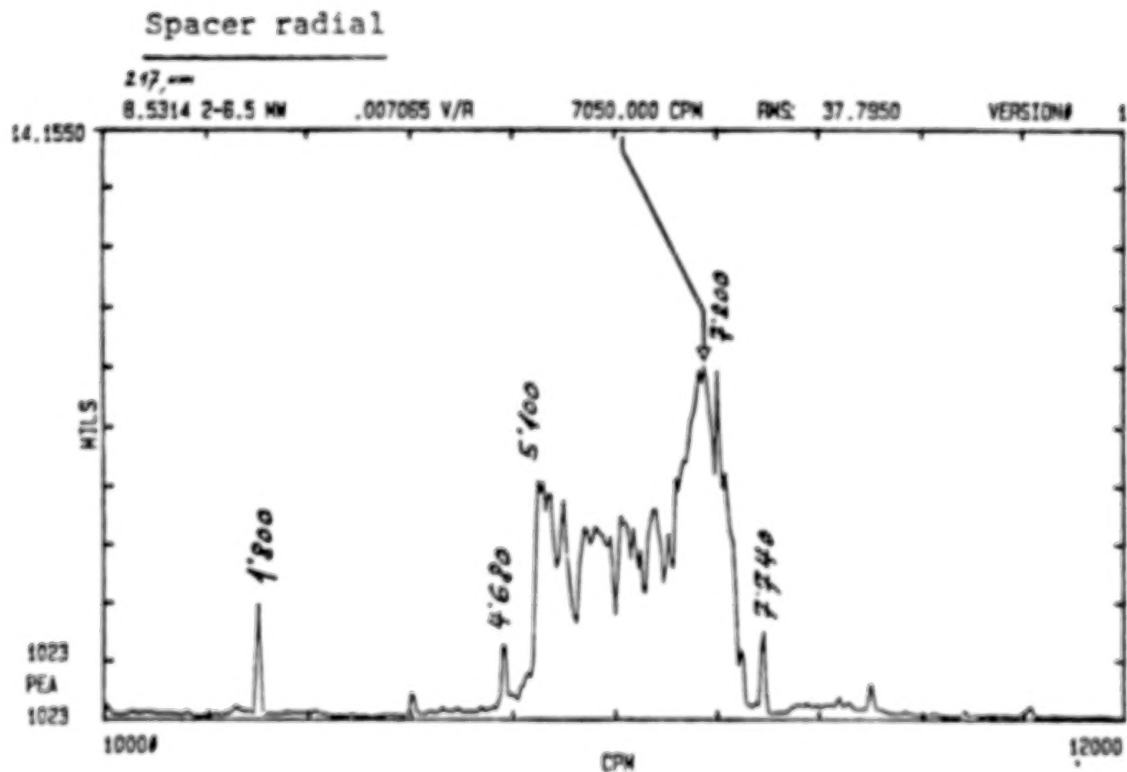


Fig. 6: Frequency Spectrum of "Peak Hold" Radial Displacement of the Coupling Spacer; Start-up Nr. 30; 2 ± 6.5 MW.

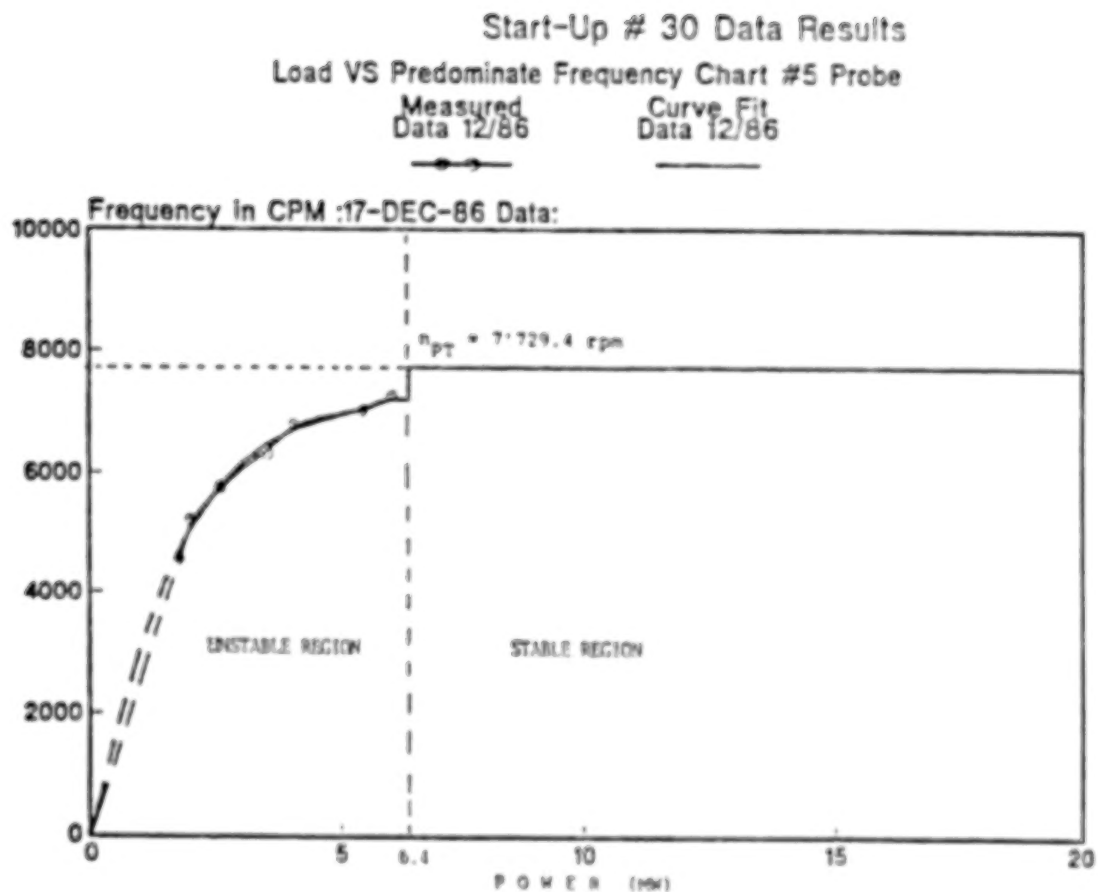


Fig. 7: Dominant Frequency as a Function of Load (Power)

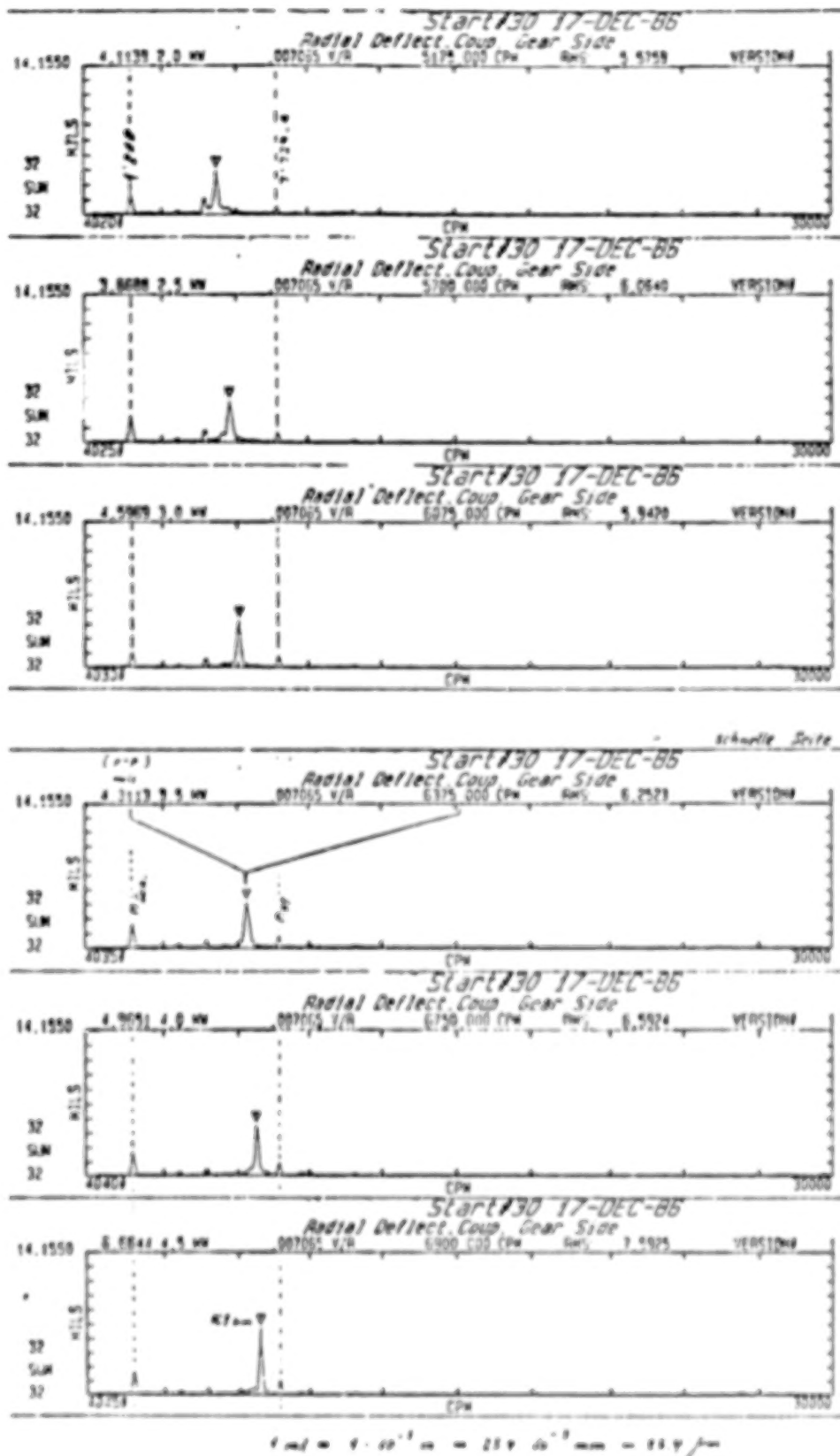


Fig. 8: Frequency Spectra of the Radial Displacement of the Coupling at Constant Speed and Load (Start Nr. 30)

BEST COPY AVAILABLE

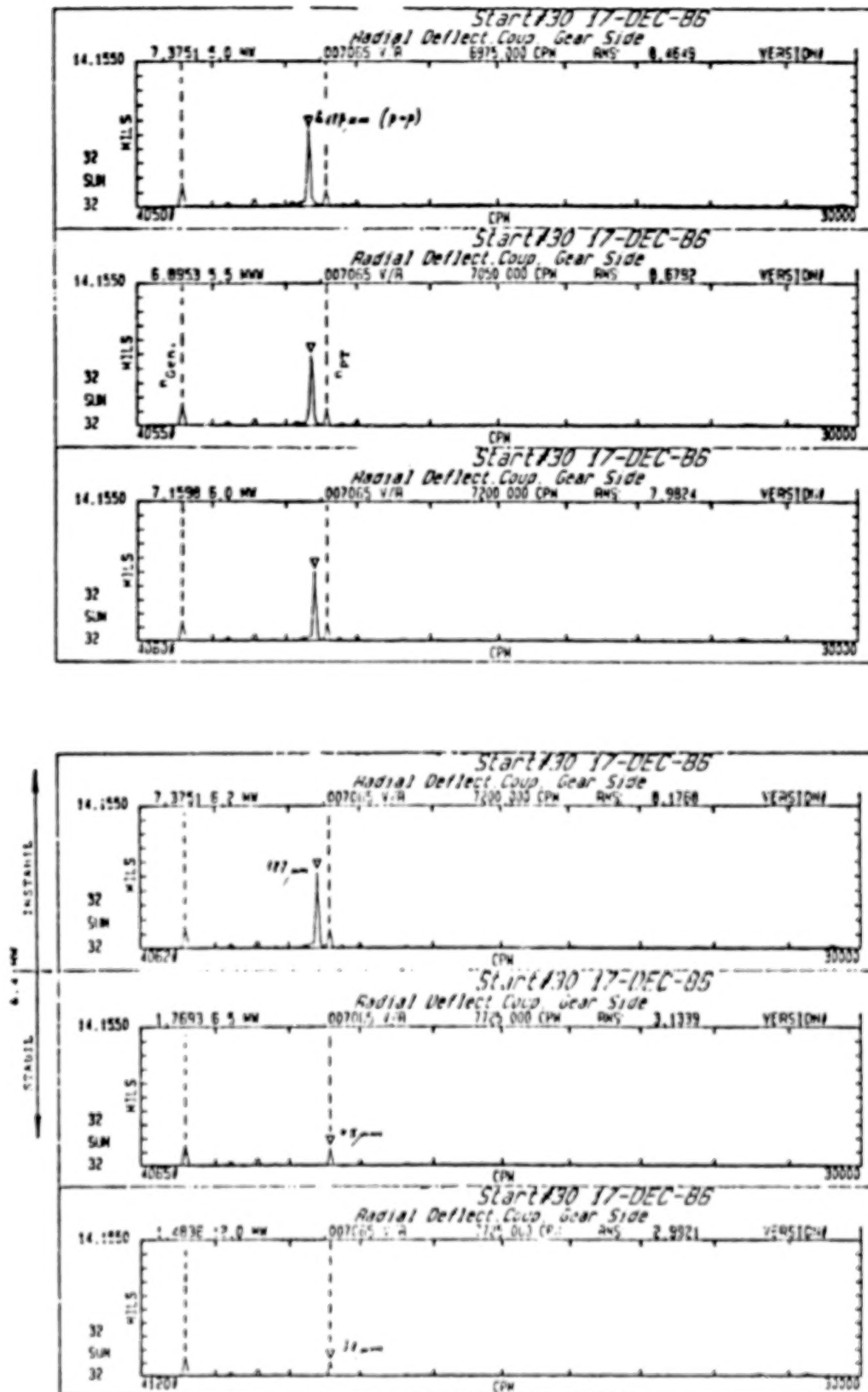


Fig. 8: Continued

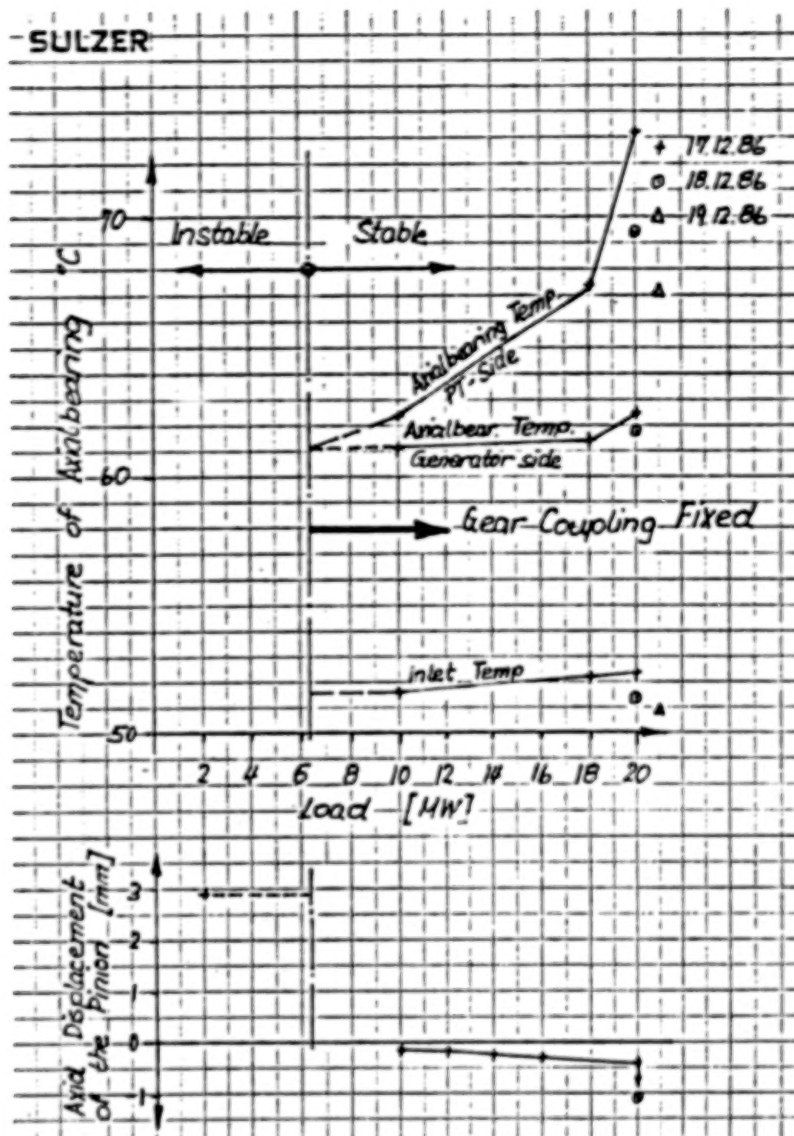
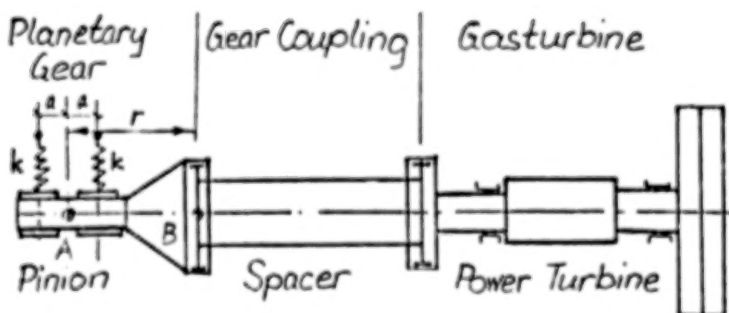
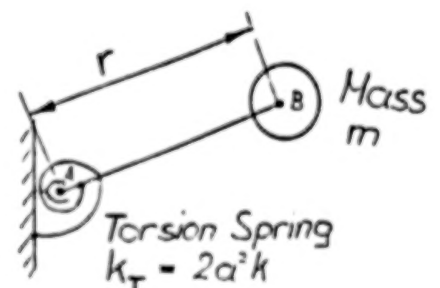


Fig. 9: Axial Bearing Temperature as a Function of Load and Time



a) Physical Model



b) Mathematical Model 1

Fig. 10.: Physical and Mathematical Models

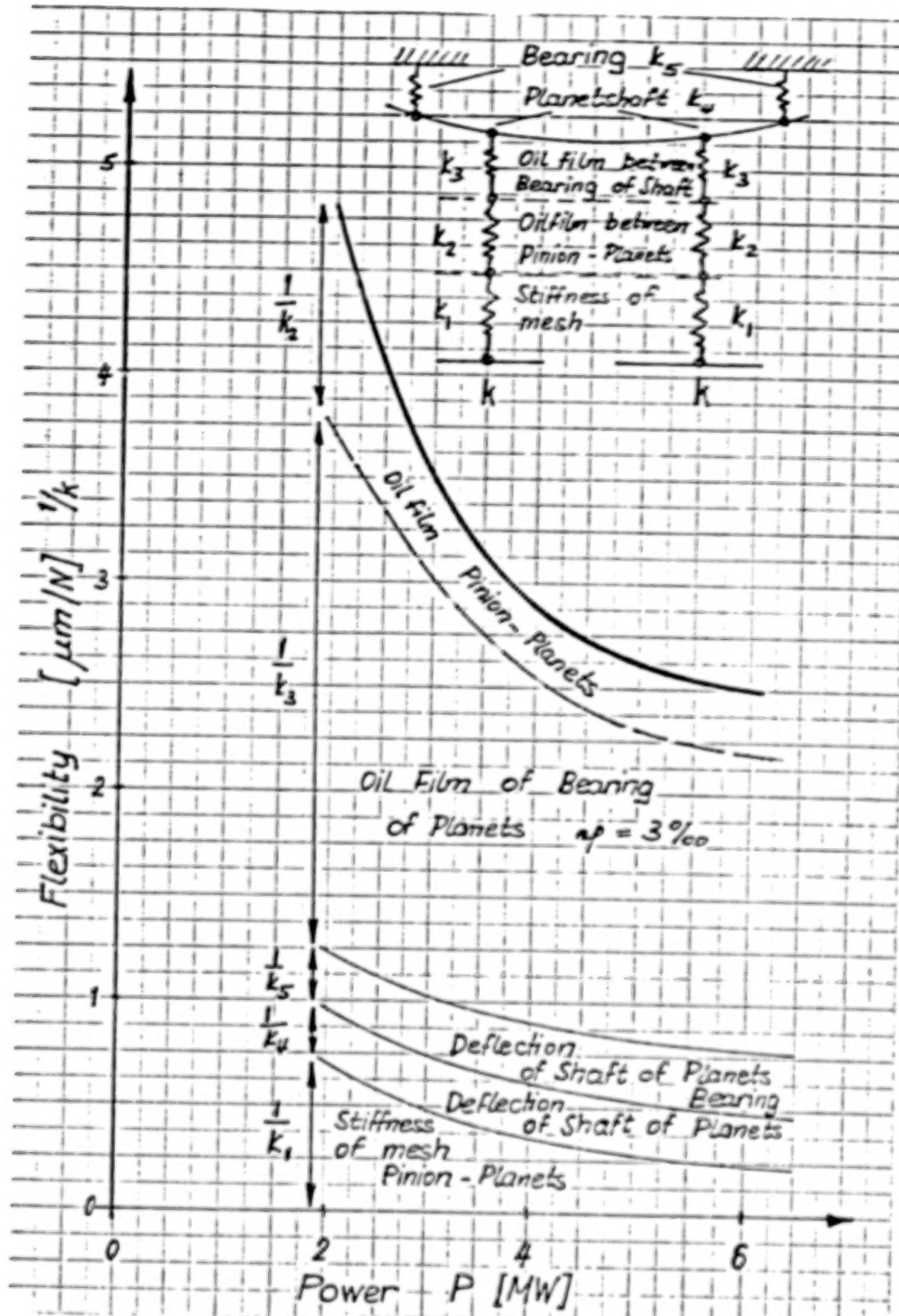
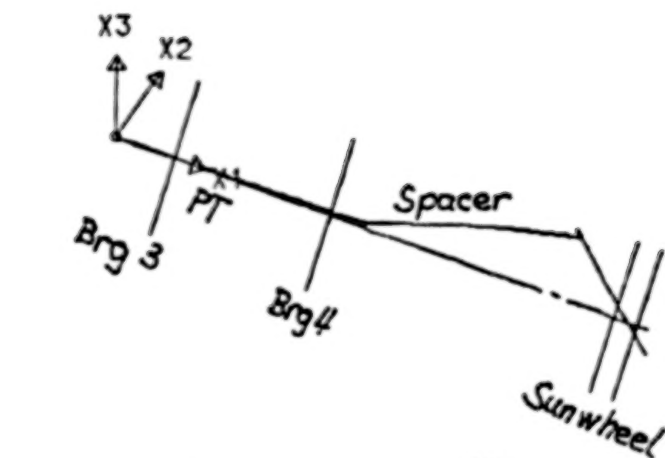


Fig. 11: Combined Spring Stiffness of the Pinion-Planet-Mesh

- Mathematical Model
- Dependence on the Load

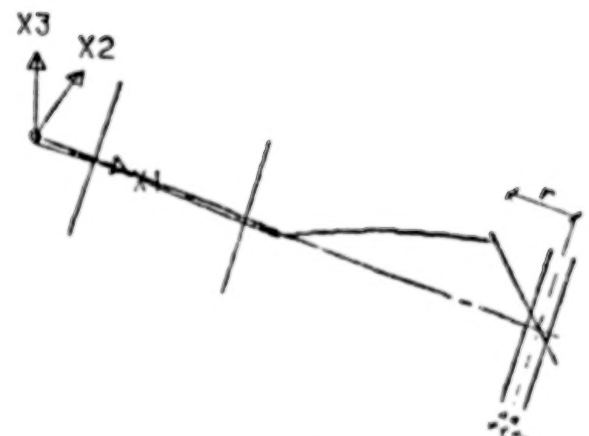


$$k = 2.086 \text{ EP } N/m$$

$$m \cong 89.238 \text{ kg}$$

7. EIGENFORM (R/RE) 86.809 Hz $D = 0.007$

$P=2MW$



$$k = 3.474 \text{ EP } N/m$$

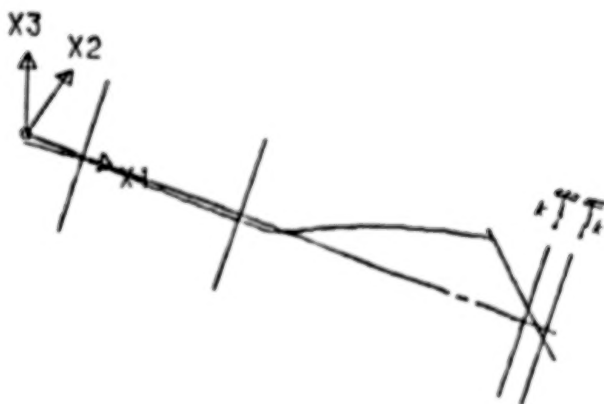
$$m \cong 88.425 \text{ kg}$$

$$r \cong 291 \text{ mm}$$

$$a \cong 75 \text{ mm}$$

8. EIGENFORM (R/RE) 112.233 Hz $D = 0.014$

$P=4MW$



$$k = 3.907 \text{ EP } N/m$$

$$m \cong 89.042 \text{ kg}$$

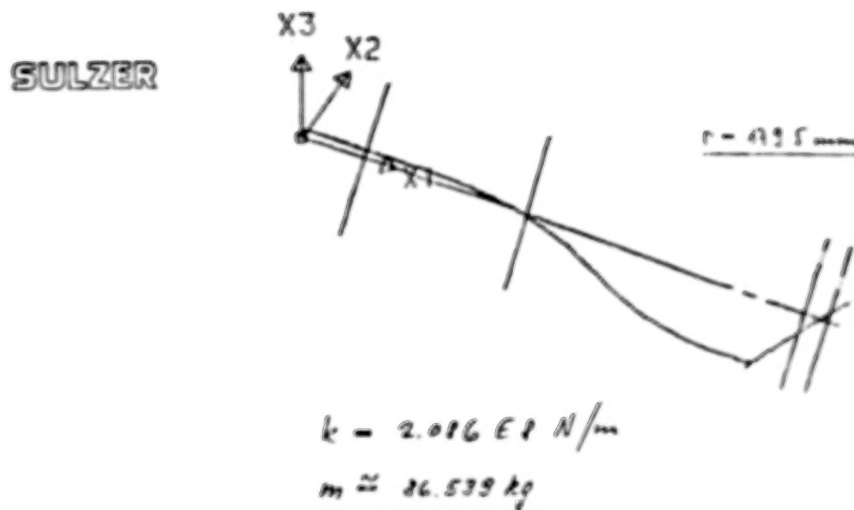
9. EIGENFORM (R/RE) 119.388 Hz $D = 0.016$

$P=6MW$

Fig. 12: Modeshape of the Unstable Natural Frequency having its Maximum Displacement at the Pinion-Spacer Hub for $P = 2, 4$ and 6 MW .



Fig. 13: Improved and Final Design of Pinion and Gear Coupling with Reduced Length of Pinion Shaft



11. EIGENFREQ. (Hz) 148.010 Hz $\delta = 0.014$

Fig. 14: Mode Shape of the Improved Design for Load $P = 2 \text{ MW}$ having its Natural Frequency at $f_n = 146 \text{ Hz}$, and well above the Speed of Operation $f_o = 128.8 \text{ Hz}$

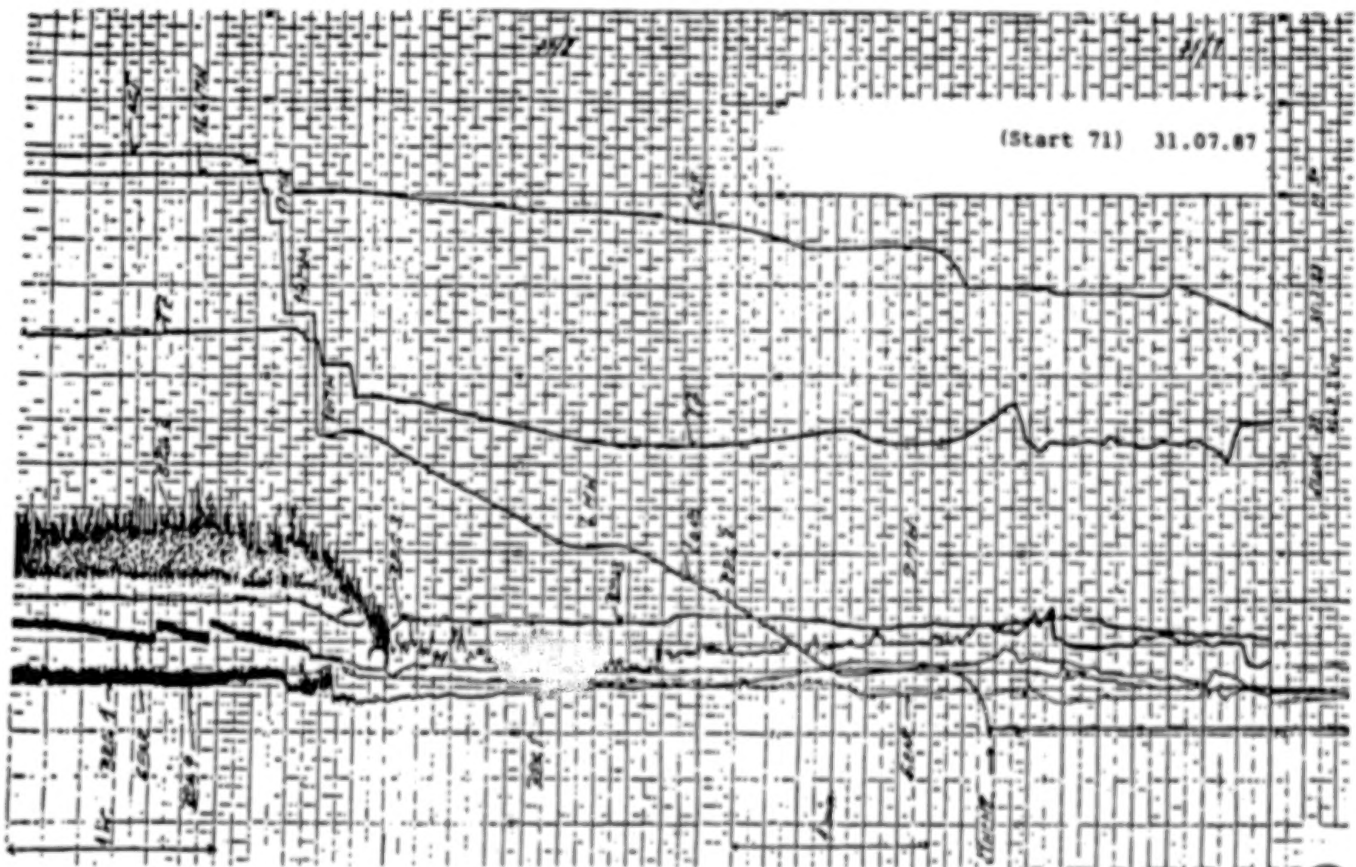


Fig. 15: Record of Start-up Nr. 71 with the Improved Design

BLANK PAGE

SOME IN-FIELD EXPERIENCES OF NON-SYNCHRONOUS VIBRATIONS

IN LARGE ROTATING MACHINERY

Giuseppe Colnago
CESI
Via Rubattino 54
20134 Milano, Italy

Claudio Frigeri, Andrea Vallini, and Gian Antonio Zanetta
ENEL
Via A. Volta 1
20093 Cologno Monzese, Milano, Italy

The paper analyzes some problems associated with non-synchronous vibrations by describing three cases experienced with fairly large rotating machines in operating conditions.

In each case, a brief description is first given of the machine and of the instrumentation used. The experimental results are then presented, with reference to time or frequency domain recordings. The lines followed in diagnosis are then discussed and, lastly, the corrective action undertaken is presented.

INTRODUCTION

Self-excited vibrations have always been a major concern in the field of the dynamics of rotating machinery, since they constitute a serious risk to the integrity of the machines, apart from leading to important losses in production.

In past years difficulties have mostly arisen from the fact that these problems were not well known and from a lack of appropriate experimental and analytical tools to cope with them. Nowadays, troubles are more often caused by the more exacting demands made of rotating machinery.

In any case, a great effort has always been made to identify these phenomena and to give them a proper theoretical description, with the result that an extensive literature now exists on the subject. However, most literature is still concerned with analytical investigations or laboratory tests, in which, of course, experiments are prepared in such a way that it is only possible to know parameters and to consider their influence one at a time.

But this does not apply to the diagnosis of real cases. As a matter of fact, in-field experience shows that, nearly always, a large

number of factors have to be taken into account at the same time, and it is neither easy to keep them apart nor to know or measure them exactly. Furthermore, when comparing one's own experimental measurements with references found in literature, one is faced with an inconsistent and rather confusing vocabulary and, for some topics, even by sharp discrepancies between different authors. All this, in turn, makes diagnosis more difficult and, sometimes, less definite.

The paper presents three case histories of sub-synchronous vibrations that recently occurred on fairly large rotating machines and in one way or another exemplify the above remarks. The first case regards the excitation of the first critical speed of an alternator rotor. The second concerns the hydraulic instability of a boiler feed-pump. The last one is about an instability with a component at exactly half the running speed on an H.P. turbine.

SUB-SYNCHRONOUS EXCITATION OF THE FIRST CRITICAL SPEED OF AN ALTERNATOR ROTOR

The machine was an alternator rotor weighing about 520 kN, supported by 2 cylindrical oil-film bearings, in service at a plant for short circuit tests; its operating speed ranged from about 47 to 62 Hz.

The machine had 2 eddy-current probes applied on each bearing. For our investigation 2 accelerometers were added on each bearing support and, together with a phase reference, all the signals provided by these transducers were recorded on a magnetic tape for subsequent digital analysis. It was thus possible to obtain the harmonic analysis of the vibrations throughout the speed range, the center loci of the journal in bearings, vibration orbits and spectrum analysis. Inlet and outlet oil temperatures at each bearing were also recorded.

Staff in charge at the plant and the manufacturer's technicians, reported that the rotor developed occasional sudden, very high vibration levels when spinning at maximum speed. Oil-film instability was immediately suspected. Nevertheless, tests on oil temperature failed to yield the usual results, since raising the oil temperature did not cause the phenomenon to disappear. On the contrary it seemed to grow a little worse. Although this could not lead to any definite conclusion about the nature of the instability, since it was only apparent at maximum speed, in case of oil-whip a higher oil temperature should have succeeded in making it disappear.

Owing to the specific features of the machine, it was possible to follow a number of run-ups and shut-downs and to keep it at maximum speed at different oil temperatures. The results of these tests may be summarized as follows:

-The machine had a number of critical speeds, with significant differences in the vertical and horizontal planes. The first critical

speed of the rotor was at about 1070 r.p.m. in the horizontal and at 1420 r.p.m. in the vertical plane. A 2nd critical rotor speed was most probably at about 3250 r.p.m. in the horizontal and quite near the maximum speed in the vertical plane. Other resonances might be attributed to flexibility of the supports and foundation and, for all of them, the phases indicated a 2nd vibration mode above 2000 r.p.m. (Fig. 1).

-The machine was in a rather poor balancing state for the 2nd vibration mode.

-The machine showed markedly non-repetitive behaviour when running at its first critical speeds, most probably due to considerable movement of the coils in relation to the rotor body.

-The centre loci of journal in bearings showed that, at the higher speeds, the shaft moved strongly towards the bearing centre (Fig. 2).

Specifically as regards instability, the following point may be made:

-During the investigation the phenomenon was observed only once, which confirmed its purely random nature. Moreover, no definite link with oil temperature could be established.

-In the presence of the phenomenon, the high vibration levels were mainly determined by a sub-synchronous vibration component at 20.4 Hz (1250 r.p.m.), while running speed frequency was 62.4 Hz (3750 r.p.m.). Maximum amplitude was reached by relative displacement in the horizontal plane and was of about 650 μ m, very close to total bearing clearance at the design stage. A number of much smaller harmonics of that component were also found and were considered to be due to non-linear behaviour of the oil film (Fig. 3). Though it almost coincided with 1/3 of the running speed, the frequency of the sub-synchronous component was considered as corresponding to excitation of the first critical speed of the rotor in those conditions.

-When filtering signals around the sub-synchronous component at 20.4 Hz, it was observed that the growth of these vibrations was rather slow and during some cycles they even kept stable (Fig. 4). The expansion coefficient, equivalent to a critical damping coefficient for the introduction of energy, was found to be equal to 0.005, taking into account the logarithmic increment. The orbits showed that the journal followed a forward whirl. Figure 5 shows a subsequent series of orbits.

-The instability disappeared as soon as the running speed of the rotor was lowered, developing and disappearing in the space of about 10 seconds.

-At maximum speed, a small component at about 20.4 Hz was always present, but appeared and disappeared continuously without reaching a significant level, when the instability did not develop fully.

A numerical investigation was then undertaken, in order to determine the threshold speed of instability for the oil film bearings. The simple Routh-Hurwitz's criterion, applied to the oil-film only, indicated a value of 1200. r.p.m., but did not take into account the characteristics of the supports and of the rotor. An estimate of the flexibility values of supports and rotor around the first critical speed was obtained by comparing the experimental results with the numerical values given by a model of the shaft (ref. 1). Calculations were then performed in accordance with 2 slightly different methods (ref. 1, 2). The results indicated a threshold speed value of 2500 r.p.m. according to reference 2 and a value of 2560 r.p.m. according to reference 3.

Lastly, for a number of speeds, a coefficient R_{eq} , proportional to the energy E_d dissipated in the oil-film bearings during one orbit of revolution, was calculated. The coefficient was obtained by dividing E_d by the mean square value of the relative vibration amplitudes in each bearing multiplied by the frequency of rotation and adding together the results for all bearings, according to the following formula:

$$R_{eq} = \frac{\sum_{i=1}^n E_{d_i}}{\omega \cdot \frac{1}{2} \cdot \sum_{i=1}^n X_{r_i}^2} \quad (1.1)$$

Thus, R_{eq} has the dimensions of a damping coefficient. The E_d terms were calculated by taking into account the theoretical values for the oil-film coefficients and the experimental values for the relative vibrations. In spite of a marked decrease with speed (Fig. 6), the coefficient was always positive, even at maximum speed.

More refined models were not used. These are most useful, if not absolutely necessary, at the design stage; but for diagnostic purposes in a real case, in our opinion, the uncertainty as to which values to assign to the different parameters into action makes it difficult to obtain results much more reliable than those obtained by simpler methods at a lower cost.

At the same time, some of the existing literature on the subject was analyzed (see reference 4 to 14) and compared with experimental and numeric results. An oil-whip phenomenon was likely, but even a hysteretic whirl could not be ruled out. In fact, the excitation of the first critical speed, the high vibration levels reached and the forward whirl are common to both phenomena, according to most authors (ref. 4, 5, 6, 7). Others (ref. 8, 9) associate hysteretic whirl with the presence of a component at half-frequency. Some facts (movements of the coils in relation to the rotor body, the low expansion coefficient of the vibrations, the erratic occurrence of instability, the fact that the phenomenon did not persist when the speed decreases just after its appearance) accorded well with a hysteretic whirl. On the other hand, the numerical results were in favour of oil-whip instability. The high ratio between the actual onset speed and the calculated threshold speed of instability, as well as its random appearance could also be explained by limits of the methods used,

uncertainties in the parameters introduced (wear, angular misalignment), actual oil temperature in bearings (ref. 10) and effects of synchronous excitation. On this last subject, significant disagreements were found in literature (compare references 5, 11, 12, 13). Other tests suggested by some authors (ref. 6) to improve the diagnosis could not in practice be performed on a machine of that size.

Luckily, both phenomena could be obviated by the same remedial action, by substituting partial arc bearings (with an arc of 60 degrees) for the existing cylindrical ones. The threshold speed for the new kind of bearings was found to be about 4000 r.p.m., according to the above-mentioned methods. Furthermore, the new bearings introduced a larger asymmetry between the horizontal and vertical planes in bearing characteristics. This should have improved stability for both phenomena under examination (ref. 5, 14). Moreover, calculations were performed with a model of the rotor, to evaluate the power loss in the oil film with cylindrical and partial arc bearings. Excitation of the 1st and 2nd vibration mode were considered separately, at both critical and maximum speeds. In all cases, the amount of dissipated energy in one orbit of revolution was greater for partial arc bearings, whose only drawback was to increase the horizontal vibrations. This low-cost solution was finally implemented and gave the expected results. So far, this problem has no longer reappeared.

SUB-SYNCHRONOUS VIBRATIONS ON A BOILER FEED PUMP

The problem was encountered on one of the 9 boiler feed-pumps of identical design installed in a thermal power plant with four 320 MW turbogenerator units. These centrifugal pumps had 5 stages with plain interstage seals and grooved seals at the glands and on the balancing-drum. The operating speed ranged from 4200 to 6200 r.p.m., the maximum capacity and pressure being 640 Tons/h and 18 MPascal, respectively. The pump was driven by an electric motor, and the power was transmitted through a gear mesh, controlled in turn by 4 hydraulic units. After a few years of normal operation the pump in question began to register high vibrations, so that it could no longer be kept in service.

In an initial set of measurements by the manufacturer, spectrum analysis revealed the presence of a subsynchronous component at about 95 per cent of the rotational speed. It was reported that the fault was more likely to occur below a certain pump capacity, yet was not repeatable under seemingly the same conditions. No conclusions were drawn as to its causes. The machine was then considered as a spare pump, but its behaviour was most unreliable and, after some other unsuccessful attempts to get it to work, a deeper investigation was called for.

First of all an excitation test was performed with the machine at rest. The force was applied on one bearing support by a sinusoidal

sweep over the frequency range in question; measurement points were set up on both bearing supports, on the casing and on the pump foundation. In the horizontal plane, 2 distinct maxima in the response were observed at about 95 and 110 Hz, but they were strongly damped and the measured compliance was not greater than 600 $\mu\text{m/kN}$. No specific information was obtained for the vertical plane. So important structural problems could be ruled out.

Then the machine was fitted with 2 eddy-current probes at each bearing, a pressure transducer on the delivery side of the pump, a phase reference on the shaft, while retaining 2 accelerometers on each support, and 3 other accelerometers on the foundation and on the driving unit. The signals so obtained, together with the capacity signal, were recorded on a magnetic tape for subsequent analysis.

The aim of the tests was to find out which parameter, such as capacity, rotational speed, pressure, or which combination of them, could start the phenomenon. In fact, the anomalous behaviour of the pump and the very high vibrations prevented from achieving the planned program in an orderly way. The following remarks may be made:

- The highest vibration levels were reached in the horizontal direction on both bearings, with a maximum on the bearing next to the electric motor. The foundation and the driving units were only marginally affected by the vibration.

- The pump was in poor balancing state with synchronous vibrations far beyond admissible levels. Recordings at variable speed showed a possible resonance at 6000 r.p.m. in the horizontal plane, but with a low amplification factor and deformation shape in the 2nd vibration mode.

- The instability developed in no more than 10 cycles and, once fully established, the vibration was not steady (Fig. 7).

- Spectrum analysis during the instability indicated that, in such conditions, the vibration was mostly determined by a sub-synchronous component whose frequency ranged from 0.85 to 0.97 of the running speed (Fig. 8, 9). The frequency of this component was not related to the rotational frequency, nor to the pressure or to the flow rate, as evidenced in figure 8, where the spectrum, obtained by a peak-hold average on only one time record 5 seconds long, showed 3 sub-synchronous components with different frequencies.

- With lower pressure at delivery it was possible to reach the maximum flow rate, but at that point the instability showed up again and vibrations up to 400 $\mu\text{m/p}$ were reached on that occasion.

- By correlating the support vibrations with frequency responses to external excitation, it was possible to get a rough estimate of the forces in play. These reached 30 kN on the support next to the coupling end with the motor.

-An auxiliary mass damper, tuned to the middle of the frequency range in question, was added in order to introduce some damping into the system, but that was not enough to suppress the instability. Under those circumstances, when the instability appeared, it was calculated from the displacement of the support to which the damper was attached that the inertial force of the auxiliary mass was about 7 kN.

-Moreover, relative vibration values at the bearing locations greater than clearances and the deformation shape of the shaft at those frequencies indicated the possibility of significant wear in one bearing and in some seals.

By comparing these experimental results with the literature available on the subject (ref. 15, 16, 17), a diagnosis of hydraulic instability was arrived at. Most likely, it was due to forces generated by the interaction of diffuser and impeller, on which a negative influence could be exerted by the generally bad conditions of the pump (balancing state or bent shaft and wear). Contrary to what is stated in references 16 and 17, the problem was also present at high flow rates.

Initially, a general overhaul of the pump was suggested; but changes of bearings and to some details in seals or clearances between impeller and diffuser, even at the cost of somewhat reduced efficiency, were considered essential. The machine was opened and, in fact, the bearing next to the coupling end and a number of seals, especially on the balancing drum, were found to be badly damaged. After maintenance, the pump was restarted again in the original design condition, since the changes suggested had not been completely defined. During the first tests and for a little while after, it looked as though the instability had disappeared. But afterwards, it reappeared again. So, in spite of proper diagnosis, it had not thus far been possible to get rid of the problem.

EXACT HALF FREQUENCY WHIRL IN AN H.P. TURBINE ROTOR

The machine in question was an H.P. turbine in an old 70 MW turbogenerator unit. The 3 rotors, H.P. and L.P. sections and the generator, were supported on 6 cylindrical bearings. The H.P. rotor weighed about 90 kN. The seal-rings of the steam glands were made of steel and very stiff. The operating speed was 3000 r.p.m. (50 Hz).

Two months after overhaul, the H.P. rotor showed a sudden increase in vibration in bearing No 1, after load reductions during normal operation. Surveillance instruments showed the phenomenon as a sharp peak in the overall absolute shaft vibration of that bearing only, the other bearings being apparently unaffected (Fig. 10). Moreover, the phenomenon only lasted a few minutes, then disappeared without tripping the unit. It was preceded by a continuous increase in vibration level at the same bearing, starting with the load reduction

transient and in good correlation with metal and steam temperature changes in the impulse wheel chamber. It is worth adding that load reductions were achieved by partialization of steam admission.

Since then, a rubbing effect had been suspected. Detailed investigation was therefore decided on and the absolute shaft vibration at the 6 bearings plus the support vibration at each of the four turbine bearings, plus a number of other quantities (metal and steam temperatures, active and reactive power, vacuum of the condenser, oil temperatures) were collected by a digital acquisition system able to carry out the harmonic analysis after a synchronous acquisition. Furthermore, it was possible to store 4 channels of time history data for subsequent spectrum analysis. Although they would have proved very useful on such an occasion, eddy-current probes could not be used until the machine was stopped.

A few tests were devised with the machine still in service. First of all, the operation sequence that had given rise to the phenomenon (load reduction from 70 MW to about 47 MW) was repeated, being careful to start from and to arrive at steady thermal conditions. In fact, the phenomenon appeared again, in almost the same way as shown in figure 10. Frequency analysis indicated that, during the first phase of load and thermal transient, vibration rises at bearing No 1 were caused mostly by a fundamental component of the signal, and 2nd harmonic variations appeared after a certain vibration level, probably due to non-linearities in the oil film. When the fundamental component arrived at about 90 μmpp a sub-synchronous component became visible; but it was not yet stable and it appeared and disappeared suddenly between one series of orbits of revolution and another. With a further increase in the fundamental component over 100 μmpp , the phenomenon continued to be present and the sub-synchronous vibration stabilized on a definite value (Fig.11). Values as high as 200 μmpp were read for this component. In any case, its frequency was 25 Hz, exactly half the frequency of the running speed. Moreover, higher harmonics at 75 and 125 Hz were present, the others, at 50 and 100 Hz, being hidden in the fundamental and 2nd harmonic components. The 25 Hz component was very low for the absolute shaft vibration at bearing No 2, while it was marked on both supports of bearings No 1 and No 2. Finally, when the thermal transient died out and the vibration decreased to below the above-mentioned levels, the sub-synchronous component disappeared.

The same test was repeated with the oil temperature in bearings 7 °C higher, but gave the same results. This time, with the machine at a 47 MW output and after reaching steady thermal conditions, a 40 °C drop in the inlet steam temperature again caused a vibration rise and, in turn, the sub-synchronous component made its appearance once more.

An analysis of bearing data showed that bearing No 1 was underloaded and the first critical speed was found to correspond to about 2000 r.p.m. (33 Hz) by a model of the shaft line, at least when in theoretical alignment. If the stiffness of bearing No 1 was reduced significantly, as it could be for the partialization effect, the turbine behaved like a cantilever. In this way, the critical speed might be less than 25 Hz and the deformation might resemble that

corresponding to the experimental measurements of the component at 25 Hz.

At this point, an oil whirl instability was ruled out, because the latter is characterized by a frequency content that is always slightly less than exactly half the rotational speed (ref. 5). The rise in oil temperature did not affect the phenomenon, which appeared only after the synchronous vibrations had reached a high level. In most authors' opinions, as already mentioned in the first case history, high vibrations should counteract oil whirl instability. Moreover, time recordings made here were not typical of that kind of instability.

On the contrary the lifting of the rotor for partialization effects, the shaft bending due to the thermal transient and the increase in the vibrations themselves were enough to explain a light rubbing effect, causing instability of a parametric kind, or due to friction forces, with a sub-synchronous frequency content equal to exactly half the rotating speed and its harmonics, like that described in references 18 or 19. However, the results referred to in these papers stem from theoretical developments and the experimental evidence given in reference 19 is limited to a small model. According to other authors (ref. 20), subharmonic components are unlikely to be found in actual turbogenerator sets and, as far as we know, only very few cases have been reported (ref. 21, 22). Vibration orbits might have made a definite opinion possible, but unfortunately they were not available.

In an initial attempt, it was suggested the turbine case be raised by 0.2 mm in relation to the rotor. The operation sequence able to produce the fault was repeated and this time only a little track of the subsynchronous component around 25 Hz in the presence of the fundamental component vibration levels was found.

During a subsequent short overhaul, the seal-rings were replaced by others of a much more flexible type and the clearances were finally revised. The problem has not so far reappeared. The rotor naturally maintained high sensitivity to thermal transients and to partialization effects. In order to reduce the influence of such effects, it was suggested that the cylindrical bearing be replaced by a tilting-pad bearing or, at least, be shortened, to increase the equivalent load. This action, however, though scheduled, has not yet been put into effect.

CONCLUSIONS

Three different in-field experiences of instability problems that occurred in large rotating machines under operating conditions have been discussed. Two of them were not so common and are scarcely referred to in literature, at least as in-field cases.

The lines followed in the diagnostic process have been emphasized. It has been shown that frequency analysis alone is not always enough to perform a definite diagnosis, since different phenomena often give rise to the same, or almost the same, frequency content. Knowledge of the structural characteristics of the whole mechanical system and the correlation of vibrations with other quantities are usually necessary, as well as comparison with other experiences and studies. Mathematical models, too, may prove very useful as an aid to diagnosis.

Once the problem has been correctly identified, the subsequent remedial action is often quite straightforward. In other cases, the complexity of the phenomena calls for special effort, and good results can be achieved only if it is possible to delve deeper into design details and experimentation.

REFERENCES

1. DYTS04-USER'S GUIDE-CEGB-RD/L/P 15/80-JOB No. VE316
2. Mechanical Technology Incorporated
Rotor-Bearing Dynamics Design Technology-Part III: Design Handbook for Fluid Film Type Bearings.
Technical Report AFAPL-TR-65-45, PART III - May 1965
3. Glienicke, J.
Experimentelle Ermittlung der statischen und dynamischen Eigenschaften von Gleitlagern für schnellaufende Wellen.
VDI Zeitschriften, Reihe 1, Nr. 22, Aug. 1970
4. Tondl, A.
Some Problems of Rotor Dynamics.
Publishing House of the Czechoslovak Academic of Sciences, Prague-1965
5. Rieger, N.F.
Stability of Rotors in Bearings-4 Lectures.
CISM, Udine-Rotordynamics Colloquium-October 12:16, 1980
6. Bentley, D.E.
The Re-Excitation of Balance Resonance Regions by Internal Friction.
ASME paper No. 72-Pet-89
EPRI CS-3716-Project 1648-5-Final Report-September 1984
7. Sacchi, G.-Moro, B.
Vibratory Problems on Gas Turbine Rotors.
IFTOMM-International Conference 'Rotordynamic Problems in Power Plants'- September 28-October 1, 1982-Rome-Italy

8. D'Ans, G.-Vanlerberghe, C.-Geradin, M.-Pirlot, A.-Suleau, M.
Some Case Studies of Modal Analysis, Signature Analysis and
Finite Element Modelling.
VibraRoMa Meeting-Milan-Italy-September 1981
9. Harris, C.M.-Crede, C.E.
Shock & Vibration Handbook
McGraw-Hill Book Company-2nd Edition-1976
10. Wagner, L.F.-Raimondi, A.A.
Effect of Oil Film Properties and Support Characteristics on Oil-
Whip Instability.
EPRI CS-4024-Contract WS 81-240-Proceedings-June 1985
11. Barret, L.E.-Akers, A.-Gunter, E.J.
Effect of Unbalance on a Journal Bearing Undergoing Oil Whirl.
Proc. IMech E-Vol.190 31/76
12. Bannister, R.H.
The Effects of Unbalance on Stability and Its Influence on Non-
Synchronous Whirling.
IMech E-2nd International Conference 'Vibrations in Rotating
Machinery' 1980-Paper No. C310/80
13. Adams, M.L.Jr.
Large Unbalance Vibration Analysis of Steam Turbine Generators.
EPRI CS-3716-Project 1648-5-Final Report-September 1984
14. Inoue, T.-Matsukura, Y.
Effect of Bearing Asymmetry on the Motion of an Asymmetric Rotor.
Proc. of the 27th Japan National Congress for Applied Mechanics,
1977
15. Black, H.F.
Lateral Stability and Vibrations of High Speed Centrifugal Pump
Rotors.
IUTAM Symposium 'Dynamics of Rotors'-Lyngby/Denmark 1974
16. Makay, E.
Centrifugal Pump Hydraulic Instability
EPRI CS-1445-Research Project 1266-18-Final Report-June 1980
17. Brown, R.D.
Vibration Phenomena in Boiler Feed Pumps Originating from Fluid
Forces.
IFTOMM-International Conference 'Rotordynamic Problems in Power
Plants'- September 28-October 1, 1982-Rome-Italy
18. Childs, D.W.
Fractional-Frequency Rotor Motion Due to Nonsymmetric Clearance
Effects.
Journal of Engineering for Power-July 1982, Vol.104/533

19. Muszynska, A.
Partial Lateral Rotor to Stator Rubs.
IMech E-Third Int. Conference in 'Vibrations in Rotating Machinery'-11:13 September 1984-University of York-Heslington, Yorkshire
20. Curami, A.-Pizzigoni, G.-Vania, A.
On the Rubbing Phenomena in Turbomachinery.
IFTOMM-International Conference on 'Rotordynamics'-September 14-17, 1986, Tokyo
21. Benanti, A.-Gadda, E.
Analysis of Turbogenerator Malfunctioning on the Basis of Vibrational Behaviour.
6th Thermal Generation Specialists Meeting-Madrid, May -56, 1981
22. Gao Jin Ji-Qi Qi Min
Rotor to Stator Rub Vibration in Centrifugal Compressor.
Symposium on 'Instability in Rotating Machinery'-Carson City, June 10-14, 1985-NASA Conference Publication 2409

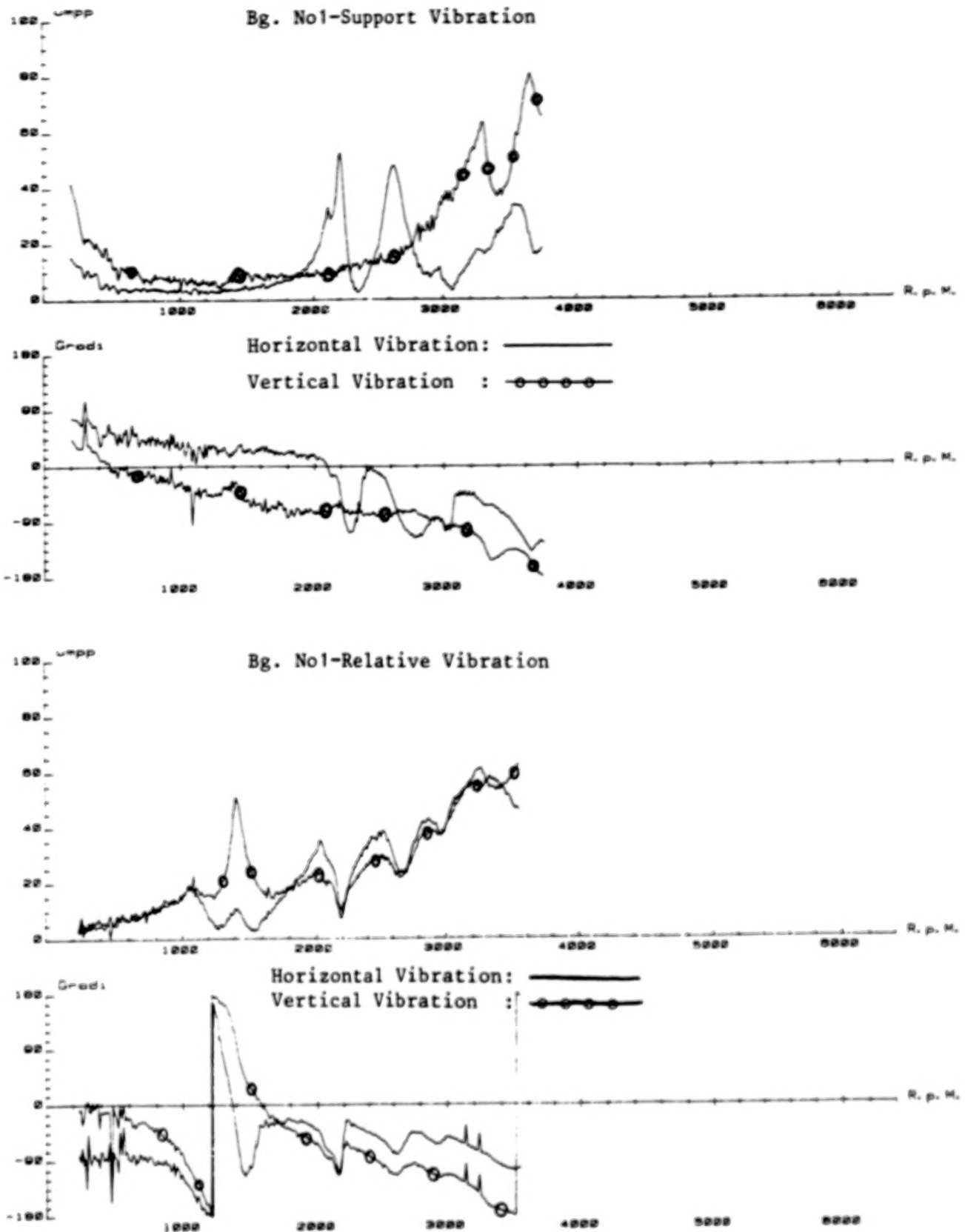


Fig.1 - Speed transient of the alternator rotor

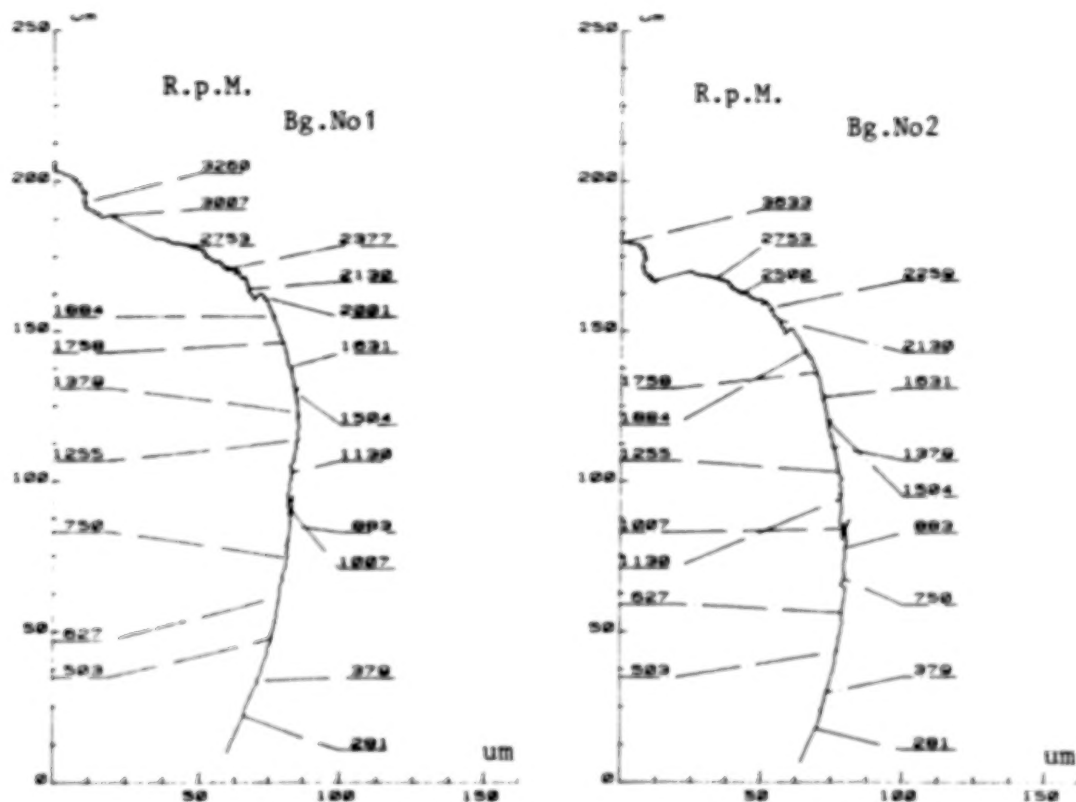


Fig. 2 - Center loci of journal in alternator rotor bearings

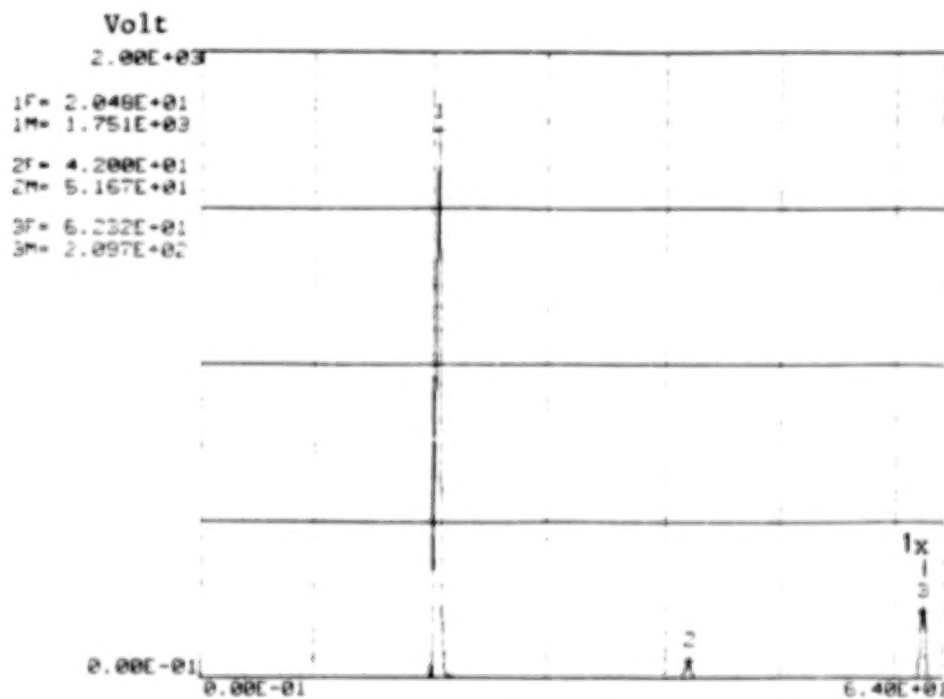


Fig. 3 - Spectrum during the instability of the alternator rotor

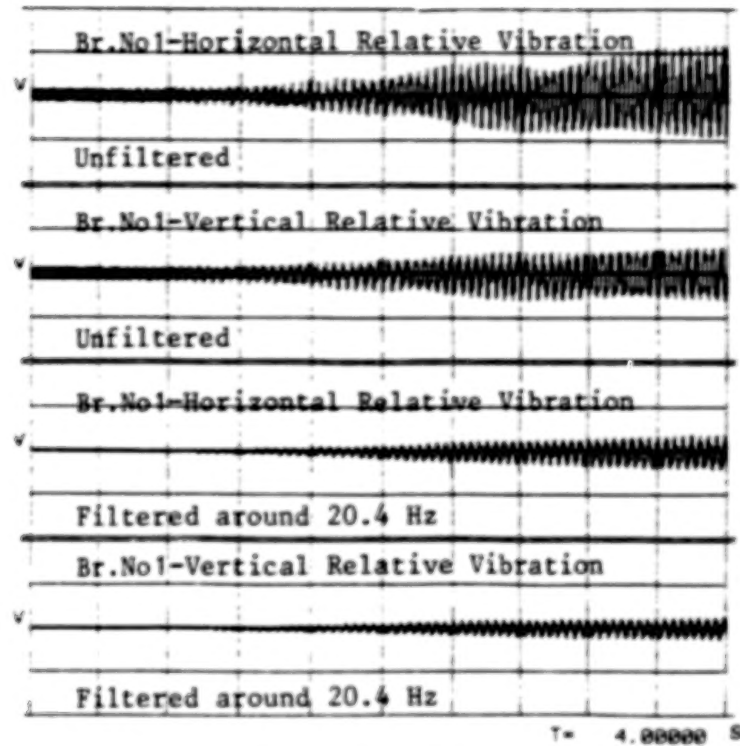


Fig.4 - Development of the instability on the alternator rotor

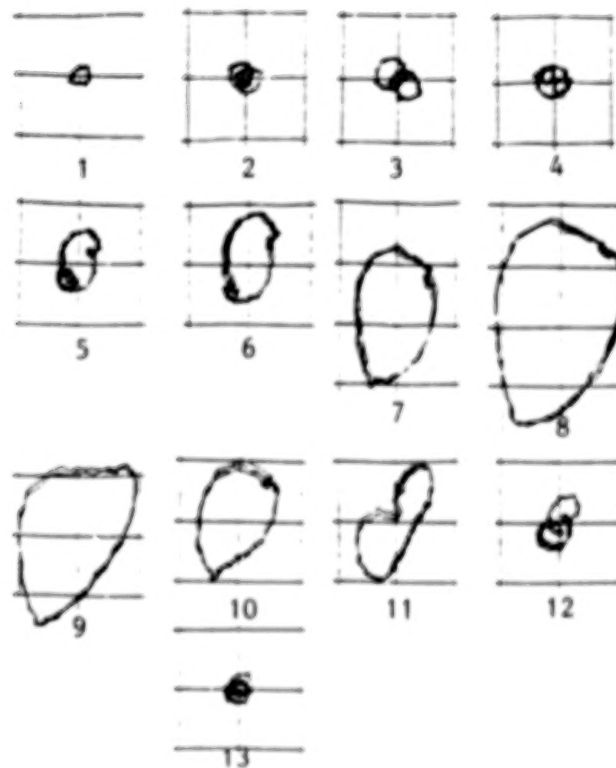


Fig.5 - Journal orbits in bearing No1 during the instability of the alternator rotor

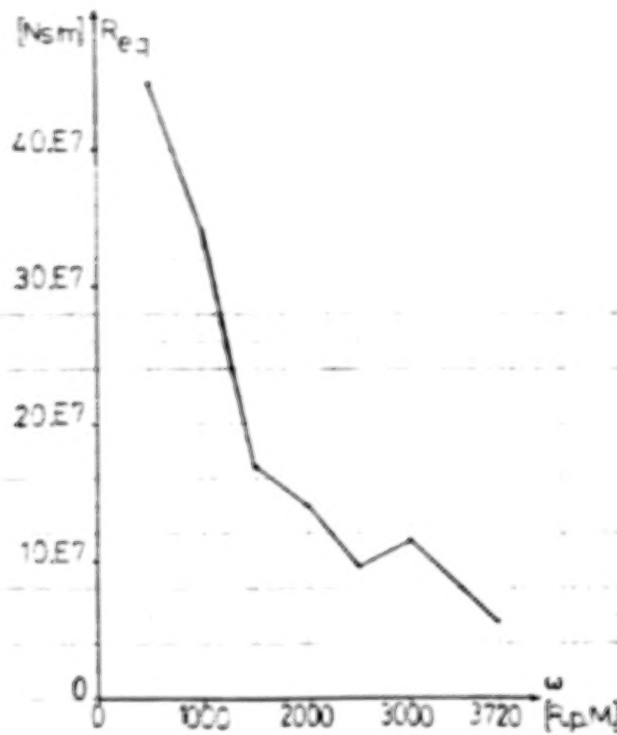


Fig.6 - Equivalent damping coefficient at different speeds of the alternator rotor

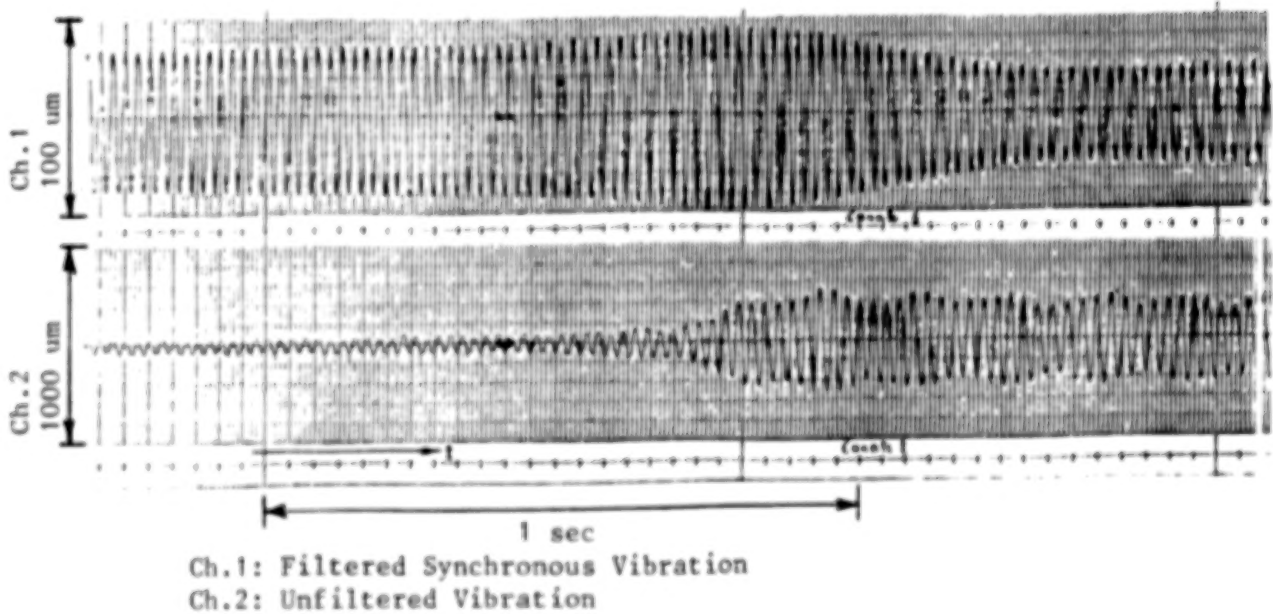


Fig. 7 - Development of the instability in the boiler feed-pump

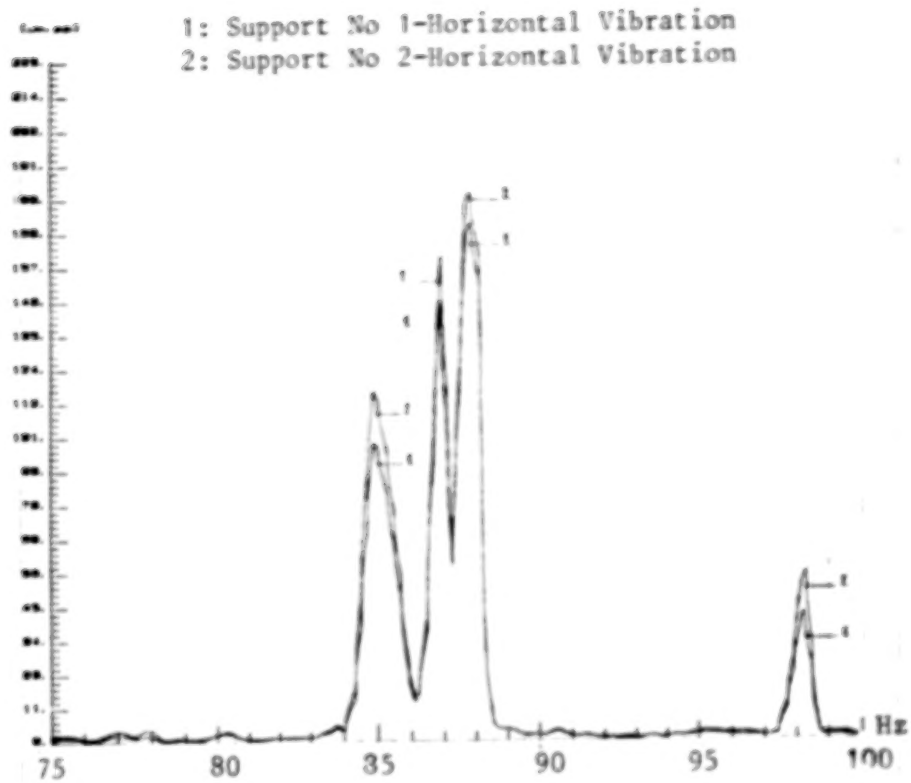


Fig. 8 - Typical spectrum analysis during the instability of the boiler feed pump

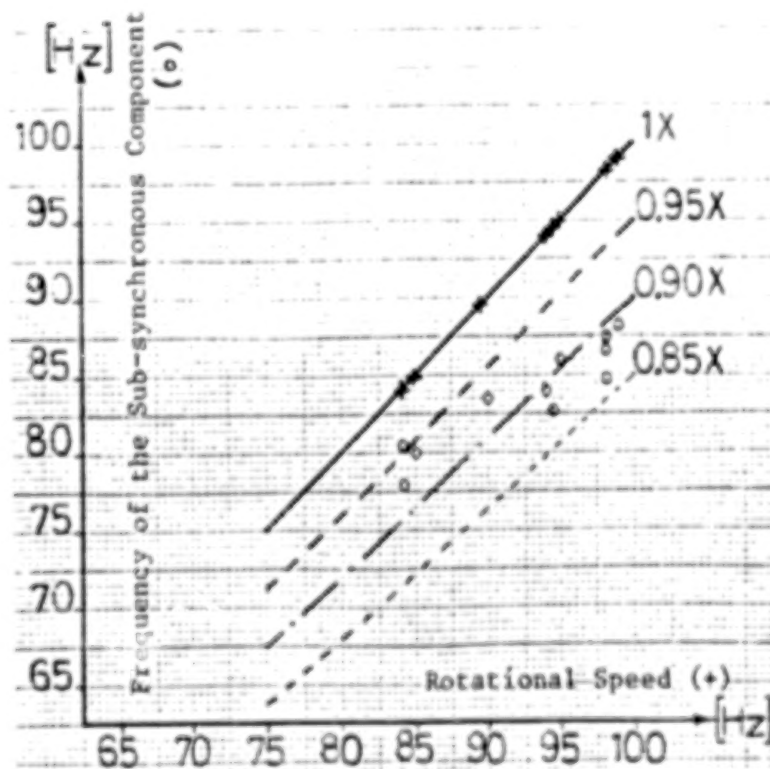


Fig. 9 - Frequency of the sub-synchronous component versus the rotating speed in the instability of the boiler feed-pump

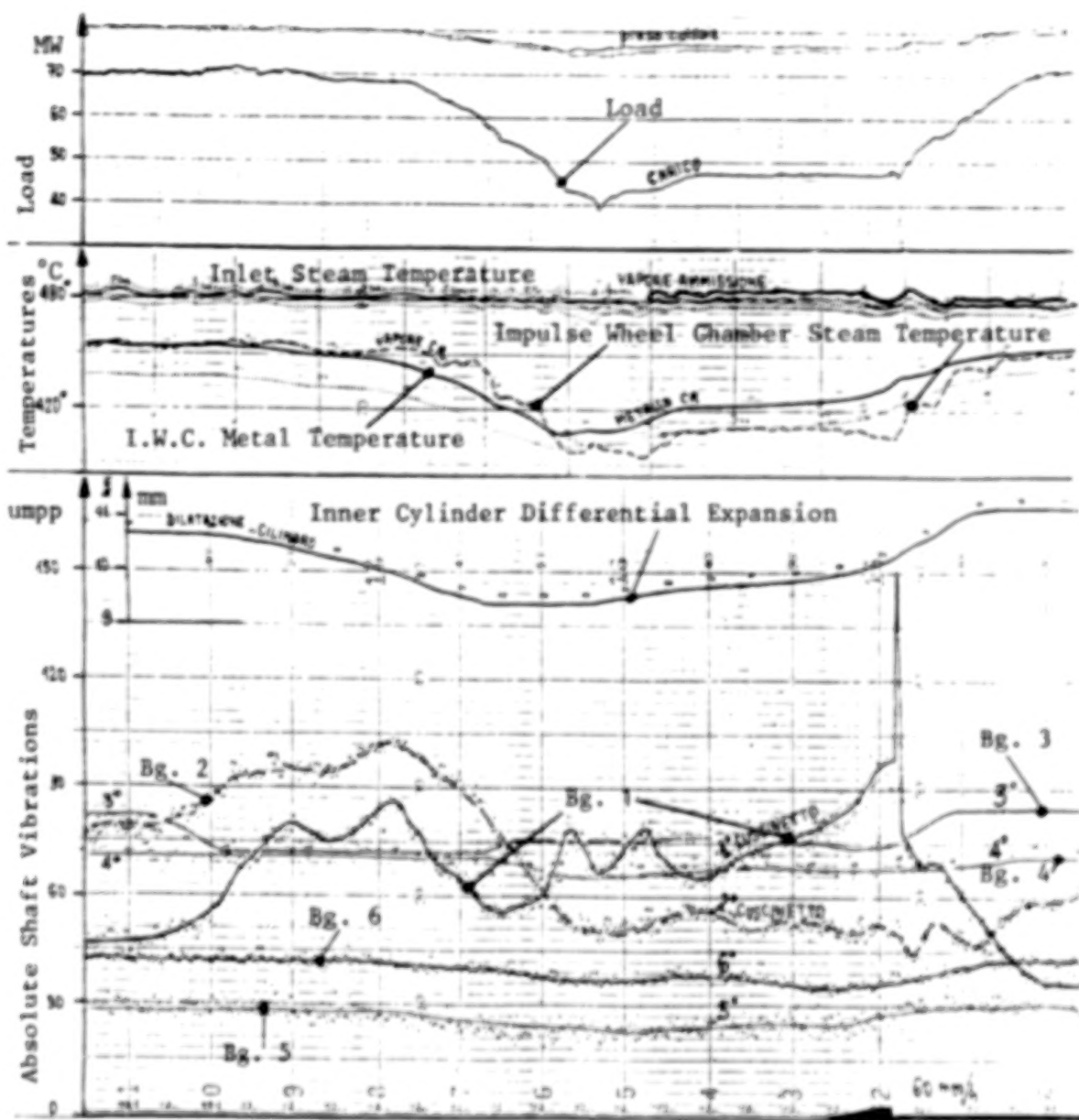


Fig.10 - Surveillance system recordings during a load transient of the H.P. turbine

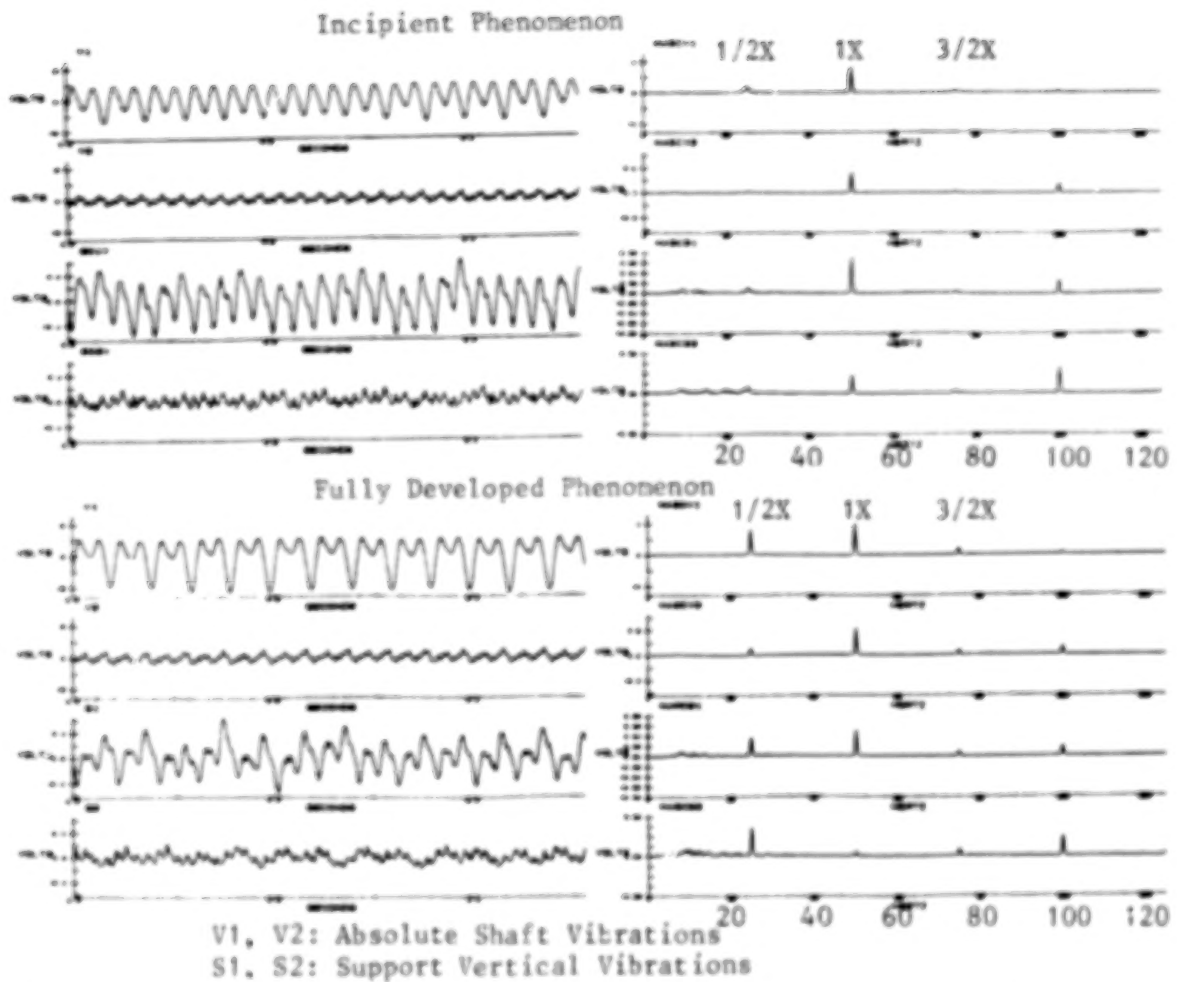


Fig.11 - Time records and spectrum analysis in the instability of the H.P. turbine

BLANK PAGE

THE SPECTRAL ANALYSIS OF AN AERO-ENGINE ASSEMBLY

INCORPORATING A SQUEEZE-FILM DAMPER

R. Holmes and M.M. Dede
Department of Mechanical Engineering
University of Southampton
Southampton, England

Aero-engine structures have very low inherent damping and so artificial damping is often introduced by pumping oil into annular gaps between the casings and the outer races of some or all of the rolling-element bearings supporting the rotors.

The thin oil films so formed are called squeeze film dampers and they can be beneficial in reducing rotor vibration due to unbalance and keeping to reasonable limits the forces transmitted to the engine casing. However, squeeze-film dampers are notoriously non-linear and as a result can introduce into the assembly such phenomena as subharmonic oscillations, jumps and combination frequencies.

The purpose of the research described in this paper is to investigate such phenomena both theoretically and experimentally on a test facility reproducing the essential features of a medium-size aero engine.

The forerunner of this work has been published in refs. [1],[2]. It was concerned with the examination of a squeeze-film damper in series with housing flexibility when supporting a rotor. The structure represented to a limited extent the essentials of the projected Rolls Royce RB401 engine. That research demonstrated the ability to calculate the oil-film forces arising from the squeeze film from known motions of the bearing components and showed that the dynamics of a shaft fitted with a squeeze film bearing can be predicted reasonably accurately.

An aero-engine will normally have at least two shafts and so in addition to the excitation forces which are synchronous with the rotation of one shaft, there will also be forces at other frequencies from other shafts operating on the squeeze-film damper. The present paper is concerned with theoretical and experimental work to consider severe loading of squeeze-film dampers and to include these additional effects. The theoretical methods are similar to those discussed in references [1] and [2].

* Now with General Electric Company, Cincinnati, U.S.A.

NOTATION

a	Mass ratio m_{e2}/m_h
b	Linear damping coefficient
c	Radial clearance of the squeeze-film bearing
d	Seal end-gap
D	Diameter of squeeze-film bearing
F	Amplitude of force transmitted to engine frame
k	Stiffness of the flexible bars 6 in Fig. 2
l	Squeeze-film bearing land width
L	Radial depth of sealing ring
L_g	Width of groove
$m_e c \omega_2^2$	Normalising parameter for forces
m	Rotor mass
$m_{e1,2}$	Effective mass of rotor 1,2.
m_h	Effective mass of rotor 1 plus bell housing 4, squeeze-film bearing housing 5 and flexible bars 6 in Fig. 2.
P_{cav}	Cavitation pressure
P_s	Oil supply pressure
$P_{c1,2}$	Unbalance force on rotor 1, 2
R	Radius of the squeeze-film bearing
$r_{1,2}$	Radius of unbalance of mass $m_{1,2}$ from axis of rotation.
T	Transmissibility = force reaching ground - unbalance force
x	Amplitude of rotor vibration
$u_{1,2}$	Effective radius of unbalance of rotor (1,2) mass from axis of rotation
\bar{w}	$g/c \omega_n^2$

α	ω_1/ω_2
β_n	$\frac{\mu R}{\pi e^2 \omega_n} \left(\frac{l}{c}\right)^3$
λ	Boundary-condition factor
ψ	Attitude angle
e	Eccentricity ratio
μ	Dynamic viscosity
$\mu \omega_n (R/c)^2$	Normalising parameter for pressures
$\omega_{1,2}$	Angular velocity of rotor 1,2.
ω_n	Undamped natural frequency
'	Differentiation with respect to ωt

THE TEST FACILITY

Fig. 1 shows diagrammatically a section through the front end of a modern aero-engine, having two nested rotors. The structure is subjected to a variety of forces, for example forces arising from unbalance in the H.P. rotor are transmitted into bearing housings supporting the L.P. rotor, which often incorporate squeeze film dampers. A test facility was designed to reproduce such essential features of the aero-engine assembly, in particular to examine the vibration of a rotor employing a squeeze-film damper, whose housing can be under the influence of an excitation force which is different in frequency from that of its shaft rotation.

A drawing of the test facility is shown in Fig. 2. The assembly consists of two sub-assemblies comprising rotors 1 and 2, representing the aero engine HP and LP shafts respectively. These are capable of being driven at different speeds by variable-speed motors through pin-and-cord couplings. The unbalance mass 3 produces a dynamic force which is transmitted through the bell-housing 4 to the housing of the squeeze-film damper 5, which is itself flexibly supported at 6 and contains the roller bearing 7. The outer race of this bearing is surrounded by the squeeze-film damper 8, which is provided with either R10 oil or Shell calibration fluid. These have viscosities at room temperature of 15cp and 5cp respectively. The unbalance mass 9 provides a further force at the inner race of the roller bearing, whose movement is permitted by the self-aligning bearing 10 and whose location represents a node of rotor 2.

The damper has two bearing lands which are separated by a central circumferential oil-supply groove. End-plates are attached at both ends of the squeeze film to afford some sealing. The axial end clearance between the plates and the dampers and thus the extent of the sealing can be varied by the

insertion of spacing shims. The rotation of the damper journal is prevented by dogs located in one of the end plates, providing sufficient clearance to allow the journal to move in any part of the squeeze-film clearance space. The squeeze-film damper diameter is set by the outer race of the roller bearing 7 (140 mm). The damper land length and its radial clearance are typical of aero engine application (Fig. 3).

The rig parameters

Preliminary impulse tests were carried out to define the total effective stiffness of the flexible bars 6 and to find the effective masses of rotors 1 and 2 at the squeeze-film location. From tests on the flexibly-mounted housing alone, its natural frequency was found to be 192 Hz. Using an effective housing mass of 3.9 kg the total stiffness of the flexible bars was found to be about 5.68×10^6 N/m. With rotor 2 alone in position, the natural frequency was 75 Hz in the horizontal and 71 Hz in the vertical direction. The difference was almost certainly due to the movement of bearing 7 within its squeeze film annulus. This was empty of oil at the time of testing and promoted bouncing of bearing 7. By taking 73 Hz as an averaged frequency, the effective mass of rotor 2 was found to be 22.16 kg. A similar test was carried out with rotor 1 in position and with rotor 2 removed, and finally with both rotors in position. Table 1 shows the findings of all the tests in a concise form.

Table 1

Arrangement	Horizontal (Hz)	Vertical (Hz)	Effective mass (kg)	Accepted Natural Freq. (Hz)
Squeeze film (SF) housing only	192	192	3.9	192
Rotor 2 and SF assembly	75	71	22.2 (rotor 2 only)	73
Rotor 1 and SF assembly	94	103	10.0 (rotor 1 only)	98
Rotors 1 and 2	61.2	63.6	32.4	62

The undamped natural frequency of the complete assembly was taken as 62 Hz (3720 c/min) and it can be seen that the effective mass in the last case is about equal to the sum of those in the previous two cases. The static load

provided by rotor 2 on the squeeze-film was half its weight, corresponding to 50/2 or 25 kg. The dynamic loads arose from the unbalance masses 3 and 9, and can be expressed as $P_{c1} = m_1 r_1 \omega_1^2$ and $P_{c2} = m_2 r_2 \omega_2^2$, where m_1 and m_2 are respectively the unbalance masses on rotors 1 and 2, r_1 , r_2 are the radii of the mass locations from the centre of rotation of each shaft, and ω_1 and ω_2 are the speeds of the shafts. However, in the analysis it is more convenient to consider the unbalance mass-radius product to have a magnitude equal to the total effective mass of each rotor at an effective unbalance radius u .

SINGLE-SHAFT VERSION OF THE TEST FACILITY

The test facility was first separated into its two rotor components by removing the bell housing 4. Tests were carried out on the LP rotor (2) alone mounted in the squeeze-film damper to investigate its performance characteristics.

A diagrammatic representation of the test facility in this configuration is given in Fig. 4. The degree of damping offered by the squeeze-film is quite critical. If it is too great the damper operates rather like a rigid link and conveys little benefit to the system. On the other hand if the damping is too small, excessive movements take place in the squeeze film annulus.

Assuming for a moment that the damping is linear, its effect in series combination with the rotor mass and housing flexibility is shown in Figs. 5a, b, c. From these figures it can be seen that there is likely to be an optimum value of damping b to ensure reasonable levels of rotor vibration relative to the engine frame (Fig. 5a), relative to the bearing housing (Fig. 5b) and of transmissibility (Fig. 5c). Complications are introduced by the fact that due to non-linearity of the squeeze-film its damping increases greatly with eccentricity ratio e . Fig. 5b indicates that high values of e can arise over a considerable frequency range, particularly at low values of b . Under these conditions the apparent benefits of low damping indicated in Figs. 5a and 5c may not be realised.

The most critical operating condition occurs at a speed corresponding to the natural frequency of the assembly, $\frac{\omega^2}{\omega_n^2} = 1$. From Figs. 5a,b,c. three distinctive features can be observed.

- a) The non-dimensional amplitude of vibration of the rotor x_2/u increases with non-dimensional damping b/\sqrt{km} .
- b) The non-dimensional eccentricity of the rotor in the squeeze-film damper, $e/(u/c)$, is independent of non-dimensional damping b/\sqrt{km} , where $e = (x_2 - x_1)/c$.
- c) The transmissibility T increases with non-dimensional damping b/\sqrt{km} .

Thus the assembly is quite unlike one having a damper in parallel with its flexibility.

BEST COPY AVAILABLE

Preliminary tests were first run on the reduced test facility to ascertain whether these trends were exhibited in the actual non-linear system. Various means were adopted by which the effective damping could be altered. For example, damping could be increased by

- i) increasing the oil viscosity
- ii) tightening the sealing, or
- iii) increasing the supply pressure.

Figs. 6a, b, c show the results obtained for various sealing conditions, oil viscosities and supply pressures. From these, conclusions can be drawn which are consistent with the three distinctive features using the linear damping model. This model thus provides a reasonable qualitative guide to damper performance in the most critical region of rotor operation.

The next purpose of the reduced test facility was to look for evidence of jump phenomena and sub-harmonic vibrations in the frequency responses as these had been observed in certain engine tests where the oil viscosity was low.

Efforts were therefore made to produce conditions on the test facility, which were likely to be conducive to such jumps. This indeed proved to be possible when the support flexibility was locked out and when the supply pressure to the squeeze-film was at a fairly low level. Fig. 7a shows a sequence of orbits of rotor vibration relative to the squeeze-film damper housing using a supply pressure of 5 psi. At about 3450 rev/min a pronounced jump up was observed. This was almost certainly due to a change in the effective parameters governing system performance. This change was probably brought about by sudden venting of the squeeze film clearance space from atmosphere, resulting in a change of level at which the negative hydrodynamic pressure in the squeeze film was curtailed. Fig. 7a shows a set of pressure recordings which seem to bear this out. This would result in much smaller squeeze-film forces and hence a much larger orbit of vibration of the rotor centre, and can be predicted by numerical computation (Fig. 7b). For the latter purpose, the hydrodynamic squeeze-film forces were numerically derived by integrating the oil-film pressure around the circumference of the damper. These forces depend on the oil-film cavitation model used and on the end-plate clearance expressed as a λ factor [2]. The λ -factor describes the boundary conditions imposed at the ends of the squeeze-film damper by the tightness of the end-seals and in the present research has been extended to cover various l/d ratios (Fig. 7c). In the present case where the l/d ratio is 0.045 a λ -factor of 0.09 was used, being appropriate to an end plate gap/clearance ratio of 0.23 and an end-plate clearance of 0.053 mm. The non-linear equations of motion were then solved by integration at each time step of a marching scheme.

With regard to subharmonic vibrations, Fig. 8a shows a succession of orbits of the LP shaft (2) relative to the squeeze-film housing for a u/c value of 0.33 and using Shell calibration fluid as the lubricant. The speed range covered was 3630 to 5075 rev/min, with the undamped natural frequency at 4300 rev/min (71 Hz). The centre of the LP rotor executed a butterfly type of motion, such that it completed each "wing" for alternate revolutions of the

rotor. This half-engine order motion persisted over a wide range of operational speed. Eventually the "wings" coalesced after the critical speed was passed to produce an essentially single orbit. The predicted orbits for the same speeds are shown in Fig. 8b, in which the same double looping is clearly evident. Coalescing is predicted somewhat later in the speed range than was measured.

Z-MODULATION

The z-mod technique presents a great deal of useful information on the harmonic content of a signal in a very compact way and by this means it is possible to appreciate an overall performance signature of an engine over a wide speed range. A z-mod is similar to a "waterfall" diagram used in rotating machinery diagnostics except that engine speeds are arranged along the x axis, instead of along the y axis, frequency content is displayed along the y axis instead of along the x axis and the strength of a frequency component is represented as a colour (or as a degree of blackness) instead of a laid-back peak.

By way of elucidating this technique, consider Fig. 9a which shows an experimental z-mod of horizontal components of LP rotor vibration relative to the squeeze-film housing using a specially-adapted commercial spectral analyser. It will be observed that half-integer order frequency components manifest themselves strongly around the natural frequency of 73 Hz.

Software was developed to obtain theoretical z-mods with the wide range of colours available on many microcomputers. This made possible direct comparisons of predictions with the experimental z-mods.

The z-mod presentation of numerically-predicted horizontal LP shaft vibration relative to the squeeze-film damper housing is shown in Fig. 9b, and compares well with the experimental z-mod of Fig. 9a. Half engine orders are indeed predicted around 73Hz. This is due to squeeze-film non-linearities manifesting themselves when the overall vibration becomes appreciable, as it does around the natural frequency of 73Hz.

Half-integer orders are a common feature in loose assemblies [3]. It is not unreasonable to suppose that in the present case the squeeze-film damper clearance was acting as a loose assembly on account of the fairly high unbalance load together with the fairly short squeeze-film damper lands and the low viscosity of the oil supplied. When heavier oil was introduced all half-integer order harmonics disappeared.

A non-linear system can be conceived in which a subharmonic may be excited, whose frequency is half that of the excitation frequency. To show that this is possible, consider a system with a square-law restoring force subject to a steady force (such as gravity) and to harmonic excitation (such as that due to unbalance), both of which are provided by the test facility. Let the system satisfy the differential equation,

$$m\ddot{x} + \gamma\dot{x} + \alpha x^2 = P_0 + P_1 \cos \omega t. \text{ say}$$

that is, the effective stiffness of the squeeze film is $\gamma - \Omega x$.

Let us assume that a possible solution is

$$x = A \cos \frac{\omega}{2} t.$$

$$\text{Thus } A(\gamma - \frac{m\omega^2}{4}) \cos \frac{\omega t}{2} - \frac{\Omega A^2}{2} + \frac{\Omega A^2}{2} \cos \omega t = P_0 + P_1 \cos \omega t$$

This equation is satisfied for

$$A = \left(\frac{2P_0}{\Omega} \right)^{\frac{1}{2}}$$

$$A = \left(\frac{2P_1}{\Omega} \right)^{\frac{1}{2}}$$

$$\text{and } \omega = 2\sqrt{\frac{\gamma}{m}}$$

The first two conditions imply that $P_0 = P_1$, which happens to be conducive to rattle since then the gravity force P_0 is just neutralised by the dynamic lift-off force P_1 . This example shows that a second harmonic, resulting from the non-linear term, can prevail, being compensated by a certain intensity of excitation at some specific frequency. This frequency is illustrated most strikingly when a squeeze-film damper is accompanied by a parallel spring of stiffness γ . In that case ω corresponds to twice the first undamped natural frequency and a subharmonic resonance of order $\frac{1}{2}$ is exhibited [4].

Since both harmonics and subharmonics can occur simultaneously, oscillations having any half integer ratios to the excitation frequency are possible, given the correct form of non linearity. These oscillations are in fact combination frequencies and will be discussed later.

THEORETICAL ANALYSIS FOR COMPLETE CONFIGURATION OF THE TEST FACILITY

The dynamically-equivalent structure of the test facility with both rotors connected is shown in Fig. 10. It may be shown [2] that a set of non-dimensional parameters which describe this non-linear system can be expressed as \bar{W} , \bar{P}_n , $u_{1,2}/c$, α , ω_2/ω_n , $P_{cav}/\mu\omega_n(R/c)^2$, and $P_s/\mu\omega_n(R/c)^2$.

The non-linear equations of motion were solved by again integrating at each time step of a marching scheme. To obtain a feel for the kind of results obtained, Fig. 11a shows a typical vibration orbit for the housing of the squeeze-film bearing relative to ground while Fig. 11b shows the vibration

orbit of rotor 2 relative to ground. In Fig. 11c the orbit of rotor vibration relative to the squeeze-film housing is shown. For these cases the following values were applied:

No-end sealing	$\bar{W} = 0.25$	$\alpha = 2.0$
	$\mu_n = 0.016$	$\alpha = 1.5$
	$\mu \omega_n (R/c)^2 = 154.5 \text{ psi}$	$\omega_2/\omega_n = 0.93$
	$u_1/c = 0.23$	$P_{cav} = -20 \text{ psi}$
	$u_2/c = 0.23$	$P_s = 20 \text{ psi}$

By putting $\alpha = -2.0$, counter-rotation of rotor 1 relative to rotor 2 is represented. The resulting orbits for this condition are shown in Fig. 12 in the same sequence as for Fig. 11. The same cases were then treated with end-plates included (Fig. 13). These last orbits indicate a much more stable system and steady states are achieved much more quickly, due to the higher damping ensured by the end plates.

COMPARISON OF NUMERICAL ORBITS AND EXPERIMENTAL OBSERVATIONS FOR COMPLETE CONFIGURATION OF THE TEST FACILITY

Fig. 14 shows a specimen set of comparisons of rotor 2 vibration orbits relative to the ground, when rotating at 3000 rev/min with rotor 1 stationary. For these comparisons the full non-linear equations were solved again using the λ -factor approach developed in ref. [2]. Fig. 14 is for a case of fairly tight sealing ($\lambda = 0.0356$) and the agreement between experimental and predicted orbits of vibration is seen to be reasonable, the scale factors used for each set of orbits being the same. This agreement is representative of comparisons over a wide range of speeds, oil viscosities, supply pressures and unbalances and a cavitation pressure of -20 psi has been used throughout.

Consider now cases in which rotors 1 and 2 rotate in first co-rotation and then counter-rotation relative to each other. Detailed comparisons between predicted and experimental orbits are not appropriate here due to the indeterminacy of the phasing between shafts 1 and 2 arising from slight drifts in speed. However it is possible to observe certain distinctive features from comparisons of experimental orbits of rotor vibration relative to ground for the co-rotating and counter-rotating cases. The same distinctive features can then be sought in the comparison of the numerically-predicted orbits.

Some experimental orbits are shown in Figs. 15 and 16 (upper) for $\omega_1/\omega_2 = \pm 1.3$. The most distinctive differences are observed to be the rounded nature of the orbits for the co-rotating cases as opposed to the spiky nature for the counter-rotating. The same features can be observed in the numerically-predicted orbits, Fig. 15 and 16 (lower). In addition, there is broad agreement on orbit size.

BEST COPY AVAILABLE

It was noticeable during running that the test facility was much more noisy for counter rotation, suggesting that transmitted forces were higher, perhaps due to the more sudden reversals in the orbits.

FREQUENCY CONTENT OF SYSTEM VIBRATION WHEN SHAFTS ARE IN CO-ROTATION AND IN COUNTER-ROTATION : COMBINATION FREQUENCIES

In a linear system resonance occurs when the system is excited by a harmonic force of frequency near to the undamped natural frequency of the system. In a non-linear system other kinds of resonance are possible.

Consider a non-linear system subject to an excitation consisting of two harmonic components as we have in this test facility. Thus,

$$m\ddot{x} + f(x) = P_1 \cos(\omega_1 t - \theta_1) + P_2 \cos(\omega_2 t - \theta_2)$$

in which we can expand $f(x)$ in the form of a Taylor series,

$$f(x) = a_1 x + a_2 x^2 + a_3 x^3 + \dots$$

Now assume that x is roughly harmonic, that is

$$x = X_1 \cos \omega_1 t + X_2 \cos \omega_2 t$$

Thus $f(x)$ will consist of terms in

$$\cos \omega_{1,2} t$$

$$\cos^2 \omega_{1,2} t = \frac{1}{2} (1 + \cos 2\omega_{1,2} t)$$

$$\cos^3 \omega_{1,2} t = \frac{3}{4} \cos \omega_{1,2} t + \frac{1}{4} \cos 3\omega_{1,2} t$$

$$\cos \omega_1 t \cos \omega_2 t = \frac{1}{2} \cos(\omega_1 - \omega_2)t + \frac{1}{2} \cos(\omega_1 + \omega_2)t$$

$$\cos 2\omega_1 t \cos \omega_2 t = \frac{1}{2} \cos(2\omega_1 - \omega_2)t + \frac{1}{2} \cos(2\omega_1 + \omega_2)t \text{ etc.}$$

All possible linear combinations of the two frequencies ω_1 and ω_2 thus appear and in general it can be said that the solution will contain the frequencies

$$n\omega_1$$

$$m\omega_2$$

$$\text{and } n\omega_1 \pm m\omega_2$$

where m and n are whole numbers, the latter being known as combination oscillations. They also manifested themselves in half-integer orders during tests on the single-shaft version of the test facility (Fig. 9).

Fig. 17 shows experimental z-modes for cases of co-rotation and counter-rotation in which $\omega_1/\omega_2 = \pm 1.3$. These relate to vertical vibration of the squeeze-film housing relative to ground. Many LP and HP engine orders are

present in both, as are probable combination frequencies. By taking a vertical section of the z-mod at L.P. rotor speeds of say 40, 60 and 75 rev/s, frequency spectra can be constructed. Figs. 15a, b show such spectra for co-rotation and counter-rotation respectively. Some suggestions are made on Fig. 15 as to what these frequencies might be in terms of HP and LP rotor speeds.

CONCLUSIONS

The purpose of the research described in this paper has been to reproduce on a test facility phenomena exhibited in aero-engine tests. These included subharmonic oscillations, jumps in frequency response and combination frequencies. All of these effects were reproduced and could be predicted by numerical computation or by appreciation of non-linear mechanics. Furthermore, at speeds in the vicinity of the undamped natural frequency, a linear treatment gave a sound understanding of trends in vibration performance.

A method was presented by which the above features could be appreciated in a comprehensive way. This is known as the z-modulation technique and utilises up-to-date computer graphics facilities.

REFERENCES

- [1] Holmes, R. and Dogan, M. 'Investigation of a rotor bearing assembly incorporating a squeeze film damper bearing.' Proc. Instn. Mech. Engrs. vol. 24, No. 3, 1982.
- [2] Holmes, R and Dogan, M. 'The performance of a sealed squeeze-film bearing in a flexible support structure.' Proc. Instn. Mech. Engrs. vol. 199, No. C1, 1985.
- [3] Angelo, M. 'Vibration Monitoring of Machines. Brüel nd Kjoer Technical Review No. 1 1987, pp.5,6.
- [4] Nikolajsen, J.L. and Holmes, R. 'Investigation of squeeze-film isolator for the vibration control of a flexible rotor.' Proc. Instn. Mech. Engrs. vol. 21, No. 4, 1979.

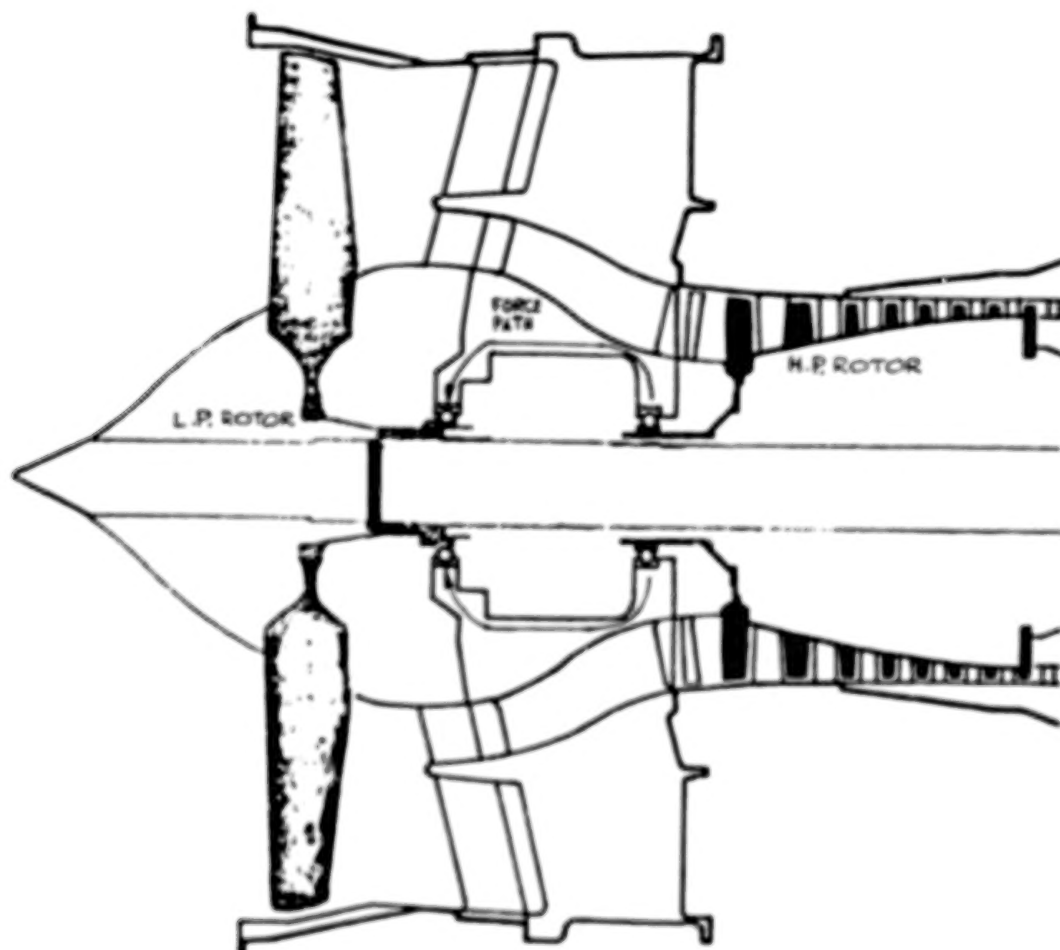


Fig. 1 : Diagrammatic section through aero-engine front end.

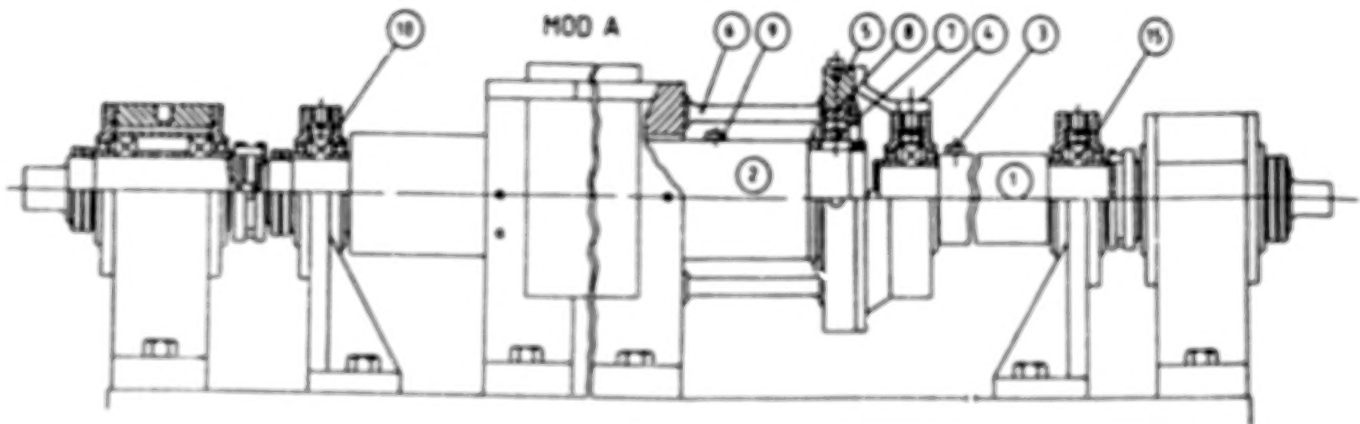
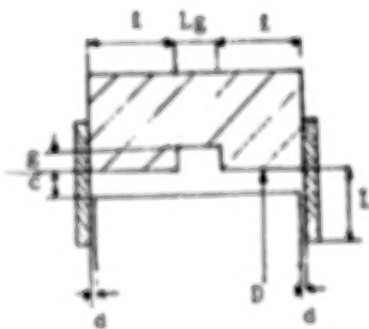


Fig. 2 : Experimental test facility.

- 1 Rotor 1
- 2 Rotor 2
- 3 Unbalance mass
- 4 Bell housing
- 5 Squeeze-film housing
- 6 Flexible bars
- 7 Roller bearing
- 8 Squeeze-film damper
- 9 Unbalance mass
- 10 Self-aligning bearing



$c = 0.23 \text{ mm}$
 $d = 0.076 \text{ mm}$
 $D = 140 \text{ mm}$
 $g = 0.63 \text{ mm}$
 $l = 6.26 \text{ mm}$
 $Lg = 7.00 \text{ mm}$
 $L = 7.76 \text{ mm}$

Fig. 3 : Damper geometry.

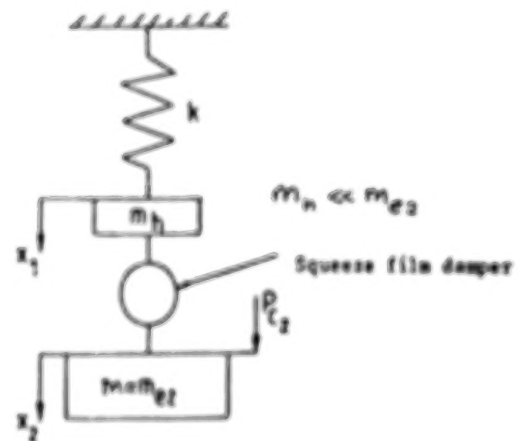


Fig. 4 - Mathematical model of the rig.

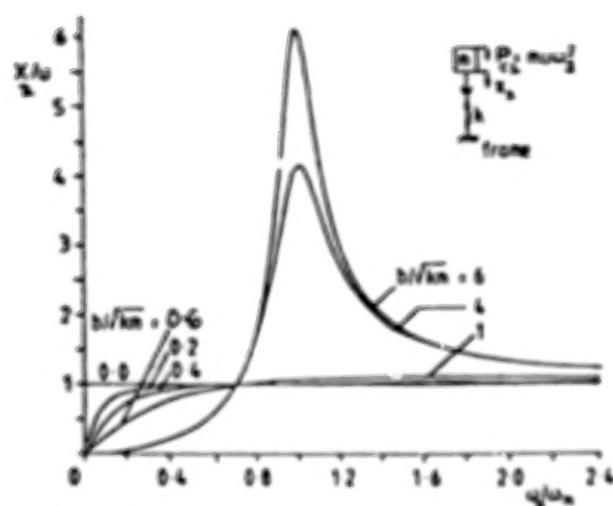


Fig. 5a - Amplitude of rotor vibration relative to engine frame.

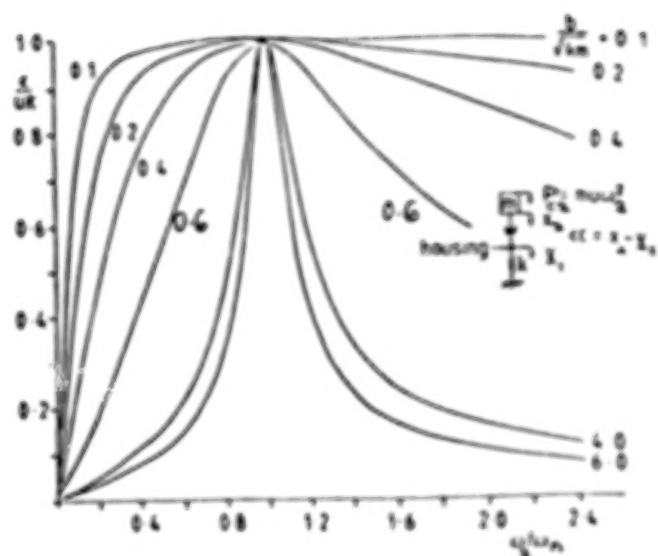


Fig. 5b - Amplitude of rotor vibration relative to damper housing.

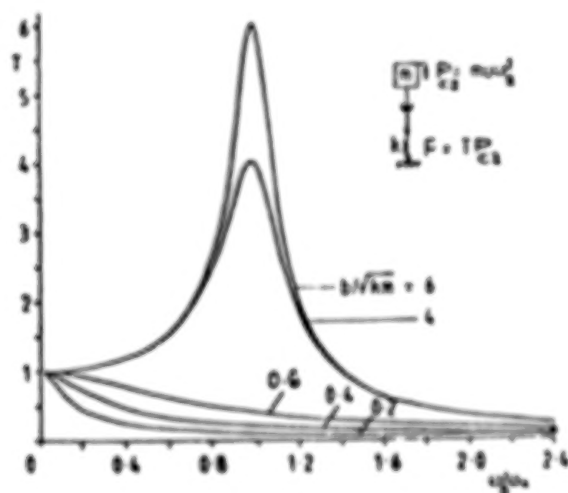
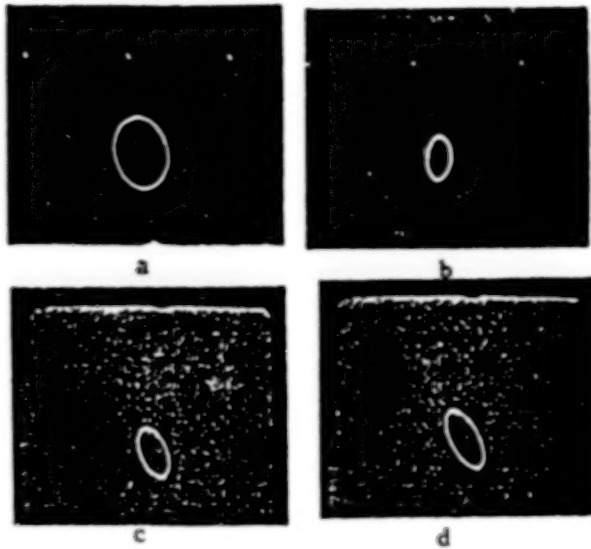


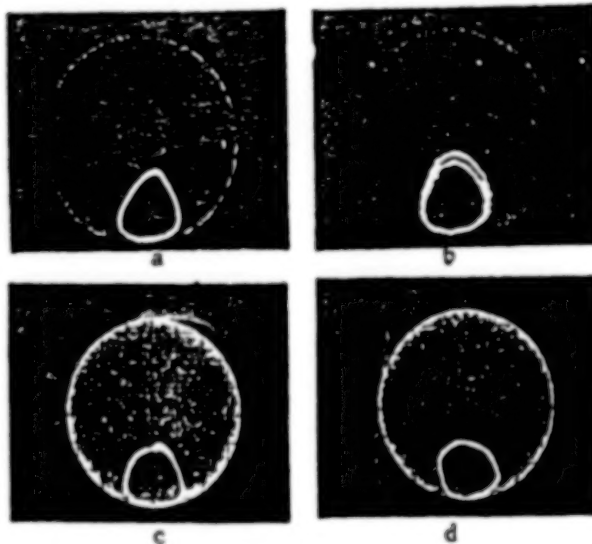
Fig. 5c - Transmissibility.



Rotor vibration relative to engine frame

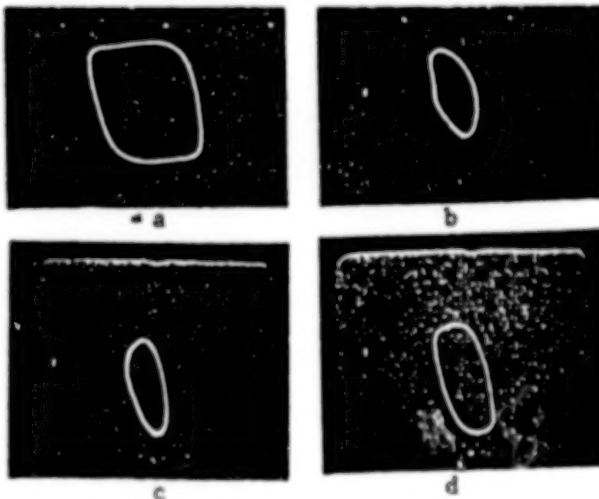
Fig. 6 : Experimental orbits.

$$\frac{\omega_2}{\omega_n} = 1, \frac{u}{c} = 0.23$$



Rotor vibration relative to the bearing housing

- a) sealing tight
viscosity high
supply pressure low
- b) sealing loose
viscosity high
supply pressure low
- c) sealing tight
viscosity low
supply pressure low
- d) sealing tight
viscosity low
supply pressure high



Transmissibility

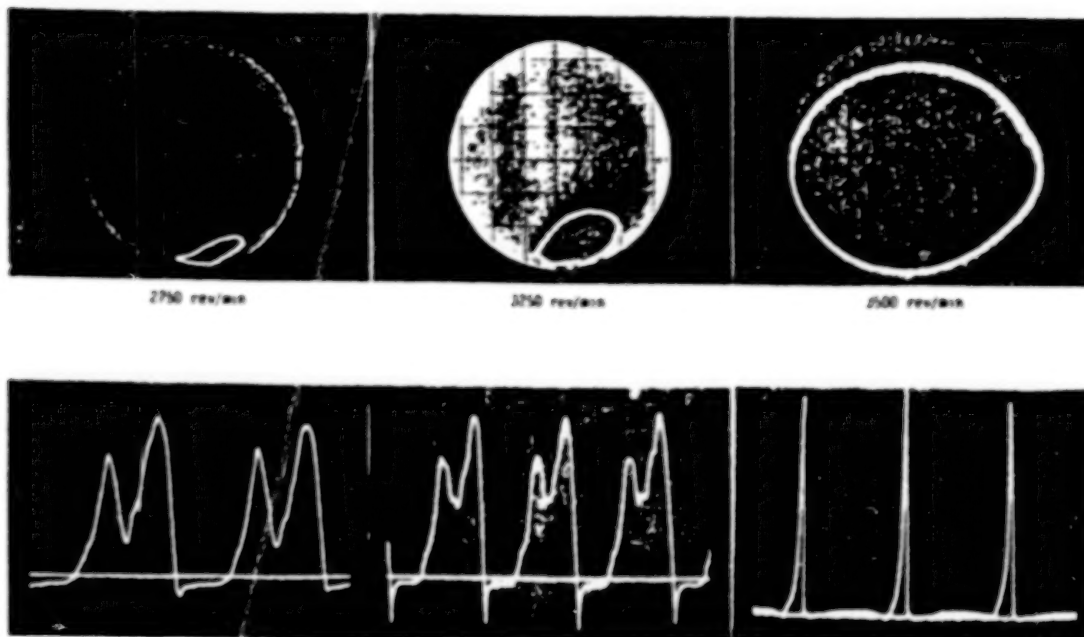


Fig. 7 : (a) Experimental orbits and pressure recordings
(1 cm = 200 psi), $u/c = 1.055$.

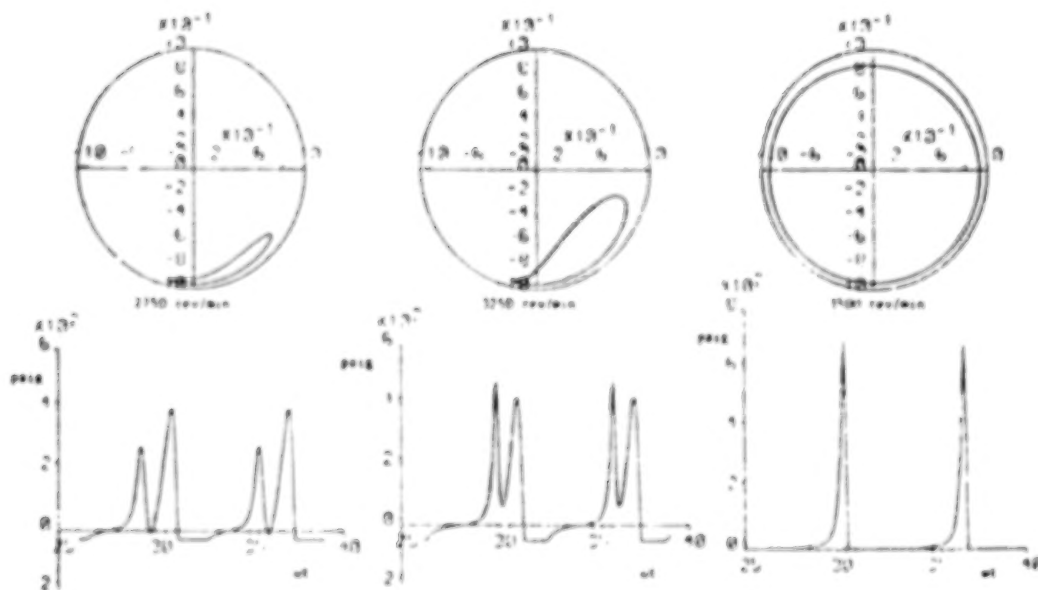


Fig. 7 : (b) Numerical orbits and pressures, $u/c = 1.055$.

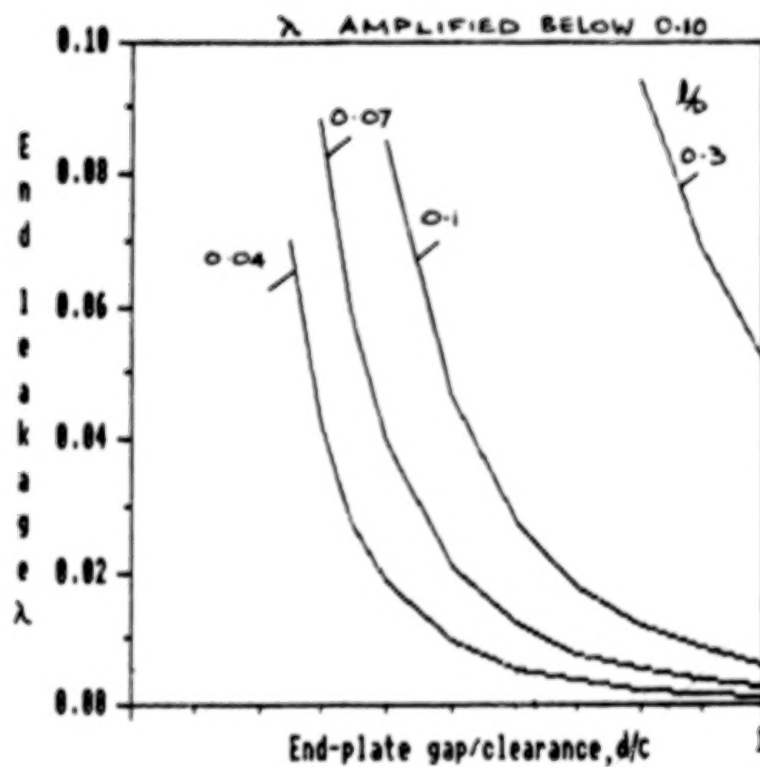
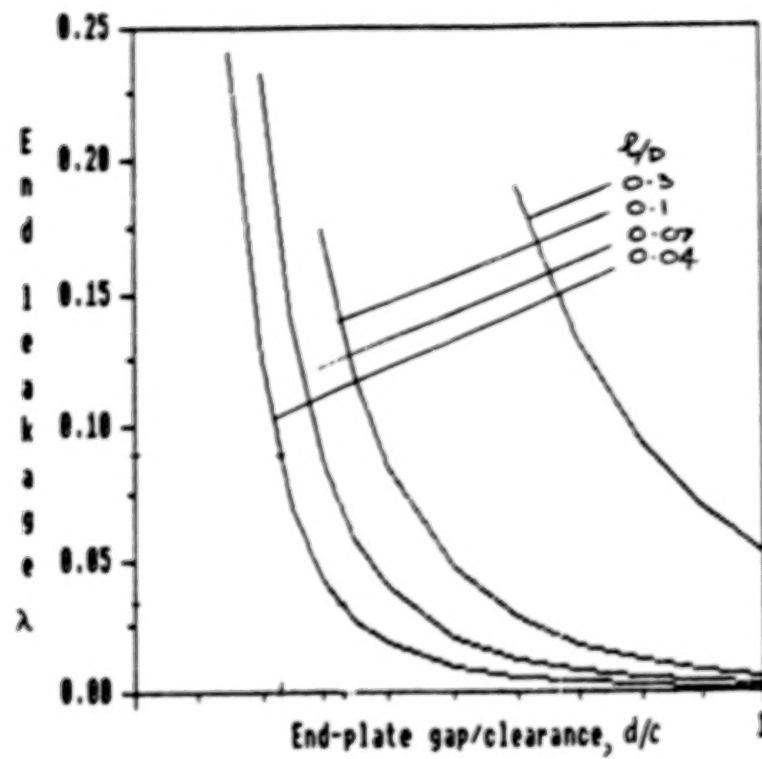
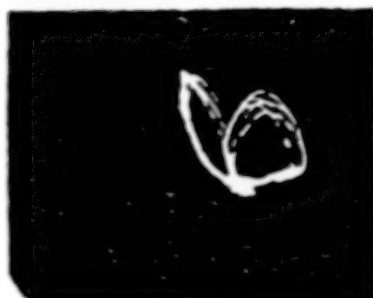


Fig. 7c - λ values for different l/D ratios.



3680 rev/min



4059 rev/min



5075 rev/min

a) Experimentally-observed orbits



3680 rev/min



4059 rev/min



5075 rev/min

b) Numerically-predicted orbits

Fig. 8 : Subharmonic vibrations.

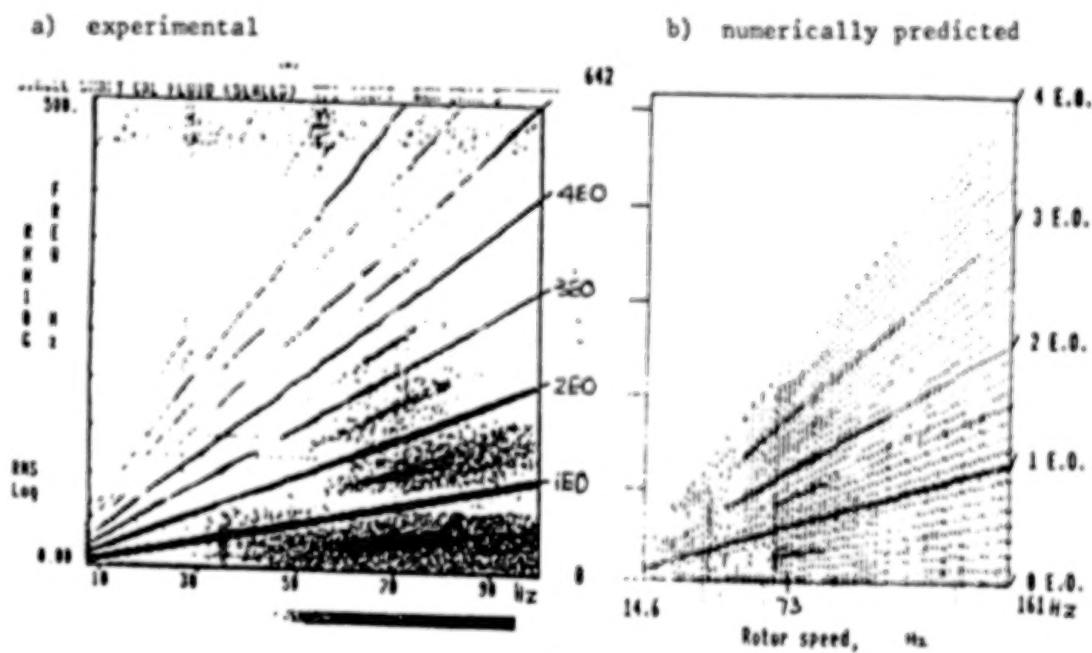


Fig. 9 : z-modulations of horizontal LP rotor vibration relative to the squeeze-film housing.

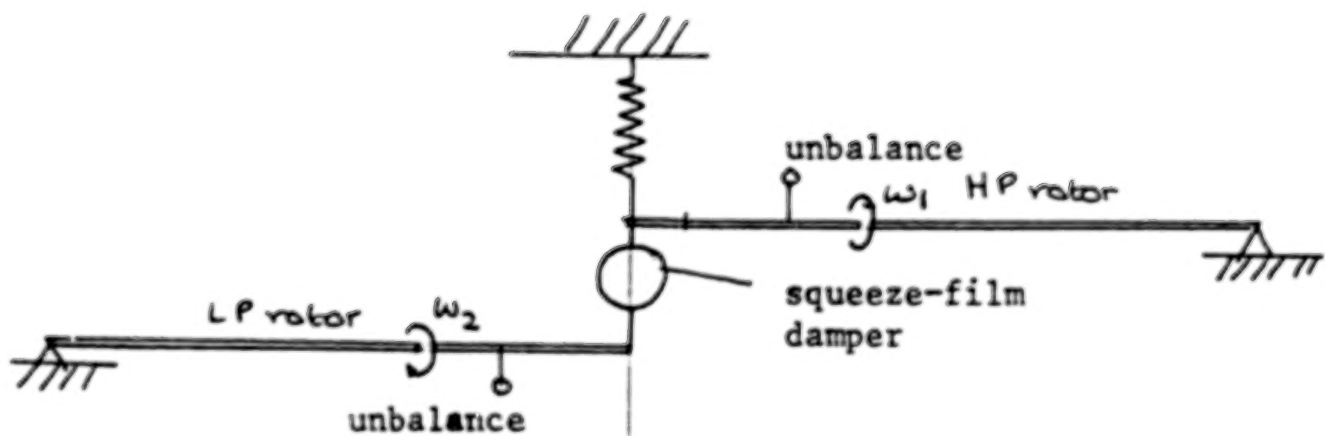
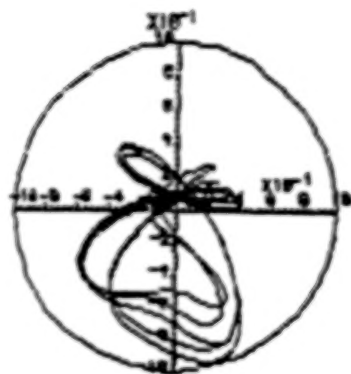
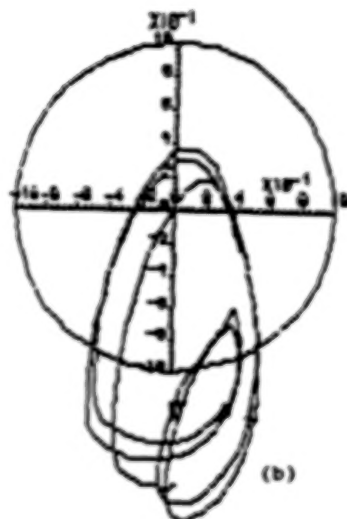


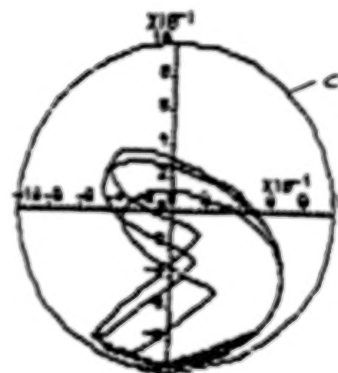
Fig. 10 - Line diagram of test rig.



(a)



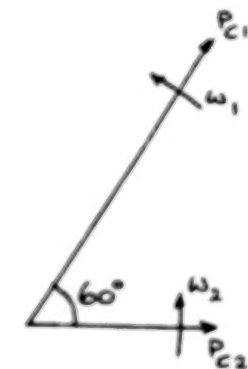
(b)



(c)

clearance circle

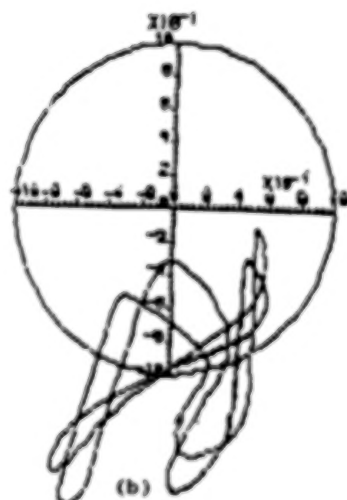
Fig.11 $\omega_{1,2}$ in same directions.
 $\omega_1/\omega_2 = 2$



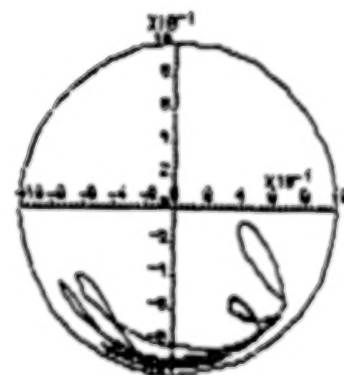
phasing at $t=0$



(a)

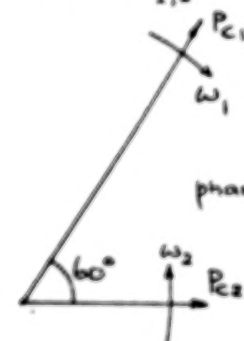


(b)

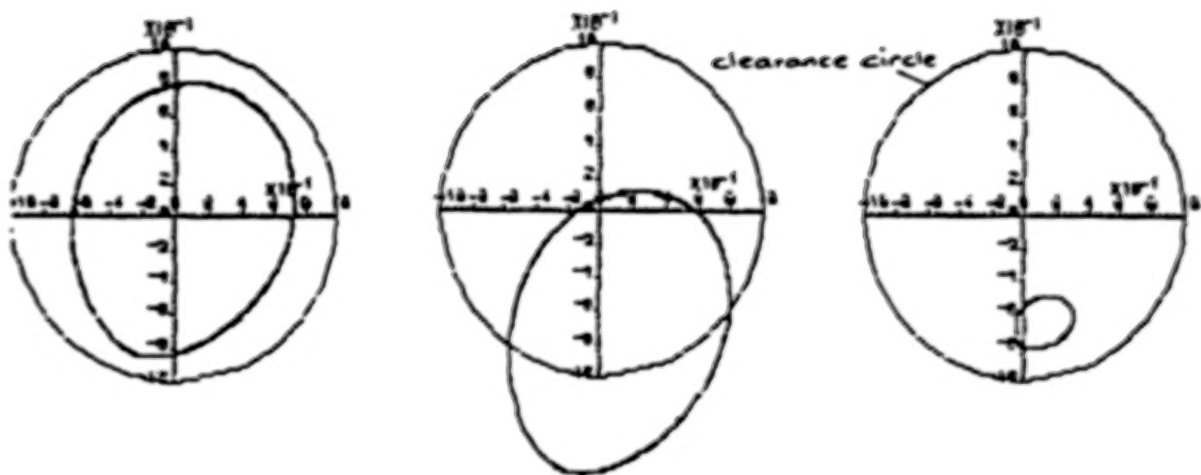


(c)

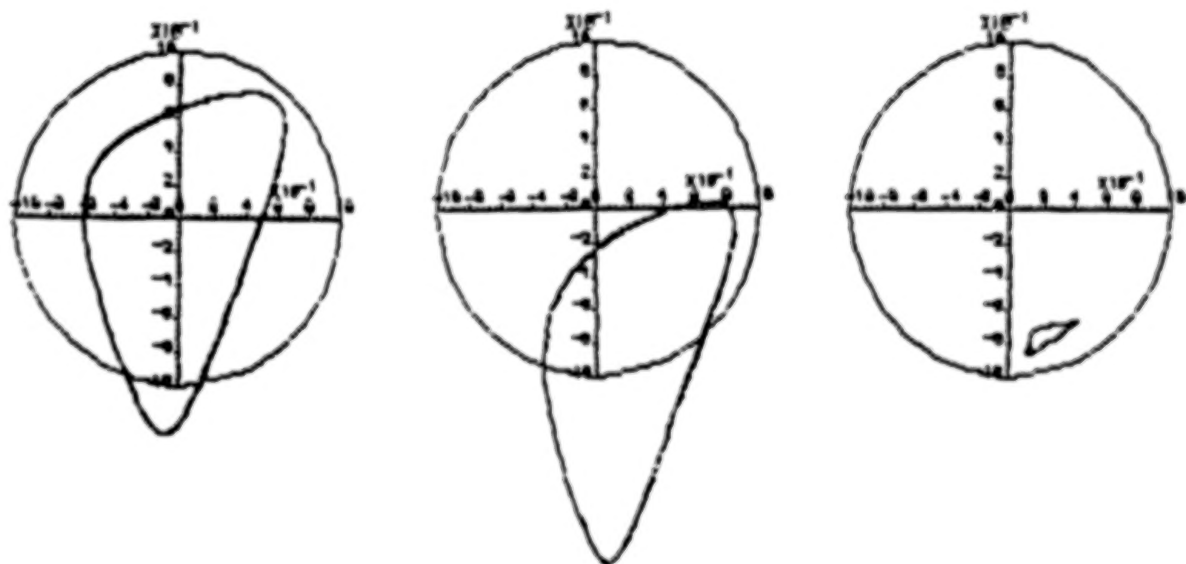
Fig.12 $\omega_{1,2}$ in opposite directions.
 $\omega_1/\omega_2 = 2$



phasing at $t=0$

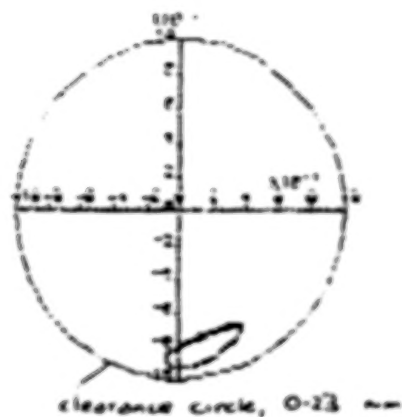


$\omega_{1,2}$ in same directions



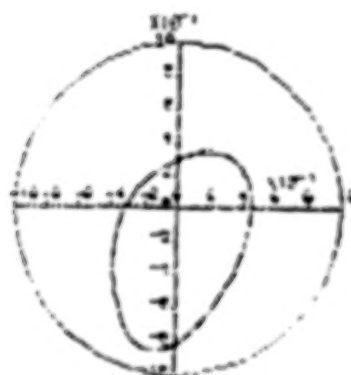
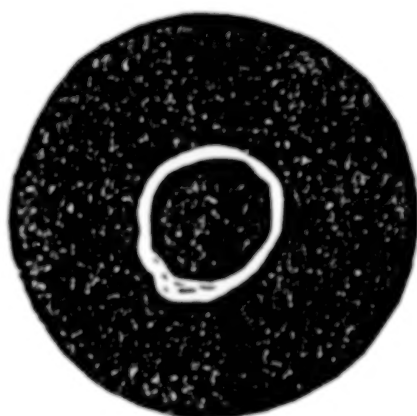
$\omega_{1,2}$ in opposite directions

Fig3: Vibration orbits for the cases of Figs.5,6
but with end plates
 $\lambda = 0.1$.

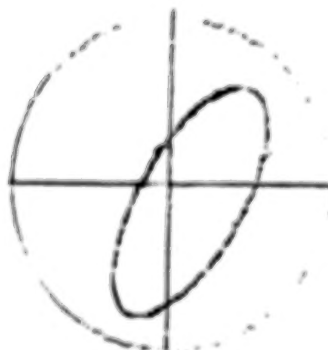


clearance circle, 0.23 mm

Rotor vibration relative to housing



Housing vibration relative to ground



Rotor vibration relative to ground

Fig14 .R10 oil shaft 2 rotating at 3000 rev/min

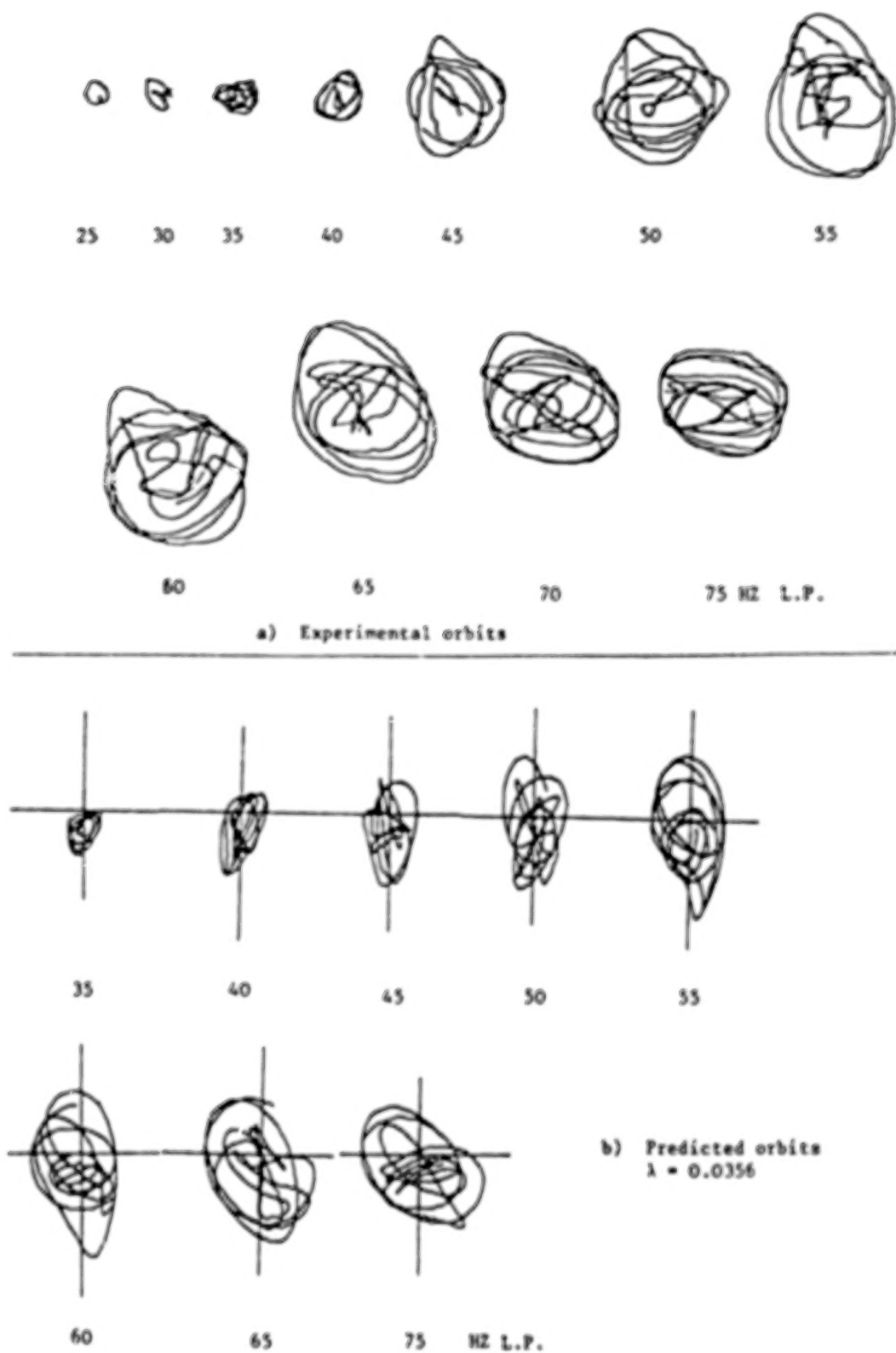
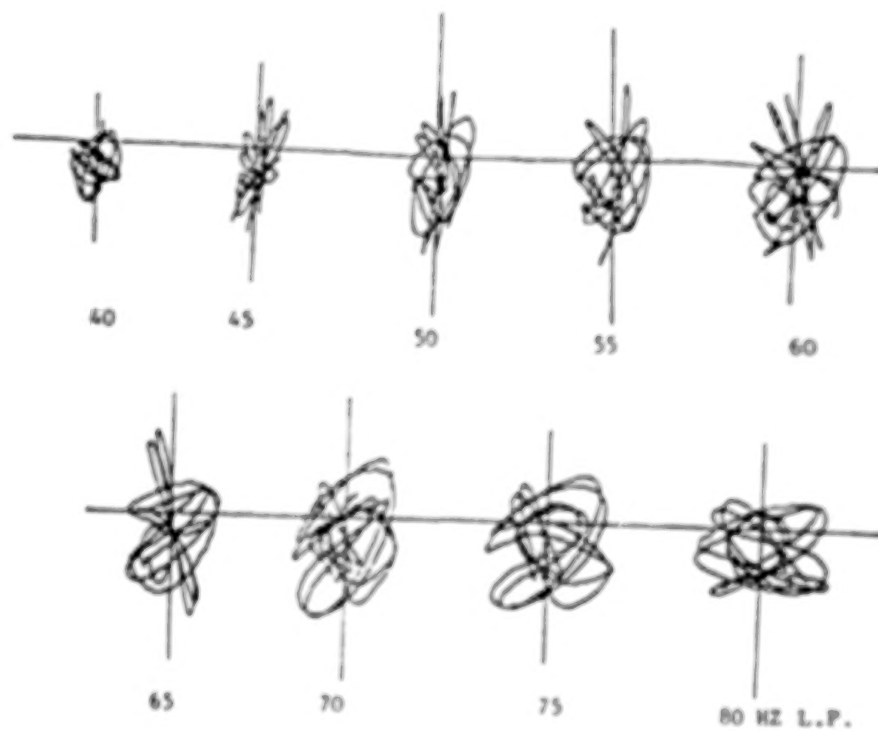
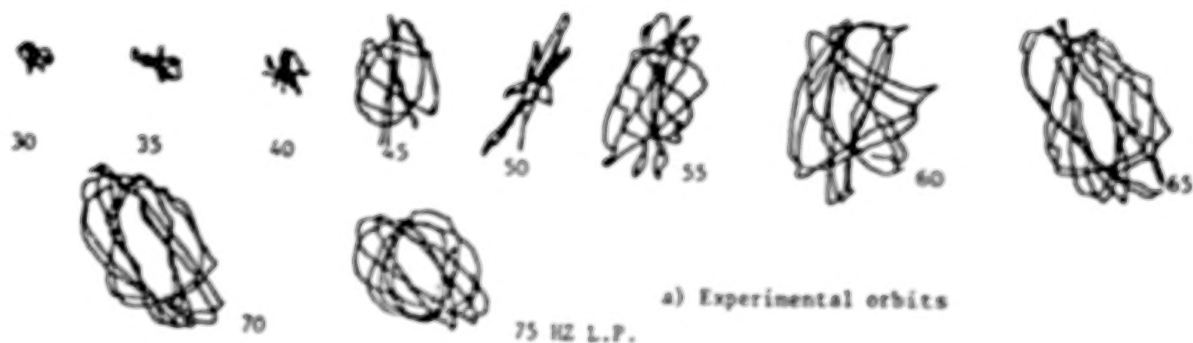


Fig. 15 : Experimental and numerically-predicted orbits of rotor vibration relative to ground, co-rotation ω_1
 $\frac{\omega_1}{\omega_2} = +1.3$
scale 1 mm = 1.413 cm



b) predicted orbits, $\lambda = 0.0356$

Fig. 16 : Experimental and numerically-predicted orbits of rotor vibration relative to ground, counter-rotation, $\frac{\omega_1}{\omega_2} = -1.3$
scale 1 mm \approx 1.413 cm

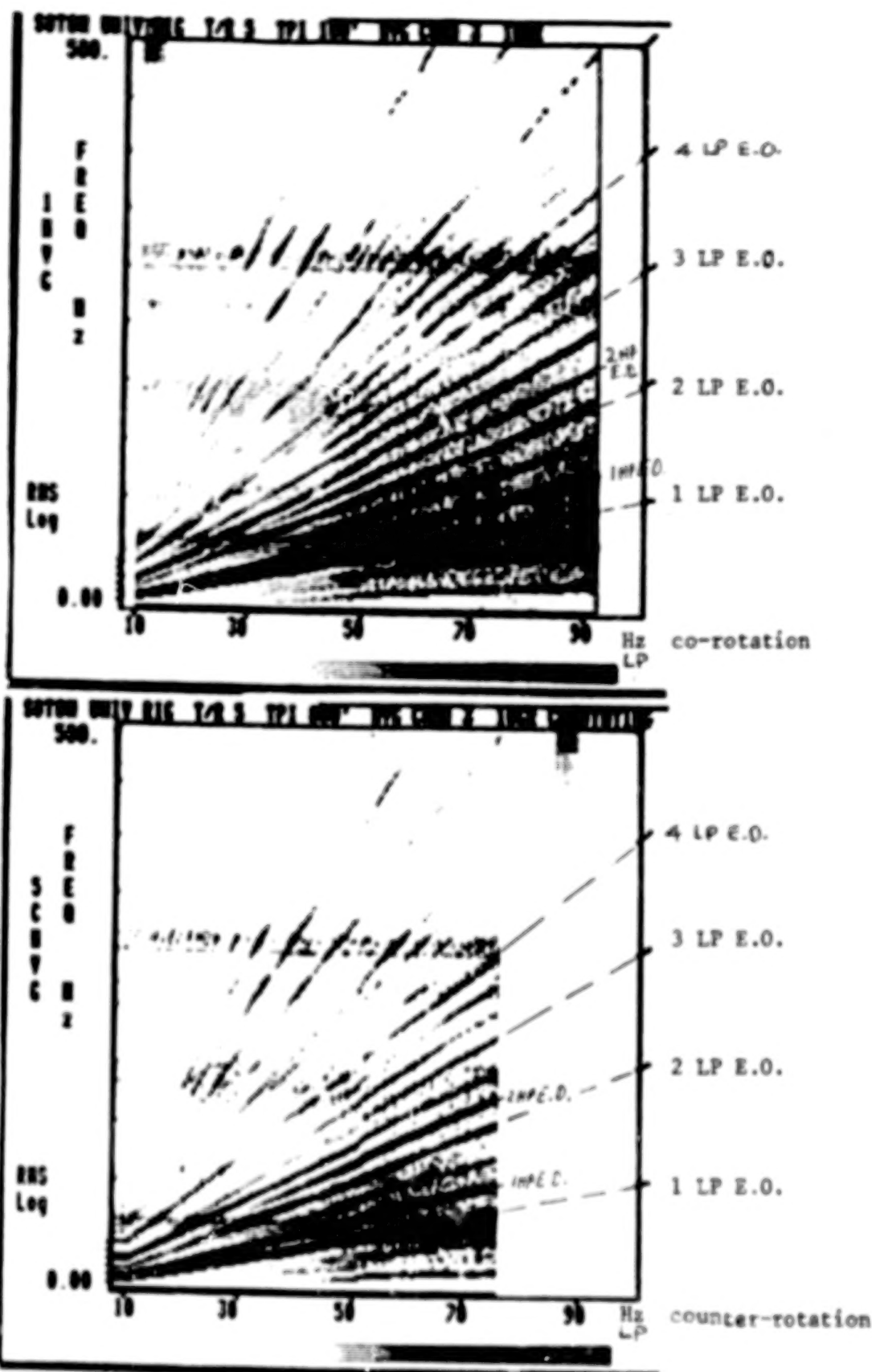


Fig. 17 : z-mods for co-rotation and counter rotation,
 $\frac{\omega_1}{\omega_2} = \pm 1.3$

BLANK

PAGE

BEST COPY AVAILABLE

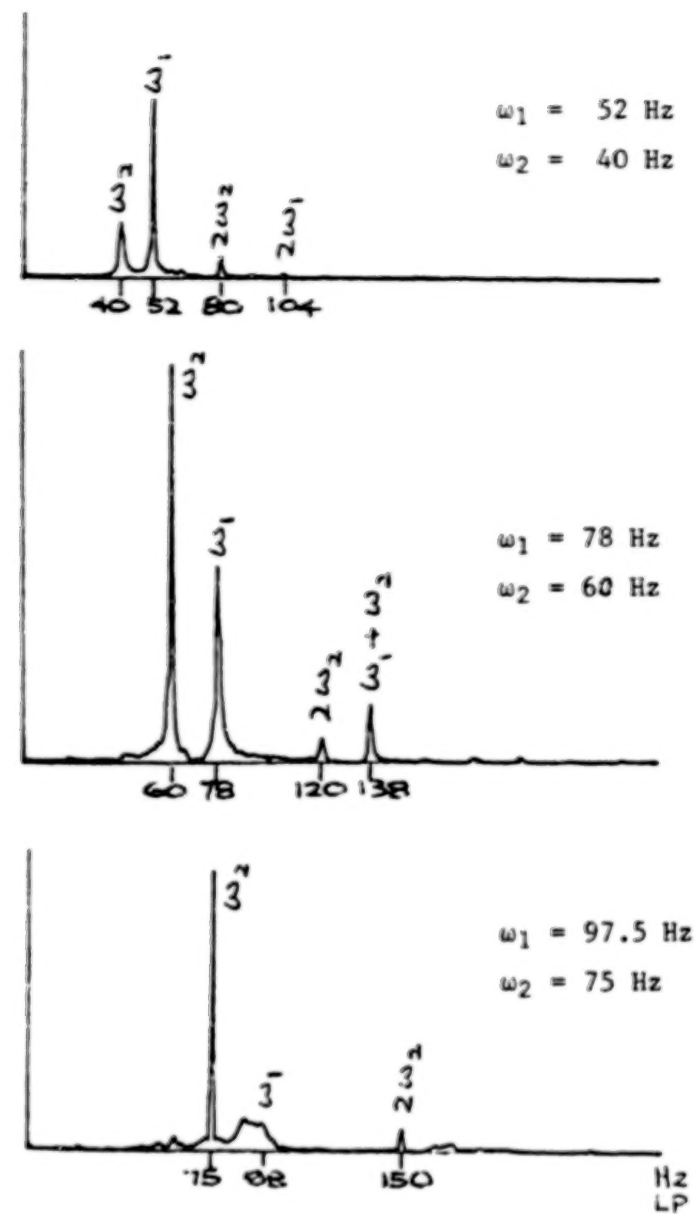
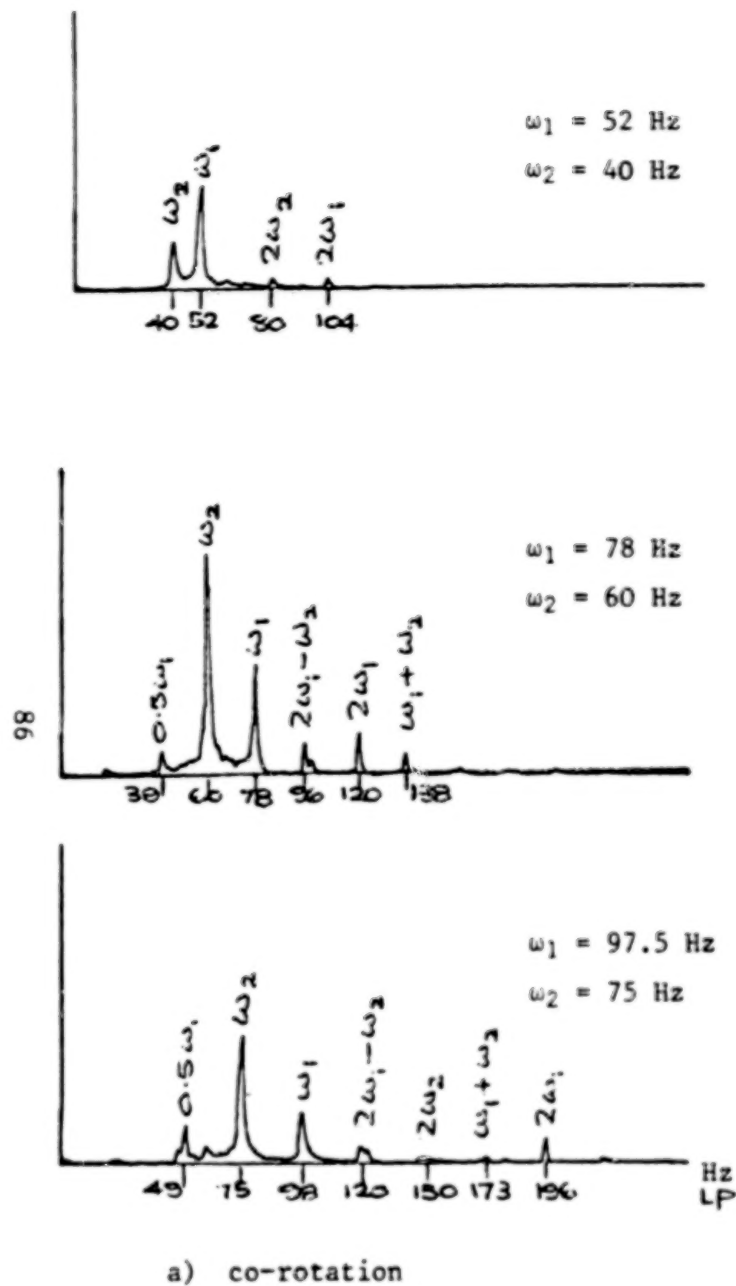


Fig. 18 : Frequency spectra.

**PIEZOELECTRIC PUSHERS FOR ACTIVE VIBRATION CONTROL
OF ROTATING MACHINERY**

A.B. Palazzolo
Department of Mechanical Engineering
Texas A&M University
College Station, Texas 77843-3123, U.S.A.

A.F. Kascak
Propulsion Directorate
U.S. Army Aviation Research and Technology Activity - AVSCOM
Lewis Research Center, MS 23-3
Cleveland, Ohio 44135, U.S.A.

R.R. Lin
Department of Mechanical Engineering
Texas A&M University
College Station, Texas 77843-3123, U.S.A.

J. Montague
Sverdrup Technology
NASA Lewis Research Center Group
Cleveland, Ohio 44135, U.S.A.

R.M. Alexander
Department of Mechanical Engineering
Texas A&M University
College Station, Texas 77843-3123, U.S.A.

The active control of rotordynamic vibrations and stability by magnetic bearings and electromagnetic shakers has been discussed extensively in the literature. These devices, though effective, are usually large in volume and add significant weight to the stator. The use of piezoelectric pushers may provide similar degrees of effectiveness in light, compact packages. This paper contains analyses which extend quadratic regulator, pole placement and derivative feedback control methods to the "prescribed displacement" character of piezoelectric pushers. The structural stiffness of the pusher is also included in the theory.

Tests are currently being conducted at NASA Lewis Research Center with piezoelectric pusher-based active vibration control. The paper presents results performed on the NASA test rig as preliminary verification of the related theory.

NOMENCLATURE

$[A^{Dm}]$: Coefficient matrix associated with $\{X\}$ in state space
$[B_F^{Dm}]$: Coefficient matrix associated with $\{F_D\}$ in state space
$[B_U^{Dm}]$: Coefficient matrix associated with $\{U\}$ in state space
$[C]$: Damping matrix
$[\tilde{C}]$: Uncoupled velocity feedback damping matrix
C_i^A	: Feedback positive active damping
$[C_F]$: Feedback damping matrix
C_s	: Damping coef. of the piezoelectric stack
$[C_S]$: Coef. matrix associated with the output vector
e_1	: Eccentricity
F_i	: Imbalance forces due to mass imbalance
$\{F_D(t)\}$: External forces (disturbance)
F_{P_i}	: Force produced by the i^{th} pusher
$[G']$: System gain matrix
$[I]$: Identity (unity) matrix
I_P	: Polar moment of inertia
I_T	: Moment of inertia
min J	: Minimize the performance index J
$[K]$: Stiffness matrix
$[K^D]$: Stiffness matrix including the pusher stiffness
$[K^{DD}]$: Pusher stiffness matrix
$[K_F]$: Feedback stiffness matrix
K_p	: Preload spring inside the pusher
K_s	: Stiffness of the stack of piezoelectric discs
M	: Number of piezoelectric pushers
$[M]$: Mass matrix
N	: Number of degrees of freedom

$[P]$: Matrix solution from Riccati equation
$[Q]$: Weighting matrix associated with state vector
r	: Number of observer's output
$[R]$: Weighting matrix associated with control vector
t	: Number of modes used
$\{U\}$: Control force matrix
$\{X\}$: State vector
$\{Y\}$: Output vector
$\{Z\}$: Space coordinates
Z_i^*	: Pusher tip displacement
$\{\alpha\}$: Prescribed displacement of the pushers
ζ_i	: i^{th} modal damping
$\{\xi\}$: Modal coordinates
$[\Phi^D]$: Mode shape matrix
$[\Phi]^T$: Transpose matrix of mode shape matrix
$[\Omega_i]$: i^{th} natural frequency
$[\text{diag}()]$: Diagonal matrix

INTRODUCTION

An increasing amount of research is being devoted to developing effective active vibration control packages for rotating machinery, machine tools, large space structures, and in robotics. The advantages of active control over passive, i.e., absorbers and dampers, is the versatility of active control in adjusting to a myriad of load conditions and machinery configurations. This is clearly illustrated when one considers the very narrow bandwidth that a tuned spring mass absorber is effective in.

Electromagnetic shakers and magnetic bearings have been used for actuators in the majority of the active vibration control research mentioned in the literature. Schweitzer (1985) examined the stability and observability of rotor bearing systems with active vibration control, and

presented an analysis which related force and stiffness to electrical and geometrical properties of electromagnetic bearings.

Nikolajsen (1979) examined the application of magnetic dampers to a 3.2 meter simulated marine propulsion system. Gondholekar and Holmes (1984) suggested that electromagnetic bearings be employed to shift critical speeds by altering the suspension stiffness. Weise (1985) discussed proportional, integral, derivative (PID) control of rotor vibrations and illustrated how magnetic bearings could be used to balance a rotor by forcing it to spin about its inertial axis. Humphris et al. (1986) compared predicted and measured stiffness and damping coefficients for a magnetic journal bearing.

Several papers describe active vibration control utilizing other types of actuators. Feng (1986) developed an active vibration control scheme with actuator forces resulting from varying bearing oil pressure. Heinzmann (1980) employed loud speaker coils linked to the shaft via ball bearings, to control vibrations.

This paper develops theory and shows test results corresponding to incorporating piezoelectric pushers as actuator devices for active vibration control. The usual application for these devices is for obtaining minute position adjustments of lenses and mirrors in laser systems (Burleigh, 1986). In the proposed application the pushers force the squirrel cage - ball bearing supports of a rotating shaft. The induced vibration counteracts the unbalanced vibration of the shaft by contributing active damping to the system. The paper presents active vibration control theory and test results for the piezoelectric pushers. To the authors' knowledge this represents a new application of piezoelectric actuators although there has been previous applications to the bending vibration of non-rotating beams using layered piezoelectric materials (Tzou, 1987).

THEORY

The piezoelectric pushers consist of a stack of piezoelectric ceramic discs which are arranged on top of one another and connected in parallel electrically. The stack expands in response to an applied voltage which causes the electric field to point in the direction of polarization for each disc. The extension of the pusher depends on the number and thickness of the discs and

the force depends on the cross sectional area of the discs. Figure 1 shows a sketch of a pusher and the corresponding ideal model. The model consists of a prescribed displacement (α) which is proportional to the input voltage and a spring (K_s) representing the stiffness of the stack of piezoelectric discs. The stiffness K_p is a preload spring which is typically 0.001 to 0.01 times the stiffness K_s . The figure shows that the device has a bilinear spring unless the tip is sufficiently preloaded to maintain a zero gap at all times. The model utilized in the upcoming analysis neglects nonlinearities in the electrical and structural characteristics of the devices and damping (C_s) in the piezoelectric stack.

If pushers are attached to m distinct degrees of freedom of the model, its matrix differential equation may be partitioned and rearranged into the form,

$$[M]_{(N \times N)}\{\ddot{Z}\}_{(N \times 1)} + [C]_{(N \times N)}\{\dot{Z}\}_{(N \times 1)} + [K^D]_{(N \times N)}\{Z\}_{(N \times 1)} = \{F_D(t)\}_{(N \times 1)} - [K^{DD}]_{(N \times M)}\{\alpha\}_{(M \times 1)} \quad (1)$$

where N and M are the number of degrees of freedom of the rotor and the number of piezoelectric pushers, respectively, and

$$[K^D]_{(N \times N)} = [K]_{(N \times N)} + \begin{pmatrix} \dots & \vdots & \dots & \vdots & \dots & \vdots & \dots \\ \dots & k_1 & \dots & \vdots & \dots & \vdots & \dots \\ \dots & \vdots & \dots & k_2 & \dots & \vdots & \dots \\ \dots & \vdots & \dots & \vdots & \ddots & \vdots & \dots \\ \dots & \vdots & \dots & \vdots & \dots & k_m & \dots \\ \dots & \vdots & \dots & \vdots & \dots & \vdots & \dots \end{pmatrix} \quad (2)$$

$$[K^{DD}]_{(N \times M)} = - \begin{pmatrix} \dots & \dots & \dots & \dots \\ k_1 & \dots & \dots & \dots \\ \dots & k_2 & \dots & \dots \\ \dots & \dots & \ddots & \dots \\ \dots & \dots & \dots & k_m \\ \dots & \dots & \dots & \dots \end{pmatrix} \quad (3)$$

and

$$\{\alpha\} = \begin{pmatrix} \alpha_1 \\ \alpha_2 \\ \vdots \\ \alpha_m \end{pmatrix} \quad (4)$$

The matrices $[M]$, $[C]$, and $[K]$ are the mass, damping, and stiffness matrices of the rotor bearing system without the pushers installed, as defined in (Palazzolo, 1983). The K_i are the effective stiffness of the pushers, which from Figure 1 are $K_i = (1/K_{si} + 1/K_{pi})^{-1}$. The stiffness K_i is inserted at the degree of freedom whose motion is the same as the tip motion of the corresponding pusher. The parameter α_i is the prescribed internal displacement of pusher i , which is assumed to vary linearly with input voltage.

The following portions of the paper provide the mathematical means for incorporating the piezoelectric pusher model into three standard active vibration control algorithms.

Part I: Optimal Control

Define the modal transformation

$$\{Z\}_{(N \times 1)} = [\Phi^D]_{(N \times t)} \{\xi\}_{(t \times 1)} \quad (5)$$

where t is the number of modes used in the modal space and $[\Phi^D]$ is the mode shape matrix for the system that includes the pusher stiffness. Substitute Eq.(5) into Eq.(1) and premultiply by $[\Phi^D]^T$, the transpose matrix of $[\Phi^D]$. Furthermore, assume that the system is proportionately damped, and the mass matrix has been orthonormalized;

$$[\Phi^D]^T [M] [\Phi^D] = [I]_{(t \times t)} \quad (6)$$

Then, from the orthogonality conditions, Eq.(1) can be expressed as

$$\{\ddot{\xi}\} + [diag(2\zeta_i^D \Omega_i^D)] \{\dot{\xi}\} + [diag((\Omega_i^D)^2)] \{\xi\} = [\Phi^D]^T \{F_D\} - [\Phi^D]^T [K^{DD}] \{\alpha\} \quad (7)$$

Eq.(7) can be written as a first order (state space) form by adding an identity equation as follows.

$$\begin{aligned} \begin{pmatrix} [I_t] & \vdots & [0] \\ \dots & \dots & \dots \\ [0] & \vdots & [diag(-(\Omega_i^D)^2)] \end{pmatrix} \begin{pmatrix} \{\xi\} \\ \vdots \\ \{\dot{\xi}\} \end{pmatrix} + \begin{pmatrix} [diag(2\zeta_i^D \Omega_i^D)] & \vdots & [diag((\Omega_i^D)^2)] \\ \dots & \dots & \dots \\ [diag((\Omega_i^D)^2)] & \vdots & [0] \end{pmatrix} \begin{pmatrix} \{\xi\} \\ \vdots \\ \{\dot{\xi}\} \end{pmatrix} \\ = \begin{pmatrix} [\Phi^D]^T \{F_D\} \\ \vdots \\ [0] \end{pmatrix} + \begin{pmatrix} -[\Phi^D]^T [K^{DD}] \{\alpha\} \\ \vdots \\ [0] \end{pmatrix} \end{aligned} \quad (8)$$

Multiplying Eq.(8) by the inverse of the leading coefficient matrix yields

$$\begin{aligned} \{\dot{X}^m\}_{(2t \times 1)} &= [A^{Dm}]_{(2t \times 2t)} \{X^m\}_{(2t \times 1)} + [B_F^{Dm}]_{(2t \times N)} \{F_D\}_{(N \times 1)} \\ &+ [B_U^{Dm}]_{(2t \times M)} \{\alpha\}_{(M \times 1)} \end{aligned} \quad (9)$$

where

$$[A^{Dm}]_{(2t \times 2t)} = \begin{pmatrix} [\text{diag}(-2\zeta_i^D \Omega_i^D)] & \vdots & [\text{diag}(-(\Omega_i^D)^2)] \\ \dots & \dots & \dots \\ [I_t] & \vdots & [0] \end{pmatrix} \quad (10)$$

$$[B_F^{Dm}]_{(2t \times N)} = \begin{pmatrix} [\Phi^D]^T \\ \dots \\ [0] \end{pmatrix} \quad (11)$$

$$[B_U^{Dm}]_{(2t \times M)} = \begin{pmatrix} -[\Phi^D]^T [K^{DD}] \\ \dots \\ [0] \end{pmatrix} \quad (12)$$

$$\{X\}_{(2t \times 1)} = \begin{pmatrix} \{\dot{\xi}\} \\ \dots \\ \{\xi\} \end{pmatrix} \quad (13)$$

Since it is impractical to measure the displacement and velocity at all the system degrees of freedom (dof), an observer system may be constructed to estimate the state vector from a smaller number of measurements. This approach, however, may not be feasible for a large rotordynamic system involving many degrees of freedom and excitation at high frequencies. Another approach is output feedback, i.e., limit the control measurements to only those defined in the output vector, $\{Y\}$, defined by

$$\{Y\}_{(r \times 1)} = [C_S]_{(r \times 2N)} \begin{pmatrix} \{\dot{Z}\} \\ \dots \\ \{Z\} \end{pmatrix}_{(2N \times 1)} \quad (14)$$

The control for the prescribed "internal" displacements of the pushers is

$$\{\alpha\}_{(M \times 1)} = -[G']_{(M \times r)} \{Y\}_{(r \times 1)} \quad (15)$$

where r is the number of sensors (velocities and displacements), and M the number of pushers. Substituting Eq.(14) in Eq.(15) and converting this equation to the modal space with Eq.(5) yields

$$\{\alpha\}_{(M \times 1)} = -[G'] [C_S] \begin{pmatrix} [\Phi^D] & \vdots & [0] \\ \dots & \dots & \dots \\ [0] & \vdots & [\Phi^D] \end{pmatrix} \begin{pmatrix} \{\dot{\xi}\} \\ \dots \\ \{\xi\} \end{pmatrix} \quad (16)$$

or in abbreviated notation

$$\{\alpha\}_{(M \times 1)} = -[\tilde{G}]_{(M \times 2t)} \{X\}_{(2t \times 1)} \quad (17)$$

where

$$[\tilde{G}]_{(M \times 2t)} = [G']_{(M \times r)} [C_S]_{(r \times 2N)} \begin{pmatrix} [\Phi^D] & \vdots & [0] \\ \dots & \dots & \dots \\ [0] & \vdots & [\Phi^D] \end{pmatrix}_{(2N \times 2t)} \quad (18)$$

The objective of output feedback control in modal space can now be identified as obtaining the gain matrix $[G']$ in Eq.(15) that suppresses the modal coordinates ξ_i in Eq.(5). The linear quadratic regulator problem goes one step further and also simultaneously reduces the required control displacements $\{\alpha_i\}$. The performance index to be minimized is defined as

$$\min_{\{\alpha\}} J = \min_{\{\alpha\}} \int_0^\infty (\{X\}^T [Q] \{X\} + \{\alpha\}^T [R] \{\alpha\}) dt \quad (19)$$

where $[Q]$ and $[R]$ are symmetric, positive-definite weighting matrices which govern the relative importance of minimizing the modal coordinates ξ_i and the prescribed pusher displacements, α_k . Diminishing $[R]$ will result in larger pusher "internal" displacements but smaller vibrations (governed by the ξ_i). Optimal control theory produces the solution for Eq.(19) in the form of Eq.(17). The gain matrix $[\tilde{G}]$ is computed from

$$[\tilde{G}]_{(M \times 2t)} = [R]_{(M \times M)}^{-1} [B_U^{Dm}]_{(M \times 2t)}^T [P]_{(2t \times 2t)} \quad (20)$$

where $[P]$ is obtained as the solution matrix to the algebraic (steady state) Ricatti equation (Palazzolo, 1988). The steady state (algebraic) Ricatti equation is

$$[P][A^{Dm}] + [A^{Dm}]^T [P] - [P][B_U^{Dm}][R]^{-1}[B_U^{Dm}]^T [P] + [Q] = [0]_{(2t \times 2t)} \quad (21)$$

where the matrices $[P]$, $[A^{Dm}]$, and $[Q]$ are $2t$ by $2t$, the matrix $[B_U^{Dm}]$ is $2t$ by M , and the matrix $[R]$ is M by M .

If Eq.(18) is to be solved exactly for G' , the number of measured outputs r (sum of velocities and displacements) must equal twice the number of modes, t , used in the modal space. Define the matrix $[\beta]$ as

$$[\beta]_{(r \times 2t)} = [C_S]_{(r \times 2N)} \begin{pmatrix} [\Phi^D] & \vdots & [0] \\ \dots & \dots & \dots \\ [0] & \vdots & [\Phi^D] \end{pmatrix}_{(2N \times 2t)} \quad (22)$$

Assuming that $r=2t$ and $[\beta]$ is nonsingular, the gain matrix $[G']$ can be derived from Eq.(18) and Eq.(20) as

$$[G'] = [R]^{-1} [B_U^{Dm}]^T [P] [\beta]^{-1} \quad (23)$$

The prescribed "internal" displacement of the i^{th} pusher can now be expressed from Eq.(15) and Eq.(23) as

$$\alpha_i = - \sum_{j=1}^r G'_{ij} y_j \quad (24)$$

The force produced by the i^{th} pusher is

$$F_{P_i} = k_i (Z_i^* - \alpha_i) \quad (25)$$

where Z_i^* is the pusher tip displacement. Substituting Eq.(14) and Eq.(15) into Eq.(1) yields

$$\begin{aligned} [M]_{(N \times N)} \{\ddot{Z}\}_{(N \times 1)} + [C]_{(N \times N)} \{\dot{Z}\}_{(N \times 1)} + [K^D]_{(N \times N)} \{Z\}_{(N \times 1)} = \\ \{F_D(t)\}_{(N \times 1)} + [K^{DD}]_{(N \times M)} [G']_{(M \times r)} [C_S]_{(r \times 2N)} \begin{pmatrix} \{\dot{Z}\} \\ \vdots \\ \{Z\} \end{pmatrix}_{(2N \times 1)} = \\ \{F_D(t)\}_{(N \times 1)} + [C_F]_{(N \times N)} \{\dot{Z}\}_{(N \times 1)} + [K_F]_{(N \times N)} \{Z\}_{(N \times 1)} \end{aligned} \quad (26)$$

where

$$\left[[C_F]_{(N \times N)} \vdots [K_F]_{(N \times N)} \right] = [K^{DD}] [G'] [C_S] \quad (27)$$

Thus, the closed loop equilibrium equation becomes

$$[M]_{(N \times N)} \{\ddot{Z}\}_{(N \times 1)} + [[C] - [C_F]]_{(N \times N)} \{\dot{Z}\}_{(N \times 1)} + [[K^D] - [K_F]]_{(N \times N)} \{Z\}_{(N \times 1)} = \{F_D(t)\}_{(N \times 1)} \quad (28)$$

This equation is very useful for conducting rotordynamic simulations with feedback control utilizing piezoelectric pushers.

Part II: Pole Placement

Similar to optimal control, Eq.(1) can be written in first order (state space) form as

$$\begin{pmatrix} [M] & \vdots & [0] \\ \cdots & \cdots & \cdots \\ [0] & \vdots & [-K^D] \end{pmatrix} \begin{pmatrix} \{\ddot{Z}\} \\ \vdots \\ \{\dot{Z}\} \end{pmatrix} + \begin{pmatrix} [C] & \vdots & [K^D] \\ \cdots & \cdots & \cdots \\ [K^D] & \vdots & [0] \end{pmatrix} \begin{pmatrix} \{\dot{Z}\} \\ \vdots \\ \{Z\} \end{pmatrix} = \begin{pmatrix} [F_D(t)] \\ \vdots \\ [0] \end{pmatrix} + \begin{pmatrix} [-K^{DD}] \\ \vdots \\ [0] \end{pmatrix} \{\alpha\} \quad (29)$$

Premultiplication by the inverse of the leading coefficient matrix yields

$$\begin{pmatrix} \{\ddot{Z}\} \\ \vdots \\ \{\dot{Z}\} \end{pmatrix} = \begin{pmatrix} [-[M]^{-1}[C]] & \vdots & [-[M]^{-1}[K^D]] \\ \cdots & \cdots & \cdots \\ [I_N] & \vdots & [0] \end{pmatrix} \begin{pmatrix} \{\dot{Z}\} \\ \vdots \\ \{Z\} \end{pmatrix} + \begin{pmatrix} [M]^{-1} \\ \vdots \\ [0] \end{pmatrix} \{F_D\} + \begin{pmatrix} -[M]^{-1}[K^{DD}] \\ \vdots \\ [0] \end{pmatrix} \{\alpha\} \quad (30)$$

This equation is written in abbreviated notation as

$$\begin{aligned} \{\dot{X}\}_{(2N \times 1)} &= [A^D]_{(2N \times 2N)} \{X\}_{(2N \times 1)} + [B_F^D]_{(2N \times N)} \{F_D\}_{(N \times 1)} \\ &+ [B_\alpha]_{(2N \times M)} \{\alpha\}_{(M \times 1)} \end{aligned} \quad (31)$$

where

$$\{X\}_{(2N \times 1)} = \begin{pmatrix} \{\dot{Z}\} \\ \vdots \\ \{Z\} \end{pmatrix} \quad (32)$$

The output vector, $\{Y\}$, and the output feedback control displacement, $\{\alpha\}$, have the same definitions as in Eq.(14) and Eq.(15), respectively. Substituting Eq.(14) into Eq.(15) yields

$$\{\alpha\}_{(M \times 1)} = -[G']_{(M \times r)}[C_S]_{(r \times 2N)}\{X\}_{(2N \times 1)} \quad (33)$$

Substitute Eq.(33) into Eq.(31) and rearrange

$$\{\dot{X}\} = ([A^D] - [B_\alpha][G']_{(M \times r)}[C_S])\{X\} + [B_F^D]\{F_D\} \quad (34)$$

Consider the unforced system with

$$\{F_D\} = \{0\} \quad \& \quad \{X\} = [\Psi]e^{\lambda t} \quad (35)$$

The characteristic equation for the closed loop system becomes

$$\det(\lambda[I]_{(2N \times 2N)} - [A^D]_{(2N \times 2N)} + [B_\alpha]_{(2N \times M)}[G']_{(M \times r)}[C_S]_{(r \times 2N)}) = 0 \quad (36)$$

Assume that λ is not an eigenvalue of the open loop system, then Eq.(36) can be rewritten as

$$\det(\lambda[I_{2N}] - [A^D])_{(2N \times 2N)} \det([I]_{(2N \times 2N)} + \{\lambda[I_{2N}] - [A^D]\}_{(2N \times 2N)}^{-1} [B_\alpha]_{(2N \times M)}[G']_{(M \times r)}[C_S]_{(r \times 2N)}) = 0 \quad (37)$$

Apply the following determinant identity (Brogan,1974)

$$\det([I_{2N}] + [PP]_{(2N \times M)}[QQ]_{(M \times 2N)}) = \det([I_M] + [QQ]_{(M \times 2N)}[PP]_{(2N \times M)}) \quad (38)$$

to Eq.(37) which then implies

$$\det([I_M] + [G']_{(M \times r)}[C_S]_{(r \times 2N)}\{\lambda[I_{2N}] - [A^D]\}_{(2N \times 2N)}^{-1}[B_\alpha]_{(2N \times M)}) = 0 \quad (39)$$

Define

$$[\Phi(\lambda)]_{(2N \times 2N)} = \{\lambda[I_{2N}] - [A^D]\}_{(2N \times 2N)}^{-1} \quad (40)$$

and

$$[\Psi(\lambda)]_{(r \times M)} = [C_S]_{(r \times 2N)} [\Phi(\lambda)]_{(2N \times 2N)} [B_a]_{(2N \times M)} \quad (41)$$

Therefore, Eq.(39) becomes

$$\det([I_M] + [G']_{(M \times r)} [\Psi(\lambda)]_{(r \times M)}) = 0 \quad (42)$$

Eq.(42) implies that the solution will be satisfied if the column vectors of

$$[I_M] + [G'] [\Psi(\lambda)] \quad (43)$$

are linearly dependent. Following (Fahmy, 1982) and (Stanway, 1984) this condition is expressed by

$$([I_M] + [G'] [\Psi(\lambda_i)]) \{f_i\}_{(M \times 1)} = \{0\}_{(M \times 1)} \quad (44)$$

for some $\{f_i\} \in \mathbf{R}^m$. For r prescribed values of λ , Eq.(44) can be expressed as

$$[f_1 : f_2 : \dots : f_r]_{(M \times r)} + [G'] [\Psi(\lambda_1) f_1 : \dots : \Psi(\lambda_r) f_r]_{(r \times r)} = [0]_{(M \times r)} \quad (45)$$

or in abbreviated notation,

$$[L]_{(M \times r)} + [G'] [W]_{(r \times r)} = [0]_{(r \times r)} \quad (46)$$

The output feedback gain matrix is obtained from

$$[G'] = -[L]_{(M \times r)} [W]_{(r \times r)}^{-1} \quad (47)$$

Note that r poles have to be assigned to compute the matrix inverse $[W]^{-1}$. Eq.(47) provides the gain matrix for prescribing r eigenvalues where r is the total number of sensor measurements including velocities and displacements.

Physically, the gain matrix $[G']$ should be a real matrix, thus for each prescribed complex eigenvalue λ_i the complex conjugate λ_{i+1} should be prescribed too. In this case, set $\{f_{i+1}\} = \{f_i\}$

or let both $\{f_i\}$ and $\{f_{i+1}\}$ be real vectors. This implies that $\frac{\tau}{2}$ complex eigenvalue pairs $(\lambda_i, \lambda_{i+1})$ may be prescribed.

The pusher internal displacements are again obtained from Eq.(24). Furthermore, the feedback equivalent damping and stiffness matrices are exactly those shown in Eq.(27) and Eq.(28).

Part III: Uncoupled Velocity Feedback Damper

This is the simplest vibration control scheme in that it only involves the internal displacement of the pusher and the velocity of it's tip. If the tip of the i^{th} pusher is in constant contact with the l_i degree of freedom, the control law becomes

$$\alpha_i = -G'_{ii} \dot{Z}_{l_i}, \quad i = 1, 2, \dots, m \quad (48)$$

Then

$$[K^{DD}]\{\alpha\} = \begin{pmatrix} 0 \\ \vdots \\ k_1 \alpha_1 \\ 0 \\ \vdots \\ k_m \alpha_m \\ 0 \\ \vdots \\ 0 \end{pmatrix} = \begin{pmatrix} 0 \\ \vdots \\ 0 \\ -k_1 G'_{11} \\ 0 \\ \vdots \\ \vdots \\ 0 \end{pmatrix} \dot{z}_1 + \dots + \begin{pmatrix} 0 \\ \vdots \\ \vdots \\ \vdots \\ 0 \\ -k_m G'_{mm} \\ 0 \\ 0 \end{pmatrix} \dot{z}_m \quad (49)$$

Substitution of Eq.(49) into Eq.(1) produces the closed loop equilibrium equation;

$$[M]_{(N \times N)} \{\ddot{Z}\}_{(N \times 1)} + [\tilde{C}]_{(N \times N)} \{\dot{Z}\}_{(N \times 1)} + [K^D]_{(N \times N)} \{Z\}_{(N \times 1)} = \{F_D(t)\}_{(N \times 1)} \quad (50)$$

where

$$[\tilde{C}] = [C] + \begin{pmatrix} \dots & \vdots & \dots & \vdots & \dots & \vdots & \dots \\ \dots & C_1^A & \dots & \vdots & \dots & \vdots & \dots \\ \dots & \vdots & \dots & C_2^A & \dots & \vdots & \dots \\ \dots & \vdots & \dots & \vdots & \ddots & \vdots & \dots \\ \dots & \vdots & \dots & \vdots & \dots & C_m^A & \dots \\ \dots & \vdots & \dots & \vdots & \dots & \vdots & \dots \end{pmatrix} \quad (51)$$

and

$$C_i^A = -k_i G'_{ii}, \quad i = 1, 2, \dots, m \quad (52)$$

Eq.(52) shows how positive active damping may be added into the rotor bearing system via the simple control law in Eq.(48).

EXPERIMENTAL RESULTS

An air turbine driven rotor rig was instrumented to check the Uncoupled Velocity Feedback Damper theory described in the previous section. The piezoelectric actuators utilized in the tests were Burleigh Pusher PZL-100's, being driven by Burleigh PZ-150/150M Amplifier Drivers. Figure 2 shows a typical voltage vs. tip displacement plot for this arrangement. The curve in this plot provides an approximate description of the internal displacement (α) vs. voltage relation, since the tip is unloaded and the preload spring in Figure 1 is very light ($\approx 20,000$ N/M). Therefore it is assumed that the voltage sensitivity for α is $S_A = -57,000.0$ V/M. This value was nearly constant for the three pushers that were tested.

Load deflection characteristics of the pushers were obtained by securing each one in a solid cylinder, applying load to the protruding tip of the pusher, and measuring the tip deflections shown in Figure 3. Repeated tests with 3 separate pushers yielded an average stiffness of approximately 3.5×10^6 N/M.

Figure 4 shows a simple sketch of the test rig, which consists of a 2.5 cm diameter shaft, 61.0 cm in length; a 14.0 N overhung disc, 13.0 cm in diameter; and two squirrel cage mounted ball bearings. The outboard bearing is externally forced by an orthogonal pair of piezoelectric pushers, which are in turn positioned opposite to the two eddy current displacement probes d_3 and d_4 . The control law in Eq.(48) applied to the test setup becomes

$$\alpha_{hor} = -G'_{hor} \dot{d}_4 \quad (53)$$

$$\alpha_{ver} = -G'_{ver} \dot{d}_3 \quad (54)$$

The horizontal and vertical active damping were set equal in the control arrangement of Figure 5. The figure outlines how an effective damping value can be computed once the probe and actuator sensitivities and actuator stiffness are known. The calculations for this test setup show that the "active" damping coefficient is estimated to vary according to

$$C_A = (275) \times G \frac{N \text{ sec}}{M} \quad (55)$$

where G is the amplifier gain in Figure 5. The rotor was carefully balanced, and then intentionally unbalanced by a known amount (10.2 gm-cm), in order to compare the test results with those predicted by an unbalance response computer program.

Figure 6 and Figure 7 show the test vibration amplitude vs. speed plots for the disc probes d_1 and d_2 in Figure 4. The family of curves is generated by switching amplifier gains in Figure 5 and computing the effective damping according to Eq.(55). The computer simulation results for either probe d_1 or d_2 , over the same range of damping values is shown in Figure 8. A comparison of Figures 6, 7 and 8 show that although the test damping is less than the predicted value from Eq.(55) a considerable amount of damping (10,000. N sec/M, 57 lb sec/in) is still produced.

Figure 9 and Figure 10 show the measured unbalanced response plots at the vertical (d_3) and horizontal (d_4) bearing probes, respectively. Figure 11 shows the theoretical response for the same probes. The results again indicate that Eq.(55) overpredicts the active damping, however by comparing the plots the pushers do provide approximately 14,000. N sec/M (80.0 lb sec/in) damping at the highest amplifier-gain setting.

The above comparison was also performed including gyroscopics in the theoretical model. This effect only caused minor changes in the predicted response.

SUMMARY AND CONCLUSIONS

This paper has examined the possible use of piezoelectric pushers for active control of rotor-bearing system vibrations. Although their most common application is currently micro-positioning of laser system mirrors and lenses; their stroke, force and frequency response make

them potentially very useful for vibration control. The obvious advantage of piezoelectric pushers over other actuators is their compact size and light weight.

Three active theories were extended to treat the special prescribed "internal" displacement (α) character of piezoelectric pushers. The Uncoupled Velocity-Feedback Damper theory was then tested by comparison to experimental results. The study showed that although the theory overpredicts the amount of damping produced by the pusher the actual level is significant, being in the range of 10,000-14,000. N sec/M (57.0-80.0 lb sec/in). The discrepancy between predicted and measured results most likely arises from the nonlinearity and hysteresis in the voltage-deflection and load-deflection characteristics of the pushers, and from the neglect of the structural damping of the piezoelectric stroke, by the theory. We are currently working with the pusher manufacturer, Burleigh Inc., to produce pushers that have reduced nonlinearity, hysteresis and stack damping. Construction of a feedback box to perform optimal control (OC) and pole placement control (PPC) is in progress. The device will accomodate up to 12 sensors and produce outputs to two actuators, which corresponds to a 2×12 dimension for the $[G']$ matrix in Eq.(15). Test results from application of OC and PPC will be forthcoming in the literature.

ACKNOWLEDGEMENTS

The authors wish to express their sincere gratitude for the following funding sources: NASA grant NAG3-763, ASEE-NASA Summer Faculty Fellowship Program, and the Texas A&M Turbomachinery Research Consortium (TRC). The invaluable assistance of the following people is also gratefully acknowledged: NASA (Tom Lokatos, Erwin Meyn, and John Ropchock) and Burleigh, Inc., (Dr. Jim Kaufer and Mark Palvino).

REFERENCES

- Brogan, W.L. (1974) "Modern Control Theory," Quantum Publishers, Inc., New York, N.Y. 10010.
- Burleigh Instruments (1986), Burleigh Park, Fishers, NY, 14453.

Fahmy, M.M. (1982) "On Eigenstructure Assignment in Linear Multivariable Systems," IEEE Trans. on Automatic Control, Vol. AC-27, No. 3.

Feng, G., and Xin, N. (1986), "Automatic Control of the Vibration of the Flexible Rotor with Microcomputer," Int. Conf. on Rotordynamics, IFTOMM and JSME, Tokyo, Sept. pp.14-17.

Gondholekar, V., and Holmes, R. (1984), "Design of Electromagnetic Bearing for Vibration Control of Flexible Transmission Shaft," Rotor Dynamic Instability Problem in High Performance Turbomachinery, Texas A&M Univ., NASA report.

Heinzmann, J. et al. (1980), "The Implementation of Automatic Vibration Control in a High Speed Rotating Test Facility," Univ. of Virginia Report UVA/464761/MAE80/160.

Humphris, R., et al. (1986), "Effect of Control Algorithms on Magnetic Journal Bearing Properties," J. Eng. Gas Turbines and Power, ASME, Oct., Vol. 108, pp.624-632.

Nikolajsen, J., Holmes, R., and Gondholekar, V. (1979), "Investigation of an Electromagnetic Damper for Vibration Control of a Transmission Shaft," Proc. Instn. Mech. Engr., Vol, 193, pp. 331-336.

Palazzolo, A.B., Wang, B.P., and Pilkey, W.D. (1983), "Eigensolution Reanalysis of Rotordynamic Systems by the Generalized Receptance Method," Jour. of Engin. for Power, Vol. 105, July, pp.543-550.

Palazzolo, A.B., Lin, R.R., Kascak, A.F., and Alexander, R.M. (1988), "Active Control of Transient Rotordynamic Vibration by Optimal Control Methods," Paper No. 88-GT-73, Presented at Gas Turbine Conf., June 5-9, 1988, Amsterdam, Accepted for publication (Jour. of Engr. for Gas Turbine and Power, April 1989).

Schweitzer, G. (1985) "Magnetic Bearings for Vibration Control," Bently Nevada Instability Seminar, Minden, Nevada. NASA CP-2409, p.317.

Stanway, R., and O'Reilly, C. (1984), "State Variable Feedback Control of Rotor Bearing Suspension Systems," Inst. Mech. Engr. Rotordynamics Conf. C274/84, pp.515-524.

Tzou, H.S. (1987), "Active Vibration Control of Flexible Structures Via Converse Piezoelec-

tricity," Presented at the 20th Midwestern Mechanics Conference, 8/31-9/2, 1987, Developments in Mechanics, pp.1201-1206, Vol. 14-c.

Weise, D., (1985), "Active Magnetic Bearings Provide Closed Loop Servo Control for Enhanced Dynamic Response," Proc. 27th IEEE Machine Tool Conf., October.

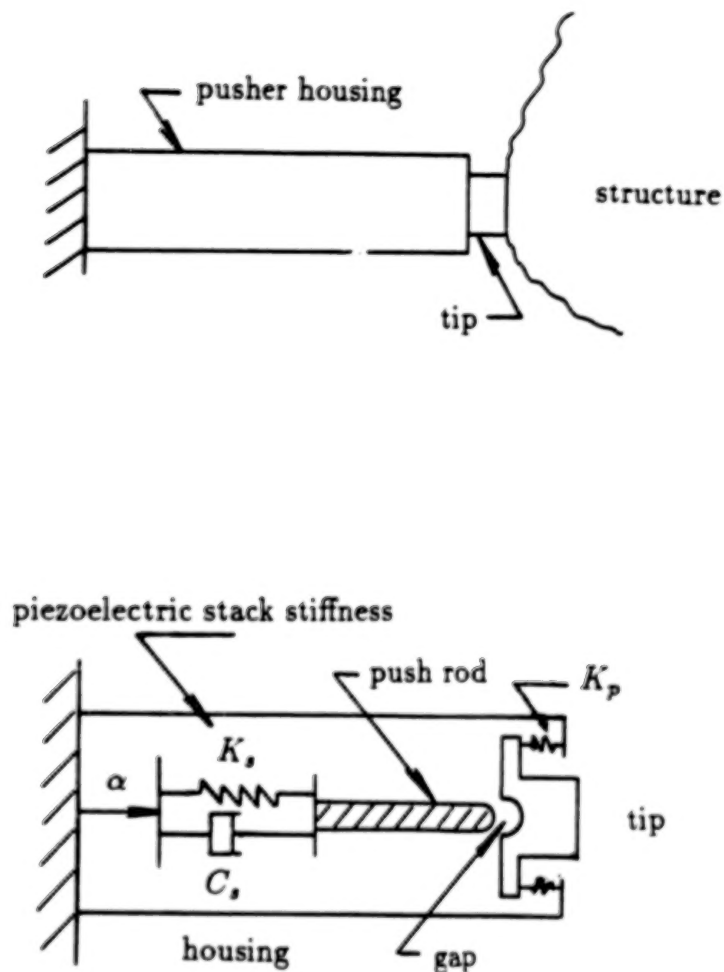


Figure 1 Sketch of piezoelectric pusher and corresponding analytical model.

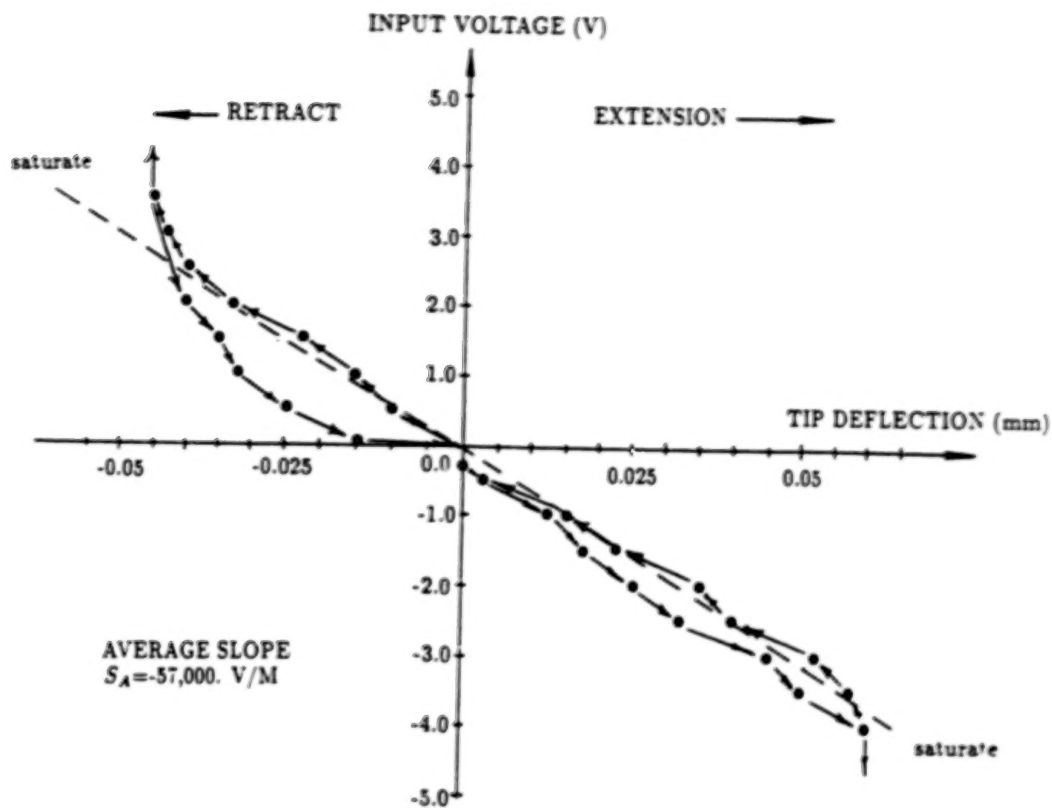


Figure 2 Typical pusher tip deflection vs. input voltage.

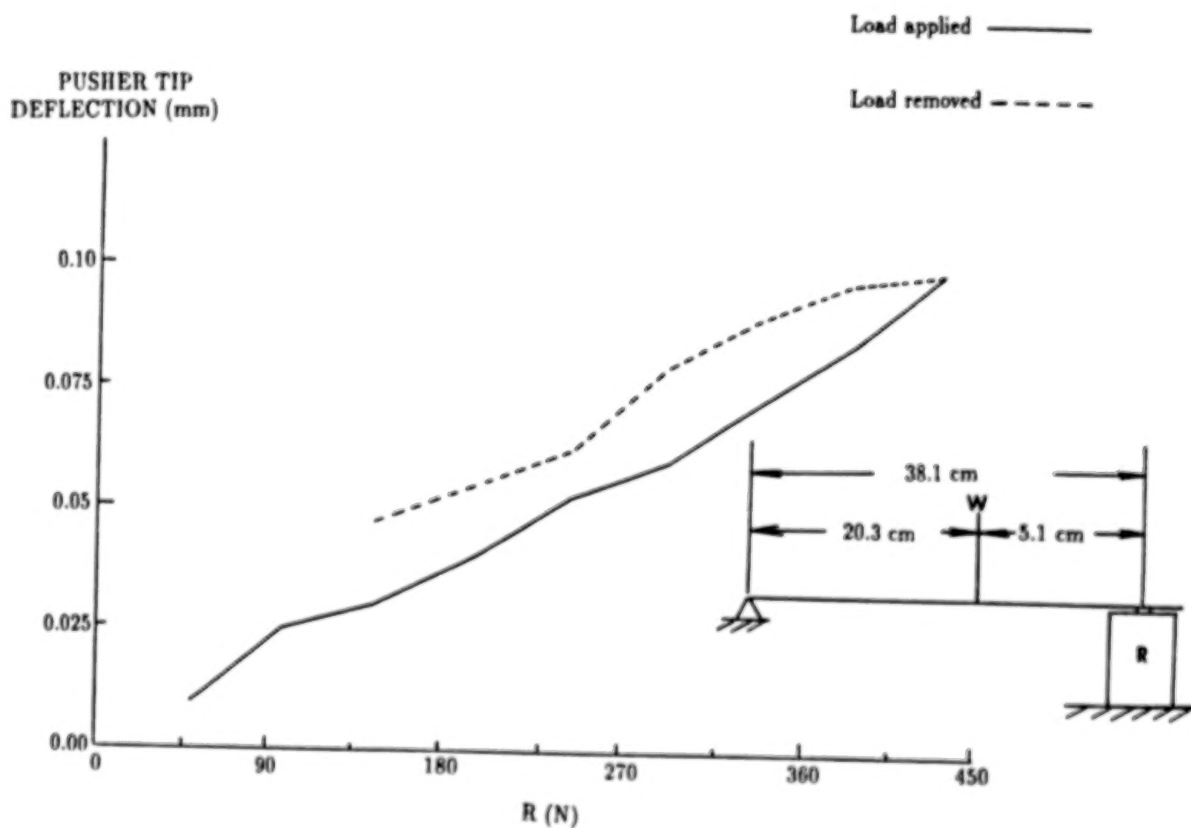


Figure 3 Typical pusher tip deflection vs. pusher tip load.

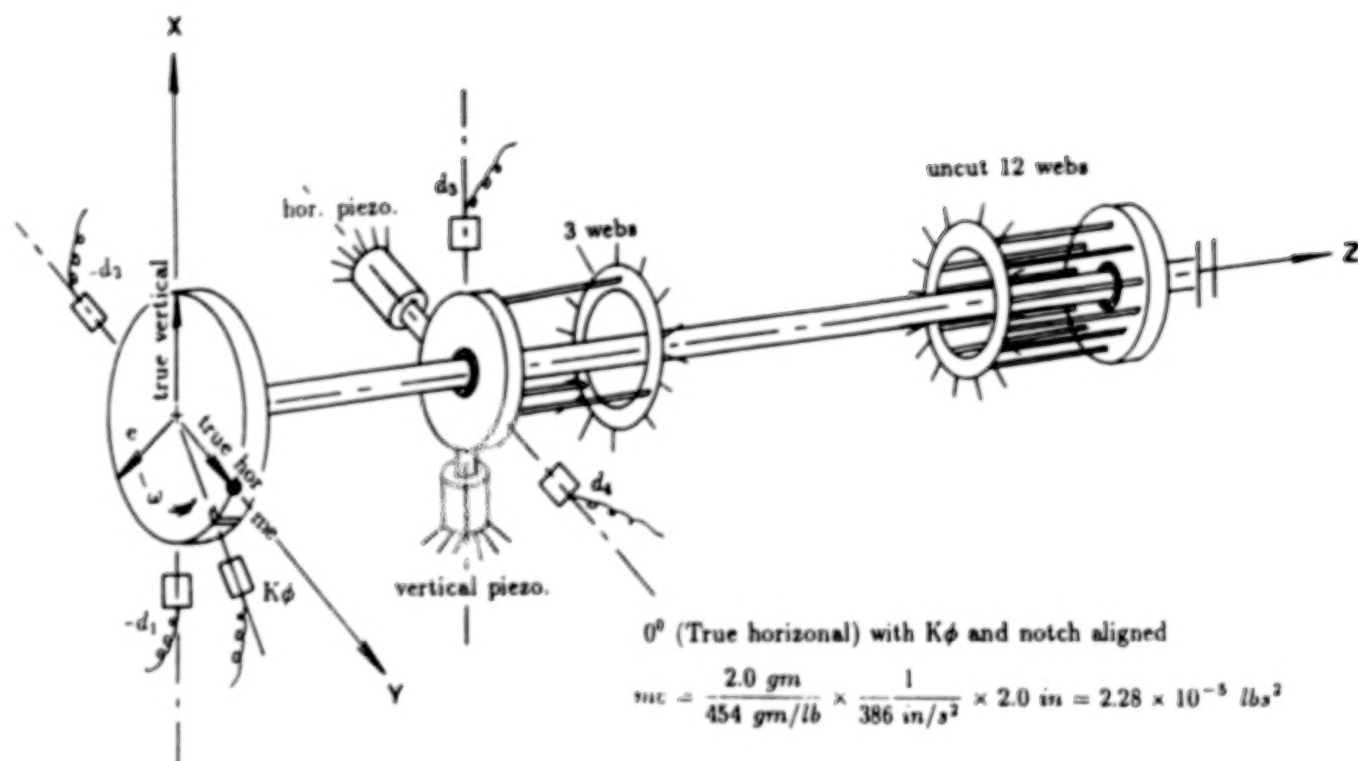
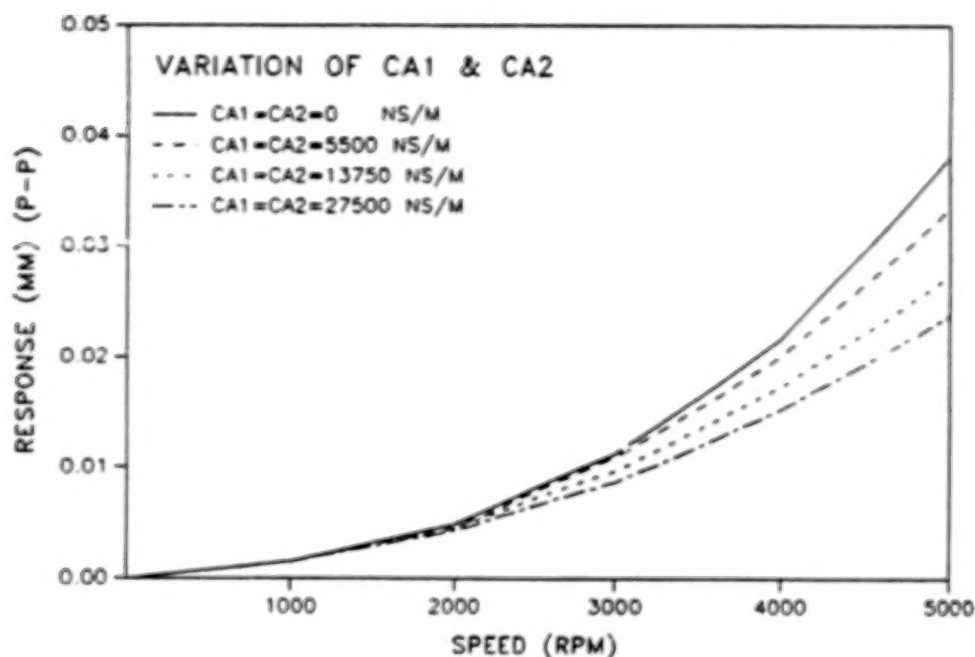


Figure 4 Diagram test rig with piezoelectric pushers.

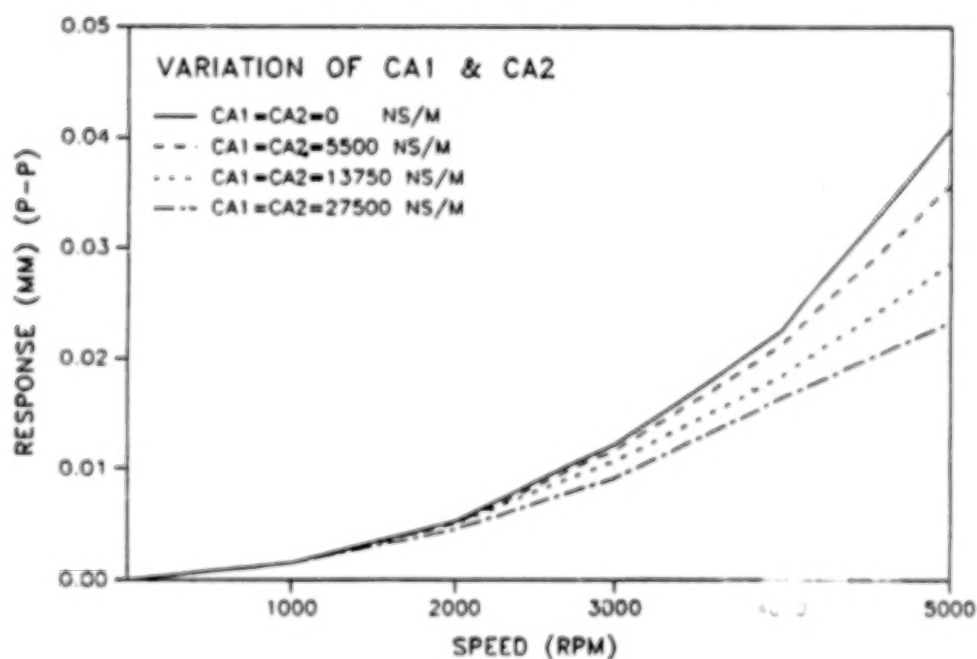
PRESCRIBED PUSHER DISPLACEMENT

D1 PROBE (DOF(1)) EXPERIMENT DATA

Figure 6 Prescribed pusher displacement at probe d_1 (DOF 1).

PRESCRIBED PUSHER DISPLACEMENT

D2 PROBE (DOF(3)) EXPERIMENT DATA

Figure 7 Prescribed pusher displacement at probe d_2 (DOF 3).

PRESCRIBED PUSHER DISPLACEMENT

D1 PROBE (DOF(1))

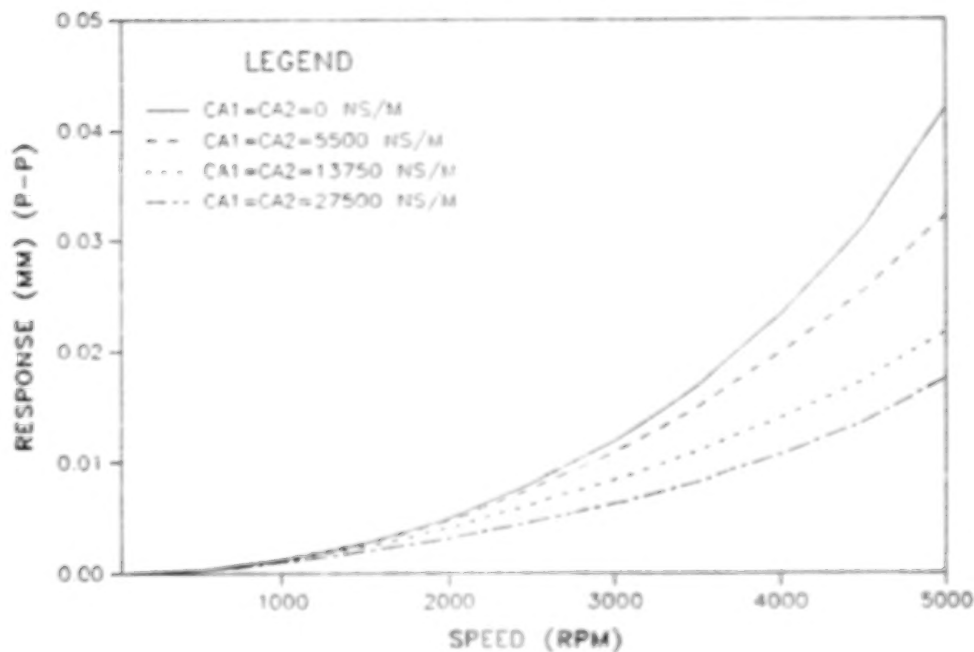


Figure 8 Computer simulation results of prescribed pusher displacement, d_1 probe.

PRESCRIBED PUSHER DISPLACEMENT

D3 PROBE (DOF(5)) EXPERIMENT DATA

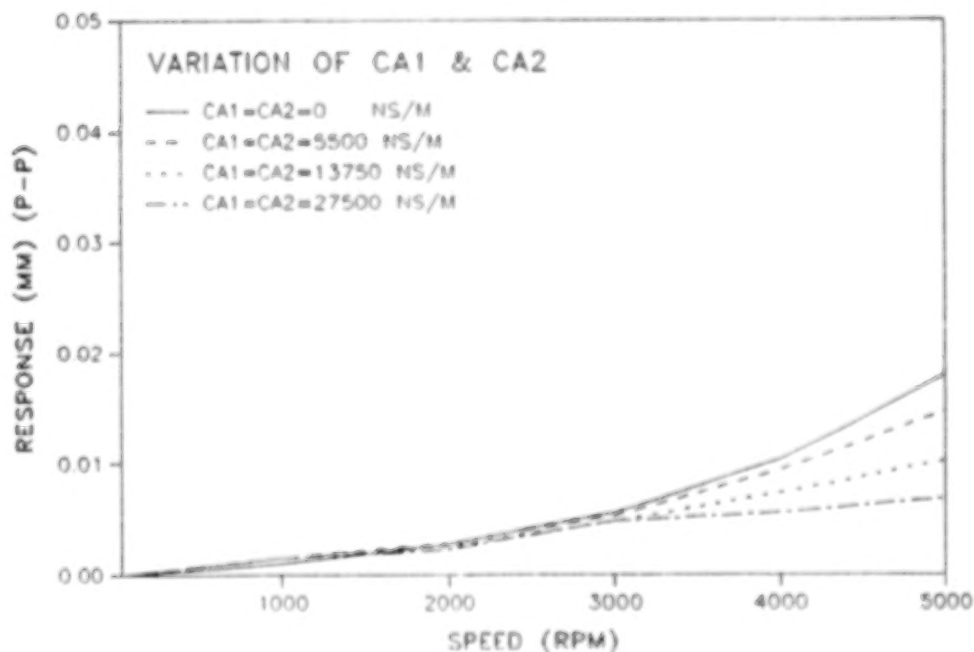
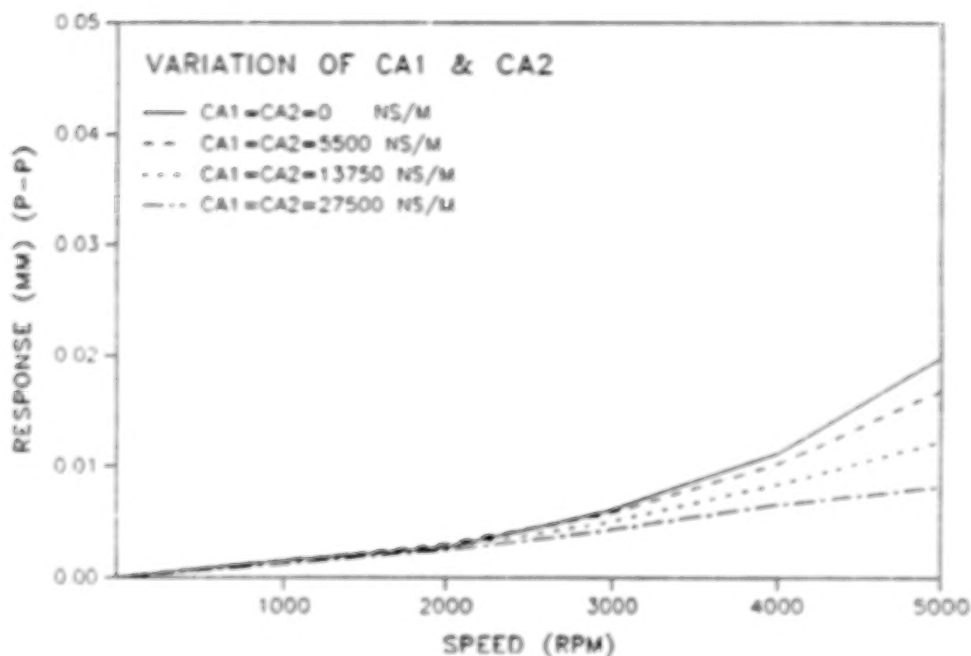


Figure 9 Measured unbalanced response plot at vertical, d_3 , probe.

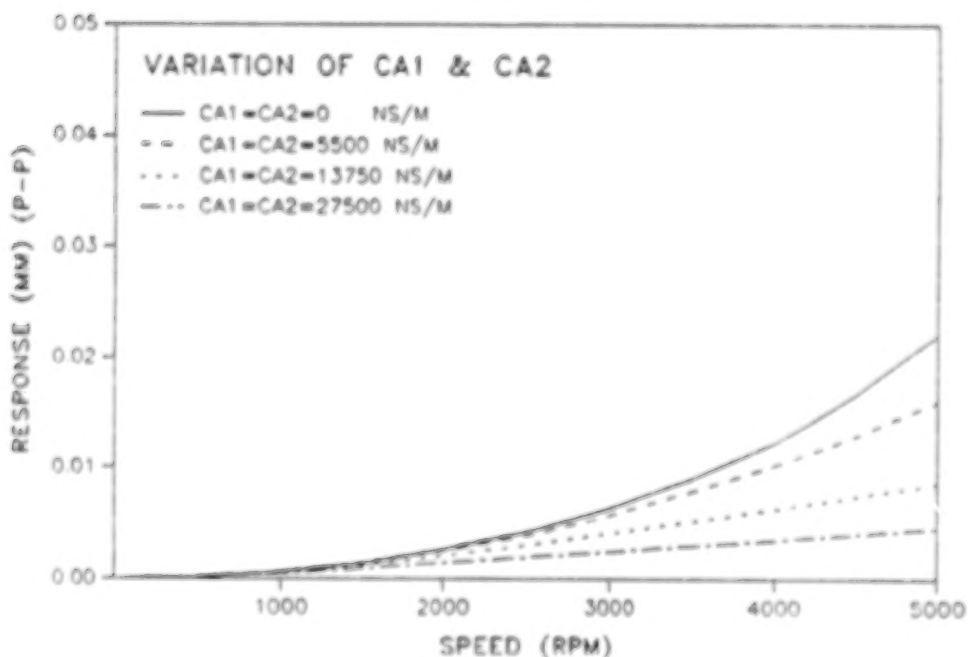
PRESCRIBED PUSHER DISPLACEMENT

D4 PROBE (DOF(7)) EXPERIMENT DATA

Figure 10 Measured unbalanced response plot at horizontal, d_1 , probe.

PRESCRIBED PUSHER DISPLACEMENT

D3 PROBE (DOF(5))

Figure 11 Computer simulation (theoretical) predicted response at probe d_3 .

CAVITATION EFFECTS ON THE PRESSURE DISTRIBUTION OF A SQUEEZE FILM DAMPER BEARING

Fouad Y. Zeidan and John M. Vance
Department of Mechanical Engineering
Texas A&M University
College Station, Texas 77843, U.S.A.

High speed motion pictures have revealed several operating regimes in a squeeze film damper. Pressure measurements corresponding to these distinct regimes were made to examine their effect on the performance of such dampers. Visual observation also revealed the means by which the pressure in the feed groove showed higher amplitudes than the theory predicts. Comparison between vapor and gaseous cavitation are made based on their characteristic pressure wave, and the effect this has on the total force and its phase.

INTRODUCTION

Squeeze film damper bearings have become an integral part of most modern jet engines. Their performance prediction is an important part of the rotordynamic analysis which requires an accurate representation of the dynamic forces generated within the damper. When operating in a cavitated regime and at high eccentricities, the bearing exhibits a non-linear hardening spring behaviour. Mohan, Rabinwitz, and Hahn [1-3] investigated the effect this nonlinearity has on the synchronous response of rigid and flexible rotors. Nikolajsen and Holmes [4] reported the existence of non-synchronous vibrations which was witnessed on experimental as well as on industrial installations. Since most if not all of squeeze film dampers in actual installations operate in a cavitated mode, and in light of the alarming characteristics described in [1-4], it becomes very important to be capable of properly predicting the type and extent of cavitation. The resulting influence on the radial and tangential forces generated by the squeeze film should also be examined.

The treatment of cavitation in squeeze film damper bearings has for the

Portions of the work reported here were supported by General Electric-Aircraft Engine Business Group; technical monitor, A. F. Storace

most part been an extension of the treatment of cavitation in steadily loaded journal bearings. The experimental work of Cole and Hughes [5] on a bearing subjected to a rotating load, led them to believe that the region of cavitation moved around the bearing and was similar to that in a steadily loaded journal bearing. Thus the boundary conditions often utilized in the analysis of journal bearings were directly applied to dynamic and squeeze film damper bearings. White [6] provided experimental evidence that contradicted the assumption stated above. He reported cavitation bubbles that persisted in the high pressure region when operating at eccentricities larger than 0.3. Hibner and Basnal [7] showed significant deviations in their measurements from predictions of the theory as the cavitation extent in the damper increased. Other investigators [8-10] also experienced significant deviations between theory and measurements. The deviations were attributed to various reasons which ranged from inertial effects that are commonly neglected in the classical lubrication theory, to the presence of turbulence, vorticity, and rotordynamic effects. While it is clear that there is a lack of consensus on the exact source for the deviations, there is a general agreement on the notion that cavitation in squeeze film dampers is far more complex than that in steadily loaded journal bearings. Squeeze film dampers usually have seals to limit side leakage, and in general have different configurations of oil feed such as circumferential grooves or inlet holes. These features make the analysis and specification of the boundary conditions a much more complex problem than that associated with rotating journal bearings.

Partly because of the complexities associated with squeeze film dampers, the treatment of the cavitation in these bearings lags far behind that for the simpler journal bearings. To date cavitation in squeeze film dampers is treated by assuming a π -film model which neglects altogether the negative pressure region. This model is often referred to as "unpressurized," while the term "pressurized" refers to the 2π -film model or the uncavitated case. Furthermore, the pressure in the circumferential feed groove is often assumed constant and set equal to zero or equal to the supply pressure. The intent of this paper is to investigate these underlying assumptions and check their validity. It is also hoped that a better understanding will emerge from identifying the various forms of cavitation that can take place in a squeeze film damper bearing.

EXPERIMENTAL APPARATUS

Experimental test rigs utilized in the study of squeeze film dampers have for the most part been low speed and of large clearances mainly for the convenience of such designs in the laboratory and in order to reduce the dynamic effects inherent in high speed operation. San Andres and Vance [11] used a low speed test rig with a large clearance to investigate the inertial effects of the squeeze film. The new test rig utilized in the current investigation is an outgrowth of the

previous apparatus, and was designed to operate at higher speeds incorporating a clearance closer to industry practice in order to determine if there are variables pertinent to high speed operation that have not been adequately simulated by the lower speed test rig.

The test rig is shown in figure 1. It consists of a rigid shaft supported on three super precision angular contact ball bearings with the squeeze film journal mounted on an eccentric piece to provide a controlled orbit. The shaft is driven by a variable speed DC motor through a toothed belt at speeds up to 5000 rpm. Oil is introduced to the circumferential feed groove through four inlet holes 2.38 mm (3/32 in) in diameter and located 90 degrees apart. A solid piston ring prevents leakage out of the feed groove with two serrated piston rings located at the inlet and outlet of the squeeze film land and are shown in figure 2. The serrated piston rings allow adequate flow through the damper and prevent distortion of the pressure wave normally experienced with the presence of inlet and outlet holes. They also produce higher pressures in the film than an open end. The journal is 166 mm (6.539 in) in diameter and 25.4 mm (1 in) long with a radial clearance of 0.635 mm (0.025 in) and an operating eccentricity of 0.45.

IDENTIFICATION OF CAVITATION REGIMES

The dynamic oil pressure is measured using piezoelectric pressure transducers located axially and circumferentially around the housing or outer ring. In the early stages of this study it was desired to obtain an overall view of the characteristics exhibited by this test rig throughout its operating speed range. To accomplish this in a fast and efficient way, the peak to peak pressures were obtained from a digital vector filter (DVF-2) as a function of speed and are shown in figure 3. The oil flow for this measurement was kept around (0.4 gal/min), a value determined by the heat transfer requirements for a typical squeeze film damper configuration. This pressure measurement identified three distinct regions of operation. The lowest speed region has the damper operating uncavitated. The second regime shows a slight drop in the slope of the pressure curve which is attributed to the presence of cavitation in the damper. The last region shows a drastic drop in pressure and an erratic signal. Based on observations of the oil condition at the outlet of the damper, this behaviour is attributed to a bubbly mixture of air and oil.

The characteristic exhibited in this measurement prompted a flow visualization experiment in order to verify the hypothesis just presented and to further clarify the type and extent of cavitation that takes place in a squeeze film damper bearing. Details of the flow visualization experiment were reported in reference [12]. Once the different regimes were identified through the use of high speed photography, pressure measurements were obtained at conditions that corre-

sponded to these regimes in order to outline and characterize the qualitative visualization experiment by quantitative pressure measurements.

Regime I- uncavitated 2π -film: This region is characterized by a full film in the bearing with no apparent film rupture. Operation in this regime takes place when the test rig is operated in the low speed range, or at small orbit eccentricities. It is also possible to achieve an uncavitated operation provided the supply pressure is increased to at least the peak pressure in the oil film and arranged so as to prevent the entrainment of atmospheric air into the damper. A pressure wave characteristic of operation in this regime is shown in figure 4. The pressure signal shows no discontinuity and is characterized by a slightly larger negative pressure region. Integration of the pressure along and perpendicular to the line of centers verifies the presence of a radial force directed outwards, and this has been attributed to the effect of fluid inertia in the damper [11]. The possibility for an engine to operate in such a regime with contemporary bearing configurations and available supply pressures is considerably remote. In spite of the limited need for the analysis of a damper operating in this regime, the efforts have been numerous mainly due to the simplicity such a model provides, and in many cases to highlight special effects such as those of fluid inertia where uncavitated operation facilitates the separation of damping and inertial coefficients.

Regime II- cavitation bubble following the journal: In this regime a ventilated cavity bubble forms and follows the journal around without affecting the positive pressure region. Cole and Hughes [5] witnessed such a behaviour on a dynamically loaded journal bearing operating at a relatively low speed. This evidence has been relied upon to treat cavitation in dynamically loaded journal bearings in a similar manner to that in steadily loaded journal bearings. Figure 5 shows a photograph that identifies such a regime in a squeeze film damper bearing when operated at a low speed, and an inlet oil flow of 0.4 gal/min. This flow corresponded to an inlet supply pressure of 3 psig which allowed air to enter the damper when the negative pressure exceeded that value. A pressure measurement which corresponds to operation in this regime is shown in figure 6. The pressure in the positive region is not affected by the presence of the cavitation bubble. This was also confirmed by the flow visualization experiments which did not reveal the presence of any bubbles in the positive portion of the cycle. The operation in this regime can occur in low speed dynamically loaded bearings, but in the case of squeeze film damper bearings this would more appropriately represent a transition regime as the engine is accelerated to full speed. The persistence of this regime once steady state conditions have been reached are considerably remote.

Regime III- oil-air mixture: As speed is further increased transition from regime II to regime III takes place. The higher speed operation traps portions of

the air bubble, and in the presence of the higher pressure region the bubbles will breakup into smaller cavities or diffuse into the oil. The higher speed operation results in larger negative pressures which means the entrainment of greater amounts of air into the damper. The air bubbles do not collapse as vapor bubbles do, but compress and reduce in size as evident by the photograph shown in figure 7. This ultimately results in a reduction of the pressure amplitude. The size and amount of bubbles are found to be very much speed and pressure dependent. The higher the speeds and pressures, the finer and more numerous the bubbles are. The fluid content in the positive region of the cycle mainly consists of a cloudy oil mixture of finely dispersed air bubbles, and fewer large patches of air cavities. In the negative pressure region, the fine air bubbles and the larger air cavities coalesce and expand to form larger cavities. The presence of air bubbles in this region prevent the oil from achieving the high negative pressure values it would otherwise attain. A pure oil in the absence of air cavities would sustain a larger tensile force until vaporization can take place. Figure 8 shows a pressure measurement that is representative of operation in this regime. One of the distinguishing features is of course the relatively low positive pressure amplitude, but of more importance is the reduced circumferential extent of the positive pressure region. Another feature of importance is a phase shift of the positive pressure peak further downstream, and a delay in the buildup of the positive pressure which is attributed to the presence of the compressible air bubbles as evident in the flow visualization experiment. The negative pressure region occupies a much larger extent as compared to the uncavitated case. It is the authors' belief that the majority of current squeeze film dampers inevitably operate in such a regime considering the supply pressure and flows that are typical of existing squeeze film damper applications.

Parkins and May-Miller [13] utilizing two flat plates with the top plate oscillating normal to the oil film identified a regime which had some similarities to the one just described. They referred to this type of cavitation as a cavitation regime with bubbles fed from outside the film.

Regime IV- vapor cavitation: It is possible to operate in this regime if the end seals have a very tight configuration so as to prevent the ingress of air from the atmosphere, and provided the supply pressure is just below the peak pressure in the film. In order to simulate this condition, the supply pressure to the damper was increased from the 3 psig level utilized in generating the previous regime to 25 psig. This served to prevent air bubbles from entering the damper, and allowed the negative pressure to reach the vapor pressure level during a certain speed range. Figure 9 shows a photograph obtained from the high speed visualization experiment which provided a good indication of the circumferential and axial extent of the vapor cavitation regime. The vapor cavities exist only during the negative portion of the cycle and are seen to immediately collapse as soon as the local pressure increases beyond the vapor pressure of the oil. Thus

their influence is limited to the negative pressure region and does not affect the positive pressure region, a fact that was confirmed by the pressure measurements which corresponded to operation in this regime as shown in figure 10. The pressure signal shows a flat horizontal response once the vapor cavitation has been reached. As the vapor bubble collapses, the pressure immediately resumes the value it is predicted to attain. To further highlight the distinctive features of this regime and that of regime III, additional measurements were carried out as shown in figure 11. In this set-up the test rig was run at 4000 rpm in both cases but with a supply pressure of 40 and 25 psig respectively. The case with the 40 psig simulated the vapor cavitation case, and clearly showed the effect the vapor collapse has on the pressure measurement which was evident by the overshoot in the pressure as a result of the implosion that takes place. It is this phenomenon which is associated with vapor cavitation that causes damage to bearing surfaces resulting in pitting marks. The positive and negative regions in this case occupy equal circumferential extents, unlike the gaseous cavitated case where the negative pressure occupies almost three quarters of the cycle. The gaseous cavitation case shows a lower positive amplitude, and a delay in the buildup of the pressure region, in addition to a shift in phase of the peak pressure as compared to that of the vapor cavitation case. The presence of bubbles in the gaseous cavitation case prevented the negative pressure from achieving the value of the vapor pressure. Walton et al.[14] were able to produce vapor cavitation in a damper bearing through the use of Teflon backup rings to provide tight sealing.

Regime V- vapor and gaseous cavitation: This regime follows directly from the previous regime as the speed is further increased until the peak pressure in the film exceeds the oil supply pressure thus drawing in air bubbles from the atmosphere due to the pressure drop across the seals. In this regime vapor cavitation takes place first, followed by the ingress of air into the bearing. The photograph shown in figure 12 illustrates the conditions in the negative portion of the cycle where the trailing edge of the vapor cavity is seen to collapse at the same time air bubbles are being drawn into the damper. This also demonstrates the ability of the air bubbles to withstand the high pressure region where they are seen to shrink in size but continue to exist throughout the high pressure region of the cycle. As the speed is further increased more air bubbles enter the damper and interfere with the vapor bubble collapse reducing the effect of the implosions as shown in the pressure wave of figure 13. In this figure vapor cavitation is noted first as indicated by the flat portion of the negative pressure followed by a slight reduction in the negative pressure caused by the ingress of air into the damper. The ingress of air bubbles delays the increase of positive pressure, and eliminates the overshoot that was associated with the implosion. This last effect seems favorable however, and has been used to advantage in certain applications [15] to reduce the severity of vapor cavitation which normally results in rapid pitting and erosion of adjacent surfaces. Further increase in speed increased

the amount of air bubbles in the fluid until there was enough air to completely prevent the formation of vapor cavitation, thus in effect transforming this regime to that of regime III which was dominated by gaseous cavitation effects.

EFFECTS OF SUPPLY PRESSURE

The conditions which determine the type of cavitation regime a squeeze film damper operates in depends on many design parameters which include the type of seals and their effectiveness, the speed and operating eccentricity, and most importantly the supply pressure. A squeeze film damper bearing features a non-rotating journal, and so differs considerably from journal bearings and dynamically loaded bearings. The pressure normally generated in all types of bearings causes oil to be expelled from the bearing. In the case of journal bearings, the oil is drawn into the high pressure region of the film by viscous shear at the surface of the spinning journal. In dynamically loaded journal bearings which normally operate in a flooded reservoir, oil is introduced by the spinning journal as was described for journal bearings. In addition, the dynamic motion results in separation of the bearing surfaces during a part of the cycle, and as they do so they draw oil into the bearing lands from the sides since no end seals are utilized with this type of bearings. This mechanism with the exception of rotation is similar to that in squeeze film damper bearings, but these do not normally operate in a flooded reservoir and are usually equipped with end seals. This leaves the oil supply pressure as the only means of introducing oil into such a bearing. Thus it is not surprising to learn how critical the supply pressure is on the performance of squeeze film dampers. Despite the importance of the supply pressure, some investigators including the authors have treated it superficially, and addressed the effects of pressurization by considering its two extremes. The term "pressurized" is often used to indicate an uncavitated bearing, while the term "unpressurized" is used to imply a π -film model, a condition that is similar to that described in regime IV with the additional simplification of neglecting all the negative pressure region. The justification given for neglecting this region which extends from zero pressure to about -35 psig, relies on the assumption that the positive pressure region in actual engine applications which operate at higher speeds and lower clearances extrapolates to positive peak pressure values in the range of 500 to 1000 psig. This would render the negative pressure region negligible in comparison. Simandiri and Hahn [16] have recognized the effect of pressurization on the squeeze film damper, notably the elimination of the jump phenomenon once the pressure was increased to prevent the bearing from operating in a cavitated condition. They cite an equation from which one can determine the required supply pressure to achieve the uncavitated operation. However, these pressures in the case of a typical engine configuration translate to a supply pressure in excess of 500 to 1000 psig, while most existing installations

are only capable of providing pressures in the range of a few psig to about 60 or 80 psig. The required high pressures will also result in excessive flows which the present scavenge pump installation would have difficulty in handling. Operation in the uncavitated region is particularly unattractive for squeeze film dampers that are not equipped with a centering spring, since the damper in this case would have to be relied upon to provide or generate the stiffness required for the load carrying capability as demonstrated by Holmes and Humes [17].

Based on these current limitations, a cavitated damper is the most probable model to consider for existing squeeze film damper installations. The question however, is to determine the type of cavitation and the effect different supply pressures have on the dynamic pressure and the resulting radial and tangential forces. A plot of the dynamic peak to peak pressure for three different inlet pressures is shown in figure 14. Unlike the plot in figure 3 this figure was obtained by taking measurements at discrete speeds, however the general trend and characteristics remained the same. The transition to the bubbly region is still evident by the characteristic knee shape of the pressure curve, which occurs at a speed of approximately 1500 rpm for the case of 3 psig supply pressure. The upper two curves are for the supply pressures of 8 and 25 psig respectively. The net effect of increasing the pressure is to cause a shift in the characteristic knee shape of the pressure curves up in speed. Increasing the supply pressure delays the onset of gaseous cavitation regime or "bubbly region", but it is always reached as speed is increased or when the test rig is operated at higher eccentricities. The supply pressure should theoretically have no effect on the dynamic pressure, and this is actually reflected in the plots at the low speed range where all three cases of supply pressures result in uncavitated regimes. The influence of the supply pressure becomes more apparent as speed is increased and the cavitation extent is expanded. The dynamic pressure in the feed groove was also measured and is shown in the lower three curves of figure 14. The groove pressure reflects the variations of pressure in the squeeze film land indicating that the commonly utilized assumption of constant pressure in the feed groove is not appropriate. The pressures in the feed groove seem to follow the pressures in the squeeze film land, despite the fact that in this damper configuration a serrated piston ring is placed between the feed groove and the squeeze film land. The flow visualization experiments provide a clue to explain the mechanism by which the pressure in the feed groove can reach these unpredicted values. The high speed motion pictures reveal that axial flow from the squeeze film land into the groove is the major contributing factor. The oil exits the squeeze film land at a relatively high axial velocity and is decelerated as it enters the larger clearance in the feed groove. The velocity head transforms into a pressure head at the interface and causes the pressure increase in the feed groove.

CAVITATION EFFECTS ON THE SQUEEZE FILM FORCES

The radial and tangential forces are obtained by integration of the measured pressures along and across the line of centers. The radial and tangential damping coefficients can then be derived from these forces as shown in the Appendix. For the case of an uncavitated damper executing a circular centered orbit, the cross coupled damping and inertia terms are zero. This allows straight forward evaluation of the direct inertia and direct damping coefficients from the radial and tangential forces respectively. For the case of a cavitated damper it is not possible to separate the inertia and damping coefficients. Instead, equivalent radial and tangential damping coefficients are defined, noting that the radial coefficient represents the effect of the direct inertia plus the cross coupled damping term, while the tangential coefficient represents the direct damping plus the cross coupled inertia term. Figure 15 shows a plot of the radial and tangential dimensionless coefficients for the three different cases of supply pressure. While in the uncavitated regimes the tangential coefficient is more or less constant, the effect of gaseous cavitation is to reduce it drastically. The traditional π -film model predicts damping coefficients of half the value obtained from the 2π -film model. This does not seem to be reflected by these measurements as operation progresses from uncavitated to cavitated conditions. The inertial coefficient which is the only term contributing to the radial force in the uncavitated region is soon negated by the cross coupled damping term which dominates as the cavitation extent in the damper increases. This fact is further verified by calculating the phase angle from the measured radial and tangential force components. The phase angle, which represents the angle between the total damper force and the line of centers measured from location of maximum film thickness, was obtained using equation (A10) for the three supply pressure cases as shown in figure 16. In all three cases, a phase angle larger than 90 degrees is obtained when operating in the uncavitated region indicating that the radial force is directed outwards. As air enters the bearing, the gaseous cavitation effects increase. This tends to shift the phase angle from above 90 degrees to around 50 to 60 degrees depending on the extent and amount of gaseous cavities present. The radial force at this instant has reversed directions and is oriented inwards. It is interesting to note that the curve for the supply pressure of 25 psig showed a region of vapor cavitation in which the phase angle was actually above 90 degrees and increasing just as was the case for the uncavitated regime. This is one more feature that distinguishes the two types of cavitation and is shown schematically in figure 17. It is of interest to further check the phase angle for the forces in the feed groove and see whether they are in phase with the forces in the squeeze film land. The phase in the squeeze film land and feed groove for the case of 8 psig supply pressure is shown in figure 18. We note that the difference is minimal in the uncavitated region, but as gaseous cavitation increases the phase shift in the squeeze film land deviates further because the

gaseous cavities occupy a larger portion of the total fluid in this region than those in the feed groove.

CONCLUSION

The cavitation regimes in a squeeze film damper bearing are much more complex and varied in nature than those for journal and dynamically loaded bearings. Five distinct operating regimes were identified through the use of high-speed motion pictures, and were subsequently characterized through pressure measurements. A proper transient analysis requires adequate modeling of the fluid film forces corresponding to each regime. This requirement further highlights the inadequacy of the π -film model for transient analysis.

Air entrainment was shown to drastically modify the pressure wave. Its effect is to reduce the negative pressure amplitude and prevent vapor cavitation from taking place. The circumferential extent of the negative pressure is enlarged, and subsequently the positive pressure region is reduced. The delay of the positive pressure buildup is attributed to the presence of bubbles. The bubbles are also responsible for the reduction of the positive pressure amplitude. While in the uncavitated and vapor cavitation regimes, the measured force has a phase angle of larger than 90 degrees. The effect of gaseous cavitation is to shift the peak pressure further downstream and results in phase angles smaller than 90 degrees. This effect is opposite to that of fluid inertia.

The pressure in the groove was verified to be a direct consequence of the axial flow from the squeeze film land into the groove.

This investigation highlights ways that existing squeeze film dampers could be improved. The oil feed mechanism, seals, and outlet holes, in addition to the supply pressure could be modified to reduce the entrainment of air into the bearing and to enhance damper performance.

APPENDIX

For a squeeze film journal executing a circular centered orbit, the radial and tangential forces can be obtained by integration of the pressure wave,

$$f_r = \int_0^1 \oint P \cos \theta \, d\theta \, d\beta \quad (A1)$$

$$f_t = \int_0^1 \oint P \sin \theta \, d\theta \, d\beta \quad (A2)$$

where $P = \mu \omega R^2 / c^2$ Dimensionless pressure

$$f_r = -C_r \omega \quad (A3)$$

$$f_t = -C_t \omega \quad (A4)$$

where

$$C_r = C_{rt} - D_{rr} \omega \quad (A5)$$

$$C_t = C_{tt} + D_{tr} \omega \quad (A6)$$

for the case of an uncavitated damper $C_{rt} = D_{tr} = 0$
and

$$C_r = -D_{rr} \omega \quad (A7)$$

$$C_t = C_{tt} \quad (A8)$$

The total film force:

$$F_i = [(f_{r_i})^2 + (f_{t_i})^2]^{1/2} \quad (A9)$$

and the force phase angle:

$$\phi_i = 90 + \tan^{-1}(f_{r_i}/f_{t_i}) \quad (A10)$$

measured from maximum gap location.

REFERENCES

- [1] Mohan, S., and Hahn, E. J., "Design of Squeeze Film Damper Supports for Rigid Rotors," *Journal of Engineering for Industry, Trans. ASME*, Vol. 96, No.3, 1974, pp. 976-982.
- [2] Rabinowitz, M. D., and Hahn, E. J., "Steady State Performance of Squeeze Film Damper Supported Flexible Rotors," *Journal of Engineering for Power, Trans. ASME*, 99, 4, pp. 552-558 (1977).
- [3] Hahn, E. J., "Stability and Unbalance Response of Centrally Preloaded Rotors Mounted in Journal and Squeeze Film Bearings," *Journal of Lubrication Tech., Trans. ASME*, 101, 2, pp. 976-982 (1979).
- [4] Nikolajsen, J. L. and Holmes, R., "Investigations of Squeeze-film Isolators for the Vibration, Control of a Flexible Rotor," *J. Mech. Eng. Sci.* (1979).
- [5] Cole, J. A. and Hughes, C. J., "Visual Study of Film Extent in Dynamically Loaded Complete Journal Bearings," *Proc. Lub. Wear Conf.* 1957, (I. Mech. E.) 147-149.
- [6] White, D. C., "Squeeze Film Journal Bearings," Ph.D. dissertation. Cambridge University, December 1970.
- [7] Hibner, D. H., and Bansal, P. N., "Effects of Fluid Compressibility on Viscous Damper Characteristics", Proceedings of the Conference on The Stability and Dynamic Response of Rotors with Squeeze Film Bearings, University of Virginia, 1979.
- [8] Thomsen, K. K., and Andersen, H., "Experimental Investigation of a Simple Squeeze Film Damper," *ASME Paper No. 73-DET-101*.
- [9] Botman, M., "Experiments on Oil-Film Dampers for Turbomachinery," *Journal of Engineering for Power, Trans. ASME*, Series A, Vol. 98, No. 3 July 1976, pp. 393-400.
- [10] Sharma, R. K., "An Experimental Study of the Steady- State Response of Oil-Film Dampers," *Journal of Mechanical Design, Trans. ASME* Vol. 100, April 1978, pp. 216-221.
- [11] San Andres, L. A., and Vance, J. M., "Experimental Measurement of The Dynamic Pressure Distribution in a Squeeze Film Damper Executing Circular- Centered Orbits," *ASLE Trans.* Vol. 30, No. 3, July 1987.

- [12] Zeidan, F. Y., and Vance, J. M., "Cavitation Leading to a Two Phase Fluid in a Squeeze Film Damper," Accepted for presentation at the STLE Annual meeting, Cleveland, Ohio, May 1988.
- [13] Parkins, D. W., and May-Miller, R., "Cavitation in an Oscillatory Oil Squeeze Film," *Journal of Tribology, Trans. ASME*, Vol. 106, July 1984, pp. 360-367.
- [14] Walton, J., Walowit, E., Zorzi, E. and Schrand, J., "Experimental Observation of Cavitating Squeeze Film Dampers," *ASME Trans.*, Vol. 109, April 1987, pp. 290-295.
- [15] Ramussen, R. E. H., "Some Experiments on Cavitation Erosion in Water Mixed with Air," *NPL Symp. Cavitation in Hydrodynamics*, 20 HMSO 1956.
- [16] Simandiri, S., and Hahn, E. J., "Effect of Pressurization on the Vibration Isolation Capability of Squeeze Film Bearings," *Journal of Engineering for Industry, Trans. ASME*, Feb. 1976, pp. 109-117.
- [17] Holmes, R., and Humes, B., "An Investigation of Vibration Dampers in Gas-turbine Engines," *Proc. 52nd AGARD Symp.*, Cleveland, U.S.A. (Oct. 1978).

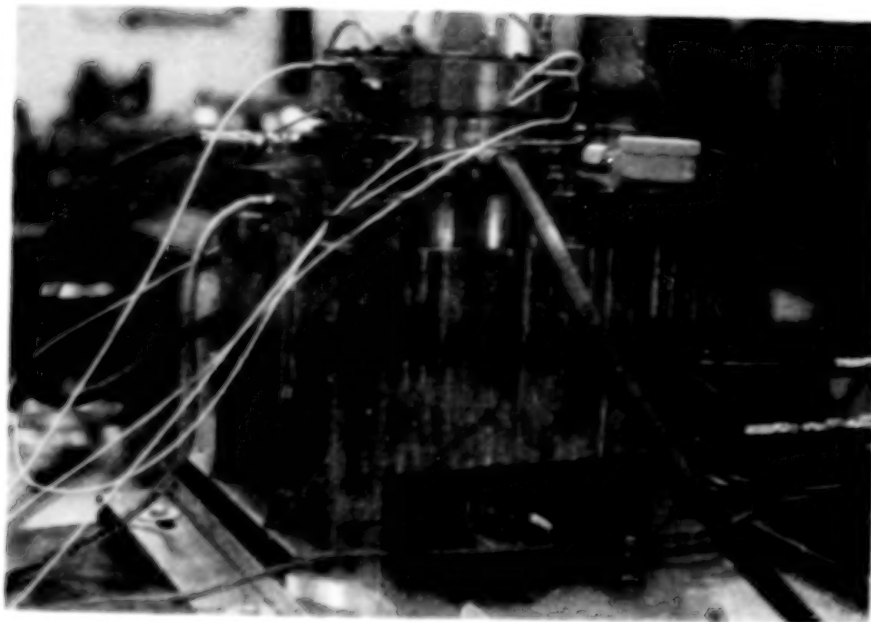


Figure 1: Controlled Orbit Squeeze Film Damper Test Rig.

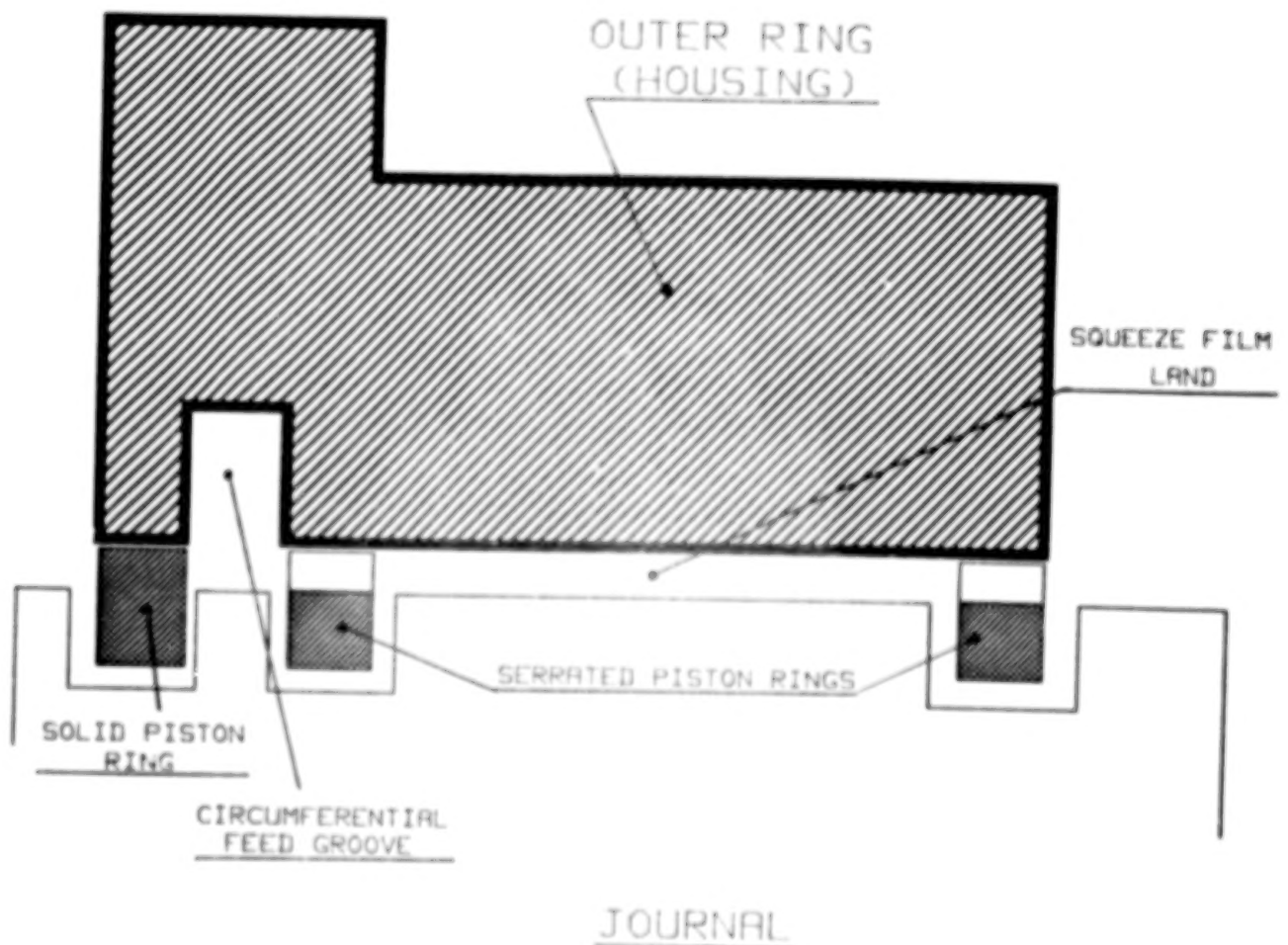


Figure 2: Schematic of Damper Configuration.

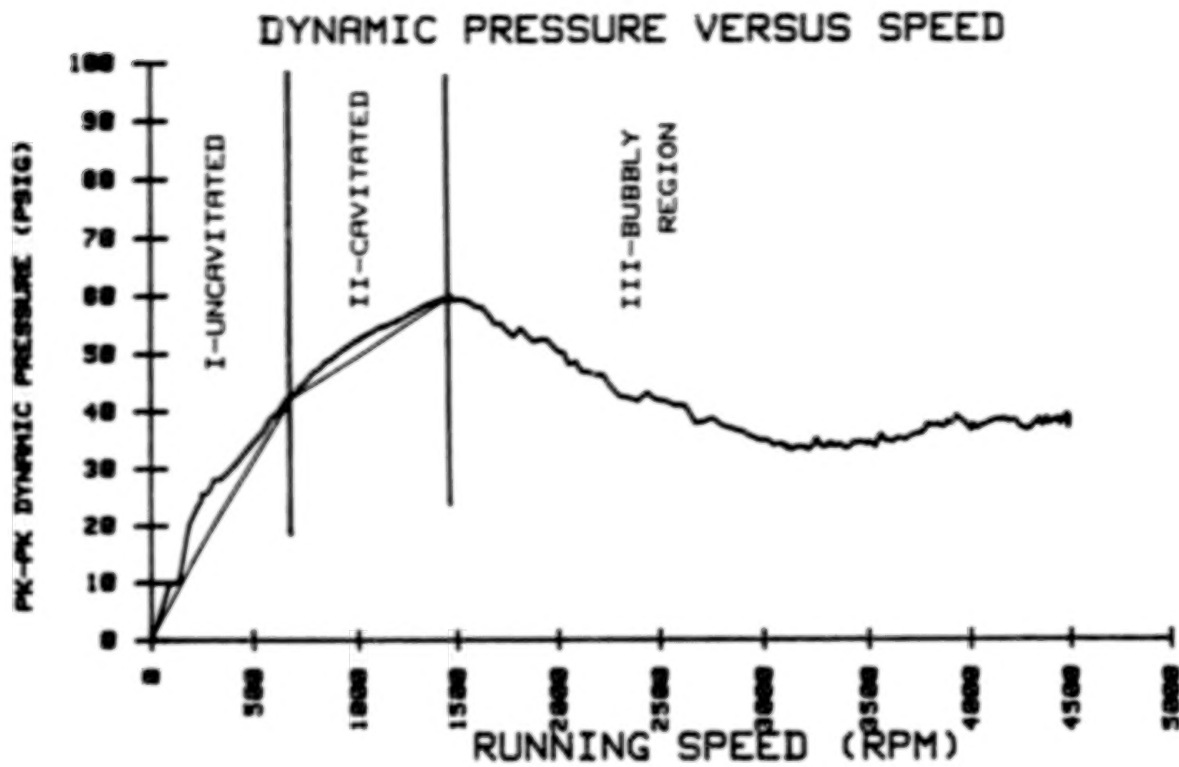


Figure 3: Peak to Peak Pressures vs Speed Identifying Three Distinct Regions of Operation at a Flow of 1.5 L/min (0.4 gal/min).

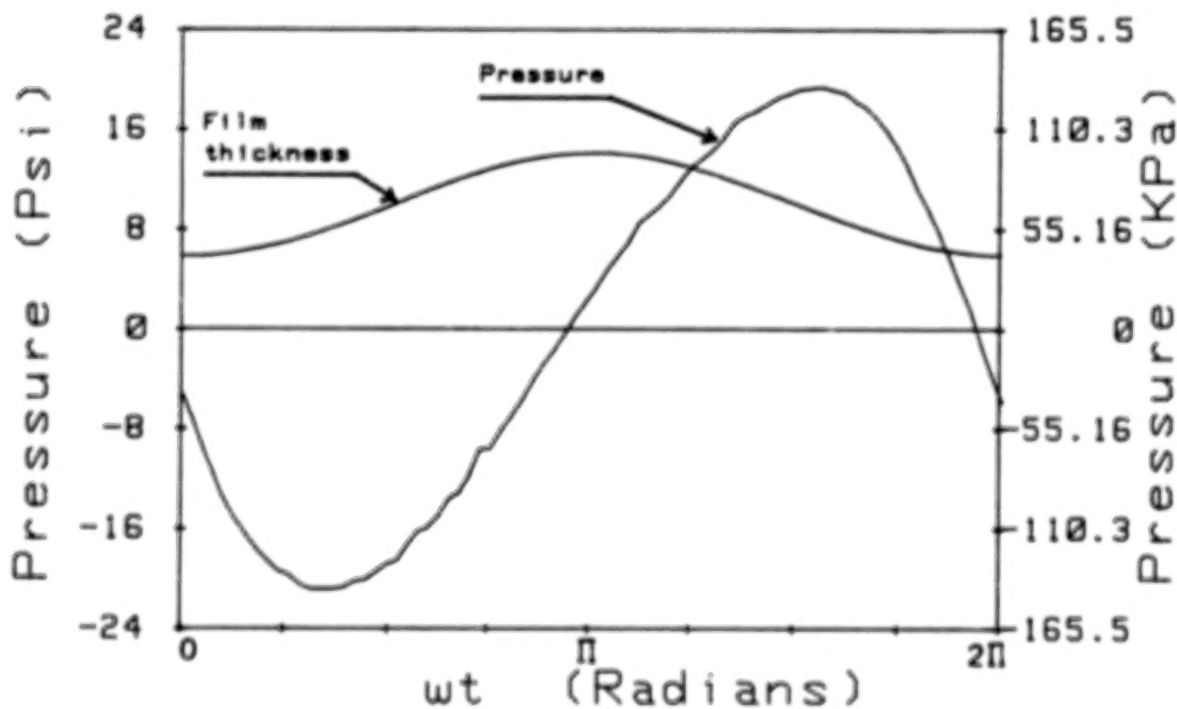


Figure 4: A Typical Uncavitated Pressure Wave.

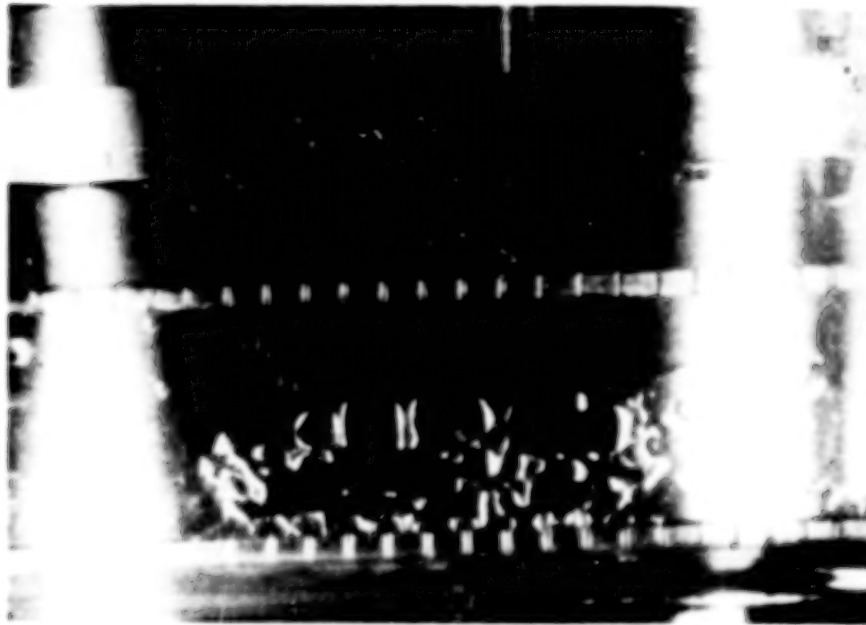


Figure 5: Gaseous Cavitation Bubble (A-A).

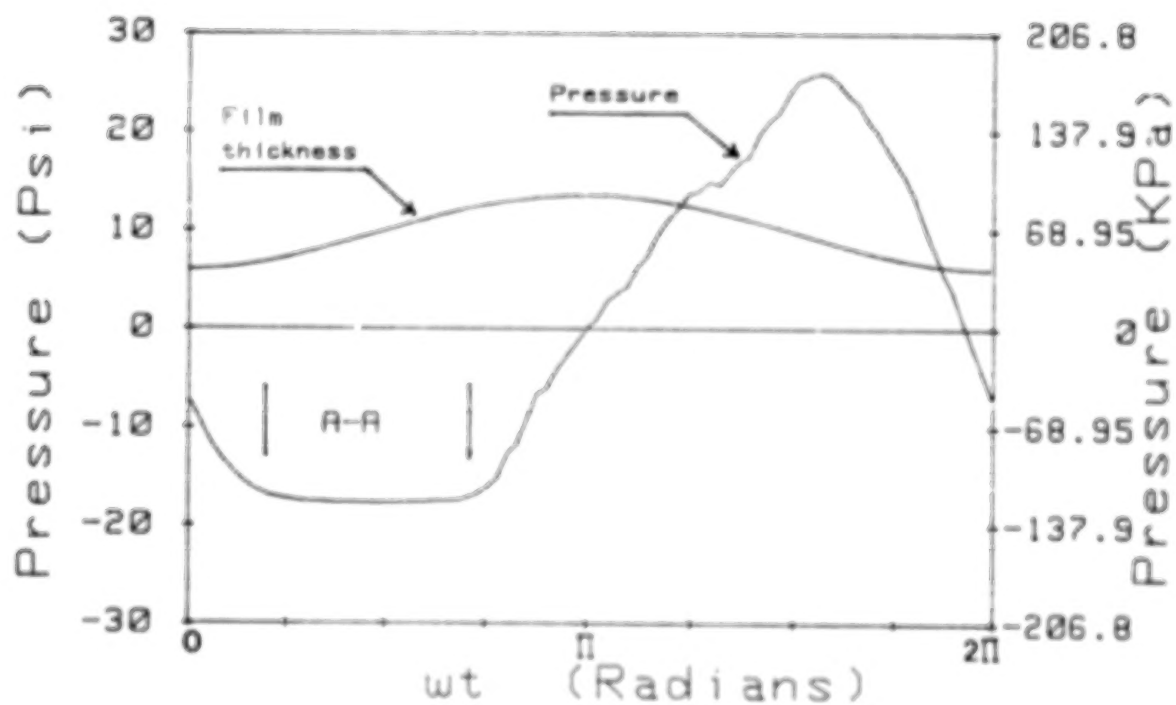


Figure 6: A Pressure Wave which Corresponds to The Cavitation Regime (II) shown in Fig. 5

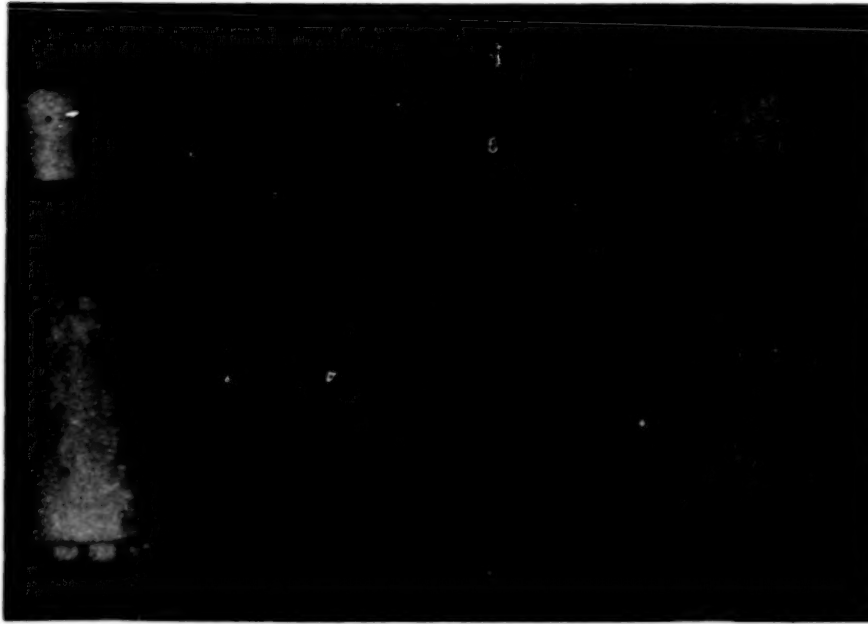


Figure 7: Air Bubbles in the High Pressure Region of Regime III.

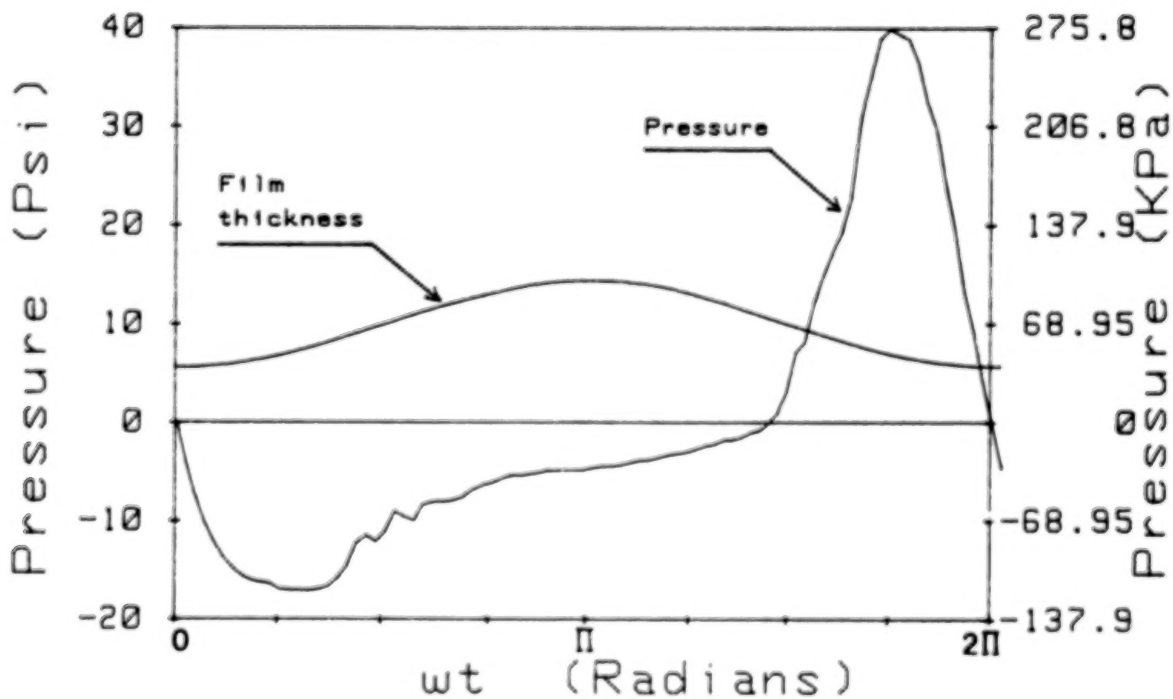


Figure 8: A Pressure Wave which Corresponds to The Gaseous Cavitation in Regime (III).

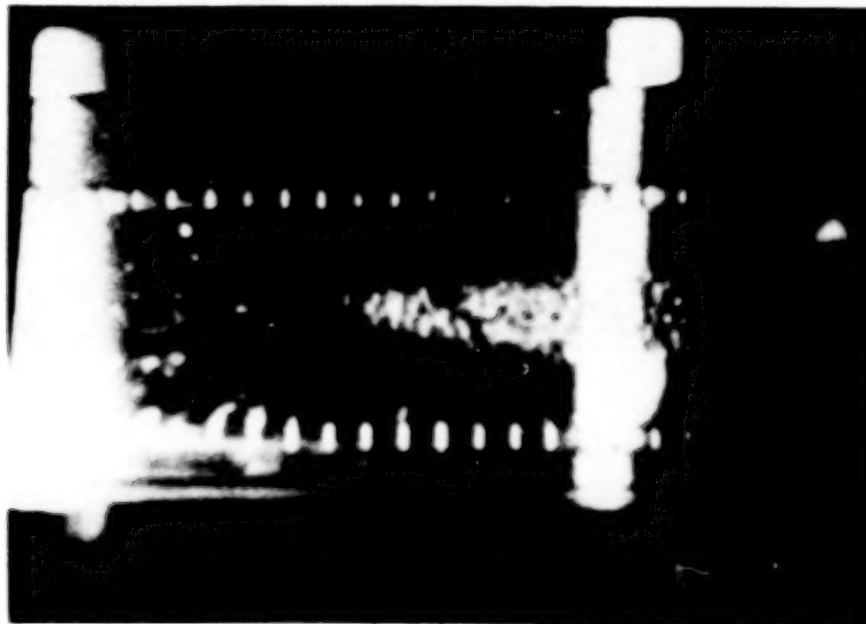


Figure 9: Vapor Cavitation in Regime (IV).

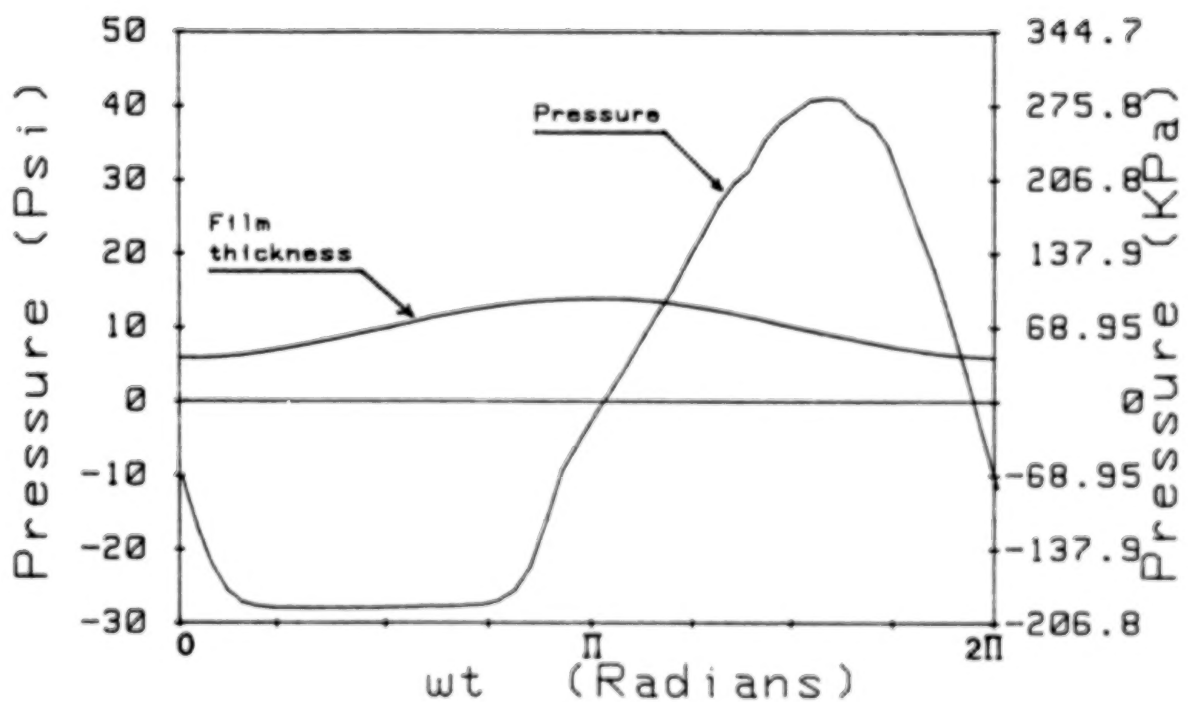


Figure 10: A Pressure Wave which Corresponds to The Vapor Cavitation in Regime (IV).

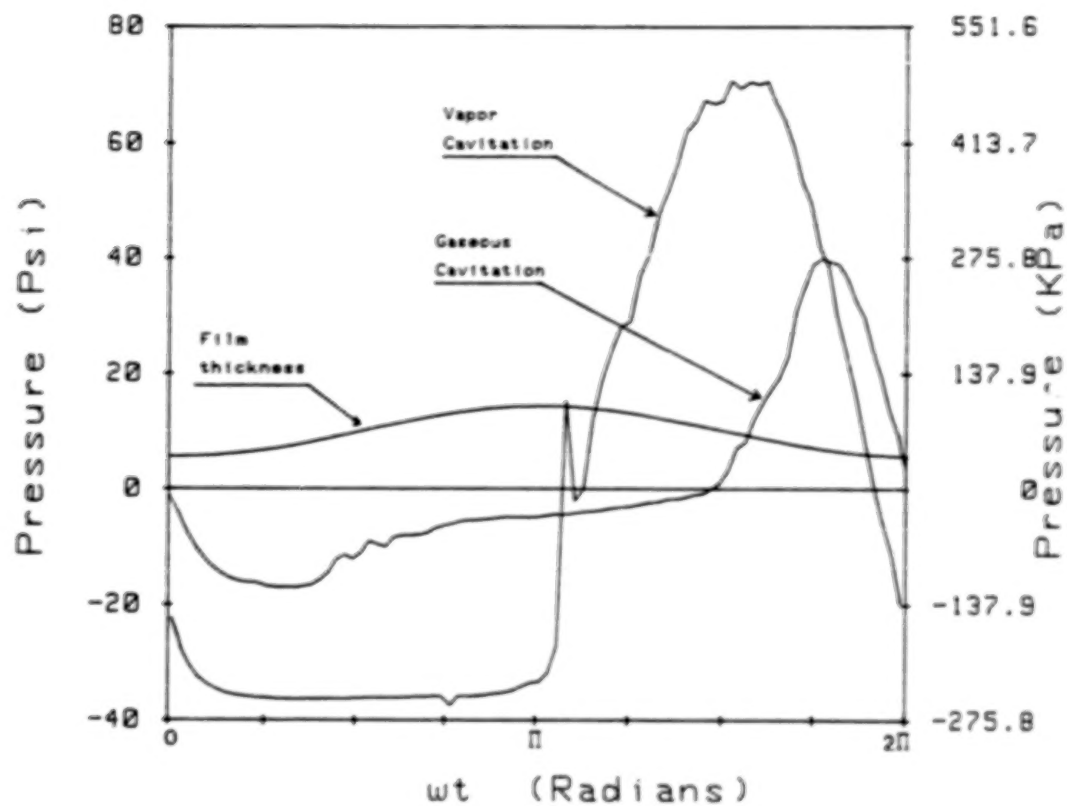


Figure 11: Comparison of Pressure Waves Corresponding to The Gaseous and Vapor Cavitation Regimes



Figure 12: The Trailing End of the Vapor Cavitation Cloud is Shown as Air Bubbles just to the Left Enter Through the Piston Ring Seals.

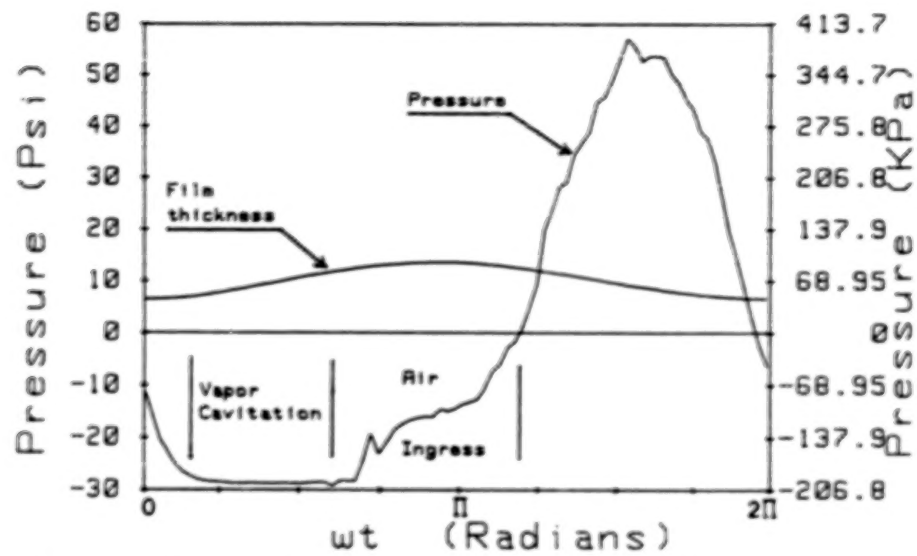


Figure 13: A Pressure Wave which Corresponds to The Vapor Plus Gaseous Cavitation in Regime (V).

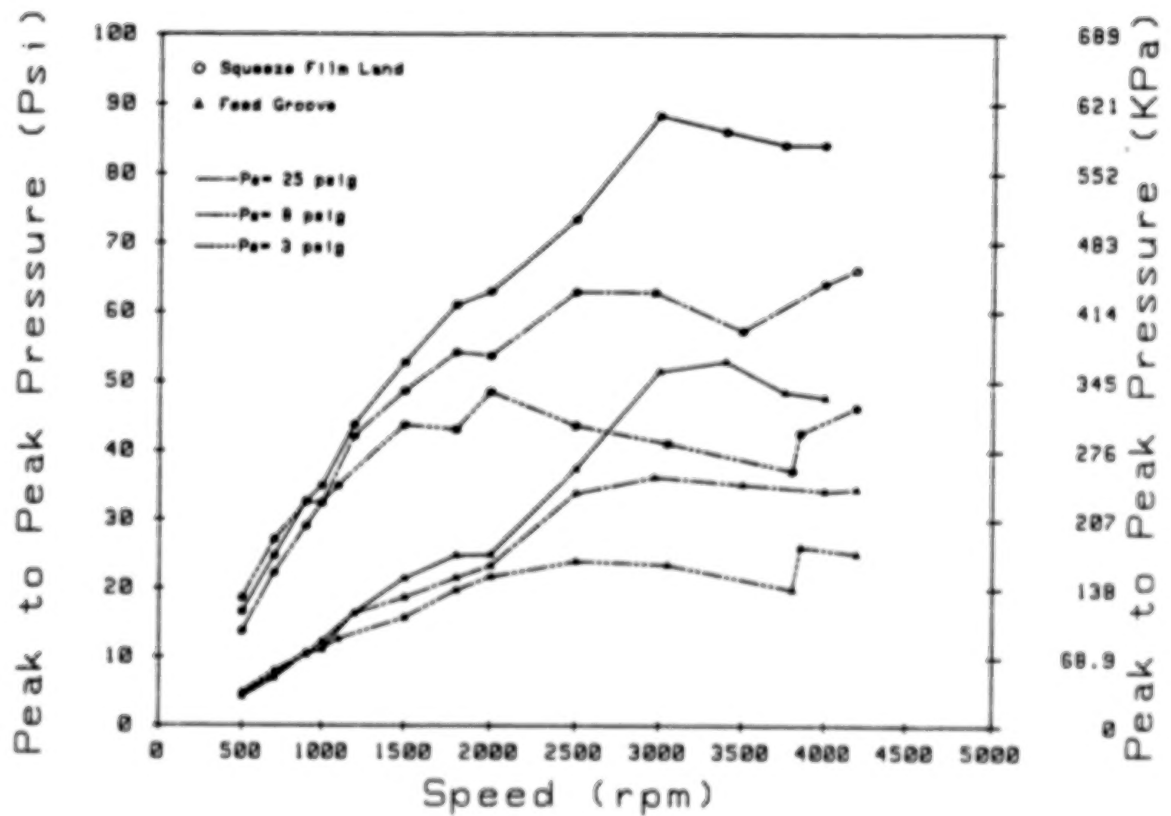


Figure 14: Measured pressures in the squeeze film land and Feed Groove at The Three Different Supply Pressures

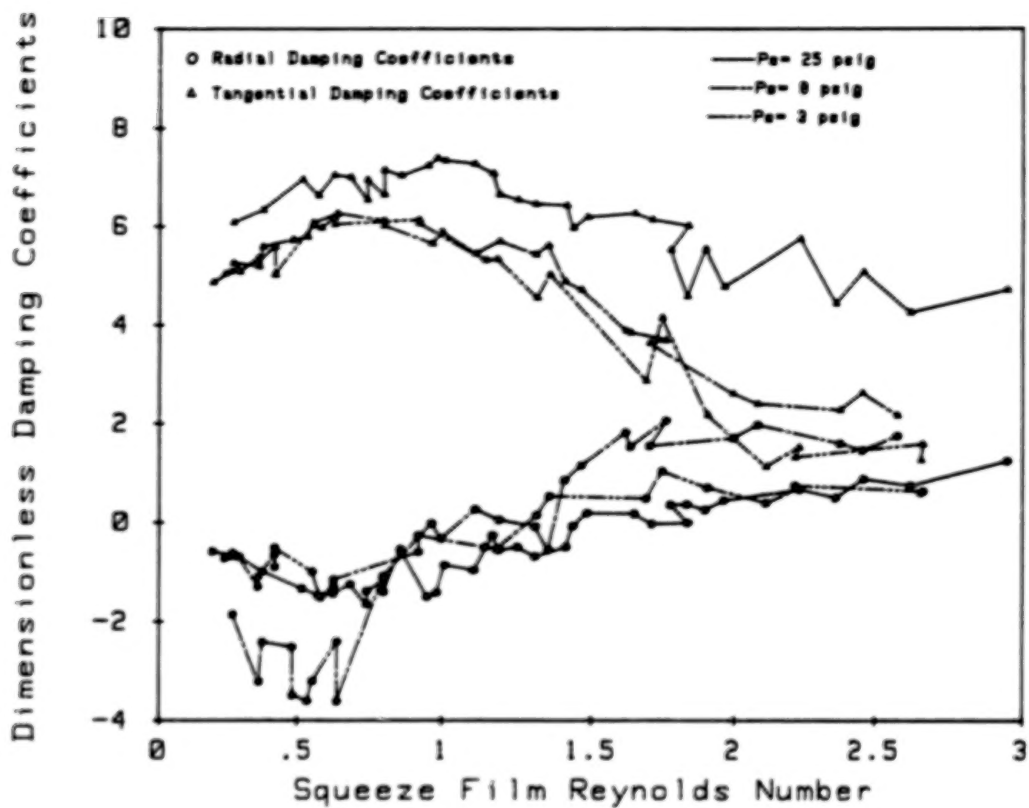


Figure 15: Dimensionless Damping Coefficients at The Three Different Supply Pressures

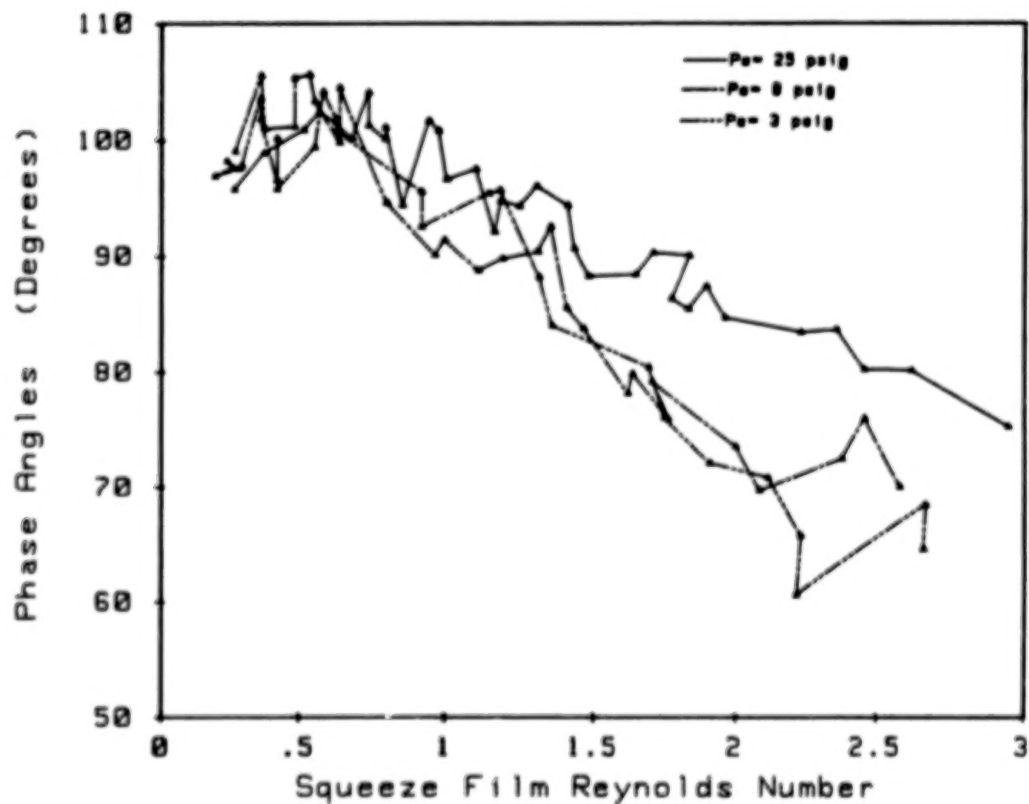


Figure 16: Phase Angles at The Three Different Supply Pressures

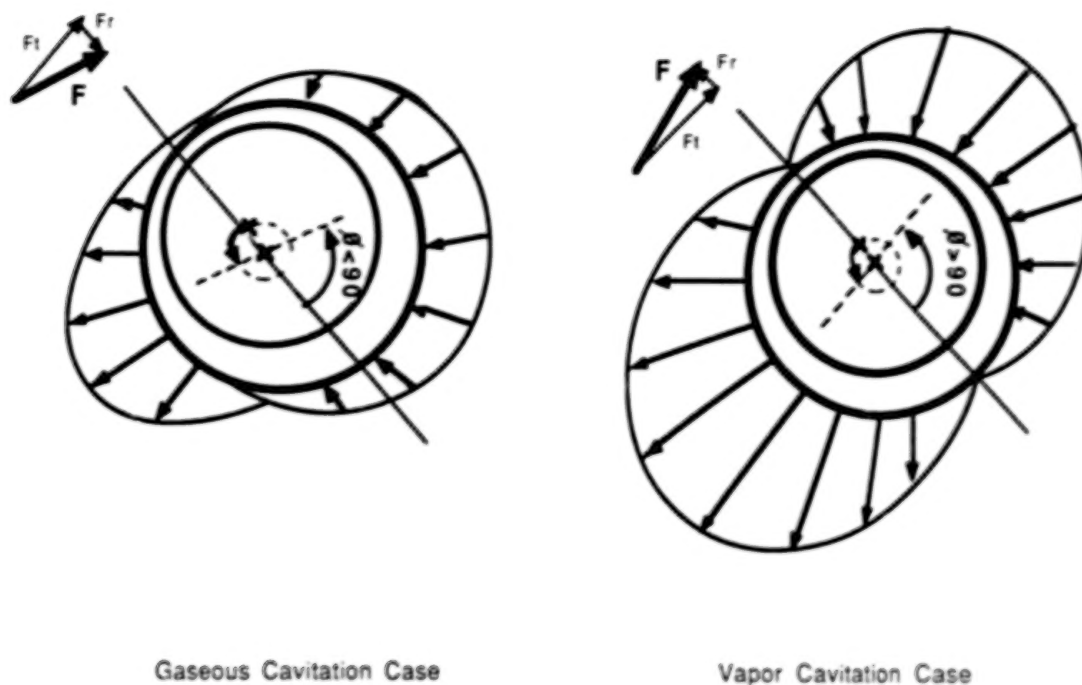


Figure 17: A Comparison Between Gaseous and Vapor Cavitation Highlighting their Effect on the Pressure Distribution and Squeeze Film Forces.



Figure 18: Phase Angles in the Squeeze Film Land and Feed Groove

AN ELECTROVISCOUS DAMPER¹

J.L. Nikolajsen and M.S. Hoque
Department of Mechanical Engineering
Texas A&M University
College Station, Texas 77843-3123, U.S.A.

A new type of vibration damper for rotor systems has been developed and tested. The damper contains electroviscous fluid which solidifies and provides Coulomb damping when an electric voltage is imposed across the fluid. The damping capacity is controlled by the voltage. The damper has been incorporated in a flexible rotor system and found to be able to damp out high levels of unbalanced excitation. Other proven advantages include controllability, simplicity, and no requirement for oil supply. Still unconfirmed are the capabilities to eliminate critical speeds and to suppress rotor instabilities.

INTRODUCTION

Electroviscous fluids have been known for almost a century. In 1885, Koenig [1] tried unsuccessfully to demonstrate a viscosity change in a fluid due to an imposed voltage. Duff [2] and Quincke [3] succeeded in 1896-97 with glycerin and other liquids. It has since been found that a wide variety of fluids and fluid/solid mixtures (e.g. starch in silicone oil) exhibit some level of electroviscosity [4],[5]. However, the effect remained too weak for practical applications until the early 1980's when advances in polymer research led to electroviscous or EV-fluids with sufficient strength to warrant patent protection, e.g. [6].

The main effect in the modern fluids is not the viscosity change but the creation of a solid consistency with an initial shear strength which must be overcome before the "fluid" will flow. In fluid dynamics terminology, the fluid turns into a Bingham plastic when subjected to a voltage, see Fig.1. Some important characteristics of the modern fluids are as follows: the composition is roughly a 1:1 suspension of 10 μ DIA polymer particles in silicone oil; the optimum thickness of the fluid layer to be sheared is 1-2 mm; the required voltage for full activation is 5,000-10,000V; the maximum current is less than 10 mA; the maximum yield strength obtainable is about 5-10 kPa; the fluid activation and deactivation time is less than 1 ms. The invention of the modern fluids led to a profusion of suggested applications in the early 1980's, e.g. [7], [8], [9]. However, to the authors' knowledge, the damper proposed in this

1. This work was supported by the TAMU Turbomachinery Research Consortium. The rig hardware was donated by John Crane-Houdaille, Inc., and the EV-fluid was donated by Castrol Research Laboratories, U.K.

paper represents the first application of EV-fluids to vibration control of rotor systems.

THE EV-DAMPER PRINCIPLE

The electroviscous, or EV-damper design is shown in principle in Fig. 2. A rotating shaft is supported by a bearing with the outer race connected to the damper housing via a so-called squirrel-cage which provides radial support flexibility. The outer bearing race also supports a non-rotating disk located inside the damper housing. The housing is filled with EV-fluid. Two annular rubber membranes seal the damper housing. The fluid films between the disk and the housing solidify when a DC voltage is applied between the disk and the housing. The solidified fluid provides Coulomb damping which impedes the radial motion of the disk, thereby attenuating the radial vibration of the shaft. The damping capacity is controlled by the applied voltage.

THE EXPERIMENTAL APPARATUS

Rig Hardware

An EV-damper with six moving disks and five stationary disks was designed and built and incorporated in a simple flexible rotor system as shown in Figs. 3 and 4. The entire apparatus is made of steel. The design configuration simulates the low pressure shaft of a gas turbine engine with the rotating disk simulating the fan stage. This configuration was chosen to demonstrate the capability of the damper to attenuate the high load excitation that follows a fan blade loss. The rotor is driven by a small air-motor through a flexible rubber coupling. A small electric pump slowly circulates the EV-fluid through the damper to prevent the polymer particles from settling out.

The multidisk damper configuration was designed to ensure that optimum system damping could be reached. The optimum equivalent viscous damping C was found by rotor analysis to be about 4000 Ns/m. The total area A for fluid shearing in the damper was then estimated from

$$C = \frac{4F_0}{\pi\omega x_0} + b \quad (1)$$

see [10], with $F_0 = pA$. F_0 is the constant Coulomb damping force; p is the maximum shear strength of the EV-fluid; ω is the rotational speed; x_0 is the vibration amplitude; and $b = \mu A/h$ is the viscous damping coefficient between the disks where μ is the fluid viscosity and h is the fluid-film thickness. Thus, the total required area A of fluid shearing was estimated to be roughly 4000 cm² with a fluid-film thickness $h = 1.6$ mm. The maximum possible radial rotor excursion at the damper location is 1 cm.

The squirrel-cage consists of three outer beams and three inner beams connected via an electrically insulating disk. The beams are 120° apart. Each beam is 4.8 cm long by 4.8 mm dia. The shaft is electrically insulated from the damper at the bearing outer race. The damper housing is electrically insulated from the base plate.

EV-Fluid

The EV-fluid used here has the following known characteristics:

Composition: 12 μ dia particles in silicone oil

Max. yield strength: 4 kPa at 3.5 kV/mm

Viscosity: 100 cP at 30°C (deactivated)

Density: 1110 kg/m³ at 25°C

Damper Power Supply

The circuit diagram of the damper power supply is shown in Fig. 5. The damping capacity is controlled manually via the variable transformer.

Instrumentation

Two perpendicular pairs of inductive proximity probes pick up the shaft displacements near midspan and near the damper as shown in Figs. 3 and 4. The DC-offsets of the probes are removed by standard op-amp summer circuits. The signals are then A/D-converted and recorded on a micro-computer in the usual fashion. The signals are also displayed live on an oscilloscope for critical speed identification and as a safety precaution. The rotational speed is derived from a photodiode facing a black and white painted stripe on the rotating disk. The speed signal is also recorded digitally and displayed live by a digital timer/counter.

RESULTS

Controllability

The rotor system shown in Figs. 3 and 4 was run up to its first critical speed (rigid body pitching mode) at about 1400 rpm and voltage was applied to the damper. The shaft whirl orbit near the damper was reduced by a factor 4 as shown in Fig. 6. Rapid voltage application resulted in slightly smaller orbits which grew to the steady-state size shown within a few seconds.

High Load Damping Capability

The rotor was run up to about 2000 rpm and an 8040 g.mm balance weight was knocked off to simulate a blade loss. The rotor was then allowed to decelerate slowly down through its critical speed. Fig. 7 shows the

response, including the initial transient, with and without voltage application. The reduction of the response after voltage application is substantial. The critical speed is almost eliminated.

CRITICAL SPEED ELIMINATION

The EV-damper also has the potential capability to eliminate critical speeds as shown in Fig. 8. As the rotational speed approaches the critical speed Ω_c , maximum voltage is applied at Ω_1 . The EV-fluid will solidify and it will remain solidified provided the yield strength of the "fluid" films exceeds the unbalance force transmitted through the damper. The effective rotor support stiffness will therefore increase so the critical speed will increase and the response curve will move to the dashed location in Fig. 8. The response at Ω_1 will then drop as shown and the rotational speed can be increased to Ω_2 . The voltage is then disconnected and the response curve jumps back to its original position as the fluid relaxes. The fluid relaxation time is less than one millisecond which, for most applications, is too short for any vibrations to build up. Thus, the critical speed has virtually been eliminated. Rotor deceleration is analogous.

The minimum response that can be achieved is represented by the bottom point of the valley between the peaks. The elevation of this point depends on the sensitivity of the critical speed to changes in rotor support stiffness. It also depends on the bandwidth of the response peak which is a function of the residual damping with the EV-fluid relaxed.

With the current damper, the response peaks could not be sufficiently separated because the residual damping, due to fluid viscosity and the rubber seals, is too large. The damper will be redesigned with fewer disks and better seals to demonstrate the critical speed elimination. It is expected that a reduction of the residual damping will also result in a more dramatic rate of reduction of the unbalance response than demonstrated in this paper.

CONCLUSION

A new type of rotor-damper has been built and tested for the first time. The damper contains an electroviscous fluid which provides Coulomb damping at a variable rate controlled by a DC-voltage applied to the fluid.

Widespread industrial application of this damper is anticipated due to its simplicity, controllability, high-load damping capability and its potential capability to eliminate critical speeds.

REFERENCES

1. Koenig, W., "Bestimmung einiger Reibungskoeffizienten und Versuche über den Einfluss der Magnetisierung und Electricisierung auf die Reibung der Flüssigkeiten," *Annalen der Physik und Chemie*, Vol. XXV, No. 8, 1885, pp. 618-625.
2. Duff, A.W., "The Viscosity of Polarized Dielectrics," *Physical Review*, Vol. 4, No. 1, 1896, pp. 23-38.
3. Quincke, G., "Die Klebrigkeit isolirender Flüssigkeiten im constanten electrischen Felde," *Annalen der Physik und Chemie*, Vol. 62, No.9, 1897, pp. 1-13.
4. Winslow, W.M., "Method and Means for Translating Electrical Impulses into Mechanical Force," U.S. Patent No. 2,417,850, 1947, (filed 1942).
5. Winslow, W.M., "Induced Fibration of Suspensions," *Journal of Applied Physics*, Vol. 20, No. 12, 1949, pp. 1137-1140.
6. Stangroom, J.E., "Electroviscous Fluids," U.S. Patent No. 4,502,973, 1985.
7. Kerr, J., "Freeze! A Solid Chance to Jam Liquid Flow Lines," *The Engineer*, July 1981, pp. 63 and 67.
8. Brooks, D.A., "Electro-Rheological Devices," *Chartered Mechanical Engineer*, Sept. 1982, pp. 91-93.
9. Scott, D., "Amazing Hardening Fluid," *Popular Science*, April 1984, pp. 82-85.
10. Den Hartog, J.P., "Mechanical Vibrations," 4th Ed., McGraw-Hill, 1956.

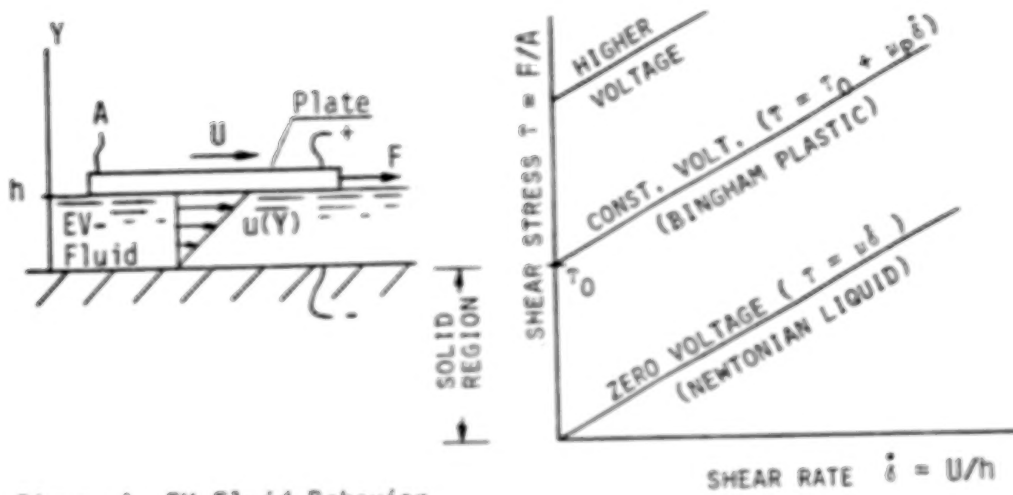


Figure 1 EV-Fluid Behavior

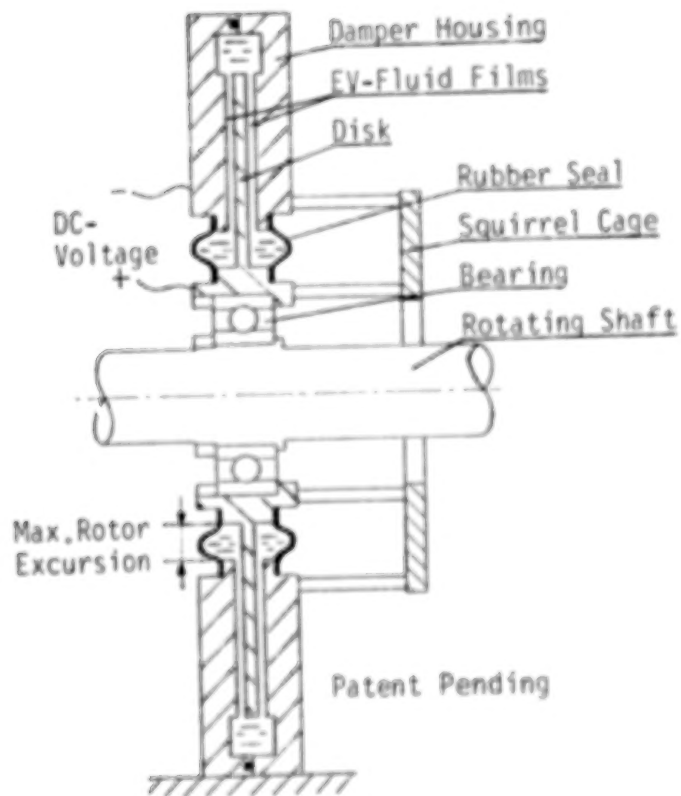


Figure 2 EV-Damper Principle

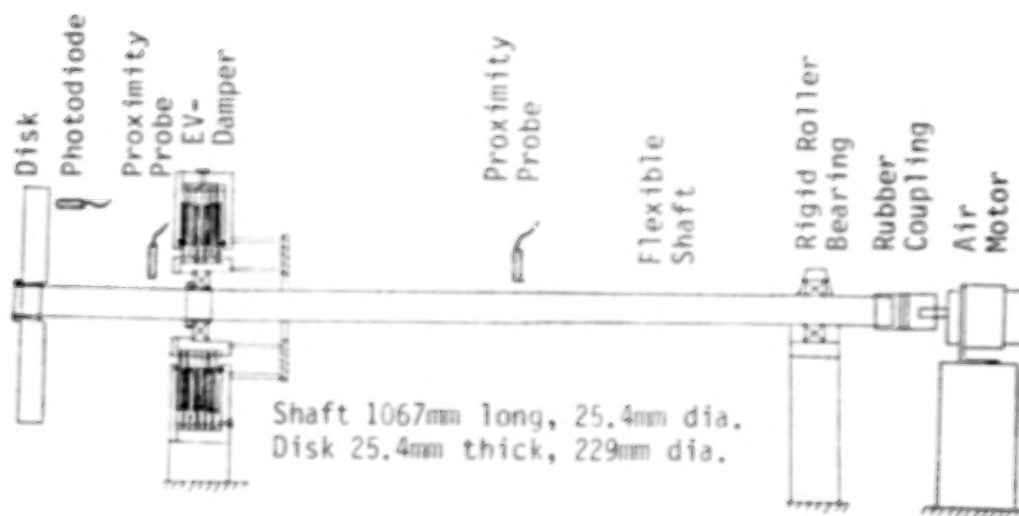


Figure 3 EV-Damper Test Rig (Schematic)

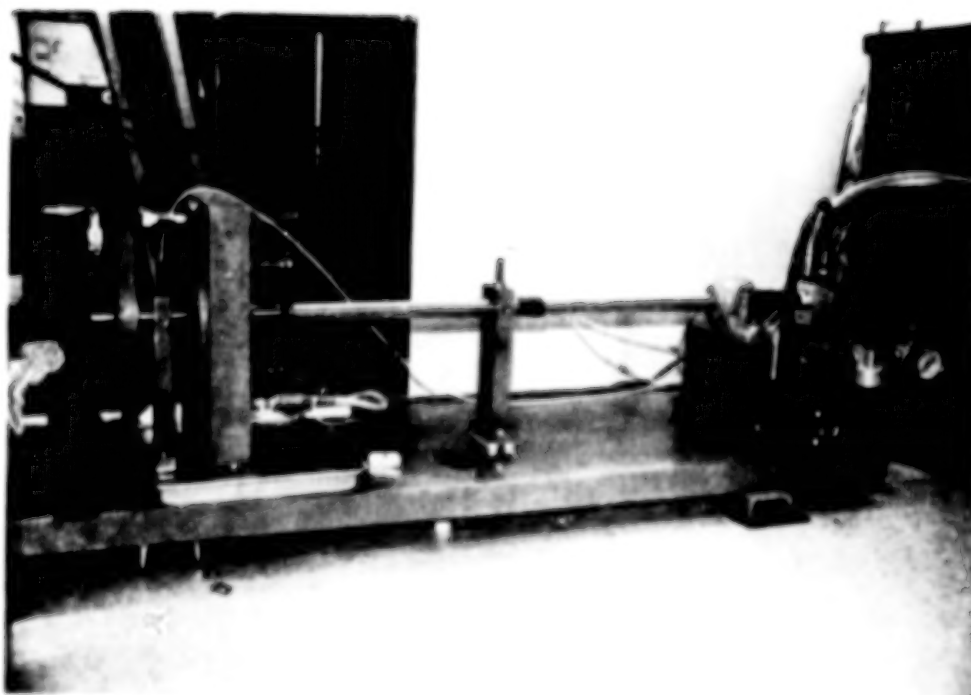


Figure 4 EV-Damper Test Rig

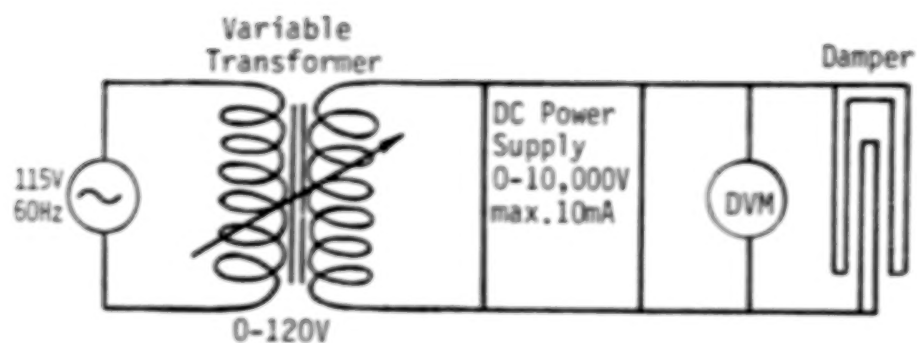


Figure 5 Damper Power Supply



Figure 6 Trace of Shaft Whirl
Orbits Near Damper

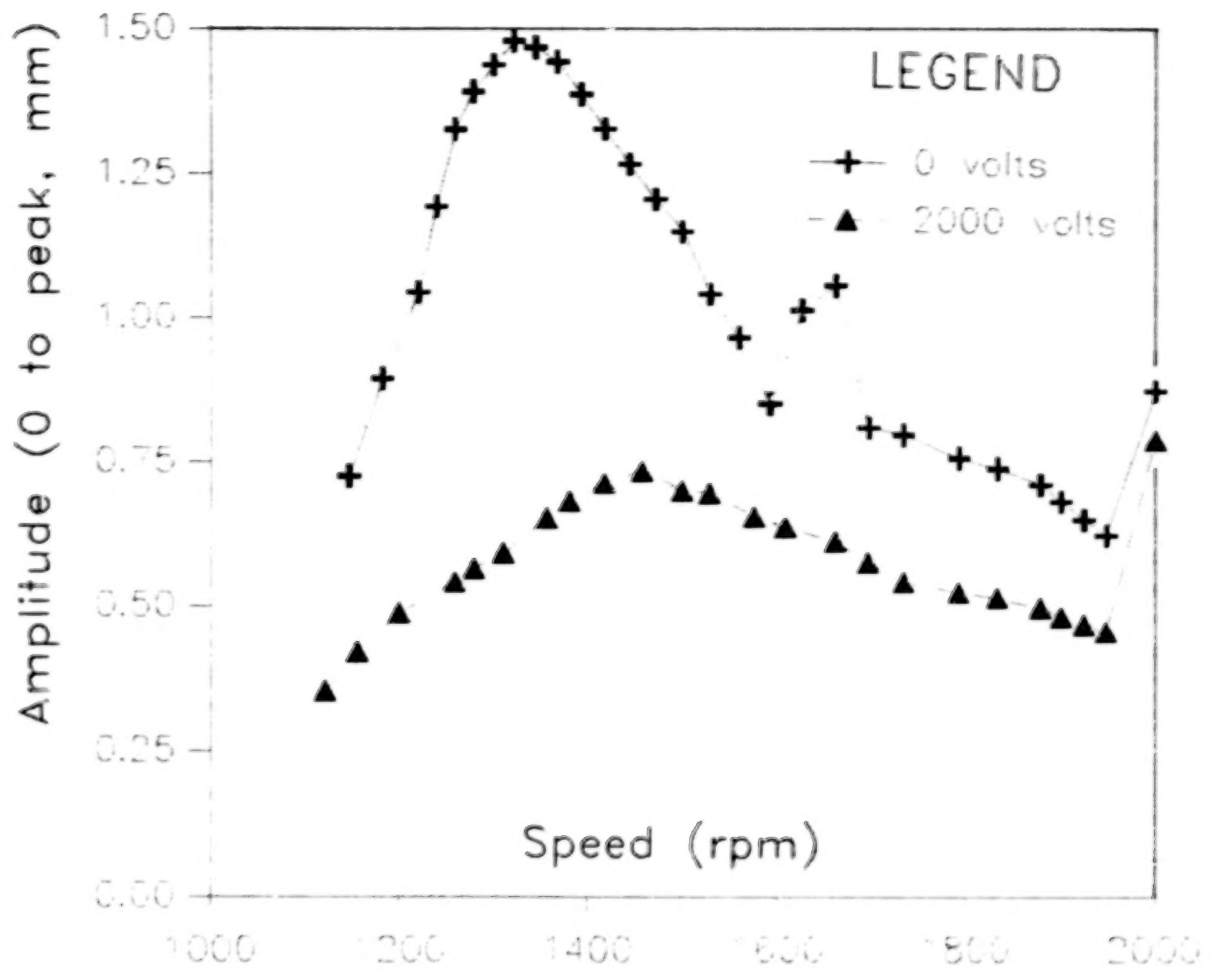


Figure 7 Simulated Blade Loss Response as a Function of Voltage

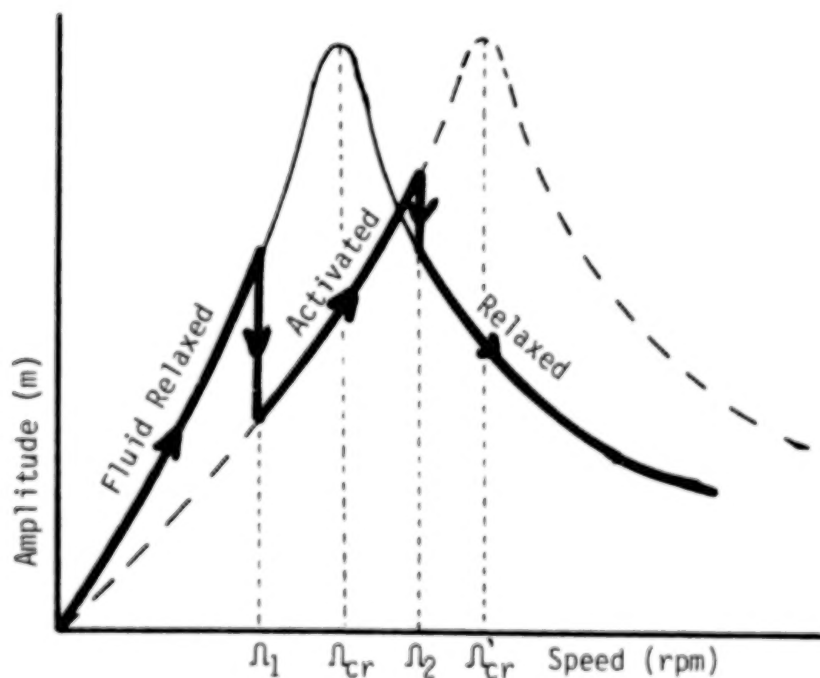


Figure 8 Critical Speed Elimination (Schematic)

BLANK PAGE

ANNULAR HONEYCOMB SEALS: TEST RESULTS FOR LEAKAGE
AND ROTORDYNAMIC COEFFICIENTS; COMPARISONS
TO LABYRINTH AND SMOOTH CONFIGURATIONS¹

Dara Childs, David Elrod, and Keith Hale
Texas A&M University
College Station, Texas 77843, U.S.A.

Test results are presented for leakage and rotordynamic coefficients for seven honeycomb seals. All seals have the same radius, length, and clearance; however, the cell depths and diameters are varied. Rotordynamic data, which are presented, consist of the direct and cross-coupled stiffness coefficients and the direct damping coefficients. The rotordynamic-coefficient data show a considerable sensitivity to changes in cell dimensions; however, no clear trends are identifiable.

Comparisons of test data for the honeycomb seals with labyrinth and smooth annular seals show the honeycomb seal had the best sealing (minimum leakage) performance, followed in order by the labyrinth and smooth seals. For prerotated fluid entering the seal, in the direction of shaft rotation, the honeycomb seal has the best rotordynamic stability followed in order by the labyrinth and smooth. For no prerotation, or fluid prerotation against shaft rotation, the labyrinth seal has the best rotordynamic stability followed in order by the smooth and honeycomb seals.

¹This work was supported in part by NASA Grant NAG3-181 from NASA Lewis Research Center (Technical Monitor, Robert Hendricks) and AFOSR Contract F49620-82-K-0033 (Technical Monitor, Tony Amos)

NOMENCLATURE

C, c	Direct and cross-coupled damping coefficients (FT/L)
\bar{C}, \bar{c}	Normalized direct and cross-coupled damping coefficients (T), defined in Eq. (3)
Cr	Radial clearance (L)
D	Diameter (L)
F	Seal reaction-force magnitude (F)
$f = k/C\omega$	Whirl frequency ratio (dimensionless)
K, k	Direct and cross-coupled stiffness coefficients (F/L)
\bar{K}, \bar{k}	Dimensionless direct and cross-coupled stiffness coefficients, defined in Eq. (3)
L	Seal length (L)
P	Fluid pressure (F/L^2)
R	Seal radius (L)
R_c	Gas constant for air
T	Fluid temperature (K)
$U_{\theta o}$	Seal inlet tangential velocity (L/T)
$u_{\theta o} = U_{\theta o}/R\omega$	Nondimensionalized seal inlet tangential velocity
X, Y	Rotor to stator relative displacement components (L)
Φ	Flow coefficient, defined in Eq. (4)
ω	Shaft angular velocity ($1/T$)

Subscripts

b	Sump value (dimensionless)
r	Reservoir value, radial component

Introduction

Annular seals using honeycomb stators and smooth rotors are occasionally used in turbomachinery, although not as commonly as labyrinths. This type of seal is illustrated in figure 1.

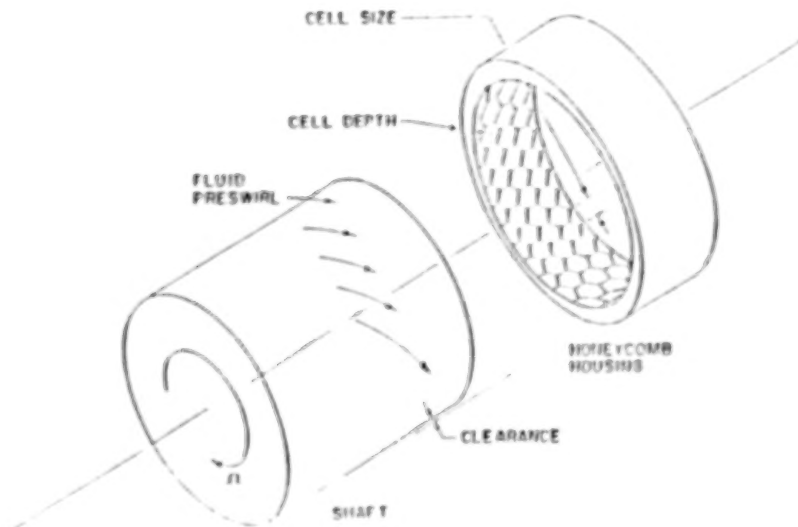


Figure 1. Honeycomb seal geometry.

The model used to define the reaction-force/motion relationship for a centered gas seal is

$$-\begin{Bmatrix} F_X \\ F_Y \end{Bmatrix} = \begin{bmatrix} K & k \\ -k & K \end{bmatrix} \begin{Bmatrix} X \\ Y \end{Bmatrix} + \begin{bmatrix} C & c \\ -c & C \end{bmatrix} \begin{Bmatrix} \dot{X} \\ \dot{Y} \end{Bmatrix}. \quad (1)$$

The test apparatus used here can separately measure the four coefficients of Eq. (1); however, the magnitude of the cross-coupled damping coefficient c is comparable to our measurement uncertainty, and is accordingly not presented. Fortunately this coefficient has a minor influence on compressor and turbine rotordynamics. Data are presented for the direct stiffness K , although (for gas seals) this coefficient also does not have a major influence on rotordynamics. The cross-coupled stiffness k and direct damping C coefficients are of primary influence with respect to rotordynamic stability, since k and C oppose each other in trying to destabilize/stabilize a rotor.

The whirl frequency ratio

$$f = \frac{k}{C\omega} \quad (2)$$

is a useful nondimensional parameter for comparing the stability properties of seals. For circular synchronous orbits, it provides a ratio between the destabilizing force component due to k and the stabilizing force component due to C .

To the authors' knowledge, Benckert and Wachter (1980) have presented the only prior test data for honeycomb seals. Their test rig could only measure stiffness coefficients. Their data, for a single honeycomb configuration, showed large values for k as compared to results for labyrinth seals. Experience with the SSME (Space Shuttle Main Engine) HPOTP (High Pressure Oxygen Turbopump) provides contrary evidence which suggests that honeycomb

seals are more stable than labyrinth seals; viz., replacement of a labyrinth turbine interstage seal with a honeycomb configuration eliminated a rotordynamic instability problem and reduced synchronous vibration levels. The data presented here were stimulated by the SSME experience and is the first presentation of damping data for honeycomb seals and the first systematic presentation of rotordynamic data for a range of honeycomb - cell dimensions.

TEST APPARATUS AND APPROACH

The contents of this section review the test apparatus, test variables, and nondimensionalization of these results before presenting leakage and rotordynamic data.

Test Apparatus

A complete description of the test apparatus is provided by Childs et al. (1986). As illustrated in figure 2, the rotor shaft is suspended, pendulum fashion, from an upper, rigidly-mounted, pivot shaft. This arrangement allows horizontal (harmonic) motion of the rotor. A cam within the pivot shaft provides vertical (static) positioning of the rotor. The rotor is excited, horizontally, by a hydraulic-shaker head which acts on the rotor-shaft housing. The design of the test rig, which is further illustrated in figure 3, permits the installation of various rotor/stator combinations. The test apparatus has been modified since the 1986 reference to permit an increase in top operating speeds from 8,000 to 16,000 *cpm*. Changes include the use of a hydraulically fitted rotor, the introduction of high-speed carbon seals, and the replacement of a roller-element thrust bearing with a Torrington, water-lubricated, swing-pad bearing. The stator of figure 3 is supported in the test section housing by three piezo-electric, quartz, load cells in a trihedral configuration. These load cells measure the pressure-induced forces due to rotor motion within the stator. Accelerometers are provided on the stator to correct for acceleration-induced forces which are measured by the load cell.

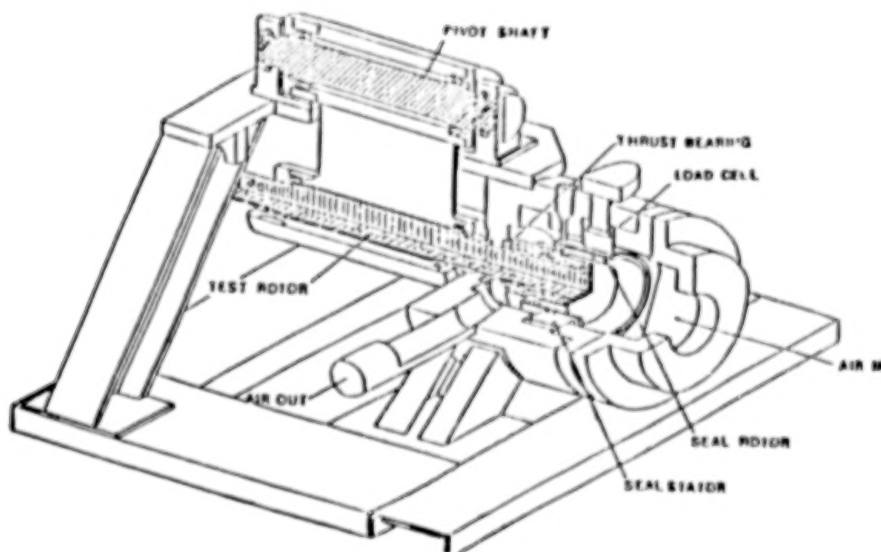


Figure 2. Test Apparatus.

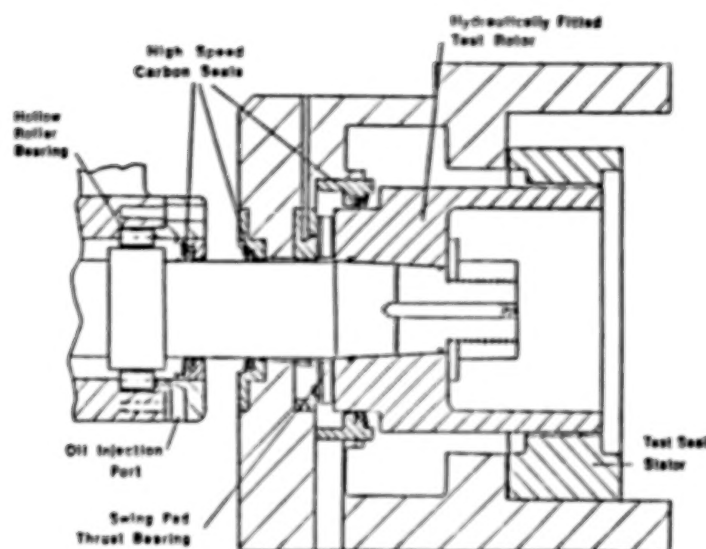


Figure 3. Test-section cross section.

Honeycomb-Seal Dimensions

Table 1 Contains dimensions for the honeycomb seals. The cell sizes cover the normal range for gas-turbine and compressor applications. The 0.74 mm cell depths tend to be smaller than common practice because of earlier experience with liquid seals, Childs and Kim (1985); however, the depths, 1.47 and 1.91 mm, are comparable to industrial practice.

Table 1. Honeycomb Seal Dimensions;
 $L = 50.8\text{mm}$, $C_r = 0.41\text{mm}$, $R = 151.36\text{mm}$.

Seal	Cell Size	Cell Depth
1	0.51 mm	0.74 mm
2	0.51 mm	1.47 mm
3	0.79 mm	0.74 mm
4	0.79 mm	1.47 mm
5	1.57 mm	0.74 mm
6	1.57 mm	1.47 mm
7	1.57 mm	1.91 mm

Test Variables

When shaking about the centered position, the dynamic-seal-apparatus is capable of controlling the following four independent variables: *pressure ratio*, *rotor speed*, *shake frequency*, and *inlet circumferential velocity*. The actual test points for three of these variables are shown in table 2.

Table 2. Test Variables

Pressure Ratio	Rotor Speeds	Inlet Circumferential Velocities
1 - 3.03	1 - 3000 cpm	-2 - High velocity against rotation
2 - 4.45	2 - 6000 cpm	-1 - Low velocity against rotation
3 - 5.70	3 - 9500 cpm	0 - Zero circumferential velocity
4 - 6.95	4 - 13000 cpm	1 - Low velocity with rotation
5 - 8.00	5 - 16000 cpm	2 - High velocity with rotation

The inlet circumferential velocities are controlled using the inlet guide vanes shown in figure 4. The guide vanes are contained in sleeves and located immediately upstream of the test seal. The no-prerotation case is obtained without guide vanes. "High" and "low" prerotation velocities are obtained for the different, guide-vane-depths "A" of figure 4. The inlet circumferential velocity is calculated from measured values for the volumetric flow rate, upstream temperature and pressure, and a flow-turning correction in accordance with Cohen et al. (1972). The circumferential velocity can not be varied arbitrarily, because it depends on the supply pressure and the flow resistance of the seal being tested.

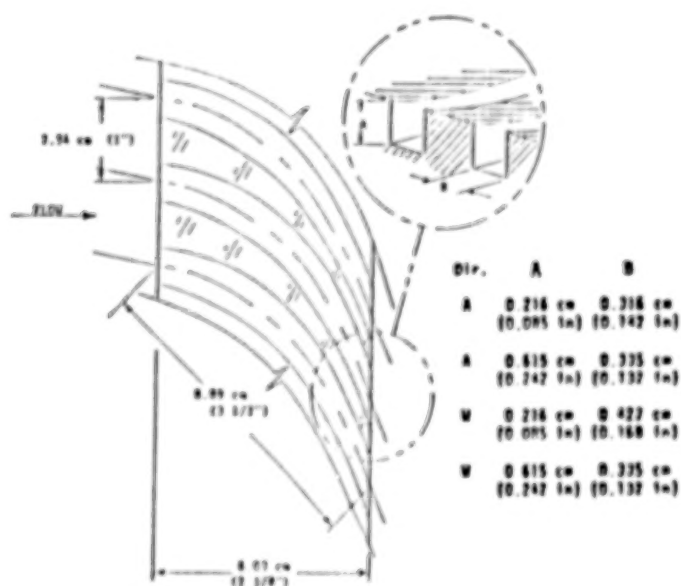


Figure 4. Inlet-guide-vane detail.

Figure 5 illustrates the inlet circumferential velocity versus pressure ratio for the five vane settings. The results are for 3,000 cpm and show $U_{\theta o}$ to be insensitive to changes in the pressure ratio for a given vane setting. Although not illustrated, the velocity tends to decrease with rotor speed, mainly because the rotor grows with increasing speed and reduces the leakage. The ratio of inlet circumferential velocity to rotor surface velocity, $u_{\theta o}$, ranged from about -3.1 to about 3.8. Although the larger numbers are unrealistic, they give insight into the effects of inlet circumferential velocity that would otherwise go unnoticed. The insensitivity of $U_{\theta o}$ to changes in pressure ratio illustrated in figure 5 are typical for all annular gas seals which have been tested.

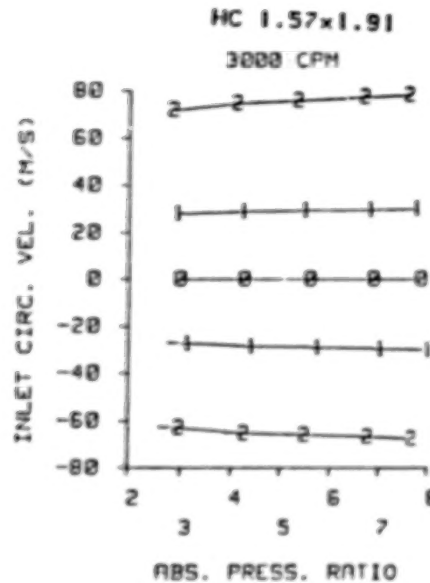


Figure 5. Inlet-circumferential velocity versus pressure ratio for seal 7 of table 1.

HONEYCOMB SEAL ROTORDYNAMIC COEFFICIENT RESULTS

Relative Uncertainty

The uncertainty in the dynamic coefficients can be determined using the method described by Holman (1978). The uncertainty in the force, excitation frequency, and displacement measurements are 0.44 N (0.1 lb), 0.065 Hz, and 0.0013 mm (0.05 mils), respectively. Before normalization, the maximum calculated uncertainty in the stiffness and damping coefficients is 24.1 N/mm (138 lb/in), and 0.072 N-s/mm (0.41 lb-s/in), respectively.

Frequency Dependency of Rotordynamic Coefficients

The stiffness coefficients of the honeycomb seals are shake-frequency-dependent. Previously, frequency-dependent results have been observed for an interlock seal, Childs et al. (1987). However, this characteristic has not been evident in tests of smooth (constant-clearance or taper-geometry) seals, labyrinth-rotor/smooth-stator seals, or labyrinth-rotor-seals. Figures 6 and 7 illustrate K for seals 1 and 7 for the three test frequencies; 38.7, 56.8, and 74.6 Hz. Seals 1 and 7 represent extremes of frequency dependency. Seal 1 is one of the stiffest seals and displays little or no frequency dependency, while seal 7 has low stiffness values and considerable frequency dependency. The results for seal 7 are repeatable and the frequency dependency exceeds the relative uncertainty.

Although not illustrated, the effect on k of changing the shake frequency is greatest for seals 5 and 7, which have the lowest cross-coupled stiffnesses. Changing the shake frequency has little effect on the cross-coupled stiffness of the other five honeycomb seals. The direct damping C is independent of shake frequency.

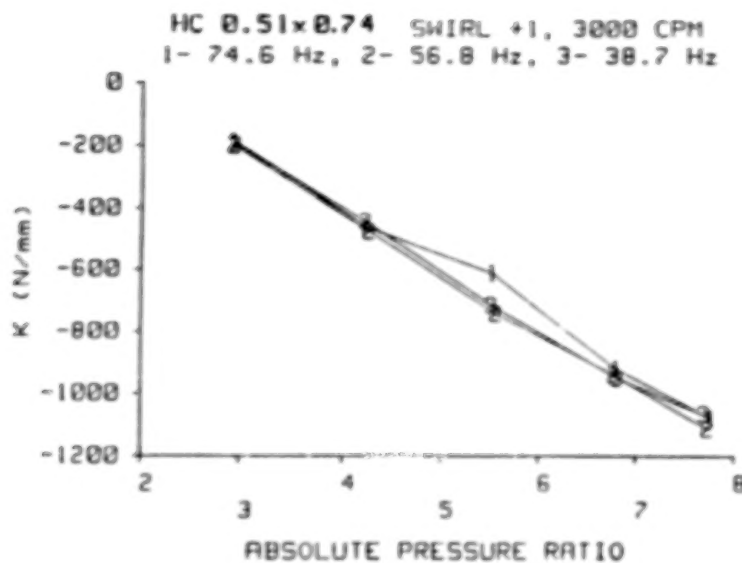


Figure 6. K versus pressure ratio for three excitation frequencies of seal 1 of table 1.

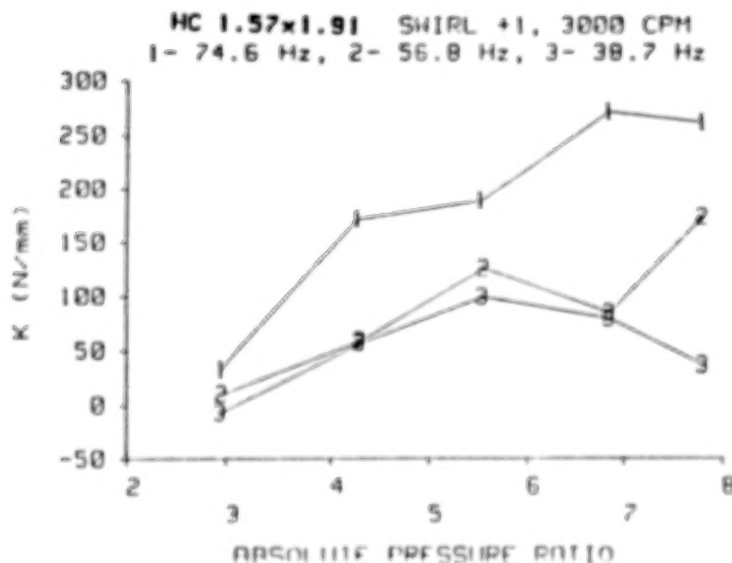


Figure 7. K versus pressure ratio for three excitation frequencies of seal 7 of table 1.

Normalization of Coefficients

Due to thermal and mechanical stresses, the seal rotor grows with changes in the shaft speed. To account for the resulting changes in the radial clearance, the growth was measured over the range of speeds tested. To remove the effect of clearance change, the coefficients are normalized in the following manner:

$$\begin{aligned} \bar{K} &= \frac{KCr}{LD(P_r - P_b)} & \bar{C} &= \frac{CCr}{LD(P_r - P_b)} \\ \bar{k} &= \frac{kCr}{LD(P_r - P_b)} & \bar{c} &= \frac{cCr}{LD(P_r - P_b)} \end{aligned} \quad (3)$$

Cross-Coupled Stiffness Results

Figure 8 illustrates \bar{k} versus $u_{\theta 0}$ at the highest inlet pressure and running speed of table 1 for the seven seals of table 1. Although not illustrated, similar results were obtained at the lowest pressure and highest speed. The figure shows that \bar{k} is positive, i.e., destabilizing, even for negative $u_{\theta 0}$. The figure also shows that destabilizing forces are highest for seal 1 and lowest for seal 7. For the two smaller cell sizes, \bar{k} decreases with increasing cell depth. For the largest cell size, \bar{k} increases and then decreases with increasing cell depth. For seals 2, 4, 5, 6, and 7 of table 1, there is little dependence of \bar{k} on $u_{\theta 0}$.

Figure 9 shows \bar{k} versus ω for the high inlet pressure of table 2 with $u_{\theta 0} = 0$. Similar results are obtained at the lowest pressure. Seal 7 has the best (smallest) \bar{k} of all the seals tested. There is no obvious pattern between changes in \bar{k} and changes in the cell honeycomb dimensions, although the deepest cell depth (seal 7) yields a minimum \bar{k} .

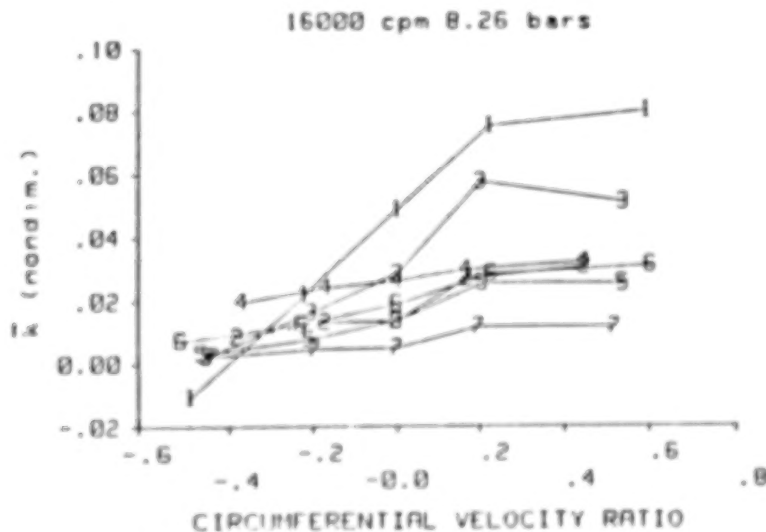


Figure 8. \bar{k} versus $u_{\theta 0}$ for the seven honeycomb seals of table 1.

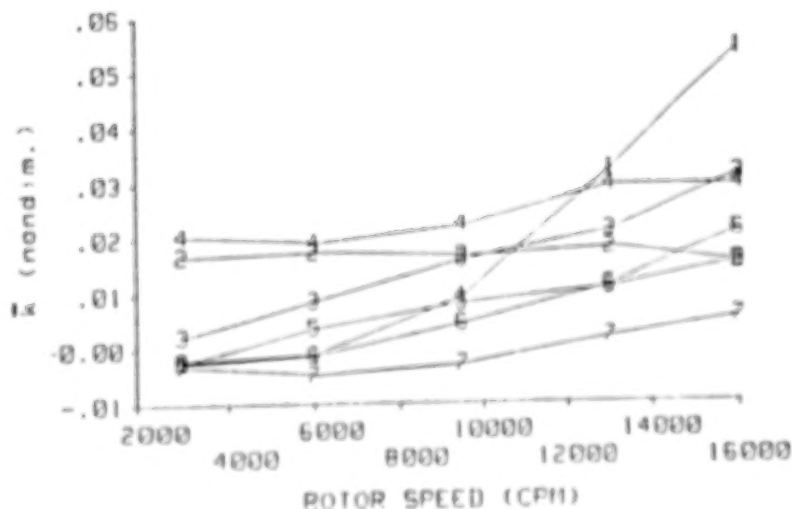


Figure 9. \bar{k} versus ω for the seven honeycomb seals of table 1.

Direct Damping Results

Figure 10 shows \bar{C} versus $u_{\theta 0}$ for the lowest and highest inlet pressures and highest rotor speed of table 2. Seals 1 and 3 of table 1 have the highest values of \bar{C} . Figure 11 shows that the normalized damping of honeycomb seals 1 and 3 increases with increasing rotor speed. There is no clear trend with increasing ω for the remainder of the honeycomb seals. The highest (best) damping values are generally obtained for seals 1, 3, and 4. The worst damping performance is provided by seals 6 and 7 which have the largest cell sizes and depth.

Whirl Frequency Ratio Results

Figure 12 provides comparisons of the whirl frequency ratio f for the seven honeycomb seals at the highest inlet pressure and rotor speed. For the two smaller cell sizes, an increase in cell depth results in a more stable seal (lower f). Seal 5, however, with large shallow cells, is more stable than seal 6. Only seal 1 is less stable than seal 6. Seal 7, with 0.44 mm deeper cells than seal 6, is the most stable seal tested. Obviously, for the larger cell size, f can be quite sensitive to cell depth changes.

Direct Stiffness Results

Figure 13 shows \bar{K} versus $u_{\theta 0}$ for the seven honeycomb seals at the highest inlet pressure and rotor speed. \bar{K} is generally negative for seals 1 and 3 and positive for seals 2, 5, 6, and 7. \bar{K} is highest for seal 6, and generally lowest for seal 1. Figure 14 illustrates \bar{K} versus rotor speed for no prerotation of the inlet air. Except for seals 1 and 3, \bar{K} increases as ω increases at both the lowest and highest inlet pressures. About the same results are obtained for the lowest pressure.

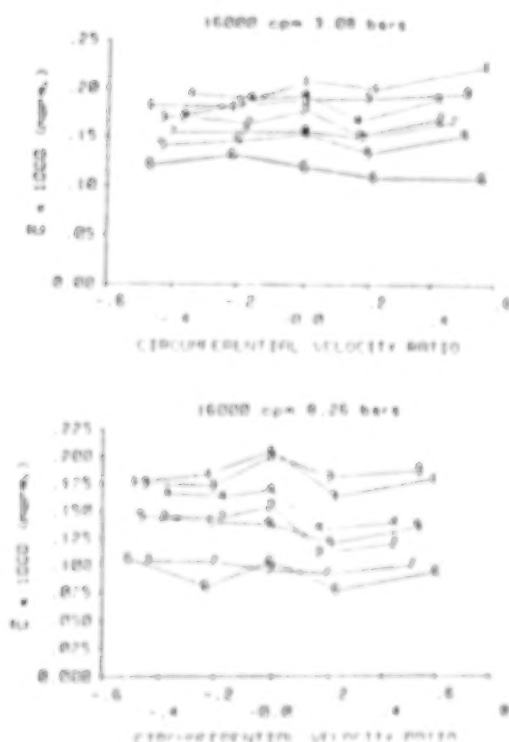


Figure 10. \bar{C} versus $u_{\theta 0}$ for the seven honeycomb seals of table 1.

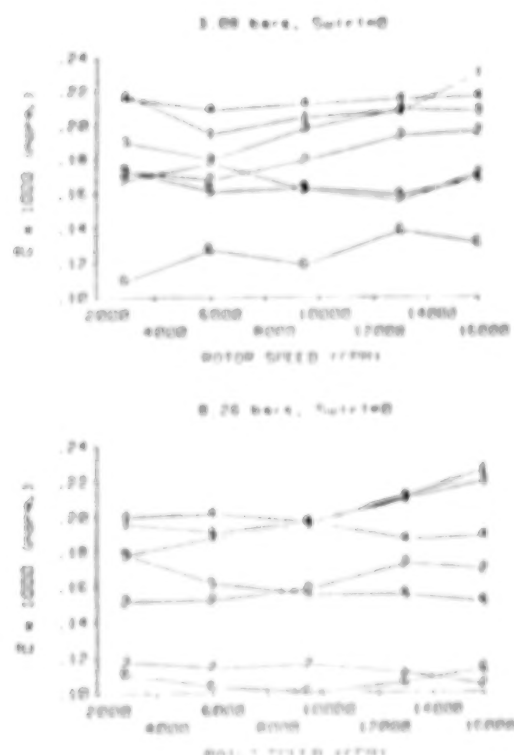


Figure 11. \bar{C} versus ω for the seven honeycomb seals of table 1.

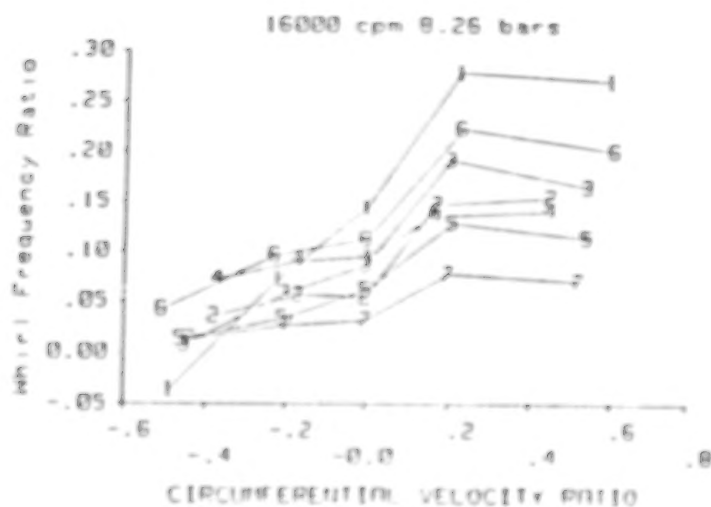


Figure 12. Whirl frequency ratio versus u_{p0} for the seven honeycomb seals of table 3.

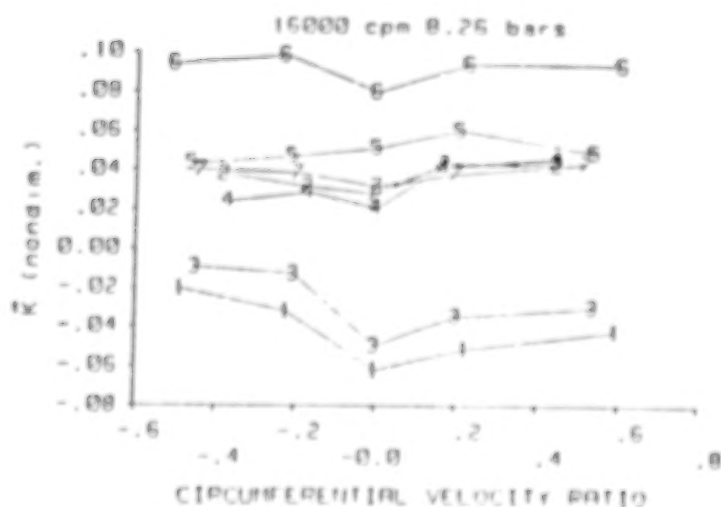


Figure 13. \bar{K} versus u_{p0} for the seven honeycomb seals of table 1.

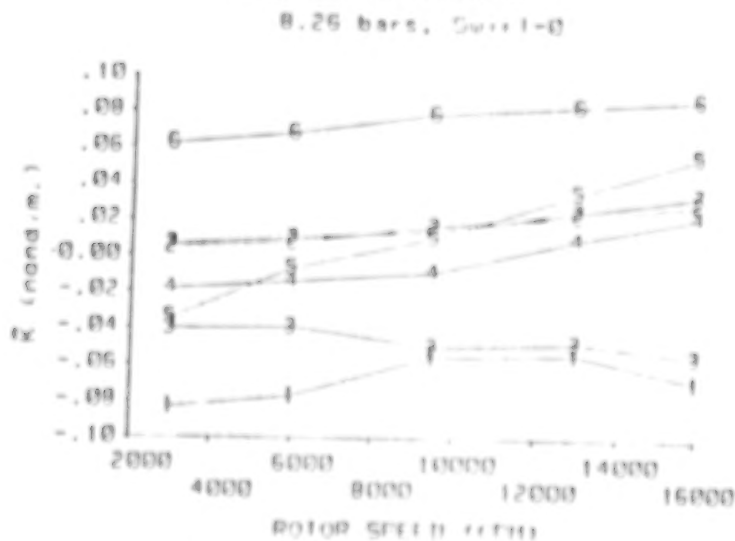


Figure 14. \bar{K} versus ω for the seven honeycomb seals of table 3.

ROTORDYNAMIC COEFFICIENTS: COMPARISONS BETWEEN HONEYCOMB, LABYRINTH, AND SMOOTH SEALS

Comparisons are made in this section for the rotordynamic coefficients of the following seal stators:

- (a) honeycomb seal 7 of table 1,
- (b) the labyrinth stator of figure 15, and
- (c) a smooth stator.

Seal 7 is the most stable honeycomb seal tested, based on a minimum whirl frequency ratio. All seals have the same length (50.8 mm), radial clearance (0.41 mm) and rotor diameter (151.36 mm). The comparative rotordynamic stability of the three seals is of interest in this section. In the following figures, smooth, labyrinth, and honeycomb seal data are labeled S, L, and H, respectively.

Rotordynamic Coefficients

Cross-Coupled Stiffness Results

Figure 16 shows \bar{k} versus $u_{\theta o}$ at the lowest and highest inlet pressure rotor speed of table 2. For the smooth and labyrinth seals (curves S and L, respectively), \bar{k} is negative, i.e. stabilizing, for negative $u_{\theta o}$. For the labyrinth seal, \bar{k} is even stabilizing for no prerotation of the inlet air. For the honeycomb seal, \bar{k} is positive (destabilizing) for all inlet circumferential velocities. For positive $u_{\theta o}$, \bar{k} is almost equally destabilizing for the labyrinth and honeycomb seals. A comparison of figures 8 and 16 reveals that, for positive $u_{\theta o}$, \bar{k} is larger for most of the honeycomb seals than the labyrinth seal as reported earlier by Benckert and Wachter (1980). Although not illustrated, the results of figure 16 also hold for other test pressure conditions.

Figure 17 shows \bar{k} versus ω for the three seals. The results shown are from tests with no prerotation of the inlet air and an inlet pressure of 3.08 bars. For the smooth and honeycomb seals, \bar{k} increases as the rotor speed increases. For the labyrinth seal, \bar{k} is increasingly negative as the rotor speed increases. Childs and Scharrer (1987) have previously noted this type of results for labyrinth seals, as did Hisa et al. (1986). One would expect \bar{k} to eventually begin increasing as ω increases.

Direct Damping Results

Figure 18 shows \bar{C} versus $u_{\theta o}$ for the smooth, labyrinth, and honeycomb seals. \bar{C} for the honeycomb seal is five or six times \bar{C} for the labyrinth seal. At an inlet pressure of 3.08 bars, the smooth and honeycomb seals have about the same normalized direct damping. At 8.26 bars, \bar{C} for the smooth seal is about one-half of \bar{C} for the honeycomb seal when $u_{\theta o}$ is positive. For non-positive $u_{\theta o}$, \bar{C} for the smooth seal is greater than \bar{C} for the honeycomb seal. Note by comparison to figure 10, that most of the other honeycomb seals have substantially higher damping values than seal 7.

Figure 19 shows \bar{C} versus ω for no prerotation of the inlet air and 3.08 bars inlet pressure. In this figure, \bar{C} for the smooth seal increases with increasing rotor speed. For the labyrinth and honeycomb seals, there is little change in \bar{C} with increasing ω .

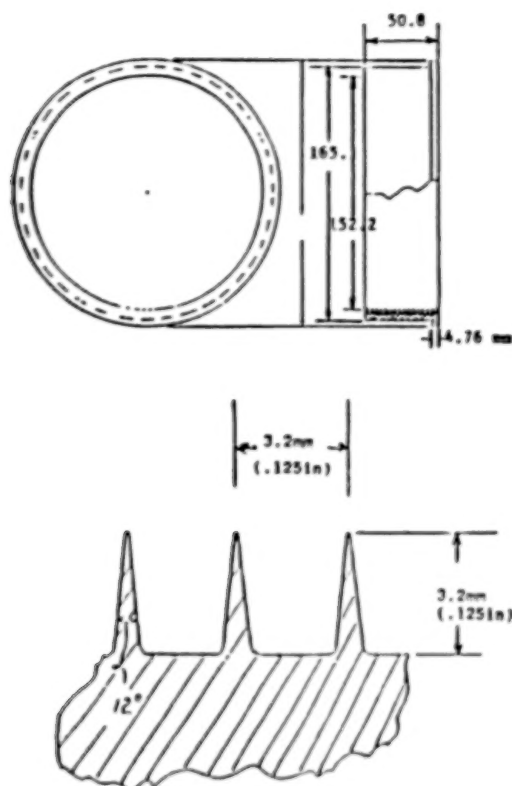


Figure 15. Labyrinth seal geometry.

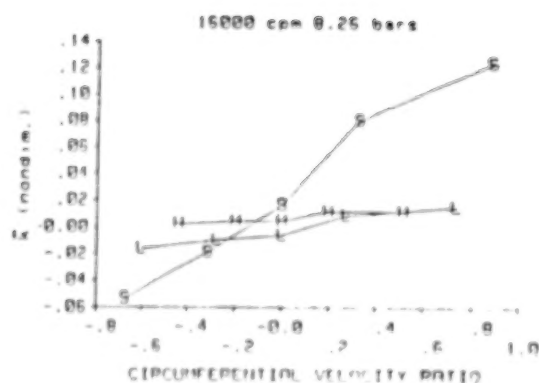


Figure 16. \bar{k} versus $u_{\theta 0}$ for smooth, labyrinth, and honeycomb seals.

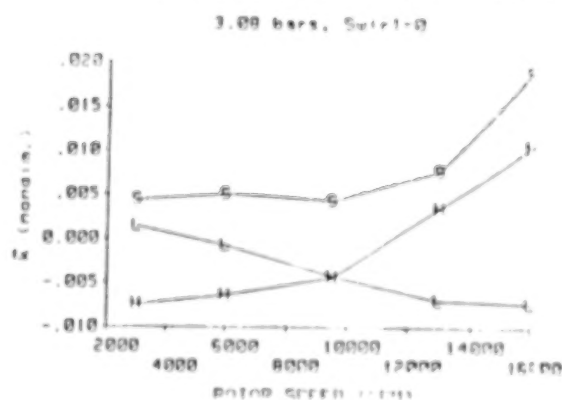
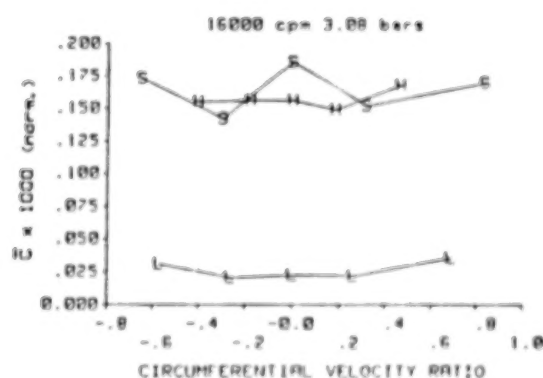


Figure 17. \bar{k} versus ω for smooth, labyrinth, and honeycomb seals.

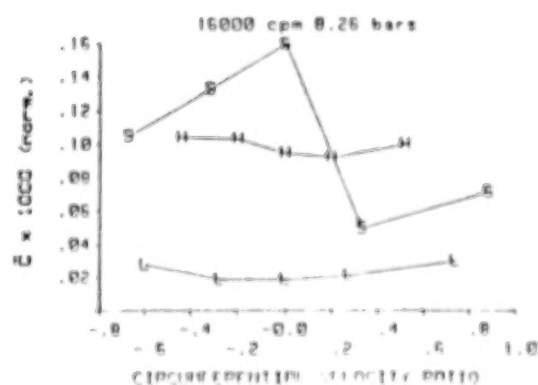


Figure 18. \bar{U} versus $u_{\theta 0}$ for smooth, labyrinth, and honeycomb seals.

3.08 bars, Swirl=0

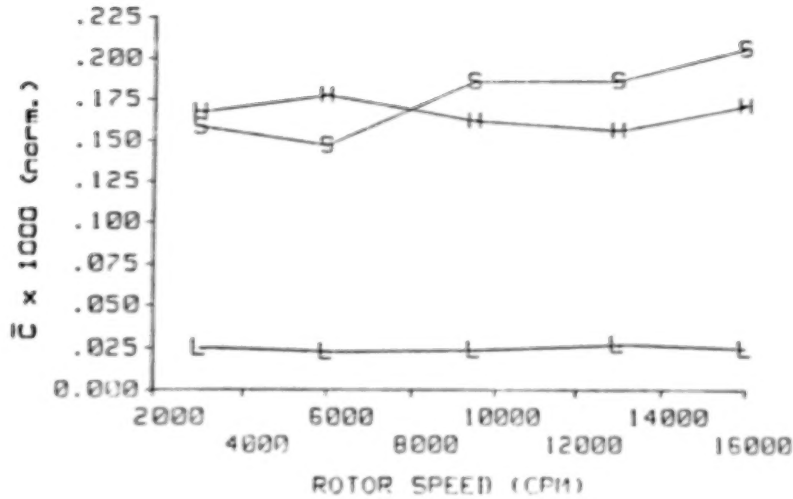


Figure 19. \bar{C} versus ω
for smooth, labyrinth, and honeycomb seals.

Whirl Frequency Ratio Results

Figure 20 shows f versus $u_{\theta 0}$ for the smooth, labyrinth, and honeycomb seals. For negative $u_{\theta 0}$, the labyrinth seal is the most stable, and the honeycomb seal is the least stable. For $u_{\theta 0} = 0$, the labyrinth seal is the most stable, and the smooth seal is the least stable. For positive $u_{\theta 0}$, the honeycomb seal is the most stable, and the smooth seal is the least stable. A comparison of figures 20 and 12 reveals that the least stable honeycomb seal tested (seal 1 of table 1) is more stable than the smooth and labyrinth seals for positive $u_{\theta 0}$.

Direct Stiffness Results

Figure 21 illustrates \bar{K} versus $u_{\theta 0}$ for a rotor speed of 16000 cpm, and an inlet pressure of 8.26 bars. For the honeycomb seal, \bar{K} is positive and relatively insensitive to changes in $u_{\theta 0}$. For the labyrinth seal, \bar{K} is negative and independent of $u_{\theta 0}$. For the smooth seal, \bar{K} is negative for no prerotation of the inlet air and increasingly positive for increasing, positive $u_{\theta 0}$. Recall from figures 13 and 14 that honeycomb-cell-dimension differences yield markedly different direct stiffness values. Fortunately, the K values for annular gas seals tend to have a second-order influence on rotor response and stability.

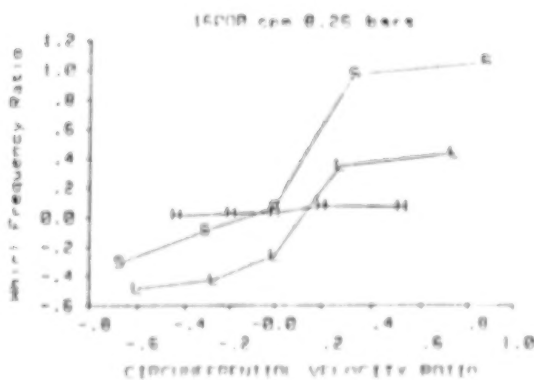


Figure 20. Whirl frequency ratio versus $u_{\theta 0}$
for smooth, labyrinth, and honeycomb seals.

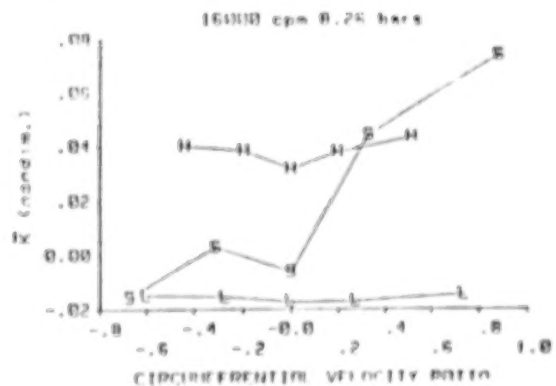


Figure 21. \bar{K} versus $u_{\theta 0}$ for
smooth, labyrinth, and honeycomb seals.

LEAKAGE PERFORMANCE

Honeycomb Seal Results

Figure 22 illustrate the flow coefficient,

$$\Phi = \frac{\dot{m}\sqrt{R_c T_r}}{\pi D C r P_r}, \quad (4)$$

for the seven honeycomb seals in table 1. All seven seals are unchoked at an inlet pressure of 3.08 bars, and choked at 8.26 bars. Φ is relatively insensitive to changes in the supply pressure. By comparison to figure 8, note the absence of correlation between leakage performance and \bar{k} . Changes in effective stator roughness which increase or decrease leakage do not yield corresponding changes in \bar{k} .

Relative Performance for Honeycomb, Labyrinth, and Smooth Stators

Figure 23 illustrates Φ versus $u_{\theta 0}$ for the smooth, labyrinth, and honeycomb (seal 7 of table 1) stators. These are the same seals for which rotordynamic characteristics were compared in the preceding section. The results of figure 23 show that the honeycomb seal leaks the least, followed in order by the labyrinth and smooth seals. Although not illustrated, the results are insensitive to changes in running speed and supply pressure. By comparison to figure 22, note that all of the honeycomb seals leak less than the labyrinth.

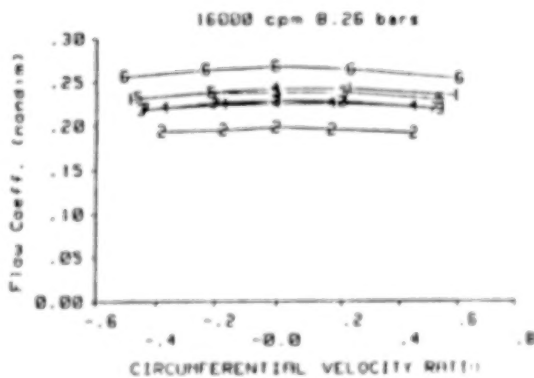


Figure 22. Flow coefficient versus $u_{\theta 0}$ at 8.26 bars for the honeycomb seals of table 1.

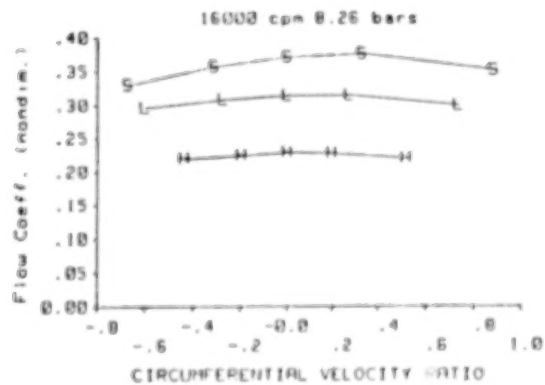


Figure 23. Flow coefficient versus $u_{\theta 0}$ for the smooth, labyrinth, and honeycomb seals.

Discussion and Conclusions

The test results presented here show that honeycomb seals are sensitive to changes in cell dimensions; however, no clear patterns emerged for the seven seal configurations tested. Test results are needed for additional (deeper) cell depths to try to establish patterns of changes in rotordynamic coefficients and leakage due to changes in cell dimensions. Honeycomb seals are "damper" seals in the sense of von Pragenau (1982) in that the rough stator reduces the tangential velocity. By comparison between honeycomb and smooth seals, their effectiveness in reducing k (and presumably the tangential velocity) is clearly demonstrated. However, there is no correlation between leakage performance (effective roughness) and cross coupled stiffness magnitudes. Seals 2 and 6 are, respectively, the

best and worst leakage performers of figure 22; however, k for seal 6 is equal to or less than k for seal 2 in figure 9. Clearly, some physical factor other than surface roughness must be accounted for to explain the effectiveness of honeycomb stators in reducing k .

The frequency dependency of the honeycomb-seal rotordynamic coefficients may be explained, in part, by Tam et al.'s paper (1987). Their numerical solutions show that "small" motion of a rotor which is sufficient to excite measureable dynamic forces, may create secondary flow and disturb the "base" flow solution. The cell depths are much too short to yield Helmholtz resonances of the gas within the honeycomb seal cavities within the frequency range of interest. The fact that frequency-independent coefficients are obtained for other seal configurations would seem to eliminate the dynamic response of the test rig as a source of the observed frequency dependency. Future tests are planned for honeycomb seals using a swept-sine-wave excitation which may provide additional physical insight of the observed frequency dependence.

Leakage comparisons, at the same minimum clearances, demonstrate the superiority of honeycomb stators followed in order by labyrinth and smooth stators. Rotordynamic measurements show that the direct damping of honeycomb and smooth stators are greater by a factor of approximately six than labyrinth stators. Obviously, increased damping means reduced rotor response when operating near or through critical speeds. With respect to rotordynamic stability, the honeycomb stators are best if the flow entering the seal is prerotated in the direction of rotation. However if the fluid is not prerotated, the labyrinth seal is better. In practical terms, the honeycomb seal is better, in the absence of an effective swirl brake, and the labyrinth seal is better if used with an effective swirl brake. There is no reason to use a swirl brake with a honeycomb seal.

As noted at the beginning of this section, the characteristics of honeycomb seals are sensitive to changes in cell dimensions; hence, the present test results should be viewed as preliminary. Additional tests are required at deeper cell depths and additional clearances.

REFERENCES

- Benckert, H, and Wachter, J., (1980), "Flow Induced Spring coefficients of Labyrinth Seals for Applications in Rotordynamics," proceedings of a workshop held at Texas A&M University, 12-14 May 1980, NASA CP2133, *Rotordynamic Instability Problems in High Performance Turbomachinery*, pp. 189-212.
- Childs, D. W., Elrod, D. A., Hale, R. K., (1986), "Rotordynamic Coefficient and Leakage Test Results for Interlock and Tooth-on-Stator Labyrinth Seals," accepted for presentation at the ASME International Gas Turbine Conference, May 1988.
- Childs, D., and Kim, C-H, (1985) "Analysis and Testing for Rotordynamic Coefficients of Turbulent Annular Seals with Different Directionally Homogeneous Surface Roughness Treatment for Rotor and Stator Elements," *ASME Transaction Journal of Tribology Technology*, Vol. 107, July 1985, pp. 296-306.

Childs, D. W., Nelson, C. C., Nicks, C., Scharrer, J., Elrod, D., Hale, K., (1987), "Theory Versus Experiment for the Rotordynamic Coefficients of Annular Gas Seals: Part 1, Test Facility and Apparatus," *ASME Trans. J. of Tribology*, Vol. 108, pp. 426-432.

Childs, D. W. and Scharrer, J. K., (1987), "Theory Versus Experiment for the Rotordynamic Coefficients of Labyrinth Gas Seals: Part II - A Comparison to Experiment," *ASME Rotating Machinery Dynamics*, Vol. 1, pp. 427-434.

Cohen, H., Rogers, C. F. G., and Saravanamutto, H. H., (1972), *Gas Turbine Theory*, Longman Group Limited.

Hisa, S., Sahakida, H., Asata, S., and Sakamoto, T., (1986) "Steam Excited Vibration in Rotor-bearing System, proceedings of the IFToMM International Conference, Tokyo, Japan, 14-17 September 1986, pp. 635-641.

Holman, J. P., (1978), *Experimental Methods for Engineers*, McGraw-Hill, New York, NY, pp. 45.

Tam, L. T., Przekwas, A. J., Muszynska, A., Hendricks, R. C., Braun, M. J., and Mullen, R. L., (1987), "Numerical and Analytical Study of Fluid Dynamic Forces in Seals and Bearings," *ASME Rotating Machinery Dynamics*, Vol. 1, pp. 359-370.

von Pragenau, G. L., (1982), "Damping Seals for Turbomachinery," NASA Technical Paper 1987.

BLANK PAGE

ROTORDYNAMIC COEFFICIENTS FOR LABYRINTH SEALS CALCULATED BY MEANS OF A FINITE DIFFERENCE TECHNIQUE

R. Nordmann and P. Weiser
Department of Mechanical Engineering
University of Kaiserslautern
Kaiserslautern, Federal Republic of Germany

The compressible, turbulent, time dependent and three dimensional flow in a labyrinth seal can be described by the Navier-Stokes equations in conjunction with a turbulence model. Additionally, equations for mass and energy conservation and an equation of state are required. To solve these equations, a perturbation analysis is performed yielding zeroth order equations for centric shaft position and first order equations describing the flow field for small motions around the seal center. For numerical solution a finite difference method is applied to the zeroth and first order equations resulting in leakage and dynamic seal coefficients respectively.

SYMBOLS

F_1, F_2	Forces on the shaft in z, y direction
U_1, U_2	shaft displacements
K, k	direct and cross-coupled stiffness
C, c	direct and cross-coupled damping
u, v, w	axial, radial and circumferential velocity
p, k, ϵ	pressure, turbulence energy, turbulent energy dissipation
T	temperature
μ_1, μ_t, μ_e	laminar, turbulent and effective viscosity ($\mu_e = \mu_1 + \mu_t$)
ρ	density
c_p	specific heat for constant pressure
t	time
z, r, θ	axial, radial and circumferential coordinate
η	radial coordinate after transformation
Pr	turbulent Prandtl number
$\sigma_k, \sigma_\epsilon$	constants of the k- ϵ model
C_μ, C_1, C_2	constants of the k- ϵ model
G	production term in turbulence model
$Diss$	laminar dissipation
ϕ	general variable
S_ϕ	general source term
C_o	seal clearance for centric shaft position
δ	seal clearance for eccentric shaft position
r_o	radius of the precession motion of the shaft

$e = r_o / C_o$	perturbation parameter
ω	rotational frequency of the shaft
Ω	precession frequency of the shaft
r_i	radius from seal center to end of seal fin
r_a	radius from seal center to stator
D_{1-10}	Transformation constants

SUBSCRIPTS

0	zeroth order variables
1	first order variables
R	Rotor
S	Stator
c	cosine
s	sine

INTRODUCTION

The problem of subsynchronous vibrations in high performance turbomachinery has been investigated for many years. However, for some destabilizing effects there is no satisfactory solution from the qualitative as well as quantitative points of view. In machines like turbocompressors and turbines, gas seals and especially labyrinths have an important influence on the dynamic behavior. These elements with turbulent flow conditions have the potential to develop significant forces

$$-\begin{bmatrix} F_1 \\ F_2 \end{bmatrix} = \begin{bmatrix} K & k \\ -k & K \end{bmatrix} \begin{bmatrix} U_1 \\ U_2 \end{bmatrix} + \begin{bmatrix} C & c \\ -c & C \end{bmatrix} \begin{bmatrix} \dot{U}_1 \\ \dot{U}_2 \end{bmatrix} \quad (1)$$

which may lead to self-excited vibrations of the shaft.

To predict the stability behavior of a high performance rotating machinery, the rotordynamic coefficients (eq. 1) of the turbulent seals have to be known. Many theoretical studies, numerical calculations and measurements have been carried out to determine the stiffness and damping characteristics. Most of the recent theoretical developments are based on a bulk flow theory, considering the shear stresses only at the wall but not within the fluid. Nelson (ref. 1) has derived a procedure with a 'one volume' model for straight and tapered seals. Iwatsubo (ref. 2) as well as Childs (ref. 3) have also used the one volume model for labyrinth seals. However, in case of such complicated seal geometries difficulties may occur, when neglecting the local turbulence characteristics within the fluid, particularly at locations with strong velocity changes.

Wyssmann et al. and Wyssmann (ref. 4 and 5) have extended the bulk flow theory for labyrinth seals, working with a two volume model. The latter takes into account the shear stresses between the core flow and the jet flow. Wyssmann's two volume model is derived from results of a finite difference calculation for a rotationally symmetric single cavity turbulent flow (centered position of the shaft), based on the time averaged Navier-Stokes equations with a $k-\epsilon$ model. A first attempt to apply finite difference methods to labyrinth seals was made by Rhode et.al. (ref. 6), who

calculated only one chamber seals for centric shaft position. However, bulk flow theories show a substantial lack in the prediction of labyrinth seal coefficients. As already shown by Nordmann, Dietzen and Weiser (ref. 7), the solution of the time-averaged conservation equations for momentum, mass and energy in conjunction with a $k-\epsilon$ turbulence model by means of a finite difference technique is a physically more realistic way for calculating rotordynamic coefficients of gas seals.

This paper is concerned with the extension of the already mentioned calculation procedure for annular seals to straight-through labyrinths.

GOVERNING EQUATIONS

To describe the flow in a labyrinth seal, we use the time-averaged conservation equations for momentum, mass and energy and the equation of state for a perfect gas. The correlation terms of the turbulent fluctuation quantities are modelled via the $k-\epsilon$ turbulence model of Launder and Spalding (ref. 8).

All these differential equations can be arranged in the following generalized form:

$$\begin{aligned} \frac{\partial}{\partial t}(\rho\phi) + \frac{1}{r} \frac{\partial}{\partial r}(\rho r v \phi) + \frac{1}{r} \frac{\partial}{\partial \theta}(\rho w \phi) + \frac{\partial}{\partial x}(\rho u \phi) = \\ \frac{1}{r} \frac{\partial}{\partial r}(r \Gamma \frac{\partial \phi}{\partial r}) + \frac{1}{r} \frac{\partial}{\partial \theta}(\Gamma \frac{1}{r} \frac{\partial \phi}{\partial \theta}) + \frac{\partial}{\partial x}(\Gamma \frac{\partial \phi}{\partial x}) + S_\phi \end{aligned} \quad (2)$$

where ϕ stands for any of the dependent variables, and the corresponding values of $\Gamma\phi$ and S_ϕ are indicated in Table 1 (see Appendix A).

PERTURBATION ANALYSIS

Obviously, this set of equations is not solvable due to the limited performance capabilities of today's computers. Therefore, a stepwise procedure is performed in order to reduce the three dimensional and time dependent flow problem to a two dimensional time independent one.

First, the governing equations are transformed to another coordinate system by introducing a new radial coordinate η whereby the eccentrically moving shaft is converted to a shaft rotating in the center of the seal (Fig. 1).

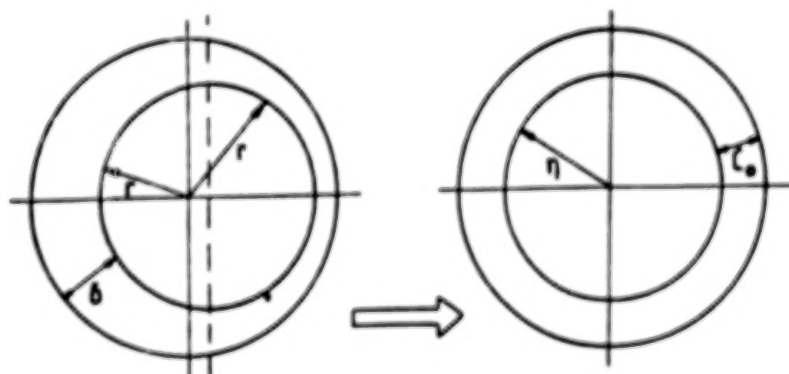
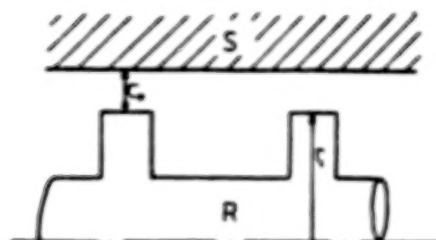


Fig. 1: Coordinate Transformation $\eta = \eta(r, t, \theta)$

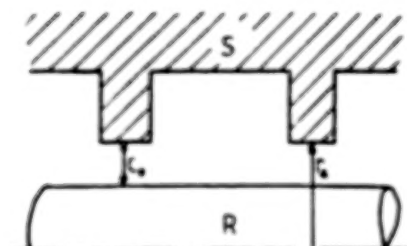
The transform functions are given in Fig. 2.



Strips on rotor:

$$\eta = r_1 + \frac{C_o \delta (r - r_1)}{(C_o - \delta)(r - r_1) + C_o \delta}$$

(3)



Strips on stator:

$$\eta = r_a + \frac{C_o \delta (r_a - r)}{(C_o - \delta)(r_a - r) - C_o \delta}$$

Fig. 2: Transform functions

Assuming small shaft motions on a circular orbit around the centric position we perform a perturbation analysis by introducing the following expressions for the dependent variables into the governing equations:

$$\begin{aligned} u &= u_o + e u_1 & v &= v_o + e v_1 & w &= w_o + e w_1 \\ p &= p_o + e p_1 & T &= T_o + e T_1 & \rho &= \rho_o + e \rho_1 \end{aligned} \quad (4)$$

This procedure yields a set of zeroth order equations governing the centric flow field and a set of first order equations describing the flow field for small eccentric shaft motions.

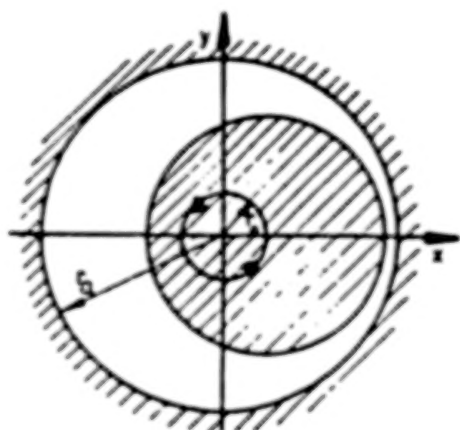
The first order equations depend also on the circumferential coordinate θ and on time t . To eliminate the circumferential derivations, we insert circumferentially periodic solutions for the first order variables in the corresponding set of equations:

$$\begin{aligned} u_1 &= u_{1c} \cos \theta + u_{1s} \sin \theta & v_1 &= v_{1c} \cos \theta + v_{1s} \sin \theta \\ w_1 &= w_{1c} \cos \theta + w_{1s} \sin \theta & p_1 &= p_{1c} \cos \theta + p_{1s} \sin \theta \\ T_1 &= T_{1c} \cos \theta + T_{1s} \sin \theta & \rho_1 &= \rho_{1c} \cos \theta + \rho_{1s} \sin \theta \end{aligned} \quad (5)$$

After separating the equations into sine and cosine terms and rearranging them by introducing the following complex variables,

$$\begin{aligned}
 \bar{u}_1 &= u_{1c} + iu_{1s} & \bar{v}_1 &= v_{1c} + iv_{1s} & \bar{w}_1 &= w_{1c} + iw_{1s} \\
 \bar{p}_1 &= p_{1c} + ip_{1s} & \bar{T}_1 &= T_{1c} + iT_{1s} & \bar{\rho}_1 &= \rho_{1c} + i\rho_{1s}
 \end{aligned} \quad (6)$$

a circular shaft precession orbit (Fig. 3) with frequency Ω and corresponding solutions for the first order variables are assumed whereby the temporal derivations can be eliminated:



$$\begin{aligned}
 \bar{h}_1 &= r_o e^{i\Omega t} \\
 &\text{(change in clearance)}
 \end{aligned}$$

Fig. 3: Circular shaft orbit

$$\begin{aligned}
 \bar{u}_1 &= \hat{u}_1 e^{i\Omega t} & \bar{v}_1 &= \hat{v}_1 e^{i\Omega t} & \bar{w}_1 &= \hat{w}_1 e^{i\Omega t} \\
 \bar{p}_1 &= \hat{p}_1 e^{i\Omega t} & \bar{T}_1 &= \hat{T}_1 e^{i\Omega t} & \bar{\rho}_1 &= \hat{\rho}_1 e^{i\Omega t}
 \end{aligned} \quad (7)$$

Finally the zeroth and first order equations are arranged to a generalized form:

$$\frac{\partial}{\partial x}(\rho_o u_o \phi) - \frac{\partial}{\partial x}(\Gamma_\phi \frac{\partial \phi}{\partial x}) + \frac{1}{\eta} \frac{\partial}{\partial \eta}(\eta \rho_o v_o \phi) - \frac{1}{\eta} \frac{\partial}{\partial \eta}(\Gamma_\phi \eta \frac{\partial \phi}{\partial \eta}) = S_\phi \quad (8)$$

Table 2 (see Appendix B) indicates the values for the zeroth and first order equations.

The constants D_1 - D_{10} (given in the Appendix C) arise from the coordinate transformation and depend only on zeroth order variables. These terms are zero for the labyrinth chambers.

FINITE DIFFERENCE METHOD

For the numerical solution of the governing equations we apply a finite difference technique in the same manner as suggested in many publications (see e.g. ref. 9). First the calculation domain is covered by a finite difference grid (Fig. 4). Discretizing the equations results in algebraic expressions linking every node point to his four neighbours. Solution of zeroth order equations results in flow field, pressure distribution, and leakage. For first order solution, the equations for the turbulence quantities k , ϵ can be dropped due to assumed small rotor motions.

Because Eq. (1) contains four unknown parameters (K, k, C, c), first order solution is performed for two different shaft precession frequencies Ω . This results in two sets of dynamic forces F_1 , F_2 obtained from the integration of the pressure perturbations (see Eq. 9).

$$\begin{aligned} -\frac{F_1}{r_o} &= \frac{\pi r_i}{C_o} \int_L p_{1c} dx \\ -\frac{F_2}{r_o} &= \frac{\pi r_i}{C_o} \int_L p_{1s} dx \end{aligned} \quad (9)$$

Finally the dynamic coefficients are calculated from Eq. 10.

$$\begin{aligned} -\frac{F_1}{r_o} &= K + c\Omega \\ -\frac{F_2}{r_o} &= -k + C\Omega \end{aligned} \quad (10)$$

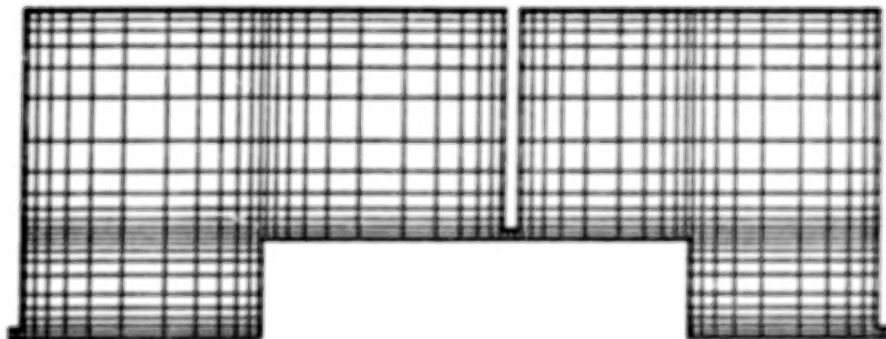


Fig. 4: Nonuniform finite difference grid for labyrinths

BOUNDARY CONDITIONS

- Zeroth order equations

For the velocities the near wall regions are represented by the logarithmic wall law. The entrance conditions are iteratively calculated depending on entrance Mach number and loss coefficient. The entrance swirl is assumed to be known.

- First order equations

Due to shaft precession and coordinate transformation, one has to pay attention to the following boundary conditions for the radial and circumferential velocities:

$$\begin{aligned} v_{1S} &= (0., 0.) & \hat{w}_{1S} &= (0., 0.) \\ \hat{v}_{1R} &= (0., (\Omega - \omega)c_o) & \hat{v}_{1R} &= (\Omega c_o, 0.) \end{aligned}$$

For the pressure, the exit perturbation is zero in case of exit Mach number less than one ("undercritical" flow) which occurred in the application examples.

APPLICATION

For testing our program, we made comparative calculations to measurements performed by Benckert (ref. 10).

Seal Data:

Shaft diameter:	0,150 m
Strip height :	5,5 mm
Strip pitch :	8 mm
Clearance :	0,5 mm
Number of chambers :	3
Entrance pressure p_o :	1,425 bar
Exit pressure p_a :	0,950 bar
Reservoir temperature:	300 K
Laminar viscosity :	$1,8 \cdot 10^{-5}$ Pa s
Perfect gas constant :	287,06 J/kgK
Specific heat ratio :	1,4
Rotor surface velocity:	0 m/s

The calculation grid, the flow field and the pressure distribution are shown in Fig. 5-7.

In Fig. 8-10 mass flow, direct and crosscoupled stiffness are plotted versus the swirl parameter, as defined by Benckert ($E_o = 0,5 \cdot p_o \cdot w_o^2 / (p_o - p_a)$).

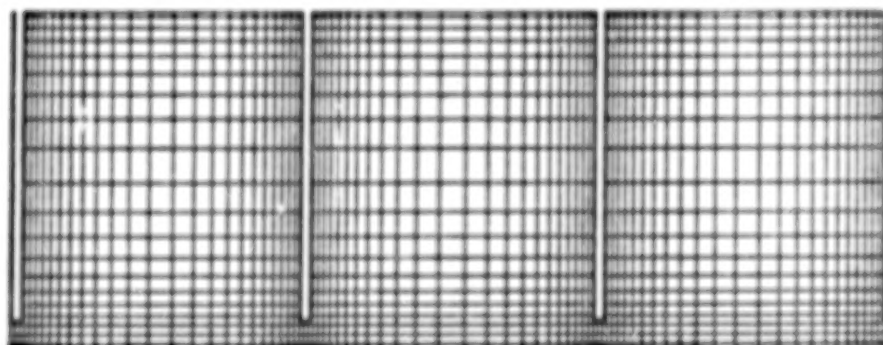


Fig. 5: Finite difference grid

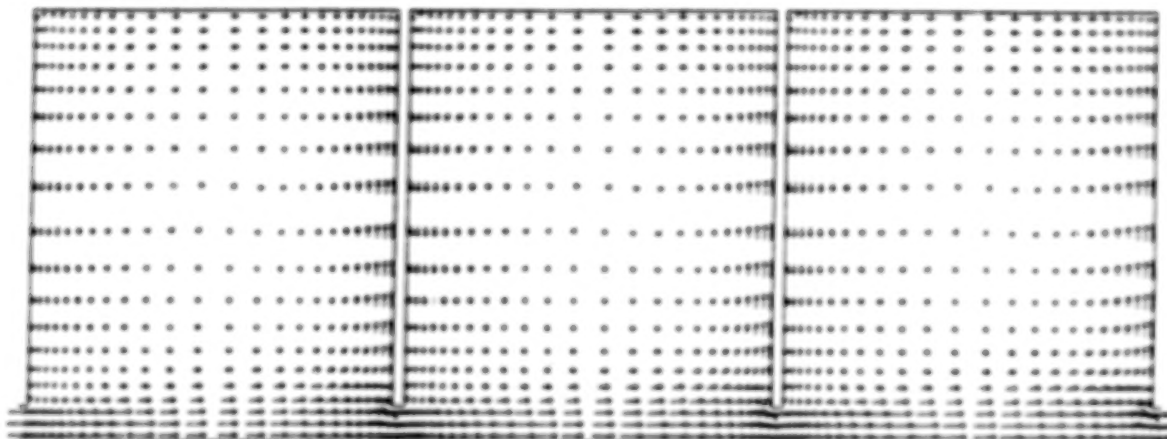


Fig. 6: Flow field

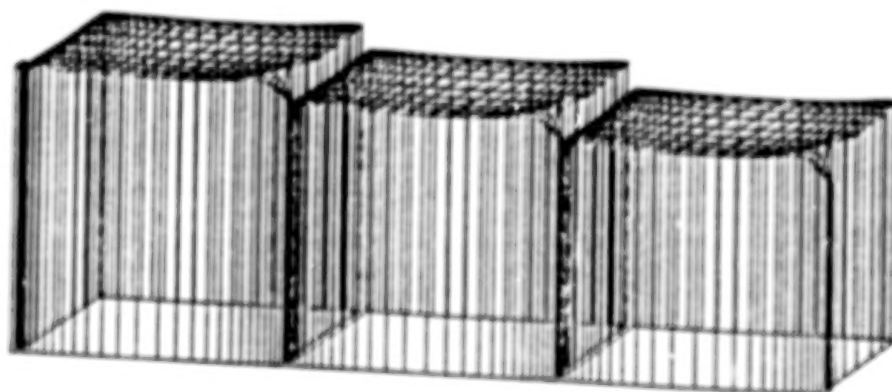


Fig. 7: Pressure distribution

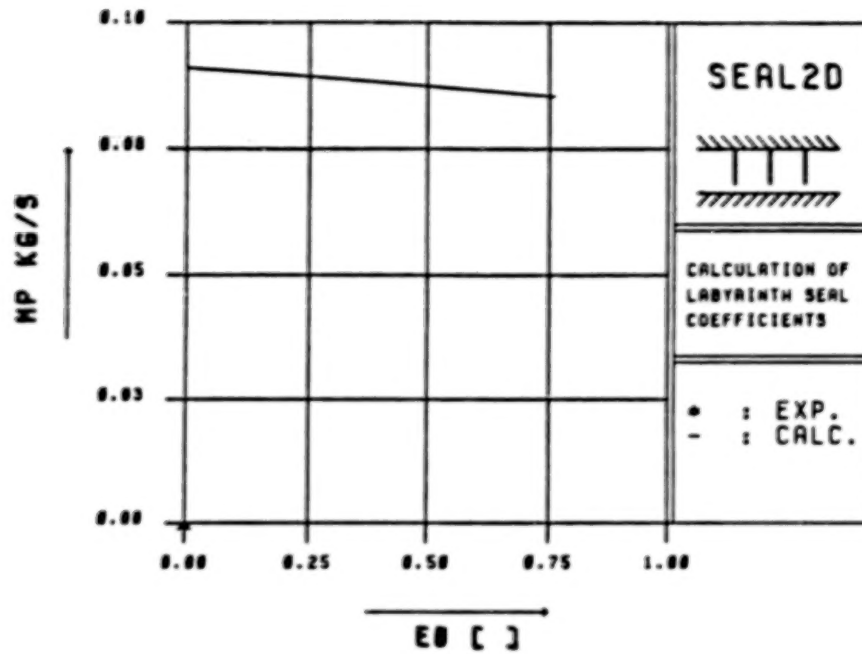


Fig. 8: Mass flow

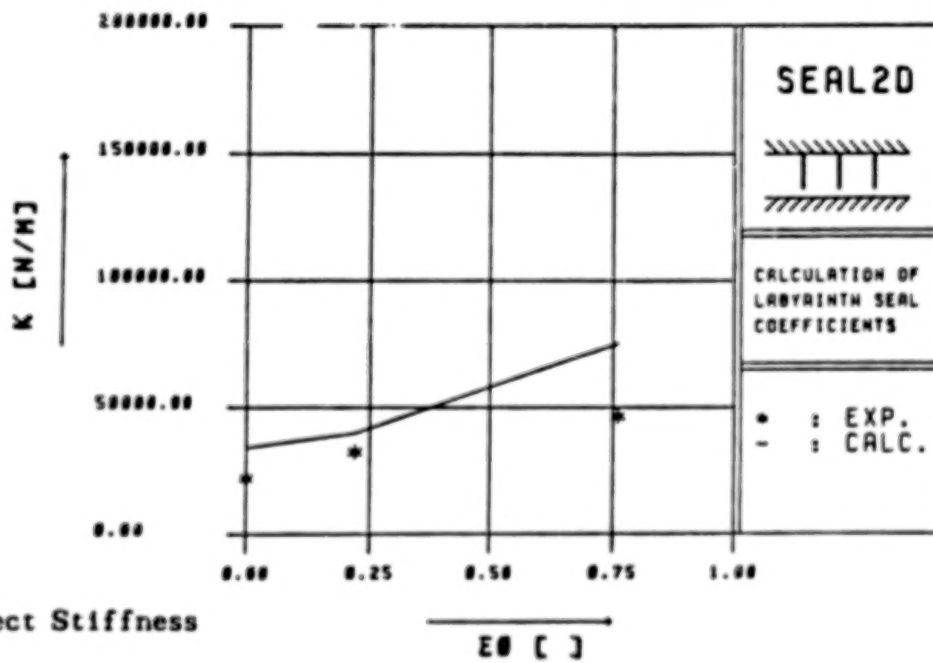


Fig. 9: Direct Stiffness

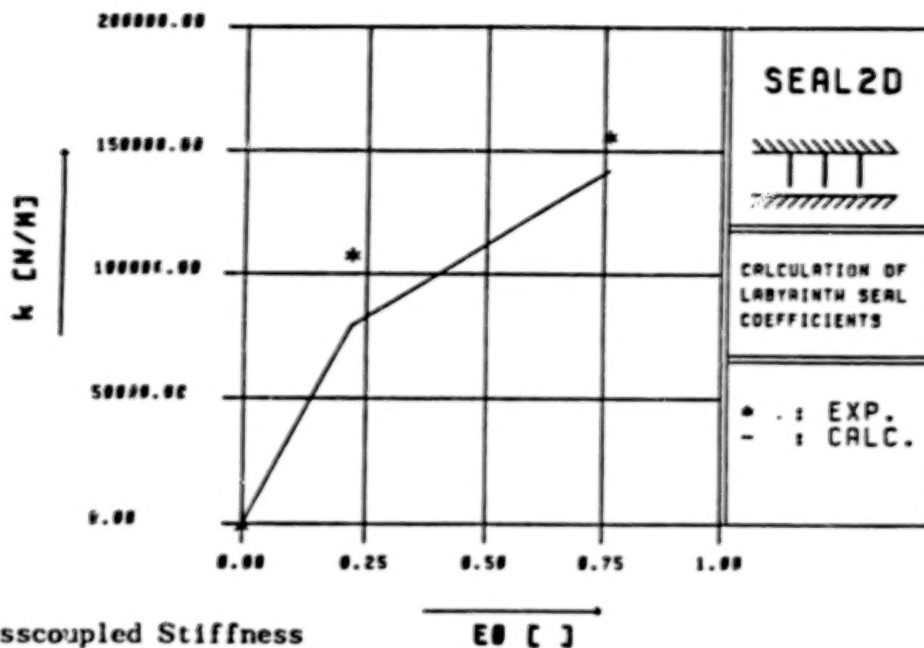


Fig. 10: Crosscoupled Stiffness

CONCLUSION

We have shown that a finite difference method based on the Navier-Stokes equations in conjunction with a turbulence model is more suitable to describe the dynamic coefficients of gas seals than the simpler models based on bulk flow theories. Of course the calculation time is also much greater. But great progress is still possible. For example, advanced solution algorithms like Multi-Grid, Newton-Schemes, SIP (strongly implicit procedure) can be implemented to speed up the computer program.

Further on, a three dimensional calculation procedure is currently under development to determine the coefficients of more complex geometries like stepped and interlocking labyrinths (Fig. 11,12).

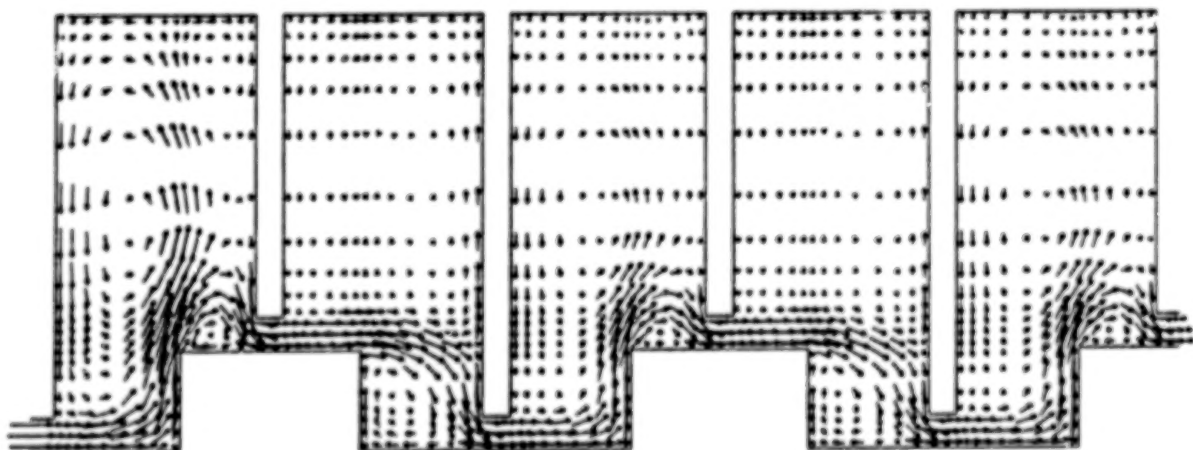


Fig. 11: Stepped seal

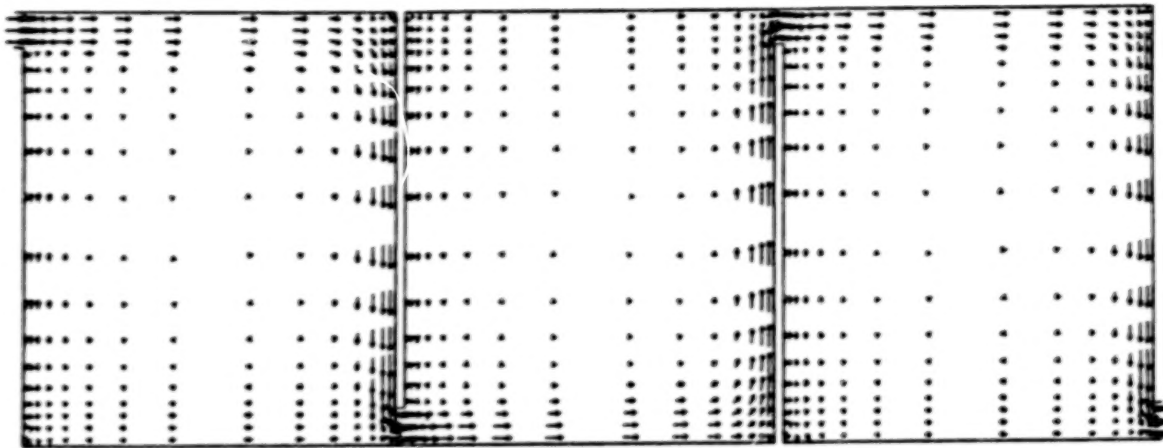


Fig. 12: Interlocking seal

APPENDIX A

Table 1: Governing equations of turbulent seal flow

ϕ	r_ϕ	S_ϕ
u	μ_e	$-\frac{\partial p}{\partial x} + \frac{\partial}{\partial x}(\mu_e \frac{\partial u}{\partial x}) + \frac{1}{r} \frac{\partial}{\partial r}(r\mu_e \frac{\partial v}{\partial x}) + \frac{1}{r} \frac{\partial}{\partial \theta}(\mu_e \frac{\partial w}{\partial x})$
v	μ_e	$-\frac{\partial p}{\partial r} + \frac{\partial}{\partial x}(\mu_e \frac{\partial u}{\partial r}) + \frac{1}{r} \frac{\partial}{\partial r}(r\mu_e \frac{\partial v}{\partial r}) + \frac{1}{r} \frac{\partial}{\partial \theta}(r\mu_e \frac{\partial v}{\partial r})$ $-\frac{2}{r^2} \mu_e \frac{\partial w}{\partial \theta} - \frac{2}{r^2} \mu_e v + \frac{\rho}{r} w^2$
w	μ_e	$-\frac{1}{r} \frac{\partial p}{\partial \theta} + \frac{\partial}{\partial x}(\frac{1}{r} \mu_e \frac{\partial u}{\partial \theta}) + \frac{1}{r} \frac{\partial}{\partial r}(\mu_e \frac{\partial v}{\partial \theta}) + \frac{1}{r} \frac{\partial}{\partial \theta}(\frac{1}{r} \mu_e \frac{\partial w}{\partial \theta})$ $+ \frac{1}{r^2} \mu_e \frac{\partial v}{\partial \theta} - \frac{w}{r^2} \frac{\partial}{\partial r}(r\mu_e) + \frac{1}{r} \frac{\partial}{\partial \theta}(\frac{2}{r} \mu_e v) - \frac{\rho}{r} vw$
p	0	0
T	μ_e/Pr	$\frac{1}{c_p}(\frac{\partial p}{\partial t} + u \frac{\partial p}{\partial x} + v \frac{\partial p}{\partial r} + \frac{w}{r} \frac{\partial p}{\partial \theta}) + \frac{1}{c_p} (Diss + \rho \epsilon)$
k	μ_e/σ_k	$G - \rho \epsilon$
ϵ	μ_e/σ_ϵ	$C_1 \frac{\epsilon G}{k} - C_2 \rho \frac{\epsilon^2}{k}$

Equation of State for a perfect gas:

$$p = \rho RT$$

Constants of the k- ϵ model

$$C_\mu = 0.09 \quad C_1 = 1.45 \quad C_2 = 1.91 \quad \sigma_k = 1.0 \quad \sigma_\epsilon = 1.22 \quad Pr = 0.9$$

Production term in the equations for the turbulence quantities:

$$G = \mu_e \left[2 \left(\left(\frac{\partial v}{\partial r} \right)^2 + \left(\frac{\partial u}{\partial x} \right)^2 + \left(\frac{1}{r} \frac{\partial w}{\partial \theta} + \frac{v}{r} \right)^2 \right) + \left(\frac{\partial v}{\partial x} + \frac{\partial u}{\partial r} \right)^2 + \left(\frac{1}{r} \frac{\partial v}{\partial \theta} + \frac{\partial w}{\partial r} - \frac{w}{r} \right)^2 \right. \\ \left. + \left(\frac{\partial w}{\partial x} + \frac{1}{r} \frac{\partial u}{\partial \theta} \right)^2 - \frac{2}{3} \left(\frac{\partial u}{\partial x} + \frac{1}{r} \frac{\partial w}{\partial \theta} + \frac{1}{r} \frac{\partial}{\partial r} (rv) \right)^2 \right]$$

Laminar Dissipation in the energy equation:

$$Diss = \mu_l \left[2 \left(\left(\frac{\partial v}{\partial r} \right)^2 + \left(\frac{\partial u}{\partial x} \right)^2 + \left(\frac{1}{r} \frac{\partial w}{\partial \theta} + \frac{v}{r} \right)^2 \right) + \left(\frac{\partial v}{\partial x} + \frac{\partial u}{\partial r} \right)^2 + \left(\frac{1}{r} \frac{\partial v}{\partial \theta} + \frac{\partial w}{\partial r} - \frac{w}{r} \right)^2 \right. \\ \left. + \left(\frac{\partial w}{\partial x} + \frac{1}{r} \frac{\partial u}{\partial \theta} \right)^2 - \frac{2}{3} \left(\frac{\partial u}{\partial x} + \frac{1}{r} \frac{\partial w}{\partial \theta} + \frac{1}{r} \frac{\partial}{\partial r} (rv) \right)^2 \right]$$

APPENDIX B

Table 2a: Zeroth order equations

ϕ	Γ_ϕ	S_ϕ
u_o	μ_e	$-\frac{\partial p_o}{\partial x} + \frac{\partial}{\partial x} \left(\mu_e \frac{\partial u_o}{\partial x} \right) + \frac{1}{\eta} \frac{\partial}{\partial \eta} \left(\mu_e \eta \frac{\partial v_o}{\partial x} \right)$
v_o	μ_e	$-\frac{\partial p_o}{\partial \eta} + \frac{\partial}{\partial x} \left(\mu_e \frac{\partial u_o}{\partial \eta} \right) + \frac{1}{\eta} \frac{\partial}{\partial \eta} \left(\mu_e \eta \frac{\partial v_o}{\partial \eta} \right) - \frac{2}{\eta} \mu_e v_o \frac{\partial v_o}{\partial \eta}$
1	0	0
w_o	μ_e	$-\frac{v_o}{\eta} \frac{\partial}{\partial \eta} (\eta \mu_e) - \frac{p_o}{\eta} v_o v_o$
k_o	$\frac{\mu_e}{\sigma_k}$	$G - p_o \epsilon$
ϵ_o	$\frac{\mu_e}{\sigma_\epsilon}$	$C_1 \frac{\epsilon}{k} G - C_2 p_o \frac{\epsilon^2}{k}$
T_o	$\frac{\mu_e}{Pr}$	$\frac{1}{c_p} \left(u_o \frac{\partial p_o}{\partial x} + v_o \frac{\partial p_o}{\partial \eta} \right) + \frac{1}{c_p} (Diss + p_o \epsilon)$

Equation of State: $\rho_o = \frac{p_o}{R \cdot T_o}$

Table 2b: First order equations

Equation of State: $\hat{\rho}_1 = \rho_o \left[\frac{\hat{p}_1}{p_o} - \frac{\hat{T}_1}{T_o} \right]$

\bullet r \bullet	S
$\hat{u}_1 \quad \mu_e$	$-\frac{\partial \hat{p}_1}{\partial x} + \frac{\partial}{\partial x} \left(\mu_e \frac{\partial \hat{u}_1}{\partial x} \right) + \frac{1}{\eta} \frac{\partial}{\partial x} \left(\eta \mu_e \frac{\partial \hat{v}_1}{\partial x} \right) - \frac{\partial}{\partial x} (\rho_o u_o \hat{u}_1)$ $- \frac{1}{\eta} \frac{\partial}{\partial \eta} (\eta \rho_o u_o \hat{v}_1) - \frac{\mu_e}{\eta} \hat{u}_1 + i \rho_o \left(\frac{\omega}{\eta} \Omega \right) \hat{u}_1 + i \frac{\rho_o}{\eta} u_o \hat{w}_1 - i \frac{\mu_e}{\eta} \frac{\partial \hat{w}_1}{\partial x}$ $- \frac{\partial}{\partial x} (u_o u_o \hat{\rho}_1) - \frac{1}{\eta} \frac{\partial}{\partial \eta} (\eta v_o u_o \hat{\rho}_1) + i \frac{u_o \omega}{\eta} \hat{\rho}_1 - i \Omega u_o \hat{\rho}_1 + D_1 + i D_2$
$\hat{v}_1 \quad \mu_e$	$-\frac{\partial \hat{p}_1}{\partial \eta} + \frac{\partial}{\partial x} \left(\mu_e \frac{\partial \hat{u}_1}{\partial \eta} \right) + \frac{1}{\eta} \frac{\partial}{\partial \eta} \left(\eta \mu_e \frac{\partial \hat{v}_1}{\partial \eta} \right) - \frac{\partial}{\partial x} (\rho_o v_o \hat{u}_1)$ $- \frac{1}{\eta} \frac{\partial}{\partial \eta} (\eta \rho_o v_o \hat{v}_1) - i \mu_e \frac{\partial}{\partial \eta} \left(\frac{\omega}{\eta} \right) - 3 \frac{\mu_e}{\eta} \hat{v}_1$ $+ i \rho_o \left(\frac{\omega}{\eta} - \Omega \right) \hat{v}_1 + \left(2 \frac{\rho_o}{\eta} \frac{\omega}{\eta} + i 2 \frac{\mu_e}{\eta} + i \frac{\rho_o}{\eta} v_o \right) \hat{w}_1$ $- \frac{\partial}{\partial x} (u_o v_o \hat{\rho}_1) - \frac{1}{\eta} \frac{\partial}{\partial \eta} (\eta v_o v_o \hat{\rho}_1) + \frac{\omega}{\eta} \hat{\rho}_1 + i \frac{v_o \omega}{\eta} \hat{\rho}_1$ $- i \Omega v_o \hat{\rho}_1 + D_3 + i D_4$
$\hat{w}_1 \quad \hat{\mu}_e$	$i \frac{\hat{p}_1}{\eta} - i \frac{\partial}{\partial x} \left(\frac{\mu_e}{\eta} \hat{u}_1 \right) - i \frac{1}{\eta} \frac{\partial}{\partial \eta} (\mu_e \hat{v}_1) - \frac{\partial}{\partial x} (\rho_o \omega_o \hat{u}_1)$ $- \frac{1}{\eta} \frac{\partial}{\partial \eta} (\rho_o \eta^2 \omega_o \hat{v}_1) - \frac{\mu_e}{\eta} \hat{w}_1 - i 3 \frac{\mu_e}{\eta} \hat{v}_1$ $- \left(\frac{\rho_o}{\eta} v_o + i \rho_o \Omega + \frac{1}{2} \frac{\partial \eta \mu_e}{\partial \eta} - i 2 \frac{\rho_o}{\eta} \omega_o \right) \hat{w}_1$ $\frac{\partial}{\partial x} (u_o \omega_o \hat{\rho}_1) - \frac{1}{\eta} \frac{\partial}{\partial \eta} (\eta v_o \omega_o \hat{\rho}_1) - \frac{v_o \omega_o}{\eta} \hat{\rho}_1 + i \frac{\omega_o \omega_o}{\eta} \hat{\rho}_1$ $- i \omega_o \Omega \hat{\rho}_1 + D_5 + i D_6$
$T_1 \quad \frac{\mu_e}{Pr}$	$\frac{1}{c_p} \left(u \frac{\partial \hat{p}_1}{\partial x} + v \frac{\partial \hat{p}_1}{\partial \eta} + \omega \frac{\partial \hat{p}_1}{\partial \eta} + v \frac{\partial \hat{p}_1}{\partial \eta} - i \frac{\omega_o}{\eta} \hat{p}_1 \right) - \frac{\mu_e}{Pr} \frac{1}{\eta} \hat{T}_1$ $- \frac{\partial}{\partial x} (\rho_o T_o \hat{u}_1) - \frac{1}{\eta} \frac{\partial}{\partial \eta} (\eta \rho_o T_o \hat{v}_1) + \frac{1}{\eta} (\rho_o T_o \hat{w}_1 + \rho_o \omega_o \hat{T}_1)$ $+ i \Omega \left(\frac{\hat{p}_1}{c_p} - \rho_o \hat{T}_1 \right) - \frac{\partial}{\partial x} (u_o T_o \hat{\rho}_1) - \frac{1}{\eta} \frac{\partial}{\partial \eta} (\eta v_o T_o \hat{\rho}_1)$ $+ i \frac{T_o \omega_o}{\eta} \hat{\rho}_1 - i \Omega T_o \hat{\rho}_1 + \frac{c_p}{c_p} \hat{\rho}_1 + D_7 + i D_8$

BEST COPY AVAILABLE

Only the first order continuity-equation to determine \hat{p}_1 shows a slightly modified form.

$$\begin{aligned} \frac{\partial}{\partial x}(\rho_o \hat{u}_1) + \frac{1}{\eta} \frac{\partial}{\partial \eta}(\eta \rho_o \hat{v}_1) &= i \frac{\rho_o}{\eta} \hat{w}_1 - \frac{\partial}{\partial x}(u_o \hat{p}_1) - \frac{1}{\eta} \frac{\partial}{\partial \eta}(\eta v_o \hat{p}_1) \\ &+ i \frac{w_o}{\eta} \hat{p}_1 - i \Omega \hat{p}_1 + D_9 + i D_{10} \end{aligned}$$

APPENDIX C

First order transformation constants

Note: $r_x = r_a$ for strips on stator

$r_x = r_i$ for strips on rotor

$$\begin{aligned} D_1 &= \frac{2(r_x - \eta)}{c_o} \frac{\partial}{\partial \eta} (\mu_{eo} \frac{\partial u_o}{\partial \eta} + \mu_{eo} \frac{\partial v_o}{\partial x} - u_o v_o \rho_o) \\ &- \frac{(r_x - \eta)^2}{c_o \eta^2} (\mu_{eo} \frac{\partial u_o}{\partial \eta} + \mu_{eo} \frac{\partial v_o}{\partial x} - u_o v_o \rho_o) \end{aligned}$$

$$\begin{aligned} D_2 &= \frac{(r_x - \eta)^2}{c_o \eta} \frac{\partial}{\partial \eta} (\mu_{eo} \frac{\partial w_o}{\partial x} - \rho_o u_o v_o) \\ &+ \Omega \frac{(r_x - \eta)^2}{c_o} \frac{\partial}{\partial \eta} (\rho_o u_o) \end{aligned}$$

$$\begin{aligned} D_3 &= \frac{2(r_x - \eta)}{c_o} \frac{\partial}{\partial \eta} (2\mu_{eo} \frac{\partial v_o}{\partial \eta} - \rho_o v_o v_o) \\ &- \frac{(r_x - \eta)^2}{c_o \eta^2} (2\mu_{eo} \frac{\partial v_o}{\partial \eta} + \rho_o v_o v_o - \rho_o v_o v_o - 2\mu_{eo} \frac{v_o}{\eta}) \\ &- \frac{2(r_x - \eta)}{c_o} \frac{\partial p_o}{\partial \eta} \end{aligned}$$

$$\begin{aligned} D_4 &= \frac{(r_x - \eta)^2}{c_o \eta} \frac{\partial}{\partial \eta} (\mu_{eo} \eta \frac{\partial}{\partial \eta} (\frac{v_o}{\eta}) - \rho_o v_o v_o) \\ &+ \Omega \frac{(r_x - \eta)^2}{c_o} \frac{\partial}{\partial \eta} (\rho_o v_o) \end{aligned}$$

$$\begin{aligned} D_5 &= \frac{2(r_x - \eta)^2}{c_o \eta^2} (\rho_o v_o v_o - \mu_{eo} \eta \frac{\partial}{\partial \eta} (\frac{v_o}{\eta})) \\ &- \frac{2(r_x - \eta)}{c_o} \frac{\partial}{\partial \eta} (\rho_o v_o v_o - \mu_{eo} \eta \frac{\partial}{\partial \eta} (\frac{v_o}{\eta})) \end{aligned}$$

$$\begin{aligned} D_6 &= \frac{(r_x - \eta)^2}{c_o \eta} \frac{\partial}{\partial \eta} (2\mu_{eo} \frac{v_o}{\eta}) - \frac{\partial}{\partial \eta} (\rho_o v_o v_o - \frac{\partial p_o}{\partial \eta}) \\ &+ \Omega \frac{(r_x - \eta)^2}{c_o} \frac{\partial}{\partial \eta} (\rho_o v_o) \end{aligned}$$

$$\begin{aligned} D_7 &= \frac{(r_x - \eta)^2}{c_o \eta^2} (\rho_o v_o T_o - \frac{\mu_{eo}}{Fr} \frac{\partial T_o}{\partial \eta}) \\ &+ \frac{2(r_x - \eta)}{c_o} \frac{\partial}{\partial \eta} (\frac{\mu_{eo}}{Fr} \frac{\partial T_o}{\partial \eta} - \rho_o v_o T_o) \\ &+ \frac{1}{c_p} \frac{2(r_x - \eta)}{c_o} v_o \frac{\partial p_o}{\partial \eta} \end{aligned}$$

$$\begin{aligned} D_8 &= \frac{1}{c_p} \frac{v_o}{\eta} \frac{(r_x - \eta)^2}{c_o} \frac{\partial p_o}{\partial \eta} \\ &- \frac{(r_x - \eta)^2}{\eta c_o} \frac{\partial}{\partial \eta} (\rho_o v_o T_o) \\ &+ \Omega \frac{(r_x - \eta)^2}{c_o} \frac{\partial}{\partial \eta} ((\rho_o T_o) - \frac{p_o}{c_p}) \end{aligned}$$

$$D_9 = \frac{(r_x - \eta)^2}{c_o \eta^2} \rho_o v_o - \frac{2(r_x - \eta)}{c_o} \frac{\partial}{\partial \eta} (\rho_o v_o)$$

$$\begin{aligned} D_{10} &= \Omega \frac{(r_x - \eta)^2}{c_o} \frac{\partial p_o}{\partial \eta} \\ &- \frac{(r_x - \eta)^2}{c_o \eta} \frac{\partial}{\partial \eta} (\rho_o v_o) \end{aligned}$$

REFERENCES

- /1/ Nelson, C.C.; 1985: Rotordynamic coefficients for compressible flow in tapered annular seals. *Journal of Tribology*, Vol. 107, July 1985
- /2/ Iwatsubo, T.; 1980: Evaluation of instability forces of labyrinth seals in turbines or compressors. NASA conference publication 2133, May 1980
- /3/ Childs, D.W.; Scharrer, J.K.; 1984: An Iwatsubo-based solution for labyrinth seals-comparison with experimental results. NASA conference publication 2338 Rotordynamic instability problems in high performance turbomachinery 1984
- /4/ Wyssmann, H.R.; Pham, T.C.; Jenny, R.J.; 1984: Prediction of stiffness and damping coefficients for centrifugal compressor labyrinth seals. *ASME Journal of Engineering for Gas Turbines and Power*, Oct. 1984, Vol. 106, pp. 920-926
- /5/ Wyssmann, H.R.; 1986: Theory and measurements of turbocompressors. The fourth workshop on rotordynamics instability problems in high performance turbomachinery. June 2-4, 1986 Texas A&M University, College Station, Texas
- /6/ Rhode, D.L.; Sobolik, S.R.; 1986: Simulation of Subsonic Flow Through a Generic Labyrinth Seal. *Journal of Engineering for Gas Turbines and Power*, Vol. 108, Oct. 1986, pp. 674-680
- /7/ Nordmann, R.; Dietzen, F.J.; Weiser, H.P.; Calculation of Rotordynamic Coefficients and Leakage for Annular Gas Seals by Means of Finite Difference Techniques. The 11th Biennial Conference on Mechanical Vibration and Noise. Sept. 27-30, 1987 Boston, Massachusetts
- /8/ Launder, B.E.; Spalding, D.B.; 1974: The numerical computation of turbulent flows. *Computer methods in applied mechanics and engineering*, 3 (1974) 269-289
- /9/ Gosman, A.D.; Pun, W.; 1974: Calculation of recirculation flows. Imperial College London, Mech. Eng. Dept., HTS/74/2
- /10/ Benckert, H.; Strömungsbedingte Federkennwerte in Labyrinthdichtungen. Dissertation Universität Stuttgart, 1980.

BLANK PAGE

ROTORDYNAMIC COEFFICIENTS FOR STEPPED

LABYRINTH GAS SEALS

Joseph K. Scharrer

Rockwell International, Rocketdyne Div.
Canoga Park, California 91304, U.S.A.

The basic equations are derived for compressible flow in a stepped labyrinth gas seal. The flow is assumed to be completely turbulent in the circumferential direction where the friction factor is determined by the Blasius relation. Linearized zeroth and first-order perturbation equations are developed for small motion about a centered position by an expansion in the eccentricity ratio. The zeroth-order pressure distribution is found by satisfying the leakage equation while the circumferential velocity distribution is determined by satisfying the momentum equations. The first order equations are solved by a separation of variables solution. Integration of the resultant pressure distribution along and around the seal defines the reaction force developed by the seal and the corresponding dynamic coefficients.

The results of this analysis are presented in the form of a parametric study, since there are no known experimental data for the rotordynamic coefficients of stepped labyrinth gas seals. The parametric study investigates the relative rotordynamic stability of convergent, straight and divergent stepped labyrinth gas seals. The results show that, generally, the divergent seal is more stable, rotordynamically, than the straight or convergent seals. The results also show that the teeth-on-stator seals are not always more stable, rotordynamically, than the teeth-on-rotor seals as was shown by experiment by Childs and Scharrer (1986b) for a 15 tooth seal.

INTRODUCTION

The problem of self excited vibration in turbomachinery due to labyrinth seals has led to the development of many analyses for the straight-through type of labyrinth seal, e.g. Childs and Scharrer (1986a), Iwatsubo (1980), Jenny et al. (1984) and Scharrer (1987). There has also been an extensive amount of experimental data collected for the rotordynamic coefficients of straight-through labyrinth seals, e.g. Childs and Scharrer (1986b), Leong (1983), Scharrer (1987) and Wachter and Benckert (1980). The stepped labyrinth seal is as prevalent in turbomachinery as the straight-through labyrinth seal; however, there has been very little or no experimental or analytical work done to quantify the rotordynamic characteristics of this type of seal. This paper presents an analysis of the stepped labyrinth seal which is a derivative of the straight-through analysis of Childs and Scharrer (1986a). The results of this analysis will be presented in the form of a parametric study, since there are no known experimental data.

PROCEDURE

The analysis presented here is developed for the stepped type of labyrinth seal shown in figure 1. The continuity and momentum equations will be derived for a single cavity control volume as shown in figures 2,3,4 and 5. A leakage model will be employed to account for the axial leakage. The governing equations will be linearized using perturbation analysis for small motion about a centered position. The zeroth-order continuity and momentum equations will be solved to determine the steady state pressure and velocity for each cavity. The first-order continuity and momentum equations will be reduced to linearly independent, algebraic equations by assuming an elliptical orbit for the shaft and a corresponding harmonic response for the pressure and velocity perturbations. The force and force coefficients for the seal are found by integration of the first-order pressure perturbation along and around the shaft.

ASSUMPTIONS

- (1) The fluid is an ideal gas.
- (2) Pressure variations within a chamber are small compared to the pressure differences across a seal strip.
- (3) The lowest frequency of acoustic resonance in the cavity is much higher than that of the rotor speed.
- (4) The eccentricity of the rotor is small compared to the radial seal clearance.
- (5) Although the shear stress is significant in the determination of the flow parameters (velocity, etc.), the shear stress forces on the rotor are small when compared to the pressure forces.
- (6) The cavity flow is turbulent and isothermal.
- (7) Added mass terms are neglected.
- (8) The seal strip is midway between steps.

GOVERNING EQUATIONS

Continuity Equation

The control volumes of figures 2 and 3 have a unit circumferential width. Their continuity equation is

$$\frac{\partial(\rho A)}{\partial t} + \frac{1}{R_{s_i}} \frac{\partial(\rho V A)}{\partial \theta} + \frac{R_{s_{i+1}}}{R_{s_i}} \dot{m}_{i+1} - \dot{m}_i = 0 \quad (1)$$

where the transverse surface area, A , is defined by

$$A_i = (B_i + H_i + B_{i+1} + H_{i+1})L_i/2$$

Momentum Equations

The momentum equation (2) is derived using figures 4 and 5 which show the pressure forces and shear stresses acting on the control volume.

$$\frac{\partial \rho V_i A_i}{\partial t} + \frac{2\rho V_i A_i}{Rs_i} \frac{\partial V_i}{\partial \theta} + \frac{\rho V_i}{Rs_i} \frac{\partial A_i}{\partial \theta} + \frac{V_i A_i}{Rs_i} \frac{\partial \rho}{\partial \theta} + \frac{Rs_{i+1} \dot{m}_{i+1} V_i}{Rs_i} - \dot{m}_i V_{i-1} = -\frac{A_i}{Rs_i} \frac{\partial P_i}{\partial \theta} + \tau_{ri} ar_i (L_i + d) - \tau_{si} as_i (L_i + d) \quad (2)$$

The shear stress model is the same as that used by Childs and Scharrer (1986a). The differences are in the dimensionless shear stress lengths and the hydraulic diameter. The dimensionless shear stress length is defined for the teeth-on-rotor labyrinth by

$$as_i = 1 \quad ar_i = (2B_i + L_i + d)/(L_i + d) \quad (3)$$

and for teeth-on-stator seals by

$$ar_i = 1 \quad as_i = (2B_i + L_i + d)/(L_i + d) \quad (4)$$

The hydraulic diameter, D_{hi} is defined by

$$D_{hi} = \frac{2(B_i + H_i)(L_i + d)}{H_i + B_i + L_i + d} \quad (5)$$

Reduced Equations

If equation (1) times the circumferential velocity is now subtracted from equation (2), the following reduced form of the momentum equation is obtained:

$$\begin{aligned} \rho A_i \frac{\partial V_i}{\partial t} + \frac{\rho V_i A_i}{Rs_i} \frac{\partial V_i}{\partial \theta} + \dot{m}_i (V_i - V_{i-1}) \\ = -\frac{A_i}{Rs_i} \frac{\partial P_i}{\partial \theta} + \tau_{ri} ar_i L_i - \tau_{si} as_i L_i \end{aligned} \quad (6)$$

The number of variables is reduced by using the ideal gas law to eliminate the density terms.

$$P_i = \rho_i RT \quad (7)$$

Leakage Equation

The leakage equation (8), flow coefficient, kinetic energy carryover coefficient, and the choked flow solution algorithm are the same as those used by Childs and Scharrer (1986a). The kinetic energy carryover coefficient has the added restriction of being unity when the step height is greater than the clearance.

$$\dot{m}_i = \mu_{1i} \mu_{2i} H_i \sqrt{\frac{P_{i-1}^2 - P_i^2}{RT}} \quad (8)$$

Perturbation Analysis

The solution procedure will be summarized here as the details are given in Childs and Scharrer (1986a). Introduction of the following perturbation variables into the governing equations yields zeroth and first order continuity and momentum equations.

$$\begin{aligned} P_i &= P_{oi} + \epsilon P_{1i} & H_i &= Cr_i + \epsilon H_1 \\ V_i &= V_{oi} + \epsilon V_{1i} & A_i &= A_o + \epsilon L_i H_1 \end{aligned}$$

where $\epsilon = e_o/Cr_i$ is the eccentricity ratio.

Zeroth-Order Solution

The zeroth-order leakage equation is

$$\frac{Rs_{i+1}\dot{m}_{i+1}}{Rs_i} = \dot{m}_i = \dot{m}_o \quad (9)$$

and can be solved iteratively to yield zeroth-order cavity pressure values.

The zeroth-order circumferential momentum equation is

$$\dot{m}_o(Rs_{i+1}V_{oi}/Rs_i - V_{oi-1}) = (\tau_{ro}\alpha r_i - \tau_{so}\alpha s_i)L_i \quad (10)$$

and is solved using a Newton root finding technique to yield zeroth-order cavity circumferential velocity components.

First-Order Solution

The governing first-order equations (11,12), define the pressure and velocity fluctuations resulting from the seal clearance function. The continuity and momentum equations follow in order:

$$\begin{aligned} G_{1i}\frac{\partial P_{1i}}{\partial t} + G_{1i}\frac{V_{oi}}{Rs_i}\frac{\partial P_{1i}}{\partial \theta} + G_{1i}\frac{P_{oi}}{Rs_i}\frac{\partial V_{1i}}{\partial \theta} + G_{3i}P_{1i} \\ + G_{4i}P_{1i-1} + G_{5i}P_{1i+1} = -G_{6i}H_{1i} - G_{2i}\frac{\partial H_{1i}}{\partial t} - G_{2i}\frac{V_{oi}}{Rs_i}\frac{\partial H_{1i}}{\partial \theta} \end{aligned} \quad (11)$$

$$\begin{aligned} X_{1i}\frac{\partial V_{1i}}{\partial t} - \frac{X_{1i}V_{oi}}{Rs_i}\frac{\partial V_{1i}}{\partial \theta} + \frac{A_{oi}}{Rs_i}\frac{\partial P_{1i}}{\partial \theta} + X_{2i}V_{1i} - \dot{m}_oV_{1i-1} \\ + X_{3i}P_{1i} + X_{4i}P_{1i-1} = X_{5i}H_{1i} \end{aligned} \quad (12)$$

where the X's and G's are defined in Appendix A. With an assumption of an elliptical shaft orbit, these equations can be reduced to the following system of linear algebraic equations:

$$[A_{i-1}](X_{i-1}) + [A_i](X_i) + [A_{i+1}](X_{i+1}) = \frac{a}{\epsilon}(B_i) + \frac{b}{\epsilon}(C_i) \quad (13)$$

where

$$\begin{aligned} (X_{i-1}) &= (P_{si-1}^+, P_{oi-1}^+, P_{si-1}^-, P_{oi-1}^-, V_{si-1}^+, V_{oi-1}^+, V_{si-1}^-, V_{oi-1}^-)^T \\ (X_i) &= (P_{si}^+, P_{oi}^+, P_{si}^-, P_{oi}^-, V_{si}^+, V_{oi}^+, V_{si}^-, V_{oi}^-)^T \\ (X_{i+1}) &= (P_{si+1}^+, P_{oi+1}^+, P_{si+1}^-, P_{oi+1}^-, V_{si+1}^+, V_{oi+1}^+, V_{si+1}^-, V_{oi+1}^-)^T \end{aligned}$$

The A matrices and column vectors B and C are given in Childs and Scharrer (1986a). To use equation (13) for the entire solution, a system matrix can be formed which is block tridiagonal in the A matrices. The size of this resultant matrix is (8NC X 8NC) since pressure and velocity perturbations at the inlet and the exit are assumed to be zero. This system is easily solved by various linear equation algorithms, and yields a solution of the form:

$$\begin{aligned}
P_{si}^+ &= \frac{a}{\epsilon} F_{asi}^+ + \frac{b}{\epsilon} F_{bsi}^+ \\
P_{si}^- &= \frac{a}{\epsilon} F_{asi}^- + \frac{b}{\epsilon} F_{bsi}^- \\
P_{ai}^+ &= \frac{a}{\epsilon} F_{asi}^+ + \frac{b}{\epsilon} F_{bsi}^+ \\
P_{ai}^- &= \frac{a}{\epsilon} F_{asi}^- + \frac{b}{\epsilon} F_{bsi}^-
\end{aligned} \tag{14}$$

DETERMINATION OF DYNAMIC COEFFICIENT

The force-motion equations for a labyrinth seal are assumed to be of the form

$$-\begin{Bmatrix} F_x \\ F_y \end{Bmatrix} = \begin{bmatrix} K & k \\ -k & K \end{bmatrix} \begin{Bmatrix} X \\ Y \end{Bmatrix} + \begin{bmatrix} C & c \\ -c & C \end{bmatrix} \begin{Bmatrix} \dot{X} \\ \dot{Y} \end{Bmatrix} \tag{15}$$

The solution of equation (15) for the stiffness and damping coefficients is the objective of the current analysis. The solution procedure used for this analysis is the same one used by Childs and Scharrer (1986a). The desired solution for the stiffness and damping coefficients is

$$\begin{aligned}
K &= \pi R s \sum_{i=1}^{NC} (F_{asi}^+ + F_{asi}^-) L_i \\
k &= \pi R s \sum_{i=1}^{NC} (F_{bsi}^+ + F_{bsi}^-) L_i \\
C &= -\frac{\pi R s}{\omega} \sum_{i=1}^{NC} (F_{asi}^+ + F_{asi}^-) L_i \\
c &= \frac{\pi R s}{\omega} \sum_{i=1}^{NC} (F_{bsi}^+ + F_{bsi}^-) L_i
\end{aligned} \tag{16}$$

RESULTS

The geometry used in the parametric study is given in table 1. The pitch of the teeth, the step height, the radial clearance, the tooth height and the inlet radius were all kept constant. The number of teeth were varied between 5 and 15 for the three types of seals investigated: straight, converging and diverging which are shown in figure 6. The operating conditions used for the study are given in table 2. The only variable is the inlet circumferential velocity ratio which was varied between 0.25 and 1.0.

Table 1. Basic Geometry Studied

<i>Radial Clearance, Cr</i>	$= 0.127 \text{ mm (0.005 in)}$
<i>Tooth Height, B</i>	$= 3.175 \text{ mm (0.125 in)}$
<i>Tooth Pitch, L</i>	$= 2.175 \text{ mm (0.125 in)}$
<i>Seal Radius, Rs</i>	$= 75.6 \text{ mm (2.979 in)}$
<i>Tooth Width, tp</i>	$= 0.152 \text{ mm (0.006 in)}$
<i>Step Height, d</i>	$= 1.000 \text{ mm (0.04 in)}$
<i>Number of Teeth, NT</i>	$= 5, 10, 15$

Table 2. Operating Conditions

<i>Reservoir Pressure, Pr</i>	$= 7.0 \text{ bar (101.0 psi)}$
<i>Sump Pressure, Ps</i>	$= 1.01 \text{ bar (14.7 psi)}$
<i>Shaft Speed, ω</i>	$= 20,000 \text{ cpm (rpm)}$
<i>Temperature, T</i>	$= 300 \text{ K (80 deg F)}$
<i>Inlet Swirl Ratio, $V_i/Rs\omega$</i>	$= 0.25, 0.5, 0.75, 1.0$
Fluid is air	

Leakage

Figures 7 and 8 show leakage versus number of teeth and configuration for teeth-on-rotor and teeth-on-stator seals, respectively. The figures show that the leakage decreases with increasing number of teeth for both teeth-on-rotor and teeth-on-stator seals. The figures also show that the diverging seal yields maximum leakage while the converging seal has the minimum leakage. This result is expected since the effective area of the diverging seal is greater than that of the converging or straight seal.

Stiffness

Figures 9 and 10 show direct stiffness versus number of teeth and configuration for an inlet circumferential velocity ratio of 1.0 for teeth-on-rotor and teeth-on-stator seals, respectively. Figure 9 shows that for converging and straight teeth-on-rotor seals a maximum stiffness occurs for the 10 tooth seal. For the teeth-on-stator seal, figure 10 shows that there is an optimum only for the diverging seal. A maximum may occur for geometries other than those investigated in this study. This phenomenon did not occur for inlet circumferential velocity ratios of 0.25 or 0.5. Both figures also show that the diverging seal yielded the largest value of stiffness. This was true for all of the geometries and operating conditions investigated.

Figures 11 and 12 show cross-coupled stiffness versus configuration and number of teeth for an inlet circumferential velocity ratio of 1.0 for teeth-on-rotor and teeth-on-stator seals, respectively. Figure 11 shows that the straight teeth-on-rotor seal yields the maximum cross-coupled stiffness for both the 10 and 15 tooth seals. This phenomenon did not occur for the 0.25 inlet circumferential velocity ratio case. Figure 12 shows that the same is true for the 10 tooth teeth-on-stator seal. This phenomenon did not occur for any inlet circumferential velocity ratio case other than 1.0. The figures also show that the cross-coupled stiffness increases as the number of teeth increase.

Damping

Figures 13 and 14 show direct damping versus configuration and number of teeth for an inlet circumferential velocity ratio of 1.0 for teeth-on-rotor and teeth-on-stator seals, respectively. Figure 13 shows that the straight teeth-on-rotor seal yields a maximum value of damping for the 10 and 15 tooth seals. This did not occur for an inlet circumferential velocity ratio of 0.25 or 0.5. Figure 14 shows that direct damping is a maximum for the diverging teeth-on-stator seal and a minimum for the converging seal for the 10 and 15 tooth seals. The opposite is true for the 5 tooth seal. The figures also show that direct damping increases as the number of teeth increases.

Relative Rotordynamic Stability

The relative stability of the seal configurations investigated will be compared using the whirl frequency ratio which is a ratio of the destabilizing influence divided by the stabilizing influence and is defined as

$$\frac{k}{\omega C}$$

When this ratio is greater than 1.0, the seal is a destabilizing influence. The seal with the lowest value is considered to be the most stable. Figures 15 and 16 show the whirl frequency ratio versus seal configuration for inlet circumferential velocity ratios of 0.25 and 1.0, respectively. Both figures show that the teeth-on-rotor seal is more stable than the teeth-on-stator seal for the 5 tooth configuration while the opposite is true for the 15 tooth configuration. The latter result is supported by the test data of Childs and Scharrer (1986b). The 10 tooth configuration seems to be in a transition region. The figures also show that except for the 5 tooth seals at inlet swirls of 1.0, the diverging seal configuration is more stable than the converging and straight configurations. A more complete stability analysis would show that the converging seal may in some cases be a more unstable seal due to the large negative direct stiffness values illustrated in figures 9 and 10.

CONCLUSIONS

This paper has presented an analysis for the rotordynamic coefficients of stepped labyrinth gas seals. The results of this analysis were presented in the form of a parametric study, since no known experimental data existed. The results of this study support the following conclusions:

- 1) The converging stepped labyrinth seal leaks less than either the straight-through or the divergent seals.
- 2) The diverging stepped labyrinth seal had a higher value of direct stiffness than either the straight-through or convergent seals for both the teeth-on-rotor and teeth-on-stator case.
- 3) A maximum direct stiffness was obtained for a 10 tooth convergent teeth-on-rotor seal and a 10 tooth divergent teeth-on-stator seal for inlet circumferential velocity ratios of 0.75 or larger.
- 4) Cross-coupled stiffness increases as the number of teeth, and therefore length (in this study), increase.

5) Direct damping increases as the number of teeth, and therefore length (in this study), increase.

6) For most of the cases studied, the diverging seal is more stable, rotordynamically, than either the straight-through or converging seals for both teeth-on-rotor and teeth-on-stator seals.

7) For the 5 tooth seals, the teeth-on-rotor seal was more stable, rotordynamically, than the teeth-on-stator seals. The opposite was true for the 15 tooth seals.

NOMENCLATURE

A	Cross-sectional area of control volume (L^2); illustrated in figure (3)
B	Height of labyrinth seal strip (L); illustrated in figure (1)
C	Direct damping coefficient (Ft/L)
Cr	Nominal radial clearance (L); illustrated in figure (1)
D_h	Hydraulic diameter of cavity (L); introduced in equation (5)
H	Local radial clearance (L)
K	Direct stiffness coefficient (F/L)
L	Pitch of seal strips (L); illustrated in figure (1)
NT	Number of seal strips
$NC = NT - 1$	Number of cavities
P	Pressure (F/L^2)
R	Gas constant (L^2/Tt^2)
Rs	Radius of control volume (L); illustrated in figure (1)
R_{sw}	Surface velocity of rotor (L/t)
T	Temperature (T)
TP	Tooth tip width (L); illustrated in figure (1)
V	Average circumferential velocity for control volume (L/t); illustrated in figure (2)
ar, as	Dimensionless length upon which shear stress acts; introduced in equation (3) and (4)
c	Cross coupled damping coefficient (Ft/L); in equation (16)
d	Step height (L), illustrated in figure 1
e_o	Displacement of the seal rotor from centered position (L)
k	Cross coupled stiffness coefficient (F/L); in equation (16)
\dot{m}	Leakage mass flow rate per circumferential length (M/Lt)
mr, nr, ms, ns	Coefficients for friction factor
t	Time (t)
ω	Shaft angular velocity (1/t)
ρ	Density of fluid (M/L^3)
ν	Kinematic viscosity (L^2/t)
$\epsilon = e_o/Cr$	Eccentricity ratio
γ	Ratio of specific heats

Subscripts

<i>o</i>	Zeroth-order component
<i>1</i>	First-order component
<i>i</i>	<i>i</i> -th chamber value
<i>x</i>	X-direction
<i>y</i>	Y-direction
<i>r</i>	Reservoir value
<i>s</i>	Sump value

APPENDIX A: DEFINITION OF FIRST-ORDER COEFFICIENTS

$$G_1 = \frac{A_{oi}}{RT}; \quad G_2 = \frac{P_{oi} L_i}{RT}$$

$$G_3 = \frac{\dot{m}_o P_{oi}}{P_{oi-1}^2 - P_{oi}^2} + \frac{\dot{m}_o \mu_{1i+1} (\gamma - 1)}{\pi \gamma P_{oi+1}} (5 - 4S_{1i+1}) \left(\frac{P_{oi}}{P_{oi+1}} \right)^{\frac{-1}{\gamma}} \frac{Rs_{i+1}}{Rs_i} \\ + \frac{\dot{m}_o \mu_{1i} (\gamma - 1)}{\pi \gamma P_{oi}} (5 - 4S_{1i}) (S_{1i} + 1) + \frac{\dot{m}_o P_{oi}}{P_{oi}^2 - P_{oi+1}^2} + \frac{\dot{m}_o P_{oi}}{P_{oi}^2 - P_{oi+1}^2} \frac{Rs_{i+1}}{Rs_i}$$

$$G_4 = \frac{-\dot{m}_o P_{oi-1}}{P_{oi-1}^2 - P_{oi}^2} - \frac{\dot{m}_o \mu_{1i} (\gamma - 1)}{\pi \gamma P_{oi}} (5 - 4S_{1i}) \left(\frac{P_{oi-1}}{P_{oi}} \right)^{\frac{-1}{\gamma}}$$

$$G_5 = \frac{-\dot{m}_o P_{oi+1}}{P_{oi}^2 - P_{oi+1}^2} \frac{Rs_{i+1}}{Rs_i} - \frac{\dot{m}_o \mu_{1i+1} (\gamma - 1)}{\pi \gamma P_{oi+1}} (5 - 4S_{1i+1}) (S_{1i+1} + 1) \frac{Rs_{i+1}}{Rs_i}$$

$$G_6 = \dot{m}_o \frac{Cr_i - Cr_{i-1}}{Cr_i Cr_{i-1}}$$

$$X_1 = \frac{P_{oi} A_{oi}}{RT}$$

$$X_3 = -\frac{\dot{m}_o (V_{oi} - V_{oi-1}) P_{oi}}{P_{oi-1}^2 - P_{oi}^2} + \frac{\dot{m}_o (V_{oi} - V_{oi-1}) (\gamma - 1)}{\pi \gamma P_{oi}} \mu_{1i} (4S_{1i} - 5) (S_{1i} + 1) \\ - \frac{\tau_{ri} ar_i L_i (1 + mr)}{P_{oi}} + \frac{\tau_{si} (1 + ms) L_i as_i}{P_{oi}}$$

$$X_4 = \frac{\dot{m}_o (V_{oi} - V_{oi-1}) P_{oi-1}}{P_{oi-1}^2 - P_{oi}^2} - \frac{\dot{m}_o (V_{oi} - V_{oi-1}) (\gamma - 1)}{\pi \gamma P_{oi}} \mu_{1i} (4S_{1i} - 5) \left(\frac{P_{oi-1}}{P_{oi}} \right)^{\frac{-1}{\gamma}}$$

$$X_2 = \dot{m}_o + \frac{\tau_{si} as_i L_i (2 + ms)}{V_{oi}} + \frac{\tau_{ri} ar_i L_i (2 + mr)}{(Rs_i \omega - V_{oi})}$$

$$X_5 = \frac{-\dot{m}_o (V_{oi} - V_{oi-1})}{Cr_i} - \frac{\tau_{si} as_i L_i ms D_{hi}}{2(Cr_i + B_i)^2} + \frac{\tau_{ri} ar_i L_i mr D_{hi}}{2(Cr_i + B_i)^2}$$

APPENDIX B: SEPARATION OF GOVERNING EQUATIONS

Continuity:

$$\begin{aligned}
\cos(\theta + \omega t) : & G_1 P_{si}^+ \left(\omega + \frac{V_{oi}}{Rs_i} \right) + G_1 \frac{P_{oi}}{Rs_i} V_{si}^+ + G_3 P_{ci}^+ + G_4 P_{ci-1}^+ \\
& + G_5 P_{ci+1}^+ = G_6 \frac{(a-b)}{2} \\
\sin(\theta + \omega t) : & -G_1 P_{ci}^+ \left(\omega + \frac{V_{oi}}{Rs_i} \right) - G_1 \frac{P_{oi}}{Rs_i} V_{ci}^+ + G_3 P_{si}^+ + G_4 P_{si-1}^+ \\
& + G_5 P_{si+1}^+ = \frac{G_2}{2} \left(\frac{V_{oi}}{Rs_i} + \omega \right) (b-a) \\
\cos(\theta - \omega t) : & -G_1 P_{si}^- \left(\frac{V_{oi}}{Rs_i} - \omega \right) + G_1 \frac{P_{oi}}{Rs_i} V_{si}^- + G_3 P_{ci}^- + G_4 P_{ci-1}^- \\
& + G_5 P_{ci+1}^- = G_6 \frac{(a+b)}{2} \\
\sin(\theta - \omega t) : & -G_1 P_{ci}^- \left(\omega - \frac{V_{oi}}{Rs_i} \right) - G_1 \frac{P_{oi}}{Rs_i} V_{ci}^- + G_3 P_{si}^- + G_4 P_{si-1}^- \\
& + G_5 P_{si+1}^- = \frac{G_2}{2} \left(\omega - \frac{V_{oi}}{Rs_i} \right) (a+b)
\end{aligned}$$

Momentum:

$$\begin{aligned}
\cos(\theta + \omega t) : & X_1 V_{si}^+ \left(\frac{V_{oi}}{Rs_i} + \omega \right) + \frac{A_{oi}}{Rs_i} P_{si}^+ + X_2 V_{ci}^+ - \dot{m}_o V_{ci-1}^+ + X_3 P_{ci}^+ \\
& + X_4 P_{ci-1}^+ = X_5 \frac{(b-a)}{2} \\
\sin(\theta + \omega t) : & -X_1 V_{ci}^+ \left(\frac{V_{oi}}{Rs_i} + \omega \right) - \frac{A_{oi}}{Rs_i} P_{ci}^+ + X_2 V_{si}^+ - \dot{m}_o V_{si-1}^+ + X_3 P_{si}^+ \\
& + X_4 P_{si-1}^+ = 0 \\
\cos(\theta - \omega t) : & X_1 V_{si}^- \left(\frac{V_{oi}}{Rs_i} - \omega \right) + \frac{A_{oi}}{Rs_i} P_{si}^- + X_2 V_{ci}^- - \dot{m}_o V_{ci-1}^- + X_3 P_{ci}^- \\
& + X_4 P_{ci-1}^- = -X_5 \frac{(a+b)}{2} \\
\sin(\theta - \omega t) : & X_1 V_{ci}^- \left(\omega - \frac{V_{oi}}{Rs_i} \right) - \frac{A_{oi}}{Rs_i} P_{ci}^- + X_2 V_{si}^- - \dot{m}_o V_{si-1}^- + X_3 P_{si}^- \\
& + X_4 P_{si-1}^- = 0
\end{aligned}$$

DEFINITION OF MATRIX ELEMENTS

 A_{i-1} MATRIX

$$A_{1,2} = A_{2,1} = A_{3,4} = A_{4,3} = G_4$$

$$A_{5,2} = A_{6,1} = A_{7,4} = A_{8,3} = X_4$$

$$A_{5,6} = A_{6,5} = A_{7,8} = A_{8,7} = -\dot{m}_o$$

The remaining elements are zero.

 A_i MATRIX

$$A_{1,1} = -A_{2,2} = G_1 \left(\omega + \frac{V_{oi}}{Rs_i} \right)$$

$$A_{3,3} = -A_{4,4} = G_1 \left(\frac{V_{oi}}{Rs_i} - \omega \right)$$

$$A_{1,2} = A_{2,1} = A_{3,4} = A_{4,3} = G_3$$

$$A_{5,2} = A_{6,1} = A_{7,4} = A_{8,3} = X_3$$

$$A_{5,1} = -A_{6,2} = A_{7,3} = -A_{8,4} = \frac{A_{oi}}{Rs_i}$$

$$A_{1,5} = -A_{2,6} = A_{3,7} = -A_{4,8} = G_1 \frac{P_{oi}}{Rs_i}$$

$$A_{5,5} = -A_{6,6} = X_1 \left(\omega + \frac{V_{oi}}{Rs_i} \right)$$

$$A_{7,7} = -A_{8,8} = X_1 \left(-\omega + \frac{V_{oi}}{Rs_i} \right)$$

$$A_{5,6} = A_{6,5} = A_{7,8} = A_{8,7} = X_2$$

The remaining elements are zero.

 A_{i+1} MATRIX

$$A_{1,2} = A_{2,1} = A_{3,4} = A_{4,3} = G_5$$

The remaining elements are zero.

B and C Column Vectors

$$B = \begin{pmatrix} \frac{G_4}{2} \\ -\frac{G_2}{2} \left(\frac{V_{oi}}{Rs_i} + \omega \right) \\ \frac{G_4}{2} \\ \frac{G_2}{2} \left(\omega - \frac{V_{oi}}{Rs_i} \right) \\ -\frac{X_3}{2} \\ 0 \\ -\frac{X_3}{2} \\ 0 \end{pmatrix} \quad C = \begin{pmatrix} -\frac{G_4}{2} \\ \frac{G_2}{2} \left(\frac{V_{oi}}{Rs_i} + \omega \right) \\ \frac{G_4}{2} \\ \frac{G_2}{2} \left(\omega - \frac{V_{oi}}{Rs_i} \right) \\ \frac{X_3}{2} \\ 0 \\ \frac{X_3}{2} \\ 0 \end{pmatrix}$$

REFERENCES

1. Childs, D.W., and Scharrer, J.K., 1986a, "An Iwatsubo Based Solution for Labyrinth Seals: A Comparison to Experimental Results," *ASME Journal of Engineering for Gas Turbines and Power*, April, Vol. 108, pp. 325-331
2. Childs, D.W. and Scharrer, J.K., 1986b, "Experimental Rotordynamic Coefficient Results for Teeth-On-Rotor and Teeth-On-Stator Labyrinth Gas Seals," ASME Paper No. 86-GT-12.
3. Iwatsubo, T., 1980, "Evaluation of Instability Forces of Labyrinth Seals in Turbines or Compressors," NASA CP2133 Proceedings of a workshop at Texas A&M University 12-14 May, entitled Rotordynamic Instability Problems in High Performance Turbomachinery, pp. 139-167.
4. Jenny, R., Wyssmann, H., and Pham, T., 1984, "Prediction of Stiffness and Damping Coefficients for Centrifugal Compressor Labyrinth Seals," ASME Paper No. 84-GT-86. Presented at the 29th International Gas Turbine Conference and Exhibit, Amsterdam, The Netherlands, June 4-7.
5. Leong, Y.M.S., 1983, "Lateral Forces Induced by Flow Through Model Labyrinth Glands," PhD Diss., Heriot-Watt University, Edinburgh, June.
6. Scharrer, J.K., 1987, "A Comparison of Experimental and Theoretical Results for Labyrinth Gas Seals," PhD Dissertation, Texas A&M University, May.
7. Wachter, J. and Benckert, H., 1980, "Flow Induced Spring Coefficients of Labyrinth Seals for Applications in Rotordynamics," NASA CP 2133, Proceedings of a workshop held at Texas A&M University, 12-14 May, Entitled Rotordynamic Instability Problems of High Performance Turbomachinery, pp. 189-212.



Figure 1. A Typical Stepped Labyrinth Seal.

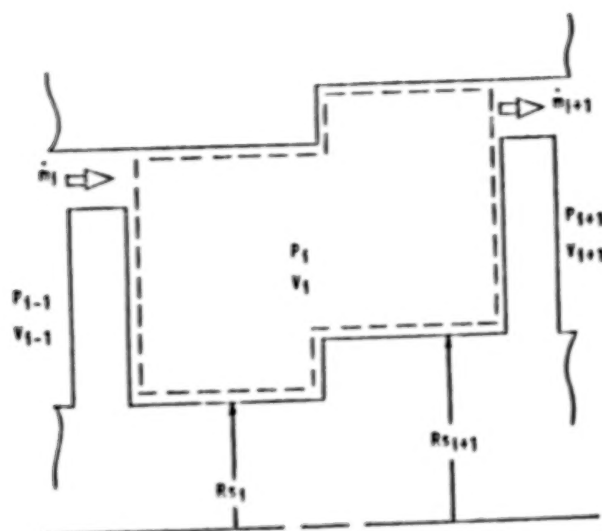


Figure 2. Cavity Control Volume.

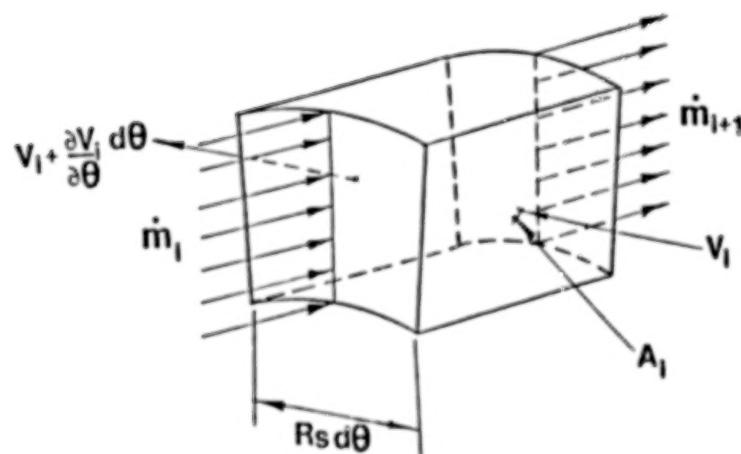


Figure 3. Isometric View of control Volume.

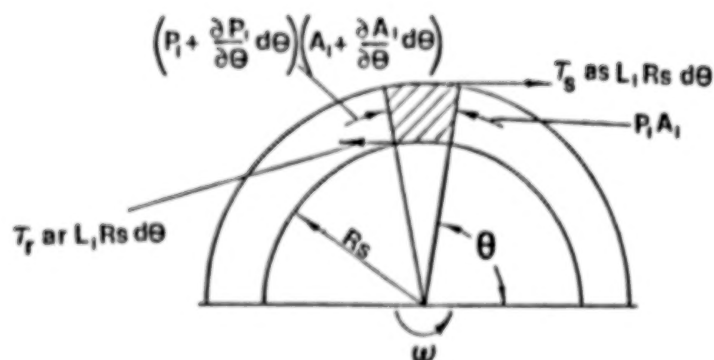


Figure 4. Forces on Control Volume.

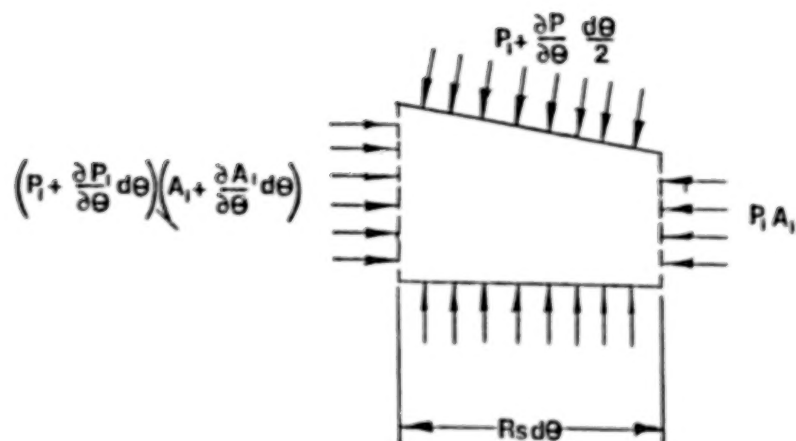


Figure 5. Pressure Forces on Control Volume.

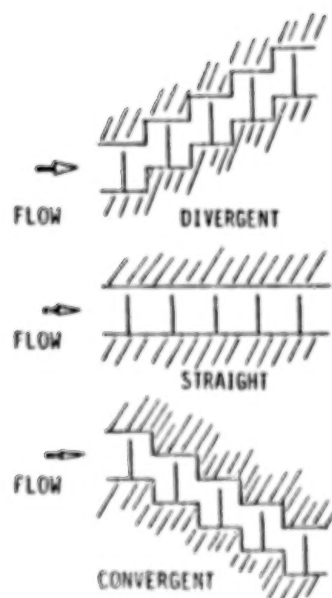


Figure 6. Configurations Studied.

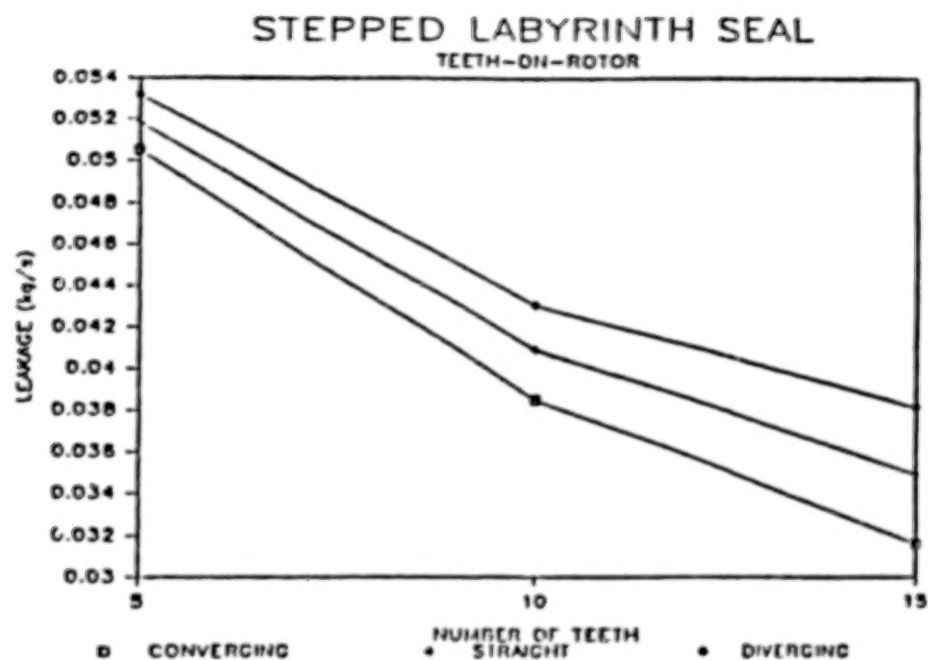


Figure 7. Leakage versus number of teeth and seal configuration for a teeth-on-rotor seal.

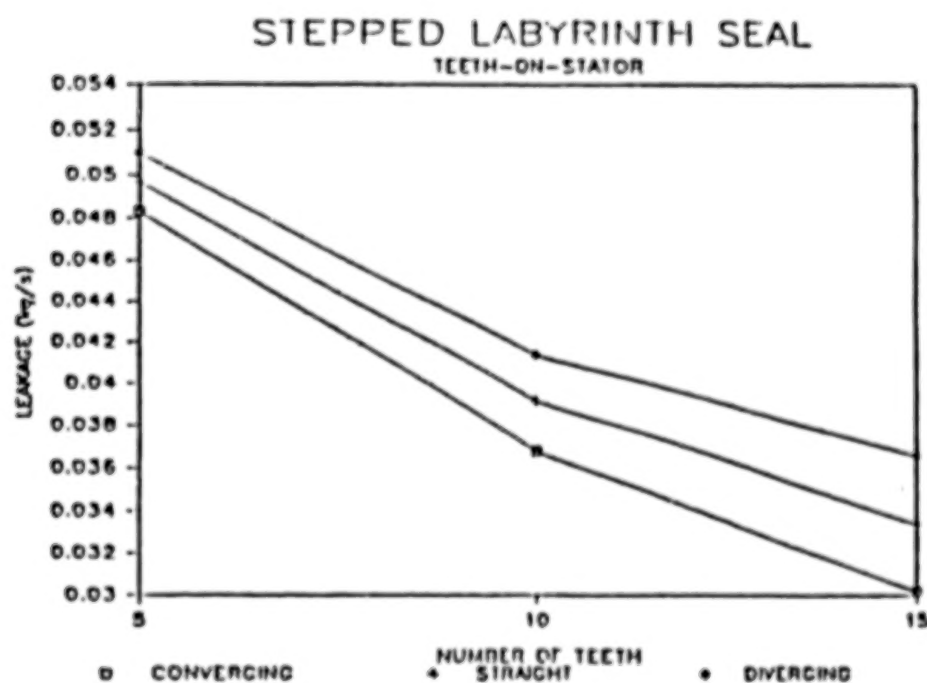


Figure 8. Leakage versus number of teeth and seal configuration for a teeth-on-stator seal.

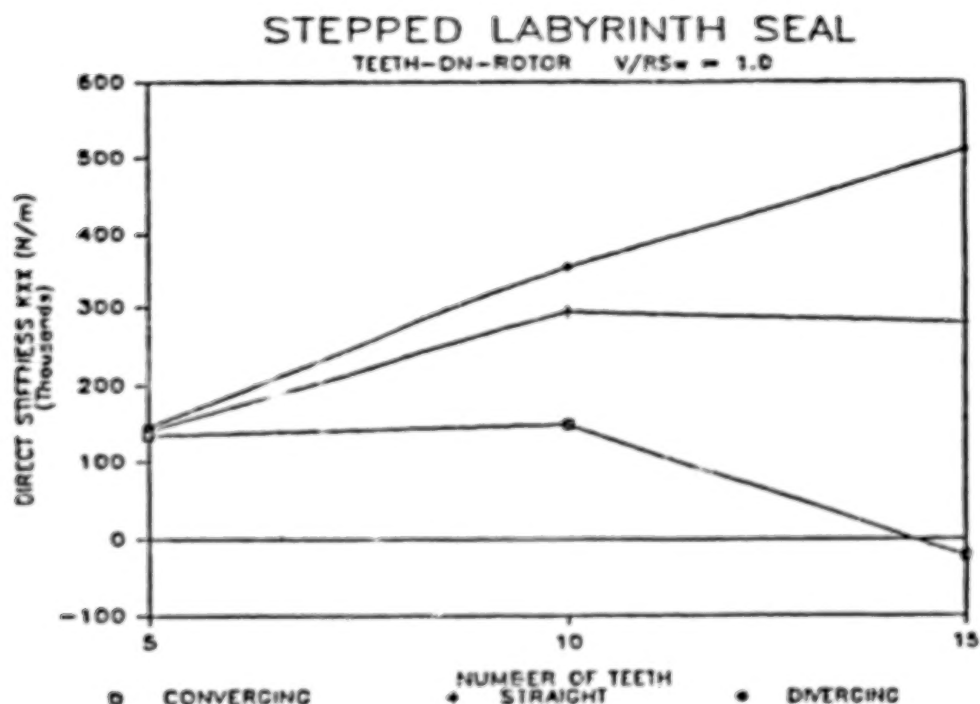


Figure 9. Direct Stiffness versus number of teeth and seal configuration for a teeth-on-rotor seal. Inlet circumferential velocity ratio is 1.0.

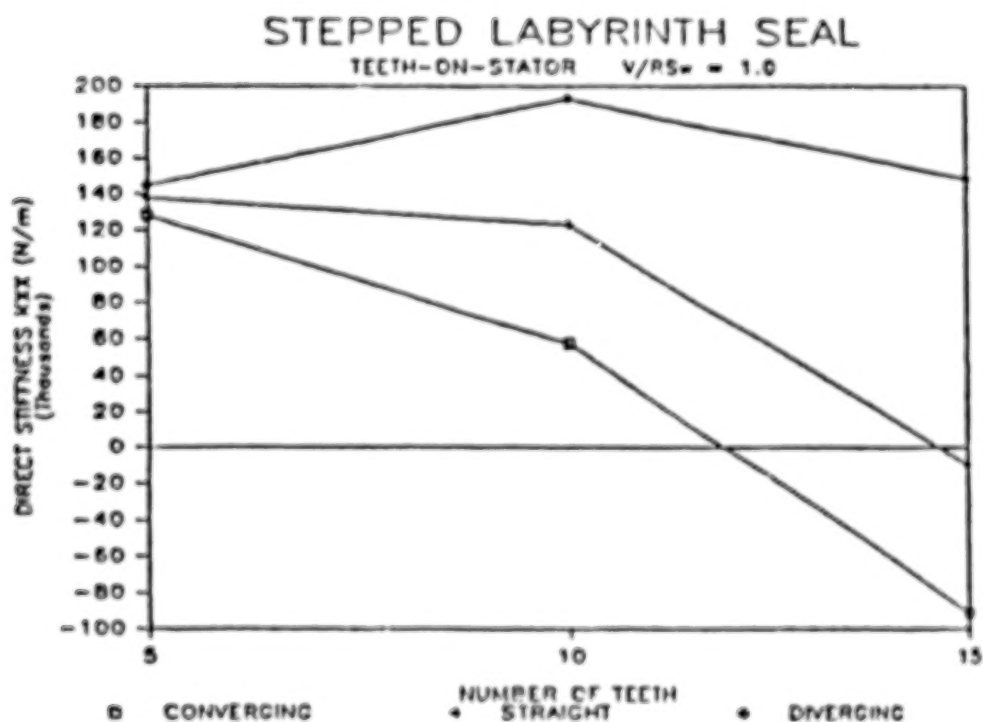


Figure 10. Direct Stiffness versus number of teeth and seal configuration for a teeth-on-stator seal. Inlet circumferential velocity ratio is 1.0.

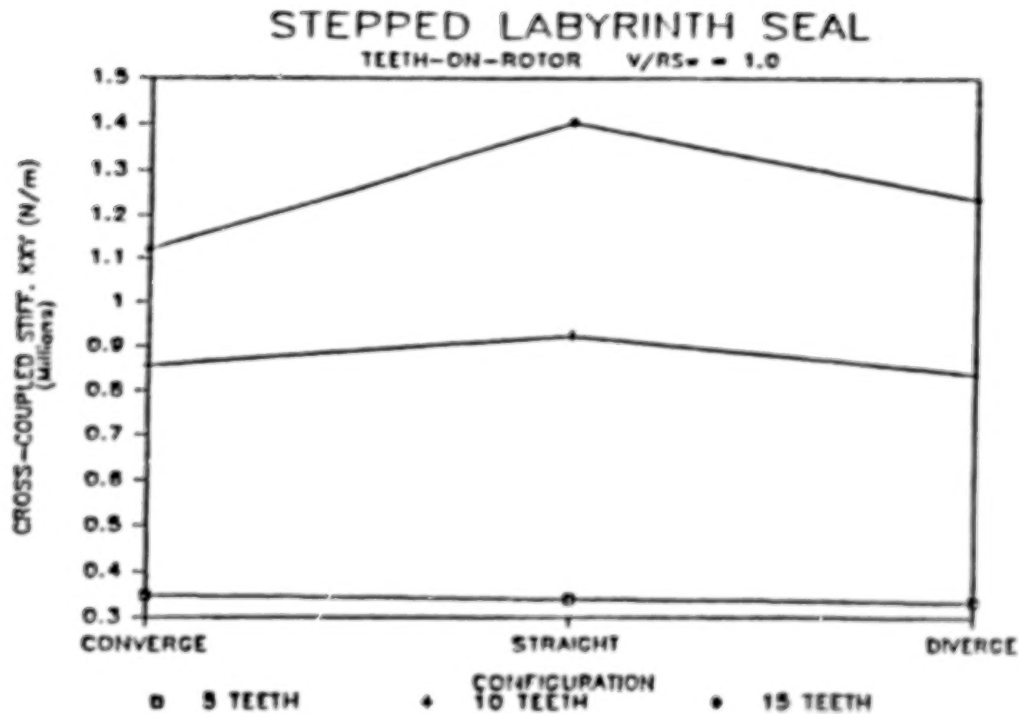


Figure 11. Cross-coupled stiffness versus seal configuration and number of teeth for a teeth-on-rotor seal. Inlet circumferential velocity ratio is 1.0.

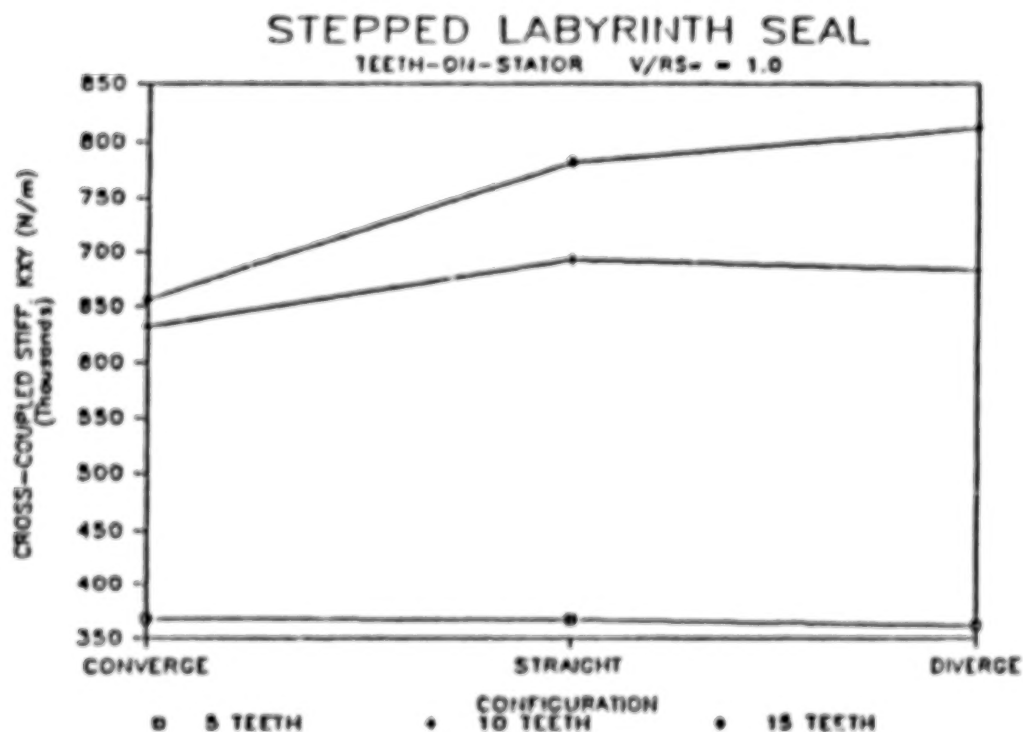


Figure 12. Cross-coupled stiffness versus seal configuration and number of teeth for a teeth-on-stator seal. Inlet circumferential velocity ratio is 1.0.

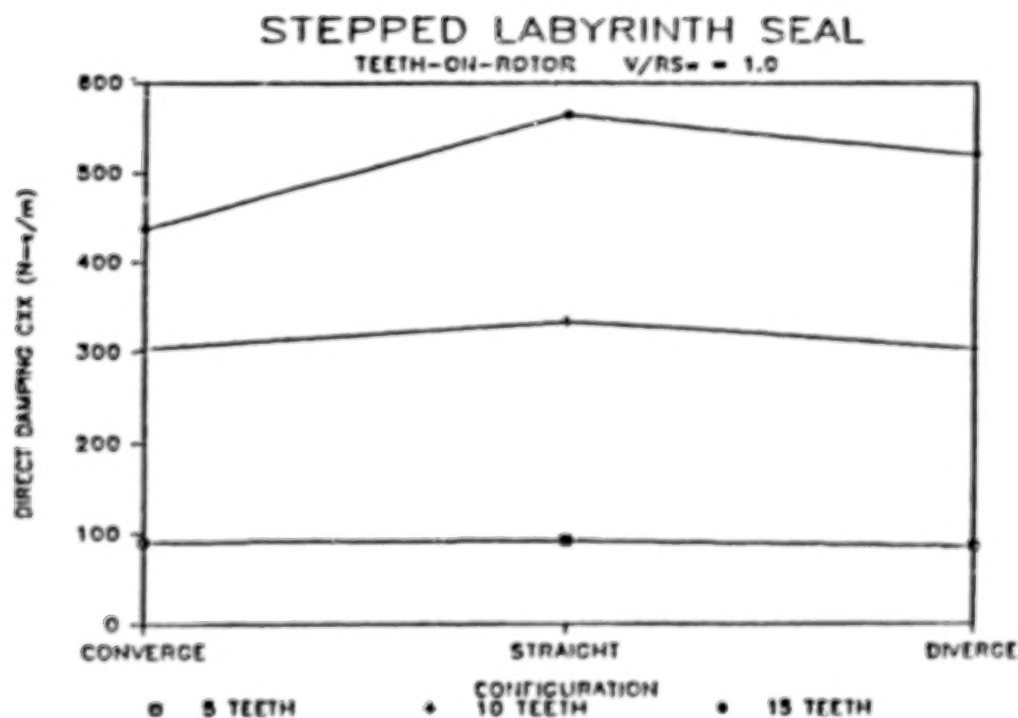


Figure 13. Direct damping versus seal configuration and number of teeth for a teeth-on-rotor seal. Inlet circumferential velocity ratio is 1.0.

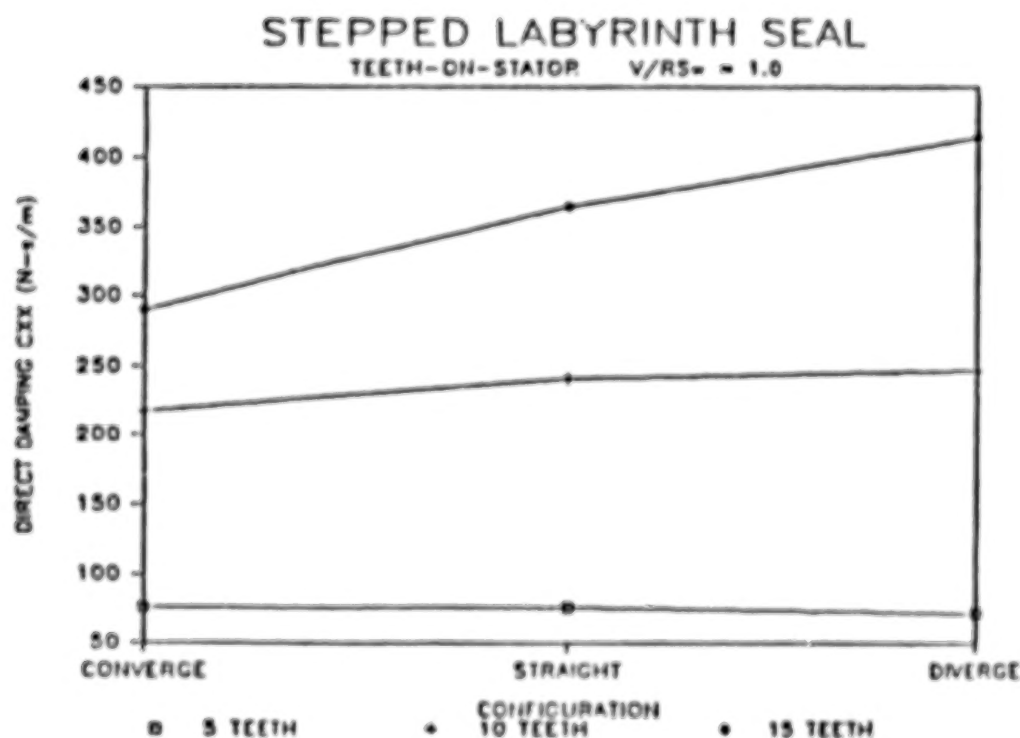


Figure 14. Direct damping versus seal configuration and number of teeth for a teeth-on-rotor seal. Inlet circumferential velocity ratio is 1.0.

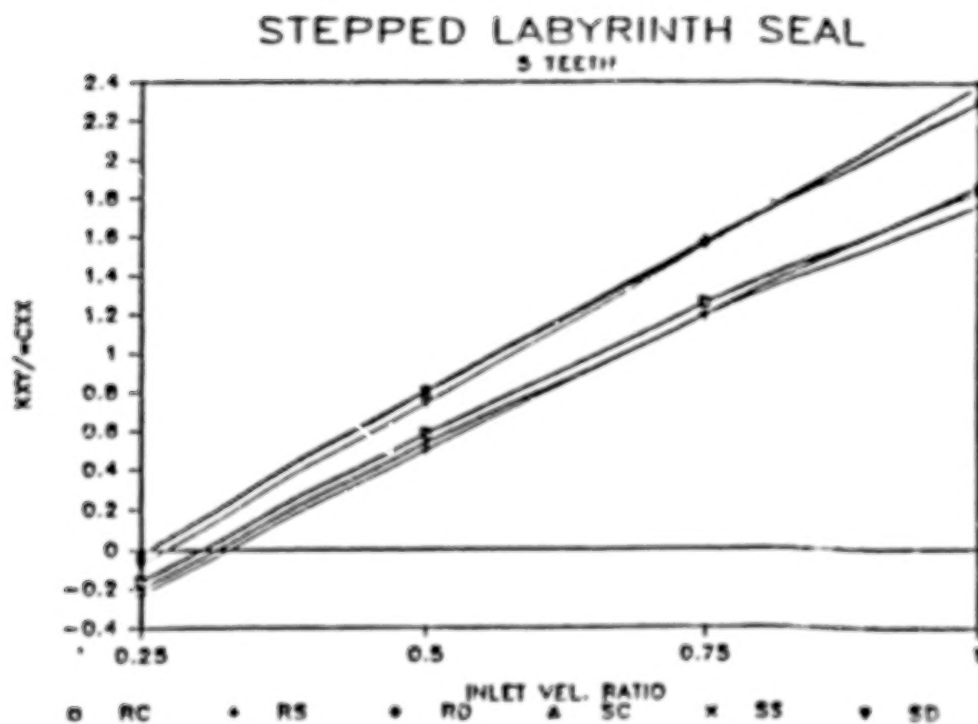


Figure 15. Whirl frequency ratio versus seal configuration for an inlet circumferential velocity ratio of 0.25.

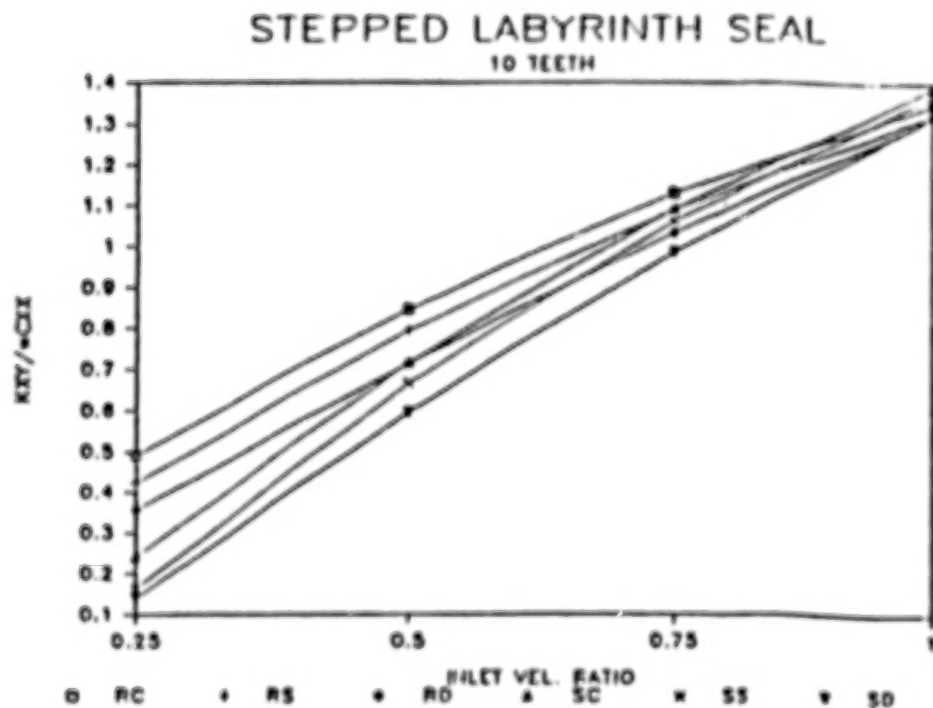


Figure 16. Whirl frequency ratio versus seal configuration for an inlet circumferential velocity ratio of 1.0.

BLANK PAGE

INFLUENCE OF DIFFERENT TYPES OF SEALS ON THE STABILITY BEHAVIOR OF TURBOPUMPS

W. Dieward and R. Nordmann
Department of Mechanical Engineering
University of Kaiserslautern
6750 Kaiserslautern, Federal Republic of Germany

One of the main problems in designing a centrifugal pump is to achieve a good efficiency while not neglecting the dynamic performance of the machine. The first aspect leads to the design of grooved seals in order to minimize the leakage flow. But the influence of these grooves to the dynamic behavior is not known very well. This paper presents experimental and theoretical results of the rotordynamic coefficients for different groove shapes and depths in seals. Finally the coefficients are applied to a simple pump model.

NOTATION

C	seal clearance
c_L	leakage coefficient = $[\dot{Q}/(2\pi R^2)][(\rho/2\Delta p)^{0.5}]$
D,d	direct and cross-coupled damping
d_{ij}	dynamic coefficients for damping
F_x, F_y	external forces
H	groove depth
K,k	direct and cross-coupled stiffness
k_{ij}	dynamic coefficients for stiffness
L	seal length
M,m	direct and cross-coupled inertia
m_{ij}	dynamic coefficients for inertia
Δp	pressure drop
R	shaft radius
\dot{Q}	volumetric flow rate
v	leakage velocity
x,y	coordinates for two orthogonal directions

α	damping coefficient (real part of the eigenvalue)
ξ	modal damping = $-\alpha/(\alpha^2 + \omega^2) - 0.5$
Ω	rotational frequency
ω	eigenfrequency (imaginary part of the eigenvalue)
ω_0	eigenfrequency of the "dry" shaft
Ω	rotational frequency

INTRODUCTION

Like all kinds of machines, centrifugal pumps must operate with a good efficiency. Because of the high rotational speeds, contactless seals have to be used to separate areas of different pressures in the pump. But the leakage flow through these seals reduces the efficiency of the machine (fig. 1).

As a result of this aspect, pump manufacturers very often use grooved seal surfaces to give more resistance to the fluid flow and so to reduce the leakage.

Besides the efficiency, also the dynamic behavior of the seals is an important aspect for today's turbopumps. The operational speed usually is much higher than the first critical speed of the "dry" shaft. But a resonance problem is avoided because during operation the seals introduce a great amount of stiffness to the system. Therefore they are also called wear rings. Not only stiffness, but also damping arises from the seals, and the physical mechanisms can cause instability for the centrifugal pump.

So the influence of seals to the dynamic behavior of turbopumps is very important and has to be taken into account (ref. 1). Especially the influence of grooved seal surfaces has to be investigated because these kind of seals are used for better effectiveness as mentioned before.

These influences are studied in this paper. For three different groove shapes with various depths (fig. 2) the dynamic coefficients of the seals are determined theoretically and experimentally. The results are discussed, and the influence to the rotordynamic behavior of a simple pump model is demonstrated.

THEORETICAL APPROACHES TO DETERMINE SEAL COEFFICIENTS

It is the aim of the theoretical approaches to describe the relations between external forces acting on a seal and the motions of the shaft by a mathematical expression. The results can be easily included in a finite element procedure for the overall behavior of a pump, if they are described in a matrix equation:

$$\begin{bmatrix} m_{11} & m_{12} \\ m_{21} & m_{22} \end{bmatrix} \begin{bmatrix} \ddot{x} \\ \ddot{y} \end{bmatrix} + \begin{bmatrix} d_{11} & d_{12} \\ d_{21} & d_{22} \end{bmatrix} \begin{bmatrix} \dot{x} \\ \dot{y} \end{bmatrix} + \begin{bmatrix} k_{11} & k_{12} \\ k_{21} & k_{22} \end{bmatrix} \begin{bmatrix} x \\ y \end{bmatrix} = \begin{bmatrix} F_x \\ F_y \end{bmatrix} \quad (1)$$

m_{ij}, d_{ij}, k_{ij} dynamic coefficients for inertia, damping and stiffness

x, y coordinates for two orthogonal directions

F_x, F_y external forces

In the following chapters two ways of calculating these dynamic seal coefficients are briefly described. Both theories come out with skewsymmetric matrices.

$M_{11} = m_{22} = M$ direct inertia

$m_{12} = -m_{21} = m$ cross-coupled inertia

$d_{11} = d_{22} = D$ direct damping

$d_{12} = -d_{21} = d$ cross-coupled damping

$k_{11} = k_{22} = K$ direct stiffness

$k_{12} = -k_{21} = k$ cross-coupled stiffness

Finite Length Theory

In 1982 CHILDS published a finite length theory (ref. 2,3) to calculate seal coefficients. It is based on a bulk-flow model (fig. 3a) for the fluid behavior in the seal. The force equilibrium equations together with continuity equations can be solved by a perturbation method. Integrating the resulting pressure distribution over the seal surface leads to the seal forces from which the dynamic coefficients can be extracted.

Contained in this calculation are empirical constants to include the friction at the rotor and stator surfaces, which have to be determined experimentally.

In regards to grooved seals it is possible to extend the model. The continuity equation in the circumferential direction is enlarged by the additional cross sections of the grooves, and the empirical friction factors are determined separately for the circumferential and axial directions. Also the friction of the circumferential fluid flow at the groove walls is taken into account.

This extended bulk-flow theory was developed by NORDMANN (ref. 4) and is applicable to grooved seals, but some empirical constants have to be measured in addition.

Finite Difference Theory

In 1986 DIETZEN and NORDMANN (ref. 5) published a method to calculate seal coefficients by means of a finite difference technique. The method is based on the Navier-Stokes Equations, continuity equation and energy equation, so that every fluid flow can be modelled.

To calculate the fluid flow in a seal, the seal gap is described with a grid of calculation points (fig. 3b). Using also a disturbance method the fluid velocities

and pressure values are calculated for all nodal points as a function of the values of the surrounding grid points.

The wall stresses are modelled by a logarithmical law, which only influences the first grid line at the wall. So it is possible to calculate the fluid flow for all seal geometries without using any empirical values. Again the resulting pressure distribution is integrated yielding the forces and finally the desired seal coefficients.

A disadvantage for this finite difference theory is the high computational time it takes, but the results are very good compared to measurements as the next chapter will show.

MEASUREMENTS OF SEAL COEFFICIENTS

Test Rig

A test rig to measure rotordynamic seal coefficients was built at the University of Kaiserslautern by MASSMANN and NORDMANN (fig. 4), (ref. 6).

Between a stiff shaft which is rigidly supported and a stiff housing, two symmetrical seal inlets are situated. During operation the shaft rotates and water is pumped through the seals. Their dynamic behavior is measured by impacting the housing with a hammer and recording the input (force) and output signal (motion of the housing in relation to the shaft). A FFT-Analyser calculates the transfer function from which the dynamic coefficients are extracted.

Because of the large mass of the housing, which is moved during measurements, the inertia coefficients cannot be evaluated by this test rig.

Leakage

A first result for the seal geometries shown in fig. 2 is the leakage performance. Fig. 5 presents the dimensionless leakage coefficient c_L for the different seal geometries versus groove depth.

It is obvious that the smooth seal has the highest leakage. For increasing groove depths, the coefficient goes down in general. Only the rectangular groove shape shows an increasing leakage for larger depths. Overall, rectangular and sawshaped grooves show the best performance.

Dynamic Coefficients

The resulting seal coefficients for one operational point are given in fig. 6. They are compared with theoretical results coming from the two theories mentioned before. The inertia coefficients are not shown in this figure, because they could not be measured as mentioned before.

For all geometries the values for the direct stiffness term are influenced very much by the various groove depths; they decrease. Cross-coupled stiffnesses also decrease slightly, while cross-coupled damping stays nearly constant. Especially

for the rectangular groove shapes direct damping also goes down with increasing depths.

The comparison with the calculated data shows very good agreement for the finite difference theory in all parameters. Finite length theory predicts higher direct stiffness terms, but shows good agreement for the other coefficients.

The results for other operational points are qualitatively similar.

Discussion

Using the finite difference technique it is possible to calculate accurate dynamic seal coefficients for all seal geometries, but it is very time consuming, and so it is also of interest to find out the case in which the finite length method works satisfactorily.

Direct damping is calculated pretty well by finite length theory, but this may arise from the fact that measured friction factors have to be included in the calculation.

Also finite length theory shows reasonable results for rectangular groove shapes, but is very wrong for other geometries especially for the very important direct stiffness terms. This can be explained regarding the fluid flow in the seals calculated by finite difference technique (fig. 7). One can see a recirculation inside rectangular grooves which does not affect the main flow very much. So the bulk flow model, with an extended circumferential continuity equation can be applied successfully. For other groove geometries the main flow direction is very much influenced by the grooves, so that the bulk flow model is not applicable.

INFLUENCE OF EIGENVALUES

For real machines not the single dynamic coefficients are important but the resulting overall behavior, for example critical speed, damping and stability behavior. These data are given by the eigenvalues of a centrifugal pump which consist of eigenfrequencies and damping values.

In order to demonstrate the effect of different seal geometries on the rotordynamics of turbopumps, a simple rotor model is chosen. Fig. 8 shows a Jeffcott rotor as a model for a double suction feed pump.

The coefficients for the different seal geometries are applied to this model. The results at operational speed are shown in fig. 9. A smooth seal increases the first eigenfrequency of the dry shaft by 96% and all grooved seals have less stiffening effect, getting smaller with increasing groove depths. The best groove geometry to introduce stiffness to the system is the sawshaped groove. Values for modal damping are improving for grooved seals, but a general characteristic cannot be observed. It has to be pointed out that modal damping is determined by both the real and imaginary part of the eigenvalue. The real parts of the eigenvalues decrease for grooved seals (fig. 10).

In fig. 10 eigenvalues and unbalance responses are shown versus running speed for rectangular groove shapes. For a constant pressure drop versus speed, which is not realistic for a pump, eigenfrequencies don't change very much, damping slightly

decreases and the unbalance responses show no dramatic differences for various groove depths. The pressure drop in a real machine would be nearly proportional to running speed squared. In this case the eigenfrequencies and damping values increase with running speed. The unbalance responses for grooved seals are now much worse compared to plain seals.

Finally the calculated eigenvalues of a multistage boiler feed pump are shown using the data for grooved seals and plain seals respectively (fig. 11). With one exception all eigenfrequencies are increased using plain seals. The results for modal damping show no uniform characteristics.

So from the dynamic point of view it is hard to tell whether one should use plain or grooved seals. The special application has to be investigated.

CONCLUSIONS

The design of grooved seals for turbopumps reduces the leakage flow and so increases the efficiency.

The influence of these kinds of seals to the dynamic performance is investigated for different types of seals. Rotordynamic seal coefficients are evaluated experimentally and the results are compared to calculated ones coming from finite length theory and finite difference technique respectively. The latter gives the best results for all seal geometries, while finite length theory seems to be applicable for rectangular grooves only.

The influence to the eigenvalues of a simple pump model shows less stiffening effect of grooved seals compared to plain seals. Whether, from a dynamic point of view, grooved seals are better or worse compared to plain seals cannot be stated generally. An analysis of the special application seems to be necessary.

LITERATURE

1. W. DIEWALD, R. NORDMANN, "Dynamic Analysis of Centrifugal Pump Rotors with Fluid-Mechanical Interactions," 11th Biennial Conference on Mechanical Vibration and Noise, Boston, MA, September 27-30, 1987.
2. D.W. CHILDS, "Dynamic Analysis of Turbulent Annular Seals Based on Hirs' Lubrication Equation," Journal of Lubrication Technology, ASME-Paper No. 82 - Lub - 41, 1982.
3. D.W. CHILDS, "Finite-Length Solutions for Rotordynamic Coefficients of Turbulent Annular Seals," Journal of Lubrication Technology, ASME-Paper No. 82 - Lub - 42, 1982.
4. R. NORDMANN, "Rotordynamic Coefficients and Leakage Flow of Parallel Grooved Seals and Smooth Seals," the 4th Workshop on Rotordynamic Instability Problems in High Performance Turbomachinery, Texas A&M, June 2-4, 1986.

5. F.-J. DIETZEN, R. NORDMANN, "Calculating Rotordynamic Coefficients of Seals by Finite-Difference Techniques, the 4th Workshop on Rotordynamic Instability Problems in High Performance Turbomachinery, Texas A&M University, June 2-4, 1986.
6. R. NORDMANN, H. MASSMANN, "Identification of Stiffness, Damping and Mass Coefficients for Annular Seals," Vibrations in Rotating Machinery, IMechE, York, 1984.

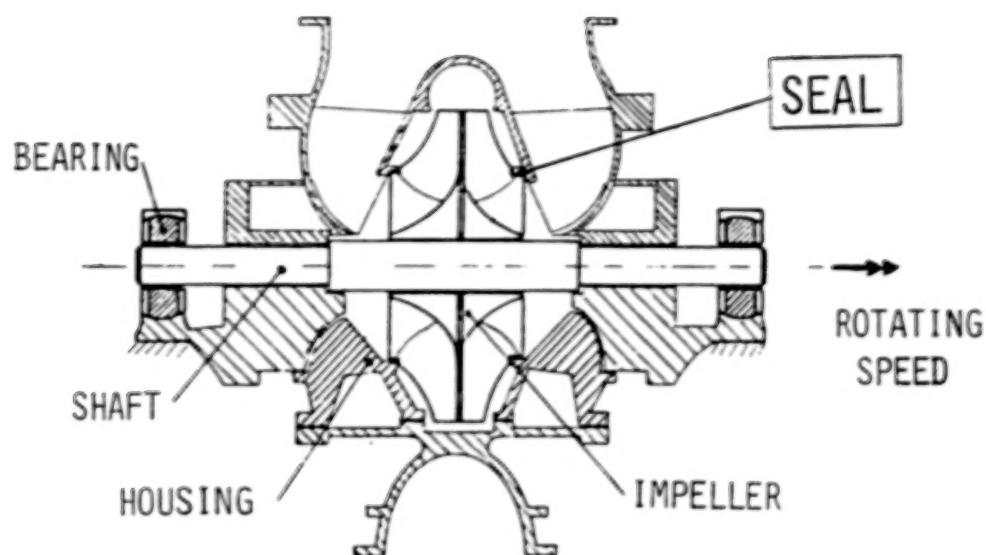


FIGURE 1: Cross section of a turbopump

smooth seal	rectangular grooves	saw shaped grooves	triangular grooves	
<p> $L = 23.5 \text{ mm}$ $R = 23.5 \text{ mm}$ $C = 200 \text{ } \mu\text{m}$ </p>				$H = 0.5 C$
				$H = 1.5 C$
				$H = 2.5 C$

FIGURE 2: Seals with different groove shapes and depths

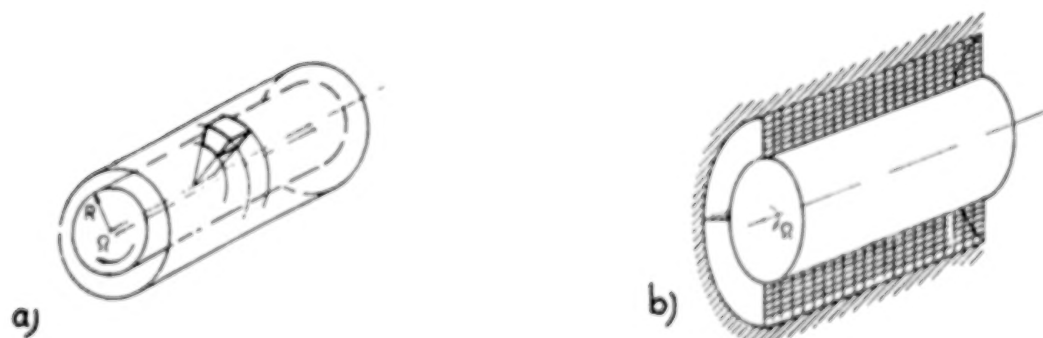


FIGURE 3: Models for a) finite length and b) finite difference theory

BEST COPY AVAILABLE

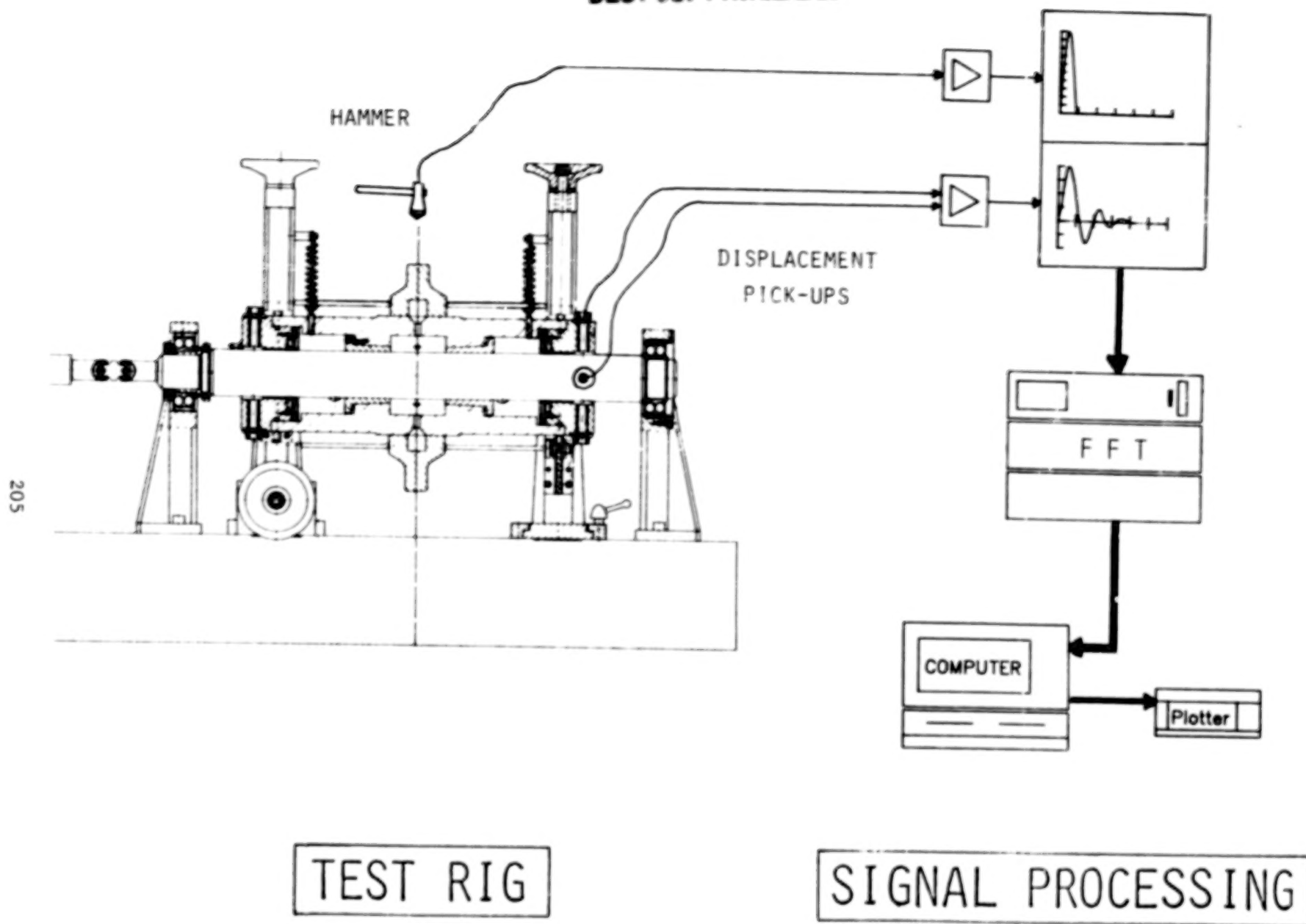


FIGURE 4: Test rig and signal processing

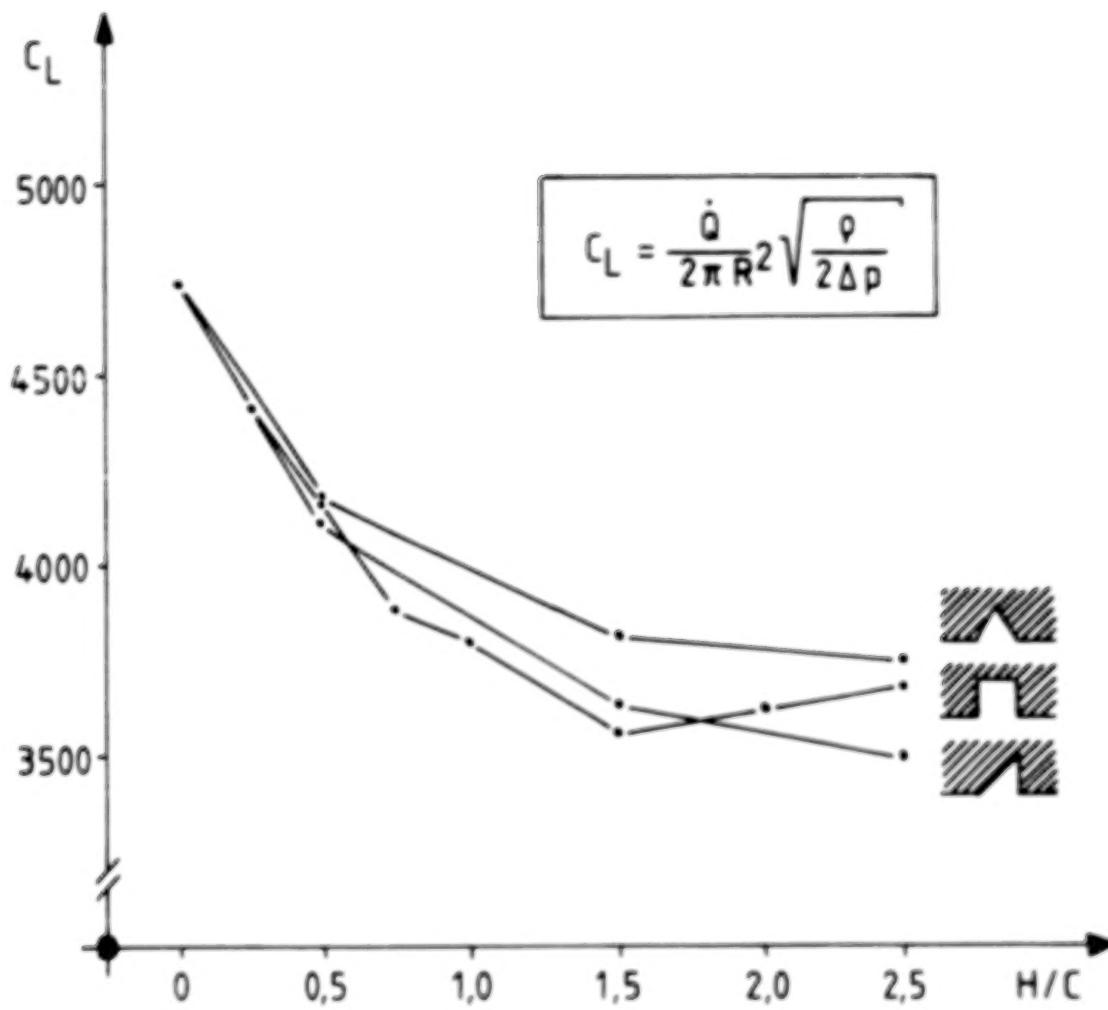


FIGURE 5: Leakage coefficients for different seal geometries versus groove depths

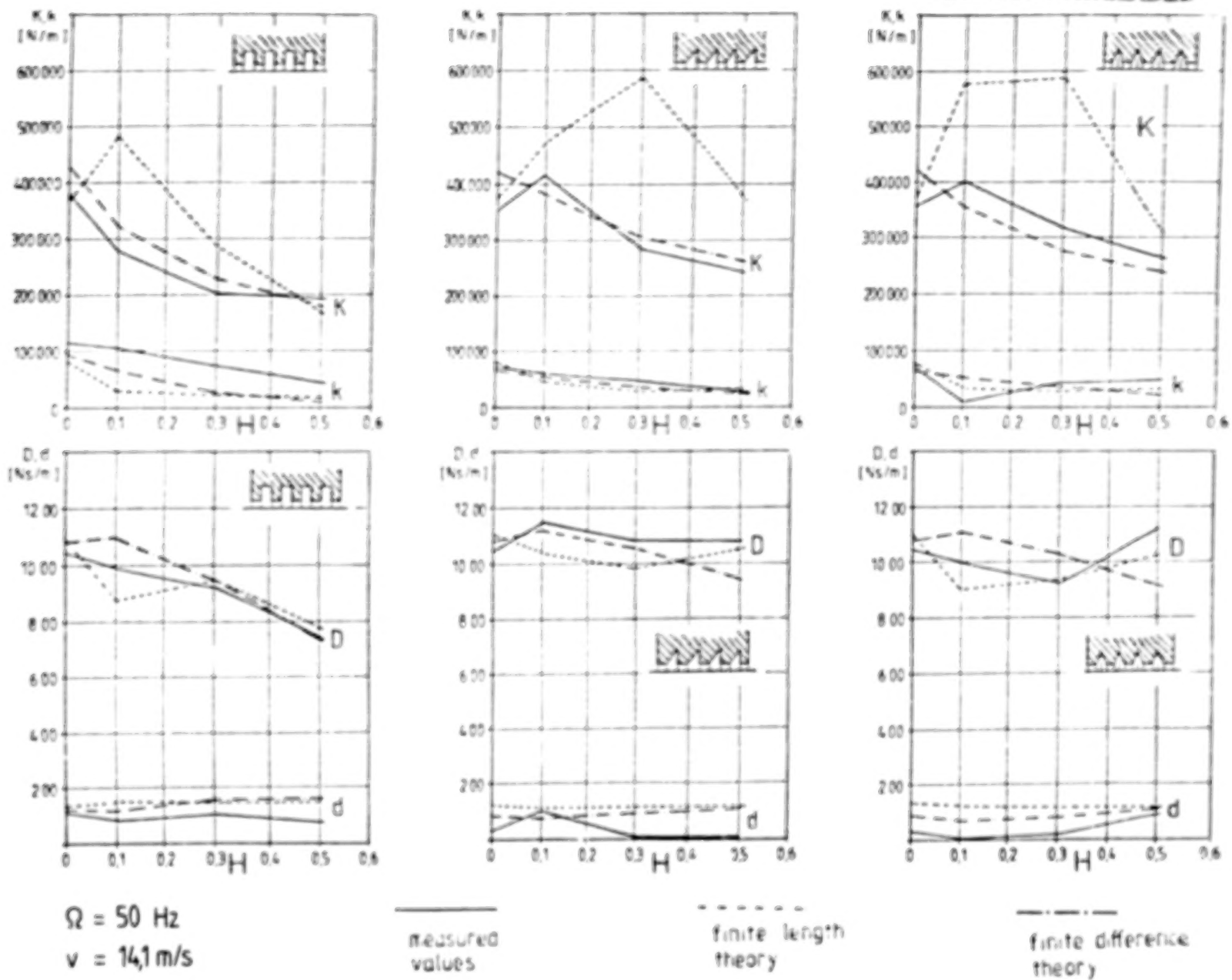


FIGURE 6: Dynamic stiffness (K,k) and damping (D,d) coefficients for different seal geometries and groove depths (H)

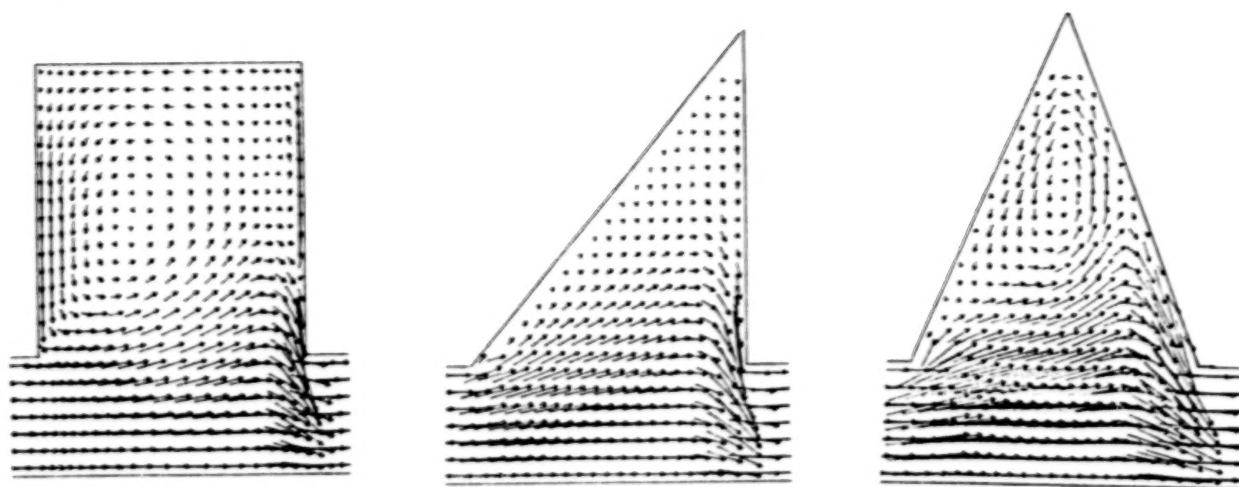


FIGURE 7: Flow fields for different groove shapes

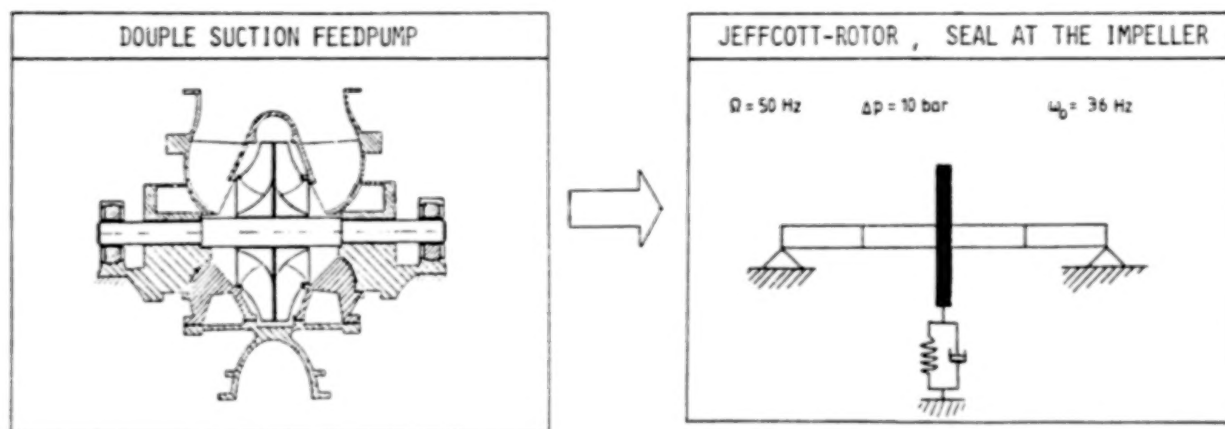


FIGURE 8: Simple model of a double suction feed pump

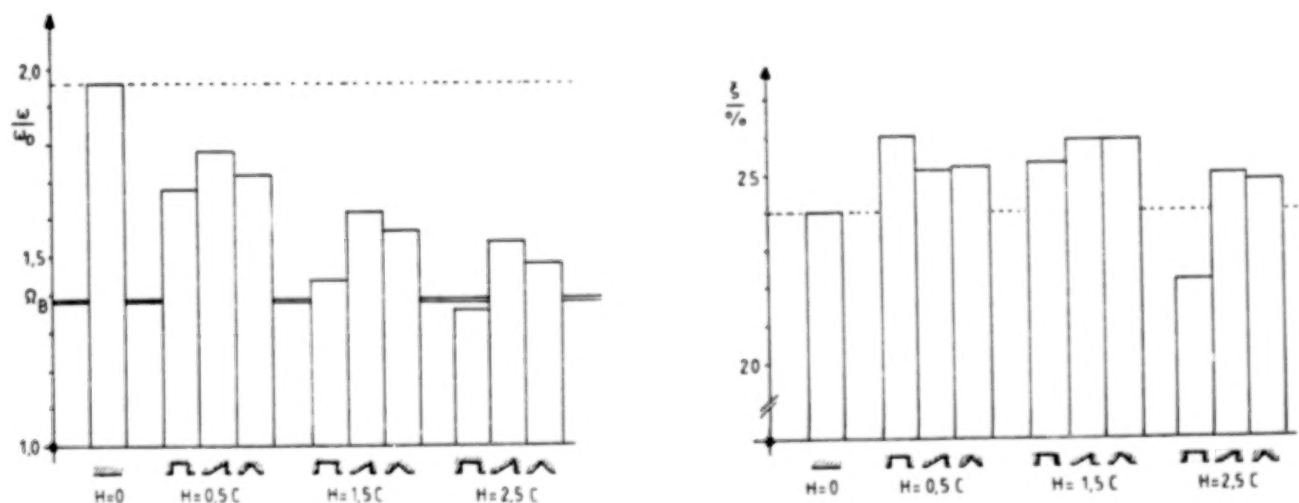


FIGURE 9: Eigenvalues of the pump model versus groove depths at operational speed for different seal geometries

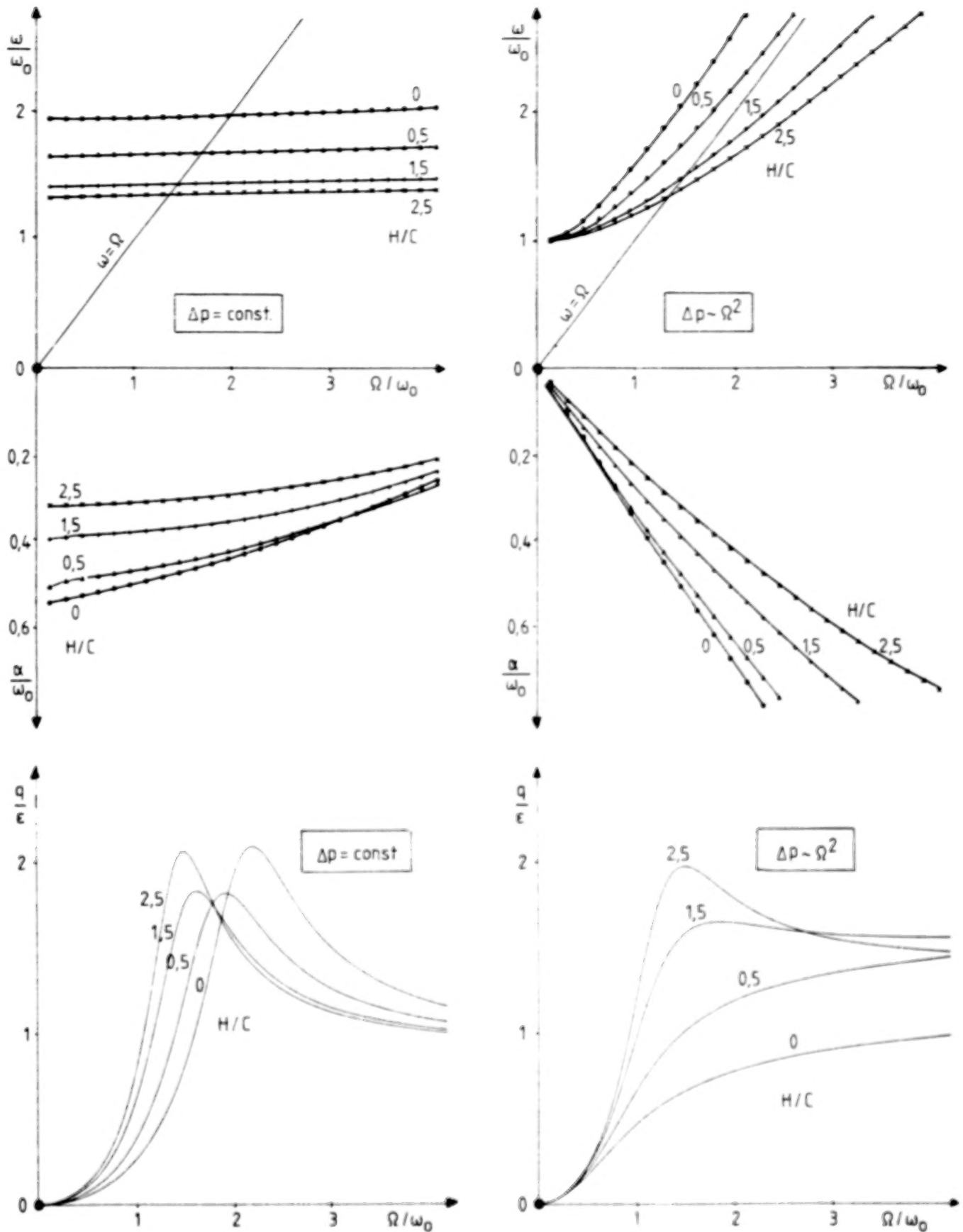


FIGURE 10: Eigenvalues and unbalance responses for rectangular groove shapes

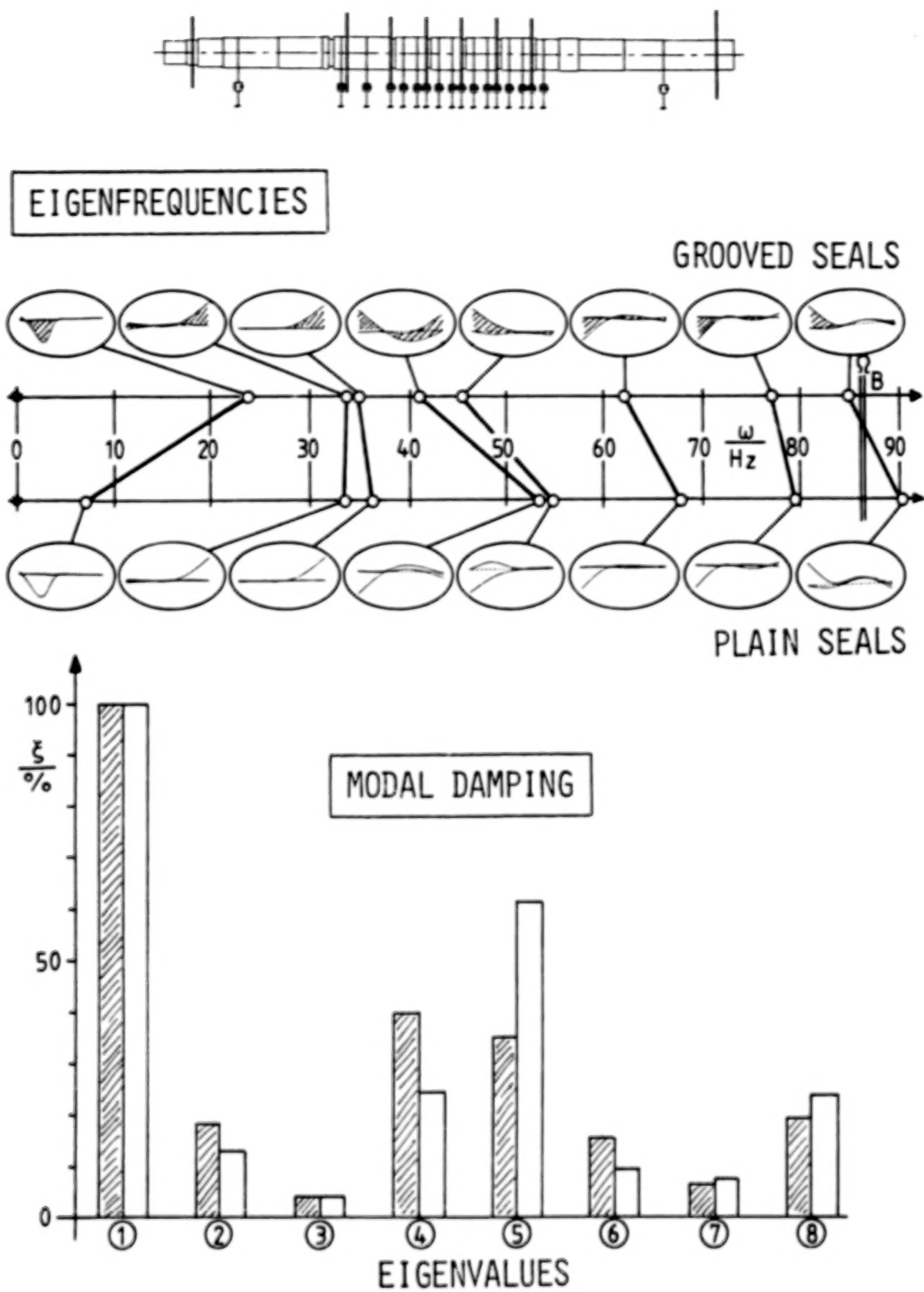


FIGURE 11: Eigenvalues of a multistage boiler feedpump

A 3-DIMENSIONAL FINITE-DIFFERENCE METHOD FOR CALCULATING

THE DYNAMIC COEFFICIENTS OF SEALS

F.J. Dietzen and R. Nordmann
Department of Mechanical Engineering
University of Kaiserslautern
Kaiserslautern, Federal Republic of Germany

This paper presents a method to calculate the dynamic coefficients of seals with arbitrary geometry. To describe the turbulent flow the Navier-Stokes equations are used in conjunction with the k - ϵ turbulence model. These equations are solved by a full 3-dimensional finite-difference procedure instead of the normally used perturbation analysis. The time dependence of the equations is introduced by working with a coordinate system rotating with the precession frequency of the shaft. The results of this theory are compared with coefficients calculated by a perturbation analysis and with experimental results.

INTRODUCTION

During the last years it has become evident that it is important to include the fluid forces caused by seals when predicting the dynamic behavior of turbopumps. To calculate these forces and the dynamic coefficients which are normally used to describe them (eq. 1)

$$-\begin{bmatrix} F_z \\ F_y \end{bmatrix} = \begin{bmatrix} K & +k \\ -k & K \end{bmatrix} \begin{bmatrix} z \\ y \end{bmatrix} + \begin{bmatrix} D & d \\ -d & D \end{bmatrix} \begin{bmatrix} \dot{z} \\ \dot{y} \end{bmatrix} + \begin{bmatrix} M & m \\ -m & M \end{bmatrix} \begin{bmatrix} \ddot{z} \\ \ddot{y} \end{bmatrix}$$

several methods which are based either on the so-called "bulk-flow" theories /1,2/ or directly on the Navier-Stokes equations /3,4/ have been published. A common feature of these methods, developed for straight pump seals /1/ straight gas seals /2,4/ or grooved seals /3/, is that they are all based on a perturbation analysis to determine the dynamic coefficients. But the perturbation analysis requires many assumptions, e.g.

1. It is assumed that the shaft moves on small orbits around the centric position, so that a perturbation analysis can be used for all flow variables

$$\phi = \phi_0 + e\phi_1 + e^2\phi_2 + \dots$$

and all terms with power of e greater than one can be neglected in the equations without loss of accuracy (e = perturbation parameter).

2. The change of the perturbation flow variables in the circumferential direction can be described by sine and cosine functions.

$$\phi_1 = \phi_{1c} \cos\theta + \phi_{1s} \sin\theta$$

3. The change in time can be described by

$$\phi_1 = \phi_1 e^{i\Omega t}$$

because the shaft moves on a circular orbit.

To check how these assumptions effect the results we have developed a 3-dimensional finite-difference procedure to calculate the dynamic coefficients. The only assumptions in this theory are that the turbulence can be described by the k- ϵ turbulence model and that the shaft moves on circular orbits around the seal center.

GOVERNING EQUATIONS

To describe the turbulent flow in a seal we have the Navier-Stokes equations and the continuity equation. The turbulent stresses occurring in the fluid can be handled like laminar stresses by introducing a turbulent viscosity. The turbulent and the laminar viscosity are then summed up to an effective viscosity μ_e

$$\mu_e = \mu_l + \mu_t$$

To describe μ_t the k- ϵ turbulence model /5,6/ is used because it is simple and often used to calculate the turbulent flow in seals /7,8,9,10/.

$$\mu_t = C_\mu \rho \frac{k^2}{\epsilon}$$

All these equations can be represented in the following form

$$\rho \frac{\partial \phi}{\partial t} + \frac{\partial}{\partial x}(\rho u \phi) - \frac{\partial}{\partial x}(\Gamma_\phi \frac{\partial \phi}{\partial x}) + \frac{1}{r} \frac{\partial}{\partial r}(r \rho v \phi) - \frac{1}{r} \frac{\partial}{\partial r}(r \Gamma_\phi \frac{\partial \phi}{\partial r}) + \frac{1}{r} \frac{\partial}{\partial \theta}(\rho w \phi) - \frac{1}{r} \frac{\partial}{\partial \theta}(\Gamma_\phi \frac{\partial \phi}{\partial \theta}) = S_\phi$$

ϕ	Γ_ϕ	S_ϕ
u	μ_e	$-\frac{\partial p}{\partial x} + \frac{\partial}{\partial x}(\mu_e \frac{\partial u}{\partial x}) + \frac{1}{r} \frac{\partial}{\partial r}(r \mu_e \frac{\partial v}{\partial x}) + \frac{1}{r} \frac{\partial}{\partial \theta}(\mu_e \frac{\partial w}{\partial x})$
v	μ_e	$-\frac{\partial p}{\partial r} + \frac{\partial}{\partial x}(\mu_e \frac{\partial u}{\partial r}) + \frac{1}{r} \frac{\partial}{\partial r}(r \mu_e \frac{\partial v}{\partial r})$ $+ \frac{1}{r} \frac{\partial}{\partial \theta}(r \mu_e \frac{\partial}{\partial r}(\frac{w}{r})) - \frac{2}{r^2} \mu_e \frac{\partial w}{\partial \theta} - \frac{2}{r^2} \mu_e v + \frac{\rho}{r} w^2$
w	μ_e	$-\frac{1}{r} \frac{\partial p}{\partial \theta} + \frac{\partial}{\partial x}(\frac{1}{r} \mu_e \frac{\partial u}{\partial \theta}) + \frac{1}{r} \frac{\partial}{\partial r}(\mu_e \frac{\partial v}{\partial \theta}) + \frac{1}{r} \frac{\partial}{\partial \theta}(\frac{1}{r} \mu_e \frac{\partial w}{\partial \theta})$ $+ \frac{1}{r^2} \mu_e \frac{\partial v}{\partial \theta} - \frac{w}{r^2} \frac{\partial}{\partial r}(r \mu_e) + \frac{1}{r} \frac{\partial}{\partial \theta}(\frac{2}{r} \mu_e v) - \frac{\rho}{r} vw$
1	0	0
k	μ_e / σ_k	$G - \rho \epsilon$
ϵ	μ_e / σ_ϵ	$C_1 \frac{\epsilon}{k} G - C_2 \rho \frac{\epsilon^2}{k}$

Table 1: Source terms of the Navier-Stokes equations, the continuity equation and the equations of the k- ϵ model.

(constants of k- ϵ model are given in Appendix A)

To determine the dynamic coefficients we assume that the shaft moves on a circular orbit with precession frequency Ω around the seal center. Since this would normally result in a time dependent problem we introduce a rotating coordinate system which is fixed at the shaft center (Fig. 1). In this system the flow is stationary. Due to the rotating coordinate system centrifugal- and coriolis-forces occur in the equations for the radial and circumferential momentum [11], which are taken into consideration by a modification of the source terms.

$$S_v^i = S_v + \Omega^2 r + 2\Omega w$$

$$S_w^i = S_w - 2\Omega v$$

So the final form of the equations is given if S_v and S_w in Table 1 are replaced by S_v^i and S_w^i .

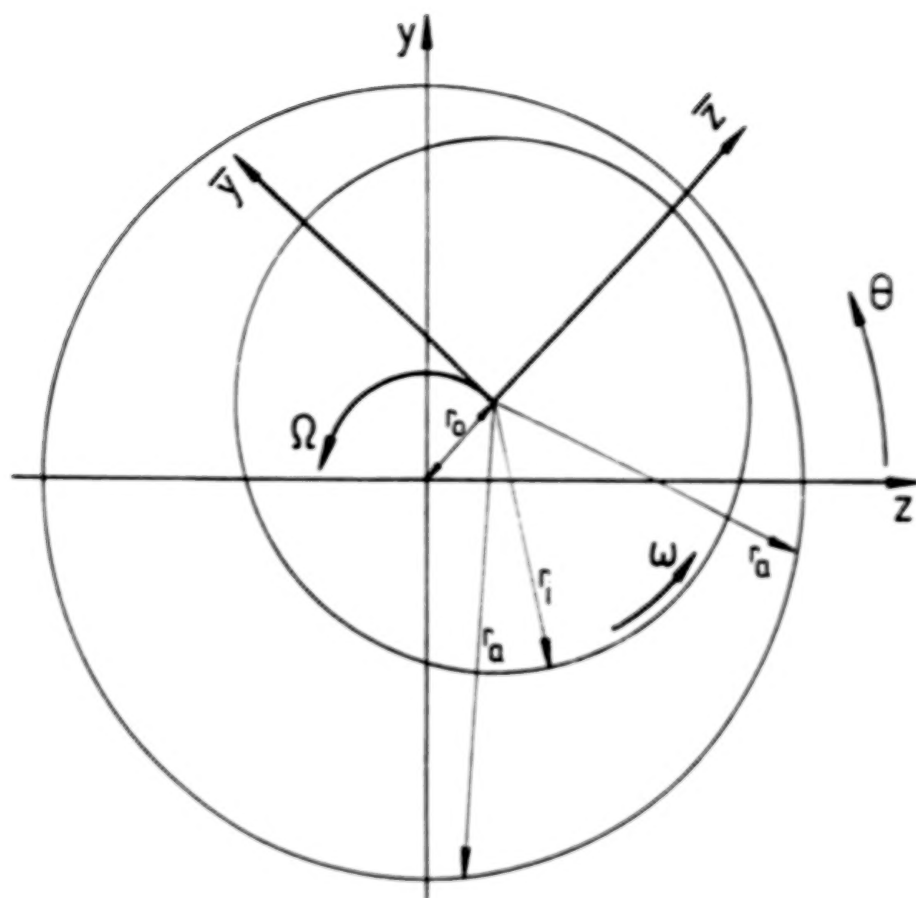


Fig. 1: Rotating coordinate system

BOUNDARY CONDITIONS

The above given equations are solved in conjunction with the following boundary conditions (Fig. 2)

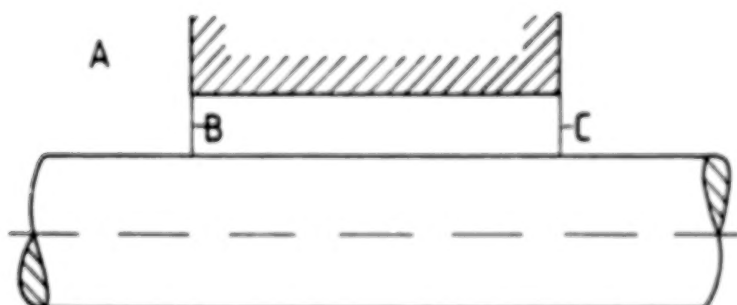


Fig. 2: Locations where the boundary-conditions must be specified

$$\begin{aligned}
 \text{Entrance: } & p_{B(\theta)} + \frac{1}{2} \rho \bar{u}_{B(\theta)}^2 (1+\xi) = p_A \\
 \text{Exit : } & p_{C(\theta)} = 0 \\
 \text{Stator : } & u = 0 \quad v = 0 \quad w = -\Omega r \\
 \text{Rotor : } & u = 0 \quad v = 0 \quad w = (\omega - \Omega) r
 \end{aligned}$$

\bar{u}_B is the average axial entrance velocity specified for every grid-plane.

For k and ϵ the standard conditions of the k - ϵ model /5,6/ are used at the walls.

FINITE-DIFFERENCE-PROCEDURE

This system of equations with the corresponding boundary conditions is solved by a 3-dimensional finite-difference procedure, based on the method published by Gosman and Pun /12/. The seal is discretized by a grid (Fig. 3) and the variables are calculated at the nodes. To determine the pressure we use the PISO /13/ algorithm instead of SIMPLE /14/.

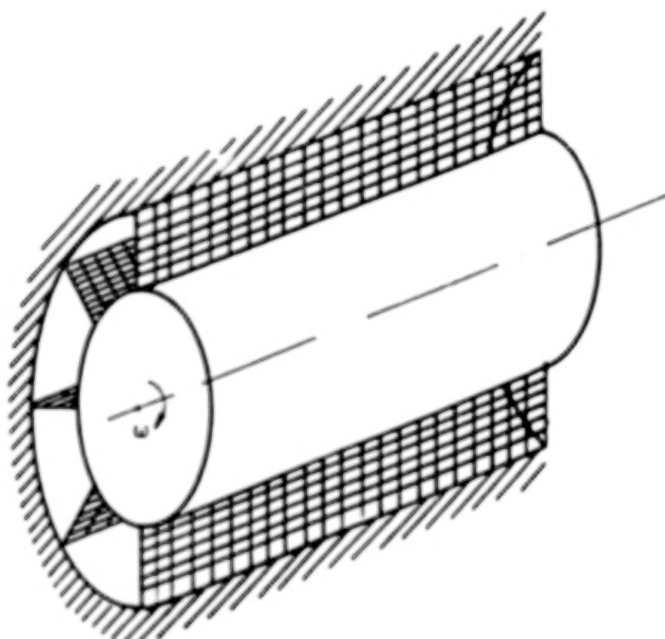


Fig. 3: Mesh arrangement in the seal

DYNAMIC COEFFICIENTS

As result of our solution procedure we get the pressure distribution in the seal and by a pressure integration in axial and circumferential direction, the forces. To simplify the integration we consider the case when the rotating coordinate system \bar{y} , \bar{z} coincides with the stationary system y , z .

$$F_z = - \int_0^L \int_0^{2\pi} p \cos \theta r_1 d\theta dx$$

$$F_y = - \int_0^L \int_0^{2\pi} p \sin \theta r_1 d\theta dx$$

When calculating the forces for 3 precession frequencies $\Omega = 0\omega$, $\Omega = 1\omega$ and $\Omega = 2\omega$ we can determine the dynamic coefficients. To save computation time we calculate k , ϵ and μ_t only for $\Omega = 0$ and keep it constant then for $\Omega = 1\omega$ and $\Omega = 2\omega$.

RESULTS

1. Example

First we compare the results of the 3-dimensional theory with those of a method, based on a perturbation analysis in the Navier-Stokes equations and in addition with experimental values.

For a straight seal with the following data the results are shown in Fig. 5.

$$L = 23.5 \text{ mm}$$

$$r_1 = 23.5 \text{ mm}$$

$$C_0 = 0.2 \text{ mm}$$

$$\bar{w}(0,0,2000 \text{ RPM})/r_1\omega = 0.13$$

$$\bar{w}(0,0,4000 \text{ RPM})/r_1\omega = 0.17$$

$$\bar{w}(0,0,6000 \text{ RPM})/r_1\omega = 0.19$$

$$\mu_1 = 0.7 \cdot 10^{-3} \text{ Ns/m}^3$$

$$\rho = 996.0 \text{ kg/m}^3$$

$$\bar{u} = 16.46 \text{ m/s}$$

$$\xi(2000 \text{ RPM}) = 0.35$$

$$\xi(4000 \text{ RPM}) = 0.37$$

$$\xi(6000 \text{ RPM}) = 0.38$$

2. Example

For a grooved seal (Fig. 4) the dynamic coefficients are shown as a function of the groove depth H_R (Fig. 6,7).

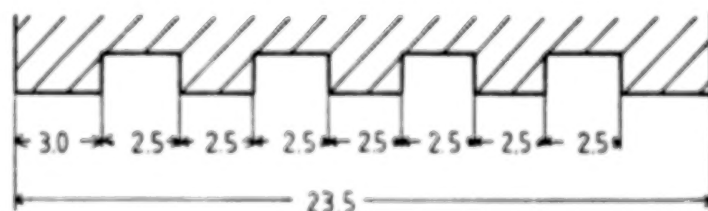


Fig. 4: Geometry of grooved seals

The seal data are

$L = 23.5 \text{ mm}$	$\mu_1 = 0.7 \times 10^{-3} \text{ Ns/m}^3$
$r_i = 23.5 \text{ mm}$	$\rho = 996.0 \text{ kg/m}^3$
$C_o = 0.2 \text{ mm}$	
$w(0, \theta, \bar{u} = 14.11 \text{ m/s})/r_i \omega = 0.20$	$\xi(14.11 \text{ m/s}) = 0.38$
$w(0, \theta, \bar{u} = 11.76 \text{ m/s})/r_i \omega = 0.22$	$\xi(11.76 \text{ m/s}) = 0.39$

In Fig. (8,9) the grid, the axial and radial velocity, the circumferential velocity and the pressure are shown for a groove depth of 0.5 mm and an average axial velocity of $\bar{u} = 14.11 \text{ m/s}$.

3. Example

In some further calculations we have investigated the influence of grooves on the rotor and stator for the seal shown in Fig. 10.

The seal data are

$L = 35.0 \text{ mm}$	$\mu_1 = 0.7 \times 10^{-3} \text{ Ns/m}^3$
$r_i = 23.7 \text{ mm}$	$\rho = 996.0 \text{ kg/m}^3$
$C_o = 0.2 \text{ mm}$	$n = 4000 \text{ RPM}$
$\xi = 0.5$	$\bar{w}(0, \theta) = 0.5 \times r_i \omega$
groove depth on rotor and stator :	0.4 mm
total pressure loss :	0.8 Mpa
radius of shaft orbit :	$r_o = C_o/40$

In Fig. 10 the total stiffness coefficients of the seal, and the portions developed in each part of the seal are shown.

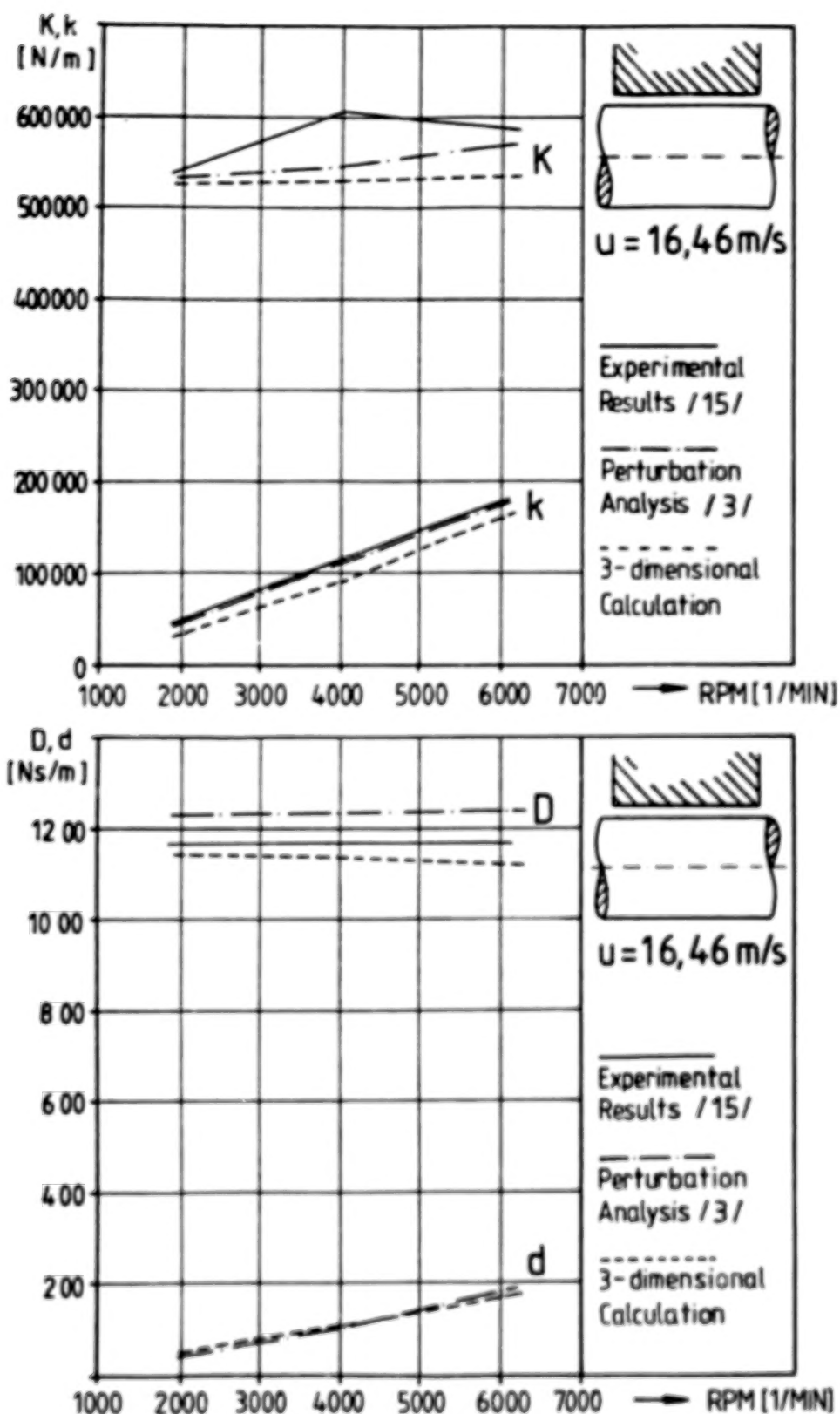


Fig. 5: Comparison of the dynamic coefficients for a straight seal.

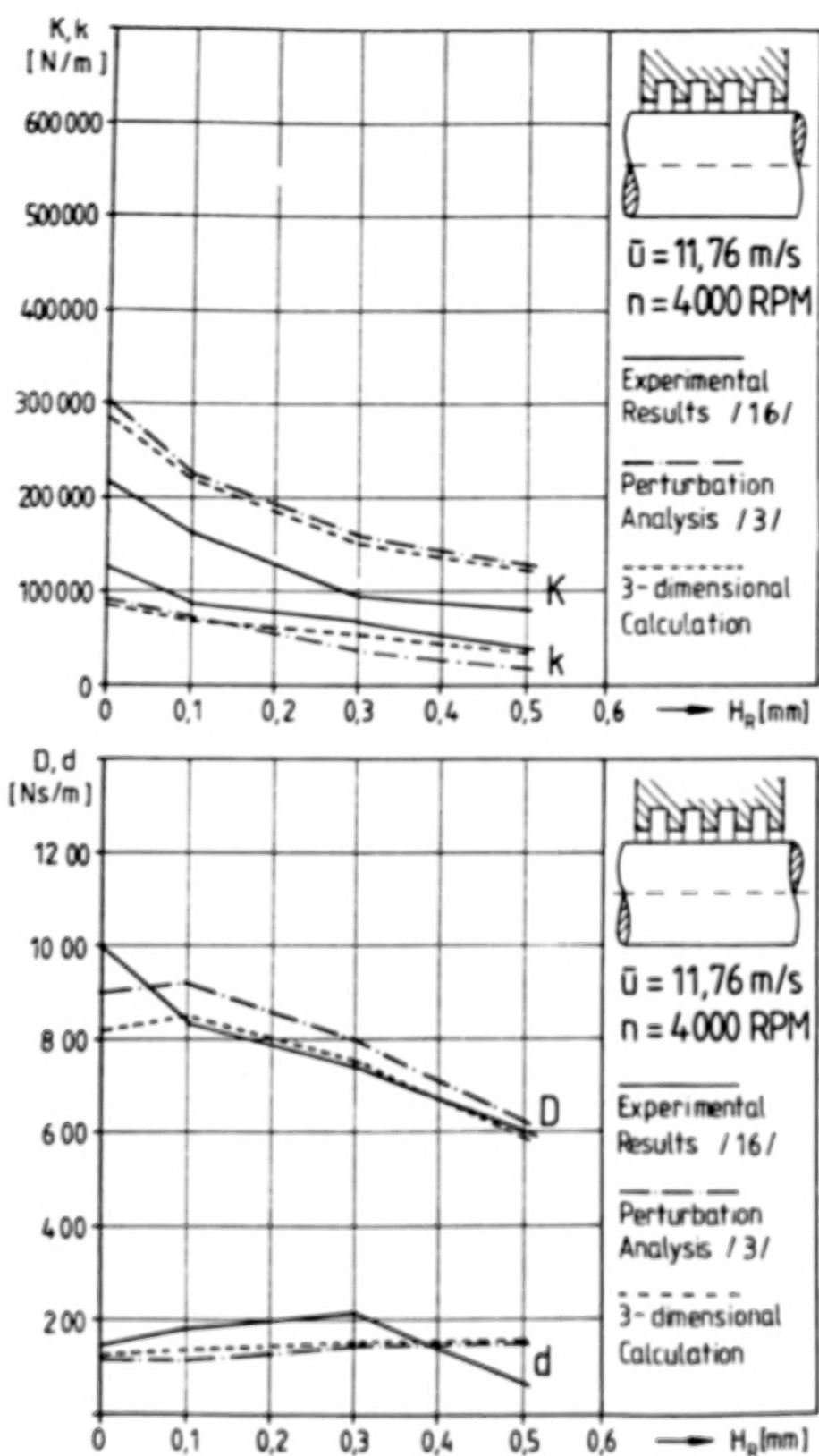


Fig. 6: Comparison of the dynamic coefficients for grooved seals.

BEST COPY AVAILABLE

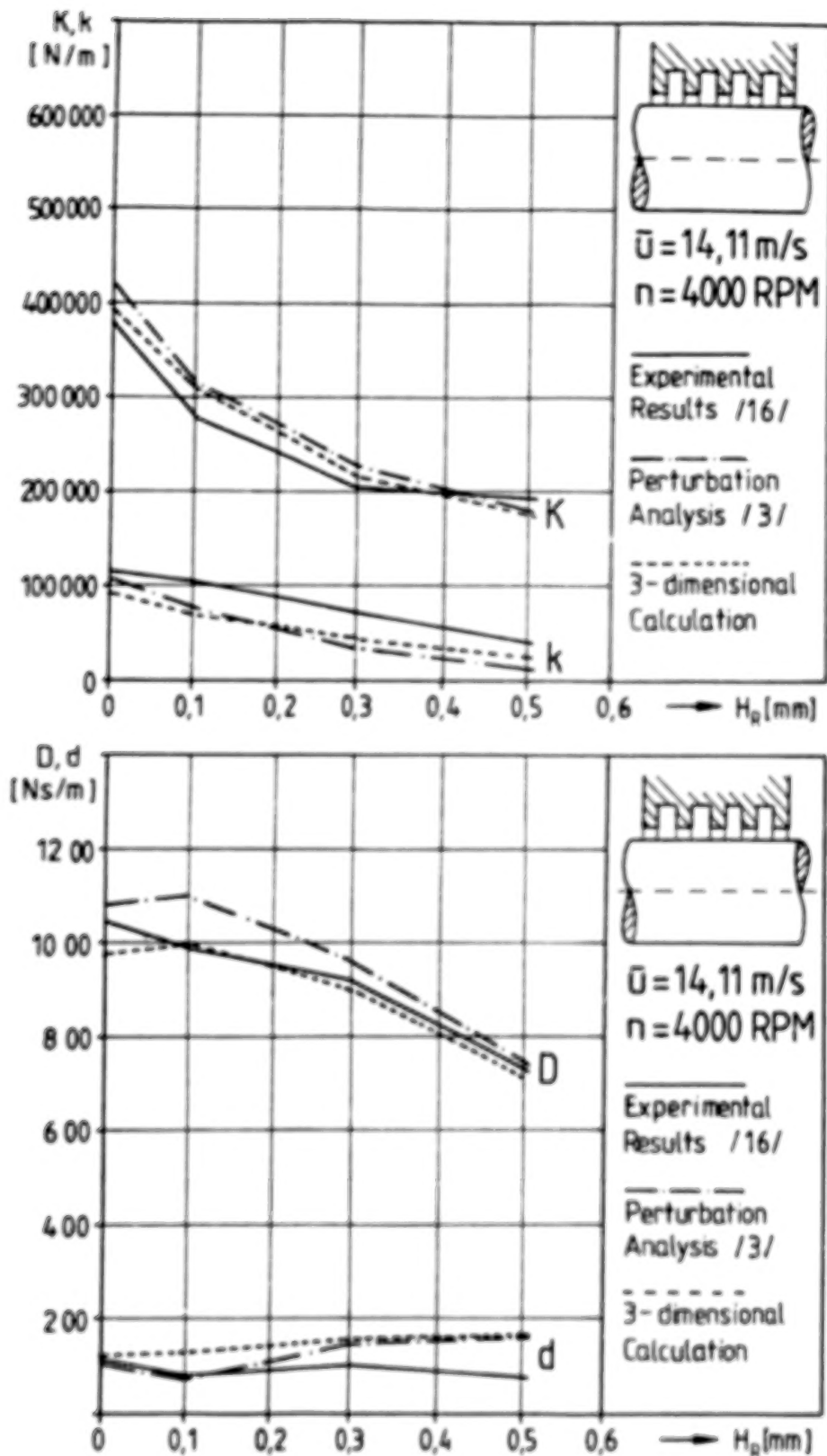


Fig. 7: Comparison of the dynamic coefficients for grooved seals.

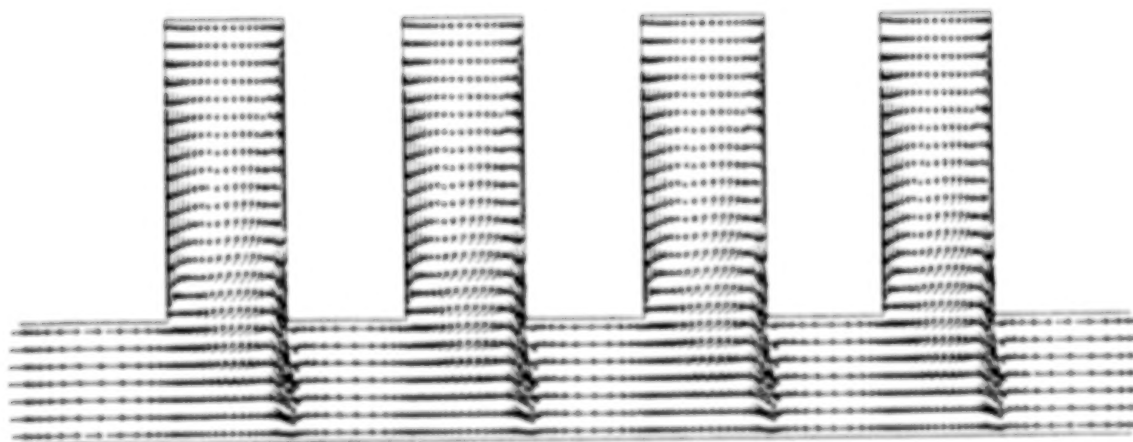
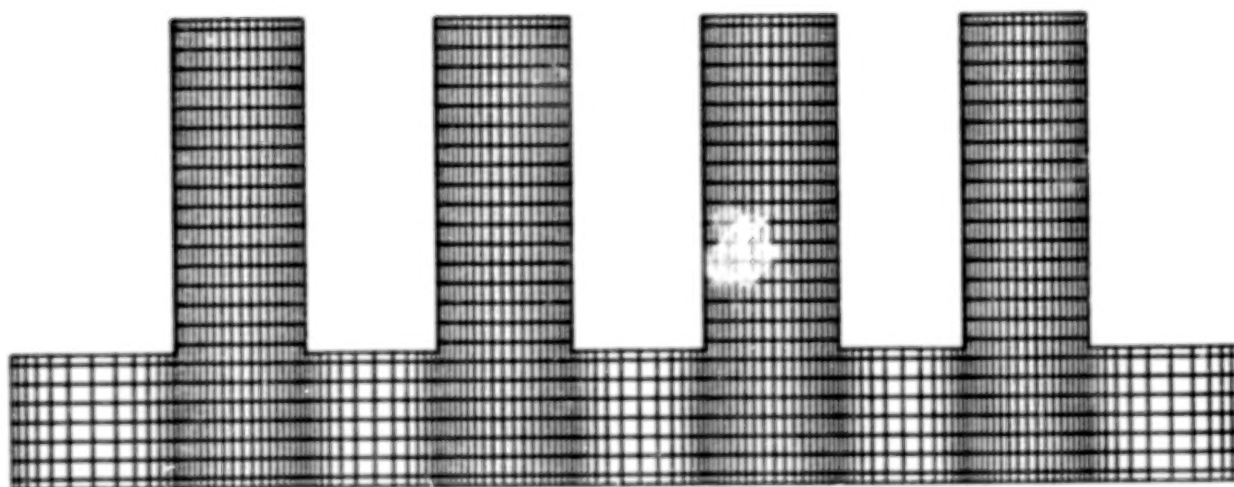


Fig. 8: Grid and axial and radial velocity for a grooved seal

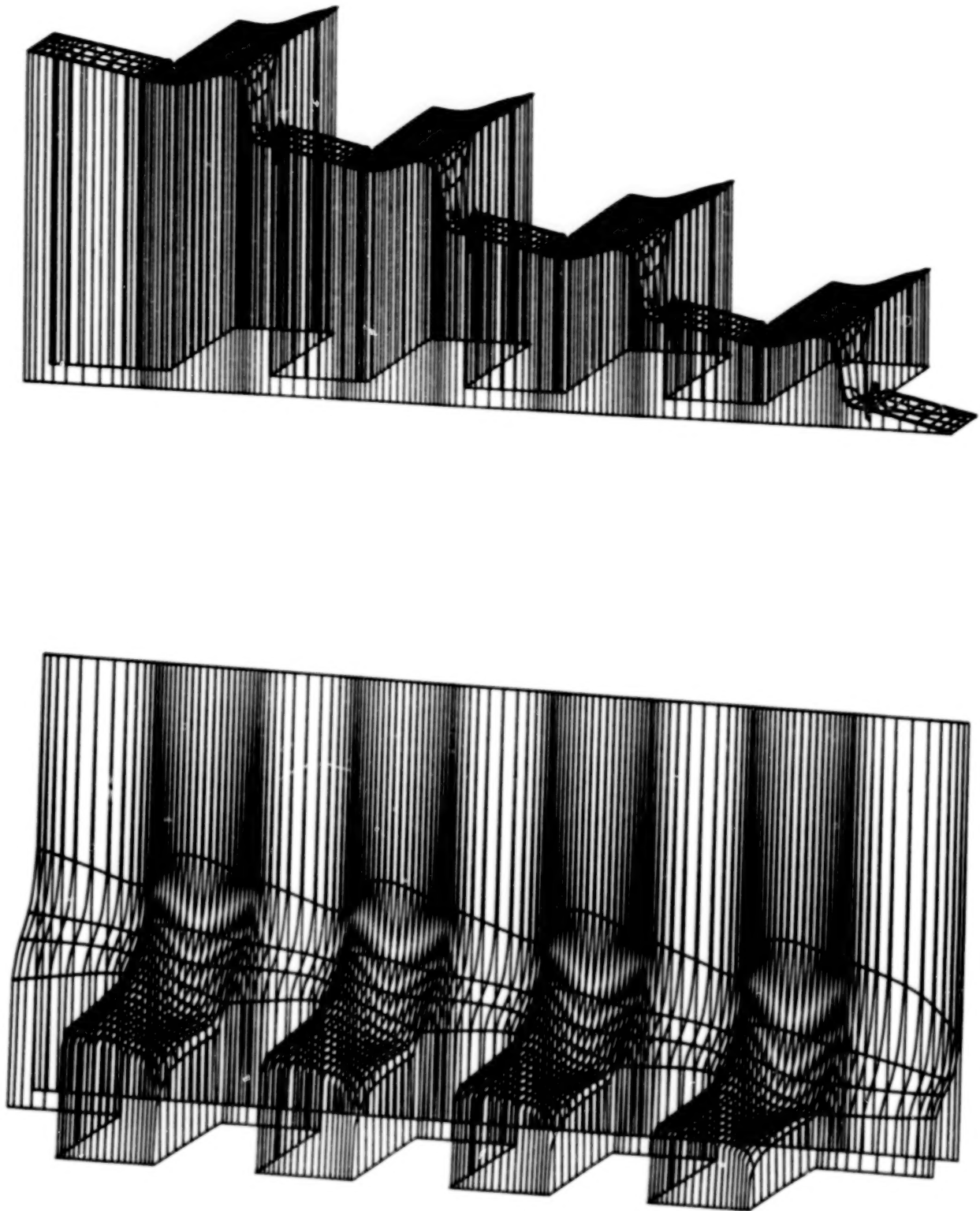


Fig. 9: Pressure distribution and circumferential velocity for a grooved seal.

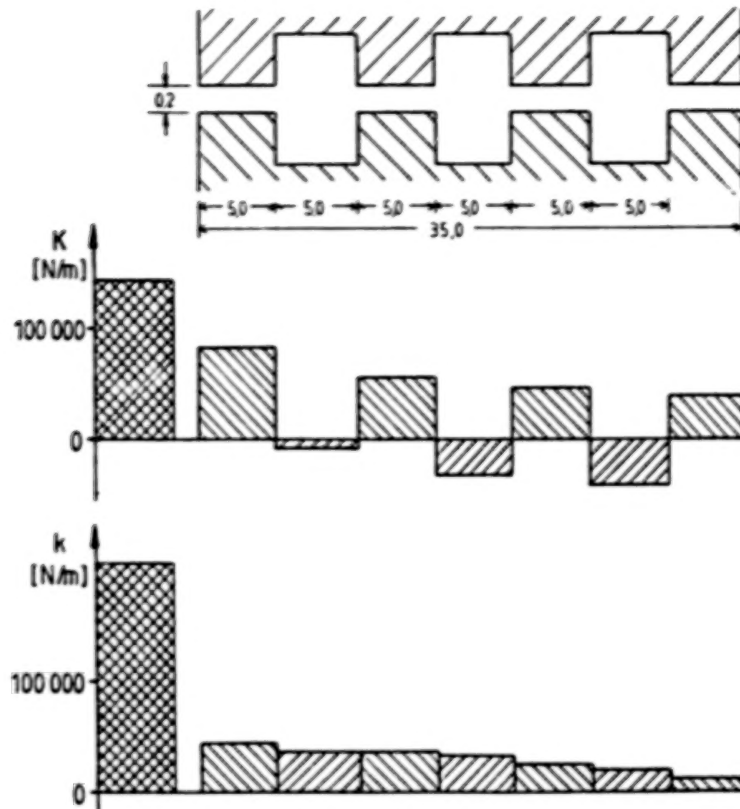


Fig. 10: Stiffness coefficients for a seal with grooves on rotor and stator

From that diagram we can draw the following interesting conclusions:

1. Although the pressure loss for a centric shaft position has the same magnitude for every land part, these lands develop different contributions to the total coefficients.
2. Although the clearance in the chambers is 5-times greater than in the land parts, the forces in the chambers can't be neglected.
3. The chambers have a strong destabilizing effect, because they cause positive radial forces and big positive tangential forces. (positive forces have the direction of the z-y axes in Fig. 1)

4. Example

We made further test calculations for the seal arrangement shown in Fig. 11. The seal data for this example are

$$\mu_1 = 0.7e^{-3} \text{ Ns/m}^2$$

$$\xi = 0.5$$

$$\rho = 1000 \text{ kg/m}^3$$

$$\bar{w}(0, \theta)/r_1 \omega = 0.5$$

$$\begin{aligned} \text{total pressure loss} & : 0.347 \text{ Mpa} \\ \text{Radius of shaft orbit} & : r_o = C_o/40 \end{aligned}$$

$$n = 2000 \text{ RPM}$$

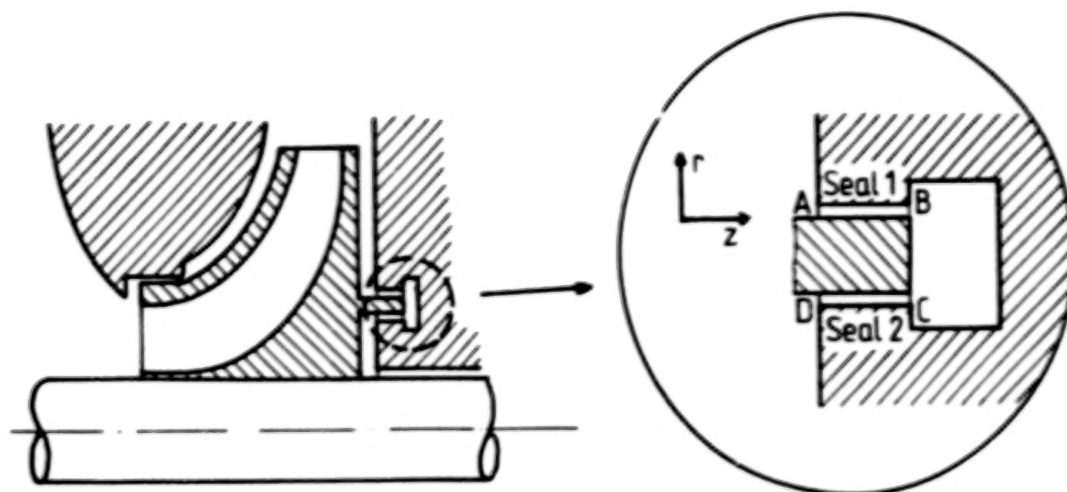


Fig. 11: Geometry of a reversing chamber

In Fig. 12 the flowfield in this seal is shown.

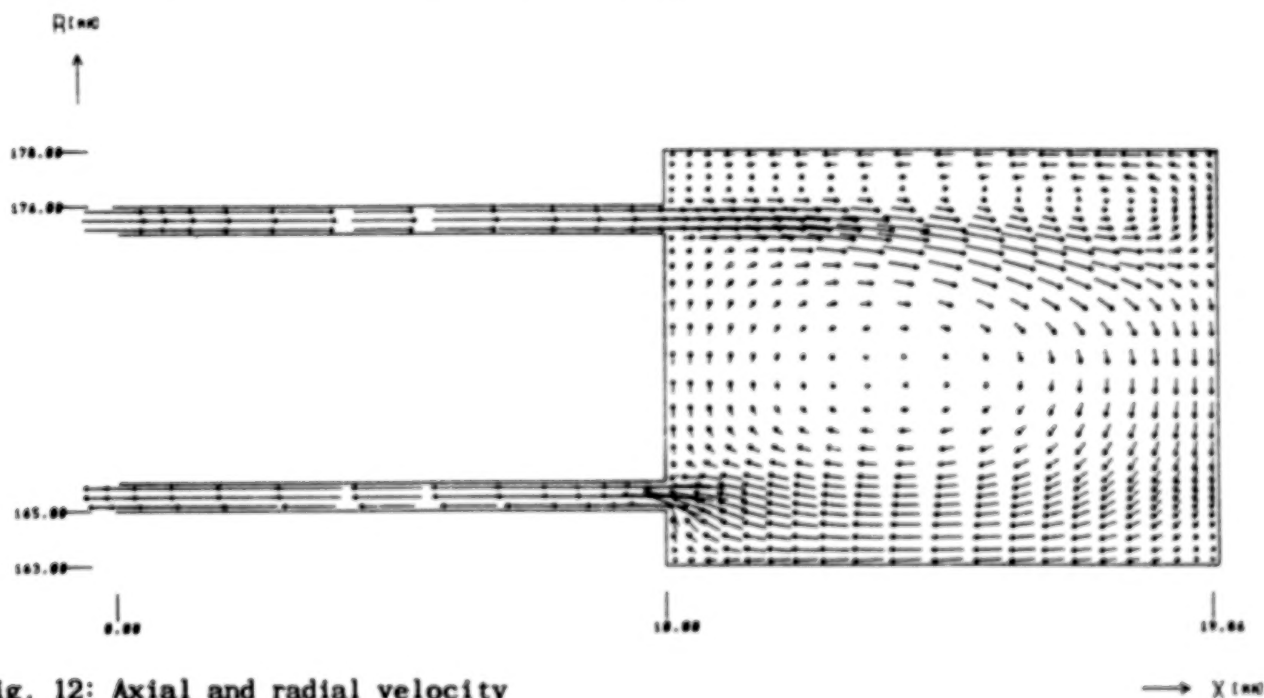


Fig. 12: Axial and radial velocity

As a result the following stiffness coefficients for seal 1 and seal 2 (Fig. 11) are obtained.

	K [N/m]	k [N/m]
Seal 1	$-0.128 \text{ e}7$	$-0.133 \text{ e}6$
Seal 2	$-0.921 \text{ e}5$	$-0.853 \text{ e}5$

The result is surprising, because seal 1 yields a negative direct stiffness instead of the expected positive. This can be explained if one looks at the pressure loss in the seal arrangement.

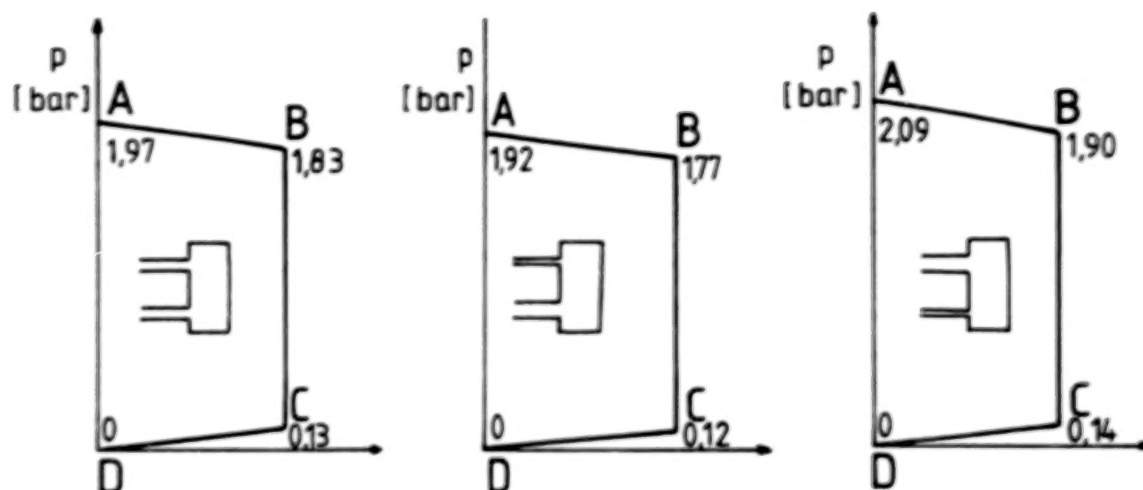


Fig. 13: Pressure loss for centric shaft position

Pressure loss in the plane with nearest gap in seal 1

Pressure loss in the plane with widest gap in seal 1

The main pressure loss is caused by the entrance loss of the flow from the chamber into seal 2 (Fig. 13). If now, the rotating part moves in the r -direction the increase of the clearance of seal 2 (in the plane considered) results in a sharp drop in the pressure loss B-C. And this drop in the pressure loss and the rise in the opposite plane is responsible for the negative value of k in seal 1.

CONCLUSIONS

The first two examples show that the perturbation analysis yields good results in comparison with the 3-dimensional theory although it requires only a fraction of the calculation time and storage needed for that method. On the other hand it is only possible to determine the coefficients of look-through seals with the perturbation analysis, while there are no restrictions concerning the geometry for the 3-dimensional procedure.

Example 3 and 4 clearly demonstrate that in an arrangement of several seals, the separated consideration of the single seals, even with big chambers between them, may lead to totally wrong results.

NOMENCLATURE

F_z, F_y	Forces on the shaft in z and y direction
K, k	direct and cross-coupling stiffness
D, d	direct and cross-coupled damping
M, m	direct and cross-coupling inertia
u, v, w	axial, radial and circumferential velocity
p	pressure
k	turbulence energy
ϵ	energy dissipation
μ_e, μ_l, μ_t	effective, laminar and turbulent viscosity
ρ	density
t	time
x, r, θ	axial, radial and circumferential coordinate
G	production term in k- ϵ -model
$\sigma_k, \sigma_\epsilon$	Constants of the k- ϵ -model
C_μ, C_1, C_2	Constants of the k- ϵ -model
ϕ	general variable standing for u, v, w, p, k, ϵ
S_ϕ	general source term
C_o	seal clearance
r_o	radius of the precession motion of the shaft
$e = r_o/C_o$	perturbation parameter
ω	rotational frequency of the shaft
Ω	precession frequency of the shaft
f	entrance lost-coefficient
L	Length of the seal
r_1	radius of the rotor (shaft)
r_a	radius of the stator

APPENDIX A: Constants and production term of the k- ϵ model

$$C_\mu = 0.09 \quad C_1 = 1.44 \quad C_2 = 1.92 \quad \sigma_k = 1.0 \quad \sigma_\epsilon = 1.3$$

$$G = \mu_e \left[2 \left(\left(\frac{\partial v}{\partial r} \right)^2 + \left(\frac{\partial u}{\partial x} \right)^2 + \frac{1}{r} \frac{\partial w}{\partial \theta} + \frac{v}{r} \right)^2 + \left(\frac{\partial v}{\partial x} + \frac{\partial u}{\partial r} \right)^2 + \left(\frac{1}{r} \frac{\partial v}{\partial \theta} + \frac{\partial w}{\partial r} - \frac{w}{r} \right)^2 + \left(\frac{\partial w}{\partial x} + \frac{1}{r} \frac{\partial u}{\partial \theta} \right)^2 \right]$$

REFERENCES

- Childs, D.W.: Finite Length solutions for rotordynamic coefficients of turbulent annular seals. Journal of Lubrication Technology, ASME-Paper, No 82 Lub. 42, 1982
- Nelson, C.C.: 1985: Rotordynamic coefficients for compressible flow in tapered annular seals. Journal of Tribology, Vol. 107, July 1985

- /3/ Dietzen, F.J.; Nordmann, R.; 1987: Calculation of rotordynamic coefficients of Seals by 'Finite-Difference' techniques. ASME Journal of Tribology, July 1987
- /4/ Nordmann, R.; Dietzen, F.J.; Weiser, H.P.: Calculation of Rotordynamic Coefficients and Leakage for Annular Gas Seals by Means of Finite Difference Techniques. The 1987 ASME Design Technology Conferences - 11th Biennial Conference on Mechanical Vibration and Noise. Boston, Massachusetts, September 27-30, 1987
- /5/ Launder, B.E.; Spalding, D.B.: The numerical computation of turbulent flows. Computer methods in applied mechanics and engineering. 3 (1974) 269-289
- /6/ Rodi, W.: Turbulence models and their application in hydraulics. Presented by the IAHR-Section on Fundamentals of Division II. Experimental and mathematical Fluid Dynamics
- /7/ Stoff, H.: Calcule et mesure de La turbulence d'un ecoulement incompressible dans le Labyrinthe entre un arbre en rotation et un cylindre stationnaire. Theses No. 342 (1949) Swiss Federal College of Technology, Lausanne, Juris Verlag Zürich, 1979
- /8/ Wyssmann, H.R.; Pham, T.C.; Jenny, R.J.: Prediction of stiffness and damping coefficients for centrifugal compressor labyrinth seals. ASME Journal of Engineering for Gas Turbines and Power, Vol. 106, Oct. 1984
- /9/ Rhode, D.L.; Demko, J.A.; Traegner, U.K.; Morrison, G.L.; Sobolik, S.R.: Prediction of incompressible flow in labyrinth seals. ASME Journal of Fluids Engineering, Vol. 108, March 1986
- /10/ Wittig, S.; Jackobsen, K.; Schelling, U.; Dörr, L.; Kim, S.: Wärmeübergangszahlen in Labyrinthdichtungen. VDI-Berichte 572.1, Thermische Strömungsmaschinen '85, p. 337-356
- /11/ Truckenbrodt, E., 1980: Fluidmechanik, Band 1. Grundlagen und elementare Strömungsvorgänge dichtebeständiger Fluide. Springer Verlag 1980, pp. 118-119
- /12/ Gosman, A.D.; Pun, W.: Lecture notes for course entitled: 'Calculation of recirculating flows'. Imperial College London, Mech. Eng. Dept., HTS/74/2
- /13/ Benodekar, R.W.; Goddard, A.J.H.; Gosman, A.D.; ISSU, R.I.: Numerical prediction of turbulent flow over surfacemounted ribs. AIAA Journal Vol. 23, No 3, March 1985
- /14/ Patankar, S.V.: Numerical heat transfer and fluid flow. McGraw Hill Book Company (1980)
- /15/ Maßmann, H., 1986: Ermittlung der dynamischen Parameter turbulent durchströmter Ringspalte bei inkompressiblen Medien. Vom Fachbereich Maschinenwesen der Universität Kaiserslautern zur Verleihung des akademischen Grades Doktor-Ingenieur genehmigte Dissertation
- /16/ Diewald, W.; Nordmann, R., 1988: Influence of Different Types of Seals on the Stability Behavior of Turbopumps. The Second International Symposium on Transport Phenomena, Dynamics and Design of Rotating Machinery; Volume 2: Dynamics. Honolulu, Hawaii April 3-6, 1988.

BLANK PAGE

AN EXPERIMENTAL STUDY ON THE STATIC AND DYNAMIC CHARACTERISTICS OF PUMP ANNULAR SEALS

T. Iwatsubo, B.C. Sheng, and T. Matsumoto
Faculty of Engineering
Kobe University
Rokko, Nada, Kobe, Japan

A new test apparatus is constructed and is applied to investigate static and dynamic characteristics of annular seals for turbopumps. The fluid forces acting on the seals are measured for various parameters such as the preswirl velocity, the pressure difference between the inlet and outlet of the seal, the whirling amplitude, and the ratio of whirling speed to spinning speed of the rotor. Influence of these parameters on the static and dynamic characteristics is investigated from the experimental results. As a result, preswirl affects the dynamic characteristics strongly. Especially, the preswirl opposing the rotating direction has a stabilizing role on the rotor system.

1. Introduction

A turbomachine such as a pump tends to be operated at high speed and high pressure because of severe performance requirements. But with increasing speed and pressure, the fluid force causes an instability of the rotating machine because of the noncontacting seal, such as the balance piston and wear ring. So, it is necessary to make the dynamic behavior clear and to supply accurate data in order to predict and prevent the unstable vibration, and still more necessary to design a stable rotating machine.

Many theoretical and experimental analyses on the characteristics of noncontacting seals are reported. As an experimental research on annular seals, Childs et al. (Refs. 2,3) investigated fluid forces acting on the seals and their characteristics with a test apparatus which has an eccentric rotor. Nordmann (Ref. 4) used an impulse force type test apparatus to carry out an experiment on the characteristics of annular seals. Kaneko et al. (Ref. 7), Kanki et al. (Ref. 8), and Hori et al. (Ref. 9) also reported their test results on the seals. All these results are important for the research on annular seals. However in these experimental apparatus, the casing inertia force of the test rig is larger than the flow-induced force due to the seal, so the signal/noise ratio is not good. Childs et al. investigated the characteristics under the condition of rotor whirling motion, but limited by the test apparatus, he only investigated the characteristics in the synchronous motion of the rotor. Recently, Kanemori and Iwatsubo (Ref. 10) used a test apparatus in which the rotor gives spinning and whirling motion independently to test a long annular seal of a submerged pump for various whirling speeds. But, they did not test for the preswirl velocity, which strongly affects the stability of a rotor system, because their interest is limited to the dynamic

characteristics of the submerged pump. The dynamic characteristics of annular seals have not been investigated yet in various operating conditions.

This paper shows the experimental results obtained by an experimental apparatus which is newly designed to obtain a high S/N ratio. In the test the fluid force acting on the seals is measured and the stiffness, damping, and inertia coefficients are obtained. Influence of the parameters such as the whirling amplitude pressure difference between the inlet and outlet of the seal, preswirl, rotating and whirling speeds, and their directions is investigated.

2. Nomenclature

F_x, F_y	: Fluid forces in x and y directions
F_r, F_t	: Fluid forces in r and t directions
$K_{xx}, K_{yy}, K_{xy}, K_{yx}$: Stiffness coefficients
$C_{xx}, C_{yy}, C_{xy}, C_{yx}$: Damping coefficients
$M_{xx}, M_{yy}, M_{xy}, M_{yx}$: Inertia coefficients
x, y, z	: Fixed coordinates
r, t	: Radial and tangential coordinates
$p(\phi, z)$: Pressure distribution
$P(\phi)$: Average pressure in axial direction
P_{in}	: Inlet pressure to the seal
P_{ex}	: Outlet pressure from the seal
ΔP	: Pressure difference between inlet and outlet of the seal
ω	: Spinning angular velocity of the rotor
Ω	: Whirling angular velocity of the rotor
e	: Whirling eccentricity of the rotor
ϕ	: Phase difference between principle force and displacement
R, D	: Rotor radius and diameter, respectively
L	: Seal length
C	: Seal clearance
V_t	: Preswirl velocity
V_{ts}	: Preswirl velocity without a rotating motion
V_a	: Fluid average velocity in axial direction

3. Test apparatus and measuring instruments

3.1 Test apparatus

Figs. 1 and 2 show the assembly of the test apparatus and the layout of the test facility, respectively. In Fig. 1, a working fluid, that is, water, is injected through three pairs of swirl passages to accomplish the different inlet swirl velocities shown in cross section B. The water passes through the clearances of the seal and flows to outlets in both sides of the housing. Cool water is continuously applied to the tank in order to maintain constant water temperature.

The inlet part consists of six tubes connected with swirl passages for injecting the water, and swirl speed is adjusted by the six valves in order to obtain the arbitrary swirl velocity in the range of 0 - 6.5 m/s.

The seal assembly consists of a seal stator and a seal rotor. The seal rotor, of which the diameter is 70 mm, is connected to the motor by a flexible coupling. The motor is controlled in the speed range 0 - 3500 r.p.m. by an electric inverter, which also selects the rotational direction. The four types of parallel annular seals shown in Table 1 were prepared for the test. The seal stator has holes to measure the dynamic pressure in the seal, as shown in cross section C. Both long

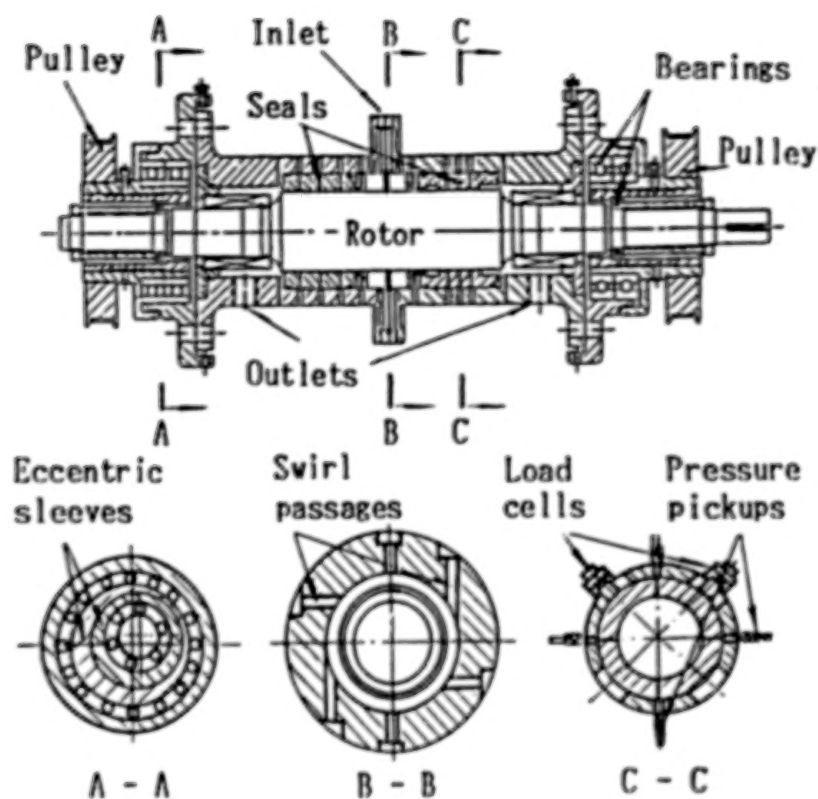


Fig.1 Test apparatus assembly

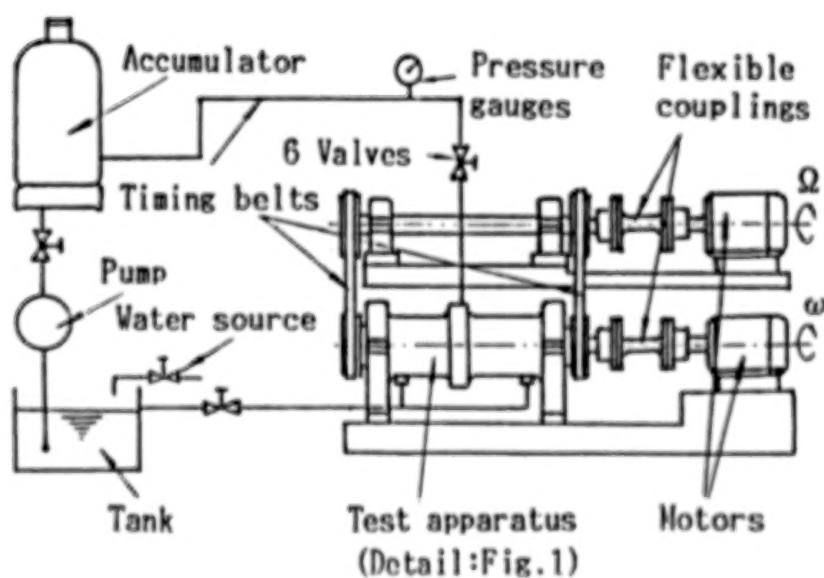


Fig.2 Test facility layout

Table 1 Specifications of seals

	Length(mm)	Diameter(mm)	L/D	Clearance(mm)
Seal 1	70	70	1.0	0.175
Seal 2	35	70	0.5	0.175
Seal 3	70	70	1.0	0.5
Seal 4	35	70	0.5	0.5

and short seals have three holes in the axial direction and four holes in the x and y directions. The dynamic pressure is measured by the strain gauge type pressure gauge shown in cross section C. The fluid dynamic force acting on the stator is also directly measured by the load cells shown in cross section C for comparison with the data of the pressure transducers.

The bearing assembly has two ball bearings to make spinning and whirling motions. To make a whirling motion, an inside sleeve and an outside sleeve, which have a 0.05 mm eccentricity to each other, are attached between the two bearings as shown in cross section A of Fig. 1. The two eccentric sleeves can be rotated, relatively. So an arbitrary eccentricity can be adjusted in the range of 0 - 0.1 mm. The sleeves of both sides are driven by a motor through the timing belts. The motor can also be controlled by an electric inverter in the rotating speed range of 0 - 3500 r.p.m., and rotational direction can be selected by an inverter.

3.2 Measuring instruments

The measuring procedure illustrated in Fig. 3 consists of four kinds of physical variables: that is, rotating and whirling speed, dynamic pressure in the seal, seal forces, and displacement of the rotor. Signals from measuring instruments are recorded by a data recorder and analyzed by a computer.

The rotating and whirling speed are measured by eddycurrent type pulse sensors and digital counters.

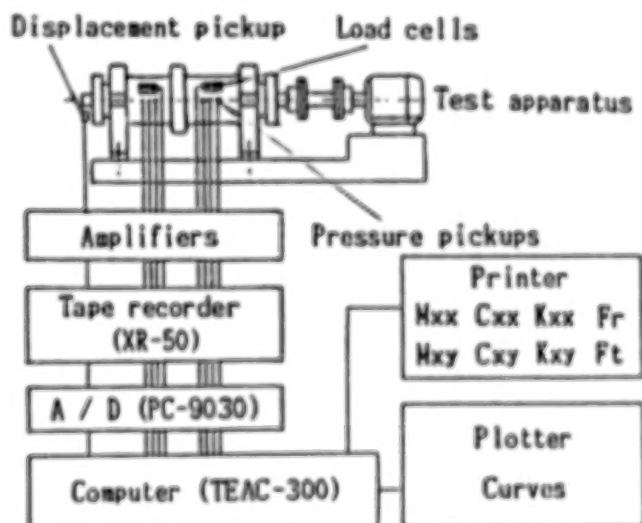


Fig.3 Measurement procedure

A pressure transducer of the semiconductor strain gauge type is used to measure the dynamic pressure through the syringe needle. The pressure in the seal is measured at the three points in the seal shown in Fig. 4. The seal stator is mounted on the housing by O-rings as shown in Fig. 4.

Dynamic fluid force can be directly measured by a load cell as shown in Fig. 5. The force measured by the load cell is calibrated to revise the influence of the O-rings and the inertia of the seal.

An eddycurrent type displacement sensor is used to measure the displacement, and this displacement is used as a reference signal to obtain the phase difference between the displacement and the flow induced force.

The test data are recorded by a data recorder and sent to the computer through an A/D converter. In the computer the pressure values are integrated in the circumferential direction to obtain the fluid force; then the characteristic coefficients are calculated.

A special pitot tube set is used to measure the preswirl velocity in the seal inlet, as shown in Fig. 6. The static and total pressures are measured by the pressure transducers instead of the usual U-tube.

Axial flow velocity in the seal and leakage are determined from the outlet flow velocity directly measured by a pitot tube.

3.3 Calibration

As a preliminary test, the static and dynamic characteristics of measuring instruments (i.e., the pressure transducer, the load cell, and the pitot tube) were calibrated.

Because the pressure measuring set is constructed by a pressure transducer and a syringe needle, a phase difference between real pressure and measured pressure was investigated. Then, it was found that the pressure measuring set has a phase lag relative to the real pressure and that the phase lag increases with the frequency.

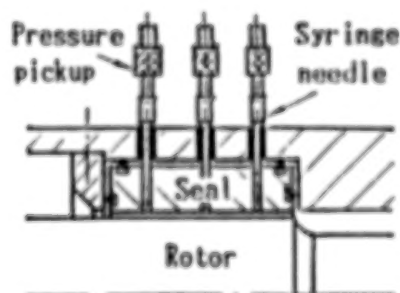


Fig. 4 Detail of pressure measurement

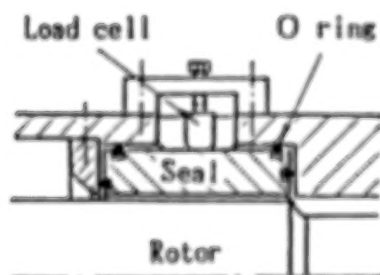


Fig. 5 Detail of force measurement

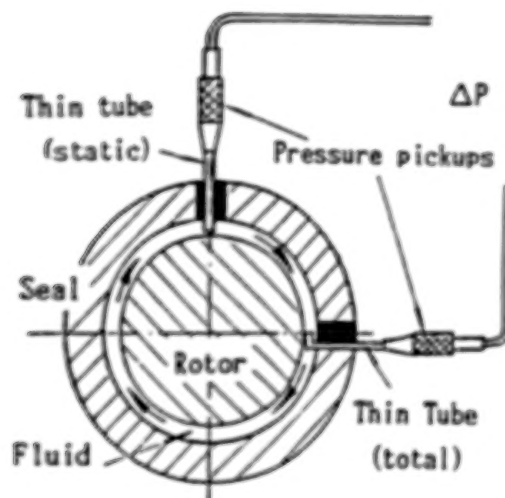


Fig.6 Detail of swirl velocity measurement

Dynamic calibration of the load cell was done in various working conditions. A periodic force was excited on the seal by a shaker, and the force was simultaneously measured by strain gauges attached to the shaking rod and by the load cell fixed on the other side. These data were used to calibrate the measured data in the real test.

A pitot tube set was used to measure the inlet preswirl velocity. Its pitot tube coefficient for calibration was determined by means of a standard pitot tube.

4. Discussions on the accuracy measured by the test apparatus

4.1 Comparison with the data by two measuring methods

Fig. 7 illustrates the fluid forces measured by the load cell unit and the pressure transducer unit. These results show a reasonable agreement because the relative error between the two results is within 5.5 percent.

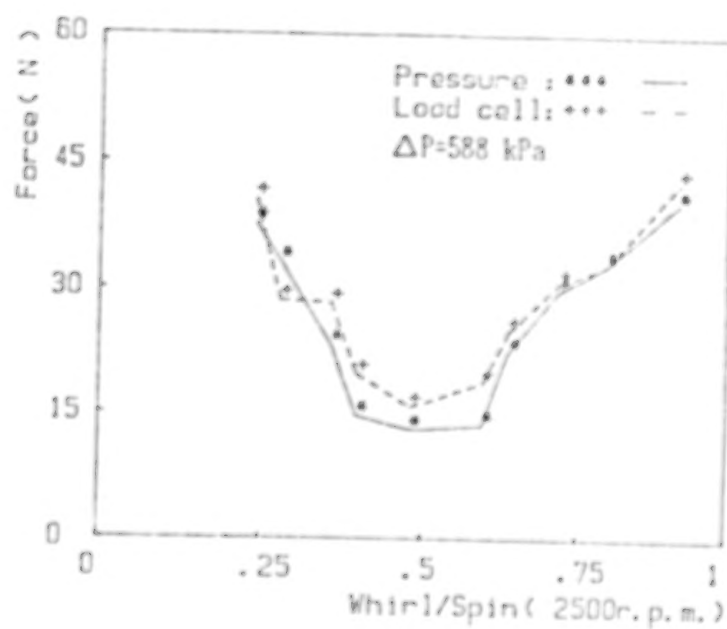
4.2 Comparison with other researcher's results

A comparison of the authors' experimental results with Childs' (Ref. 2) results is shown in Fig. 8. These results cannot be compared quantitatively, because the working fluids and test conditions are different. However, these results have the same tendencies. Fig. 9 gives the test results of Kanemori et al. (Ref. 10). These results also demonstrate good agreement with the authors' results of Fig. 10.

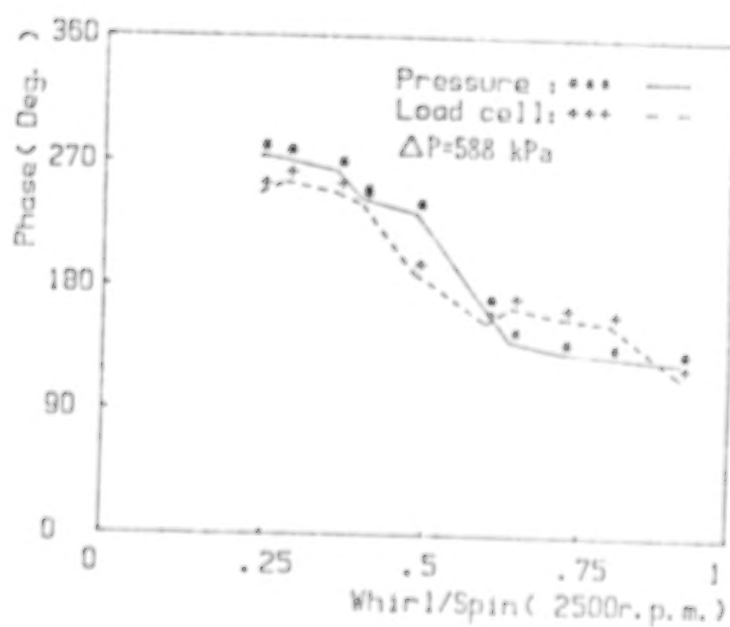
5. Calculation of fluid force and characteristic coefficients

It is assumed that the motion equation of the rotor system is represented as follows

$$[M](\ddot{X}) + [C](\dot{X}) + [K](X) = (f(t)) - (F)$$



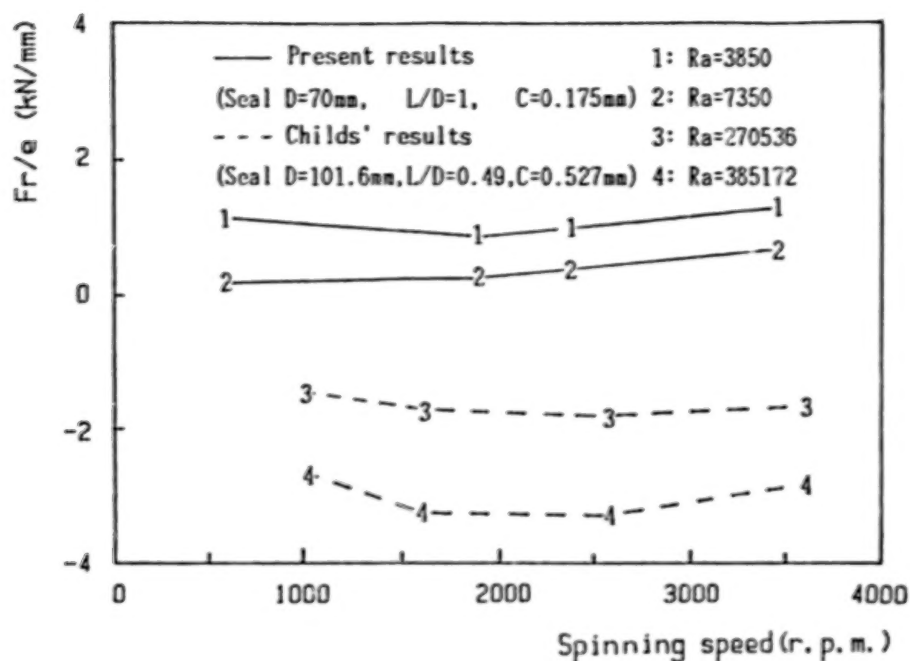
(a) Force



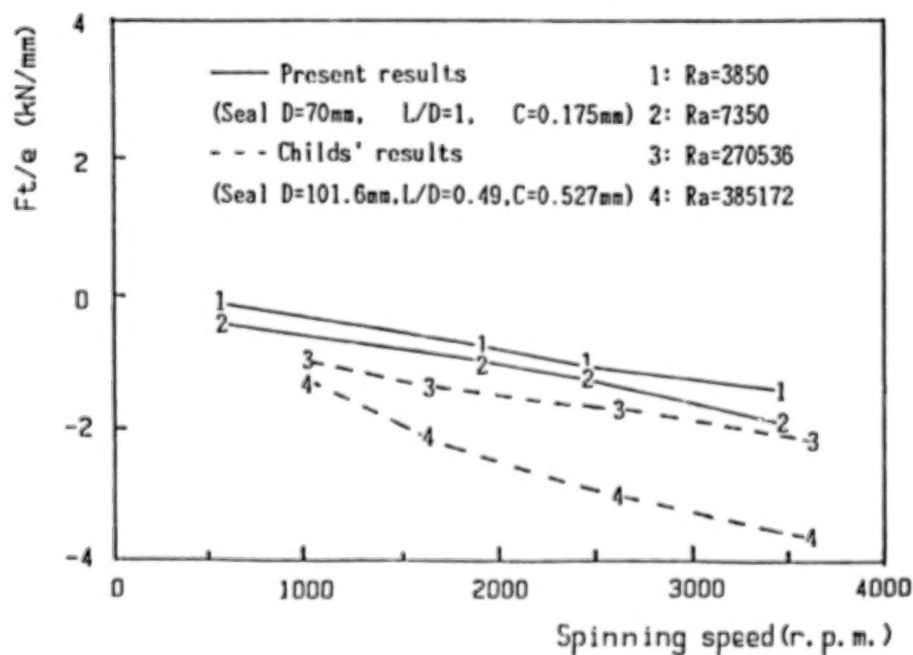
(b) Phase

Fig.7 Results measured by two measuring methods

BEST COPY AVAILABLE



(a) Radial coefficient Fr/e



(b) Tangential coefficient Ft/e

Fig.8 Comparison of experimental results and Childs' results

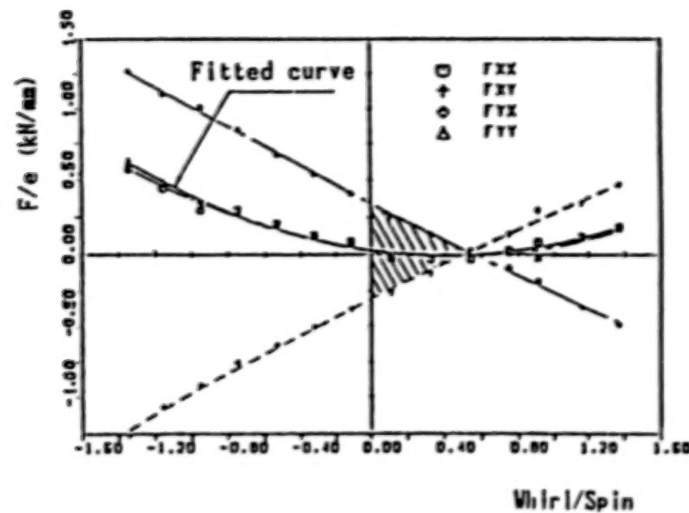


Fig.9 Kanemori's results

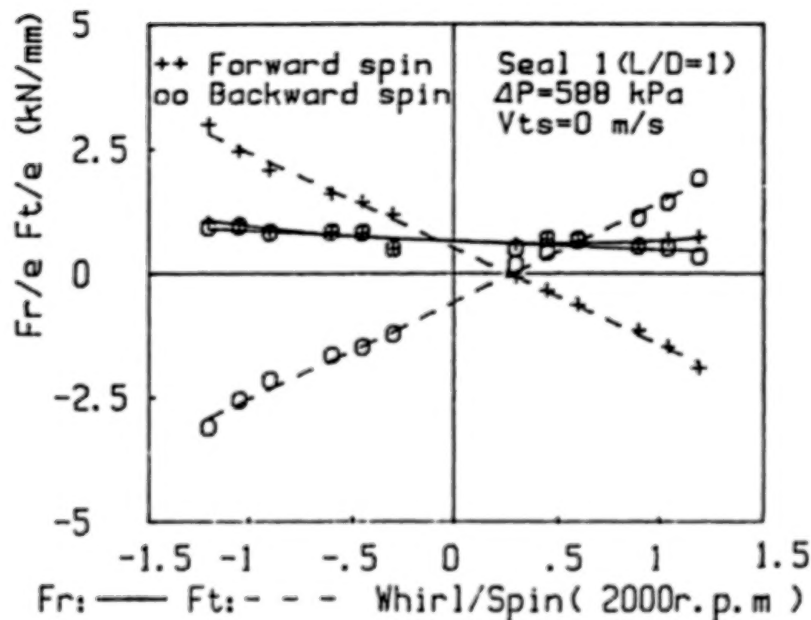


Fig.10 Results for forward and backward spinning speeds

where $[M]$, $[C]$, $[K]$ are the mass, the damping, and the stiffness matrix and $\{f(t)\}$ is the force vector. $\{F\} = \{F_x \ F_y\}^T$ is the fluid reaction force acting on a rotor and is represented as a linear function of rotor displacement, velocity, and acceleration, as follows.

$$-\begin{Bmatrix} F_x \\ F_y \end{Bmatrix} = \begin{bmatrix} M_{xx} & M_{xy} \\ M_{yx} & M_{yy} \end{bmatrix} \begin{Bmatrix} \ddot{x} \\ \ddot{y} \end{Bmatrix} + \begin{bmatrix} C_{xx} & C_{xy} \\ C_{yx} & C_{yy} \end{bmatrix} \begin{Bmatrix} \dot{x} \\ \dot{y} \end{Bmatrix} + \begin{bmatrix} K_{xx} & K_{xy} \\ K_{yx} & K_{yy} \end{bmatrix} \begin{Bmatrix} x \\ y \end{Bmatrix} \quad \dots(1)$$

For a small whirling motion about a center position, the relation of the coefficients may be expressed by

$$\begin{aligned} M_{xx} &= M_{yy}, & M_{yx} &= M_{xy} = 0, & C_{xx} &= C_{yy}, \\ C_{yx} &= -C_{xy}, & K_{xx} &= K_{yy}, & K_{yx} &= -K_{xy} \end{aligned} \quad \dots(2)$$

where the cross-coupled inertia coefficient is neglected because it is negligibly small.

A rotating coordinate system rotating with the rotor is adopted to analyze the fluid forces easily. The relation between a fixed coordinate system and a rotating coordinate system is illustrated in Fig. 11, where F_x and F_y are represented by the radial force F_r and the tangential force F_t .

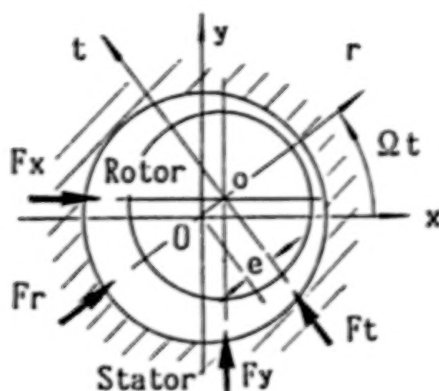


Fig.11 Model of annular seal

In the test, whirling motion is given by

$$\begin{aligned} x &= e \cdot \cos \Omega t, & y &= e \cdot \sin \Omega t \\ \dot{x} &= -e \cdot \Omega \cdot \sin \Omega t, & \dot{y} &= e \cdot \Omega \cdot \cos \Omega t \\ \ddot{x} &= -e \cdot \Omega^2 \cdot \cos \Omega t, & \ddot{y} &= -e \cdot \Omega^2 \cdot \sin \Omega t \end{aligned} \quad \dots(3)$$

Substituting Eq. (3) and Eq. (2) into Eq. (1), the following expressions are obtained

$$\begin{aligned} F_r &= e (-K_{xx} - \Omega C_{xy} + \Omega^2 M_{xx}) \\ F_t &= e (K_{xy} - \Omega C_{xx}) \end{aligned} \quad \dots(4)$$

or

$$\begin{aligned} -F_r/e &= K_{xx} + \Omega C_{xy} - \Omega^2 M_{xx} \\ -F_t/e &= -K_{xy} + \Omega C_{xx} \end{aligned} \quad \dots(5)$$

where $-F_r/e$ and $-F_t/e$ are called the restitution force coefficient and the tangential force coefficient, respectively.

The displacement of the rotor, the pressure, and the force can be directly measured by the displacement sensor, the pressure transducer, and the load cell, respectively. So the dynamic coefficients are determined from these data.

The fluid forces are obtained by integrating the pressure distribution along the axial and circumferential directions of the seal: that is,

$$\begin{aligned}
F_r &= \int_0^L \int_0^{2\pi} p(\phi, z) \cdot \cos\phi \cdot R \cdot d\phi \cdot dz \\
&= R \cdot L \cdot \int_0^{2\pi} P(\phi) \cdot \cos\phi \cdot d\phi \\
&= (L \cdot D \cdot \pi / N) \sum_{j=1}^N P(\phi_j) \cdot \cos\phi_j \\
&\dots (6) \\
F_t &= \int_0^L \int_0^{2\pi} p(\phi, z) \cdot \sin\phi \cdot R \cdot d\phi \cdot dz \\
&= R \cdot L \cdot \int_0^{2\pi} P(\phi) \cdot \sin\phi \cdot d\phi \\
&= (L \cdot D \cdot \pi / N) \sum_{j=1}^N P(\phi_j) \cdot \sin\phi_j
\end{aligned}$$

where N is the time series total number of pressures within one period. $P(\phi)$ is average pressure in the axial direction,

$$\begin{aligned}
P(\phi) &= (1/L) \int_0^L p(\phi, z) \cdot dz \\
&= (1/L) \sum_{i=1}^3 P_i \cdot L_i \\
&\dots (7)
\end{aligned}$$

where P_i is the pressure measured at different points, and L_i is the length between these points.

To determine the coefficients M_{xx} , C_{xx} , C_{xy} , K_{xx} , and K_{xy} of Eq. (5), F_r/e and F_t/e at 12 different forward and backward whirling speeds are measured for a given spinning speed, and F_t/e is approximated by a linear function, and F_r/e by a quadratic function of Ω . From Eq. (5), the inertia coefficient, damping coefficients, and stiffness coefficients are represented by the curvature, the slopes, and the crosses, respectively. The experimental conditions are shown in Table 2.

Table 2 Experimental Conditions

Pressure difference ΔP (kPa)	196, 294, 490, 588, 882
Whirling amplitude e (μm)	20, 30, 40, 50, 60
Spinning speed ω (r.p.m)	500 ~ 3500
Whirling speed Ω (r.p.m)	± 600 ~ ± 2400
Preswirl velocity V_t (m/s)	0 ~ ± 13

6. Experimental results and discussion

Since the fluid forces measured by the pressure transducer and load cell are about the same, the fluid force measured by the pressure transducer is used as the experimental results in this discussion.

6.1 Pressure distribution and leakage (static results)

The static pressure distributions in the axial direction of seal 1 and 2 are shown in Fig. 12, and the dynamic pressure distributions of seal 1 are shown in Fig. 13 for various inlet pressures. It is known from Fig. 13 that the dynamic pressure distribution is more sensitive to the inlet pressure.

The leakages of seal 1 to 4 are shown in Fig. 14. They increase as the pressure difference and the seal clearance increase but reduce slightly with increasing spinning speeds. Also they are insensitive to the preswirls, whirling amplitude, and whirling speeds of the rotor.

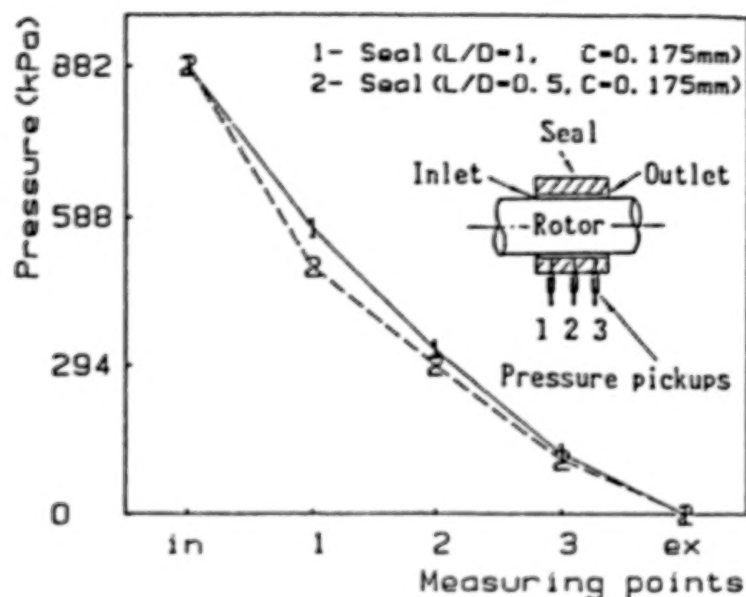


Fig.12 Static pressure falls

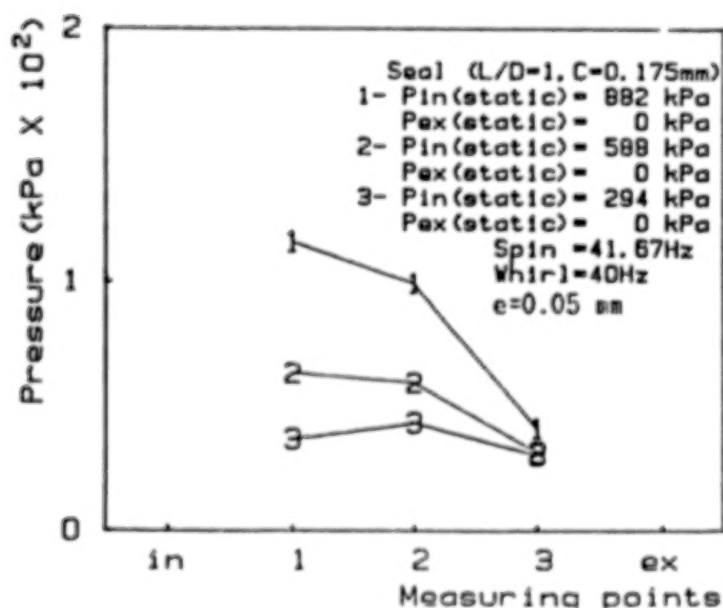


Fig.13 Dynamic pressure falls

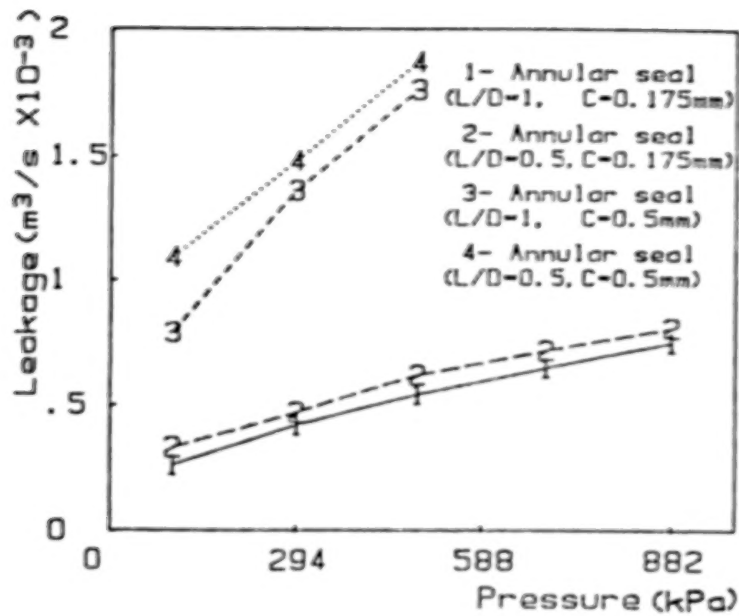


Fig.14 Leakages

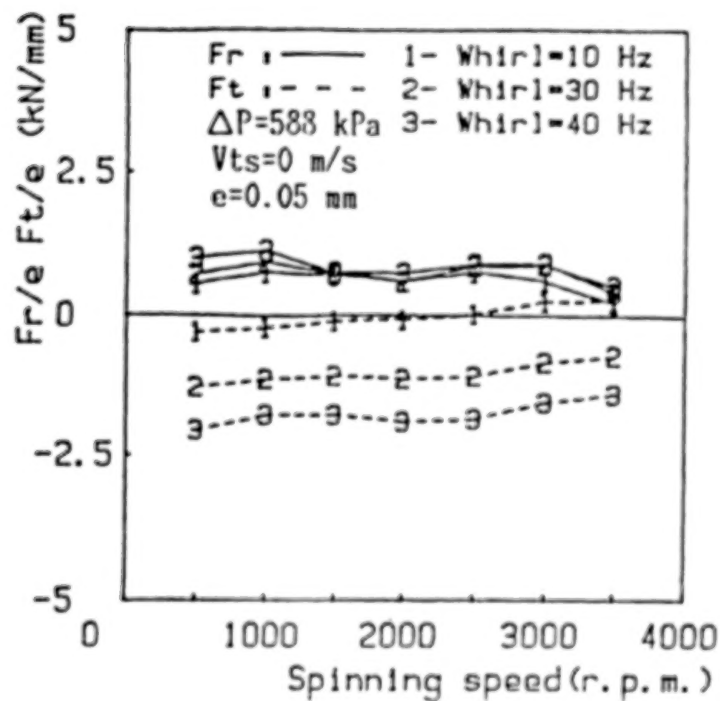


Fig.15 Force coefficients for spinning speed

6.2 Fluid force

6.2.1 Effect of spinning speed

Fig. 15 illustrates the experimental results of fluid force coefficients Fr/e and Ft/e for rotor spinning speeds. These results show that Fr/e does not

obviously vary with the spinning speed, but F_t/e increases with the spinning speed. That is, increasing the spinning speed has a destabilizing effect on the rotor system. The changes of F_r/e and F_t/e with spinning speed are independent of the pressure and the whirling amplitude, and these tendencies appear to be the same for all four types of seal.

The radial and the tangential forces (i.e., F_r/e and F_t/e) for the ratios Ω/ω are shown in Fig. 16 where the oblique fillet is the destabilizing region of F_t/e . It is known from the results that F_r/e and F_t/e vary with the spinning speed, even if the ratios of Ω/ω are the same. This may be due to fluid viscosity.

6.2.2 Effect of preswirl velocity

Fig. 17 shows the effect of the whirl ratio Ω/ω on F_r/e and F_t/e of seal 1 for various preswirl velocities. The results illustrate that the preswirl in the same direction as the spinning affects the unstable area of fluid force greatly. The preswirl in the direction of rotation extends the unstable area, but the preswirl in the direction opposite to that of rotation reduces the area, even reducing it to negative values for enough opposing swirl. However, for both of the swirls the intersection point of F_t/e and the zero axis approach about $\Omega/\omega = 0.5$ with increasing spinning speed.

This phenomenon is illustrated as the relation between the whirling speed and the average circumferential velocity rotating about $\omega R/2$. That is, when the whirling angular velocity of the rotor is lower than the average angular velocity of the fluid, the whirling motion of the rotor will be accelerated by the rotating fluid; conversely, when the whirling angular velocity is faster than the average angular velocity, the whirling motion will be restrained, so that the sign reverses about $\Omega/\omega = 0.5$. The circumferential velocity distributions in radial are shown in Fig. 18 where Figs. (b) and (c) are for the cases of enough preswirl and inverse preswirl velocities. The distribution demonstrates that the preswirl strengthens the fluid average velocity V_m , and the opposing preswirl weakens the average velocity V_m . From these effects, the unstable area varies.

In summary, the preswirl in the direction of the rotor rotation has a destabilizing effect on the rotor system, and the opposing preswirl has a stabilizing effect on the rotor system.

6.2.3 Effect of pressure difference

F_r/e and F_t/e are measured for various pressure differences between the inlet and outlet of the seal. The results show that F_r/e and F_t/e only change their values; they do not change their qualitative characteristics. One of these results is shown in Fig. 19.

6.2.4 Effect of seal length

The effect of seal length is shown in Fig. 20. The result shows that the two seals have the same tendencies for F_t/e , but not for F_r/e . Compared with that of the long seal ($L/D = 1$), the F_r of the short seal ($L/D = 0.5$) acts as a stabilizing force. This is because if the axial flow velocity increases, the tangential force which is generated by the circumferential flow decreases with the decrease of the time it takes for the flow to pass through the seal.

6.2.5 Effect of whirling amplitude

Fig. 21 shows the effect of whirling amplitude (eccentric ratio) on F_r/e and F_t/e of seal 1. The results show F_r/e and F_t/e increase with increasing whirling amplitude.

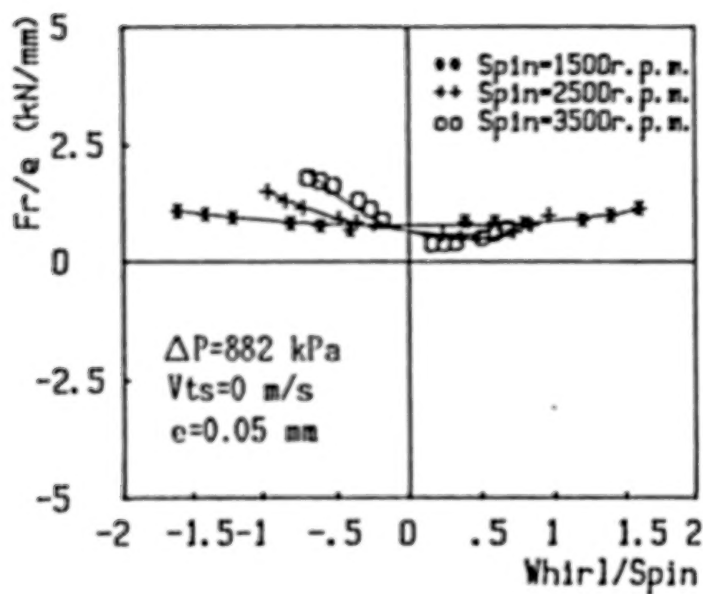
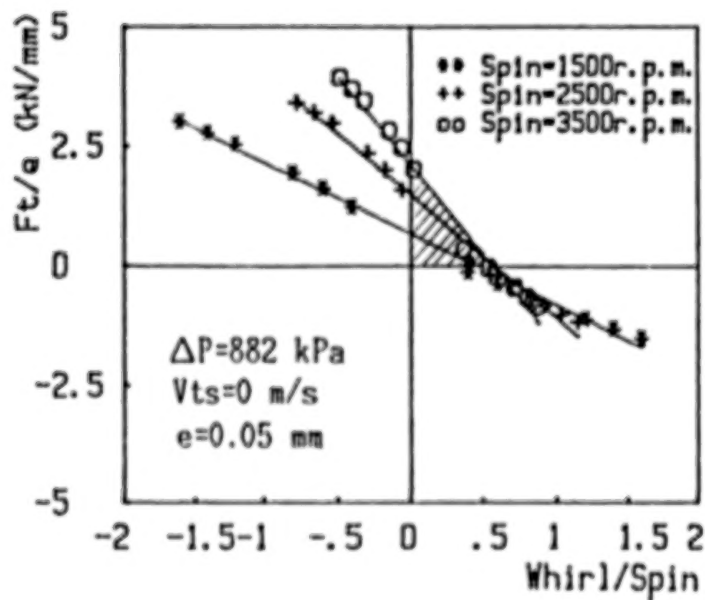
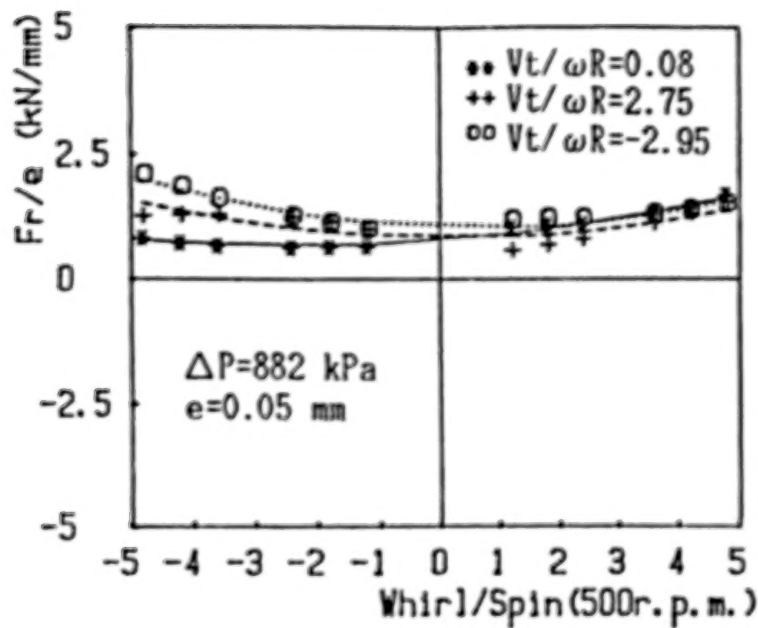
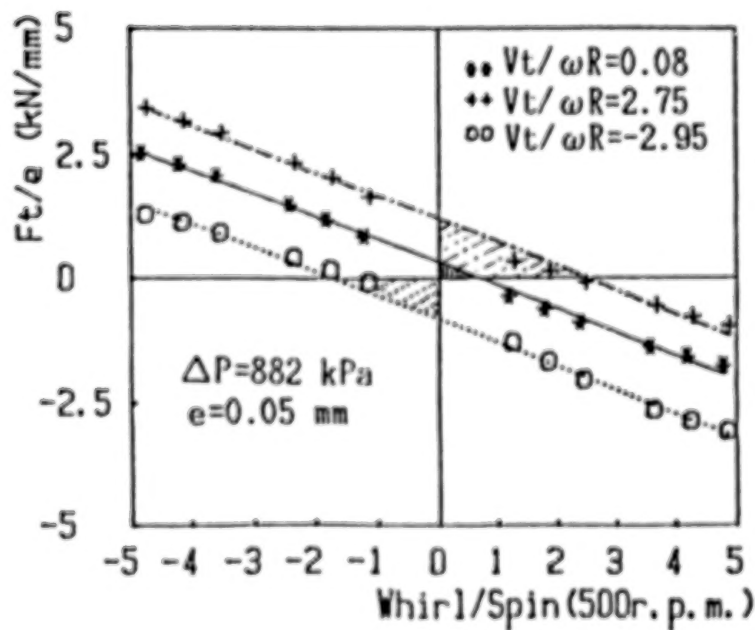
(a) Radial coefficient Fr/e (b) Tangential coefficient Ft/e

Fig.16 Effect of spinning speed on force coefficients



(a) Radial coefficient Fr/e



(b) Tangential coefficient Ft/e

Fig.17 Effect of swirling velocity on force coefficients

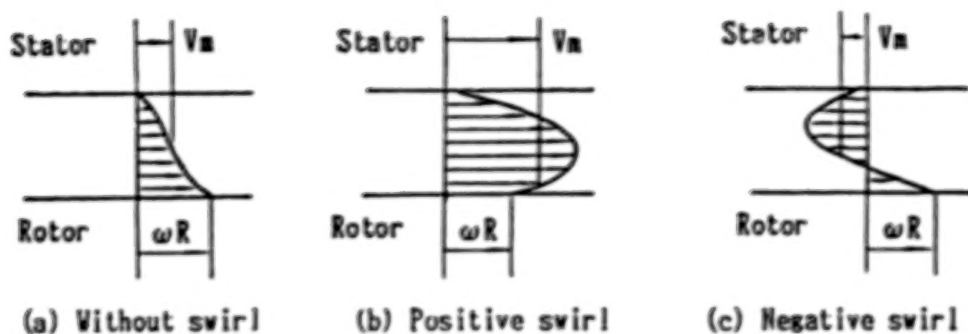


Fig.18 Velocity distributions in clearance of seal

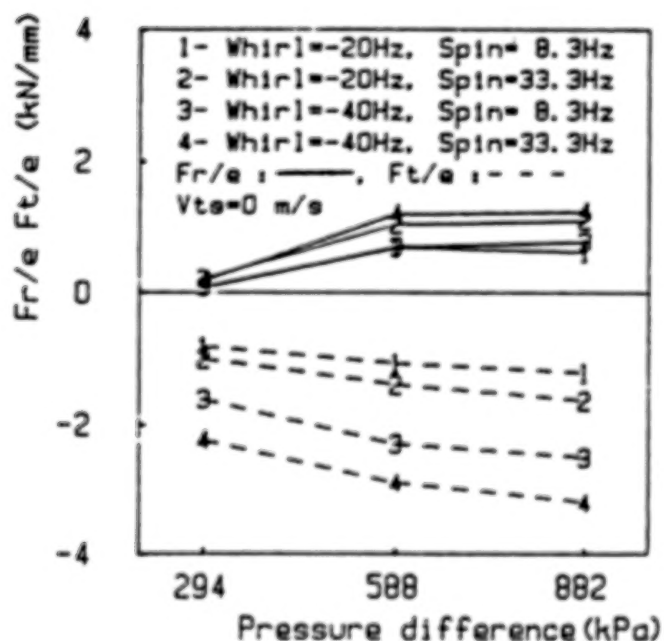


Fig.19 Effect of pressure difference on force coefficients

6.2.6 Effect of seal clearance

The results of Fr/e and Ft/e for different radial seal clearances are shown in Fig. 22. They are measured in the condition of positive preswirl velocities. Attention should be paid to Fr/e ; that is, regardless of the seal length ($L/D = 1.0$ and $L/D = 0.5$), seals with large clearance have negative values of Fr/e , in contrast to seals with small clearance. It is considered that these negative Fr/e are caused by the increase of the axial flow in the large clearance seal. In addition, the tangential force coefficients Ft/e of the large clearance seals are much more influenced by preswirl velocity than those of the small clearance seal.

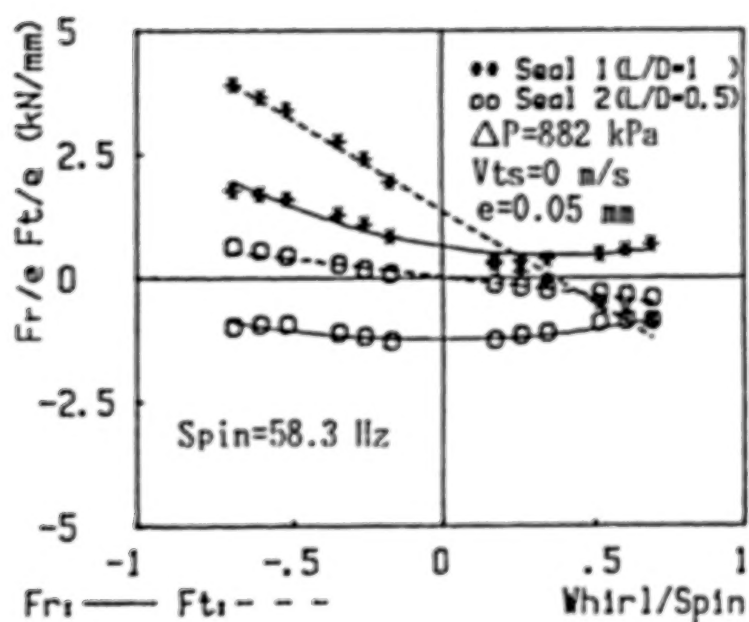


Fig.20 Effect of seal length on force coefficients

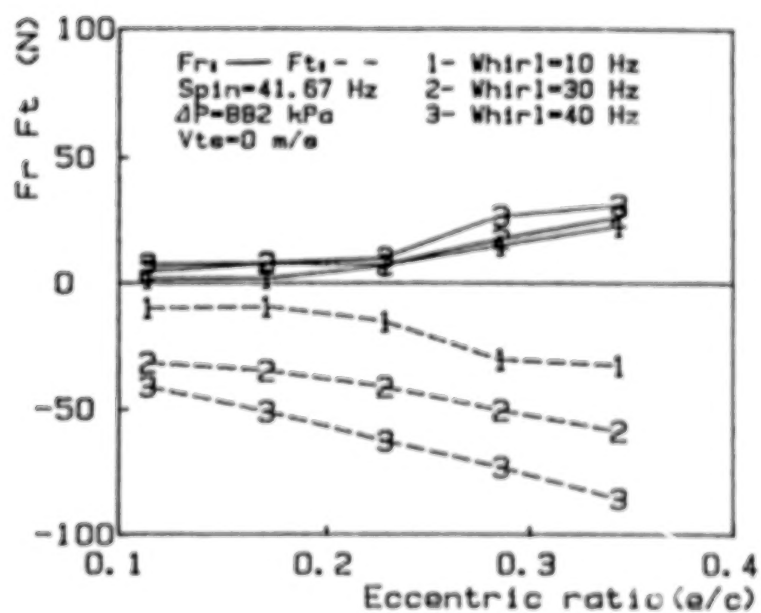
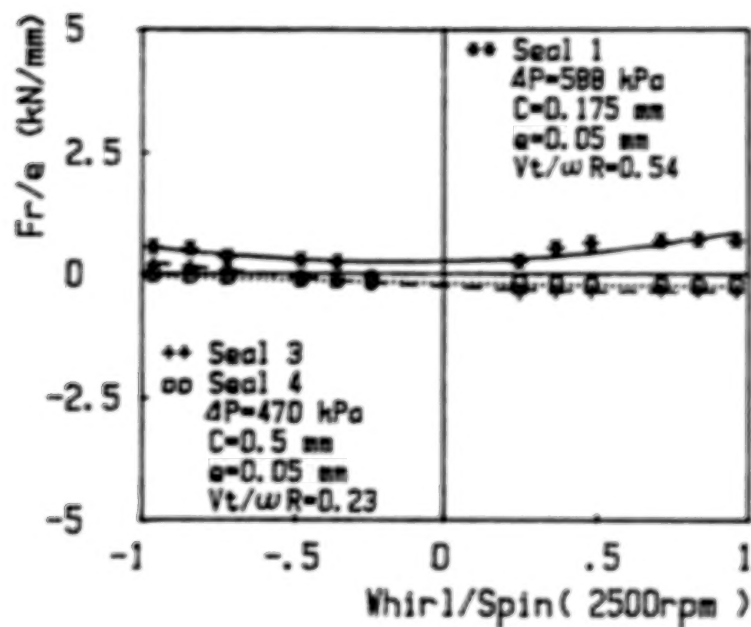
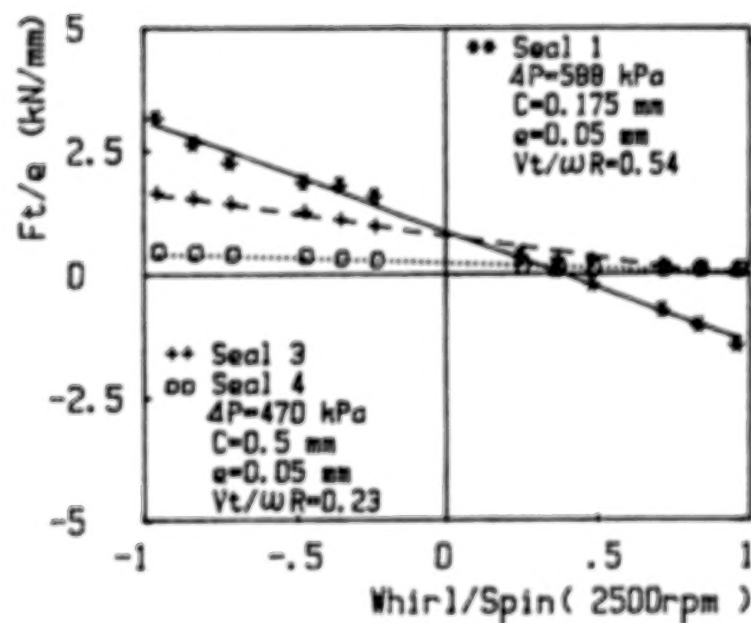


Fig.21 Forces for whirling amplitude (eccentric ratio)



(a) Radial coefficient Fr/e



(b) Tangential coefficient Ft/e

Fig.22 Effect of seal clearance

6.3 Stiffness, damping, and inertia coefficients

The stiffness coefficients, damping coefficients, and inertia coefficients obtained from the fluid forces are shown in Figs. 23 and 24. These results show that the inertia coefficients are independent of the pressure difference, the eccentric ratio, and the swirl velocity, and that they always have positive values. Therefore, the inertia force decreases an eigenfrequency of the rotor system.

The direct damping coefficients are always positive and much larger than C_{xy} , so generally, the damping forces act as stabilizing forces on the rotor system. These damping forces are not affected by swirl velocity and seal length.

The stiffness coefficients K_{xx} and K_{xy} are largely affected by the swirl velocity, especially K_{xy} . These can be recognized from Fig. 23. K_{xy} increases with the preswirl velocity and decreases with the opposing swirl velocity. That is, the stiffness force related to K_{xy} may act as a stabilizing force or as a destabilizing force according to opposing preswirl or preswirl velocities.

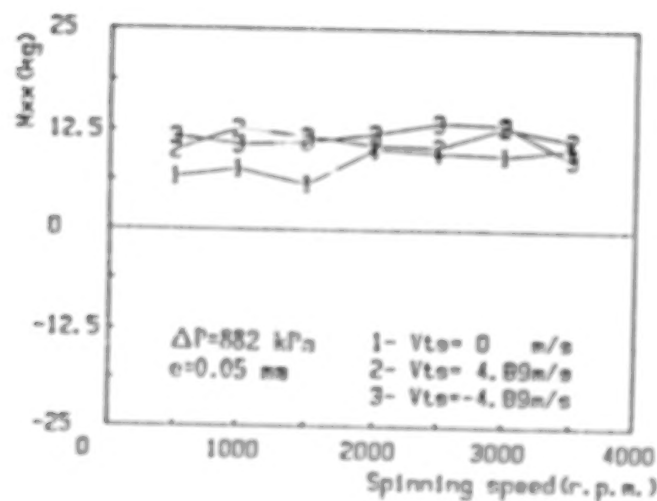
As shown in Fig. 24, the coefficient K_{xx} has a negative value for the long seal 1, but K_{xx} has a positive value for the short seal 2. Namely, the short seal is more stable than the long seal from the view point of the stiffness coefficients of diagonal terms.

7. Conclusions

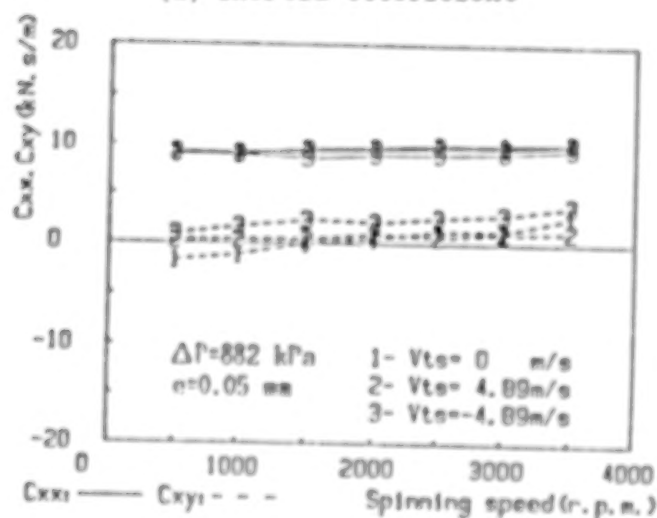
From the experimental study reported here, we derive the following conclusions:

- (1) Leakage grows with increasing pressure difference, but reduces slightly with increasing spinning speed. The leakage is insensitive to the preswirl velocity, the whirling amplitude, and the whirling speed.
- (2) Flow induced force increases with increasing whirling amplitude, but decreases with increasing seal clearance.
- (3) Preswirl velocity strongly affects the stability of the rotor system. Preswirl velocity in the rotating direction has a tendency to destabilize, but opposing preswirl has a tendency to stabilize the rotor system.
- (4) Tangential fluid force increases with rotor spinning speed; as a result, it may become a destabilizing force.
- (5) Axial flow through the seal has a tendency to stabilize the rotor system. It can be recognized from the radial force coefficients F_r/e of the short seal and the large clearance seal.
- (6) The inertia force related to the inertia coefficient M_{xx} always acts to decrease the eigenfrequency of the rotor system.
- (7) The damping force related to the damping coefficients C_{xx} and C_{xy} usually acts as a stabilizing force. As for the values, C_{xx} is larger.
- (8) The preswirl velocity has no effect on M_{xx} , C_{xx} , or C_{xy} ; however, it affects the stiffness coefficients K_{xx} and K_{xy} greatly, especially K_{xy} .

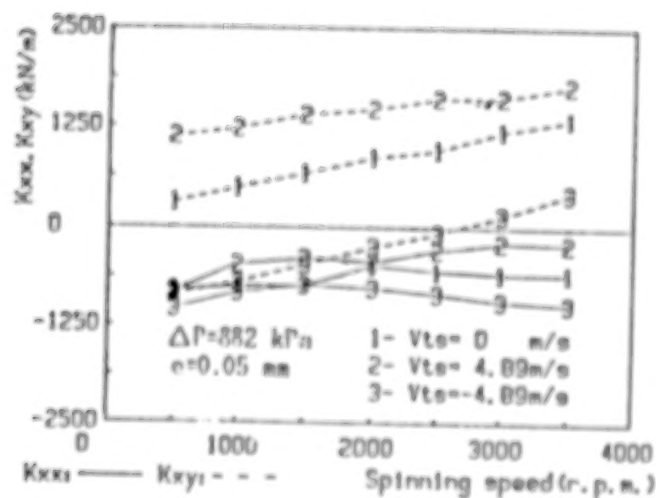
The financial support of Grant-in-Aid for Scientific Research B, Ministry of Education, and also Aero-Engine and Space Operation, Ishikawajima-Harima Heavy Industries Co. Ltd. is gratefully acknowledged. The authors wish further to thank Dr. S. Saito for his kind suggestions for this research.



(a) Inertia coefficient

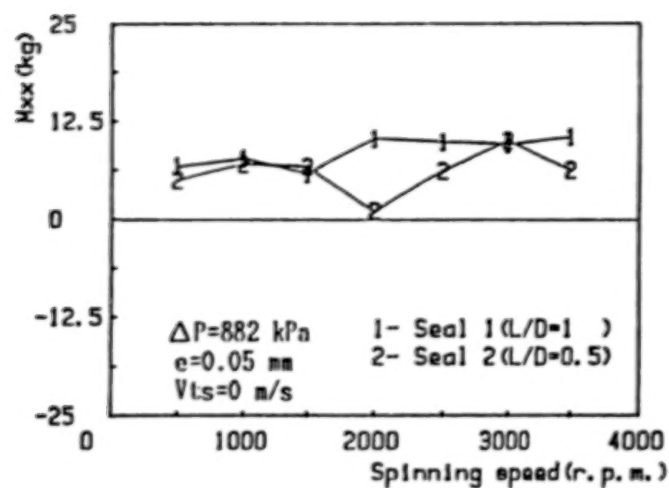


(b) Damping coefficient

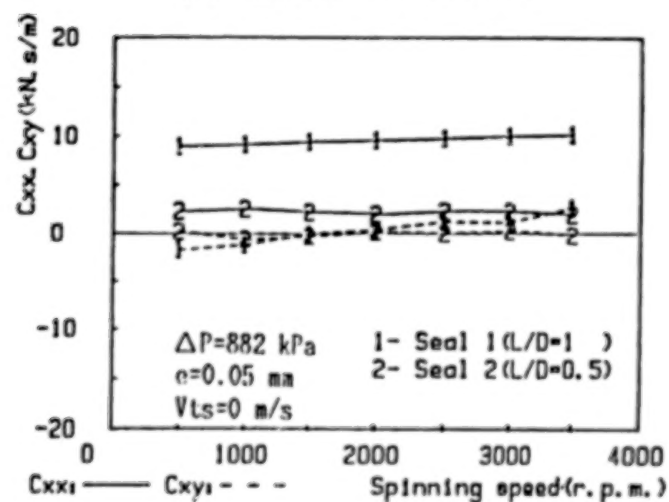


(c) Stiffness coefficient

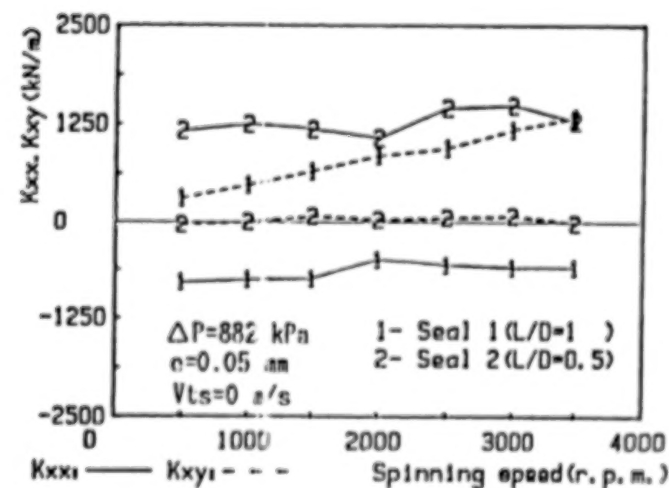
Fig.23. Effect of swirling velocity on characteristic coefficients



(a) Inertia coefficient



(b) Damping coefficient



(c) Stiffness coefficient

Fig.24. Effect of seal length on characteristic coefficients

References

1. Black, H.F., Calculation of Forced Whirling and Stability of Centrifugal Pump Rotor System. Trans. ASME J. Eng. Ind. (1974) 1076.
2. Childs, D.W., and Kim, C.H., Analysis and Testing for Rotordynamic Coefficient of Turbulent Annular Seal With Different, Directionally Homogeneous Surface-Roughness Treatment for Rotor and Stator Elements. NASA Conf. Pub. (1982) 313.
3. Childs, D.W., Dynamic Analysis of Turbulent Annular Seal Based on Hirs' Lubrication Equation. Trans. ASME No. 82-Lub-41.
4. Nordmann, R., and Massmann, H., Identification of Stiffness, Damping and Mass Coefficients for Annular Seals. I. Mech. E. (1984) 167.
5. Iwatsubo, T., Evaluation of Instability Forces of Labyrinth Seal in Turbine or Compressors. NASA. Conf. Pub. (1980) 139.
6. Yang, B.C., Iwatsubo, T., and Kawai, R., A study on the Dynamic Characteristics of Pump Seal. (1st Report, In Case of Annular Seal with Eccentricity) Trans. JSME, Vol. 49, No. 445. (1983) 1636.
7. Kaneko, H., Iino, T., and Takagi, M., An Experimental Research on Dynamic Characteristics of Annular Pump Seals. (1st Report, Dynamic Characteristics in Case of Concentricity) Proc. JSME, No. 820-3 (1982) 25.
8. Kanki, H., and Kawakami, T., Experimental Study on the Dynamic Characteristics of Pump Annular Seals. I. Mech. E. (1984) 159.
9. Kaneko, S., Hori, Y., and Tanaka, M., Static and Dynamic Characteristics of Annular Plain Seals, I. Mech. E. (1984) 205.
10. Kanemori, Y., and Iwatsubo, T., Experimental Study of Dynamic Characteristics of Long Annular Seal. Proc. 2nd China-Japan Joint Conf., Xi-an (1987) 143.

BLANK PAGE

A SEAL TEST FACILITY FOR THE MEASUREMENT OF ISOTROPIC AND ANISOTROPIC LINEAR ROTORDYNAMIC CHARACTERISTICS

M.L. Adams and T. Yang
Case Western Reserve University
Cleveland, Ohio 44106, U.S.A.

S.E. Pace
Electric Power Research Institute
Palo Alto, California 94304, U.S.A.

A new seal test facility for measuring high-pressure seal rotordynamic characteristics has recently been made operational at Case Western Reserve University (CWRU). This work is being sponsored by the Electric Power Research Institute (EPRI). The fundamental concept embodied in this test apparatus is a double-spool-shaft spindle which permits independent control over the spin speed and the frequency of an adjustable circular vibration orbit for both forward and backward whirl. Also, the static eccentricity between the rotating and non-rotating test seal parts is easily adjustable to desired values. By accurately measuring both dynamic radial displacement and dynamic radial force signals, over a wide range of circular orbit frequency, one is able to solve for the "full" linear-anisotropic model's 12 coefficients rather than the 6 coefficients of the more restrictive isotropic linear model. Of course, one may also impose the isotropic assumption in reducing test data, thereby providing a valid qualification of which seal configurations are well represented by the isotropic model and which are not. In fact, as argued in reference [1], the requirement for maintaining a symmetric total system mass matrix means that the resulting isotropic model needs 5 coefficients and the anisotropic model needs 11 coefficients.

INTRODUCTION

The new test facility described in this paper was born out of an earlier test apparatus described in reference [2]. The earlier apparatus, while conceived and designed by the first author of this paper, was assembled by a third party in their commercial test laboratory (herein called Laboratory "X"). Basically, Laboratory "X" spent all the funds allocated for the assembly, debugging and test work without ever getting beyond the debug stage. EPRI then terminated funding this Laboratory "X" work and the hardware remnants of this unsuccessful effort remained in dormant storage at Laboratory "X" for about two years, until it was transported to CWRU in late 1985. Since then, two years have been spent redesigning certain critical portions

of the apparatus and building the new facility at CWRU. In early 1988, the test facility was ready for full system testing and the results demonstrated that the facility was capable of providing reliable test results. Consequently, this work is now moving into its next phase, i.e., testing several different seal geometries and configurations for applications in power plant centrifugal pumps. Specifically, interstage sealing annulus geometries with improved wear-resistant damping characteristics will be sought and rotordynamically quantified using this new test facility. The main body of this paper contains a brief description of the test facility, details of design changes and samples of the first group of results.

SYMBOLS

$[C_{ij}]$	damping coefficient matrix
$[D_{ij}]$	inertia coefficient matrix
$\{F_j\}$	single peak amplitudes of measured-force fundamental component
$\{f_j\}$	interactive dynamic force
R	vibration orbit radius
$[K_{ij}]$	stiffness coefficient matrix
$\{\theta_j\}$	phase angles of measured-force fundamental component
Ω	vibration orbit frequency

THE ISOTROPIC VERSUS THE ANISOTROPIC MODEL

$$\begin{Bmatrix} f_x \\ f_y \end{Bmatrix} = - \begin{bmatrix} K & k \\ -k & K \end{bmatrix} \begin{Bmatrix} x \\ y \end{Bmatrix} - \begin{bmatrix} C & c \\ -c & C \end{bmatrix} \begin{Bmatrix} \dot{x} \\ \dot{y} \end{Bmatrix} - \begin{bmatrix} D & d \\ -d & D \end{bmatrix} \begin{Bmatrix} \ddot{x} \\ \ddot{y} \end{Bmatrix} \quad (1)$$

The isotropic model, equation (1), is now commonly used for seals for two apparent reasons. First, the isotropic model lends itself to test apparatus configurations which have already been successfully demonstrated to provide usable engineering inputs to rotor vibration analyses, e.g., the various published results of Childs, Nordmann and others. Second, the isotropic model is probably a reasonable engineering assumption for deep groove seal configurations and situations where the rotor-to-seal concentricity is accurately controlled by the bearings and other factors such as manufacturing/assembly tolerances and maintenance of highly axisymmetric temperature gradients within the overall machine and axisymmetric seal inlet pre-swirl velocity distribution.

Conversely, in dealing with the rotordynamic characteristics of fluid-film journal bearings, the strong anisotropic property stemming from journal-to-bearing eccentricity and from non-axisymmetric geometric properties has long been recognized. One might therefore expect that the more a seal resembles a journal bearing (i.e., smooth without serrations or grooves), the worse is the isotropic model approximation, and vice versa. In fact, the recently published results of Kanki and Kawakami [3] support this hypothesis. Their experimental results show a strong anisotropic effect of static eccentricity on the rotordynamic coefficients of a smooth (no grooves) seal and an almost negligible anisotropic effect of static eccentricity on the rotordynamic coefficients of a circumferentially screw-grooved seal.

The anisotropic linear model can be expressed as follows.

$$\begin{Bmatrix} f_x \\ f_y \end{Bmatrix} = - \begin{bmatrix} K_{xx} & K_{xy} \\ K_{yx} & K_{yy} \end{bmatrix} \begin{Bmatrix} x \\ y \end{Bmatrix} - \begin{bmatrix} C_{xx} & C_{xy} \\ C_{yx} & C_{yy} \end{bmatrix} \begin{Bmatrix} \dot{x} \\ \dot{y} \end{Bmatrix} - \begin{bmatrix} D_{xx} & D_{xy} \\ D_{yx} & D_{yy} \end{bmatrix} \begin{Bmatrix} \ddot{x} \\ \ddot{y} \end{Bmatrix} \quad (2)$$

Based on arguments made in reference [1], the seal inertia matrix should be symmetric, and this translates into $d \equiv 0$ in equation (1) and $D_{xy} \equiv D_{yx}$ in equation (2).

Most of the currently operational test rigs for experimental determination of seal rotordynamic characteristics are configured to extract only the isotropic model coefficients and are correspondingly not capable of quantifying how good is the isotropic assumption for any particular seal tested, except indirectly by computing the dynamic force signals from the extracted coefficients and comparing these with the measured dynamic force signals.

To extract all the coefficients of the anisotropic model requires not only independent control over spin speed and vibration orbit frequency, but also requires a significantly two-dimensional orbit. Thus, a synchronous orbit test can not provide the necessary data to extract the anisotropic-model coefficients. Also, even with independent control over spin speed and orbit frequency, a straight-line oscillatory orbit can not provide the necessary data to extract the anisotropic-model coefficients.

It would appear that the optimum orbit to make these measurements is a circular or nearly circular orbit. The new CWRU/EPRI test apparatus described herein utilizes an independently controlled frequency and adjustable magnitude circular orbit.

DESCRIPTION OF TEST FACILITY

Overview

Various aspects of the test facility are shown in Figures 1 through 8. The conceptual schematic of the test rig spindle and seal differential pressure chamber are shown in Figure 1(a) and a layout of the original configuration, as it was first designed and built, is shown in Figure 1(b). Figure 2 shows the floor plan and elevation views of the complete test facility and Figure 3 shows the schematic of the data acquisition system. Figure 4 shows a more detailed flow chart of the data acquisition system and data reduction steps. Both the clock and trigger for the A/D conversion is external to the PC microprocessor. A 360 slot disk rotates with the orbit-frequency shaft and is used in conjunction with a fast acting optical switch to sequentially fire all data channels.

Modifications to Original Configuration

After considerable critiquing of the original test rig, two factors became obvious. First, the links for connecting the test-seal ring to the piezoelectric load measuring transducers did not sufficiently guarantee adequate axial play to insure that the hydrostatic thrust bearing maintained a non-contacting axial load support. Second, the design of the piezoelectric load measuring system relied on the concept that the primary load path (through the piezoelectric load cells) was orders of magnitude stiffer than the parallel load path through the static seals (O-rings). After extensive thought at separate solutions to these two problems, a single design solution emerged which addressed both of these problems. This design evolution is shown in Figures 5 through 8.

This final configuration has shown itself to work to the maximum satisfaction. It contains four connecting links which are relatively flexible in the axial and tangential directions but relatively quite stiff in the radial direction. The axial flexibility permits the hydrostatic thrust bearing to function as intended. The tangential flexibility nearly eliminates measurable cross-talk between the two mutually perpendicular load measuring axes. The high radial stiffness maintains the stiff load-path concept of the original design, embodying very stiff piezoelectric load cells. Finally, by making these four support links each a strain gaged transducer, they provide a second and independent measurement system for the dynamic force signals. Thus, the accuracy of the dynamic force measurements can be confirmed independently, provided both force measuring systems are simultaneously working as intended. In effect, with independent dual force measuring systems, a very high degree of confidence is possible because the dual measurements are self checking. Furthermore, the addition of strain-gaged transducers permits measurement of the static radial force, which was not part of the original test rig capability.

In-Place Force System Calibrations

A linkage has been designed which attaches to the exposed closure bolt circle when the front closure head is removed. It allows a known force to be applied directly to the test seal ring, in any of the multitude of radial directions of the bolt circle holes. A schematic of this calibration system is shown in Figure 9. Both force measuring systems are simultaneously calibrated with this setup. It is quite easy and quick to use, thus allowing frequent recalibration, such as at the beginning and end of each test sequence, if desired. Actually, both force measuring systems are quite stable and do not require such frequent recalibration.

FIRST TEST RESULTS OBTAINED (JANUARY 1988)

Figures 10 through 13 show typical measurement output samples. Figure 10 shows a cycle of force output, time averaged over only two cycles, whereas Figure 11 shows the same case time averaged over 20 cycles. Figures 10 through 12 are from the F_x load axis piezoelectric measurements. Figure 12 shows the fundamental Fourier series component (i.e., Ω), which is the portion of the signal that is utilized in extraction of the rotordynamic coefficients. Figure 13 shows a superposition of the same F_x signal fundamental component extracted simultaneously from the independent strain-gage system and the piezoelectric system.

In making the comparison of signals shown in Figure 13, it is important to know that the seal tested was a deep groove labyrinth configuration with only a 50 psi pressure drop through it. Also, it was a concentric orbit, i.e., nominally a zero static eccentricity. The dynamic eccentricity (orbit radius) was only 1.3 mils. Consequently, the force signals were quite small (10 lb. maximum) which was intentionally devised in order to subject the two independent force measuring systems to a most stringent comparison test. With the present load measuring links, the peak dynamic load capability is approximately 700 lbs, being set by the strain-gaged links' strength limitation. The Kistler piezoelectric system has a much higher maximum load limitation. We believe these results indicate that the test rig is capable of making reliable measurements of rotordynamic characteristics.

Table 1 summarizes the data-reduction simultaneous equations for a circular orbit. Table 2 shows a sample of reduced data, comparing the two sets of rotordynamic coefficients derived from the two independent force measuring systems. It is important to bear in mind when evaluating these initial results that the dynamic forces were quite small.

CONCLUDING REMARKS

The CWRU/EPRI seal rotordynamic test facility described in this paper is now operational and all indications are that it provides reliable test data. It provides the anisotropic coefficients and thus provides a valid qualification on the validity of the isotropic model for any seal tested. The addition of a strain-gage based back-up force measuring system provides independent self-checking capability and the additional feature of measuring the static load components in addition to the dynamic load signals. Also, the adjustable static eccentricity and dynamic eccentricity (0 to 0.060 inches) allows testing to determine limits of the linear model's validity as vibration orbit magnitude is increased. Furthermore, in addition to making accurate determination of seal rotodynamic coefficients, this facility will be used to make fundamental investigations into the validity of the basic mechanical impedance hypothesis as it is now taken for granted by most investigators. These are fundamental investigations related to topics recently reviewed in reference [1].

REFERENCES

1. Adams, M.L.: Insights Into Linearized Rotor Dynamics, Part 2. Journal of Sound and Vibration, Vol. 112(1), 1987, pp. 97-110.
2. Adams, M.L. and Makay, E.: Development of Advanced Rotor-Bearing Systems for Feedwater Pumps - Phase III: Hardware Design and Fabrication. EPRI Final Report CS-3203, July 1983.
3. Kanki, H. and Kawakami, T.: Experimental Study on the Static and Dynamic Characteristics of Screw Grooved Seals. Proceedings, ASME Rotating Machinery Dynamics papers, ASME 11th Biennial Conference on Mechanical Vibration and Noise, Boston, Sept. 27-30, 1987, DE-Vol. 2, pp. 273-278.

$$(F_x \cos \theta_r) / R = -K_{xx} - \Omega_j C_{xy} + \Omega_j^2 D_{xx}$$

$$(F_x \sin \theta_r) / R = K_{xy} - \Omega_j C_{xx} - \Omega_j^2 D_{xy}$$

$$(F_y \cos \theta_r) / R = -K_{yy} - \Omega_j C_{ry} + \Omega_j^2 D_{yy}$$

$$(F_y \sin \theta_r) / R = K_{ry} - \Omega_j C_{yx} - \Omega_j^2 D_{ry}$$

$$J = 1, 2, 3$$

Table 1. Simultaneous coefficient-extraction equations for a circular orbit.

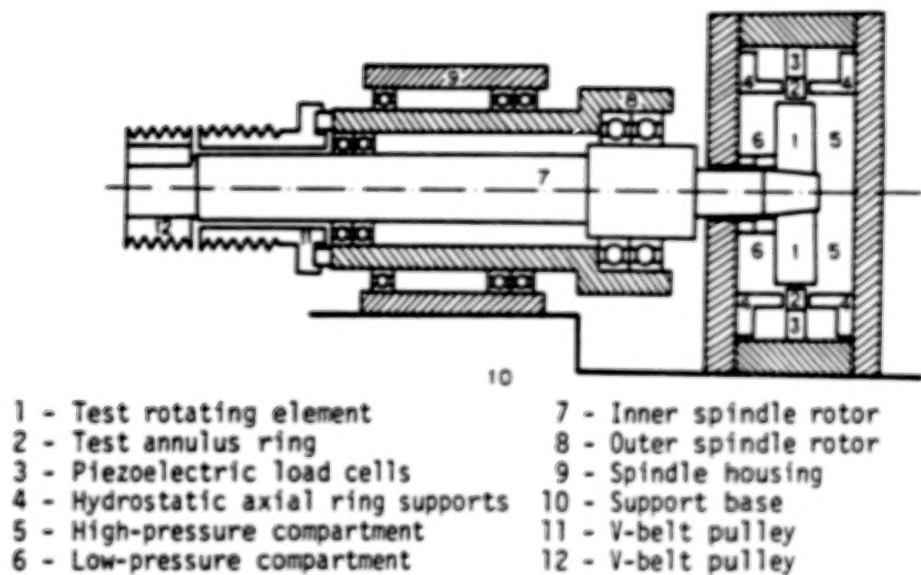
Kk	LB/INCH		Kb	LB/INCH	
[2878	1838	[2106	1954
	-2351	2654		-2172	1870
]					
Ck	LB*SEC/INCH		Cb	LB*SEC/INCH	
[67.51	11.93	[57.42	16.34
	-10.87	76.35		-9.480	66.45
]					
Dk	LB*SEC*SEC/INCH		Db	LB*SEC*SEC/LB	
[4.941E-2	-1.055E-1	[5.523E-2	-9.479E-2
	1.332E-1	3.948E-2		1.213E-1	3.788E-2
]					

SHAFT SPEED = 1500 RPM

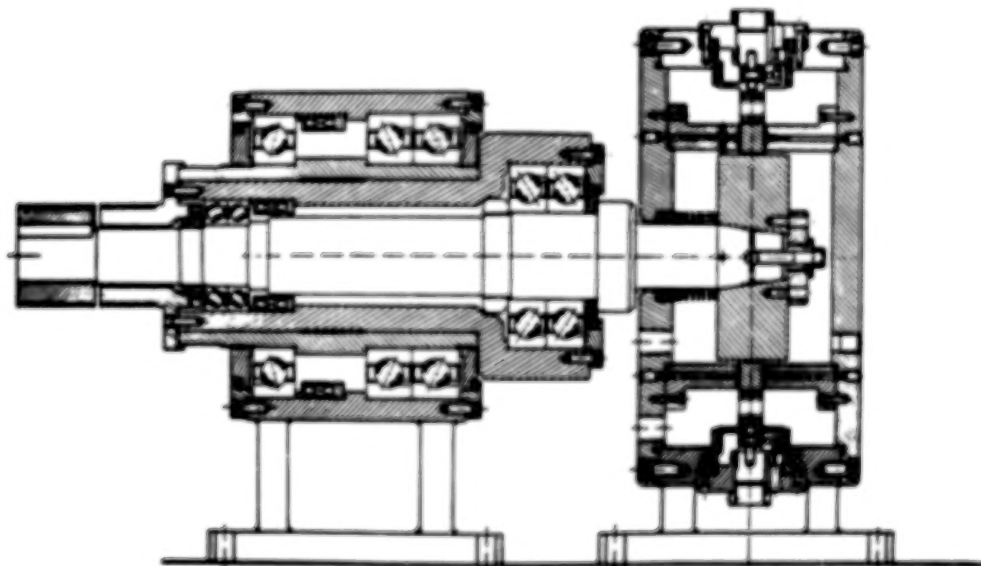
ORBIT FREQ. = 676, 1446, 1952 RPM

ORBIT RADIUS = 1.40 MIL

Table 2. Sample rotordynamic coefficients, comparing results from piezoelectric measurements with results from strain gage measurements.



1(a) Conceptual Sketch of Rotor Support Component Test Apparatus



1(b) Assembly Layout of Rotor Support Component Test Apparatus

Figure 1. Test Apparatus, Reference (3)

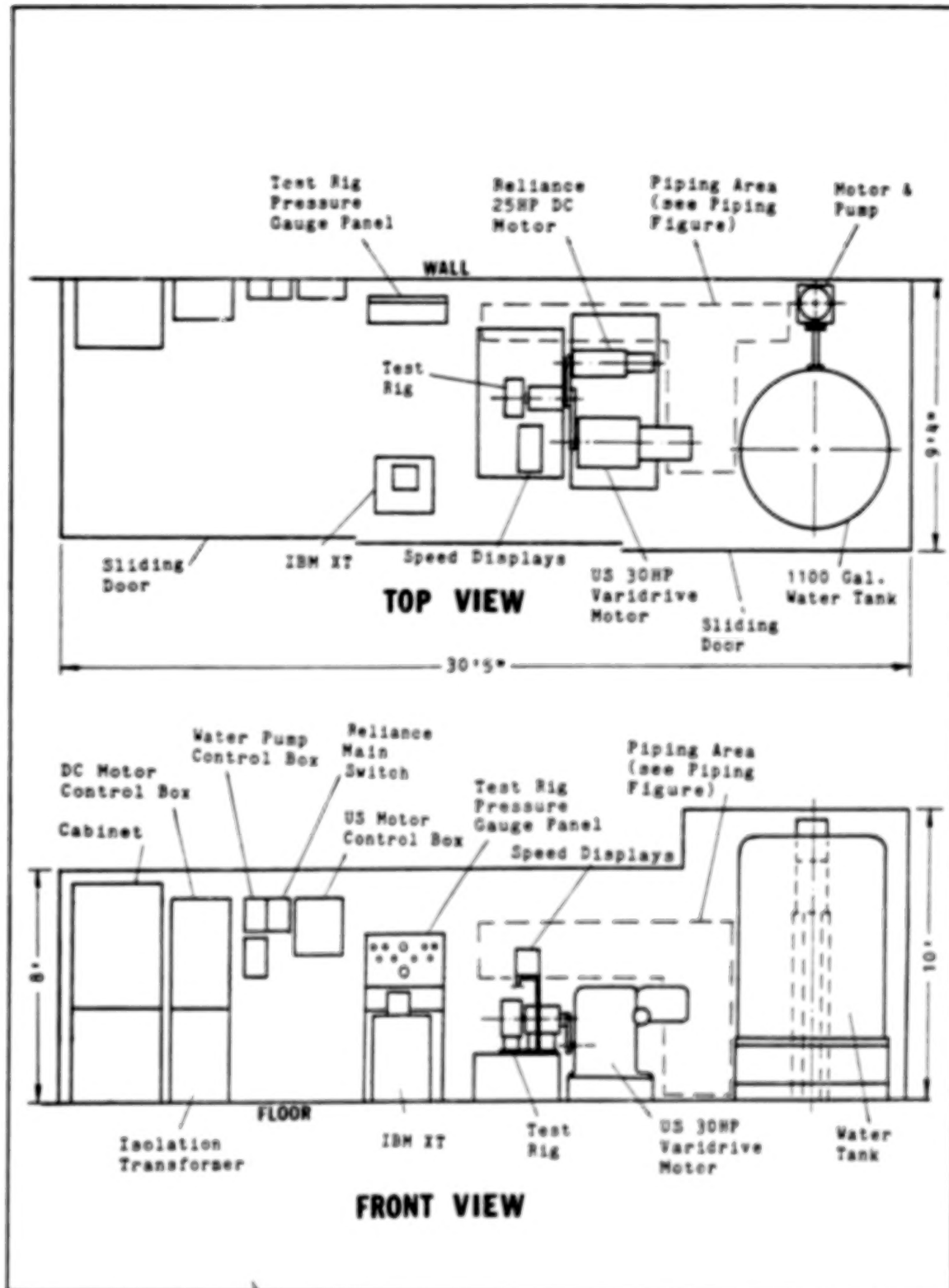


Fig. 2. Floor plan and elevation view of test facility.

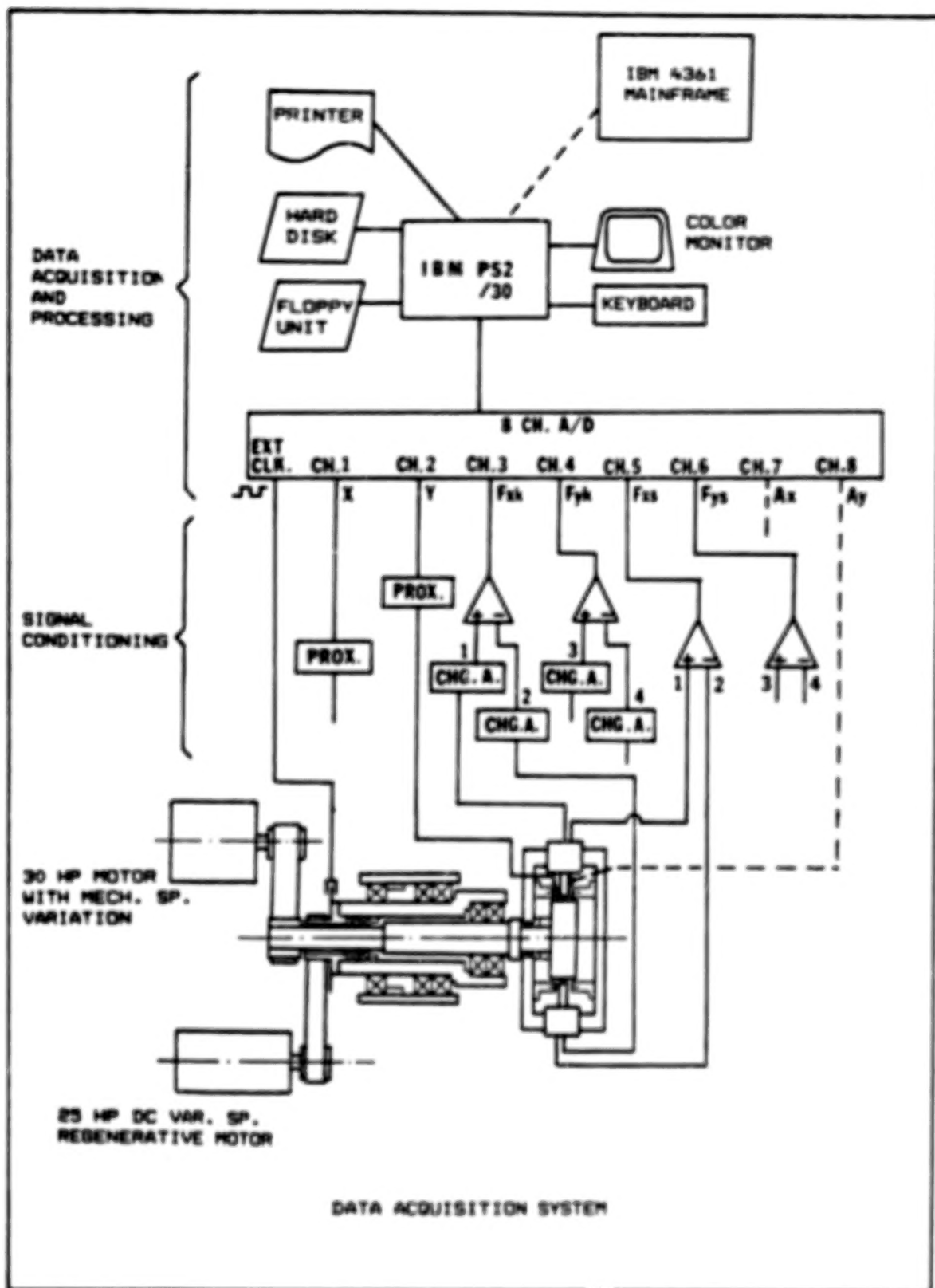


Fig. 3. Schematic of data acquisition system.

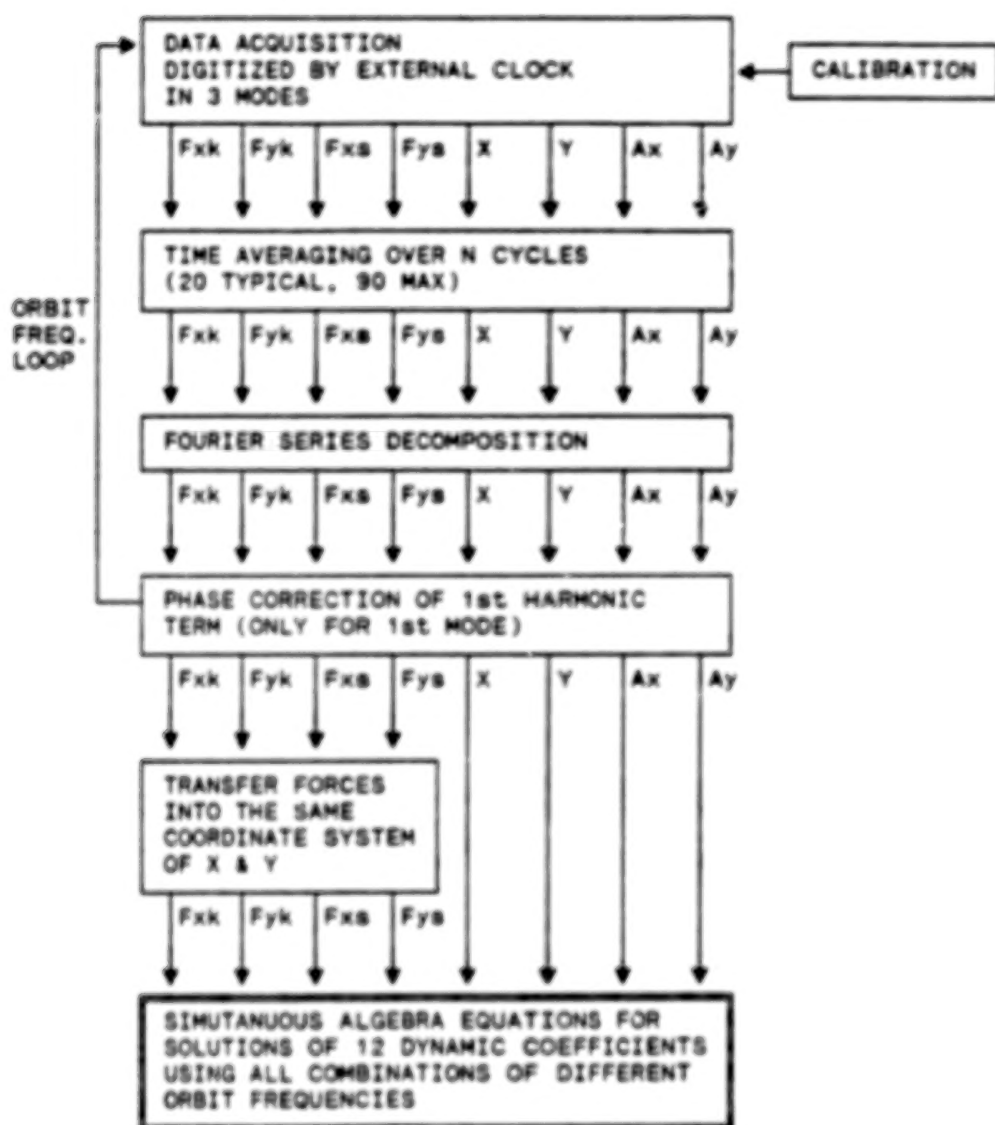


Fig. 4. Data acquisition and analysis overview.

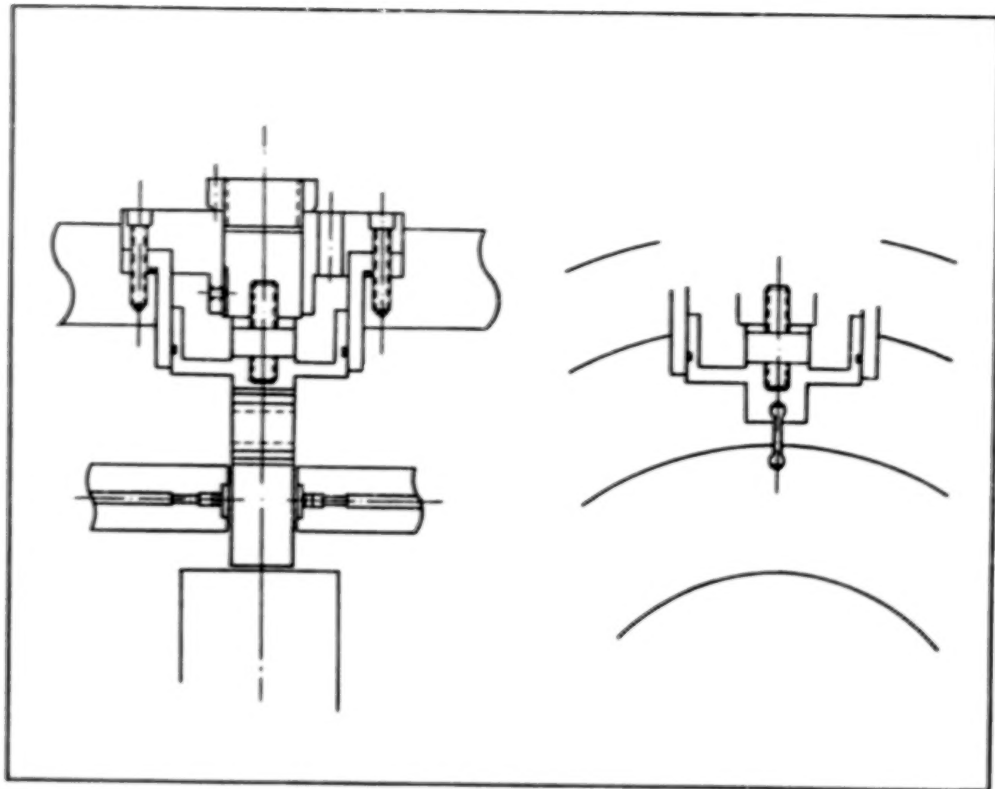


Fig. 5. Original load measuring and support system.

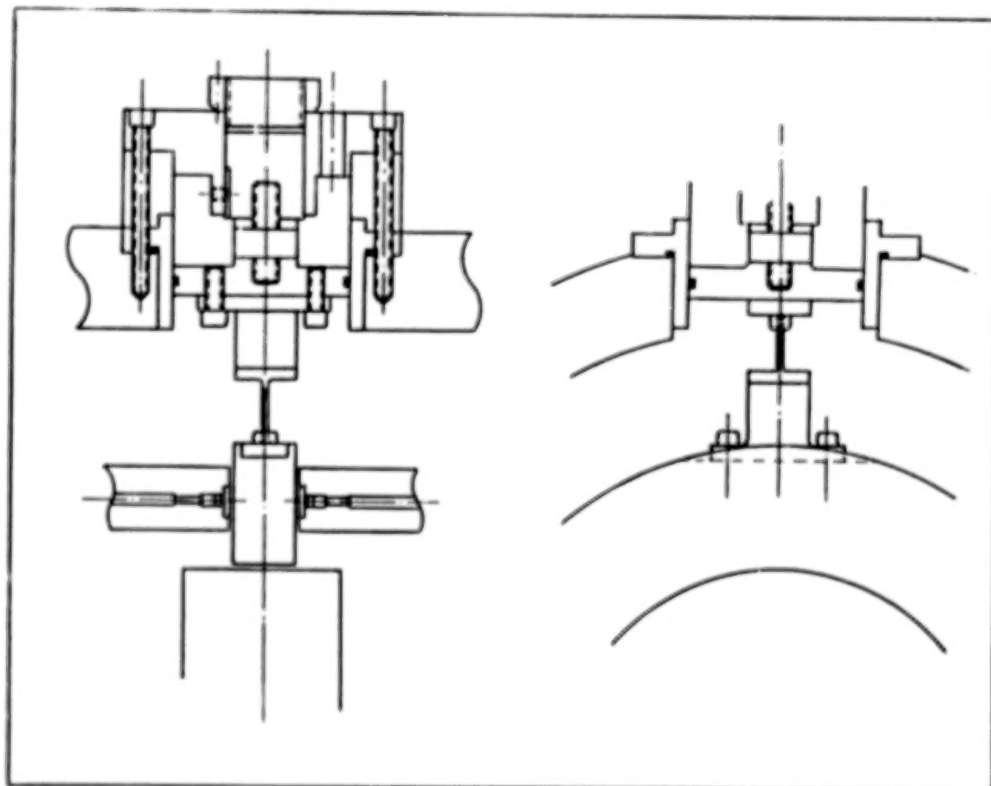


Fig. 6. New load measuring and support system.

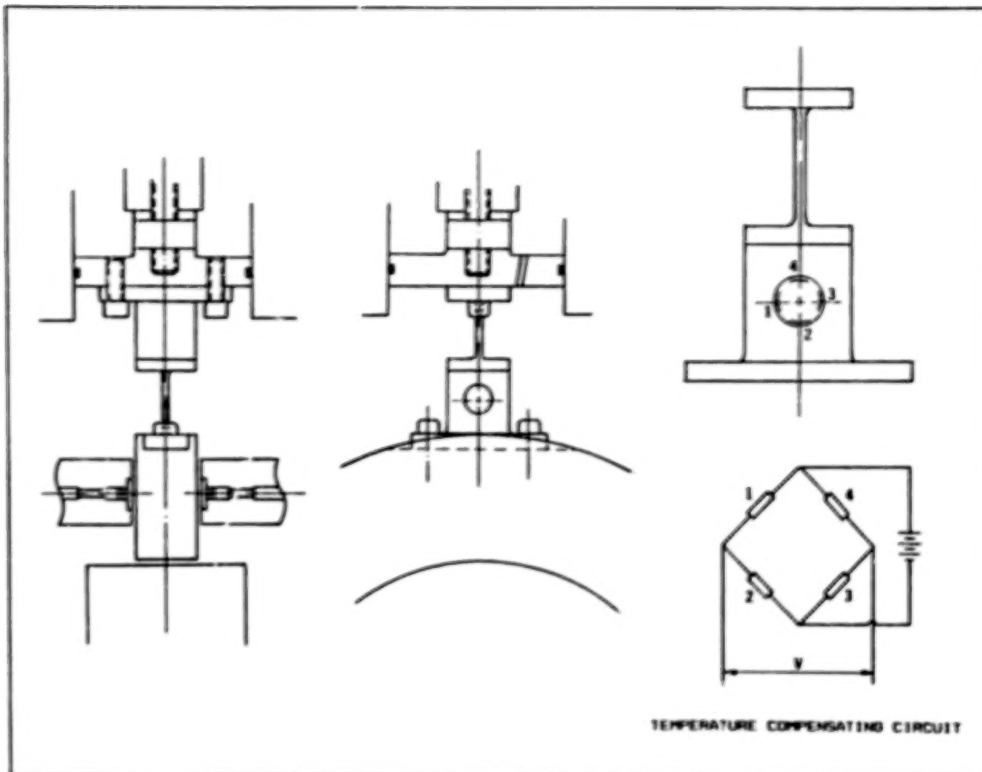


Fig. 7. New load measuring and support system with strain gage transducer.

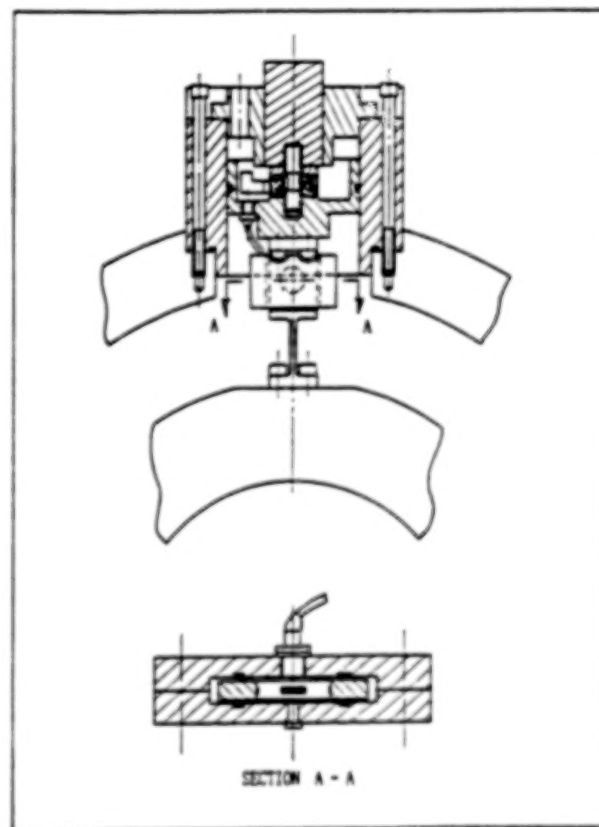


Fig. 8. New load measuring system, showing complete assembly with water-seal barrier.

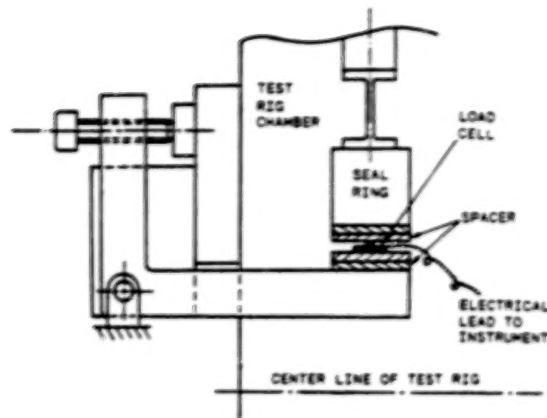


Fig. 9. In-place load calibration system.

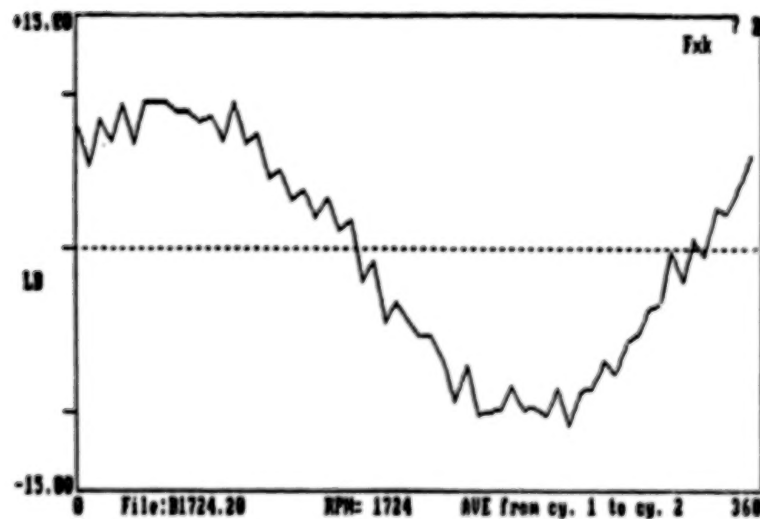


Fig. 10. Sample measurement, time averaged over 2 cycles.

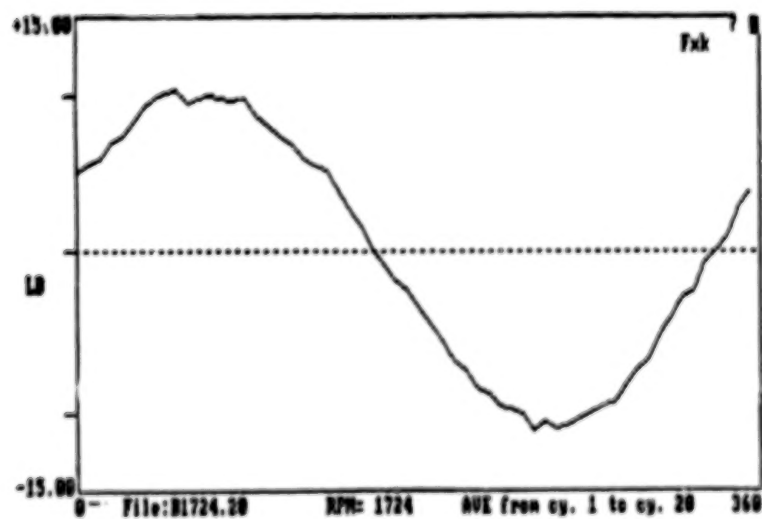


Fig. 11. Sample as in Figure 10, but time averaged over 20 cycles.

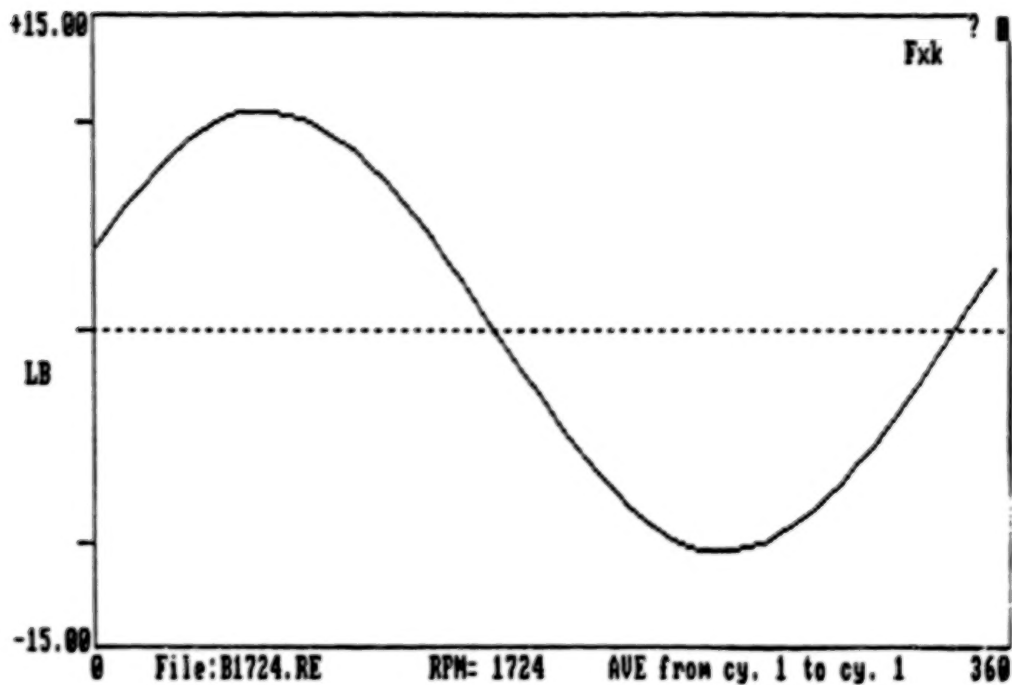


Fig. 12. The fundamental (Ω) frequency component from time-averaged signal given in Figure 11.

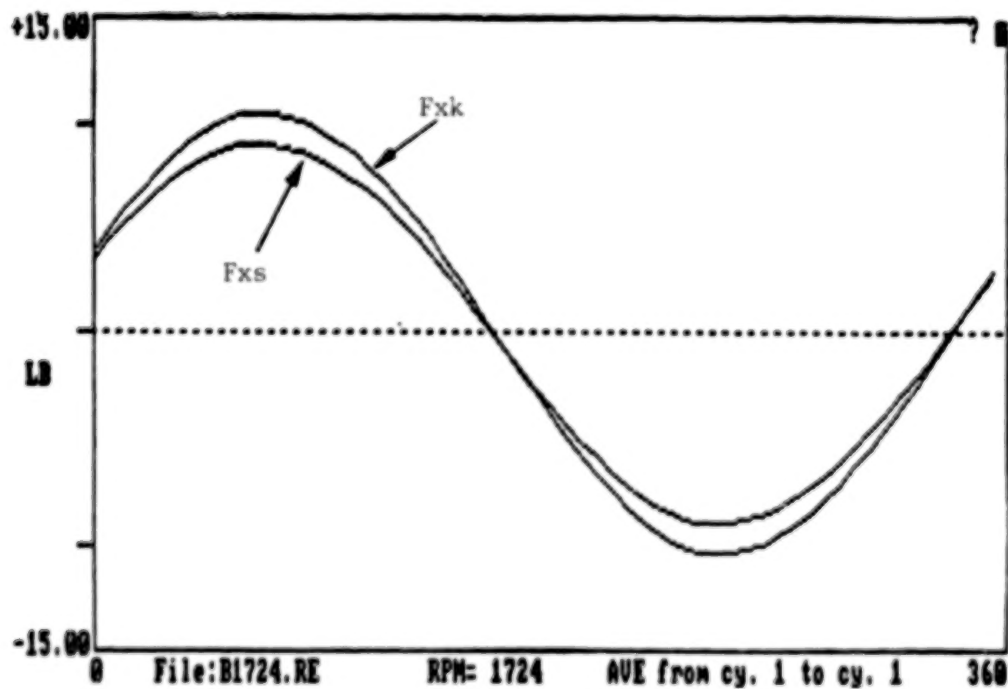


Fig. 13. Comparison of fundamental (Ω) frequency component measured simultaneously with both force measuring systems.

BLANK PAGE

FINITE DIFFERENCE ANALYSIS OF ROTORDYNAMIC SEAL COEFFICIENTS FOR AN ECCENTRIC SHAFT POSITION

R. Nordmann and F.J. Dietzen
Department of Mechanical Engineering
University of Kaiserslautern
Kaiserslautern, Federal Republic of Germany

The dynamic coefficients of seals are calculated for shaft movements around an eccentric position. The turbulent flow is described by the Navier-Stokes equations in connection with a turbulence model. The equations are solved by a finite-difference procedure.

INTRODUCTION

To model the dynamic behaviour of turbopumps properly it is very important to consider the fluid forces which are developed in the seals. This has been clearly demonstrated by some authors, like for example Diwald (1987). The fluid forces are normally described by the following equation.

$$-\begin{bmatrix} F_z \\ F_y \end{bmatrix} = \begin{bmatrix} K & k \\ -k & K \end{bmatrix} \begin{bmatrix} z \\ y \end{bmatrix} + \begin{bmatrix} D & d \\ -d & D \end{bmatrix} \begin{bmatrix} \dot{z} \\ \dot{y} \end{bmatrix} + \begin{bmatrix} M & 0 \\ 0 & M \end{bmatrix} \begin{bmatrix} \ddot{z} \\ \ddot{y} \end{bmatrix} \quad (1)$$

But this equation is only valid for a shaft moving around the center of the seal, which very seldom occurs in reality. In most machines the shaft will orbit around an eccentric position, so that the fluid forces must be described by

$$-\begin{bmatrix} F_z \\ F_y \end{bmatrix} = \begin{bmatrix} K_{zz} & k_{zy} \\ -k_{yz} & K_{yy} \end{bmatrix} \begin{bmatrix} Z \\ Y \end{bmatrix} + \begin{bmatrix} D_{zz} & d_{zy} \\ -d_{yz} & D_{yy} \end{bmatrix} \begin{bmatrix} \dot{Z} \\ \dot{Y} \end{bmatrix} + \begin{bmatrix} M_{zz} & 0 \\ 0 & M_{yy} \end{bmatrix} \begin{bmatrix} \ddot{Z} \\ \ddot{Y} \end{bmatrix} \quad (2)$$

The dynamic coefficients in such a case have been investigated by Jenssen (1970), Allaire et al. (1976) and recently in an excellent paper by Nelson and Nguyen (1987). To model the turbulent flow, all these have used so called "Bulk-Flow Theories" in which the shear stress at the wall is described as a function of the average fluid velocity relative to the wall. Because some authors affirm that in the case of great eccentricities recirculation in circumferential direction occurs (which can't be described by a bulk-flow model) and strongly effects the dynamic coefficients, we extended the theory of Dietzen and Nordmann (1987) and Nordmann (1987) to investigate the flow and the coefficients in the case of an eccentric shaft. In that theory the Navier Stokes equations in connection with the k-ε turbulence model were used to calculate the dynamic coefficients of incompressible and compressible seals for a shaft motion around the centric position.

GOVERNING EQUATIONS

In a turbulent flow, turbulent stresses occur which are often modeled like laminar stresses by introducing a turbulent viscosity. The turbulent and the laminar viscosity are then added to an effective viscosity.

$$\mu_e = \mu_l + \mu_t \quad (3)$$

The turbulent viscosity must be described by a turbulence model. We use the k-ε model, but also much simpler mixing-length models will be appropriate for a straight seal. The turbulent viscosity is given by

$$\mu_t = C_\mu \rho \frac{k^2}{\epsilon} \quad (4)$$

So we have the Navier-Stokes equations, the continuity equation and the equations of the k-ε model to describe the turbulent flow in a seal. These equations have the following form.

$$\frac{\partial(\rho\phi)}{\partial t} + \frac{\partial}{\partial x}(\rho u\phi) - \frac{\partial}{\partial x}(\Gamma \frac{\partial \phi}{\partial x}) + \frac{1}{r} \frac{\partial}{\partial r}(r \rho v\phi) - \frac{1}{r} \frac{\partial}{\partial r}(r \Gamma \frac{\partial \phi}{\partial r}) + \frac{1}{r} \frac{\partial}{\partial \theta}(\rho w\phi) - \frac{1}{r} \frac{\partial}{\partial \theta}(\Gamma \frac{\partial \phi}{\partial \theta}) = S_\phi \quad (5)$$

ϕ	Γ	S_ϕ
u	μ_e	$-\frac{\partial p}{\partial x} + \frac{\partial}{\partial x}(\mu_e \frac{\partial u}{\partial x}) + \frac{1}{r} \frac{\partial}{\partial r}(r \mu_e \frac{\partial v}{\partial x}) + \frac{1}{r} \frac{\partial}{\partial \theta}(\mu_e \frac{\partial w}{\partial x})$
v	μ_e	$-\frac{\partial p}{\partial r} + \frac{\partial}{\partial x}(\mu_e \frac{\partial u}{\partial r}) + \frac{1}{r} \frac{\partial}{\partial r}(r \mu_e \frac{\partial v}{\partial r}) + \frac{1}{r} \frac{\partial}{\partial \theta}(r \mu_e \frac{\partial}{\partial r}(\frac{w}{r}))$ $-\frac{2}{r^2} \mu_e \frac{\partial w}{\partial \theta} - \frac{2}{r^2} \mu_e v + \frac{\rho}{r} w^2$
w	μ_e	$-\frac{1}{r} \frac{\partial p}{\partial \theta} + \frac{\partial}{\partial x}(\frac{1}{r} \mu_e \frac{\partial u}{\partial \theta}) + \frac{1}{r} \frac{\partial}{\partial r}(\mu_e \frac{\partial v}{\partial \theta}) + \frac{1}{r} \frac{\partial}{\partial \theta}(\frac{1}{r} \mu_e \frac{\partial w}{\partial \theta})$ $+ \frac{1}{r^2} \mu_e \frac{\partial v}{\partial \theta} - \frac{w}{r^2} \frac{\partial}{\partial r}(r \mu_e) + \frac{1}{r} \frac{\partial}{\partial \theta}(\frac{2}{r} \mu_e v) - \frac{\rho}{r} v w$
1	0	0
k	μ_e / σ_k	$G - \rho \epsilon$
ε	μ_e / σ_ϵ	$C_1 \frac{\epsilon}{k} G - C_2 \rho \frac{\epsilon^2}{k}$

Table 1: The governing equations of the turbulent seal flow.

(The constants of the k-ε model are given in appendix A)

PERTURBATION ANALYSIS

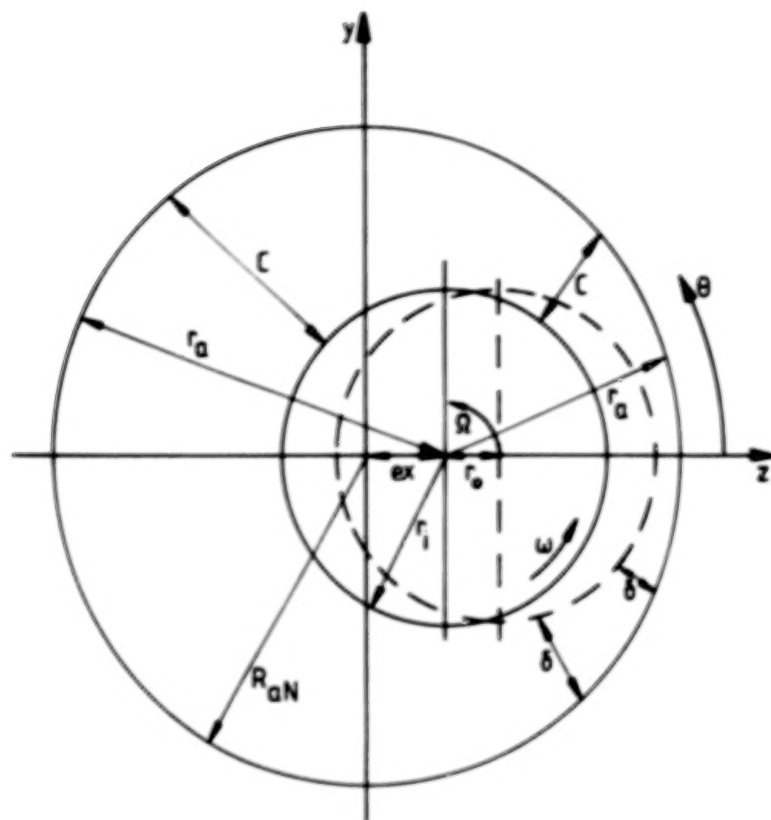


Fig. 1 Geometry of the eccentric shaft

To describe the flow if the shaft is moving around an eccentric position we follow the procedure of Dietzen and Nordmann (1987) and use a similar transformation. (see Fig. 1)

$$\eta = r_a(\theta) - \frac{r_a(\theta) - r}{\delta(\theta, t)} C_0(\theta) \quad (6)$$

But now r_a and C_0 are functions of θ . This is not so if the shaft moves around the center. δ is the seal clearance, varying with angle θ and time t .

The radius r_a can be described by the following equation:

$$r_a(\theta) = \sqrt{R_{aN}^2 - ex^2 \sin^2(\theta)} - ex \cos(\theta) \quad (7)$$

As result of this transformation the shaft orbiting around an eccentric position is transformed to the stationary eccentric position.

If we introduce this transformation into our equations, we must obey the following relations.

$$\left(\frac{\partial}{\partial \theta}\right)_r = \left(\frac{\partial}{\partial \theta}\right)_\eta + \left(\frac{\partial}{\partial \eta}\right)_\theta \left(\frac{\partial \eta}{\partial \theta}\right)_r \quad \left(\frac{\partial}{\partial t}\right)_r = \left(\frac{\partial}{\partial t}\right)_\eta + \left(\frac{\partial}{\partial \eta}\right)_t \left(\frac{\partial \eta}{\partial t}\right)_r \quad (8)$$

To calculate the rotordynamic coefficients we assume that the shaft moves around the eccentric position on small orbits, so that we are allowed to introduce a perturbation analysis.

$$\begin{aligned} \delta &= C_0 - eh_1 & u &= u_0 + eu_1 & v &= v_0 + ev_1 \\ w &= w_0 + ew_1 & p &= p_0 + ep_1 \end{aligned} \quad (9)$$

If we introduce these expressions and the coordinate transformation in our governing equation, neglecting terms with power of e greater than 1 and separating the parts with and without e we will get a set of zeroth order and first order equations. The zeroth order equations describe the stationary flow for the eccentric shaft, the first order equations the perturbation of this flow, if the shaft moves around the stationary position.

We assume that the shaft moves with the precession frequency Ω on a circular orbit with radius r_0 around the eccentric position. So the change of the clearance is given by

$$eh_1 = r_0(\cos\Omega t \cos\theta + \sin\Omega t \sin\theta) \quad (10)$$

Because this change is periodic in time we introduce also periodic functions for the flow variables.

$$\begin{aligned} u_1 &= u_{1c} \cos\Omega t + u_{1s} \sin\Omega t & v_1 &= v_{1c} \cos\Omega t + v_{1s} \sin\Omega t \\ w_1 &= w_{1c} \cos\Omega t + w_{1s} \sin\Omega t & p_1 &= p_{1c} \cos\Omega t + p_{1s} \sin\Omega t \end{aligned} \quad (11)$$

By separating now in the first order equations the terms with $\cos\Omega t$ and $\sin\Omega t$ we obtain two real equations for every first order equation. These equations are then arranged in a new form by introducing complex variables.

$$\begin{aligned} \hat{u}_1 &= u_{1c} + iu_{1s} & \hat{v}_1 &= v_{1c} + iv_{1s} \\ \hat{w}_1 &= w_{1c} + iw_{1s} & \hat{p}_1 &= p_{1c} + ip_{1s} \end{aligned} \quad (12)$$

Finally supplementary to our real zeroth order equations we have a set of complex first order equations. These equations have the following form.

$$\frac{\partial}{\partial x}(\rho u_0 \hat{\phi}) - \frac{\partial}{\partial x}(r \frac{\partial \hat{\phi}}{\partial x}) + \frac{1}{\eta} \frac{\partial}{\partial \eta}(\eta \rho v_0 \hat{\phi}) - \frac{1}{\eta} \frac{\partial}{\partial \eta}(\eta r \frac{\partial \hat{\phi}}{\partial \eta}) + \frac{1}{\eta} \frac{\partial}{\partial \theta}(\rho w_0 \hat{\phi}) - \frac{1}{\eta} \frac{\partial}{\partial \theta}(r \frac{\partial \hat{\phi}}{\partial \theta}) = S_{\hat{\phi}} \quad (13)$$

ϕ	Γ_ϕ	S_ϕ
u_0	μ_e	S_{u_0}
v_0	μ_e	S_{v_0}
w_0	μ_e	S_{w_0}
1	0	0
k_0	μ_e/σ_k	S_{k_0}
ϵ_0	μ_e/σ_ϵ	S_{ϵ_0}
\hat{u}_1	μ_e	$-\frac{\partial \hat{p}_1}{\partial x} + \frac{\partial}{\partial x}(\mu_e \frac{\partial \hat{u}_1}{\partial x}) + \frac{1}{\eta} \frac{\partial}{\partial \eta}(\eta \mu_e \frac{\partial \hat{v}_1}{\partial x}) + \frac{1}{\eta} \frac{\partial}{\partial \theta}(\mu_e \frac{\partial \hat{w}_1}{\partial x})$ $- C_{u_1} + i\rho\Omega \hat{u}_1 + D_{u_0}$
\hat{v}_1	μ_e	$-\frac{\partial \hat{p}_1}{\partial \eta} + \frac{\partial}{\partial x}(\mu_e \frac{\partial \hat{u}_1}{\partial \eta}) + \frac{1}{\eta} \frac{\partial}{\partial \eta}(\eta \mu_e \frac{\partial \hat{v}_1}{\partial \eta})$ $+ \frac{1}{\eta} \frac{\partial}{\partial \theta}(\eta \mu_e \frac{\partial \hat{w}_1}{\partial \eta}) - \frac{2}{\eta^2} \mu_e \frac{\partial \hat{w}_1}{\partial \theta} - \frac{2}{\eta^2} \mu_e \hat{v}_1 + \frac{\rho}{\eta} w_0 \hat{w}_1$ $- C_{v_1} + i\rho\Omega \hat{v}_1 + D_{v_0}$
\hat{w}_1	μ_e	$-\frac{1}{\eta} \frac{\partial \hat{p}_1}{\partial \theta} + \frac{\partial}{\partial x}(\frac{1}{\eta} \mu_e \frac{\partial \hat{u}_1}{\partial \theta}) + \frac{1}{\eta} \frac{\partial}{\partial \eta}(\mu_e \frac{\partial \hat{v}_1}{\partial \theta}) + \frac{1}{\eta} \frac{\partial}{\partial \theta}(\frac{1}{\eta} \mu_e \frac{\partial \hat{w}_1}{\partial \theta})$ $+ \frac{1}{\eta^2} \mu_e \frac{\partial \hat{v}_1}{\partial \theta} - \frac{\hat{w}_1}{\eta^2} \frac{\partial}{\partial \eta}(\eta \mu_e) + \frac{1}{\eta} \frac{\partial}{\partial \theta}(\frac{2}{\eta} \mu_e \hat{v}_1) - \frac{\rho}{\eta} v_0 \hat{w}_1$ $- C_{w_1} + i\rho\Omega \hat{w}_1 + D_{w_0}$

Table 2: Source terms of zeroth and first order equations.

Only the first order continuity equation to calculate \hat{p}_1 has a slightly different form.

$$\frac{\partial}{\partial x}(\rho \hat{u}_1) + \frac{1}{\eta} \frac{\partial}{\partial \eta}(\eta \rho \hat{v}_1) + \frac{1}{\eta} \frac{\partial}{\partial \theta}(\rho \hat{w}_1) = D_{p_0} \quad (14)$$

You get S_{u_0} , S_{v_0} , S_{w_0} , S_{k_0} , S_{ϵ_0} , if you replace in table 1 in the corresponding terms r by η and u, v, w, p, k, ϵ by $u_0, v_0, w_0, p_0, k_0, \epsilon_0$. The terms C_{u_1} , C_{v_1} , C_{w_1} result from the perturbation of the convective terms in the Navier Stokes equations. D_{u_0} , D_{v_0} , D_{w_0} , D_{p_0} are constants resulting from the coordinate transformation, which are not functions of \hat{u}_1 , \hat{v}_1 , \hat{w}_1 , \hat{p}_1 . The terms with Ω represent the time dependent parts.

Because we assume that the viscosity μ_e remains constant for the small motions, we do not need a \hat{k}_1 and $\hat{\epsilon}_1$ equation.

(D_{u_0} , D_{v_0} , D_{w_0} , D_{p_0} , C_{u_1} , C_{v_1} , C_{w_1} are given in appendix B)

BOUNDARY CONDITIONS

The zeroth order boundary conditions are

$$\begin{aligned} \text{stator} &: u_{0s} = 0 & v_{0s} = 0 & w_{0s} = 0 \\ \text{rotor} &: u_{0r} = 0 & v_{0r} = 0 & w_{0r} = R_1 N \omega \\ \text{entrance} &: p_{0En} = p_{Res} - \frac{1}{2} \rho u_{0En}^2 (1 + f) \\ \text{exit} &: p_{0Ex} = 0 \end{aligned}$$

u_{En} is the average axial entrance velocity for every plane with θ constant. p_{Res} is the reservoir pressure and ω the rotational frequency of the shaft.

The first order boundary conditions are

$$\begin{aligned} \text{stator} &: \hat{u}_{1s} = (0,0) & \hat{v}_{1s} = (0,0) & \hat{w}_{1s} = (0,0) \\ \text{rotor} &: \hat{u}_{1r} = (0,0) \\ & \hat{v}_{1r} = [C_{0N}(\Omega - \omega) \sin\theta, -C_{0N}(\Omega - \omega) \cos\theta] \\ & \hat{w}_{1r} = [C_{0N}\Omega \cos\theta, C_{0N}\Omega \sin\theta] \\ \text{entrance} &: \hat{p}_{1En} = -\rho u_{0En}(1 + f) \hat{u}_{1En} \\ \text{exit} &: \hat{p}_{1Ex} = (0,0) \end{aligned}$$

THE FINITE DIFFERENCE METHOD

For solving these equations a finite-difference procedure is used which is based on the method published by Gosman and Pun (1974). The seal is discretized by a grid (Fig.2) and the variables are calculated at the nodes. The velocities u_0, v_0, w_0 ($\hat{u}_1, \hat{v}_1, \hat{w}_1$) are determined at points which lie between the nodes where the variables p_0, k_0, ϵ_0 (\hat{p}_1) are calculated (Fig.3)

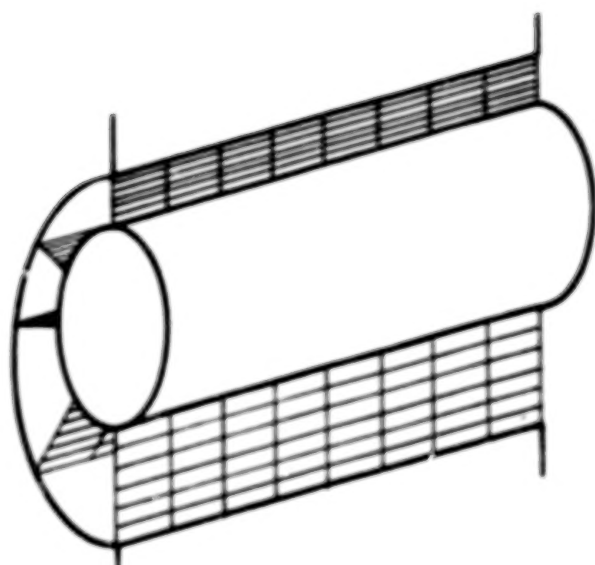


Fig. 2 3-dimensional grid in the seal.

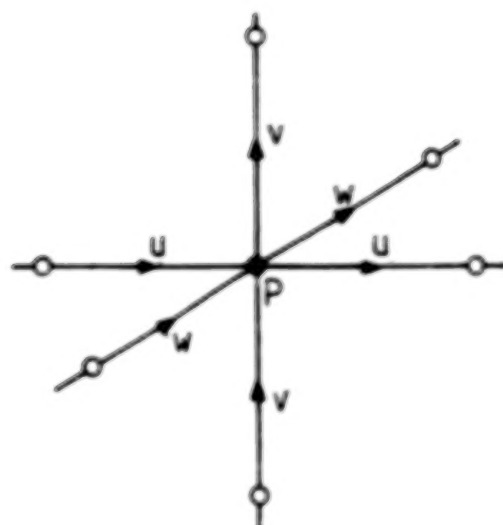


Fig. 3 Velocities and pressure in a staggered grid.

To calculate the flow we proceed as follows:

1. We start our procedure with guessed values for all variables.
2. First the velocities u_0, v_0, w_0 ($\hat{u}_1, \hat{v}_1, \hat{w}_1$) are calculated.
3. Then the velocities and the pressure are corrected to satisfy the continuity equation.
To do that we use a modified version of the 'PISO' procedure of Benodekar et al. (1985).
4. After this k and ϵ are calculated (only for the zeroth order solution).

We repeat step 2 to 4 until we reach a convergent solution. First we solve the zeroth order equations and then the first order equations.

Of course we need a 3-dimensional finite-difference method to calculate the flow in the case of an eccentric shaft, while a two-dimensional method is sufficient for movements around the centric position.

DETERMINATION OF THE DYNAMIC COEFFICIENTS

By integration the pressure \hat{p}_1 around the shaft we get forces in z and y directions.

Then we introduce $z, y, \dot{z}, \dot{y}, \ddot{z}, \ddot{y}$ from our circular orbit into equation (2). This gives us the following equations:

$$\int_0^L \int_0^{2\pi} p_{1c} \cos\theta R_{1N} d\theta dx = C_{0N} (K_{zz} + d_{zy}\Omega - M_{zz}\Omega^2)$$

$$\int_0^L \int_0^{2\pi} p_{1s} \cos\theta R_{1N} d\theta dx = C_{0N} (k_{zy} - D_{zz}\Omega)$$

$$\int_0^L \int_0^{2\pi} p_{1c} \sin\theta R_{1N} d\theta dx = C_{0N} (-k_{yz} + D_{yy}\Omega)$$

$$\int_0^L \int_0^{2\pi} p_{1s} \sin\theta R_{1N} d\theta dx = C_{0N} (K_{yy} + d_{yz}\Omega - M_{yy}\Omega^2)$$

If we calculate the forces for several precession frequencies Ω of the shaft, we can obtain the coefficients by a 'Least-Square-Fit'.

RESULTS

We compare our theory with the model of Nelson and Nguyen (1987) and some experimental results of Falco et al. (1966) which also have been published in the paper of Nelson and Nguyen (1987).

In Fig. 4-10 dynamic coefficients are calculated as a function of the eccentricity. We compare our results with Nelson and Nguyen's theory and the stiffness coefficients also with experimental and theoretical results of Falco et al.

The seal data are

length	: $L = 40.0$ mm	pressure drop	: 1.0 Mpa
shaft radius	: $R_{1N} = 80.0$ mm	shaft speed	: 4000 RPM
nominal clearance	: $C_{0N} = 0.36$ mm		
density	: $\rho = 1000$ kg/m ³		
preswirl ratio	: $\bar{w}(0, \theta)/R_{1N}\omega = 0.3$		
viscosity	: $\mu_1 = 1.0 \times 10^{-3}$ Ns/m ²		
entrance lost-coefficient	: $\xi = 0.5$		

CONCLUSIONS

We have shown that it is possible to calculate the dynamic coefficients of eccentric seals by a finite difference method based on the Navier Stokes equations. This method can also be extended to calculate the coefficients of eccentric gas seals by following the procedure of Nordmann (1987) and to calculate the dynamic coefficients of bearings by neglecting the turbulence model.

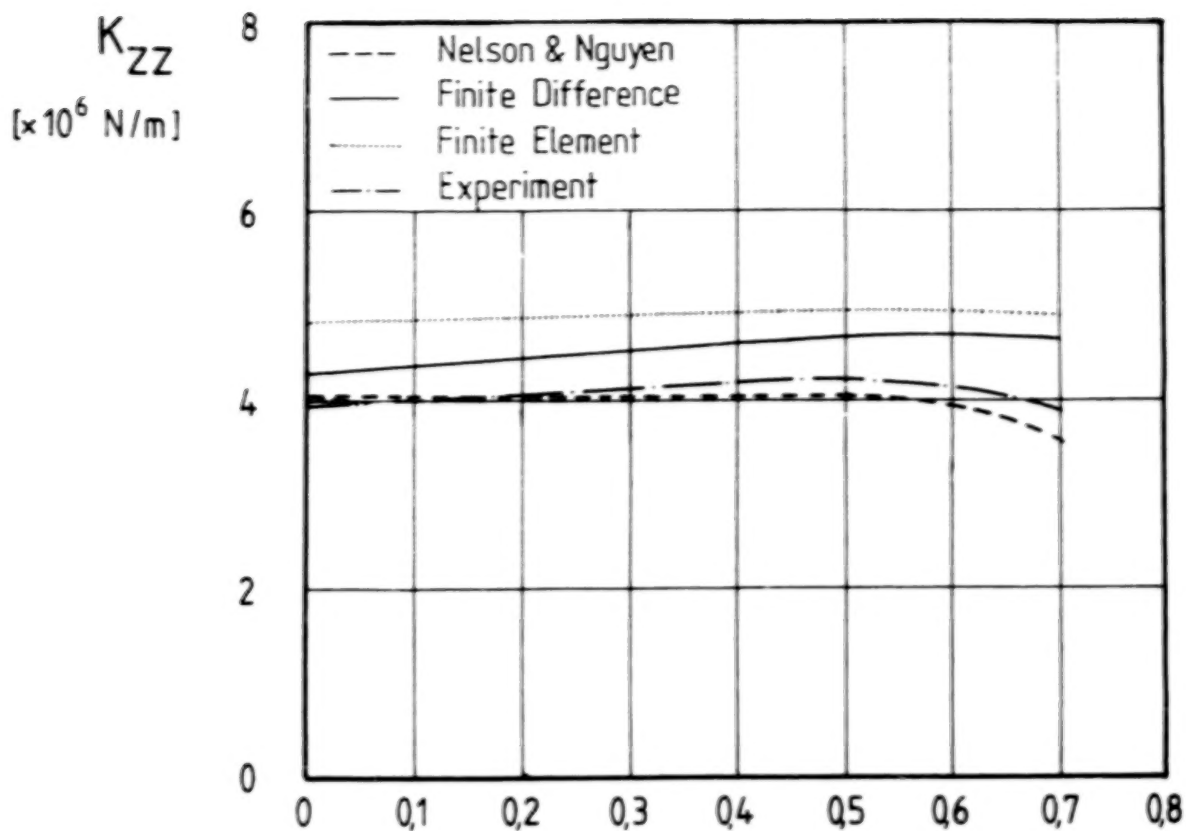


Fig. 4 Direct stiffness K_{zz} versus eccentricity.

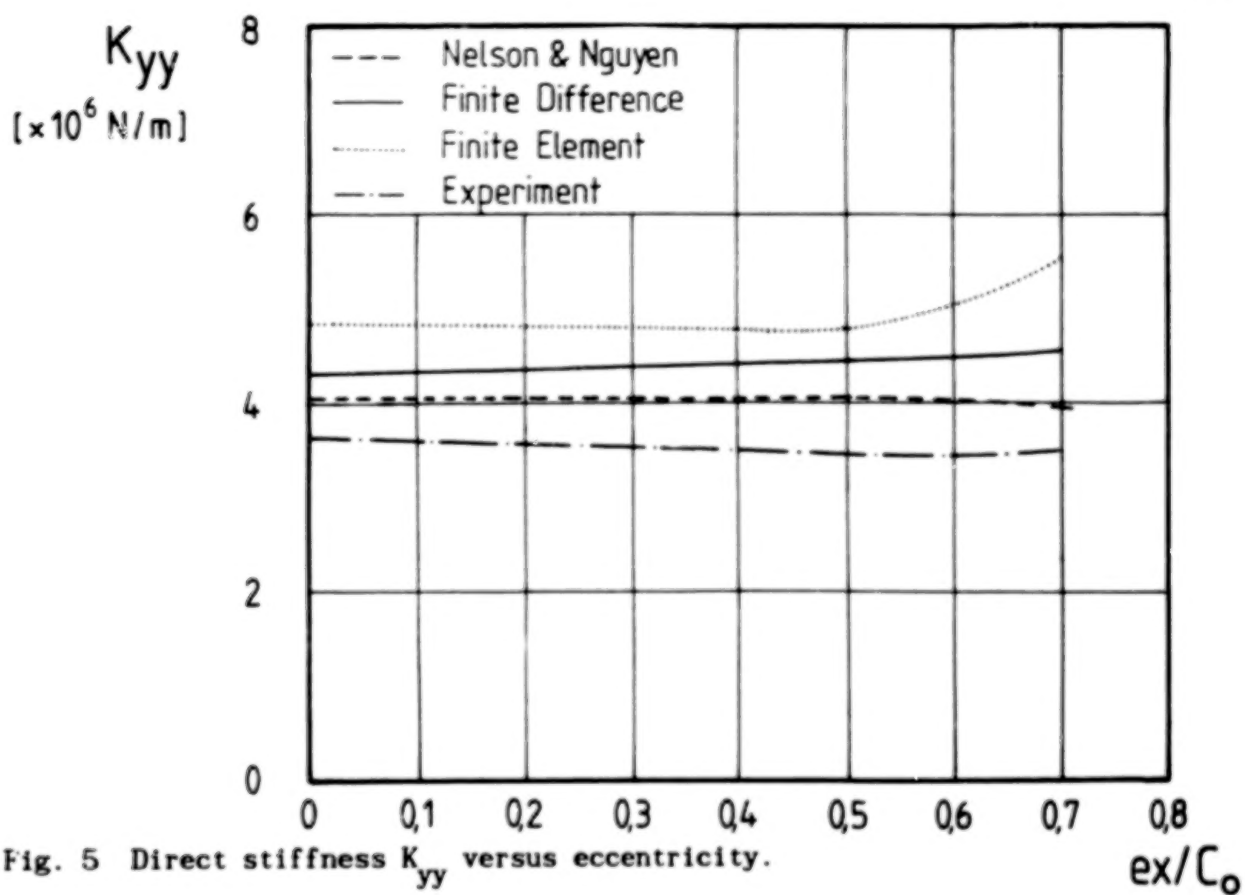
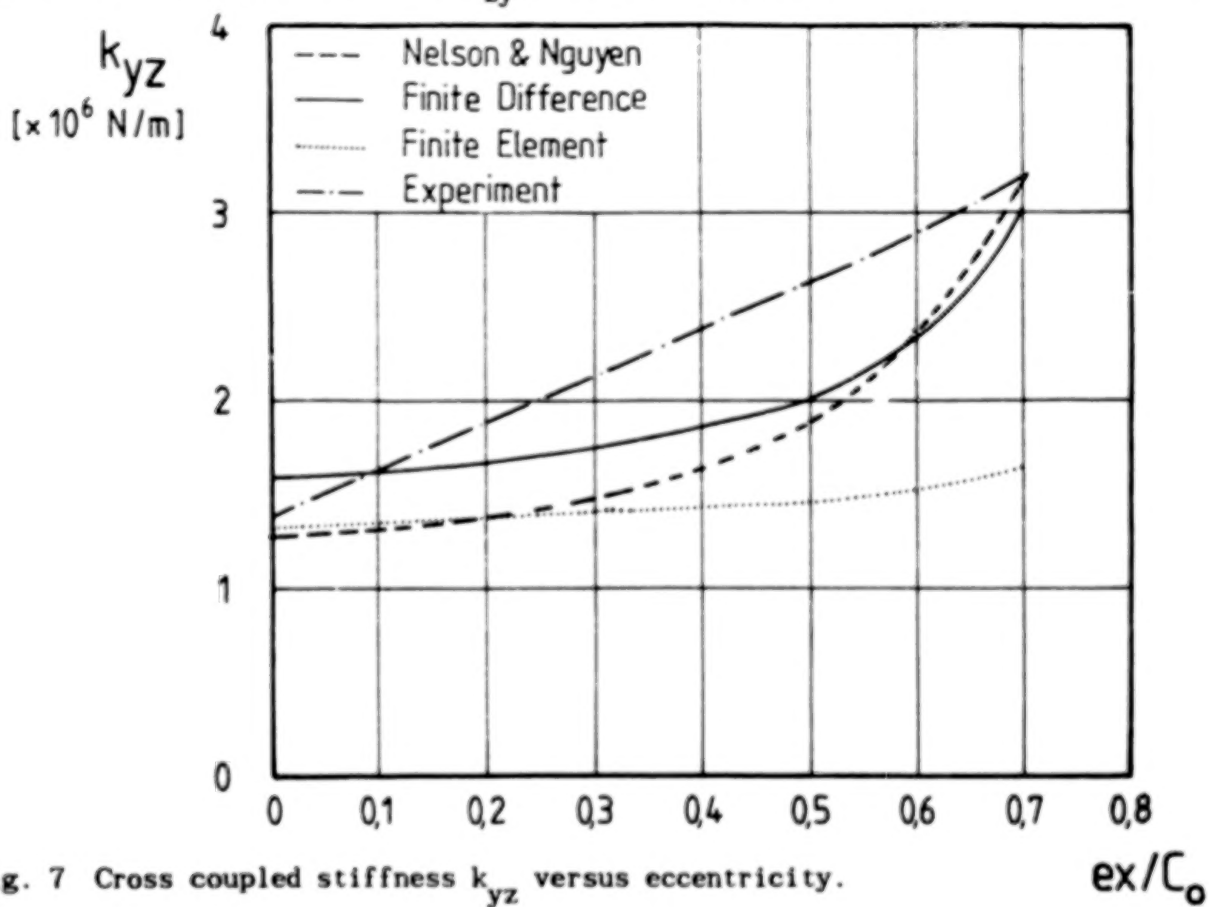
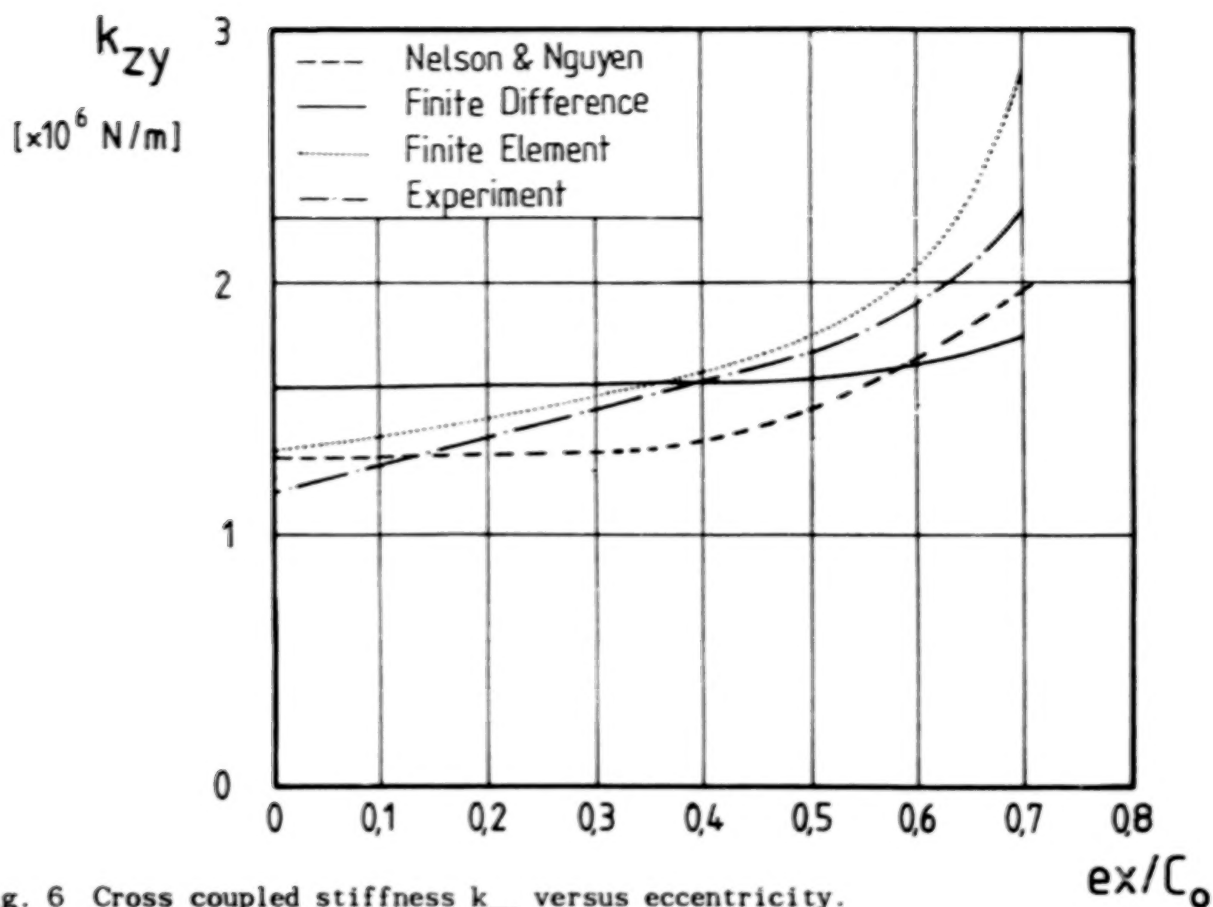


Fig. 5 Direct stiffness K_{yy} versus eccentricity.



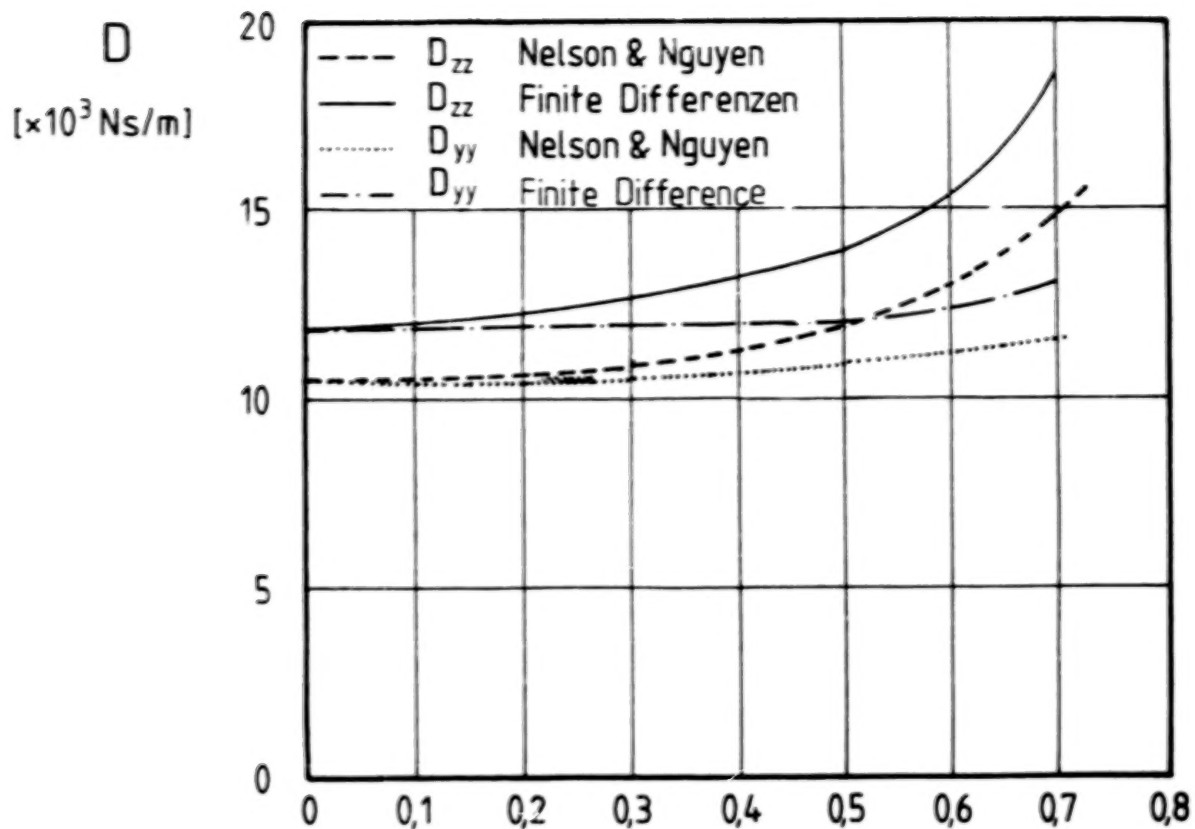


Fig. 8 Direct damping versus eccentricity.

ex/C_0

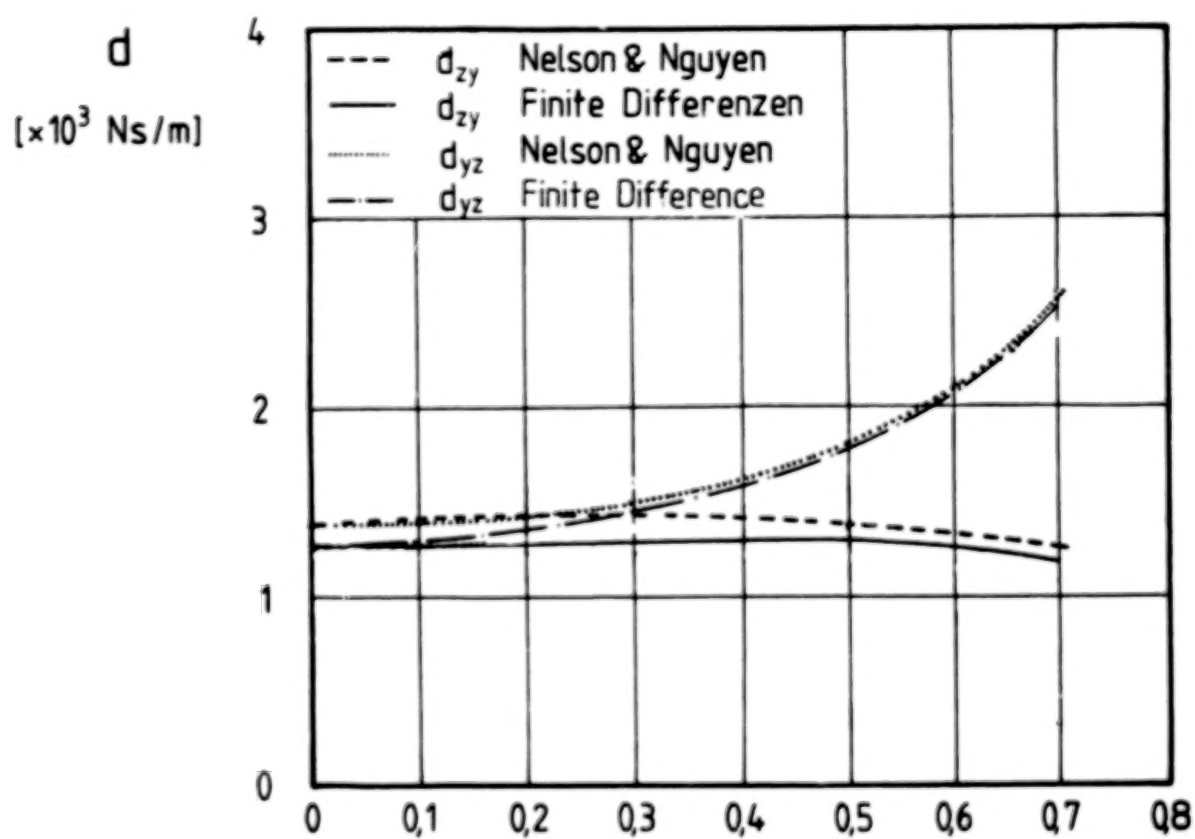


Fig. 9 Cross coupled damping versus eccentricity.

ex/C_0

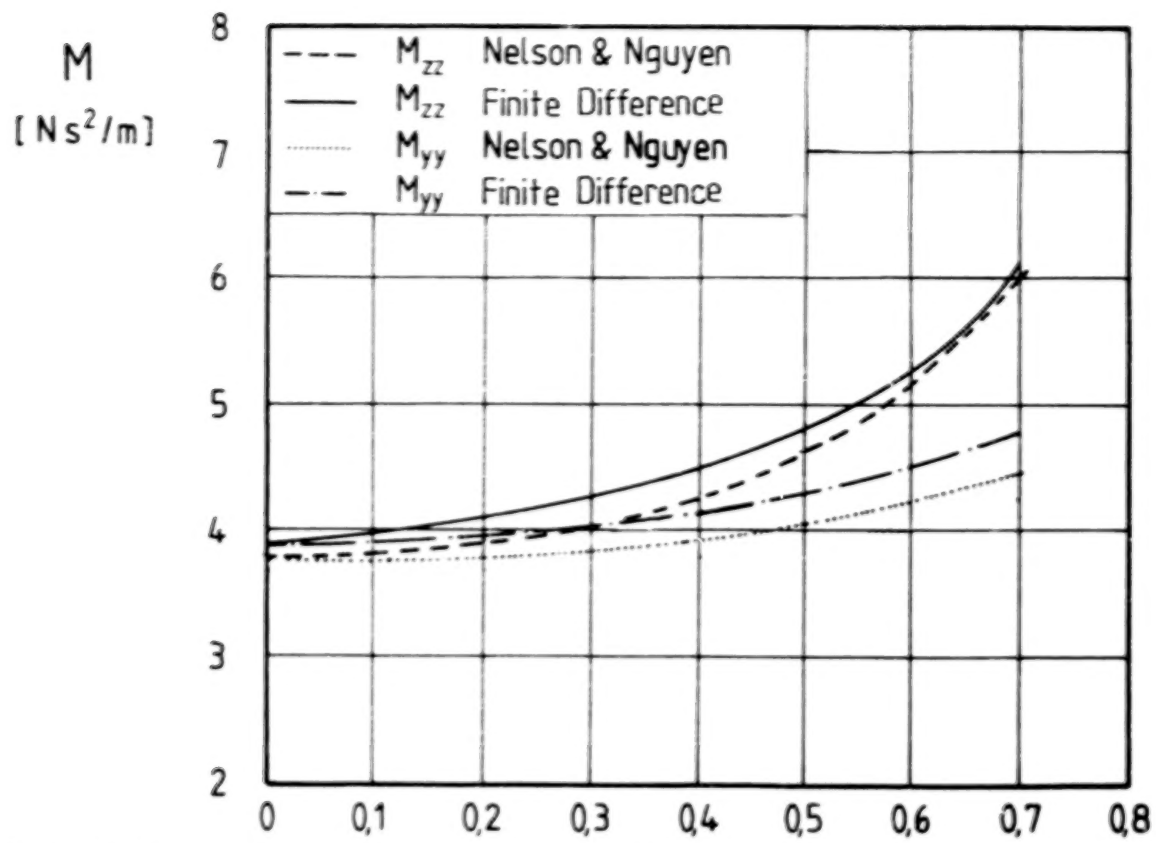


Fig. 10 Direct inertia versus eccentricity.

ex/c_o

NOMENCLATURE

F_z, F_y	Forces on the shaft in z and y direction
K, k	direct and cross-coupling stiffness
D, d	direct and cross-coupled damping
M, m	direct and cross-coupling inertia
u, v, w	axial, radial and circumferential velocity
p	pressure
k	turbulence energy
ϵ	energy dissipation
μ_e, μ_l, μ_t	effective, laminar and turbulent viscosity
ρ	density
t	time
x, r, θ	axial, radial and circumferential coordinate
x, y, z	rectangular coordinate directions
Y, Z	rotor displacements from its steady-state position
η	radial coordinate after transformation
G	production term in k- ϵ -model
$\sigma_k, \sigma_\epsilon$	constants of the k- ϵ -model
C_μ, C_1, C_2	constants of the k- ϵ -model
ϕ	general variable standing for u, v, w, p, k ϵ
S_ϕ	general source term
C_o	nominal seal clearance
C_{oN}	steady-state clearance for an eccentric shaft
δ	varying seal clearance for orbiting shaft
r_o	radius of the precession motion of the shaft
$e = \frac{r_o}{C_{oN}}$	perturbation parameter
ω	rotational frequency of the shaft = RPM $\pi/30$
RPM	revolutions per minute
Ω	precession frequency of the shaft
ξ	entrance lost-coefficient
L	Length of the seal
r_a	stator radius (Fig. 1)
R_{aN}	nominal stator radius (Fig. 1)
R_{iN}	shaft radius (Fig. 1)
h_1	change in the clearance
ex	eccentricity
\bar{w}	average circumferential velocity
u_{En}	average axial velocity at the entrance
p_{Res}	sump pressure

APPENDIX A: Constants of the k-ε model.

$$C_\mu = 0.09 \quad C_1 = 1.44 \quad C_2 = 1.92 \quad \sigma_k = 1.0 \quad \sigma_\epsilon = 1.3$$

and G is a given by

$$G = \mu_e \left[2 \left(\left(\frac{\partial v}{\partial r} \right)^2 + \left(\frac{\partial u}{\partial x} \right)^2 + \left(\frac{1}{r} \frac{\partial w}{\partial \theta} + \frac{v}{r} \right)^2 \right) + \left(\frac{\partial v}{\partial x} + \frac{\partial u}{\partial r} \right) + \left(\frac{1}{r} \frac{\partial v}{\partial \theta} + \frac{\partial w}{\partial r} - \frac{w}{r} \right)^2 + \left(\frac{\partial w}{\partial x} + \frac{1}{r} \frac{\partial u}{\partial \theta} \right)^2 \right]$$

APPENDIX B: Terms of first order source term.

$$C_{u_1} = \frac{\partial}{\partial x}(\rho u_0 \hat{u}_1) + \frac{1}{\eta} \frac{\partial}{\partial \eta}(\eta \rho u_0 \hat{v}_1) + \frac{1}{\eta} \frac{\partial}{\partial \theta}(\rho u_0 \hat{w}_1)$$

$$C_{v_1} = \frac{\partial}{\partial x}(\rho v_0 \hat{u}_1) + \frac{1}{\eta} \frac{\partial}{\partial \eta}(\eta \rho v_0 \hat{v}_1) + \frac{1}{\eta} \frac{\partial}{\partial \theta}(\rho v_0 \hat{w}_1) - \frac{\rho}{\eta} \hat{w}_0 \hat{w}_1$$

$$C_{w_1} = \frac{\partial}{\partial x}(\rho w_0 \hat{u}_1) + \frac{1}{\eta} \frac{\partial}{\partial \eta}(\eta \rho w_0 \hat{v}_1) + \frac{1}{\eta} \frac{\partial}{\partial \theta}(\rho w_0 \hat{w}_1) + \frac{\rho}{\eta} \hat{w}_0 \hat{v}_1$$

$$D_{u_0} = (((r_a - \eta)DFC + RCS)U1 + CCC * U2 + CCS * U3) + i(((r_a - \eta)DFS + RSS)U1 + CCS * U2 + CCC * U3)$$

$$D_{v_0} = (((r_a - \eta)DFC + RCS)V1 + CCC * V2 + CCS * V3) + i(((r_a - \eta)DFS + RSS)V1 + CCS * V2 + CCC * V3)$$

$$D_{w_0} = (((r_a - \eta)DFC + RCS)W1 + CCC * W2 + CCS * W3) + i(((r_a - \eta)DFS + RSS)W1 + CCS * W2 + CCC * W3)$$

$$D_{p_0} = (((r_a - \eta)DFC + RCS)P1 - CCC * P2) + i(((r_a - \eta)DFS + RSS)P1 - CCS * P2)$$

$$DFS = \frac{C_{0N}}{C_0} \left[\cos(\theta) - \frac{ex}{C_0} * \sin(\theta) \sin(\theta) * \left(1 - \frac{ex \cos(\theta)}{\sqrt{R_{aN}^2 - ex^2 \sin^2(\theta)}} \right) \right]$$

$$DFC = - \frac{C_{0N}}{C_0} \left[\sin(\theta) + \frac{ex}{C_0} * \cos(\theta) \sin(\theta) * \left(1 - \frac{ex \cos(\theta)}{\sqrt{R_{aN}^2 - ex^2 \sin^2(\theta)}} \right) \right]$$

$$RCS = ex \frac{C_{0N}}{C_0} \left[\cos(\theta) \sin(\theta) * \left(1 - \frac{ex \cos(\theta)}{\sqrt{R_{aN}^2 - ex^2 \sin^2(\theta)}} \right) \right]$$

$$RSS = ex \frac{C_{0N}}{C_0} \left[\sin(\theta) \sin(\theta) * \left(1 - \frac{ex \cos(\theta)}{\sqrt{R_{aN}^2 - ex^2 \sin^2(\theta)}} \right) \right]$$

$$\cos \theta = \frac{C_{0N}}{C_0} \cos(\theta)$$

$$\cos \theta = \frac{C_{0N}}{C_0} \sin(\theta)$$

$$\cos \theta = -\Omega \frac{C_{0N}}{C_0} \cos(\theta)$$

$$\cos \theta = \Omega \frac{C_{0N}}{C_0} \sin(\theta)$$

$$P1 = \frac{1}{\eta} \frac{\partial}{\partial \eta} (\rho w_0)$$

$$P2 = \frac{1}{\eta} \frac{\partial}{\partial \eta} (\eta \rho v_0) + (1 - \frac{r_a}{\eta}) \frac{1}{\eta} \frac{\partial}{\partial \theta} (\rho w_0) - \frac{r_a}{\eta^2} \rho v_0$$

$$U1 = \frac{1}{\eta} \left[\frac{\partial}{\partial \eta} (\rho u_0 w_0) - \frac{\partial}{\partial \eta} \left(\frac{\mu}{\eta} \frac{\partial u_0}{\partial \theta} \right) - \frac{\partial}{\partial \eta} \left(\mu \frac{\partial w_0}{\partial x} \right) \right]$$

$$U2 = \frac{1}{\eta} \frac{\partial}{\partial \eta} \left(\eta \mu \frac{\partial v_0}{\partial x} + \eta \mu \frac{\partial u_0}{\partial \eta} \right) - \frac{r_a}{\eta^2} \mu \frac{\partial v_0}{\partial x} - \frac{r_a}{\eta^2} \mu \frac{\partial u_0}{\partial \eta} + (1 - \frac{r_a}{\eta}) \frac{1}{\eta} \frac{\partial}{\partial \theta} \left(\frac{\mu}{\eta} \frac{\partial u_0}{\partial \theta} + \mu \frac{\partial w_0}{\partial x} \right) - \frac{1}{\eta} \frac{\partial}{\partial \eta} (\eta \rho v_0 u_0) + \frac{r_a}{\eta^2} \rho v_0 u_0 - (1 - \frac{r_a}{\eta}) \frac{1}{\eta} \frac{\partial}{\partial \theta} (\rho u_0 w_0)$$

$$U3 = (r_a - \eta) \frac{\partial}{\partial \eta} (\rho u_0)$$

$$V1 = \frac{1}{\eta} \left[\frac{\partial}{\partial \eta} (\rho v_0 w_0) - \frac{\partial}{\partial \eta} \left(\frac{\mu}{\eta} \frac{\partial v_0}{\partial \theta} \right) - \frac{\partial}{\partial \eta} \left(\mu \frac{\partial}{\partial \eta} \left(\frac{w_0}{\eta} \right) \right) \right]$$

$$V2 = (1 - \frac{r_a}{\eta}) \left[\frac{1}{\eta} \frac{\partial}{\partial \theta} \left(\frac{\mu}{\eta} \frac{\partial v_0}{\partial \theta} + \mu \frac{\partial}{\partial \eta} \left(\frac{w_0}{\eta} \right) \right) - \frac{2}{\eta} \left(\frac{\mu}{\eta} \frac{\partial w_0}{\partial \theta} + \frac{\mu}{\eta} v_0 \right) - \frac{1}{\eta} \frac{\partial}{\partial \theta} (\rho v_0 w_0) \right] - \frac{r_a}{\eta^2} \mu \frac{\partial v_0}{\partial \eta} + \frac{1}{\eta} \frac{\partial}{\partial \eta} \left(2 \eta \mu \frac{\partial v_0}{\partial \eta} \right) - \frac{1}{\eta} \frac{\partial}{\partial \eta} (\eta \rho v_0 v_0) + \frac{r_a}{\eta^2} \rho v_0 v_0 + \frac{\eta - r_a}{\eta} \frac{\rho}{\eta} w_0 w_0 - \frac{\partial p_0}{\partial \eta}$$

$$V3 = (r_a - \eta) \frac{\partial}{\partial \eta} (\rho v_0)$$

$$W1 = \frac{1}{\eta} \left[\frac{\partial}{\partial \eta} (\rho w_0 w_0) - \frac{\partial}{\partial \eta} \left(2 \frac{\mu}{\eta} v_0 \right) - \frac{\partial}{\partial \eta} \left(2 \frac{\mu}{\eta} \frac{\partial w_0}{\partial \theta} \right) + \frac{\partial p_0}{\partial \eta} \right]$$

$$W2 = (1 - \frac{r_a}{\eta}) \left[\frac{2}{\eta} \frac{\partial}{\partial \theta} \left(\frac{\mu}{\eta} \frac{\partial w_0}{\partial \theta} + \frac{\mu}{\eta} v_0 \right) + \frac{1}{\eta} \left(\frac{\mu}{\eta} \frac{\partial v_0}{\partial \theta} + \mu \frac{\partial}{\partial \eta} \left(\frac{w_0}{\eta} \right) \right) - \frac{\rho}{\eta} v_0 w_0 - \frac{1}{\eta} \frac{\partial p_0}{\partial \theta} - \frac{1}{\eta} \frac{\partial}{\partial \theta} (\rho w_0 w_0) \right] + \frac{1}{\eta} \frac{\partial}{\partial \eta} \left(\eta^2 \mu \frac{\partial}{\partial \eta} \left(\frac{w_0}{\eta} \right) \right) - \frac{r_a}{\eta} \mu \frac{\partial}{\partial \eta} \left(\frac{w_0}{\eta} \right) - \frac{r_a}{\eta} \frac{\mu}{\eta^2} \frac{\partial v_0}{\partial \theta} + \frac{1}{\eta} \frac{\partial}{\partial \eta} \left(\mu \frac{\partial v_0}{\partial \theta} \right) - \frac{1}{\eta} \frac{\partial}{\partial \eta} (\eta \rho v_0 w_0) + \frac{r_a}{\eta^2} \rho v_0 w_0$$

$$W3 = (r_a - \eta) \frac{\partial}{\partial \eta} (\rho w_0)$$

REFERENCES

- Allaire, P.E.; Gunter, E.J.; Lee, C.P.; and Barrett, L.E. (1976): The dynamic analysis of the space shuttle main engine-high pressure fuel turbopump. Part II - Load capacity and hybrid coefficients for the turbulent interstage seals. University of Virginia, Report NO UVA/528140/ME76/103.
- Benodekar, R.W.; Goddard, A.J.H.; Gosman, A.D.; Issa, R.I. (1985): Numerical prediction of turbulent flow over surfacemounted ribs. AIAA Journal Vol. 23, No 3, March 1985.
- Dietzen, F.J.; Nordmann, R. (1987): Calculating rotordynamic coefficients of seals by 'Finite-Difference Techniques'. ASME Journal of Tribology, 1987.
- Diwald, W.; Nordmann, R. (1987): Dynamic analysis of centrifugal pump rotors with fluid-mechanical interactions. 11th ASME Design Engineering Division Conference on Vibration and Noise, 27-30 Sept. 87, Boston.
- Falco, M.; Mimmi, G.; Marenco, G. (1986): Effects of seals on rotor dynamics. Proceedings of the International Conference on Rotordynamics, September 14-17, 1986, Tokyo, Japan.
- Gosman, A.D.; Pun, W. (1974): Lecture notes for course entitled: 'Calculation of recirculating flows'. Imperial College London, Mech. Eng. Dept., HTS/74/2.
- Jenssen, D.N. (1970): Dynamics of rotor systems embodying high pressure ring seals. Ph.D. dissertation, Heriot-Watt University, Edinburgh, Scotland, July 1970.
- Nelson, C.C.; Nguyen, D.T. (1987): Analysis of eccentrically-positioned annular incompressible seals: Part 1 - A new solution procedure using the fast fourier transform to facilitate the solution for the hydrostatic force. Will be presented in ASME Journal of Tribology.
- Nelson, C.C.; Nguyen, D.T. (1987): Analysis of eccentrically-positioned annular incompressible seals: Part 2 - Investigating the effects of eccentricity on the rotordynamic coefficients. Will be presented in ASME Journal of Tribology.
- Nordmann, R.; Dietzen, F.J.; Weiser, H.P. (1987): Rotordynamic coefficients of turbulent gas seals. ASME Applied Mechanics, Bioengineering and Fluids Engineering Conference. June 14-17, 1987, Cincinnati, Ohio.

INFLUENCE OF IMPELLER AND DIFFUSER GEOMETRIES ON THE LATERAL FLUID FORCES OF WHIRLING CENTRIFUGAL IMPELLER

Hideo Ohashi
University of Tokyo
Tokyo 113, Japan

Akira Sakurai
Kobe Steel, Ltd.
Kobe 651, Japan

Jiro Nishihama
Asahi Glass Co.
Yokohama 221, Japan

Lateral fluid forces on two-dimensional centrifugal impellers, which whirl on a circular orbit in a vaneless diffuser, were reported at the 3rd Workshop in 1984. Experiments were further conducted for the cases in which a three-dimensional centrifugal impeller, a model of the boiler feed pump, whirled in vaneless and vaned diffusers. The influence of the clearance configuration between the casing and front shroud of the impeller was also investigated.

The result indicated that the fluid dynamic interaction between the impeller and the guide vanes induces quite strong fluctuating fluid forces to the impeller, but nevertheless its influence on radial and tangential force components averaged over a whirling orbit is relatively small.

INTRODUCTION

The lateral fluid forces acting on two-dimensional (2-D) centrifugal impellers, which whirl on a circular orbit in a vaneless diffuser, were studied experimentally as well as theoretically at the authors' laboratory, and the results were reported at the 1st and 3rd Workshops in 1980 and 1984 [refs. 1 and 2]. The results were later summarized and published in references 3 and 4.

The apparatus for forced whirling motion was then replaced by a newly designed one [ref. 5], and the studies were further conducted for a three-dimensional (3-D) impeller (model of a prototype boiler feed pump) installed in vaneless and vaned diffusers.

From these experiments the following results are summarized in the present paper:

- (1) Comparison of lateral fluid forces on 2-D and 3-D impellers in a vaneless diffuser.
- (2) Comparison of lateral fluid forces on the 3-D impeller in vaneless and vaned diffusers.
- (3) Comparison of lateral fluid forces on the 3-D impeller for various clearance configurations between the casing and front shroud.
- (4) Fluid forces induced by impeller/guide vane interaction.

Similar experimental studies on whirling impeller forces have been conducted at California Institute of Technology, Sulzer Brothers, Ltd., and Mitsubishi Heavy

Industries, Ltd. A 3-D impeller installed in a volute casing was tested for forced orbital motion at the CalTech facility [refs. 6 and 7]. The results indicated that the tangential force became excitatory at a low whirl speed ratio, i.e., at high supercritical speed, regardless of the pump discharge.

A model impeller of the boiler feed pump was tested at the Sulzer facility, where the test impeller was forced to a unidirectional oscillatory motion [refs. 8 and 9]. The results were qualitatively similar to those obtained at CalTech, but the forces induced by impeller oscillation were considerably larger than those obtained at CalTech and at our laboratory. This difference could be attributed to the fact that the test impeller at Sulzer was a precise scale model of a real casing, and thus the clearance between the impeller and the surrounding casing was kept as small as possible to reduce the disk friction loss. This situation resulted in a large restrictive force for any impeller motion in the casing.

Mitsubishi built a new whirling test facility for circular orbital motion and tested a 2-D impeller in a volute casing [ref. 10]. The results indicated a quantitative tendency similar to those of CalTech and ours, and tangential force became excitatory at a low whirl speed ratio regardless of pump discharge.

The 2-D and 3-D impellers tested in our laboratory indicated less instability. The whirl excitation was observed only when the impeller operated at partial discharge [refs. 4 and 5].

The test data obtained by the above mentioned four facilities are compared briefly in Appendix A. A qualitative explanation on the nature of fluid forces on a whirling impeller in a vaneless diffuser is given in Appendix B.

TEST FACILITY

The test facility is virtually a single-stage, vertical shaft, centrifugal pump. The overall test setup, which has been fundamentally unchanged since the start of this study, is illustrated in figure 1. The new apparatus for forced whirling motion is illustrated in figures 2 and 3. The section views of figures 4 and 5 describe how the test impeller is installed in the casing for the 2-D and 3-D impellers. The experiments on 2-D impellers were done principally to compare them with theory, while those on the 3-D impeller were done to obtain impeller data for practical applications. The specifications of the test impellers and diffusers are listed in tables 1 and 2.

In the previous test facility, the main pump shaft was driven by a constant speed induction motor (530 rpm), while the whirl shaft was driven by a variable speed DC motor, so that the ratio of whirl speed Ω to rotational speed ω , Ω/ω , could be arbitrarily adjusted and kept constant. However, this made it impossible to keep the phase relation between whirl and rotation angles θ_1 and θ_2 (see fig. 6), in a prescribed way.

To improve this situation, the DC motor for whirling motion was replaced by an AC servo motor. After counting signals from encoders attached to the pump shaft (1500 ppr) and whirl shaft (3000 ppr), proper pulse series are fed to the controller of the servo motor, which keeps the whirl angle θ_1 in a prescribed relation to the rotation angle θ_2 . At $\Omega/\omega = 1/2$, for example, the impeller rotates twice and returns exactly to the same position relative to the guide vanes while the whirl shaft rotates once. By introducing this equipment, the impeller/guide vane interaction, where sensitivity varies according to the relative position between the impeller and the guide vanes, can be measured with a better resolution.

DATA EVALUATION

The data acquisition and evaluation were made fundamentally in the same way as described in the previous reports. The fluid force $F(\theta_1, \theta_2)$ is divided into radial and tangential components, F_r and F_θ , as illustrated in figure 6. The average forces on the orbit, \bar{F}_r and \bar{F}_θ , are then normalized by the equation,

$$f_r = \bar{F}_r / M\omega^2, \quad f_\theta = \bar{F}_\theta / M\omega^2 \dots\dots\dots (1)$$

where reference mass $M = \rho\pi r_2^2 b$, e = eccentricity, ρ = fluid density, r_2 = outer radius and b = impeller exit width.

In comparing normalized fluid forces on 2-D and 3-D impellers, the following difference must be kept in mind.

(1) For 2-D impellers, fluid forces acting on impeller blades, excluding all other fluid forces on front and back shrouds, impeller hub, etc., are normalized by $M\omega^2$, where b of the reference mass M is the exit width of the impeller blades only. Reference mass is therefore the mass of fluid in the volume enveloped by the rotating impeller blades.

(2) For 3-D impellers, fluid forces acting on the whole impeller (blades as well as shrouds and hub) are normalized by the quantity $M\omega^2$, where b is the exit total width of the impeller, that is, blade width plus the width of the two shrouds.

The former definition is convenient for comparing the experimental result with the theoretical one. The latter is for the convenience of practical application, since the fluid forces on impeller blades and shrouds have the same significance on the rotordynamic behavior of the rotating system.

FLUID FORCES ON 2-D AND 3-D IMPELLERS IN VANELESS DIFFUSERS

Comparison of the two impellers is dealt with in this chapter. The first is a 2-D impeller whirling in a vaneless diffuser or in free space as shown in figure 4. The other is a 3-D impeller whirling in the casing as shown in figure 5. The discharge from the impeller is diffused in the succeeding parallel walled vaneless diffuser (11 vanes are removed). The clearance between the casing and front shroud of the impeller is sufficiently large (without the spacer), and the effect of the fluid dynamic restriction due to the surrounding casing is seemingly weak.

Figures 7 (a) and (b) show how normalized tangential and radial force components of 2-D and 3-D impellers vary with whirl speed ratio, Ω/ω , at design discharge $\phi/\phi_D = 1.0$ and at partial discharge $\phi/\phi_D = 0.2$. As seen from these figures, lateral fluid forces on the 3-D impeller are slightly larger than those on the 2-D impeller. Most of this difference could be attributed to the fact that the 3-D impeller has an inlet passage that is wider than the exit and that the real volume enveloped by the rotating impeller is considerably larger than that of the reference mass, $\pi r_2^2 b$. In other words, the forces on the 3-D impeller are normalized by a relatively smaller quantity compared with the case of the 2-D impeller.

It can be concluded from the results that fluid forces on whirling impellers in a vaneless diffuser, regardless of 2-D or 3-D, are caused mostly by unsteady fluid forces on the whirling impeller blades and coincide with those predicted quantitatively by theory [refs. 3 and 4]. This is only the case, however, when the impeller is installed in the casing with ample clearance.

FLUID FORCES ON 3-D IMPELLER IN VANELESS AND VANED DIFFUSERS

In this chapter the influence of the interaction between the impeller blades and guide vanes on the whirling fluid forces is dealt with. A 3-D test impeller was installed in the casing as shown in figure 5. The eleven guide vanes attached between the two parallel walls (see fig. 10) are removable, and whirling tests were conducted for cases with and without guide vanes. The mean radial clearance between the impeller outer periphery and the guide vane inner periphery is 5 mm. When the impeller whirls with eccentricity $c = 1.5$ mm, the clearance varies between 3.5 and 6.5 mm. Every time a trailing edge of an impeller blade passes in the vicinity of a leading edge of a guide vane, a fluid dynamic interaction takes place, and the blade receives an impulsive force. The impeller/guide vane interaction can be understood as the sum of these individual impulses. The clearance between the casing and front shroud is kept wide (without a spacer) throughout this test series.

Figures 8 (a) and (b) show the comparison at design discharge $\phi/\phi_D = 1.0$ and at partial discharge $\phi/\phi_D = 0.2$. It is obvious that the fluid forces on an impeller in a vaned diffuser are about 50% larger than those on an impeller in a vaneless diffuser. It should be noted that the pressure rise in a vaned diffuser is also larger by about 15 to 20% at the same discharge. The general qualitative tendencies of both cases are essentially the same. As described in the latter chapter, impeller/guide vane interaction generates quite large fluctuating fluid forces on the whirling impeller; however, its influence on fluid forces averaged over an orbit remains relatively small.

As seen in figure 8 (b), both tangential and radial components indicate a local increase at around $\Omega/\omega = 0.1$ to 0.2 at partial discharge. These phenomena are hardly seen near design discharge and are considered as characteristics of partial discharge. The real reason is still unknown. The coupling of the whirling motion with the rotating stall in the diffuser, which is usually 10 to 20% of rotational speed, can be considered as a possible cause.

INFLUENCE OF CLEARANCE BETWEEN CASING AND FRONT SHROUD

The influence of clearance between the casing and front shroud of the impeller on whirling fluid forces is dealt with in this chapter. Tests were conducted for a 3-D impeller in three cases: (a) without a spacer (original layout); (b) with a spacer, $C1 = 2.7$ mm, $C2 = 3.0$ mm (see fig. 5); (c) 24 radial grooves with 10 mm width and 5 mm depth are added to the spacer surface facing the front shroud. Other conditions are the same as those of case (b).

The result obtained at design discharge is summarized in figure 9. As the clearance between the casing and impeller shroud gets smaller and thus the restrictive effect of the fluid contained in the narrow space becomes greater, the fluid forces on the front shroud of the whirling impeller increase. This results in the increase of the radial component and the decrease of the tangential one. Narrower clearance between the impeller and casing leads obviously to the expansion of the whirl excitation range at positive whirl.

The grooves on the spacer surface, which are expected to brake the rotation of fluid in the clearance, resulted in the increase of the tangential component in the positive direction, thus reducing the range of whirl excitation at positive whirl.

IMPELLER/GUIDE VANE INTERACTION

The fluid forces on the whirling impeller are a function of both the whirl angle θ_1 and rotation angle θ_2 . As understood from figure 10, which illustrates the relative disposition of 6 impeller blades and 11 guide vanes, the fluid force at a location of whirl orbit is different according to the relative angular position of the impeller to the guide vanes. Since six impeller blades are equally located on the periphery, the rotational condition becomes identical after every rotation of 60° .

Figure 11 illustrates how fluid force on the whirling impeller varies on the orbit because of the impeller/guide vane interaction. The measurement was done at $\Omega/\omega = 1$ and at four discharge conditions: that is, $\phi/\phi_D = 1.4, 1.0, 0.6$, and 0 (shut off). At $\Omega/\omega = 1$ the trailing edge of a specific impeller blade with the narrowest gap passes successively near the leading edges of the 11 guide vanes during one rotation. This is the reason why 11 distinct interactions can be observed during an orbit. As seen from the figures the interaction becomes obviously weaker as the flow rate decreases. At partial discharge the separation in the impeller and diffuser causes large random fluctuations of flow, and it applies a strong masking effect on the blade interaction.

Figure 12 illustrates fluid force vectors on the orbit for various whirl speed ratios, $\Omega/\omega = 2/3, 1/2, -2/3$, and -1 . The figures are for the over-discharge condition, $\phi/\phi_D = 1.4$, where the interaction takes place most distinctly. The frequency of periodicity on the orbit varies with the whirl speed ratio and can be explained by tracing the mode of the impeller/guide vane encounter near the minimum gap region.

The impeller/guide vane interaction takes place at every encounter of moving blade and stationary vane, however, the resultant fluid force on the whole impeller is predominantly induced by the blade interaction to a specific guide vane, which is located closest to the least gap point. As illustrated in figure 10, we chose the guide vane with the least gap and the blade closest to the vane. The angle α is then defined as the angle difference between the trailing edge of the blade and the leading edge of the vane. All interaction data at $\phi/\phi_D = 1.4$ are then replotted against this angle α for three whirl speed ratios, $\Omega/\omega = 1.0, 1/2$, and $1/6$, as shown in figure 13, where the tangential and radial components indicate the deviation from the average values on the orbit. This figure suggests that the interactions at various whirl speed ratios are almost identical in nature and are primarily controlled by the local geometric condition near the minimum gap point.

It should be noted again that the interaction, though it appears quite distinctly, is only a local event and has a relatively small effect on the fluid force averaged over the orbit.

CONCLUSIONS

Fluid forces on whirling centrifugal impellers are studied experimentally for various configurations of the impeller and diffuser. The results obtained are summarized as follows:

- (1) Comparison of fluid forces on 2-D and 3-D impellers whirling in a vaneless diffuser indicated no significant difference.
- (2) Fluid forces on a 3-D impeller whirling in a vaned diffuser were about 50% larger than those in a vaneless diffuser, partly due to the interaction between the impeller blades and guide vanes and partly to the increased pressure rise.
- (3) The fluid forces acting on the front shroud of the whirling impeller are affected by the clearance configuration between the casing and shroud. The smaller

the clearance, the bigger the fluid forces on the whirling shroud. Grooves cut on the spacer surface facing the shroud do augment the damping effect at positive whirl. (4) Impeller/guide vane interaction generates strong fluctuating fluid forces on the impeller. The effect of this strong interaction on fluid force characteristics is relatively mild as stated above, because high-frequency fluctuations are smoothed out during the averaging process.

SYMBOLS

F :	lateral fluid force	ϕ :	flow coefficient
f :	normalized fluid force	Ω, ω :	whirl and rotational frequency
M :	reference mass		subscript
θ_1 :	whirl angle	D :	design (shock-free entry)
θ_2 :	rotation angle	r, θ :	radial and tangential

APPENDIX A: COMPARISON OF TEST RESULTS

The facilities and test results of four research groups, that is, the University of Tokyo, California Institute of Technology, Sulzer Brothers, Ltd., and Mitsubishi Heavy Industries, Ltd., are introduced briefly as follows:

Univ. Tokyo The test facility is described in the main text and is shown in figures 1 through 5. Normalized tangential and radial components, f_θ and f_r , on the blades of a whirling 2-D impeller in a vaneless diffuser are shown in figure A-1, in which calculated results are also shown for comparison [ref. 4]. The results of a 3-D impeller whirling in a vaned diffuser are shown in figure A-2 for design flow rate and shut-off. The thin broken curves in the figure indicate the force characteristics obtained by the best fit of mass, damping, and stiffness matrices. In comparing the results of the four groups, it should be noted that the normalization of tangential and radial forces is done by the same definition; however, the sign of the tangential force defined by the Univ. Tokyo group is opposite to that of the remaining three groups.

CalTech The test facility is illustrated in figure A-3, in which a horizontal-shaft 3-D impeller installed in a volute casing is forced to a circular orbital motion and the fluid force on the impeller is measured by a rotating dynamometer. Typical results at design flow rate are reproduced in figure A-4 from reference 6.

Sulzer Figure A-5 illustrates the test facility, in which a horizontal-shaft boiler feed pump impeller in a vaned diffuser is forced to a unidirectional motion. Impeller force is measured by a rotating dynamometer. The tangential force is evaluated indirectly from the reaction force to unidirectional excitation and is given in figure A-6 [ref. 8].

Mitsubishi Figure A-7 illustrates the test facility, in which a vertical-shaft 2-D impeller in a volute casing is forced to a circular orbital motion. The results are shown in figure A-8 [ref. 10].

The comparison of the above results leads to

- (1) Very roughly speaking, tangential force is nearly linear with respect to whirl speed ratio, while radial force is parabolic with its minimum at positive whirl speed ratio in all test results.
- (2) The absolute values of fluid forces are different. The force level increases in order of Univ. Tokyo, Mitsubishi, CalTech, and Sulzer. The forces on the Sulzer impeller are almost 8 times as large as those on the blades of the 2-D impeller measured by the Univ. Tokyo.

(3) The large difference of measured fluid forces comes mostly from the difference of clearance space between the impeller shroud and the surrounding casing. The narrower the clearance, the stronger the restrictive effect of the surrounding casing to the movement of the impeller, thus resulting in a larger reaction force on the impeller.

(4) The results of CalTech, Sulzer, and Mitsubishi indicate that tangential force becomes destabilizing at a smaller positive whirl speed ratio, $\Omega/\omega < 0.4$, regardless of pump discharge. The results of the Univ. Tokyo indicate, however, that the destabilizing effect occurs only at partial discharge.

(5) The characteristics of whirling fluid forces can be represented by a linear formulation using mass, damping, and stiffness matrices to a satisfactory extent. However, peculiar behaviors such as the local increase of fluid forces observed at low whirl speed ratio and partial discharge (cf. figure A-2) are all smoothed out and neglected, when the linear formulation is adopted.

APPENDIX B: QUALITATIVE EXPLANATION OF WHIRLING IMPELLER FORCE

The questions of why whirling fluid forces occur and how they are affected by whirl speed are explained here qualitatively by using a very simple model. Let us consider the fluid dynamic forces on blades A and B, which are indicated by solid straight lines in figure B-1 (a). It is assumed that the fluid dynamic characteristics of the blades are approximated by those of an isolated airfoil neglecting interaction between blades. The figure shows the impeller geometry at the moment when absolute center O' , impeller center O , and two blades are aligned on a straight line: that is, on the x-axis in this case. This condition is not a singular one. For an impeller with a large number of blades, there are always a couple of blades that are at the same disposition as that of the figure. The two blades considered in the model symbolize the ones which happen to be in such a situation.

When there is no whirl, the lift on a blade, L_0 , is proportional to the square of peripheral speed $u = R\omega$, where R is the radius of the blade center, and its direction is normal to the relative inlet flow W as seen in the figure. If whirl occurs, the impeller center O circles along the orbit with velocity $\epsilon\Omega$. At the location shown in the figure the whole impeller moves upward with the same velocity, so that the absolute peripheral speed of blade A increases from u to $u + \epsilon\Omega$, while that of B decreases from u to $u - \epsilon\Omega$. Consequently the lift of blades A and B vary by $\pm\Delta L$, where ΔL is estimated by a small perturbation principle as $\Delta L = 2L_0\epsilon\Omega/u$.

The imbalance of lifts on blades A and B results in an impeller force F_L shown in figure B-1 (b), which is proportional to whirl velocity $\epsilon\Omega$. A body in an accelerative motion receives an inertial reaction from the surrounding fluid equivalent to apparent mass times acceleration. Let M_a be the apparent mass of impeller blades, the inertial force of the whirl motion is $M_a\epsilon\Omega^2$ in the direction normal to the orbit. This inertial force is indicated by F_M in the figure. The total fluid force F caused by the whirl motion is therefore the resultant of two force vectors, F_M and F_L . The radial and tangential components of force F are then written by

$$F_r = M_a\epsilon\Omega^2 - k_r\epsilon\Omega, \quad F_\theta = k_\theta\epsilon\Omega \quad \dots\dots\dots (B1)$$

where k_r and k_θ are proportional constants.

The force characteristics predicted by the above modelling are illustrated in figure B-2 by solid curves. The measured characteristics indicated by thin broken curves are generally similar in shape but do not necessarily cross the origin as solid curves do. Radial and tangential forces at zero whirl speed ratio correspond to direct and cross stiffness, respectively. The above analysis, though it is quite simple and qualitative, suggests the mechanism of whirling fluid force and also its relation to the whirl speed.

As seen from figure B-1 (a), the absolute center O' , which represents the center of suction pipe and thus the location of source Q , changes its relative position to impeller blades during whirl. This induces a source-oriented perturbation on the blades and results in a corresponding unsteady fluid force. This effect has only a secondary significance as compared to the primary effect due to whirl speed-oriented perturbation, however, it constitutes a part of the discrepancy between the model and reality.

REFERENCES

1. Shoji, H. and Ohashi, H., "Fluid Forces on Rotating Centrifugal Impeller with Whirling Motion," NASA CP-2133, 1980, pp. 317-328.
2. Ohashi, H. and Shoji, H., "Lateral Fluid Forces Acting on a Whirling Centrifugal Impeller in Vaneless and Vaned Diffuser," NASA CP-2338, 1984, pp. 109-122.
3. Shoji, H. and Ohashi, H., "Lateral Fluid Forces on Whirling Centrifugal Impeller: Theory," Journal of Fluids Engineering, Vol. 109, 1987, pp. 94-99.
4. Shoji, H. and Ohashi, H., "Lateral Fluid Forces on Whirling Centrifugal Impeller: Experiment in a Vaneless Diffuser," Journal of Fluids Engineering, Vol. 109, 1987, pp. 100-106.
5. Ohashi, H., Hatanaka, R. and Sakurai, A., "Fluid Force Testing Machine for Whirling Centrifugal Impeller," Proc., Intern. Conf. on Rotordynamics, JSME/IFTOMM, Sept. 1986, Tokyo, pp. 643-648.
6. Jery, B., Acosta, A.J., Brennen, C.E. and Caughey, T.K., "Hydrodynamic Impeller Stiffness, Damping and Inertia in the Rotordynamics of Centrifugal Flow Pumps," NASA CP-2338, 1984, pp. 137-160.
7. Chamie, D.S., Acosta, A.J., Brennen, C.E. and Caughey, T.K., "Experimental Measurements of Hydrodynamic Radial Forces and Stiffness Matrices for a Centrifugal Pump-Impeller," ASME Journal of Fluids Engineering, Vol. 107, No. 3, 1985, pp. 307-315.
8. Bolleter, U. and Wyss, A., "Measurement of Hydrodynamic Interaction Matrices of Boiler Feed Pump Impellers," ASME 85-DET-148, 1985.
9. Pace, S.E., Florjancic, S. and Bolleter, U., "Rotordynamic Developments for High Speed Multistage Pumps," Proc., 3rd Intern. Pump symposium, Texas, May 1986, pp. 45-54.
10. Yoshida, Y. and Tsujimoto, Y., "Experimental Study of Fluid Forces on a Centrifugal Impeller Rotating and Whirling in a Volute Casing," JSME, Paper 87-1266A, March 1988 (in Japanese).

Table 1 Specifications of 2-D impeller

Impeller:	Two-dimensional, closed type
outer blade diameter;	350 mm
inner blade diameter;	175 mm
exit blade width;	35 mm
exit total width;	45 mm
number of blades;	6
exit vane angle to radius;	68°(logarith. spiral)
mass;	4.1 kg
Diffuser:	Parallel walled, vaneless
exit diameter;	700 mm
width;	70 mm

Table 2 Specifications of 3-D impeller

Impeller:	Three-dimensional, closed type
outer blade diameter;	330 mm
inner blade diameter;	180 mm
exit blade width;	28 mm
exit total width;	43.5 mm
number of blades;	6°
exit vane angle to radius;	65.5
mass;	5.6 kg
Diffuser:	Parallel walled, vaned and vaneless
inlet diameter;	340 mm
exit diameter;	480 mm
width;	30 mm
number of vanes;	11

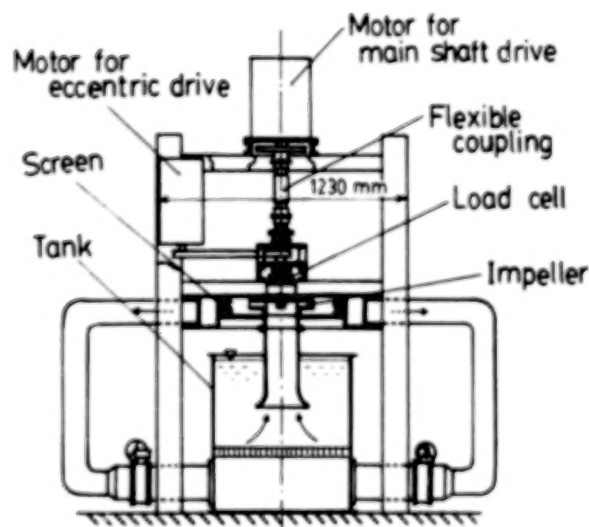


Figure 1. Layout of test facility

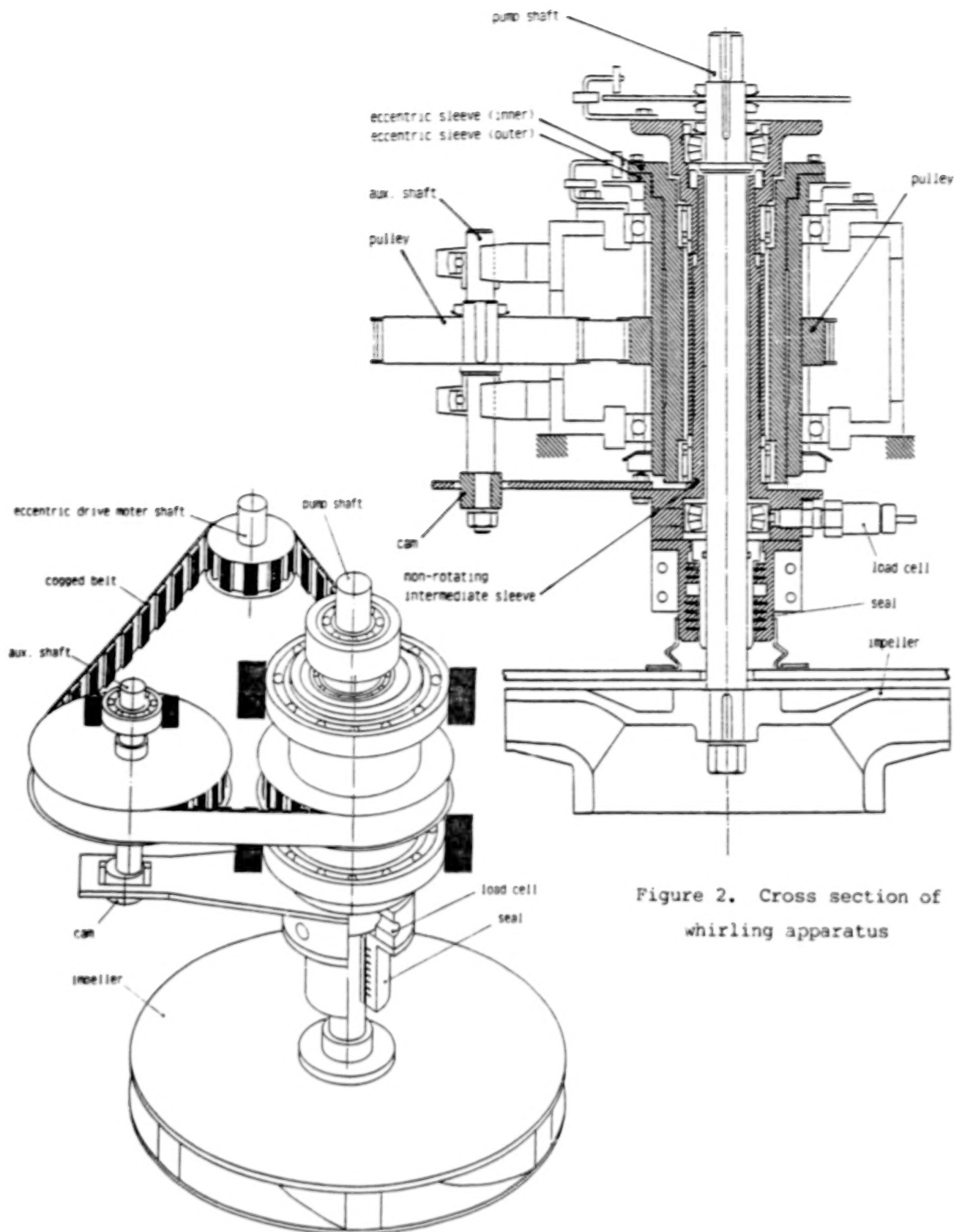


Figure 2. Cross section of whirling apparatus

Figure 3. Layout of whirling apparatus

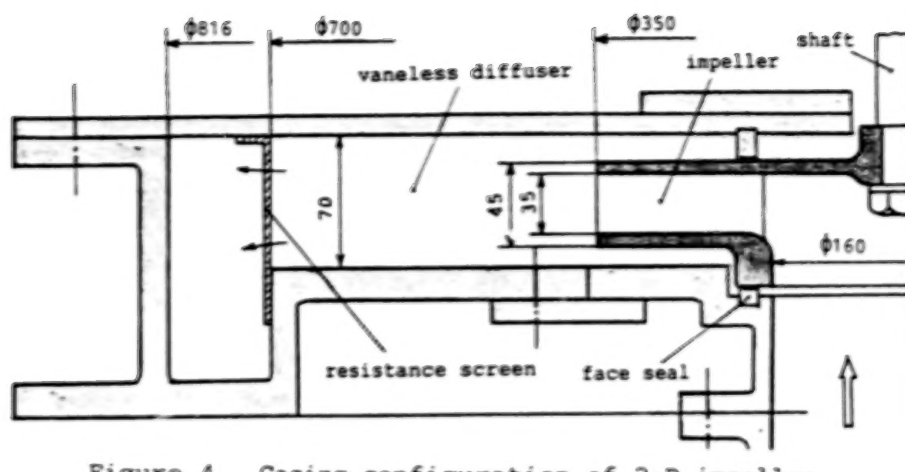


Figure 4. Casing configuration of 2-D impeller

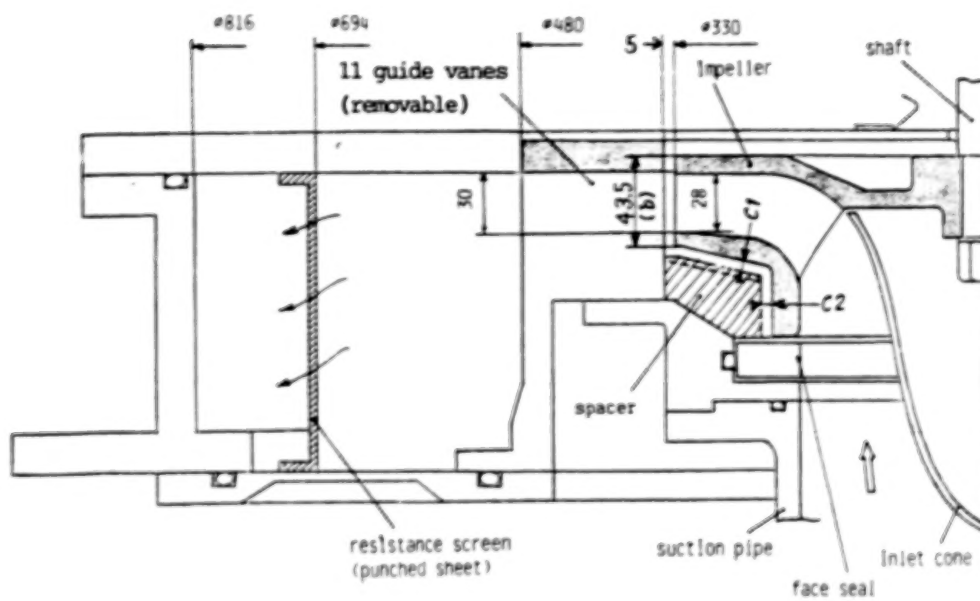


Figure 5. Casing configuration of 3-D impeller

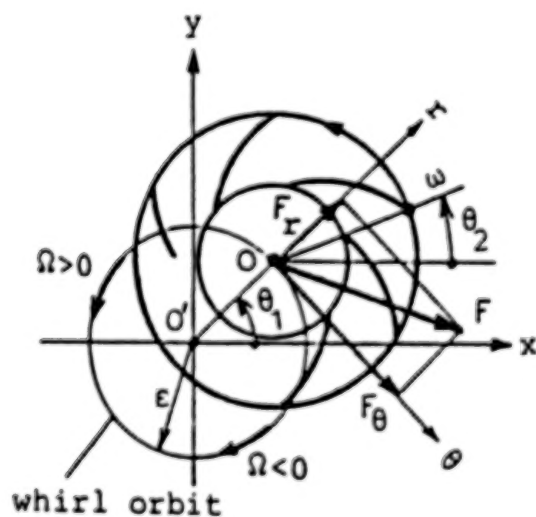


Figure 6. Coordinate system and force components

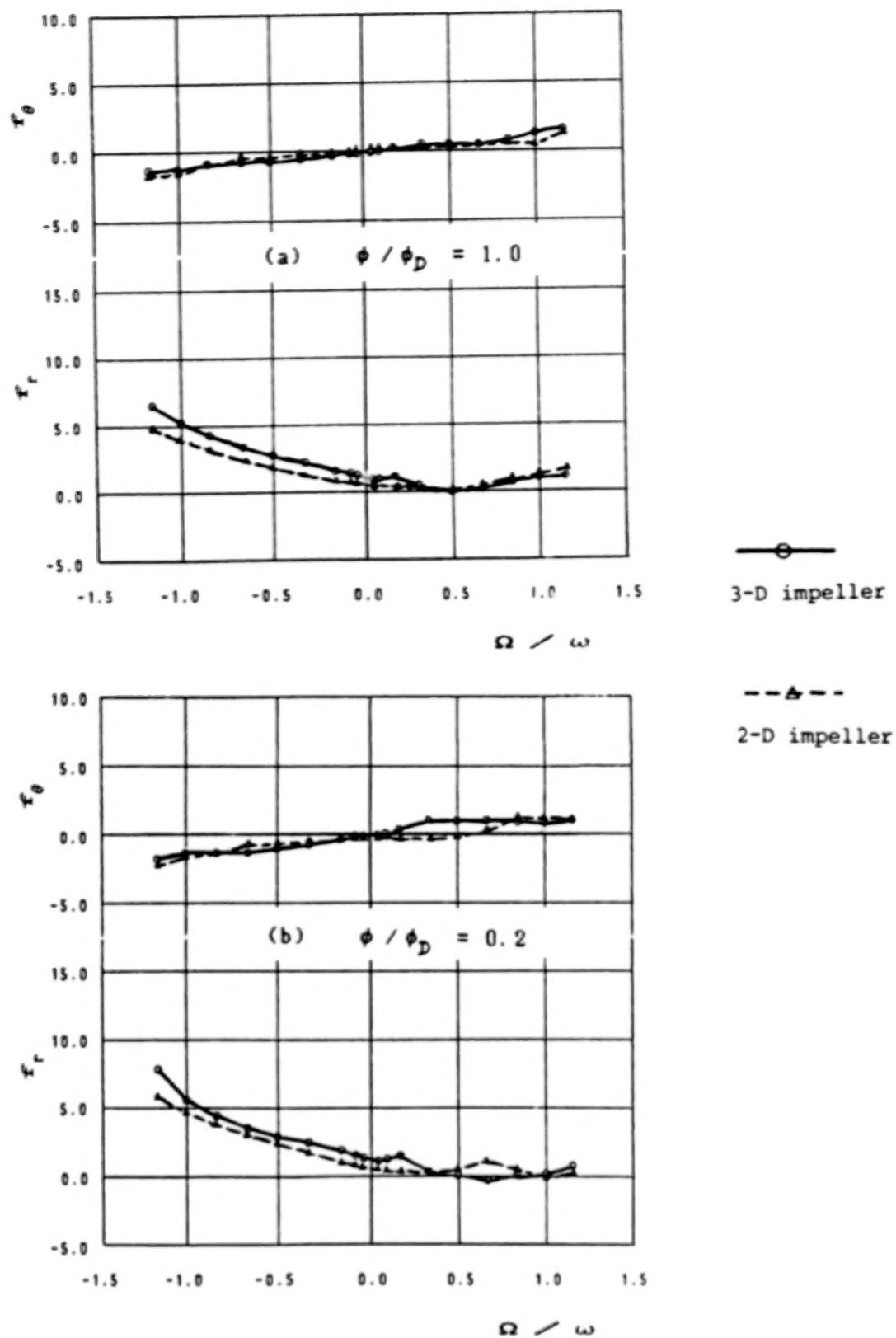


Figure 7. Normalized fluid forces on 2-D and 3-D impellers in vaneless diffuser

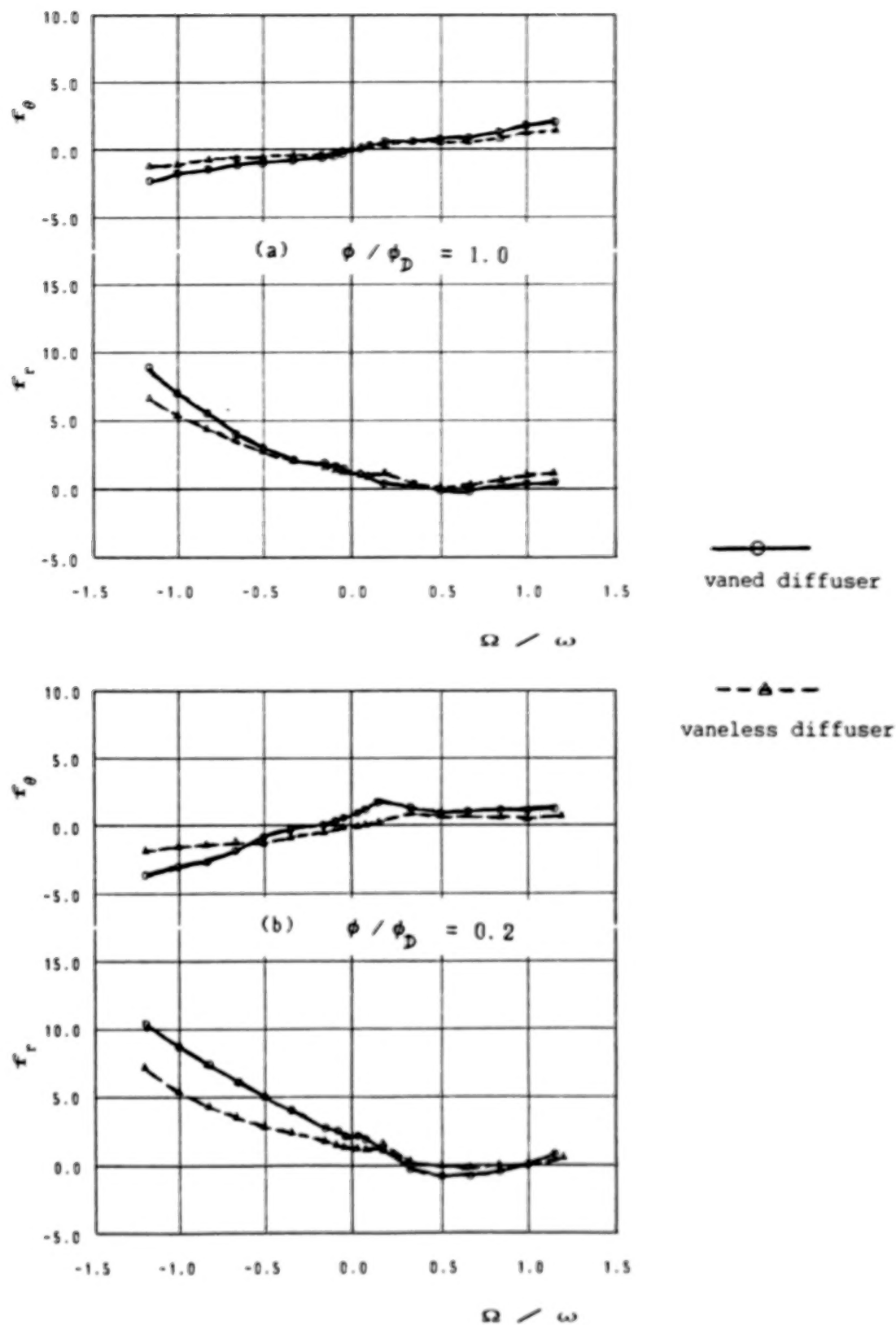
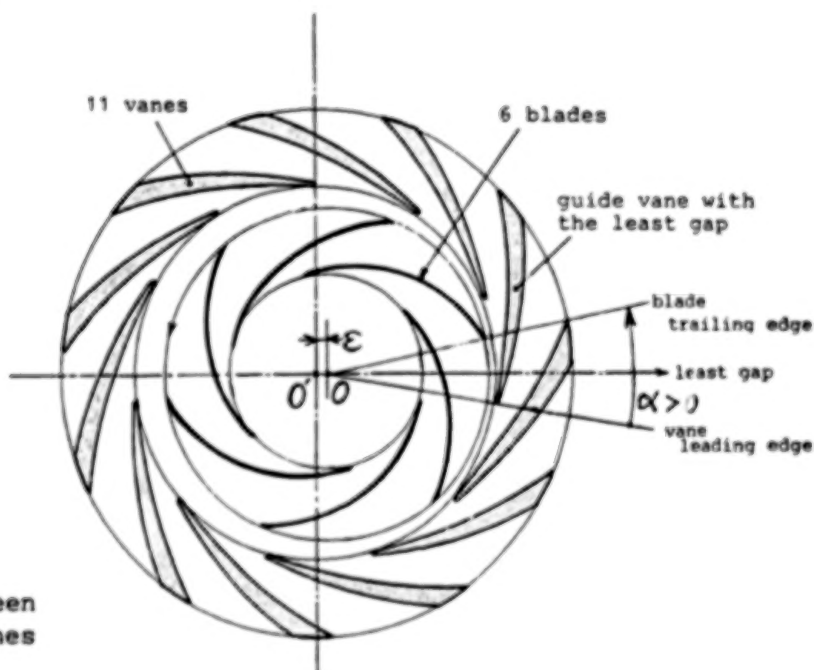
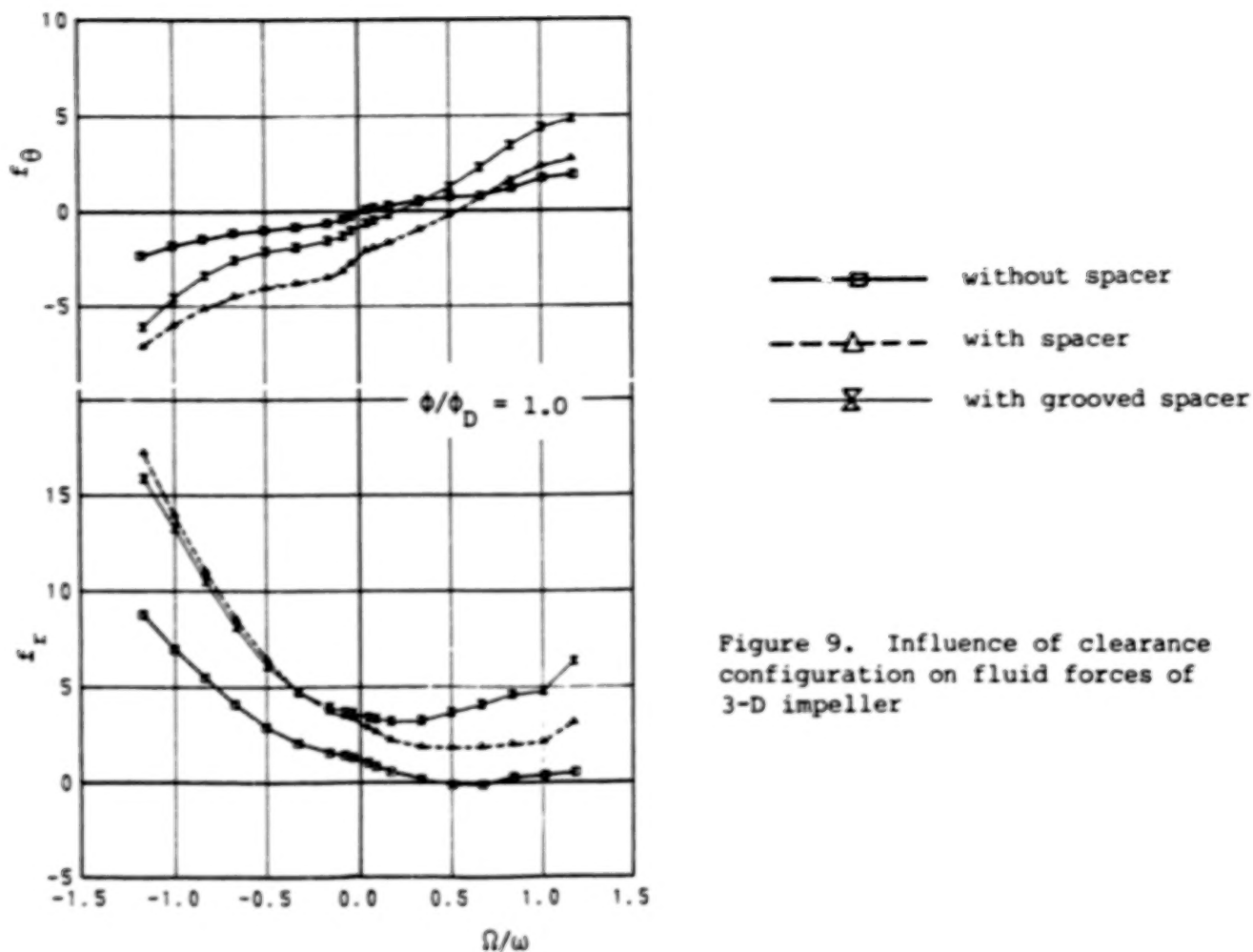


Figure 8. Normalized fluid forces on 3-D impeller in vaneless and vaned diffuser



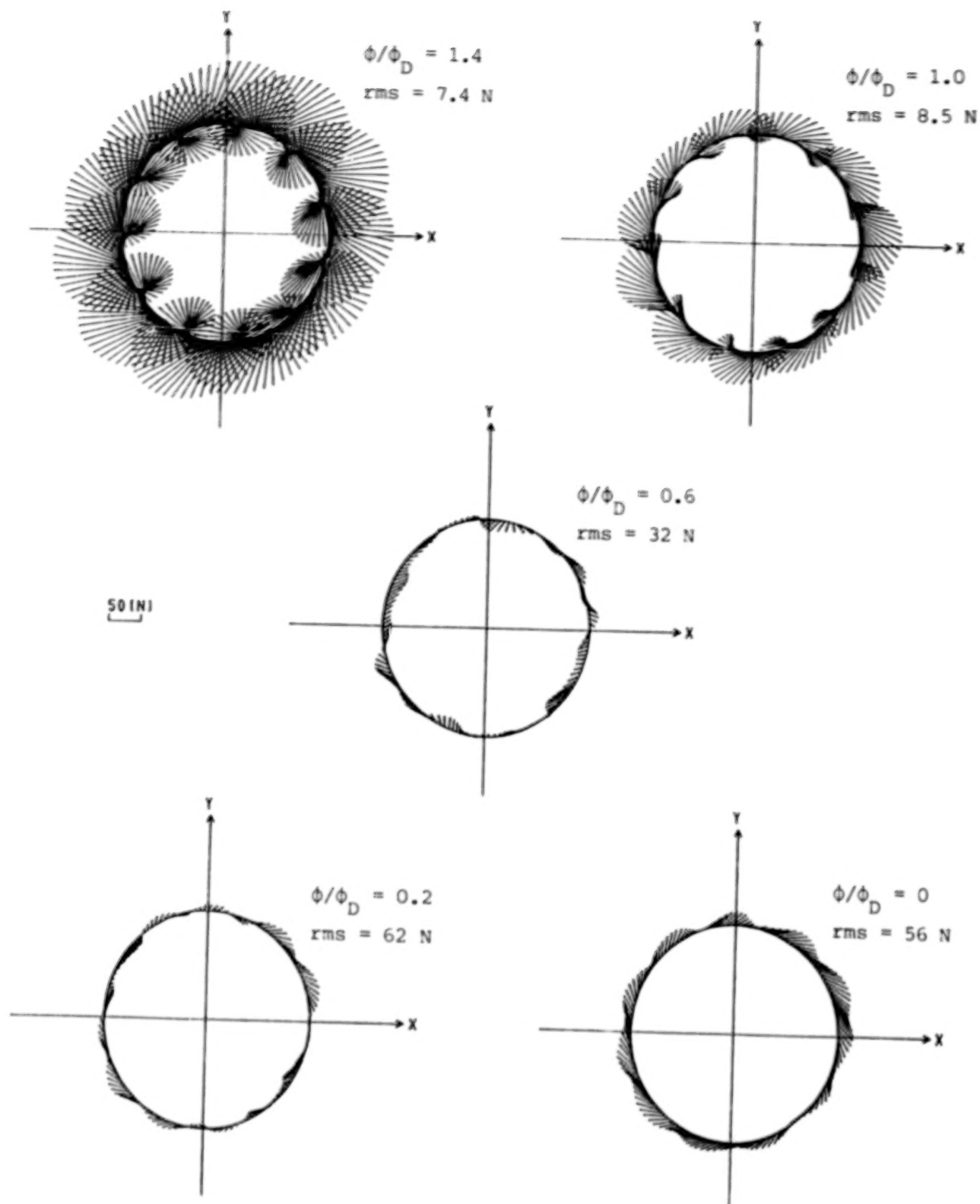


Figure 11. Impeller/guide vane interaction on the orbit at $\Omega/\omega = 1$

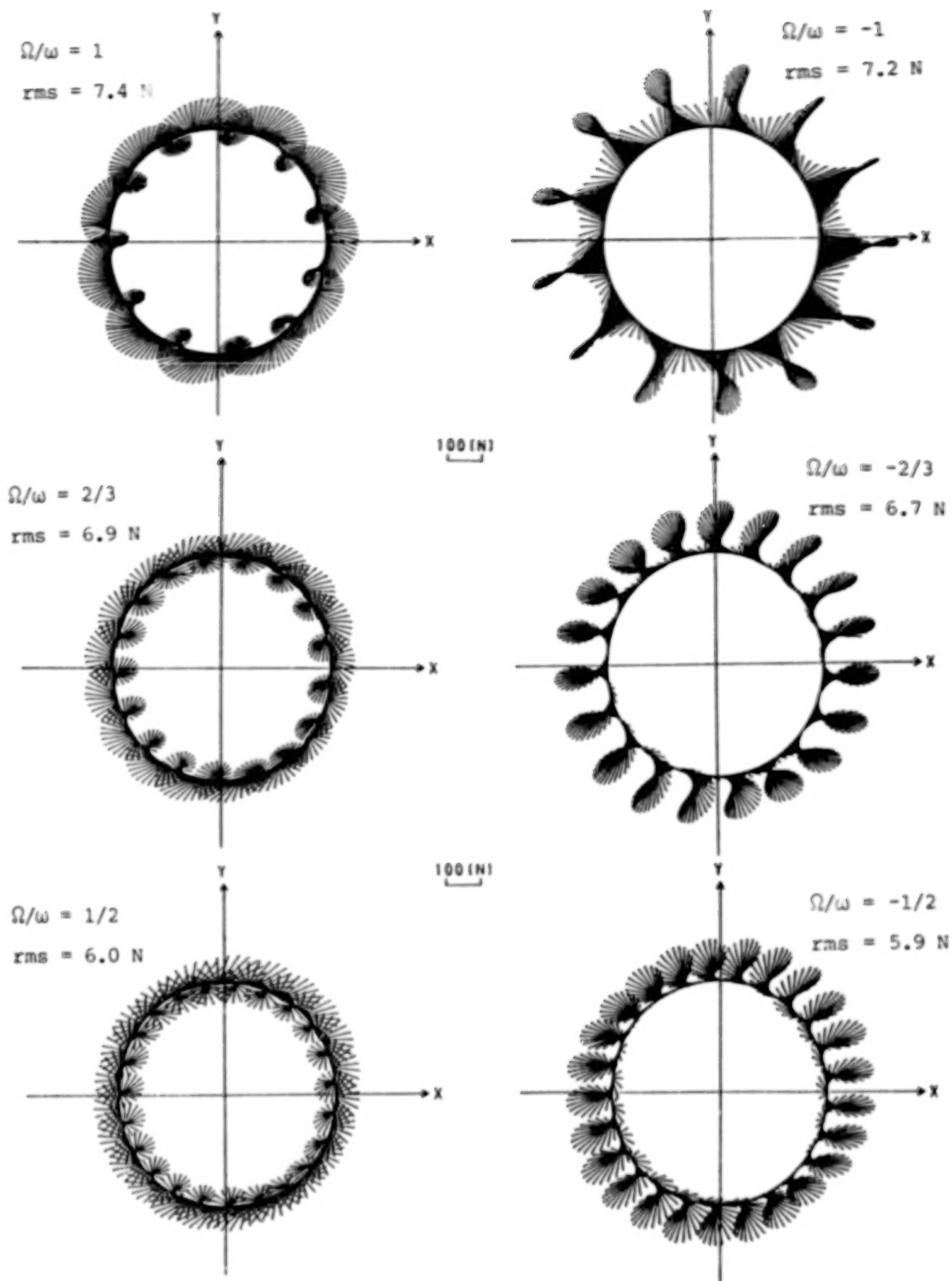


Figure 12. Impeller/guide vane interaction on the orbit at $\phi/\phi_D = 1.4$

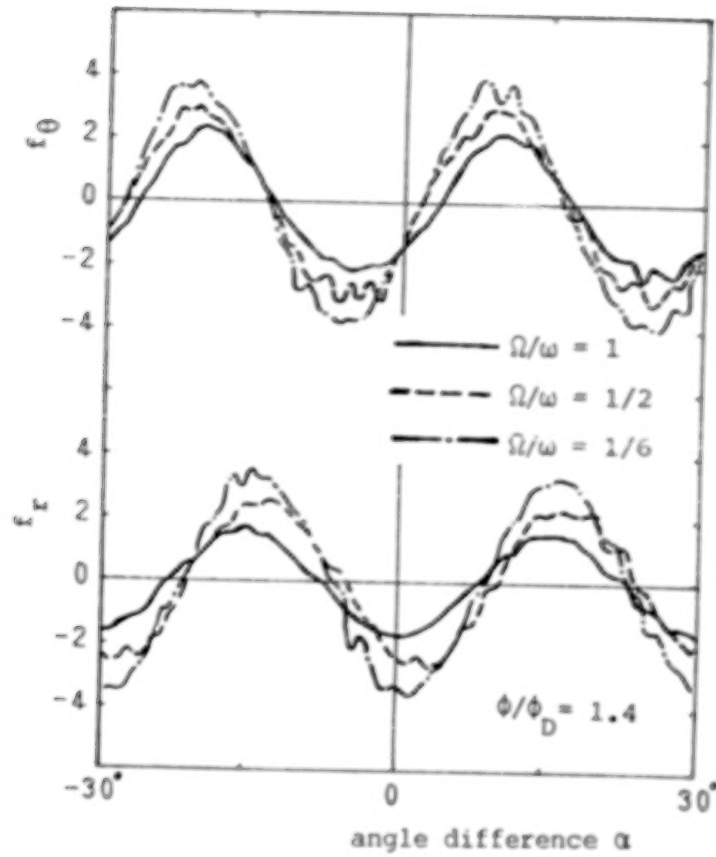


Figure 13. Force fluctuation plotted against angle α

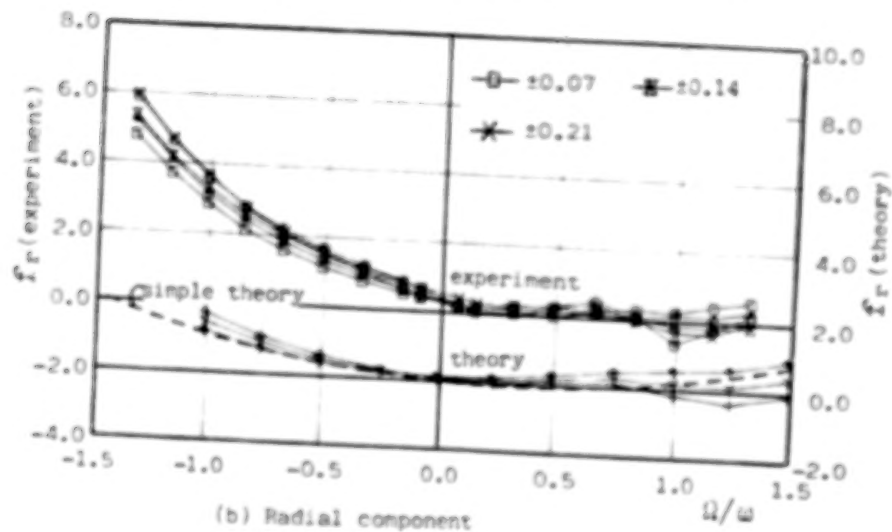
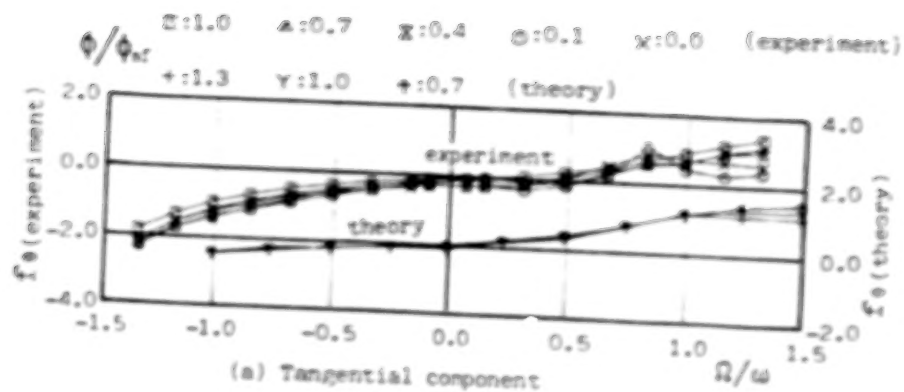


Figure A-1. Fluid forces on whirling blades of 2-D impeller in vaneless diffuser

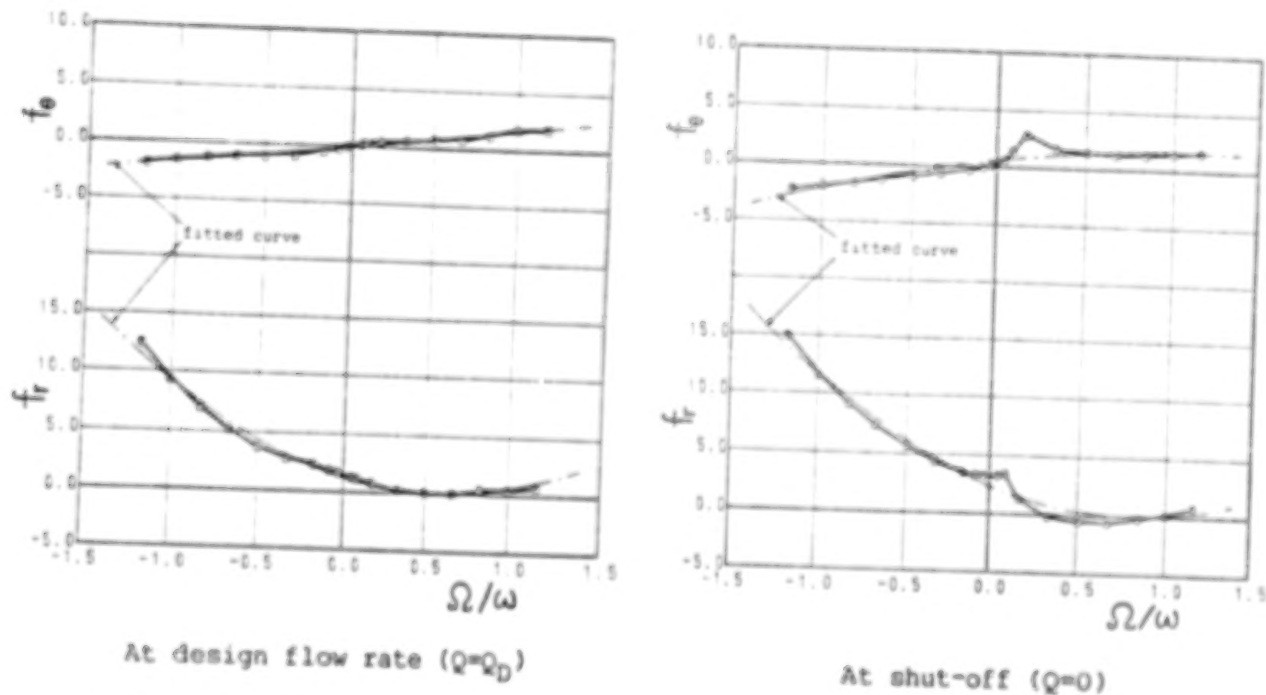


Figure A-2. Fluid forces on whirling 3-D impeller in vaned diffuser

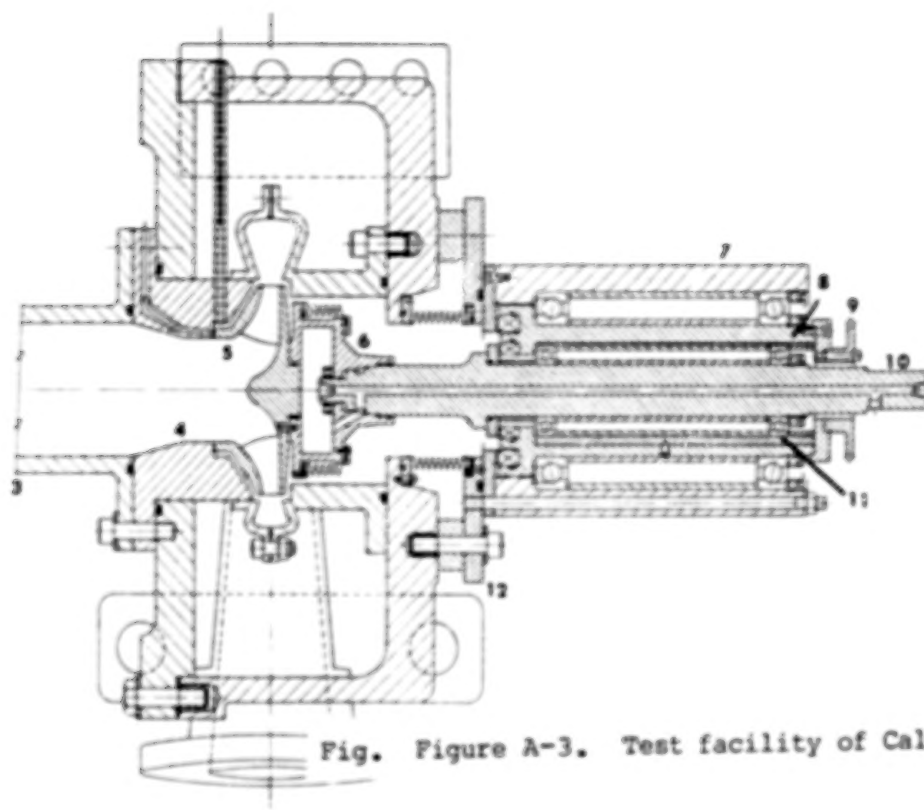


Fig. Figure A-3. Test facility of CalTech

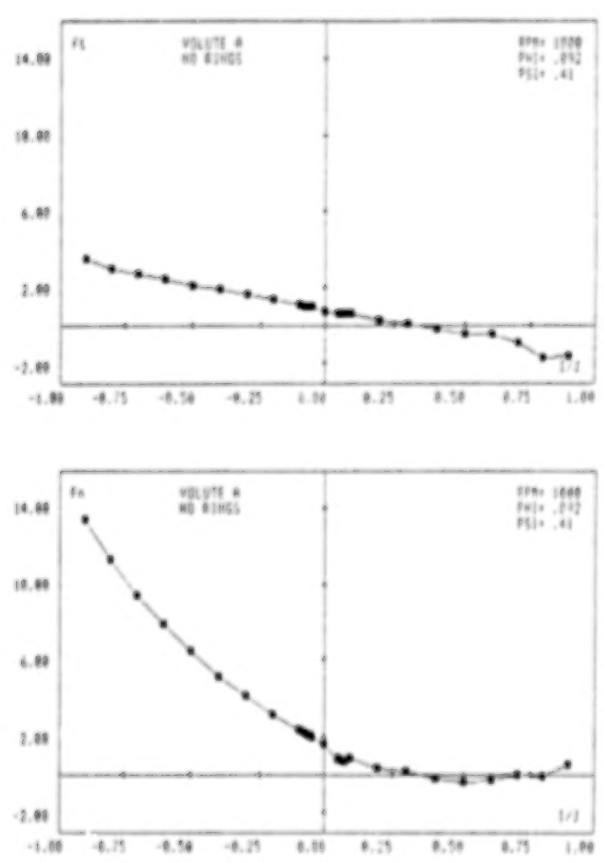


Figure A-4. Fluid forces on whirling 3-D impeller in volute casing

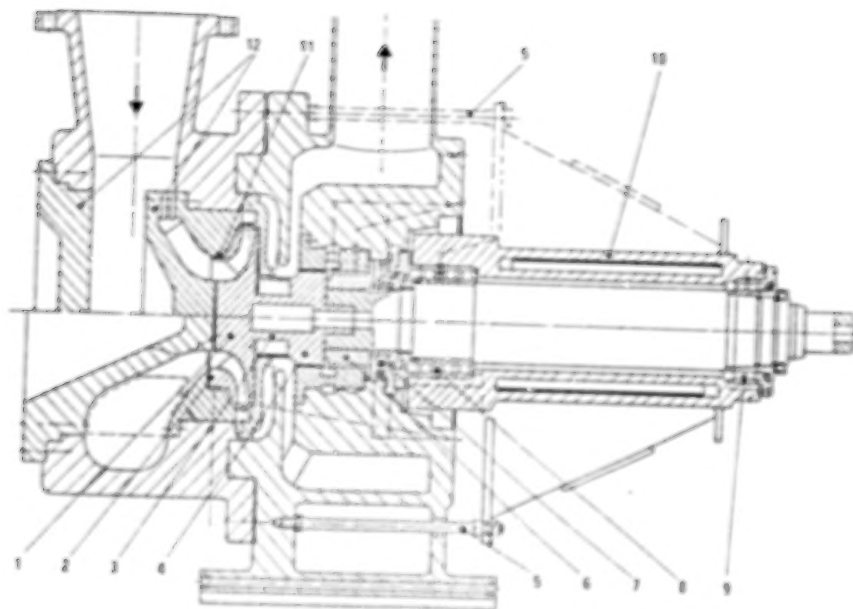


Figure A-5. Test facility of Sulzer

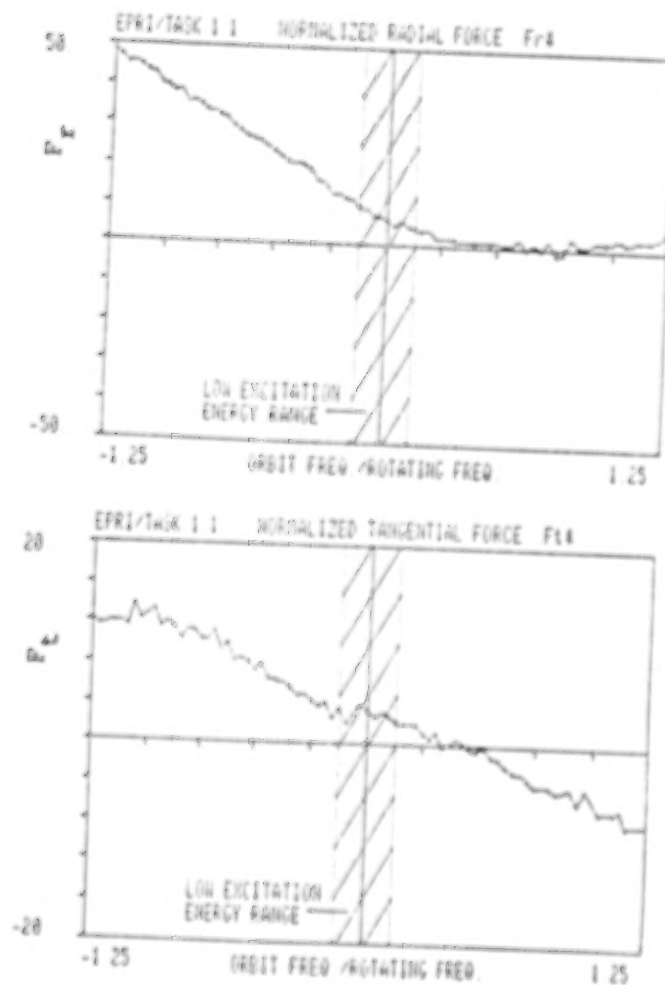


Figure A-6. Fluid force on whirling BFP impeller in vaned diffuser

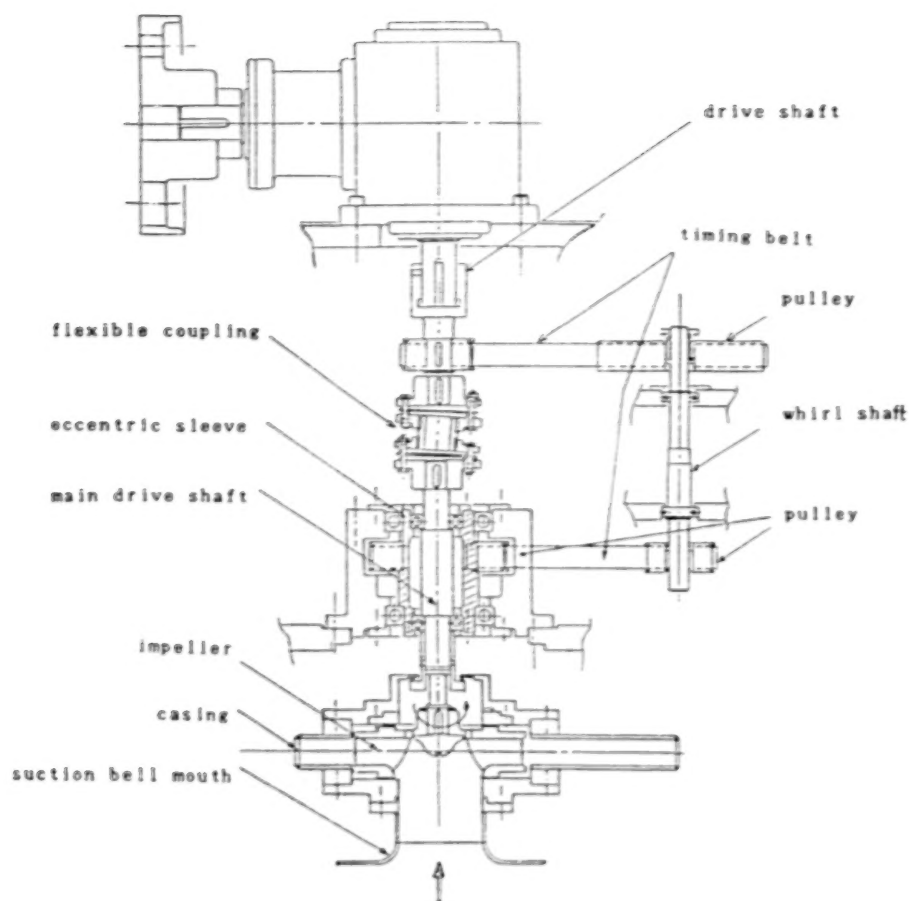


Figure A-7. Test facility of Mitsubishi

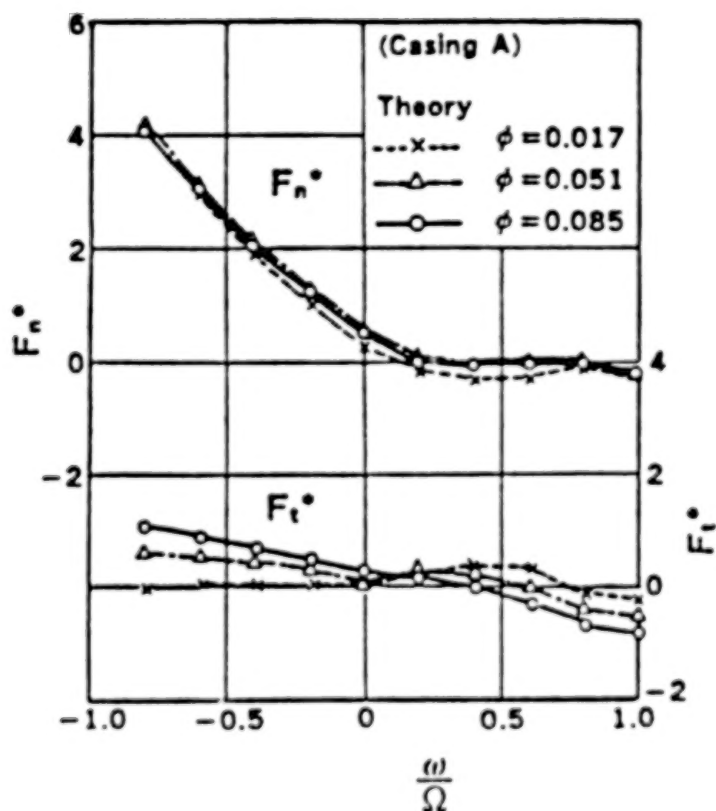


Figure A-8. Fluid forces on whirling 2-D impeller in volute casing

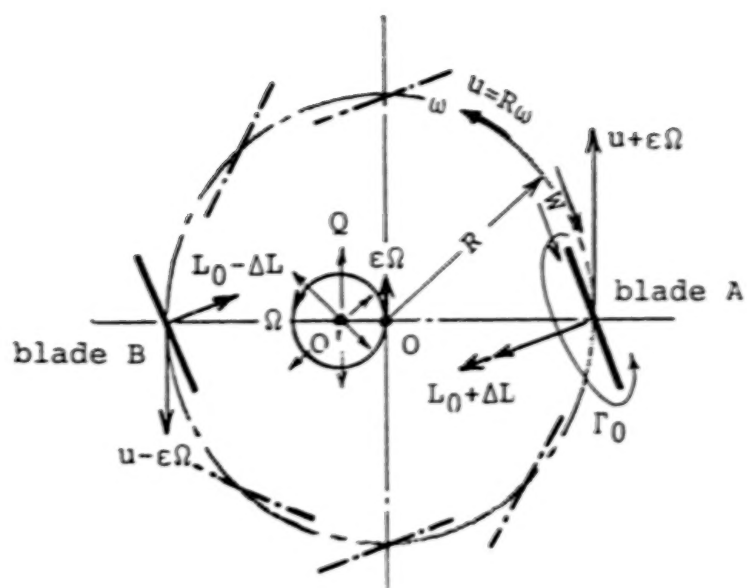


Figure B-1 (a) Flow model

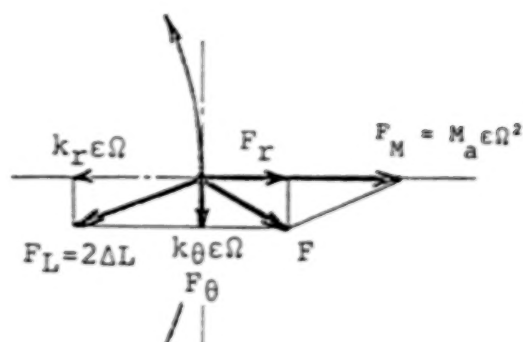


Figure B-1 (b) Force vectors

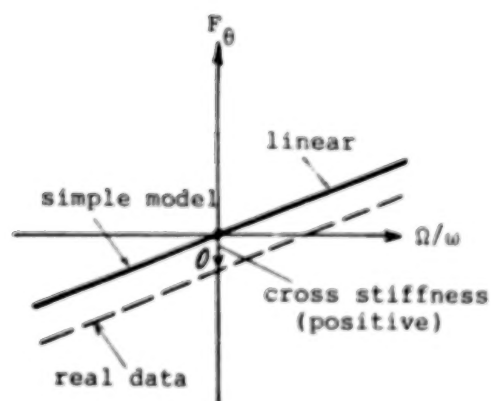
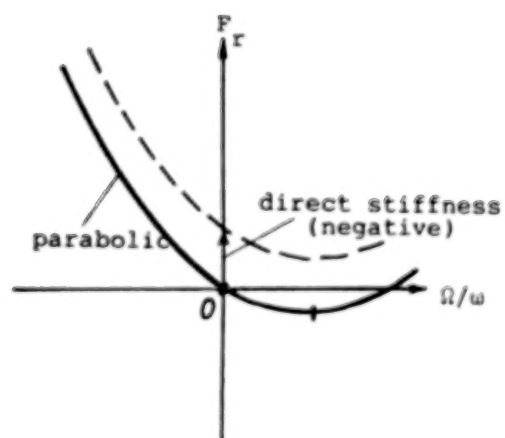


Figure B-2 Fluid forces on whirling impeller by simple model

A THEORETICAL STUDY OF FLUID FORCES ON A CENTRIFUGAL IMPELLER

ROTATING AND WHIRLING IN A VANED DIFFUSER

Yoshinobu Tsujimoto
Osaka University
Toyonaka, Osaka, 560, Japan

Allan J. Acosta
California Institute of Technology
Pasadena, California 91125, U.S.A.

Yoshiki Yoshida
Mitsubishi Heavy Industry
Takasago, Hyogo, 676, Japan

The fluid forces on a centrifugal impeller rotating and whirling in a vaned diffuser are analysed on the assumption that the number of impeller and diffuser vanes is so large that the flows are perfectly guided by the vanes. The flow is taken to be two dimensional, inviscid, and incompressible, but the effects of impeller and diffuser losses are taken into account.

It is shown that the interaction with the vaned diffuser may cause destabilizing fluid forces for whirling motion even at design flow rate. Discussions are made to elucidate the physical mechanisms that produce the destabilizing fluid forces. From these discussions, it is found that the whirling forces are closely related to the steady head-capacity characteristics of the impeller. This physical understanding of the whirling forces can be applied also to the cases with volute casings.

At partial capacities, it is shown that the impeller forces change greatly when the flow rate and whirl velocity are near to the impeller or vaned diffuser attributed rotating stall onset capacity, and the stall propagation velocity, respectively. In such cases the impeller forces may become destabilizing for impeller whirl.

INTRODUCTION

It has been made clear by pioneering experiments by Ohashi et al. (ref. 1) and Acosta et al. (refs. 2 and 3) that the fluid forces on centrifugal impellers may become destabilizing for whirling motion under certain conditions. Even if the impeller forces are stabilizing, it is important to estimate the forces since there are many cases in which the whirling instability is caused by bearing or seal forces.

So far the following examples have been reported in which the impeller forces become destabilizing for whirl. Ohashi et al. (ref. 1) have measured whirling forces on two-dimensional impellers in vaned or vaneless diffusers to capture the basic nature of the forces and to compare with their two-dimensional potential flow analyses (refs. 4 and 5). In this, it was found that the forces are basically stabilizing but become destabilizing for whirling with small positive whirl velocity

ratios at partial capacity. Recently new testing equipment was developed (ref. 6), and preliminary results on a three-dimensional boiler feed pump impeller model whirling in a vaned diffuser were reported. The impeller forces become very large compared with the 2D cases, but they are stabilizing both at design and shut off capacities.

Acosta et al. focused on the interaction with the volute casing and have shown that the forces on impellers whirling in a volute may become destabilizing even at design capacity (refs. 2, 3 and 7). A two-dimensional unsteady flow analysis (ref. 8) was carried out assuming that the impeller has an infinite number of vanes, and it was found that it can simulate the experimental results fairly well.

Bolleter and Wyss (ref. 9) used a "rocking arm" test apparatus to measure force matrices of a boiler feed pump impeller with outlet guide vanes. Whirling forces were synthesized on the assumption of the linearity of the disturbance, and it was shown that the forces are destabilizing for small positive whirl even at design capacity.

Two of the present authors have made an analysis (ref. 10) of impeller forces on a two-dimensional impeller whirling in a vaneless diffuser. There, it was shown that the whirling forces are basically stabilizing, as shown by Ohashi et al. (ref. 1), but they may become destabilizing if the flow rate and the whirling velocity are near the onset flow rate and the stall propagation velocity of rotating stalls due to the impeller or the vaneless diffuser.

The present study treats the cases when a impeller whirls in a vaned diffuser on the assumption of a two-dimensional inviscid incompressible flow. The number of impeller and/or diffuser vanes is taken to be infinite, and the total pressure losses in the impeller and the diffuser are taken into account. It is assumed that the outlet of the diffuser is open to a space of constant pressure. The problem is linearized on the assumption that the eccentricity and hence the unsteady components are sufficiently small.

FLOW ANALYSIS

We consider the case when, as shown in Fig. 1, a logarithmic centrifugal impeller with a vane angle β and inner and outer radii r_1 and r_2 rotates with an angular velocity Ω and whirls with an eccentricity ϵ and an angular velocity ω , in a logarithmic vaned diffuser with a vane angle α , inner and outer radii r_3 and r_4 . We take a stationary frame $z' = x' + iy' = r'e^{i\theta'}$ with its origin at the center of the diffuser, and a moving frame $z = x + iy = re^{i\theta}$ with its origin at the center of the impeller translating with its axes parallel to the stationary frame. We put ' on the velocities relative to the z' frame, and the velocities without ' represent the velocities relative to the z frame. The total velocity and the steady and unsteady components are represented by v , V , and v_d , respectively. For unsteady components, we use a complex representation with respect to an imaginary unit j such as $v_{rpd} = \tilde{v}_{rp} \exp(j(\omega t - \theta))$ where the suffix r means radial component and $p = 1, 2, 3, 4$ means the values at $r = r_1, r_2, r_3$, and r_4 . We consider that the real part carries the physical meaning.

Relations governing unsteady components

The results of the relations and expressions obtained for the vaneless diffuser case (ref. 10) could also be used here.

Velocity at the impeller inlet: The velocity disturbance is composed of that due to relative dislocation of a source Q at the origin of the z' frame and an unknown potential disturbance

$$\tilde{v}_{r1} = -\varepsilon Q / (2\pi r_1^2) + v_{r1}^* \quad (1)$$

$$\tilde{v}_{\theta 1} = -\varepsilon Q j / (2\pi r_1^2) - j v_{r1}^* \quad (2)$$

where v_{r1}^* is an unknown complex constant.

Velocities at the impeller outlet and the diffuser inlet ($p = 2, 3$): The steady velocity in the vaneless part ($r_2 < r < r_3$) is given by $(V_r, V_\theta) = (Q/2\pi r, \Gamma/2\pi r)$ where $\Gamma = 2\pi r_2[r_2\Omega - Q/(2\pi r_2)\cot\beta]$ is the impeller circulation. We assume a vorticity ζ shed from the impeller is transported at this steady velocity. Then the unsteady velocities can be given as a sum of the velocity induced by the vorticity field of magnitude ζ_2 and a potential flow disturbance of strength \tilde{A} .

$$\tilde{v}_{rp} = Z_{rp}\zeta_2 + A_{rp}\tilde{A} \quad (3)$$

$$\tilde{v}_{\theta p} = Z_{\theta p}\zeta_2 + A_{\theta p}\tilde{A} \quad (4)$$

where

$$Z_{rp} = (R_R - jR_I)_{rp} - (r_2/r_p)^2 e^{-2j\beta} (R_R - jR_I)_{r2}$$

$$Z_{\theta p} = (\theta_R - j\theta_I)_{rp} - j(r_2/r_p)^2 e^{-2j\beta} (R_R - jR_I)_{r2}$$

$$A_{rp} = 1 - (r_2/r_p)^2 e^{-2j\beta}, \quad A_{\theta p} = -j(1 + (r_2/r_p)^2 e^{-2j\beta})$$

$$R_R - jR_I = -j(S + T), \quad \theta_R - j\theta_I = S - T$$

$$S(r) = (1/2) \int_{r_2}^r \lambda(r_0, 0)(r_0/r)^2 dr_0$$

$$T(r) = (1/2) \int_r^{r_3} \lambda(r_0, 0) dr_0$$

$$\lambda(r, \theta) = \exp([-j(\pi\omega(r^2 - r_2^2)/Q + \theta - (\Gamma/Q)\log(r/r_2))])$$

The expressions (3) and (4) are so determined that the flow tangency condition at the impeller outlet $\tilde{v}_{\theta 2} = -\tilde{v}_{r2} \cot\beta$ is satisfied.

Continuity of mass flow between impeller inlet and outlet: Defining $\phi \equiv \theta_1 - \theta_2 = \cot\beta \log(r_2/r_1)$ as shown in Fig. 1, we obtain the following continuity relation between $r = r_1$ and r_2 .

$$r_1 \tilde{v}_{r1} = r_2 \tilde{v}_{r2} e^{j\phi} \quad (5)$$

Strength of shed vorticity: We obtain the following expression by integrating the momentum equation from inlet to outlet of the impeller and using the θ component of Euler's equation at the impeller outlet.

$$r_2 V_{r2} \zeta_2 = J \tilde{v}_{r2} + D \quad (6)$$

where

$$J = (\omega - \Omega) \{ r_2 (1 + j \cot \beta) + M \} - j L_1$$

$$D = c Q e^{-j\phi} \{ 2 r_1 (\omega - \Omega) - L_2 \} / (2 \pi r_1^2)$$

and $M \equiv \int_{r_3}^{r_2} r_2 / (r \sin \beta) ds = r_2 (\sin \beta)^{-2} \log(r_2/r_1)$ is the effective length of the flow

channel of the impeller, L_1 and L_2 are parameters representing the effects of total pressure loss in the impeller. These are given as follows. We assume that the loss can be given as a sum of incidence and hydraulic losses:

$$\Delta p_t / \rho = \{ \zeta_s (1/t_a - 1/t_{ad})^2 + \zeta^* \} v_{r1}^2 / 2 \equiv Z(t_a) v_{r1}^2 / 2 \quad (7)$$

where t_a is the tangent of the mean flow inlet angle $\bar{\beta}_1$, and $t_{ad} = \tan \beta$. The hydraulic and incidence loss coefficients ζ^* and ζ_s are evaluated from

$$\zeta^* = 2(1 - \eta_h)(r_1/r_2)^2(1 - \phi_d \cot \beta) / \phi_d^2$$

$$\zeta_s = 0.3 + 0.6 \beta^\circ / 90^\circ$$

using the shock free flow coefficient ϕ_d and the impeller efficiency η_h at ϕ_d . For simplicity, we neglect the delay of loss and evaluate the loss from quasi-steady application of equation (7). After linearization on the assumption that the disturbance is small, we obtain the following expressions for L_1 and L_2 :

$$L_1 = V_{r1} (r_2/r_1) \{ Z + (1/2) \tan \bar{\beta}_1 (1 - j \tan \bar{\beta}_1) Z' \}$$

$$L_2 = V_{r1} Z' \tan^2 \bar{\beta}_1$$

The condition at diffuser outlet

We assume that the outlet of the diffuser is connected to a space of constant pressure. From this condition, we derive a relation that should be satisfied at the diffuser inlet. Taking the total pressure loss Δp_{td} in the diffuser into account, we can express the unsteady Bernoulli's equation as follows.

$$p_3 / \rho = p_4 / \rho + 1/2 (v_4'^2 - v_3'^2) + \int_{r_3}^{r_4} \partial v_s' / \partial t \cdot ds + \Delta p_{td} / \rho \quad (8)$$

We evaluate Δp_{td} by equation (7) after replacements of $Z(t_a)$ with $Z_d(\tan \bar{\alpha}_3)$ and v_{r1} with v'_{r3} . After the linearization of equation (8) with respect to the unsteady component and the differentiation with θ' , we obtain

$$1/\rho \cdot \partial p_3 / \partial \theta_3' = -j \{ (E_d + L_{1d}) \tilde{v}_{r3}' - (\Gamma / 2 \pi r_3 + L_{2d} / 2) \tilde{v}_{\theta 3}' \} \quad (9)$$

where

$$E_d = V_{r4} (r_3/r_4) (1 + \cot^2 \alpha) - V_{r3} + j \omega M_d$$

M_d = effective length of diffuser flow channel

$$= r_3(\sin\alpha)^{-2}\log(r_3/r_4)$$

$$L_{1d} = Z_d V_{r3} + (1/2)V_{r3}Z_d' \tan\bar{\alpha}_3$$

$$L_{2d} = V_{r3}Z_d' \tan^2\bar{\alpha}_3$$

and the relation $\partial p_4/\partial\theta_3' = 0$ has been used. $\bar{\alpha}_3 = \tan^{-1}(Q/\Gamma)$ is the mean flow angle at the diffuser inlet.

The unsteady component of the absolute velocity at the diffuser inlet is given as a sum of the unsteady component in the moving frame, a component due to the dislocation of the steady flow field (V_r , V_θ), and the whirling velocity:

$$\begin{aligned}\tilde{v}_{r3}' &= \tilde{v}_{r3} + \epsilon(Q - j\Gamma)/2\pi r_3^2 + \epsilon\omega j \\ \tilde{v}_{\theta 3}' &= \tilde{v}_{\theta 3} + \epsilon(\Gamma + jQ)/2\pi r_3^2 + \epsilon\omega\end{aligned}\quad (10)$$

Putting equations (9) and (10) in the θ' component of a linearized Euler's equation, we finally obtain the following equation representing the diffuser outlet condition.

$$P_\zeta \bar{\zeta}_2 + P_A \bar{A} = G \quad (11)$$

where

$$\begin{aligned}P_\zeta &= (j\omega + V_{r3}/r_3 + jL_{2d}/2r_3)Z_{\theta 3} - j(E_d + L_{1d})Z_{r3}/r_3 + V_{r3}Z_a \\ P_A &= (j\omega + V_{r3}/r_3 + jL_{2d}/2r_3)A_{\theta 3} - j(E_d + L_{1d})A_{r3}/r_3 - jZ_b V_{r3} \\ G &= -\epsilon(j\omega + V_{r3}/r_3 + jL_{2d}/2r_3)(\omega + V_{\theta 3}/r_3 + jV_{r3}/r_3) \\ &\quad + \epsilon j(E_d + L_{1d})(V_{r3}/r_3 + j\omega - jV_{\theta 3}/r_3)/r_3 + 2\epsilon V_{r3}(V_{\theta 3} + jV_{r3})/r_3^2 \\ Z_a &= \lambda(r_3, 0) - 2S(r_3)/r_3 + 2j(r_2^2/r_3^3)e^{-2j\beta} (R_R - jR_1)r_2 \\ Z_b &= -2(r_2^2/r_3^3)e^{-2j\beta}\end{aligned}$$

Determination of flow and impeller forces

From equations (1) to (6) and (11), we obtain

$$\bar{A} = \{G(r_2 V_{r2} - JZ_{r2}) - P_\zeta D\} / \{P_\zeta JA_{r2} + P_A(r_2 V_{r2} - JZ_{r2})\} \quad (12)$$

Other unknowns are determined by the successive use of equations (1) to (6) and (11). Each term of the numerator of the above equation has a factor ϵ . By considering the case with $\epsilon = 0$, we find that the rotating stall onset conditions under the interaction of impeller and diffuser are obtained by setting the denominator of equation (12) to be zero.

The impeller forces are determined from the balance of momentum. If we separate the impeller forces into components normal to (n) and tangential to (t ; positive counter clockwise) the whirling orbit, each component stays constant. The

impeller forces (F_n , F_t) normalized with $\rho\pi(r_2\Omega)^2\epsilon$ are given by summing up the following components. ($\phi \equiv Q/2\pi r_2^2\Omega$ is a flow coefficient.)

Force due to inlet pressure

$$(F_n + jF_t)_{p1} = (r_1/r_2)[(\omega r_1/\Omega r_2)(-2j(r_2/r_1)^2\phi + \omega/\Omega) - \tilde{v}_{r2}/(\epsilon\Omega)e^{j\phi}(j\omega/\Omega + \phi(r_2/r_1)^2)] \quad (13.1)$$

Force due to inlet momentum

$$(F_n + jF_t)_{m1} = \phi[2\phi(r_2/r_1)^2 + 2j\omega/\Omega + 3e^{j\phi}\tilde{v}_{r2}(r_2/r_1)/\epsilon\Omega] \quad (13.2)$$

Force due to outlet pressure

$$\begin{aligned} (F_n + jF_t)_{p2} = & -(\omega/\Omega)^2 - je^{-j\phi}(L_2/r_2\Omega)\phi(r_2/r_1)^2 \\ & - 2j\phi(r_2/r_1)e^{-j\phi}(1 - \omega/\Omega) \\ & - (j(1 + M/r_2)(1 - \omega/\Omega) - \phi(1 + \cot^2\beta)) \\ & - L_1/(r_2\Omega)\tilde{v}_{r2}/(\epsilon\Omega) \end{aligned} \quad (13.3)$$

Force due to outlet momentum

$$(F_n + jF_t)_{m2} = -(2\phi + j(1 - 2\phi \cot\beta)\tilde{v}_{r2}/(\epsilon\Omega) - 2j\phi(\omega/\Omega)) \quad (13.4)$$

Force due to change of momentum of the fluid in the impeller

$$(F_n + jF_t)_m = -j(\omega/\Omega)(1 - (r_1/r_2)e^{j\phi})\tilde{v}_{r2}/(\epsilon\Omega) + (\omega/\Omega)^2(1 - (r_1/r_2)^2) \quad (13.5)$$

RESULTS AND DISCUSSIONS

We consider an impeller with $r_1/r_2 = 0.5$, $\beta = 30^\circ$. The shock free flow coefficient for this impeller is $\phi_d \equiv v_{r2}/(r_2\Omega) = 0.1443$, which is looked upon as the "design" condition and is also shockless for diffusers with $\alpha = 11^\circ$. The loss coefficients of the impeller were estimated from the equations shown in the last section assuming $\eta_h = 0.9$. The hydraulic loss coefficient for the diffuser was estimated from the expression of the coefficient after multiplying by $(r_2/r_1)^2$ and using $\eta_h = 0.9$. The diffuser incidence loss coefficient was obtained from the expression for the impeller after replacing β with α .

Impeller forces at design flow rate

Figure 2 shows the plots of F_n and F_t against the whirl velocity ratio ω/Ω . There, the diffuser inlet radius r_3 is changed keeping $(r_4 - r_3)/r_2$ to be 0.25. It has been known that if F_t is in the same direction as the whirl it is destabilizing, and vice versa. We find a destabilizing region for small positive whirl for $r_3/r_2 < 1.5$. This region diminishes with the increase of r_3/r_2 . A similar destabilizing region is observed also for the cases with a volute. Discussions on this will be made shortly. F_n for $\omega/\Omega < 0$ increases with the decrease in r_3/r_2 , which is considered to be caused by the increase of the apparent mass due to interaction with the vaned diffuser. If we increase r_3/r_2 , F_n and F_t tend to the values for the case with a vaneless diffuser with outer radius $r_3/r_2 = 5.25$.

Figure 3 shows the effects of r_4/r_2 . We see that F_n for $\omega/\Omega < 0$ increases with the increase in r_4/r_3 , but F_t is not affected by r_4/r_3 systematically. Note that the destabilizing region exists even for the case with $r_4 = r_3$. On the other hand, if we change the vane angle α and r_4/r_3 keeping the effective length of the diffuser M_d to be constant, as shown in Figure 4, F_n does not change much but F_t for small positive to negative ω/Ω decreases with the increase in α . Now we can say that F_n for $\omega/\Omega < 0$ is mainly affected by M_d . F_t for $\omega/\Omega \lesssim 0.4$, and hence the existence of the destabilizing region, is largely dependent on the value of α .

In Figure 5 the impeller forces are separated into components corresponding to equations (13.1) to (13.5). We see that the component due to outlet pressure is dominant for $\omega/\Omega < 0.4$. Although not shown here, the contribution of outlet pressure is larger for the cases with smaller r_3/r_2 . This is true also at partial capacities.

In all of the above calculations the effects of impeller and diffuser losses are taken into account. The above tendencies are not changed by neglecting the losses. After all, it is considered that the flow turning effect of the vaned diffuser is responsible for the existence of the destabilizing region.

Let us consider the physical mechanism with which the impeller forces become destabilizing. To simplify the problem we take the limits $r_3 \rightarrow r_2$ and $\alpha \rightarrow 0$. For such cases we can obtain a purely analytical solution without numerical integrations with respect to the shed vorticity. By letting $\alpha \rightarrow 0$ in the continuity equation $(v_4')^2 = (r_3/r_4)^2 (v_{r3}')^2 / \sin^2 \alpha$, we find that a small increase in v_{r3}' in some part of the circumference results in a large increase in v_4' and hence in p_3 there, from equation (8). Then the outflow from the impeller to that part will be diminished; a diffuser with a small α has a smoothing effect on the circumferential flow rate distribution through the diffuser. By letting $\tilde{v}_{r3}' \rightarrow 0$ and $r_3 \rightarrow r_2$ in equation (10), we obtain

$$\begin{aligned} \tilde{v}_{r2} &\rightarrow -\epsilon(Q - j\Gamma)/(2\pi r_2^2) - \epsilon\omega j \\ &= \epsilon\Omega[-\phi + \{(1 - \phi \cot\beta) - \omega/\Omega\}j] \end{aligned} \quad (14)$$

This means that an outflow distribution \tilde{v}_{r2} from the impeller is so determined as to cancel the radial absolute velocity disturbances due to the dislocation of the flow field of impeller circulation Γ and source Q and due to the whirling velocity. This equation can be obtained also by letting $\alpha \rightarrow 0$ in the analytical solution.

We estimate the impeller forces due to a pressure distribution which is obtained by assuming that the inertia on the fluid in the impeller due to \tilde{v}_{r2} is balanced by the outlet pressure distribution. Then we have

$$(F_n + jF_t)_{p2} = -j(1 - \omega/\Omega)M\tilde{v}_{r2}/(r_2\epsilon\Omega) \quad (15)$$

From the definition of complex representation, we find that the complex plot of \tilde{v}_{r2} gives the azimuthal direction where the radial velocity becomes maximum and the amplitude of the radial velocity fluctuation, in a plane with its real axis in the direction of eccentricity (n) and the imaginary axis in the tangential (t) direction. Equation (14) shows that the radial velocity will become maximum in the direction $(n, t) = (-\phi, \psi \equiv 1 - \phi \cot\beta)$ for $\omega/\Omega = 0$ and the pressure in the direction $(-\psi, -\phi)$ where ϕ and ψ are flow and head coefficients. The resulting force is,

from equation (15), in the direction of (ψ, ϕ) , i.e., outward and in the direction of rotation. Thus the impeller force is closely related to the steady impeller characteristics. F_n and F_t determined from equations (14) and (15) are given in the APPENDIX. Next is considered the effects of impeller loss. Near design flow rate, the loss becomes maximum in the direction of \tilde{v}_{r2} . There the outlet pressure is diminished and the resulting force can be expressed as $2(r_2/r_1)^2 \phi \tilde{v}_{r2}/(\epsilon\Omega)$, which is in the same direction as \tilde{v}_{r2} .

Figure 6 shows the above relations for $\alpha \rightarrow 0$ and $r_3/r_2 \rightarrow 1$ in which impeller and diffuser losses are neglected. This figure shows that equation (14) can estimate \tilde{v}_{r2} fairly well for $\alpha = 1^\circ$ and that the impeller force may be approximated by the outlet pressure force of equation (15) for $\omega/\Omega < 0$. Figure 7 shows an example for a more realistic case with $r_3/r_2 = 1.05$, $\alpha = 11^\circ$ with the effects of losses taken into account. The absolute value of \tilde{v}_{r2} is significantly smaller than that estimated from equation (14), which is mainly caused by the finiteness of α . We see that the impeller force may be estimated from the simple relations if we use the exact value of \tilde{v}_{r2} in equation (15) and take into account the effect of loss discussed above. The real part of \tilde{v}_{r2} , and correspondingly F_t for $\omega/\Omega = 0$, approaches zero by increasing r_3/r_2 and hence the destabilizing region diminishes.

From the above discussions we may understand the mechanisms of the destabilizing impeller forces as follows. A vaned diffuser with a small vane angle α has the effect to smooth out the circumferential flow rate distribution through the diffuser. This effect brings about a circumferential flow distribution through the impeller to cancel out the absolute radial velocity disturbances at the diffuser inlet due to the dislocation of the flow field of impeller circulation Γ and source Q , and to the whirling velocity. Such a flow distribution through the impeller is established by a pressure distribution around the impeller, which balances with the inertia on the fluid in the impeller caused by the flow distribution. In cases of $\alpha \rightarrow 0$ and $r_3/r_2 \rightarrow 1$ the flow through the impeller for $\omega/\Omega = 0$ becomes maximum in the direction of $(n, t) = (-\phi, \psi)$ and the impeller force (F_n, F_t) due to the outlet pressure distribution caused by the flow distribution is positively proportional to (ψ, ϕ) . This tendency is carried over to general cases of finite but small values of α and $r_3/r_2 \rightarrow 1$, resulting in a destabilizing region at small positive ω/Ω .

The tendencies that the outlet pressure force is more dominant for the cases of smaller r_3/r_2 and ω/Ω may be understood by considering that the above mechanism becomes more definitive for those cases. When the diffuser angle is not constant, the outlet angle will have a more important effect on the impeller forces. In cases with a volute, the radial velocity on the volute is strictly controlled by the volute surface. Hence the latter half of the above discussions can be applied also for the cases with a volute.

Impeller forces at partial capacity (Cases with infinitesimally small impeller/diffuser gap)

We consider the cases with $r_3/r_2 \rightarrow 0$. As mentioned before, the solution becomes purely analytical for such cases. Figures 8 and 9 show the impeller forces at partial capacities with impeller and diffuser losses considered and neglected, respectively. For $\omega/\Omega < 0$, F_n increases and F_t decreases with the decrease in ϕ . This tendency can be understood from the discussions for $\alpha \rightarrow 0$ in the last section through the effect of ϕ on \tilde{v}_{r2} . The destabilizing region is enlarged by the decrease in ϕ . It is interesting to note here that the value of ω/Ω

for which $\text{Imag}(\tilde{v}_{r2}) = 0$ increases with the decrease in ϕ . In Figure 7, the impeller forces for $\phi/\phi_d = 0.2$ change largely near $\omega/\Omega = 0.35$. This condition corresponds to the rotating stall onset flow rate and the stall propagation velocity which can be determined by putting the denominator of equation (12) to be zero. It can be shown that the onset flow rate thus determined equals the flow rate at which the difference between the diffuser outlet static pressure and the impeller inlet total pressure becomes unchanged by a change in flow rate. Those conditions agree with those obtained by Raily & Ekerol (ref. 11). The onset condition determined from equation (12) for this case is $(\phi/\phi_d, \omega/\Omega) = (0.21, 0.34)$. If we neglect the losses, as shown in Figure 8, we do not have the large change in the forces. For $\omega/\Omega < 0$, the losses have little effect on F_n but they have the effect to increase F_t near the design capacity and to decrease F_t at lower capacities. This is because the change in losses due to the change in incidence angle becomes significant at lower capacities. In Figures 8 and 9, we observe destabilizing regions in $\omega/\Omega < 0$ at very low capacities. This has not been observed experimentally, and it is questionable if the present model can be applied to such a small capacity.

Impeller forces at partial capacity (Cases with small impeller/diffuser gap)

At small capacities the impeller forces change largely with a small change in r_3/r_2 and the effect of rotating stall observed in Figure 7 for $r_3/r_2 = 1$ cannot be seen for $r_3/r_2 = 1.03$. Figure 10 shows the impeller forces for $r_3/r_2 = 1.10$. The impeller forces change greatly in the region $\omega/\Omega < 0$ at partial capacities. The denominator of equation (12) becomes zero for $(\phi/\phi_d, \omega/\Omega) = (0.288, -0.16)$. Unlike the cases with $r_3/r_2 = 1.0$ shown in Figures 8 and 9, the large change does not disappear by neglecting impeller and diffuser losses.

The vaned diffuser rotating stall onset condition can be obtained by a method similar to the present study under the assumptions that the pressure is constant at the outlet of the diffuser and that the flow upstream is irrotational. If we neglect the delay of loss, the onset flow rate coincides with that at which the difference of the inlet total pressure and the outlet static pressure is unaltered by the change in the flow rate under a constant inlet circumferential velocity. For the present case the diffuser rotating stall onset condition thus determined is $(\phi/\phi_d, \omega/\Omega) = (0.320, 0.0396)$. The impeller rotating stall onset condition for the present case determined under the condition of constant impeller outlet pressure is $(\phi/\phi_d, \omega/\Omega) = (0.349, 0.914)$ (ref. 10). Both of these conditions are far apart from the condition above mentioned.

As the flow rate gets smaller, the flow angle in the vaneless region becomes smaller and the time required for a fluid particle to pass through the region becomes larger. We consider a case when the shed vorticity decays proportionally to $\exp(-D_\alpha t)$, where D_α is a positive constant and t is the time passed after the vorticity is shed from the impeller. Such cases can be treated by simply multiplying $-D_\alpha \pi(r^2 - r_2^2)/Q$ by $\lambda(r, \theta)$ in equation (4). Figure 11 shows the results with $D_\alpha/\Omega = 2.0$. We do not have the large change in $\omega/\Omega < 0$ as seen in Fig. 10. This fact may show that the large change is caused by the interaction of the vorticity with the vaned diffuser. The denominator of equation (4) becomes zero for $(\phi/\phi_d, \omega/\Omega) = (0.40, 0.02)$, and the impeller forces change greatly near this condition. This condition is close to that of diffuser rotating stall onset. This large change in the impeller forces disappears if we neglect the diffuser loss. Hence, the large change for $D_\alpha/\Omega = 2.0$ is considered to be related to the diffuser rotating stall.

Impeller forces at partial capacity
(Cases with large impeller/diffuser gap)

Figure 11 shows the results for $r_3/r_2 = 1.5$ and $D_a/\Omega = 0.25$. The denominator of equation (12) becomes zero at $(\phi/\phi_d, \omega/\Omega) = (0.33, 0.02)$ and $(0.08, 0.98)$, near which the impeller forces change irregularly. The former and latter solutions disappear if we neglect the diffuser and impeller losses respectively. The diffuser and the impeller rotating stall onset conditions when they are alone are $(\phi/\phi_d, \omega/\Omega) = (0.328, 0.021)$ and $(0.349, 0.914)$, respectively, and these are close to the above conditions. Hence the irregular changes of the forces in Figure 12 are considered to be related to the diffuser and impeller rotating stalls. The change of the forces near the diffuser stall onset condition is smaller than that in Figure 11 for $r_3/r_2 = 1.1$. It decreases further by the increase in r_3/r_2 . On the contrary, the impeller stall onset flow rate increases with the increase in r_3/r_2 , and its effect on the impeller forces becomes more significant.

In any case the impeller forces change greatly near the diffuser and impeller rotating stall onset conditions and may become destabilizing for whirl. However, we should use a non-linear analysis for the exact determination of the impeller forces near rotating stall onset conditions, since rotating stalls are highly non-linear phenomena. In the present calculations with vaned diffusers, no phenomenon was observed which could be related to rotating stalls in the vaneless part of the diffuser.

CONCLUSIONS

Major findings of the present study may be summarized as follows.

- (1) The fluid forces on an impeller whirling in a vaned diffuser may become destabilizing for whirling motion even at design capacity. Discussions are made to elucidate the cause of the destabilizing fluid forces, and it was shown that the destabilizing fluid forces are closely related to the steady head-capacity characteristics of the impeller.
- (2) The destabilizing whirl velocity region is larger for a smaller diffuser vane angle, impeller/diffuser gap, and flow rate.
- (3) For an infinitesimally small gap between impeller and diffuser, the effects of a rotating stall on the impeller forces are observed at partial capacity. These effects disappear with a small increase in the gap, but the effects of the interaction of shed vorticity with the vaned diffuser appear instead. If we take into account the decay of shed vorticity, effects of diffuser rotating stalls are observed.
- (4) As we increase the gap further, the effects of the diffuser rotating stall become smaller. The impeller rotating stall onset flow rate increases and its effect on the impeller forces becomes more significant. In either case the impeller forces change greatly near the rotating stall onset conditions and may become destabilizing for impeller whirl.
- (5) For small positive to negative whirl velocity ratio, the contribution of the impeller outlet pressure distribution has the most significant effect on the impeller forces. It increases as the impeller/diffuser gap is decreased.

APPENDIX

(Normal and tangential forces for $r_3/r_2 \rightarrow 1$ and $\alpha \rightarrow 0$, without loss)

From equation (14) and (15) we obtain

$$F_t = (M/r_2)(1 - \omega/\Omega)\phi$$

$$F_n = (M/r_2)(1 - \omega/\Omega)(\psi - \omega/\Omega)$$

where $\phi \equiv Q/2\pi r_2^2 \Omega$ is the flow coefficient and $\psi = 1 - \phi \cot \beta$ is the head coefficient (normalized by $\rho r_2^2 \Omega^2$) of the impeller. M is the inertial length of the impeller flow channel, defined in the paragraph following equation (6).

These expressions show that F_t is linear with respect to ω/Ω and is proportional to the flow coefficient ϕ . F_n is a parabolic function of ω/Ω and dependent on the head coefficient ψ . These relations are illustrated in the following figure.

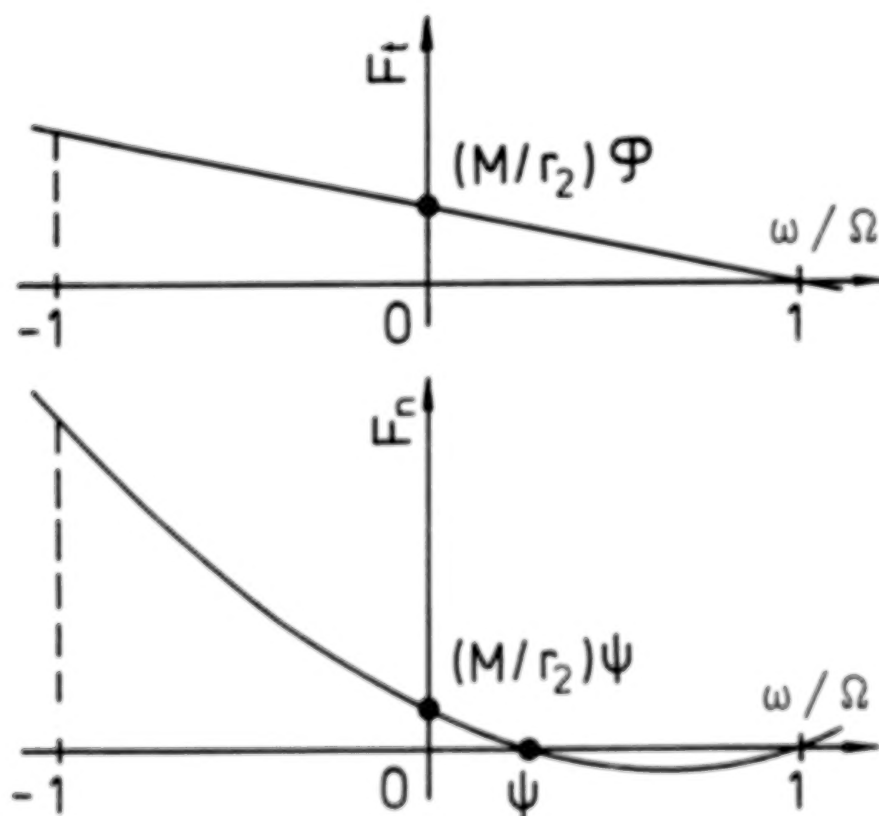


Illustration of F_t and F_n for the cases with $r_3/r_2 \rightarrow 1$ and $\alpha \rightarrow 0$, without losses.

The present authors would like to express their sincere gratitude to Professors H. Ohashi and C. Brennen for their helpful discussions. Acknowledgments are also made to Mr. S. Takatsugi for his assistance in numerical calculations.

REFERENCES

1. Ohashi, H. and Shoji, H., "Lateral Fluid Forces Acting on a Whirling Centrifugal Impeller," NASA CP-2335, May 1984, pp. 109-122.
2. Chamieh, D.S., Acosta, A.J., Brennen, C.E. and Caughey, T.K., "Experimental Measurements of Hydrodynamic Radial Forces and Stiffness Matrices for a Centrifugal Pump-Impeller," ASME Journal of Fluid Engineering, Vol. 107, No. 3, Sept. 1985, pp. 307-315.
3. Jery, B., Acosta, A.J., Brennen, C.E., Caughey, T.K. and Franz, R., "Experimental Measurements of Hydrodynamic Stiffness Matrices for a Centrifugal Pump-Impeller," NASA CP-2235, May 1984, pp. 137-160.
4. Shoji, H. and Ohashi, H., "Fluids Forces on Rotating Centrifugal Impeller With Whirling Motion," NASA CP-2133, May 1980, pp. 317-328.
5. Shoji, H. and Ohashi, H., "Theoretical Study of Fluid Forces on Whirling Centrifugal Impeller," (in Japanese), Trans. JSME, Vol. 50, no. 458, B. Oct. 1984, pp. 2518-2523.
6. Ohashi, H., Hatanaka, R. and Sakurai, A., "Fluid Force Testing Machine for Whirling Centrifugal Impeller," Proceedings of International Conference on Rotor Dynamics (IFTOMM), Sept. 1986, Tokyo, pp. 643-648.
7. Arndt, N. and Franz, R., "Measurements of Hydrodynamic Forces on a Two-Dimensional Impeller and Modified Centrifugal Pump," Division of Engineering and Applied Science, California Institute of Technology, Rept. E249.4, 1986.
8. Tsujimoto, Y., Acosta, J. and Brennen, C., "Two-dimensional Unsteady Analysis of Fluid Forces on a Whirling Centrifugal Impeller in a Volute," NASA CP-2235, May 1984, pp. 161-171. Numerical results are included in "Theoretical Study of Fluid Forces on a Centrifugal Impeller Rotating and Whirling in a Volute," by the same authors, submitted to ASME Journal of Vibration, Acoustics, Stress and Reliability in Design.
9. Bolleter, U. and Wyss, A., "Measurement of Hydrodynamic Interaction Matrices of Boiler Feed Pump Impellers," ASME Paper 85-DET-148, 1985.
10. Tsujimoto, Y. and Acosta, A.J., "Theoretical Study of Impeller and/or Vaneless Diffuser Attributed Rotating Stalls and their Effects on Whirling Instability of a Centrifugal Impeller," Proceedings of IAHR Work Group on the Behavior of Hydraulic Machinery Under Steady Oscillatory Conditions, Sept. 1987, Lille, France.
11. Raily, J.W. and Ekerol, H., "Influence of a Closely Coupled Throttle on the Stalling Behavior of a Radial Compressor Stage," ASME Journal of Engineering for Gas Turbines and Power, Vol. 107, Apr. 1985, pp. 522-527.

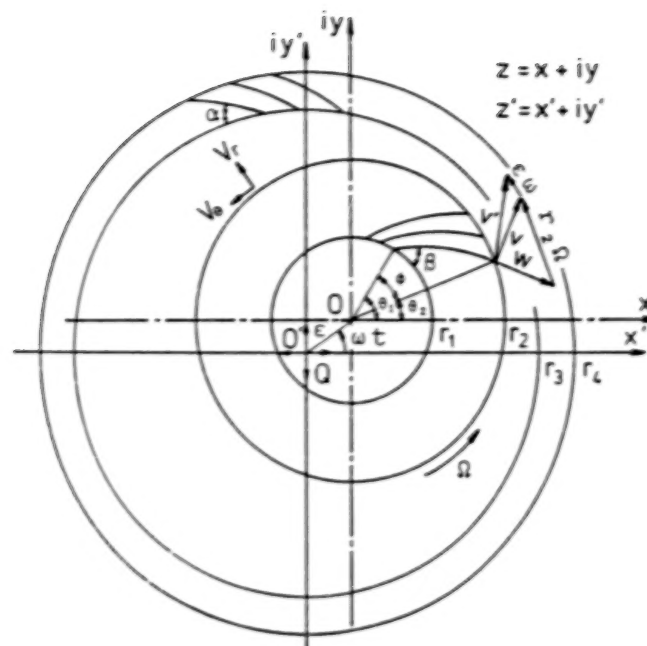


Fig.1 Impeller and vaned diffuser.

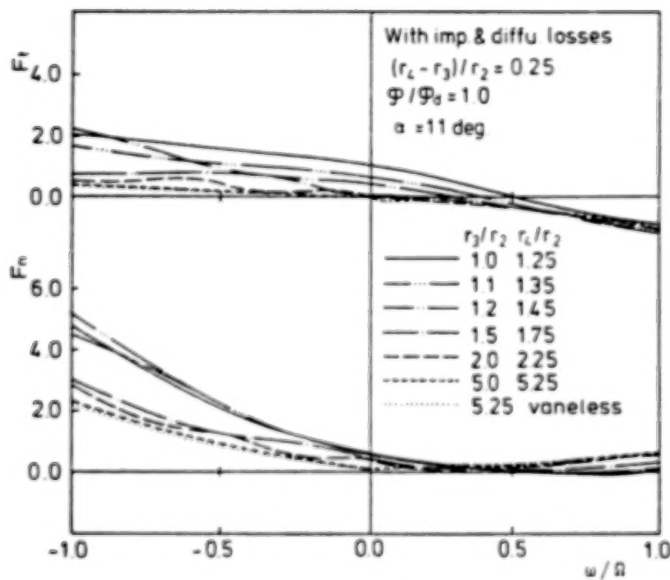


Fig.2 Effects of impeller/diffuser gap on whirling forces at design capacity.

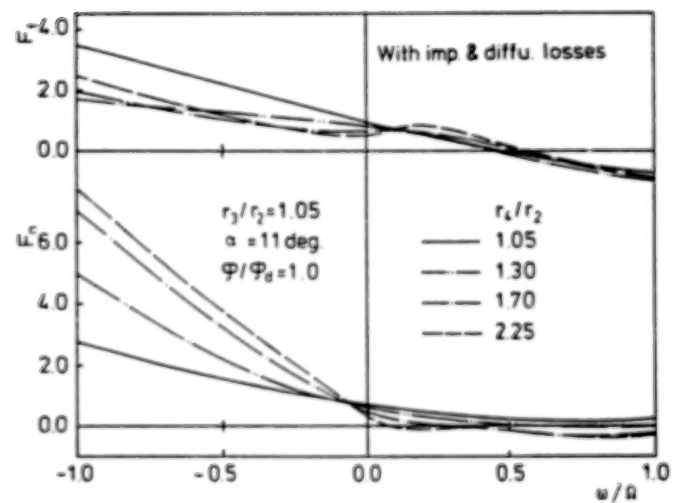


Fig.3 Effects of diffuser flow channel length on whirling forces at design capacity.

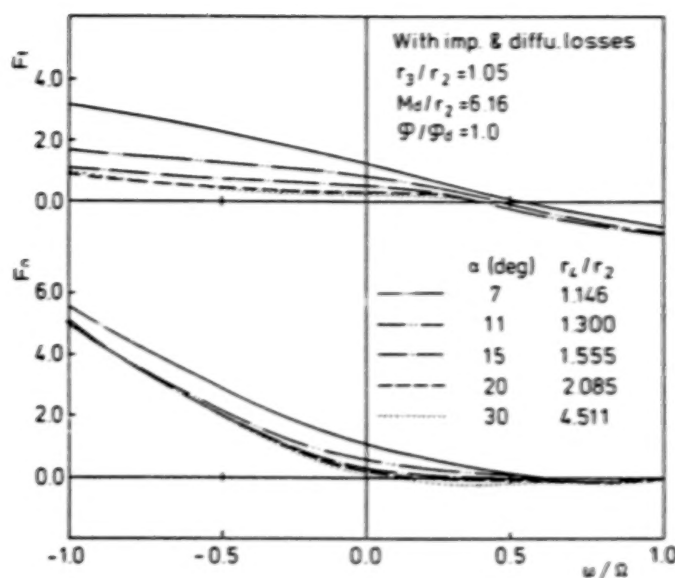


Fig. 4 Effects of diffuser vane angle on whirling forces at design capacity. The effective length of diffuser flow channel is kept constant.

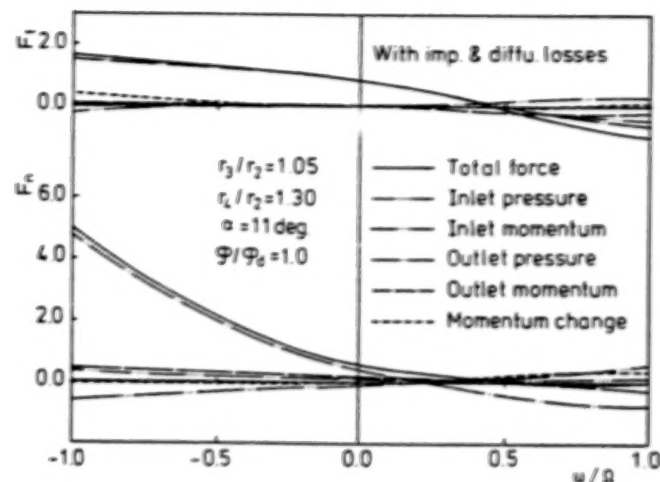


Fig. 5 Division of whirling forces. Contribution of impeller outlet pressure distribution is dominant in a range of small positive to negative whirl velocity ratio.

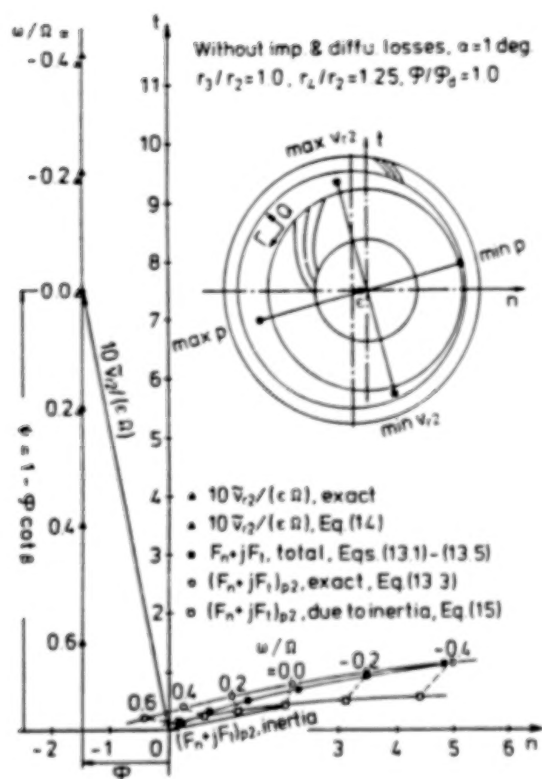


Fig. 6 Illustration of the relations among impeller outlet flow distribution, pressure distribution and impeller forces, for an idealized case with $\alpha = 0$ and $r_3 = r_2$.

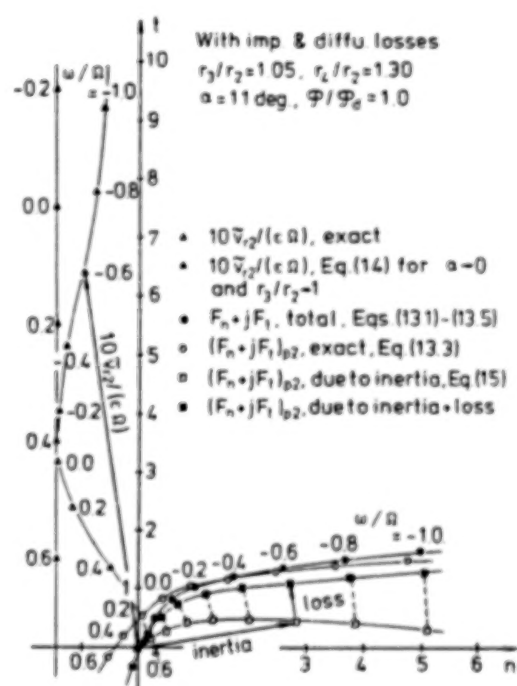


Fig. 7 Illustration of the relations among impeller outlet flow distribution, pressure distribution and impeller forces, for a realistic case.

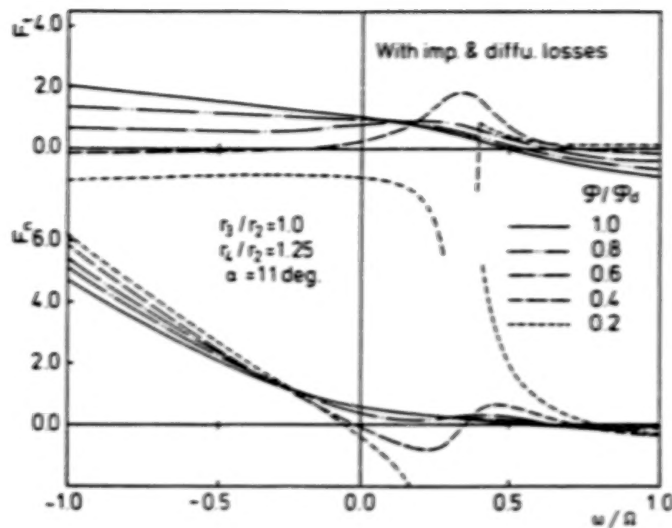


Fig.8 Impeller forces at partial capacities, for the case with infinitesimally small impeller/diffuser gap, with the effects of impeller and diffuser losses taken into account. Effects of a rotating stall are observed.

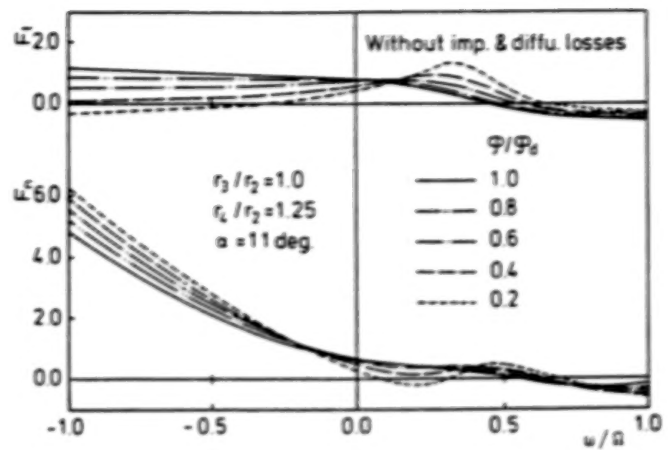


Fig.9 Impeller forces at partial capacities, for the case with infinitesimally small impeller/diffuser gap. The impeller and diffuser losses are not considered. We do not observe the effects of rotating stall.

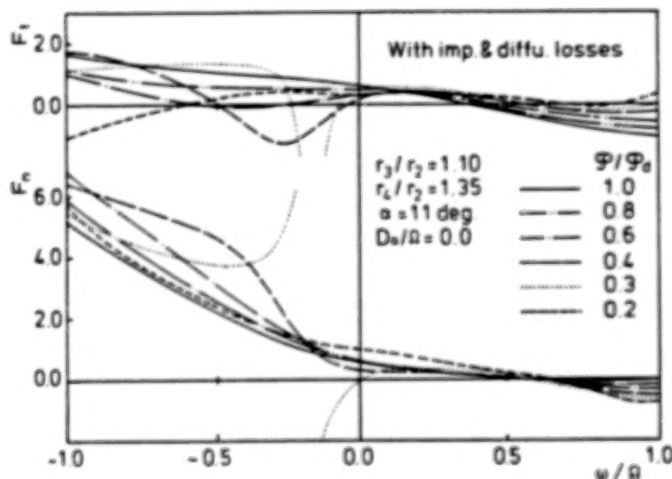


Fig.10 Impeller forces at partial capacities for the case with smaller impeller/diffuser gap. We observe fluctuations of the forces in the range of negative whirl velocity.

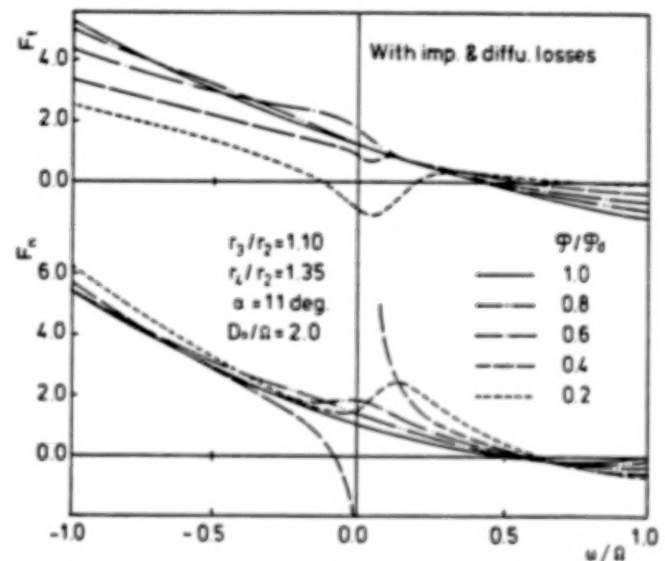


Fig.11 Impeller forces at partial capacities for the case with smaller impeller/diffuser gap. Exponential decay of shed vorticity is considered. Fluctuations in the range of negative whirl velocity diminish and the effects of diffuser rotating stall are observed at small positive whirl velocity.

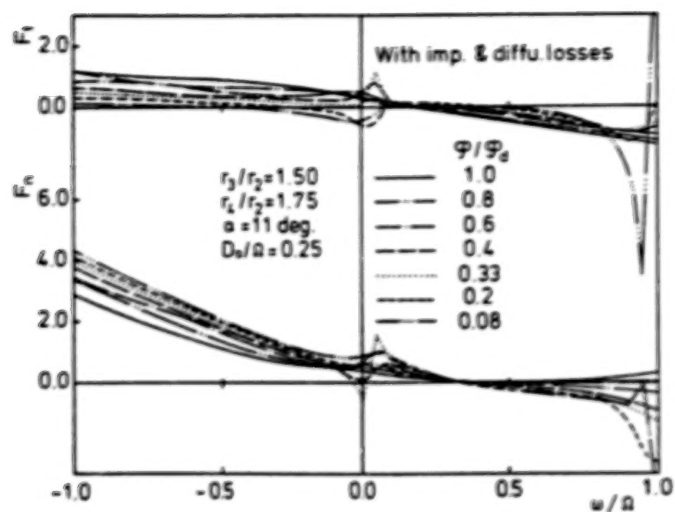


Fig.12 Impeller forces at partial capacities, for the case with larger impeller/diffuser gap. Effects of impeller rotating stall are observed

INFLUENCE OF IMPELLER SHROUD FORCES ON

TURBOPUMP ROTOR DYNAMICS

Jim P. Williams
Bell Helicopter Textron, Inc.
Group 06, Dept. 81, MS 14
Fort Worth, Texas 76101, U.S.A.

Dara W. Childs
Department of Mechanical Engineering
Texas A&M University
College Station, Texas 77843, U.S.A.

The shrouded-impeller leakage path forces calculated by Childs (1987) have been analyzed to answer two questions. First, because of certain characteristics of the results of Childs, the forces could not be modeled with traditional approaches. Therefore, an approach has been devised to include the forces in conventional rotordynamic analyses. The forces were approximated by traditional stiffness, damping and inertia coefficients with the addition of whirl-frequency-dependent direct and cross-coupled stiffness terms. The forces were found to be well-modeled with this approach. Finally, the effect these forces had on a simple rotor-bearing system was analyzed, and, therefore, they, in addition to seal forces, were applied to a Jeffcott rotor. The traditional methods of dynamic system analysis were modified to incorporate the impeller forces and yielded results for the eigenproblem, frequency response, critical speed, transient response and an iterative technique for finding the frequency of free vibration as well as system stability. All results lead to the conclusion that the forces have little influence on natural frequency but can have appreciable effects on system stability. Specifically, at higher values of fluid swirl at the leakage path entrance, relative stability is reduced. The only unexpected response characteristics that occurred are attributed to the nonlinearity of the model.

INTRODUCTION

The vibration of centrifugal pumps has received increasing attention recently because of the inability of current analysis techniques to adequately predict the dynamic characteristics of pump designs. Failure to accurately predict vibrations has resulted in the loss of considerable amounts of money in down time from severe vibration problems. Massey (1985), for example, described an eleven-stage pump that became unstable when its running speed exceeded its critical speed by 25%. In other words, it whirled at 80% of running speed. Another example occurred in the High Pressure Oxygen Turbopump (HPOTP) of the Space Shuttle Main Engine (SSME) which also whirled at 80% of running speed (Childs and Moyer, 1985).

The hydrodynamic forces generated in many of the fluid-filled gaps within the pump are well-established contributors to the problems cited above. This article is concerned specifically with the forces developed along the leakage path between the impeller and the shroud, as shown in Figure 1. As the fluid is discharged from the impeller, some will return to the lower-pressure, suction side by way of this leakage path. Leakage is minimized typically with wear ring seals, as shown. Hydrodynamic forces are developed along the entire leakage path, i.e. the shroud section as well as the seal. Note

that these are only parts of the total force on the impeller and that the impeller/volute region, balance drums, inducers, shaft, etc. also contribute to the dynamics of pumps, although they are not considered here.

Unfortunately, measurements of the total force on actual impellers have typically been obtained using pumps that have been modified to minimize leakage path forces. However, some results have been reported that are of importance here. For example, research at Cal Tech (Adkins, 1976) led to the conclusion that the pressures in the shroud annulus contributed from about 50% to 75% of the total stiffness acting on the impeller. The pump used included separation rings and an enlarged shroud clearance space to minimize leakage flow forces.

Bolleter et al. (1985) used a rocking-arm mechanism to vertically translate the spinning impeller. Their pump had normal clearances in the leakage path; and, therefore, the forces measured were more realistic. The results demonstrated that the nondimensionalized cross-coupled stiffness value was about twice that measured on the pump at Cal Tech (Jery et al., 1984). This suggests that the leakage path region in pumps can also reduce the stability of impeller motion.

Almost all of the analytical attempts at predicting leakage path forces have been concerned with seals. However, Childs has extended his previous techniques in seal analysis (1980, 81, 82a, 82b, 82c) to apply them to the flow within the clearance space surrounding the shroud (1987). His work will be used to model the seal and shroud forces in this article and will now be summarized.

Childs used a bulk-flow approach to obtain the governing equations of the flow of a differential element of fluid. In the seal problem, three equations were required: axial- and circumferential-momentum equations as well as the continuity equation. In the shroud problem, the axial-momentum equation was replaced by a path-momentum equation, introducing additional terms which described the centrifugal and Coriolis accelerations of the fluid element. After a perturbation expansion of the equations in the eccentricity ratio, the resulting relationships were solved at various values of the whirl frequency, Ω . Integration of the resulting pressure distribution on the shaft or shroud yielded the radial and tangential force as functions of whirl frequency. In addition, solution was carried out at various circumferential velocities at the shroud entrance. This variable is of primary importance in system stability (cross-coupled stiffness). Figure 2 shows the results of the shroud problem for three different values of the inlet swirl velocity. The leakage path analyzed corresponded to that used by Bolleter et al. (1985) which ran at 2000 rpm. Figure 3 provides the dimensions of the pump and other data of importance.

In the articles cited above, Childs initially suggested the following conventional, linear relationship to model the forces. It applies for small motion of the rotor about the centered position.

$$\begin{Bmatrix} F_x \\ F_y \end{Bmatrix} = \begin{bmatrix} M & 0 \\ 0 & M \end{bmatrix} \begin{Bmatrix} \ddot{x} \\ \ddot{y} \end{Bmatrix} + \begin{bmatrix} C & c \\ -c & C \end{bmatrix} \begin{Bmatrix} \dot{x} \\ \dot{y} \end{Bmatrix} + \begin{bmatrix} K & k \\ -k & K \end{bmatrix} \begin{Bmatrix} x \\ y \end{Bmatrix} \quad (1)$$

If circular whirl at frequency, Ω , and radius, Q , is assumed such that

$$\begin{aligned} x &= Q \cos \Omega t \\ y &= Q \sin \Omega t, \end{aligned} \quad (2)$$

the radial and tangential force components can be stated

$$\begin{Bmatrix} F_r \\ F_t \end{Bmatrix} = Q \begin{Bmatrix} -M\Omega^2 + c\Omega + K \\ C\Omega - k \end{Bmatrix} \quad (3)$$

After nondimensionalizing the terms as defined in (Childs, 1987), equations (3) become

$$\begin{aligned} \frac{\tilde{F}_r}{\tilde{q}} &= \tilde{M}f^2 - \tilde{c}f - \tilde{K} \\ \frac{\tilde{F}_t}{\tilde{q}} &= -\tilde{C}f + \tilde{k}, \end{aligned} \quad (4)$$

where the definitions of the coefficients are included in the List of Symbols and the other variables are defined as follows.

$$\begin{aligned} \tilde{F} &= \frac{F}{2R_L \Delta P} && , \text{ nondimensionalized force} \\ \tilde{q} &= \frac{Q}{Q_0} && , \text{ nondimensionalized clearance} \\ f &= \frac{\Omega}{\omega} && , \text{ whirl frequency ratio} \\ \frac{\tilde{F}}{\tilde{q}} &&& , \text{ force coefficient.} \end{aligned}$$

The quadratic relationships of equations (4) are to be used to obtain the dynamic coefficients of equations (1). Specifically, a least-squares curve fit of the force curves will yield the coefficients. This is an adequate approach for seal forces because they, in general, do follow a quadratic trend. However, the curves of Figure 2 illustrate that shroud forces can not be approximated by equations (4); and, therefore, a traditional linear model as expressed in equations (1) will not adequately represent the forces. Although these results are unexpected, experimental measurements made by Franz and Arndt (1986) of impellers with inducers yielded very similar results.

PROBLEM DEFINITION

At this point, it is not known, assuming the force curves of Figure 2 are valid, how they can best be included in traditional rotordynamic calculations of stability, response, critical speeds etc. To solve this problem, the present research has been conducted to answer the following questions.

1. How can the force curves found by Childs (1987) be incorporated in the traditional rotordynamic analyses of system response, stability, critical speeds etc.?

2. What effects do the forces have on a rotor-bearing system with respect to stability, natural frequencies, imbalance response, etc?

Before answering these questions, observe that the forces present no new problems in a transient analysis because they could be applied as whirl-frequency-dependent forcing functions to a simple rotor model such as that developed by Jeffcott (1919). The equations of motion would be nonlinear because the forces depend on the whirl frequency, defined kinematically as

$$f = \frac{\Omega}{\omega_s} = \frac{x\dot{y} - y\dot{x}}{\omega_s(x^2 + y^2)}, \quad (5)$$

but this could be handled by integrating the equations of motion numerically with traditional methods. However, a transient analysis alone is not sufficient to obtain an understanding of the forces, and this is why an answer to the questions posed above is necessary. The following section describes the model used to analyze the shroud forces, and results are then given for the eigenvalue problem and frequency response, respectively.

ROTORDYNAMIC MODEL

As shown in Figure 4, the model is a Jeffcott rotor (Jeffcott, 1919) under the application of seal and shroud forces. The rotor itself represents a double-suction impeller, yielding two symmetrical leakage paths. In summary, the forces on the rotor are the shaft stiffness, two identical seal forces and two identical shroud forces. The mathematical representation of each force will now be discussed.

A 90.7 kg (200 lb) rotor is assumed. In addition, the shaft stiffness used ($K_{sh} = .2987$ MN/m) makes the natural frequency of forward whirl (to be defined later) equal to 80% of shaft speed. This choice is not completely arbitrary since this frequency corresponds to that observed in the examples cited in the Introduction (Massey, 1985; Childs and Moyer, 1985).

The seals modeled are smooth, wear ring seals with a clearance and diameter of .36 mm and 236 mm, respectively. The least-squares approach of Childs described earlier has been carried out, and the resulting dynamic coefficients are given in Table 1. The analysis used under-predicts the true value of the direct stiffness coefficient which, therefore, is doubled later when the coefficients of the entire model are assembled.

Table 1. Coefficients for one wear ring seal.

\bar{u}_d --	M_s kg	C_s Ns/m	c_s Ns/m	K_s MN/m	k_s MN/m
.5	.3111	3356.0	78.6	.6121	.4628
.6	.3398	2167.0	89.6	.5443	.4611
.7	.3714	970.9	101.3	.4755	.4455

As described in the Introduction, conventional stiffness, damping and mass coefficients can not completely describe the impeller-shroud forces calculated by Childs and shown in Figure 2. Therefore, the following method has been devised. First, a curve fit of the force curves is carried out, yielding dynamic coefficients which describe the quadratic variation of the forces with respect to the whirl frequency ratio as described above. The difference between these curve fits and the actual force curves is modeled by

direct and cross-coupled stiffness coefficients which are functions of whirl frequency ratio. The mathematical equivalent of this approach will now be discussed.

The following modified forms of equations (4) express the method with which the impeller-shroud forces are modeled.

$$\begin{aligned}\frac{\tilde{F}_x}{\tilde{q}} &= \tilde{M}_L f^2 - \tilde{c}_L f - [\tilde{K}_L + \tilde{K}^*(f)] \\ \frac{\tilde{F}_y}{\tilde{q}} &= -\tilde{C}_L f + [\tilde{k}_L + \tilde{k}^*(f)],\end{aligned}\quad (6)$$

where \tilde{K}^* and \tilde{k}^* represent the nondimensionalized deviations between the force curves and the approximating quadratic expressions. Figure 5 illustrates \tilde{K}^* and \tilde{k}^* , respectively. Note that, although they represent forces proportional to displacement, they are not traditional stiffness coefficients since they are functions of whirl frequency ratio. In addition, because of the perturbation approach used by Childs, the original forces are linearly proportional to rotor displacement. This fact supports the usage of stiffness coefficients to model the forces in Figure 5. Equations (1) are now rewritten as

$$\begin{Bmatrix} F_x \\ F_y \end{Bmatrix} = \begin{bmatrix} M_L & 0 \\ 0 & M_L \end{bmatrix} \begin{Bmatrix} \ddot{x} \\ \ddot{y} \end{Bmatrix} + \begin{bmatrix} C_L & c_L \\ -c_L & C_L \end{bmatrix} \begin{Bmatrix} \dot{x} \\ \dot{y} \end{Bmatrix} + \begin{bmatrix} K_L + K^*(f) & k_L + k^*(f) \\ -k_L - k^*(f) & K_L + K^*(f) \end{bmatrix} \begin{Bmatrix} x \\ y \end{Bmatrix} \quad (7)$$

Finally, observe that equations (7) are, in general, nonlinear differential equations. To understand this statement, recall that the general definition of the whirl frequency ratio, f , is given in equation (5). If the rotor precession has a constant radius and rate, f is a constant and the motion is linear. However, for general motion, f is variable and a function of the motion.

After performing the asymptotic least-squares curve fit to Figure 2, the resulting coefficients of equation (6) are given in Table 2.

Table 2. Approximating coefficients for one leakage path.

M_L kg	C_L Ns/m	c_L Ns/m	K_L MN/m	k_L MN/m
3.469	2037	969.9	.06781	.3137

Note that the above values apply for all three inlet tangential velocities to the leakage path. The frequency-dependent coefficients, \tilde{K}^* and \tilde{k}^* , are illustrated in the curves of Figure 5.

In summary, the following equations represent how the overall coefficients for the model are defined.

$$M = M_r + 2(M_s + M_L)$$

$$C = 2(C_s + C_L) + \tilde{C}$$

$$c = 2(c_s + c_L)$$

$$K = K_{sh} + 2(2K_s + K_L) + 2K^* = \bar{K} + 2K^*$$

$$k = 2(k_s + k_L) + 2k^* = \bar{k} + 2k^* \quad (8)$$

Particular coefficients are doubled because there are two seals and two leakage paths in a double suction pump. The quantity, \bar{C} , must be added to the model to yield reasonable stability. If the eigenvalues of the overall system are obtained without adding \bar{C} , the system is found to be unstable. Therefore, by adding another damping term ($\bar{C} = 10,422$ Ns/m), reasonable stability, which is consistent with operating pump experience, is ensured.

The following equation represents the complete model used to approximate the forces on the rotor.

$$\begin{bmatrix} M & 0 \\ 0 & M \end{bmatrix} \begin{Bmatrix} \ddot{x} \\ \ddot{y} \end{Bmatrix} + \begin{bmatrix} C & c \\ -c & C \end{bmatrix} \begin{Bmatrix} \dot{x} \\ \dot{y} \end{Bmatrix} + \begin{bmatrix} K(f) & k(f) \\ -k(f) & K(f) \end{bmatrix} \begin{Bmatrix} x \\ y \end{Bmatrix} = \begin{Bmatrix} F_x \\ F_y \end{Bmatrix} \quad (9)$$

Table 3 contains the numerical values used for this analysis. These coefficients combine to make the damping for the uncoupled system, defined by $2\sqrt{\bar{K}M}$, equal to 63%, 59% and 54% of critical damping for the three swirl ratios shown, respectively. Again, \bar{K}^* and \bar{k}^* are illustrated in Figure 5 and are defined analytically with cubic-spline curve fits.

Table 3. Coefficients for overall model.

\bar{u}_d --	M kg	C Ns/m	c Ns/m	\bar{K} MN/m	\bar{k} MN/m
.5	98.240	21208	2097.1	2.8827	1.5549
.6	98.298	18830	2119.1	2.6115	1.5494
.7	98.361	16438	2142.4	2.3363	1.5184

EIGENVALUE DETERMINATION AND INTERPRETATION

The characteristic equation for equation (9) is

$$(Ms^2 + Cs + K)^2 + (cs + k)^2 = 0 \quad (10)$$

Traditionally, the roots of the above quartic polynomial in the complex variable, s , are the system eigenvalues, the real part of which determines the stability while the imaginary part is the natural frequency. However, this description is not altogether complete as will be explained below. It can be shown that the four roots of equation (10) are two pairs of complex conjugates, corresponding to the forward whirl and backward whirl modes.

In solving equation (10) for the eigenvalues, there are of four roots for any whirl frequency ratio. Figures 6 and 7 show how only the forward-whirl eigenvalue varies with whirl frequency ratio for the three inlet swirl ratios.

The physical meaning of the eigenvalues is of interest, and Figure 7 will be used to explain this. In linear systems, the frequency of free vibration is determined by the imaginary part of the eigenvalues. However, this is not exactly true in the present whirl frequency-dependent model. Free whirl of the rotor occurs only when the imaginary part of an eigenvalue equals the whirl frequency. In Figure 7, therefore, only those points where the abscissa equals the ordinate can correspond to free vibration of the rotor. Further, stability is determined at the eigenvalue whose imaginary part equals the whirl frequency ratio.

To find this "natural frequency" and stability of free whirl, the following iterative technique has been used. First, a whirl frequency ratio is assumed. From this value, the corresponding values of K^* and k^* are obtained from the data shown in Figure 5 from which the eigenvalues are found using equation (10). These first two steps are equivalent to finding a point on the curves of Figure 6 and 7. The imaginary part of the forward-whirl eigenvalue is compared to the whirl frequency used. If they are the same, the natural frequency at which free vibration takes place is defined. If they are different, the imaginary part of the forward-whirl root becomes the assumed whirl frequency ratio, and the same steps are carried out until convergence occurs.

Tables 4 and 5 show results of the above algorithm. Also included are the eigenvalues of the same model neglecting K^* and k^* , which correspond to a pure quadratic approximation of the leakage path forces as in equations (4). The eigenvalues illustrate at least two important conclusions about the effects of the values of K^* and k^* . First, the natural frequency increases when K^* and k^* are included as well as when the swirl ratio is increased. The variation of K^* in Figure 5 explains these observations. More importantly, the percent differences between the two models show that the values of K^* and k^* have very little effect on natural frequency. Second, stability is reduced when K^* and k^* are included and when the swirl ratio is increased. The variation of k^* in Figure 5 is the cause of these observations. Finally, the percent differences between the two models show that K^* and k^* can cause appreciable reductions in relative stability.

Table 4. Natural frequencies of free vibration for the pump model with and without K^* and k^* .

\bar{u}_L	$\frac{\omega_n}{\omega_s}$ with K^* and k^*	$\frac{\omega_n}{\omega_s}$ without K^* and k^*	percent decrease
.5	.747	.727	2.68%
.6	.777	.724	6.82%
.7	.800	.715	10.63%

To show that the stability and frequency of free vibration are determined only by the root obtained from the iterative approach described earlier, the equations of motion (9) were integrated in a series of transient, free-vibration simulations. Initial conditions were an initial displacement of .127 mm (.005 in) and velocity equal to $R_L \omega_s$ (synchronous whirl). Figure 8 includes the resulting orbit and a time history of the whirl frequency ratio for free vibration and an inlet swirl ratio of .7. As shown, the rotor executed a well-damped spiral

orbit. The whirl frequency ratio of the orbit was exactly .8, which corresponds to the natural frequency found earlier. The other two swirl ratios yielded similar results.

Table 5. Real parts of the eigenvalues for the model with and without K^* and k^* .

\bar{u}_d --	real part with K^* and k^* 1/sec	real part without K^* and k^* 1/sec	percent decrease --
.5	-55.9	-60.3	7.87%
.6	-31.1	-47.2	51.80%
.7	-13.8	-34.5	150.00%

To verify that the stability of the model is described only by the real part of the eigenvalues obtained with the iterative approach described above, the direct damping coefficient was reduced by 12.5% producing a range of unstable eigenvalues as shown in Figure 9 where the real part of the forward-whirl root is positive between whirl frequency ratios of .41 and .57. The natural frequency of this altered model corresponds to a stable eigenvalue and is $.825\omega_s$. Integration of the equations of motion showed that free vibration was indeed stable and occurred at the new natural frequency. In addition, the equations of motion were altered to include a harmonic forcing function with an amplitude of 5 N which forced the rotor in a circular direction at a frequency of $.5\omega_s$. Figure 10 includes the resulting orbit, whirl frequency ratio time history and a Fast Fourier Transform (FFT) of the x-coordinate, respectively. Even though the forcing frequency was within the unstable range of frequencies, the figures show that the system was stable in that its orbit did not grow without bound. The loops and limit cycle behavior are the results of the nonlinearities in the model. The FFT shows that the steady state orbit consisted of response at both the forcing frequency, $.5\omega_s$, and the natural frequency, $.825\omega_s$. Other forcing frequencies were also tried. Using a stable value of $.7\omega_s$, for example, the response did not behave in the same manner; instead, the orbit reached a steady state circular path at the excitation frequency as would be expected from a linear system. However, forcing at $.375\omega_s$, the characteristics of the results from forcing at $.5\omega_s$ occurred again, as can be seen in Figure 11, which again contains the orbit, time history of the whirl frequency ratio and an FFT of the response. Only forcing frequencies below and within the unstable zone resulted in this behavior. Only when the direct damping coefficient was reduced until the natural frequency corresponded to an unstable eigenvalue did the response become unstable in a linear sense, where the orbit grew without bound at the natural frequency. The fundamental result from this analysis is a verification that a range of whirl frequencies yielding eigenvalues with positive real parts does not cause the system response to grow without bound unless it includes the system natural frequency. In addition, the nonlinearities of the system can cause a limit cycle to occur under certain conditions.

Finally, the critical speed of the rotor can not be calculated unless force curves are available at other shaft speeds. In this case, the natural frequency is calculated with the iterative method just described, but at a number of shaft speeds. A plot of natural frequency as a function of shaft speed is then drawn, analogous to "critical speed maps" in fluid-film bearing analysis. The critical speed is defined as the speed where the natural frequency is equal to the shaft speed.

FREQUENCY RESPONSE

As discussed earlier, the following are the equations of motion of the model

$$\begin{bmatrix} M & 0 \\ 0 & M \end{bmatrix} \begin{Bmatrix} \ddot{x} \\ \ddot{y} \end{Bmatrix} + \begin{bmatrix} C & c \\ -c & C \end{bmatrix} \begin{Bmatrix} \dot{x} \\ \dot{y} \end{Bmatrix} + \begin{bmatrix} K(f) & k(f) \\ -k(f) & K(f) \end{bmatrix} \begin{Bmatrix} x \\ y \end{Bmatrix} = F \begin{Bmatrix} \cos \Omega t \\ \sin \Omega t \end{Bmatrix}, \quad (11)$$

where the right-hand side represents a harmonic forcing function appropriate to frequency response analyses. As in traditional methods, the transient solution is assumed to decay with time, and only the steady-state response of the rotor is considered. The forcing frequency is defined by Ω which has been used to represent whirl speed. Since the steady-state motion is assumed to occur at the same frequency as the excitation, this should not cause confusion. Note that the model is now linear because the whirl frequency ratio and, hence, the stiffnesses are constant. Multiplying the second equation by the complex number i , the equations can be combined into one in terms of the complex variable z .

$$M\ddot{z} + (C - ic)\dot{z} + (K - ik)z = Fe^{i\Omega t}. \quad (12)$$

Assuming steady-state motion of the following form

$$z = Re^{i\phi}, \quad (13)$$

where R denotes the whirl amplitude, and ϕ is the phase angle yields

$$\frac{R}{F/K} = \frac{K}{\sqrt{[K - M\Omega^2 + c\Omega]^2 + [C\Omega - k]^2}}$$

$$\phi = \tan^{-1} \left[\frac{k - C\Omega}{K - M\Omega^2 + c\Omega} \right]. \quad (14)$$

Equations (14) were solved using the present model data, and the results for a swirl ratio of .7 are shown in Figures 12 and 13. Also included are the same results for the model with K^* and k^* neglected. Again, in obtaining frequency response curves as shown in Figures 12 and 13, the stiffness terms must be calculated at the corresponding whirl frequency ratio.

The swirl ratio of .7, shown, exhibited the largest variation in amplitude and phase at the whirl frequency ratio of .80, the system natural frequency. An amplitude difference of about 60% is shown between the curves, suggesting that K^* and k^* have significant influence on the system primarily at this frequency. The swirl ratios of .6 and .5 exhibited similar but decreasing results in both the amplitude and phase curves, having differences in amplitude at the peak value of 35% and 6%, respectively. In fact, the curves were almost identical in the case corresponding to a swirl ratio of .5. Note that these resonance peaks occurred in all cases at the corresponding natural frequencies found in the previous section, further verifying the preceding results. The difference in the response to imbalance excitation between the two models is small, and this suggests that the leakage path forces have negligible effects at this frequency especially at low inlet swirl ratios. However, the presence of a subsynchronous excitation near the natural frequency can result in large increases in response amplitude when k^* is included. Finally, these results depend on the

choice of \bar{C} . The denominator of the first of equations (14) demonstrates that the amplitude increases as $C\Omega$ approaches k . Therefore, the observations stated above apply only for the damping values stated earlier.

SUMMARY AND CONCLUSIONS

The impeller-shroud forces have been separated into a.) constant (whirl frequency-independent) stiffness, damping and inertia coefficients and b.) direct and cross-coupled added stiffness coefficients which are functions of whirl frequency. With this approach, the model can be analyzed using traditional techniques with a few modifications. A new iterative technique was used in the determination of system stability and free vibration natural frequency. The whirl-frequency-dependent stiffness terms were seen to be convenient and effective models for the impeller-shroud force nonlinearities.

When the values of the added stiffness coefficients, K^* and k^* , were included in addition to the frequency-independent coefficients, a number of effects resulted. First, the natural frequency was seen to increase by a small amount, suggesting that K^* could be neglected when only the natural frequency is important. In addition, the stability is seen to decrease when k^* is included. This effect is appreciable, so stability calculations should include k^* . The frequency response analysis showed synchronous response to imbalance is increased by the stiffnesses although by only a small amount. Appreciable differences in response due to subsynchronous excitation occur only at or near the natural frequency and become negligible at low values of the inlet swirl ratio.

To find the natural frequency and stability of the system, a new iterative technique was used. The resulting eigenvalues were shown to completely describe the characteristics of free vibration. The nonlinearities in the model resulted in loop-filled orbits and limit cycles under specific conditions.

LIST OF SYMBOLS

$\tilde{C} = \frac{CQ_o\omega_s}{F_o}$	nondimensionalized direct damping coefficient
$\tilde{c} = \frac{cQ_o\omega_s}{F_o}$	nondimensionalized cross-coupled damping coefficient
$\tilde{F}_{r/t} = \frac{F_{r/t}}{F_o}$	nondimensionalized radial and tangential forces on the rotor
$F_o = 2R_L L \Delta P$	(Childs, 1987) (F)
$f = \frac{\Omega}{\omega_s}$	whirl frequency ratio
$\tilde{K} = \frac{KQ_o}{F_o}$	nondimensionalized direct stiffness coefficient
K^*	direct stiffness coefficient which is a function of the whirl frequency ratio (F/L)
$\tilde{k} = \frac{kQ_o}{F_o}$	nondimensionalized cross-coupled stiffness coefficient [19]
k^*	cross-coupled stiffness coefficient which is a function of the whirl frequency ratio (F/L)
L	length of seal or impeller-shroud path (L)
$\tilde{M} = \frac{MQ_o\omega_s^2}{F_o}$	nondimensionalized direct mass coefficient [19]
Q	rotor whirl radius (L)
Q_o	clearance at leakage path entrance (L)
$\tilde{q} = \frac{Q}{Q_o}$	clearance ratio
R	rotor whirl amplitude (L)
$R_{L,s}$	inlet radius of shroud leakage path or seal (L)
$\tilde{u}_{tL/s} = \frac{u_{tL/s}}{R_L\omega_s}$	nondimensionalized tangential fluid velocity at leakage path or seal entrance (inlet swirl ratio) [19]
x, y	rectangular coordinates of rotor center (L)
Z	complex rotor whirl amplitude (L)
$z = x + iy$	complex rotor coordinate (L)
ϕ	phase angle of whirl from harmonic excitation
Ω	rotor whirl frequency (1/T)
ω_n	natural frequency of free vibration (1/T)
ω_s	shaft speed (1/T)
L	shroud leakage path coefficient subscript
r	rotor coefficient subscript
s	seal coefficient subscript
sh	shaft coefficient subscript
none	overall coefficient subscript

REFERENCES

- Adtkins, D., 1976, "Analyses of Hydrodynamic Forces on Centrifugal Pump Impellers," M. S. Thesis, California Institute of Technology, Pasadena.
- Bolleter, U., Wyss, A., Welte, I. and Sturchler, R., 1985, "Measurements of Hydrodynamic Interaction Matrices of Boiler Feed Pump Impellers," ASME, Paper No. 85-DET-148.
- Childs, D., Dressman, J. and Childs, S., 1980, "Testing of Turbulent Seals for Rotordynamic Coefficients," Proc. of Workshop on Rotordyn. Inst. Prob. in High-Perf. Turbomach., Texas A&M University, NASA CP-2133, pp. 121-38.
- Childs, D., 1981, "Convergent-Tapered Annular Seals: Analysis for Rotordynamic Coefficients," Symp. Vol., Fluid/Structure Interactions Turbomach., ASME Winter Annual Meeting, pp. 35-44.
- Childs, D., 1982a, "Dynamic Analysis of Turbulent Annular Seals Based on Hirs' Lubrication Equations," ASME Paper No. 82-Lub-41.
- Childs, D., 1982b, "Finite-Length Solutions for Rotordynamic Coefficients of Turbulent Annular Seals," ASME Paper No. 82-Lub-42.
- Childs, D. and Dressman, J., 1982c, "Testing of Turbulent Seals for Rotordynamic Coefficients," Proc. of Workshop on Rotordyn. Inst. Prob. in High-Perf. Turbomach., Texas A&M University, NASA CP-2250, pp. 157-71.
- Childs, D. and Moyer, D., 1985, "Vibration Characteristics of the HPOTP (High Pressure Oxygen Turbopump) of the SSME (Space Shuttle Main Engine)," ASME Trans. Journ. of Eng. for Gas Turbine, and Power, 107, pp. 152-59.
- Childs, D., 1987, "Fluid-Structure Interaction Forces At Pump-Impeller-Shroud Surfaces For Rotordynamic Calculations," Texas A&M University, Mech. Engr. Dept., accepted for presentation at ASME Vibration Conference, Boston, Mass.
- Franz, R. and Arndt, N., 1986, "Measurement of Hydrodynamic Forces on the Impeller of the SSME," Report No. E249.2, California Institute of Technology, Pasadena.
- Jeffcott, H., 1919, "The Lateral Vibration of Loaded Shafts in the Neighborhood of a Whirling Speed - The Effect of Want of Balance," The Philosophical Magazine, 6(37), pp. 304-14.
- Jery, B., Acosta, J., Brennen, C. and Caughey, T., 1984, "Hydrodynamic Impeller Stiffness, Damping and Inertia In the Rotordynamics of Centrifugal Flow Pumps," Proc. of Workshop on Rotordyn. Inst. Prob. in High-Perf. Turbomach., Texas A&M University, NASA CP-2338, pp. 137-60.
- Massey, I. C., 1985, "Subsynchronous Vibration Problems in High Speed Multistage Centrifugal Pumps," Proc. of the 14th Turbomach. Symposium, Turbomachinery Laboratories, Texas A&M University, pp. 11-16.

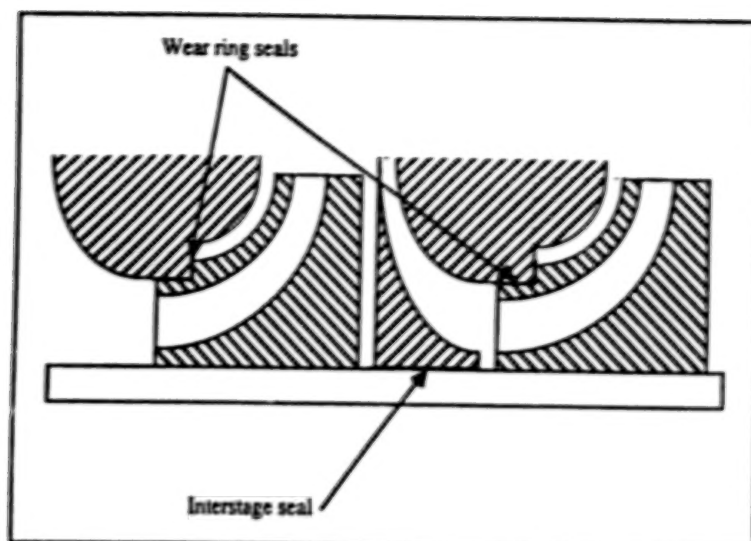


Figure 1. Typical seal configurations for a multi-stage pump.

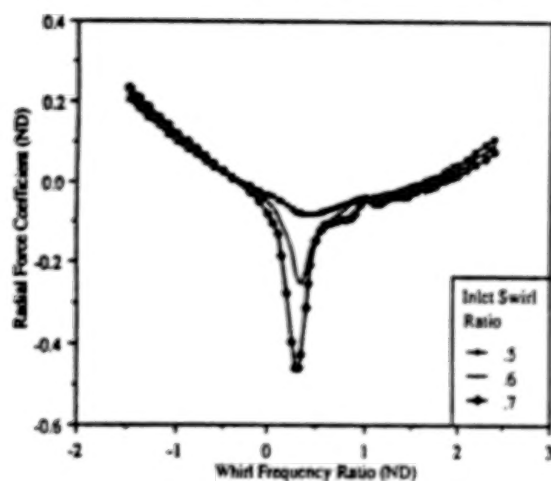


Figure 2a. Radial force coefficient curves (Childs, 1987).

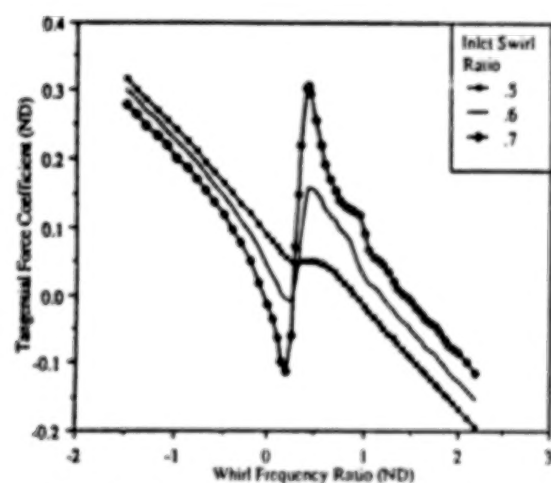
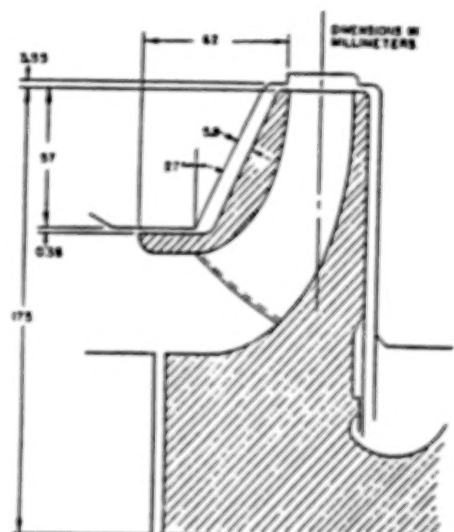


Figure 2b. Tangential force coefficient curves (Childs, 1987).



Pump data

shaft speed = $\omega_s = 2000$ rpm
 inlet clearance = $Q_0 = 3.55$ mm
 impeller exit angle = 22.5°
 flowrate = 130 l/sec
 head developed = 68 m
 seven-bladed impeller
 working fluid is water at 80 °F

Figure 3. Dimensions and data for the pump tested by Bolleter et al. (Bolleter, et al., 1985).

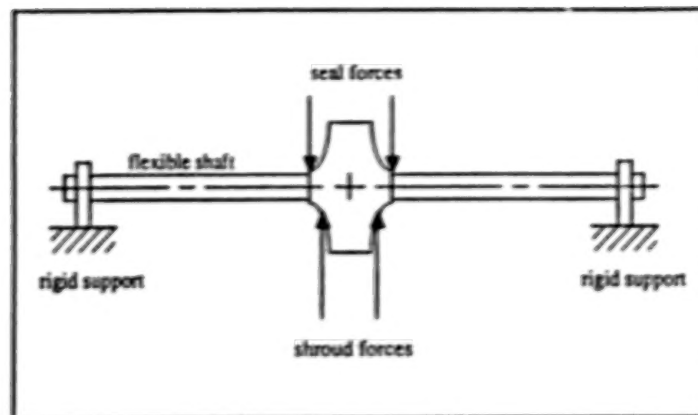


Figure 4. Jeffcoat-based, double-suction impeller leakage path model.

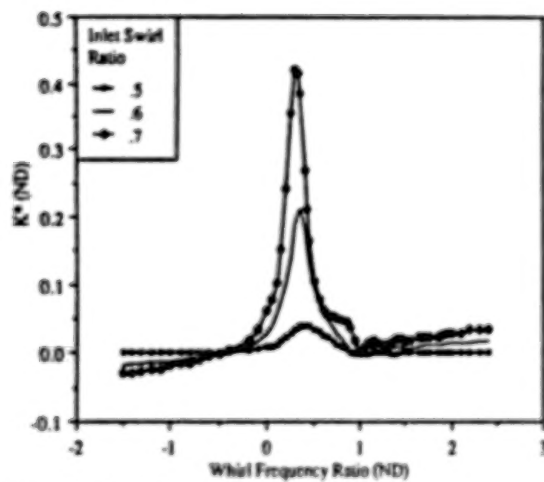


Figure 5a. Dependency of K^* on whirl frequency ratio.

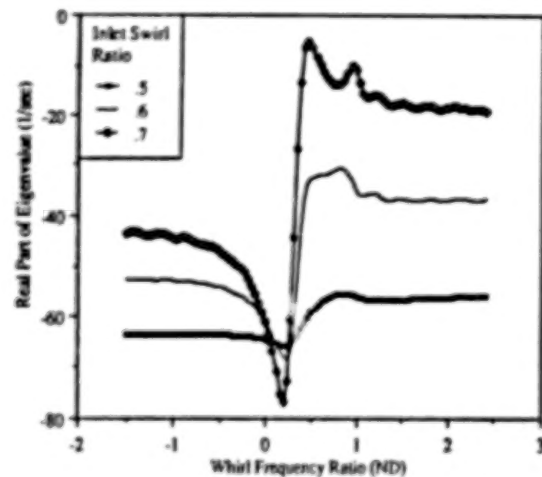


Figure 6. Real part of the eigenvalues for the forward-whirl mode.

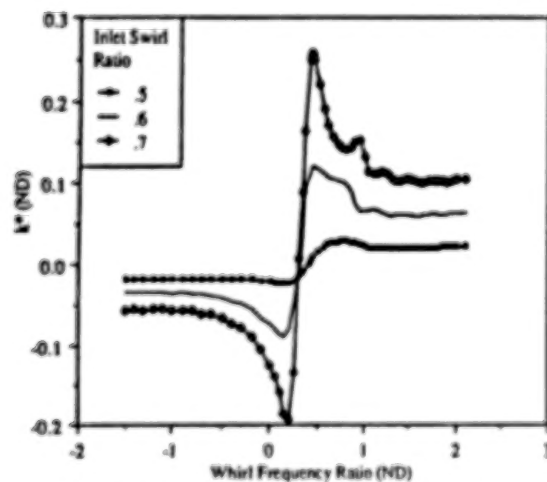


Figure 5b. Dependency of k^* on whirl frequency ratio.

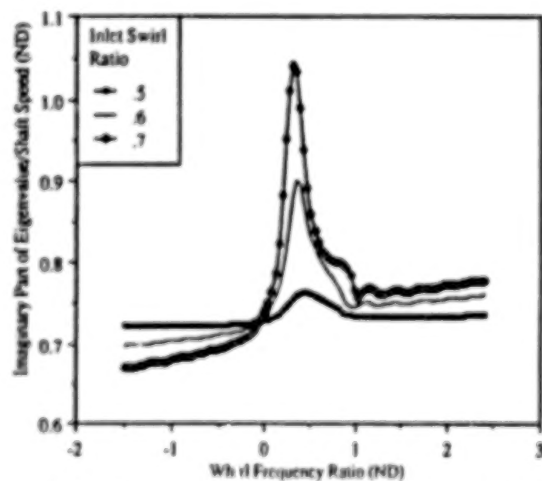


Figure 7. Imaginary part of the eigenvalues for the forward-whirl mode.

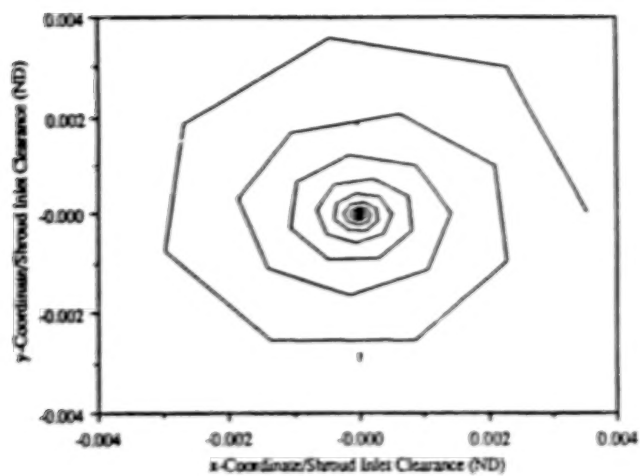


Figure 8a. Rotor orbit during free vibration.

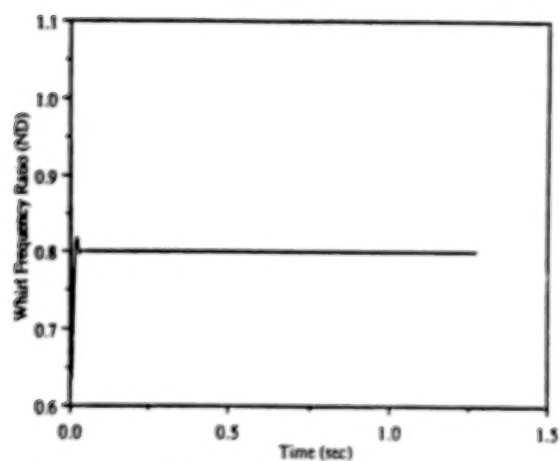


Figure 8b. Time history of rotor whirl frequency ratio during free vibration.

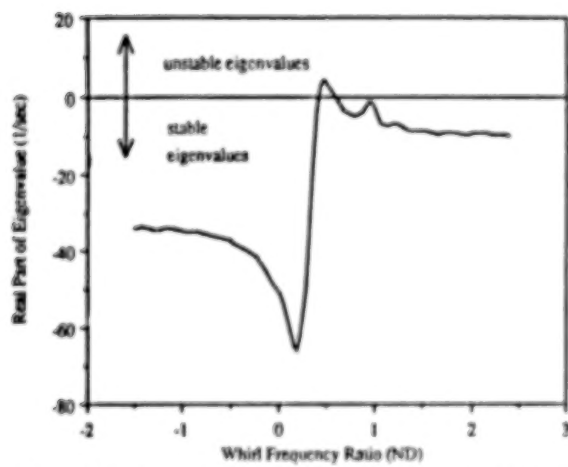


Figure 9. Real part of the eigenvalues for the forward-whirl mode with a 12.5% reduction in direct damping.

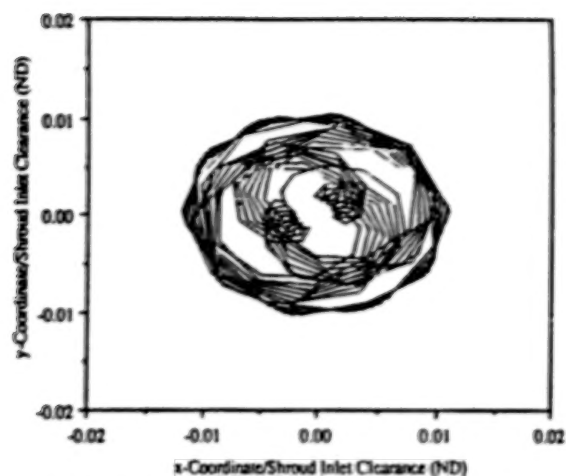


Figure 10a. Rotor orbit during harmonic excitation at 50% of shaft speed and 12.5% reduction in direct damping.

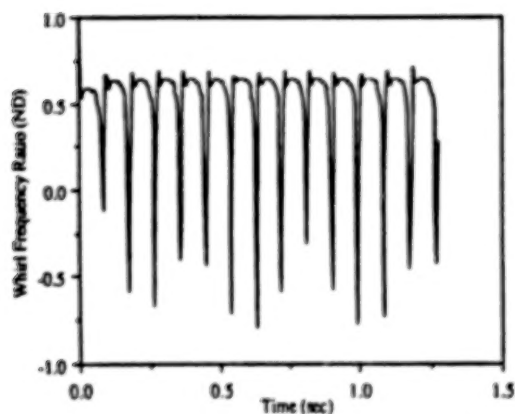


Figure 10b. Time history of rotor whirl frequency ratio during harmonic excitation at 50% of shaft speed and a 12.5% reduction in direct damping.

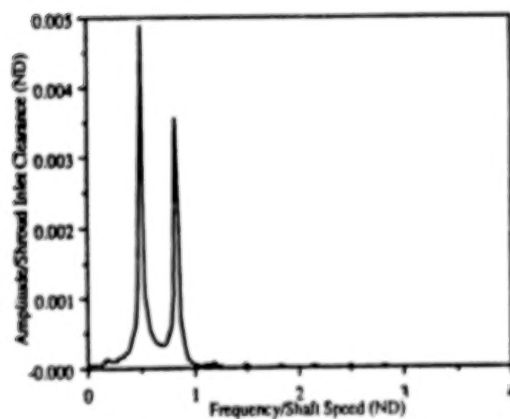


Figure 10c. FFT of the response of the rotor during harmonic excitation at 50% of shaft speed and a 12.5% reduction in direct damping.

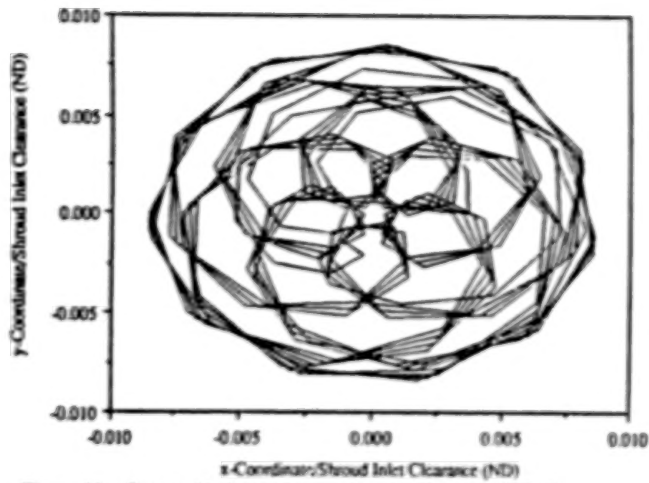


Figure 11a. Rotor orbit during harmonic excitation at 37.5% of shaft speed and a 12.5% reduction in direct damping.

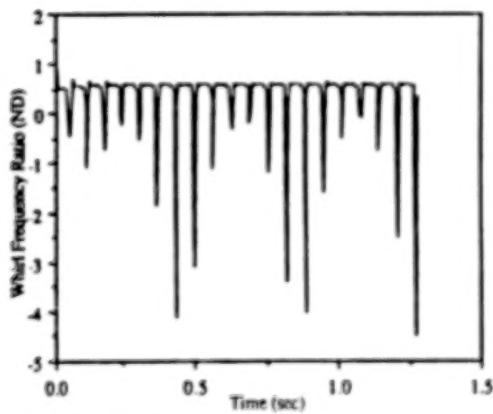


Figure 11b. Time history of rotor whirl frequency ratio during harmonic excitation at 37.5% of shaft speed and a 12.5% reduction in direct damping.

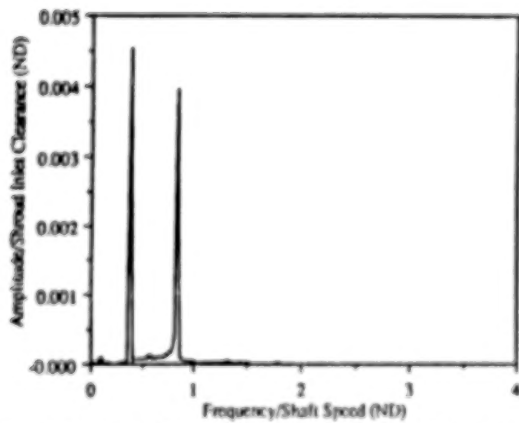


Figure 11c. FFT of the response of the rotor during harmonic excitation at 37.5% of shaft speed and a 12.5% reduction in direct damping.

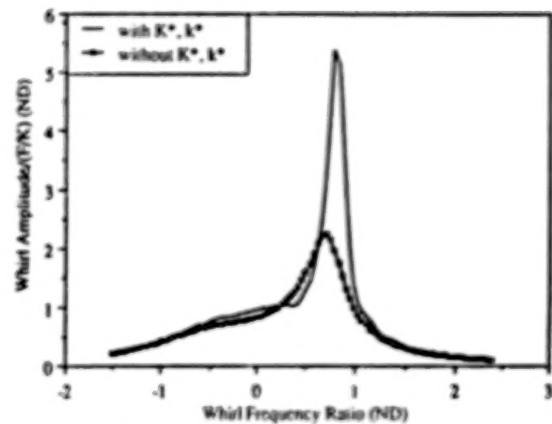


Figure 12. Frequency response: whirl amplitude.

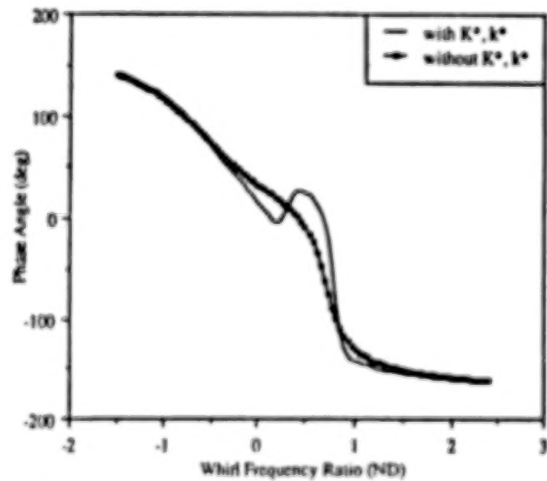


Figure 13. Frequency response: phase angle.

BLANK PAGE

MAGNETIC BEARING STIFFNESS CONTROL USING FREQUENCY BAND FILTERING

H. Ming Chen
Mechanical Technology Incorporated
968 Albany-Shaker Road
Latham, New York 12110, U.S.A.

Active magnetic bearings can be implemented with frequency band-reject filtering that decreases the bearing stiffness and damping at a small bandwidth around a chosen frequency. The control scheme has been used for reducing a rotor dynamic force, such as an imbalance force, transmitted to the bearing stator. This study reveals that the scheme creates additional system vibration modes at the same frequency. It also shows that the amount of force reduction is limited by the stability requirement of these modes.

INTRODUCTION

The attractive-type active magnetic bearings (AMBs) usually have four quadrants of electromagnets (ref. 1). A pair of opposite quadrants independently control the journal motion in one direction by a Proportional-Integral-Derivative (PID) controller (ref. 2). Steady-state (bias) currents are induced in the quadrants so that the total control current in each quadrant never changes polarity. This provides a base for linear feedback control and greatly simplifies the control circuitry (ref. 3).

There appears to be a growing interest in applying the AMBs not only for their advantageous basic bearing function, but also for their potential to be the rotor force isolator (ref. 4). An AMB can be made extra "soft" at narrow frequency bands, and the rotor forces to ground at these frequencies can be dramatically reduced at the sacrifice of large rotor runouts. For example, the well-publicized AMB control feature, "auto-balancing," was designed to reduce imbalance force to ground with the rotor rotating about its inertia axis (ref. 2). However, the creation of these stiffness "valleys" also creates instability problems for the rotor-AMB system. Herein this type of instability problem is addressed analytically while an experimental project is in progress.

NOMENCLATURE

AMB	active magnetic bearing
a	phase-lead network zero parameter
B	frequency bandwidth of band-pass filter
b	phase-lead network pole parameter
C	radial air gap
C _d	proportional feedback gain

C_v	phase-lead feedback gain
C_e	integral feedback gain
C_p	band-pass filter gain
C_{po}	band-pass filter stability threshold gain
F	regulating magnetic force
F_1, F_3	magnetic force per pole due to bias current in quadrant 1 or 3
FODE	first-order differential equation
f	band-pass factor
G	power amplifier gain
I_1, I_3	bias current in quadrant 1 or 3
i	regulating current
j	$\sqrt{-1}$
K	AMB stiffness
K_i	current stiffness
K_m	magnetic (negative) stiffness
LHS	left hand side
M	mass supported by AMB
PID	proportional-integral-derivative
Q	integrator output
R	nondimensional frequency parameter defined at a stiffness valley
RHS	right hand side
S	Laplace variable
t	time
U	real stiffness at ω_c after filter implementation
u	real stiffness at ω_c before filter implementation
u_r	RHS stiffness
u_l	LHS stiffness
V	imaginary stiffness at ω_c after filter implementation
v	imaginary stiffness at ω_c before filter implementation
Y	AMB journal displacement in Y-direction
Y_p	band-pass filter output
Z	phase-lead network output
ΔC_d	net proportional feedback gain contributing to real stiffness
ω	exciting frequency
ω_c	band-pass filter center frequency
ω_l	LHS slope frequency
ω_o	integrator cut-off frequency

ω_r	RHS slope frequency
dot	d/dt
$\Delta\omega$	$\omega_c - \omega$
θ	magnetic pole angle

AMB CONTROL WITH FREQUENCY BAND FILTERING

Assuming the bias currents are much larger than the regulating currents and the air gap is much larger than the journal's normal excursion, the two perpendicular axes of a radial AMB can be controlled independently (ref. 3). A control scheme for each axis is presented in figure 1. There are four parallel loops processing a journal displacement measurement. The top three loops, including a phase-lead network ($b > a$), form a conventional PID controller. The fourth loop comprises a typical second-order band-pass filter with the center frequency at ω_c , bandwidth B, and gain C_p (ref. 5). The filter can have a fixed center frequency or it may vary the center frequency with rotor speed. The latter is called a tracking filter and its implementation was explained by SKF (ref. 6). The filter output is subtracted from the displacement measurement that is fed into the phase-lead network. Also, the output multiplied by a gain ΔC_d is added to the basic PID signals that control the power amplifier. The gain ΔC_d is defined below.

$$\Delta C_d = C_d - K_m/(K_i G) \quad (1)$$

where

C_d = proportional loop gain, volt/m

G = amplifier gain, A/volt

K_m = magnetic stiffness
 $= 2 (F_1/C + F_3/C) \cos \theta$, lb/m

K_i = current stiffness
 $= 2 (F_1/I_1 + F_3/I_3)$, lb/amp

C = radial air gap, m

I_1, I_3 = bias current of quadrants 1 or 3, respectively, A

F_1, F_3 = magnetic forces per pole due to bias currents, N

The parameter K_m is the "negative spring" effect of the AMB magnetic field. The part of the proportional gain to overcome this effect is $K_m/(K_i G)$. Therefore, ΔC_d is the net proportional gain contributing to the AMB stiffness.

Assuming the power amplifiers are current sources in the bandwidth of interest (G = constant), the AMB regulating force across the quadrants 1 and 3 is

$$F = K_i i + K_m Y \quad (2)$$

From figure 1, the regulating current is

$$i = G [- C_d Y - C_v Z - C_e Q + \Delta C_d C_p Y_p] \quad (3)$$

where

$$Z = [(S + a)/(S + b)] (Y - C_p Y_p) \quad (4)$$

$$Q = [1/(S + \omega_o)] Y \quad (5)$$

$$Y_p = [BS/(S^2 + BS + \omega_c^2)] Y \quad (6)$$

Incorporating equations (4), (5), and (6) into equation (3), which in turn is incorporated into equation (2), the AMB reaction transfer function can be expressed by equation (7).

$$-F/Y = K_i G[(\Delta C_d + C_v(S + a)/(S + b))f + C_e/(S + \omega_o)] \quad (7)$$

where

$$f = 1 - C_p BS/(S^2 + BS + \omega_c^2)$$

The filter gain C_p ranges from 0 to 1. For AMB without frequency band rejection, i.e., $C_p = 0$, the complex stiffness as a function of exciting frequency is

$$\begin{aligned} -F/Y = & [K_i G(\Delta C_d + C_v(ab + \omega^2)/(b^2 + \omega^2)) + K_i G C_e \omega_o/(\omega^2 + \omega_o^2)] \\ & + j \omega [K_i G C_v(b - a)/(b^2 + \omega^2) - K_i G C_e/(\omega^2 + \omega_o^2)] \end{aligned} \quad (8)$$

The real part of equation (8) is the AMB stiffness and the imaginary part is the AMB damping. The second terms of both parts are the main contributors to the AMB "static stiffness" (for small ω). The stiffness and damping of a typical AMB are presented in figure 2. It may appear unusual that the bearing damping can be negative, but as long as no rotor natural vibration mode exists in the frequency range with negative damping, there should be no dynamic problem.

Figure 3 shows the magnitude of the complex stiffnesses for the same AMB with a frequency band rejection. The filter creates a stiffness valley with a depth proportional to C_p . With C_p approaching one, a dynamic force exerted on the rotor at the center frequency can be mostly balanced by the rotor inertia force. Only a small part will be resisted by the AMB and thus transmitted to the bearing stator or ground. In the following section, a potential stability problem of creating such a stiffness valley will be discussed.

AMB STABILITY AT FILTER CENTER FREQUENCY

Figure 4 is a zoomed-in view of the stiffness valley of figure 3. The local complex stiffness decreases and increases sharply but continuously around a center frequency ω_c in a small bandwidth B .

Let

M = rotor mass associated with the AMB

u, v = real and imaginary parts of complex stiffness, respectively,
at ω_c before the valley was created

and

$$\sqrt{u/M} > \omega_c$$

which implies a natural frequency exists above the filter center frequency.

Imagine applying a dynamic force to the mass at a frequency ω that is slowly increasing across the valley. There will be (if the valley is deep enough) an exciting frequency, ω_L , associated with a LHS slope stiffness, u_L , such that,

$$\sqrt{u_L/M} = \omega_L$$

Therefore, ω_L is a resonance frequency. Similarly, there is a RHS slope resonance frequency:

$$\sqrt{u_r/M} = \omega_r$$

These discussions are best illustrated by an example shown in figure 5. Note that these two resonance modes are not due to the filter circuitry alone. They are also related to the mass which the AMB sees. It is of less concern how well the modes are damped. Presumably, if the exciting force frequency, such as the rotor speed, is not drifting away from the filter center frequency, these modes can only be excited by impact type loads. Since the filters are usually implemented with narrow bandwidth, they will not be excited easily as long as they are reasonably damped and no persistent impact load exists. It is a major concern, however, that these modes may not be stable, i.e., associated with positive growth factor or negative damping. This can happen when the gain C_p is made large or approaching one. For example, the LHS slope mode at 59.4 Hz in figure 5 is unstable (growth factor = 120) with $C_p = 1$. It is therefore important in implementing this type of filter to know a threshold stable gain C_p , which is determined in the following analysis.

Let

$$\Delta\omega = \omega_c - \omega$$

and

$$R = (B/2)/\Delta\omega$$

The band-reject factor in equation (7) is

$$\begin{aligned} f &= 1 - C_p(jB\omega)/[(\omega_c^2 - \omega^2) + jB\omega] \\ &= [1 + (1 - C_p)R^2 - jC_pR]/(1 + R^2) \end{aligned} \quad (9)$$

The complex stiffness around ω_c is approximately

$$-F/Y = (u + jv) f = U + jV \quad (10)$$

where

$$U = u [1 - C_p R^2 / (1 + R^2)] + v C_p R / (1 + R^2) \quad (11)$$

$$V = v [1 - C_p R^2 / (1 + R^2)] - u C_p R / (1 + R^2) \quad (12)$$

Both U and V are functions of R , which in turn is a function of the exciting frequency near ω_c . According to equation (12), the RHS mode ($R < 0$) is always more damped than the LHS mode. Note that at the center frequency ($R = \infty$), equations (11) and (12) become

$$U = u(1 - C_p)$$

and

$$V = v(1 - C_p)$$

Also note that for effective force isolation, the frequency $\sqrt{u(1 - C_p)}/M$ should be one-third of ω_c or less. To determine the threshold gain (C_{p0}) for stability, it may not be overly conservative to require

$$V > 0$$

which implies by equation (12)

$$C_{p0} \leq (1 + R^2)/[(u/v)R + R^2] \quad (13)$$

In the range of 0 to 1, the minimum value of C_{p0} occurs at the LHS slope where

$$R = v/u + \sqrt{v^2/u^2 + 1} \quad (14)$$

Incorporating equation (14) into equation (13), the relationship between C_{p0} and v/u is plotted in figure 6. For normal AMB applications with $v/u < 1$, the gain value of C_p should be less than 0.83 according to this plot.

STABILITY OF ROTOR-AMB SYSTEM USING FREQUENCY BAND FILTERING

When two or more radial AMBs are supporting a rotor, the mass that each AMB sees is different at different critical modes. The location of the filter center frequency relative to these critical frequencies has a definite influence on the stability problem mentioned above. Since the influence is not straight forward, it would be appropriate to investigate the stability problem in a rotor-AMB dynamic system as follows.

In a conventional rotordynamics approach, the rotor is modeled as sections of circular beams using a finite element method. Concentrated masses and inertias are assigned at the nodes of the beam elements for any attachments to the rotor. Gyroscopic effect is included. For simplicity, circular orbits can be assumed and are adequate for most AMB applications. For each radial AMB there are two independently controlled axes. For each axis, there is a set of first-order differential equations (FODEs) representing the AMB dynamics. For example, the control scheme of figure 1 can be represented by four FODEs according to equations (4), (5), and (6), which include the frequency band filtering. The rotor-bearing coupling terms exist in equations (2) and (3).

Combining the dynamic equations of the rotor and AMBs, an electromechanical system model can be formulated for eigenvalue evaluation. The formulation procedure is straight forward and will not be presented here. An example eigenvalue analysis for a simple rotor supported by two identical AMBs (fig. 7) is used to demonstrate this system approach. The key AMB control parameters are identical for all four controlled axes (table I). The stiffness and damping of this AMB as functions of frequency have been plotted in figure 2.

Without the filtering, the system has natural modes at 3000 cpm, 10,000 cpm and 35,000 cpm. The rotor-AMB system has been analyzed for the filter centered at 30 Hz and 60 Hz separately. The additional LHS mode, which is less stable than the RHS one, is presented in table II for different values of C_p . The predicted values of C_{p0} using equations (13) and (14), as noted on table II, are consistently conservative.

CONCLUSIONS

A frequency band-reject scheme for reducing dynamic force to stator at a selected frequency may create AMB instability problems.

From the generic bearing point of view, this study has shown the following:

1. Depending on the mass supported by the AMB, there can be a natural vibration mode corresponding to the stiffness somewhere on each slope of the stiffness valley. Thus the frequencies of the induced modes are close to the filter center frequency.
2. There is a limit how deep the stiffness valley can be made without causing these modes to be unstable. The limit is related to the local damping-to-stiffness ratio before the valley is created. A conservative limit in terms of the ratio has been established.

From the rotor-AMB system point of view, the AMB mass varies with the rotor critical mode shapes. A rigorous approach to determine the stability is to find the eigenvalues of the electromechanical system.

REFERENCES

1. Weise, D. A.: Active Magnetic Bearings and Their Industrial Applications. 5th Annual Rotating Machinery and Controls Industrial Research Conference, San Antonio, Texas, 1985.
2. Habermann, H., and Brunet, M.: The Active Magnetic Bearing Enables Optimum Control of Machine Vibrations. ASME 85-GT-221, 1985.
3. Chen, H. M., and Darlow, M. S.: Design of Active Magnetic Bearings with Velocity Observer. ASME 11th Biennial Conference on Mechanical Vibrations and Noise, Boston, September 1987.
4. Hendrickson, T. A., et al.: Application of Active Magnetic Bearing Technology for Vibration Free Rotating Machinery. Naval Engineers Journal, May 1987, pp. 107-111.
5. Hilburn, J. L., and Johnson, D. E.: Manual of Active Filter Design. McGraw-Hill, 1973.
6. SKF Industries, Inc.: An Introduction to Active Magnetic Bearings. Technology Services Division, King of Prussia, Pennsylvania, June 1981.

TABLE I - RADIAL AMB PARAMETERS

K_i	53.5 N/A
K_m	2.27×10^5 N/m
a	163.3 rad/sec
b	978.8 rad/sec
ω_o	3.14 rad/sec
C_d	5921 volt/m
C_v	5626 volt/m
C_e	31500 volt/m-sec
C_p	0 to 1
ω_c	188.5 rad/sec or 377.0 rad/sec
B	7.54 rad/sec or 15.08 rad/sec

TABLE II - ADDITIONAL LHS MODE

	Speed = 1800 rpm $\omega_c = 30$ Hz; $v/u = 0.25$; $C_{po} = 0.4$		Speed = 3600 rpm $\omega_c = 60$ Hz; $v/u = 0.46$; $C_{po} = 0.6$	
C_p	Frequency (cpm)	log. decrement	Frequency (cpm)	log. decrement
0.0	1800	0.126	3600	0.126
0.4	1798	0.045	3597	0.064
0.5	1798	0.025	3597	0.049
0.6	1797	0.006 *	3596	0.034
0.8	1796	-0.034 *	3595	0.003 *
1.0	1794	-0.072 *	3593	-0.027 *

* marginal or unstable modes

AN ACTIVE MAGNETIC BEARING CONTROL SCHEME WITH FREQUENCY BAND-REJECT FILTERING

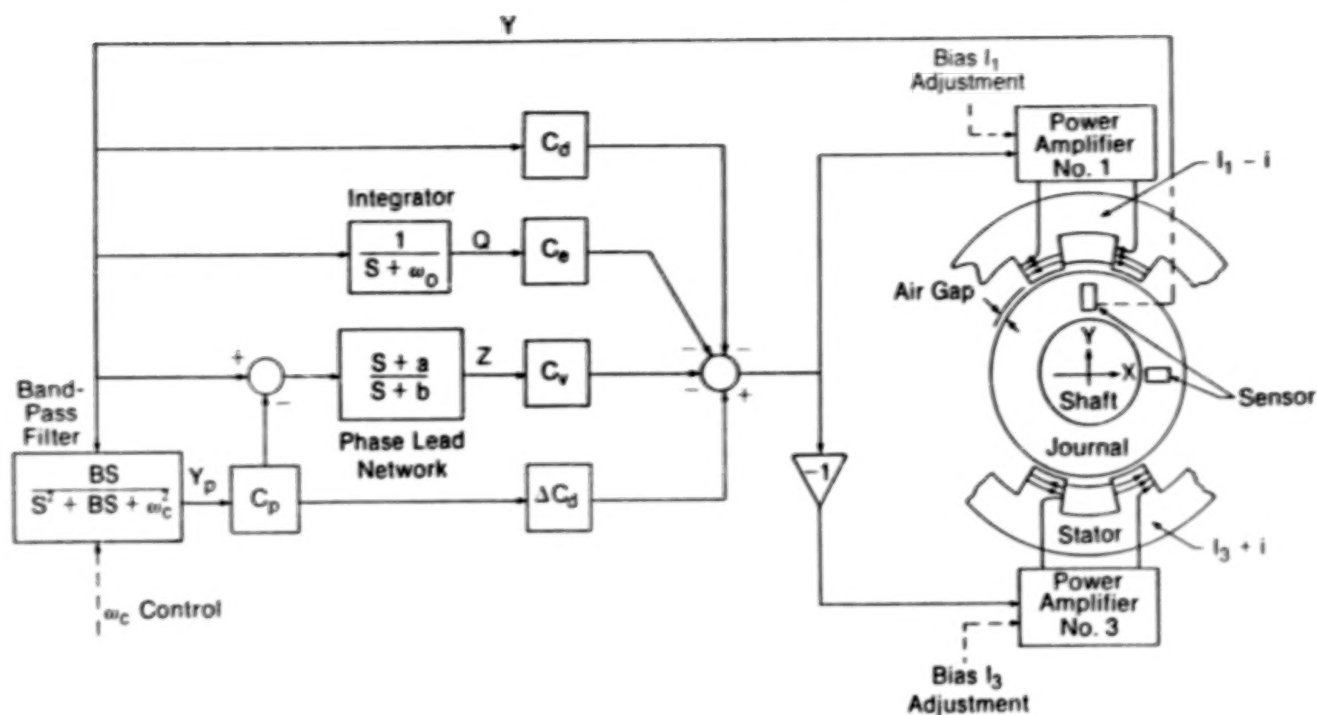
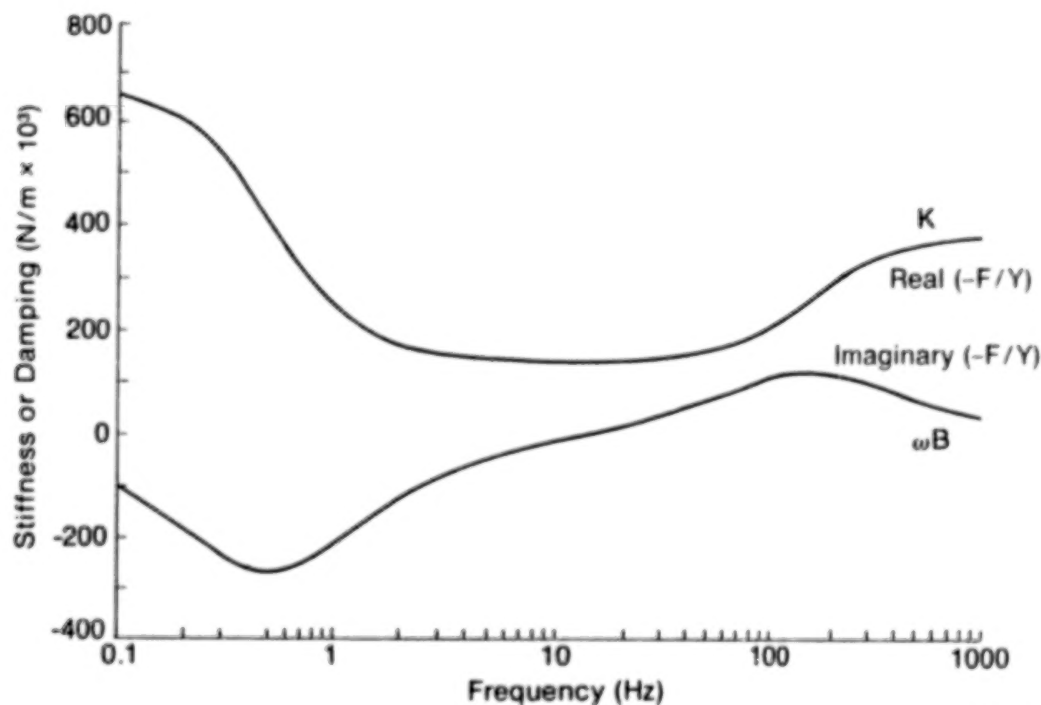


Figure 1

881081-1

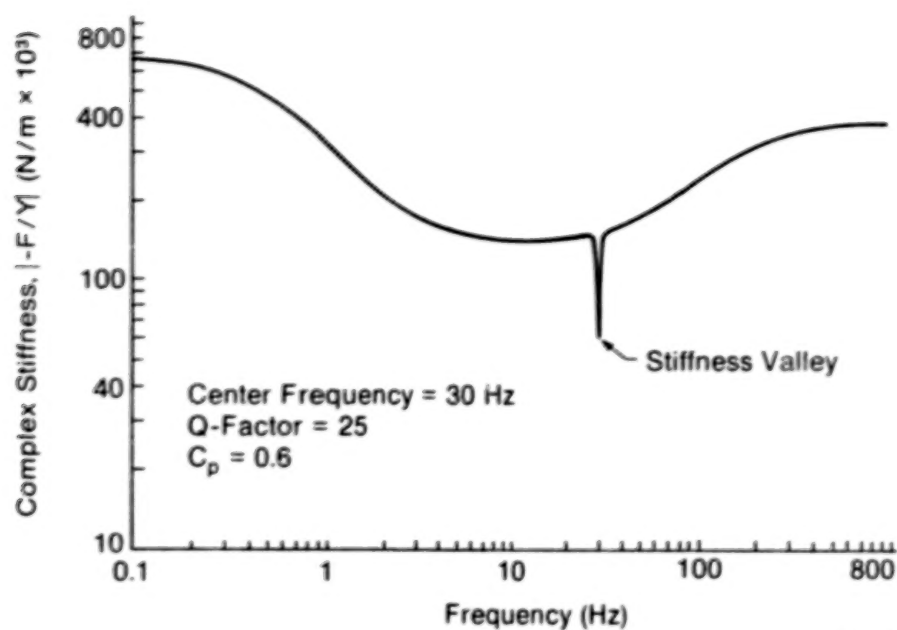
STIFFNESS AND DAMPING OF A TYPICAL ACTIVE MAGNETIC BEARING



88896

Figure 2

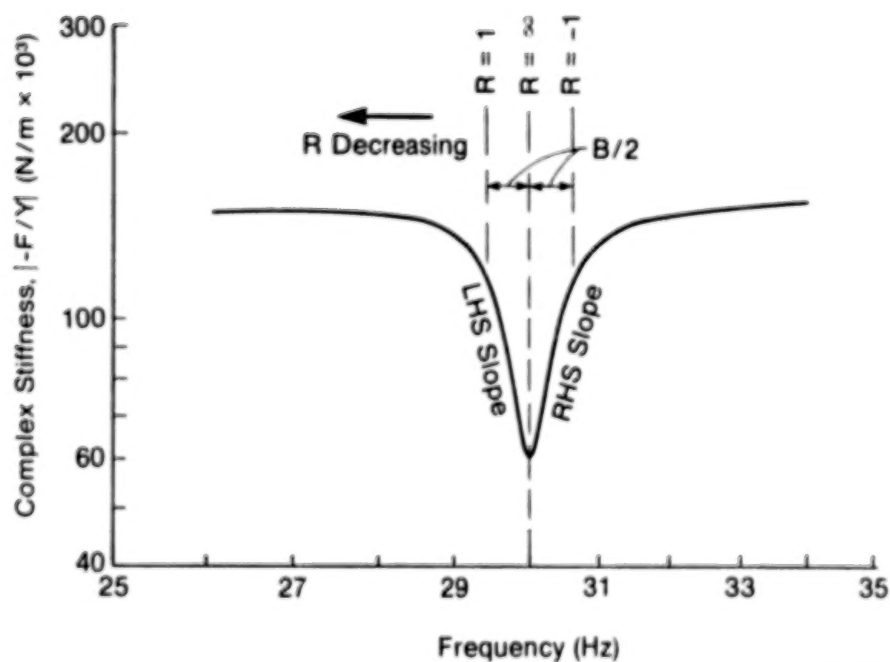
COMPLEX STIFFNESS OF A TYPICAL ACTIVE MAGNETIC BEARING WITH BAND-REJECT FILTERING



881490

Figure 3

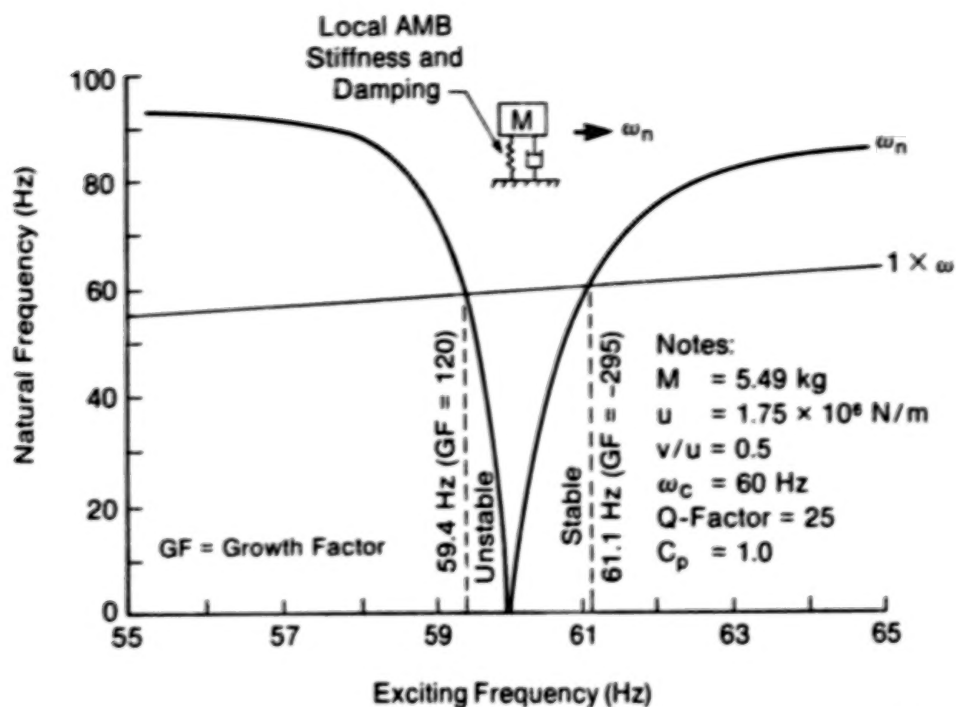
ZOOMED-IN VIEW OF A STIFFNESS VALLEY



881492

Figure 4

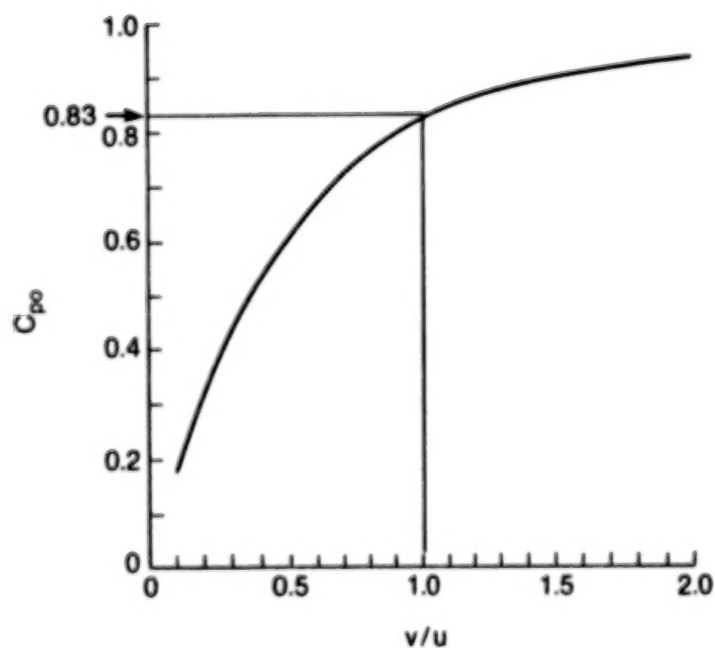
NATURAL FREQUENCY VS. EXCITING FREQUENCY



881491

Figure 5

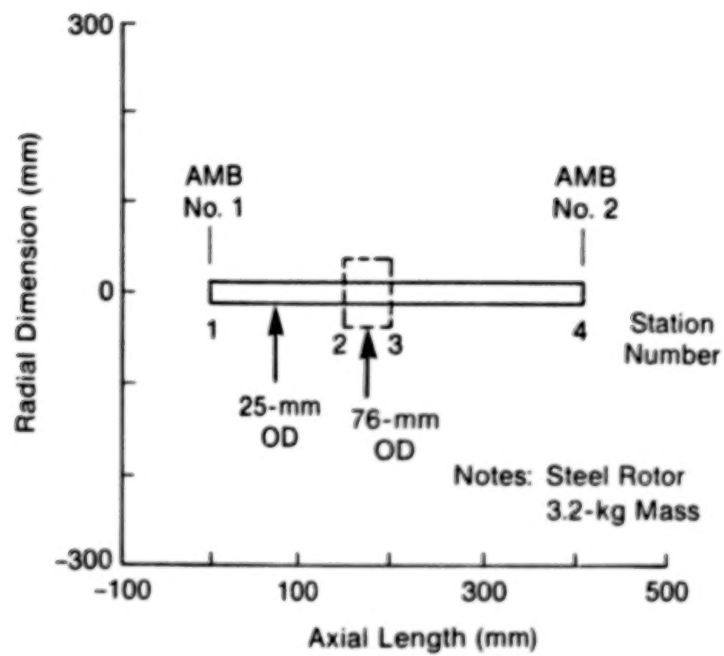
C_{po} VS v/u



881494

Figure 6

ROTOR MODEL



881493

Figure 7

A MAGNETIC DAMPER FOR FIRST MODE VIBRATION

REDUCTION IN MULTIMASS FLEXIBLE ROTORS

M.E.F. Kasarda
Rotor Bearing Dynamics, Inc.
Wellsville, New York 14895, U.S.A.

P.E. Allaire, R.R. Humphris, and L.E. Barrett
Department of Mechanical and Aerospace Engineering
University of Virginia
Charlottesville, Virginia 22901, U.S.A.

Many rotating machines such as compressors, turbines and pumps have long thin shafts with resulting vibration problems. They would benefit from additional damping near the center of the shaft. Magnetic dampers have the potential to be employed in these machines because they can operate in the working fluid environment unlike conventional bearings. This paper describes an experimental test rig which was set up with a long thin shaft and several masses to represent a flexible shaft machine. An active magnetic damper was placed in three locations: near the midspan, near one end disk, and close to the bearing. With typical control parameter settings, the midspan location reduced the first mode vibration 82%, the disk location reduced it 75% and the bearing location attained a 74% reduction. Magnetic damper stiffness and damping values used to obtain these reductions were only a few percent of the bearing stiffness and damping values. A theoretical model of both the rotor and the damper was developed and compared to the measured results. The agreement was good.

NOMENCLATURE

<u>Symbol</u>	<u>Meaning</u>
A	Area of magnetic pole face (one)
C	Capacitance
c_{eq}	Equivalent damping
F	Force
G	Controller transfer function
h	Gap thickness
h_s	Steady state gap thickness
i	Current
i_s	Steady state current
i_b	Bottom magnet current
i_t	Top magnet current
K_a	Current amplifier gain

K_{eq}	Equivalent stiffness
K_g	Proportional gain
K_i	Current stiffness
K_g	Rate gain
K_t	Controller total gain
K_y	Position stiffness
M	Mass
N	Number of turns (per leg)
R	Resistance
s	Laplace variable
W	Weight
y	Vertical position
ω	Angular velocity
ϕ	Magnetic flux
μ_0	Permeability of free space
τ	Time constant

INTRODUCTION

Compressors, turbines and other rotating machines often have long thin shafts which give rise to high vibration problems. Currently, many compressors operate above the first [1] or second critical speed. Steam turbines also operate above several critical speeds. Seals inside compressors give rise to cross coupled stiffness terms which may drive a machine into large subsynchronous vibrations [2]. Nicholas et al. [3] report on the effects of flexible supports which tend to increase vibration levels in steam turbines. Generally it is desirable to increase the damping effects near the center of these long, thin shaft machines. One method of doing this is to place a damper inside the machine casing.

The concept of using a damper inside these machines is not new. Such a damper would be located somewhere between the bearings and apply damping, and perhaps stiffness, to the rotor. What has been lacking until recent years is a damper which could operate in the environment of the working fluid. Conventional rolling element and fluid film bearings require an oil supply. A central damper in a compressor would have to be sealed so that the oil does not contaminate the gas. In most cases, the additional complications do not warrant the damper. In steam turbines, the temperature is so high that an oil damper could not be used inside the turbine.

Magnetic dampers are now a real possibility for these types of machines. Commercial magnetic bearings [4,5] are increasingly being used for compressors and other machines. These do not require oil and can operate at high temperatures, thus removing the limitations indicated above. To date, the authors are not aware of the use of a magnetic damper in a field application in North America.

A magnetic bearing can be used as a magnetic damper simply by having it carry no load. Thus the machine is completely supported in regular bearings. Typically these are oil lubricated bearings. If the damper is not active, then the machine reverts to its normal behavior without a damper effect. Some early work on simple rotors with active control was reported in [6,7] by Allaire et al.

Several studies have been carried out by Holmes et al. [8,9] on the suppression of vibrations in long transmission shafts. A magnetic damper was placed at various locations along the shaft to determine the reduction. These studies differ from the present paper because there were no large masses located along the shaft such as occur in compressors and turbines.

A magnetic bearing/damper has been developed at the University of Virginia. It was used as the damper in this work, so the relevant publications are described in some detail here. The basic bearing geometry and control algorithm was described by Humphris et al. [10]. The effects of the bearing employed to support a flexible rotor were measured and reported in Allaire et al. [11-13]. Adjustment of the bearing stiffness properties via the control system gains allowed movement of the rotor first critical speed from approximately 800 rpm to 2,000 rpm, which is more than a factor of two. Variation of the bearing damping properties gave a reduction in rotor vibrations of as much as an order of magnitude. The first results using the magnetic bearing as a damper (not supporting any steady state load) were reported in [14]. Also, initial results of employing digital control to operate magnetic bearings were published in [15].

The purpose of this paper is to report on the use of an active magnetic damper in a multimass flexible rotor. Three large disks were placed on a shaft, supported in conventional bearings, to represent a multimass compressor or steam turbine. The magnetic damper was placed in various locations to observe the vibration reduction capabilities. The magnetic damper was placed near the midspan, near one end disk, and as close to the outboard bearing as possible.

ACTIVE MAGNETIC DAMPER

An active magnetic damper is essentially an active magnetic bearing with no load support capacity. The magnetic damper used in this analysis consists of four electromagnets located radially around the rotor shaft. The electromagnet currents, which determine the force in each magnet, were determined by a controller which maintained the shaft in the center of the damper by continuously monitoring the shaft position and adjusting the electromagnet currents accordingly. There were air gaps between the shaft and the magnets and the shaft did not contact the magnets. The dynamic properties of the damper (i.e. damping and stiffness) were electronically regulated by the controller.

A diagram of the four electromagnets which made up the damper is shown in Figure 1. They were located radially around a laminated ferromagnetic disk which was attached to the rotor shaft. The purpose of this laminated disk was to provide a continuous flux path between the magnet pole faces with a minimum of eddy current losses.

Each electromagnet in the damper consisted of a solid soft iron core forming a horseshoe, with two pole faces cut to a diameter of 60.5 mm (2.38 inches). This gave a nominal radial clearance of 1.0 mm (0.040 inches). Each leg of the coil was wound with 920 turns of wire. All electromagnets were the same with equal steady state currents. Presented in appendix A is the theory of the damper characteristics.

Two proximator (eddy current) probes located vertically and horizontally near the damper (unless otherwise specified) were used as rotor position sensors for input

to the electronic controller. Various tests were previously conducted to insure that the magnetic fields from the damper did not affect the readings of the probes.

TEST RIG

A four mass laboratory rotor was constructed with a 19.0 mm (0.75 inch) shaft supported in conventional sleeve bearings with a bearing span of 660.4 mm (26.0 inches). Three steel disks were placed four inches apart at the center of the shaft leaving 190.5 mm (7.5 inches) between each outboard disk and the closest support bearing. Each of these three disks was 139.7 mm (5.5 inches) in diameter, 25.4 mm (1.0 inch) in thickness, and weighed 28.48 N (6.4 lbs). The fourth mass was the laminated ferromagnetic damper disk which weighed 4.90 N (1.1 lbs) and was 58.4 mm (2.3 in) in diameter with a thickness of 25.4 mm (1.0 inch). The total rotor length and weight, including the laminated magnetic disk, was 762 mm (30.0 inches) and 107.2 N (24.1 lb), respectively.

This damper disk was placed at three different locations on the rotor, illustrated in Figure 2, depending on the desired location of the magnetic damper. The three locations were at the midspan near the center disk, near the third disk at the quarterspan of the rotor, and at a location just inboard of the outer bearing. These locations were chosen to demonstrate the effect of a damper at optimum and less than optimum rotor locations for control of one or more modes of vibration. These locations represent situations where there may be design constraints on an actual machine as to the placement of a magnetic damper on the rotor. As shown in Figure 2, shaft displacement sensors were placed at 3 different locations to monitor shaft motion. These locations will be referred to from left to right as the disk 1 probe, midspan probe and disk 3 probe, respectively. The four mass rotor will now be referred to as the 3-mass rotor, due to the relatively small mass of the laminated ferromagnetic disk compared to the three large steel disk masses.

The 3-mass rotor was attached to an aluminum baseplate which was fixed to a large concrete block by anchor bolts. Shim stock was placed underneath the aluminum baseplate to correct a slight bow in the baseplate. The shaft was also twisted (bowed) with a significant shaft bow which could not be corrected. For example, when the shaft bow at the midspan probe was reduced to below .0254 mm (1 mil), the bow near the first disk was still close to .0508 mm (2 mils).

The rotor was driven by a 1/2 hp electric motor which was rated at 10,000 RPM. The motor transmitted power through a flexible rubber coupling as shown in Figure 2.

A total of three vertical and three horizontal proximitors were used to monitor shaft displacements. A separate proximitor probe was used as a key phasor. Signals from the probes were run to two digital vector filters, where amplitude and phase information at the probes was determined. One set of proximitor probes was also used as input sensors for the magnetic damper controller. These sensors were always located close to the damper.

The three-mass experimental rotor was used to study the effects of a magnetic damper located at the three locations on the shaft. The magnetic damper, used in conjunction with a controller, exhibited some nonlinear effects above 4,000 RPM. Therefore this paper will be limited to operation below 4000 RPM (66.7 Hz). The first rotor bending mode is located at about 1600 RPM (26.7 Hz), with all other modes located at frequencies greater than 4000 RPM (66.7 Hz).

DAMPER AT MIDSPAN

The first location of the magnetic damper to be investigated was the midspan location as shown in Figure 2a. This was expected to be the optimum position for control of first mode vibrations.

The effect of increasing rate gain (K_r) or damping and proportional gain (K_g) or stiffness of the electromagnetic damper was studied at each location. The rate gain (K_r) was varied from a nominal value of 2.0 to a maximum value of 20.0. Due to stability problems, it was not possible to use this damper with pure damping or rate gain (K_r), and therefore, the controller was set with a nominal proportional gain (K_g) of 2.5, while the rate gain (K_r) was varied for analysis. Similarly, the electromagnetic damper could not be used with pure stiffness or proportional gain (K_g), and the controller was set with a nominal rate gain (K_r) of 5.0 while the proportional gain (K_g) was varied from 2.5 to 10.0. Finally, a comparison of the effect of the damper location for fixed values of rate gain (K_r) and proportional gain (K_g) was carried out.

The effect of using the damper at the midspan is shown in Figure 3. The rotor was run with the damper off and with rate gain (K_r) equal to 2.0, 5.0 and 10.0. Proportional gain was held constant at 2.5. There was an 82% reduction in amplitude with a rate gain of 10.0 over the case with the damper off.

An unbalance response model of the rotor was developed to compare to the measured data. Stiffness and damping coefficients were evaluated for the damper as described in Appendix B. Also, the unbalance level in the rotor was determined by balancing the rotor to a low level and then adding a known unbalance weight in the center disk.

The forced response predictions for the magnetic damper at the midspan of the 3-mass rotor are plotted in Figure 4 for cases with the magnetic damper off, and with the damper on with a rate gain (K_r) equal to 2.0, 5.0, and 10.0, respectively. A maximum reduction of 88% in the amplitude of vibration occurs theoretically with $K_r = 10$ as compared to the value of 82% for the measured case.

It may be seen from these results that even a small amount of damping can greatly reduce the vibration level. For $K_r = 2.0$, the estimated damping value was 31 N-sec/m (0.18 lb-sec/in), which produces a 49% decrease in amplitude at the rotor center. The estimated bearing damping was 1050 N-sec/m (6.0 lb-sec/in). Thus the actual midspan damping is only approximately 3% of the bearing damping. At $K_r = 10$, the estimated damping was 122 N-sec/m (0.70 lb-sec/in) or approximately 12% of the bearing damping. This produced an 82% reduction in amplitudes of vibration.

Figure 5 shows the experimental values for the midspan damper location as the proportional gain (K_g) had the values 2.5, 5.0 and 7.5. The rate gain was held constant at $K_r = 5.0$. The critical speed increased from 1600 rpm (26.7 Hz) to 2570

rpm (42.8 Hz) with $K_g = 7.5$. The value of $K_g = 7.5$ corresponds to a damper stiffness of 210,000 N/m (1200 lb/in). This stiffness value is only about 10% of the bearing vertical stiffness.

The calculated forced response is shown in Figure 6. The predicted increase in critical speed is 38% for $K_g = 7.5$. This is somewhat lower than the 60% measured increase in critical speed. Also, the theory predicted a steady increase in amplitude with increasing K_g , whereas the measured values decreased and then increased. Overall, however, the agreement is good.

DAMPER AT DISK THREE

The second location of the magnetic damper is the disk three location as shown in Figure 2. This was expected to be the next best position for control of the first mode vibrations.

The effect of using the damper at disk three is shown in Figure 7. The rotor was run with the damper off and the rate gain (K_r) equal to 5.0, 10.0, and 20.0. Proportional gain was held constant at 2.5. There is a 75% reduction in amplitude with a rate gain of 20.0 over the case with the damper off.

An unbalance response model of the rotor with the damper at disk three was also developed for comparison with the measured data. The forced response predictions for this configuration are plotted in Figure 8 for cases with the magnetic damper off, and with the damper on, with a rate gain (K_r) equal to 5.0, 10.0, and 20.0, respectively. A maximum reduction of 85% in the amplitude of vibration occurred theoretically with $K_r = 20$, as compared to the value of 75% for the measured case.

Again, it may be seen from these results that even a small amount of damping can greatly reduce the vibration level. At $K_r = 20$, the estimated damping was 175 N-sec/m (1.0 lb-sec/in) or 17% of the bearing damping. This produced a 75% reduction in amplitudes of vibration.

Experimental data was also taken for the disk three damper location with proportional gain (K_g) values of 2.5, 7.5, and 10.0, while the rate gain (K_r) remains at 5.0. The critical speed increased from 1600 RPM (26.7 Hz) to 1920 RPM (32 Hz) with $K_g = 10.0$. The value of $K_g = 10.0$ corresponded to a damper stiffness of 262,000 (1500 lb/in). This stiffness value was only about 13% of the bearing vertical stiffness.

The corresponding forced response calculations predicted a 25% increase in the critical speed frequency for $K_g = 10.0$. This was somewhat higher than the measured value of 19%. Once again the theory predicted a steady increase in amplitude with increasing K_g whereas the measured values decreased and then increased. In general, however, the agreement was good.

DAMPER AT BEARING

The third location of the magnetic damper to be investigated was the bearing location as shown in Figure 2c. This was expected to be the least effective location for control of the first mode of vibrations.

The effect of using the damper at the bearing was similar to the effect of the damper at other locations. However, experimental data was taken for the rotor when the rate gain (K_r) was equal to 5.0, 10.0, and 20.0, while the proportional gain (K_g) equals 2.5. There was a significant 74% reduction in amplitude with a rate gain of 20.0, over the case with the damper off whereas forced response calculations predicted only a 52% decrease.

Similar data was taken when the proportional gain (K_g) was set at 2.5, 7.5, and 10.0, with the rate gain (K_r) equal to 5.0. There was a measured 11% increase in the first critical speed from 1620 RPM (27 Hz) with the damper off to 1800 RPM (30 Hz) with the proportional gain (K_g) equal to 10.0. Forced response calculations predicted a 6% increase in critical speed.

EFFECT OF MAGNETIC DAMPER LOCATION

A summary of the measured effect of magnetic damper location is shown in Figure 9, when the proportional gain (K_g) equals 2.5 and the rate gain (K_r) equals 5.0. As noted, the optimum control of the first mode vibrations occurs when the damper is at the midspan location, with a 70% reduction. The next best location is at disk three, with a 61% reduction in vibration. While the least optimum location for control of the first mode of vibrations is the bearing location, there is still a 48% reduction in vibrations over the case with no damper.

The corresponding forced response predictions are shown in Figure 10. There is a predicted 84% reduction when the damper is at the midspan and an 81% reduction when the damper is at disk three. Also there is a 34% predicted reduction when the damper is at the bearing.

A summary of the overall measured responses at the first mode is shown graphically in Figure 11 with $K_g = 2.5$. This figure shows the effect of the damper at various locations on the first mode response. It can also be noted that the vibration reduction approaches a minimum level as the damping is increased.

CONCLUSIONS

Overall, the magnetic damper achieves the desired result of a large reduction of first mode vibration at the center of the rotor. The largest reduction is 82% with the damper in the optimum location near the rotor center. These results indicate that even less than optimum placement or less than optimum control parameter setting value can produce very significant vibration reductions. This is very encouraging for the potential use of magnetic dampers in industrial applications.

It can also be noted, however, that there is a limit to the vibration reduction which can be attained by a single damper in the machine. Beyond a certain level, even a large increase in the stiffness and damping of the damper essentially produces very little further reduction of vibrations.

Generally, the agreement between the theoretical modeling of the shaft/damper system compared to the measured results is good. The magnitudes are close and the trends in the results are consistent. This indicates that the design of magnetic dampers, done on a theoretical basis before construction, has a high probability of success.

APPENDIX A ACTIVE MAGNETIC DAMPER

This Appendix briefly discusses basic electromagnetic theory relating to the force and control of a magnetic damper. For an active magnetic damper there are four electromagnets located radially around the shaft. For the vertical direction there would be an identical top and bottom magnet and the force is

$$F_{\text{total}} = 2F_{g(\text{top})} - 2F_{g(\text{bottom})} = \frac{\mu_0 AN^2 i_t^2}{h^2} - \frac{\mu_0 AN^2 i_b^2}{h^2} \quad (1)$$

In a damper, for steady state conditions,

$$i_t = i_b$$

The total force or load capacity in a magnetic damper is thus equal to zero.

$$F_{\text{total}} = W = 0$$

This, of course, would not be true in a magnetic bearing.

In an electromagnetic damper, two independent parameters can change -- position, x , and current, i . Define the position and current stiffness as

$$K_y = - \frac{\Delta F}{\Delta y} = \text{Position Stiffness}$$

$$K_i = - \frac{\Delta F}{\Delta i} = \text{Current Stiffness}$$

The gap thickness and current expressions are

$$h = h_s - \Delta y$$

$$i = i_s + \Delta i$$

for small changes about the steady state. The total force expression, Equation (1), becomes

$$F_{\text{total}} = \left[\frac{\mu_0 AN^2 (i_t + \Delta i)^2}{(h_s - \Delta y)^2} \right] - \left[\frac{\mu_0 AN^2 (i_b - \Delta i)^2}{(h_s + \Delta y)^2} \right]$$

or approximating by the binomial expansion,

$$F_{\text{total}} = \frac{\mu_0 AN^2 i_t^2}{h_s^2} \left(1 + 2\frac{\Delta y}{h_s} + 2\frac{\Delta i}{i_s}\right) - \frac{\mu_0 AN^2 i_b^2}{h_s^2} \left(1 - 2\frac{\Delta y}{h_s} - 2\frac{\Delta i}{i_b}\right)$$

For steady state conditions,

$$i_t = i_b = i_s$$

so the total force equation reduces to

$$F_{\text{total}} = \frac{\mu_0 AN^2 i_s^2}{h_s^2} \left(\frac{4\Delta y}{h_s} + \frac{4\Delta i}{i_s}\right)$$

The two stiffnesses K_y and K_i can now be obtained.

First setting Δi to zero,

$$F = W - K_y \Delta y = \frac{\mu_0 AN^2 i_s^2}{h_s^2} \left(\frac{4\Delta y}{h_s}\right)$$

Recalling that $W = \text{zero}$ for a damper, the total positive stiffness is

$$K_y = - \frac{4\mu_0 AN^2 i_s^2}{h_s^3} \quad (2)$$

Second, setting Δy to zero,

$$F = W - K_i \Delta i = \frac{\mu_0 AN^2 i_s^2}{h_s^2} \left(\frac{4\Delta i}{i_s}\right)$$

The total current stiffness is,

$$K_i = - \frac{4\mu_0 AN^2 i_s}{h_s^2} \quad (3)$$

Both the position and current stiffnesses for the combination top and bottom electromagnets are simply two times the position and current stiffnesses for a single electromagnet, respectively.

The purpose of the electronic controller is to condition the position voltage signals from the proximator probes and feed back the correct amount and phase of current to the magnets for optimum control of the rotor. The stiffness of the electromagnet damper is determined by the controller and can be varied by changing the proportional gain (K_g) of the controller. The damping of the electromagnetic damper is also determined by the controller. The position voltage signal from the proximator probes is electronically differentiated so that the damping can be determined by the amount of velocity or rate signal present. The damping can be varied by changing the rate gain (K_r) of the controller.

A block diagram for the controller is shown in Figure 12. A feedback control diagram of the entire magnetic damper is shown in Figure 13. The transfer function for the electronics from the sensor amplifier through the position and current amplifier is

$$G(s) = \frac{K_t K_a K_p [K_g + (K_g + K_r)RCs] (s+1/\tau_2)}{(1+\tau_1 s)(s+1/\tau_3)(1+RCs)} \quad (4)$$

Finally, the total transfer function for the magnetic damper is

$$\frac{F_{ext}^y}{F_{ext}} = \frac{\frac{1}{Ms^2 + K_y}}{1 + \frac{K_i G(s)}{Ms^2 + K_y}}$$

Simplifying

$$\frac{F_{ext}^y}{F_{ext}} = \frac{1}{Ms^2 + K_y + K_i G(s)} \quad (5)$$

It is easily seen that adjustment of controller proportional and rate gains (K_g and K_r) are used to adjust the stiffness and damping of the magnetic damper.

An effective damper stiffness and damping can also be obtained. The transfer function for an equivalent mass-spring-damper system is

$$\frac{F_{ext}^y}{F_{ext}} = \frac{1}{Ms^2 + c_{eq}s + K_{eq}}$$

Equating this expression with Equation (5) gives

$$\begin{aligned} K_{eq} &= K_y + K_i \operatorname{Re}\{G(j\omega)\} \\ c_{eq} &= \frac{-K_i \operatorname{Im}\{G(j\omega)\}}{\omega} \end{aligned} \quad (6)$$

where s has been replaced by $j\omega$ for synchronous vibrations.

APPENDIX B DETERMINATION OF DAMPER DYNAMIC PROPERTIES

A single mass rotor as shown in Figure 14 was used to experimentally evaluate the damping and stiffness characteristics of the magnetic damper for various settings of rate gain (K_r) and proportional gain (K_g). The effective stiffness of the damper is determined by the proportional gain (K_g) setting only. The effective damping of the magnetic damper is determined primarily by the rate gain (K_r) setting, but is also affected by the proportional gain (K_g) setting.

A rotor model of the single mass rotor was established, including support bearing characteristics, shaft bow, and unbalance in the rotor. The support bearings had a vertical stiffness of 4,030,000 N/m (23,000 lb/in) and a vertical damping of 10,000 N-sec/m (57 lb-sec/in). This model was used in a forced response program and the predicted response was compared to experimentally measured rotor response. Various values of stiffness and damping were added to the rotor model at the electromagnetic damper location until predicted response (i.e. frequency and amplitude of the first mode response) matched the experimental rotor response to within approximately 5%. An example of experimental data and its corresponding or "matching" calculated response is shown in Figure 15 for the case when the proportional gain (K_g) equals 2.5 and the rate gain (K_r) equals 2.0. In this manner stiffness and damping characteristics for the electromagnetic damper were determined for various values of rate gain (K_r) and proportional gain (K_g). The stiffness values are listed in Table 1 and the damping values are listed in Table 2.

The damping and stiffness characteristics of the magnetic damper determined in this manner were used in the rotor model of the 3-mass rotor for forced response calculations.

REFERENCES

1. Kludt, F. H., and Salamone, D. J., "Rotor Dynamics Modification of an Eight Stage Compressor for Safety/Reliability Improvement," Twelfth Turbomachinery Symposium, Texas A&M University, November 15-17, 1983, pp 81-96.
2. Allaire, P. E., Stroh, C. G., Flack, R. D., Kocur, J. A., and Barrett, L. E., "Subsynchronous Vibration Problem and Solution in Multistage Centrifugal Compressor," Proc. of 16th Turbomachinery Symposium, Sponsored by Texas A&M University, Dallas, TX, October 26-29, 1987.
3. Nicholas, J. C., and Barrett, L. E., "The Effect of Bearing Support Flexibility on Critical Speed Prediction," ASLE Trans., Vol. 29, No. 3, pp. 329-338, April 1986.
4. Foster, E. G., Kulle, V. and Peterson, R. A., "The Application of Active Magnetic Bearings to a Natural Gas Pipeline Compressor," ASME Gas Turbine Conference, Paper 86-GT-61, Dusseldorf, June, 1986.
5. Hustak, J. F., Kirk, R. G., and Schoeneck, K. A., "Analysis and Test Results of Turbocompressors Using Active Magnetic Bearings," Presented at ASLE Annual Meeting, Toronto, Ontario, Canada, May 12-15, 1986.
6. Allaire, P. E., Lewis, D. W., and Jain, V. K., "Feedback Control of a Single Mass Rotor on Rigid Supports," Journal of the Franklin Institute, Vol. 312, 1981, pp. 1-11.
7. Allaire, P. E., Lewis, D. W., and Knight, J. D., "Active Vibration Control of a Single Mass Rotor on Flexible Supports," Journal of the Franklin Institute, Vol. 315, 1983, pp. 211-222.

8. Nikolajsen, J. L., Holmes, R., and Gondhalekar, V., "Investigation of an Electromagnetic Damper for Vibration Control of a Transmission Shaft," The Institution of Mechanical Engineers, 1979, Vol. 193, No. 31, pp. 331-336.
9. Gondhalekar, V. and Holmes, R., "Design of an Electromagnetic Bearing for the Vibration Control of a Flexible Transmission Shaft," Rotor Dynamics Instability Problems in High Performance Turbomachinery, Texas A&M University, May 1984.
10. Humphris, R. R., Kelm, R. D., Lewis, D. W., and Allaire, P. E., "Effect of Control Algorithms on Magnetic Journal Bearing Properties," J. of Engr. for Gas Turbines and Power. Trans. ASME, Vol. 108, October 1986, pp. 624-632.
11. Allaire, P. E., Humphris, R. R., and Kelm, R. D., "Dynamics of a Flexible Rotor in Magnetic Bearings," Proc. of Rotordynamic Instability Problems in High-Performance Turbomachinery, June 2-4, 1986, NASA Conference Publication 2443, pp. 419-430.
12. Allaire, P. E., Humphris, R. R., and Barrett, L. E., "Critical Speeds and Unbalance Response of a Flexible Rotor in Magnetic Bearings," Proc. of European Turbomachinery Symposium, October 27-28, 1986.
13. Allaire, P. E., Humphris, R. R., and Imlach, J., "Vibration Control of Flexible Rotors with Magnetic Bearing Supports," AFOSR/ARO Conference, Nonlinear Vibrations, Stability, and Dynamics of Structures and Mechanisms, Virginia Tech, Blacksburg, Virginia, March 23-25, 1987.
14. Allaire, P. E., Humphris, R. R., Kasarda, M. E. F., and Koolman, M. I., "Magnetic Bearing/Damper Effects on Unbalance Response of Flexible Rotors," Proc. AIAA Conference, Philadelphia, PA, August 10-14, 1987.
15. Keith, F. J., Williams, R. D., Allaire, P. E., and Schafer, R. M., "Digital Control of Magnetic Bearings Supporting a Multimass Flexible Rotor," Presented at NASA Conference on Magnetic Suspension Technology, NASA Langley, February 2-4, 1988.

Table 1 - Horizontal and Vertical Stiffness Values of the
Magnetic Damper at Approximately 2500 RPM (41.7 Hz).

Proportional Gain (K_g)	0	2.5	5.0	7.5	10.0
K_x (N/m)	-35,000	44,000	190,000	210,000	260,000
(lb/in)	(-200)	(250)	(1100)	(1200)	(1500)
K_y (N/m)	-35,000	70,000	175,100	210,100	263,000
(lb/in)	(-200)	(400)	(1000)	(1200)	(1500)

Table 2 - Horizontal and Vertical Damping Values (lb-sec/in)
of the Magnetic Damper at 2500 RPM (41.7 Hz)

$K_r =$	0.0	2.0	5.0	10.0
K_g	$\frac{N\text{-sec}}{in}(\frac{lb\text{-sec}}{in})$	$\frac{N\text{-sec}}{in}(\frac{lb\text{-sec}}{in})$	$\frac{N\text{-sec}}{in}(\frac{lb\text{-sec}}{in})$	$\frac{N\text{-sec}}{in}(\frac{lb\text{-sec}}{in})$
0.0	$C_x = 33(C_x = .19)$ $C_y = 30(C_y = .17)$	-	-	-
2.5	U	$C_x = 49(C_x = .28)$ $C_y = 32(C_y = .18)$	$C_x = 100(C_x = .62)$ $C_y = 84(C_y = .45)$	$C_x = 150(C_x = .85)$ $C_y = 120(C_y = .70)$
5.0	U	U	$C_x = 51(C_x = .29)$ $C_y = 42(C_y = .24)$	-
7.5	U	U	U	$C_x = 47(C_x = .27)$ $C_y = 47(C_y = .27)$
10.0	U	U	U	U

U = Unstable

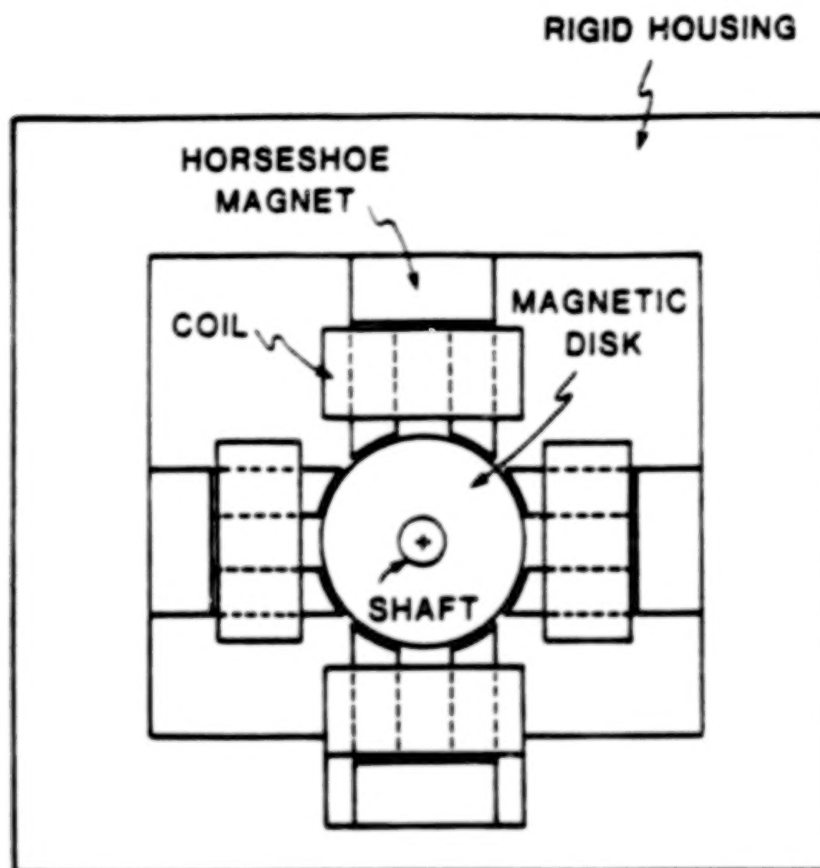
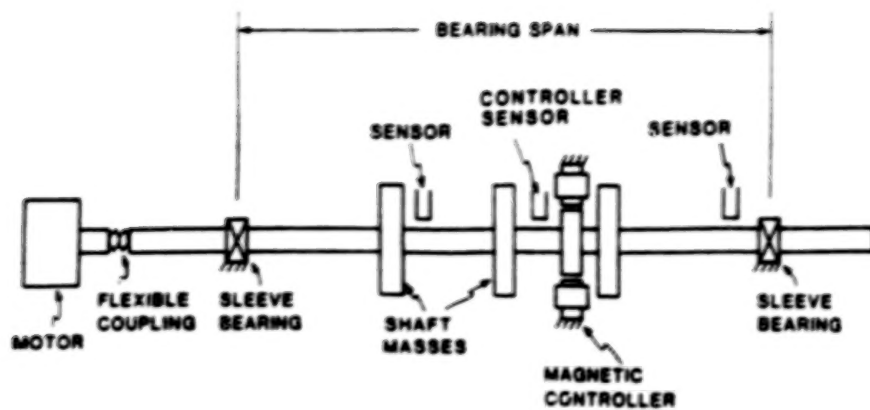
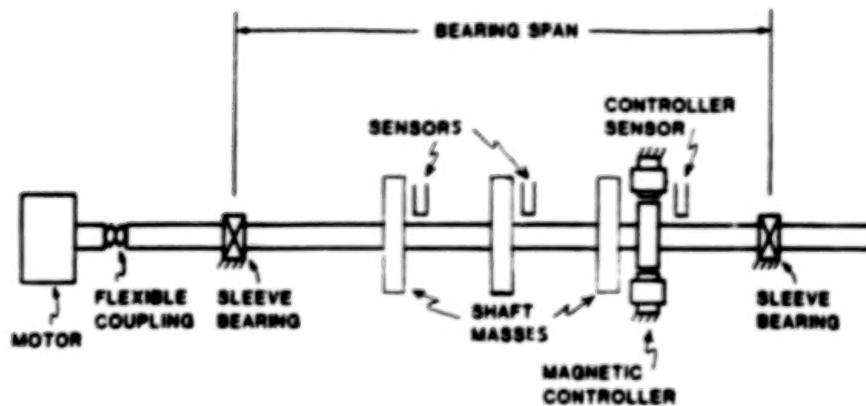


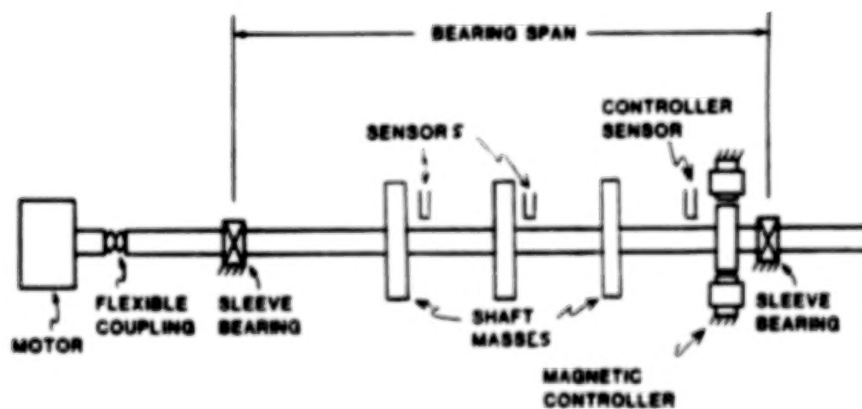
Figure 1 Magnetic Damper Model



DAMPER AT MIDSPAN



DAMPER AT DISK THREE



DAMPER AT BEARING

Figure 2 Schematic of 3-Mass Rotor with Magnetic Damper at Three Different Locations (Not to Scale)

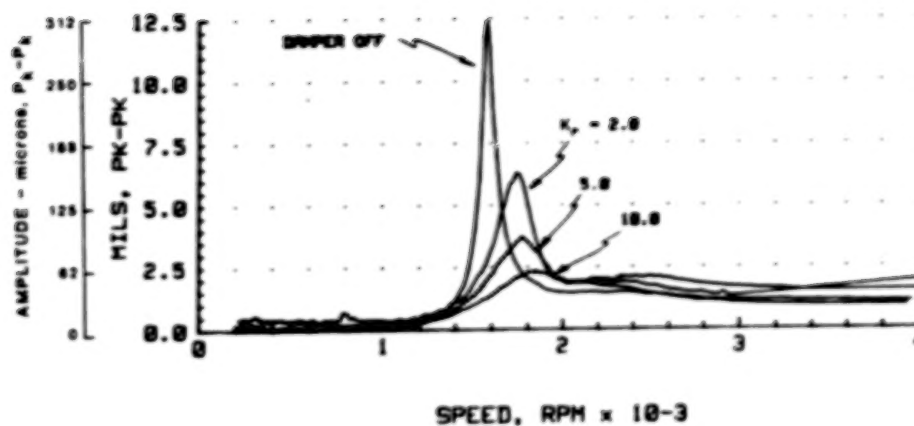


Figure 3 Experimental Results for the Damper at Midspan (Increasing Rate Gain (K_r)) at the Vertical Midspan Probe - $K_g = 2.5$

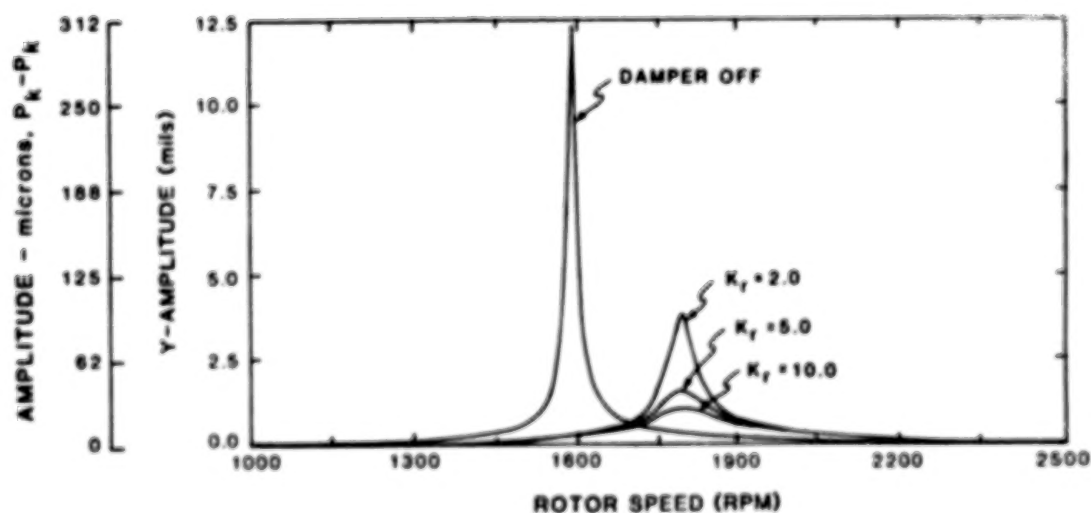


Figure 4 Forced Response Program Predictions for Damper at Midspan (Increasing Rate Gain (K_r)) at Vertical Midspan Probe - $K_g = 2.5$

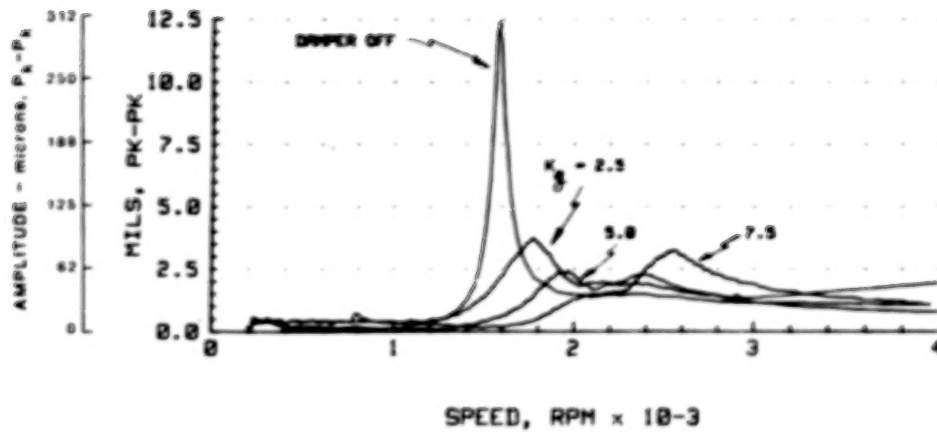


Figure 5 Experimental Results for the Damper at Midspan (Increasing Proportional Gain (K_g)) at the Vertical Midspan Probe - $K_r = 5.0$

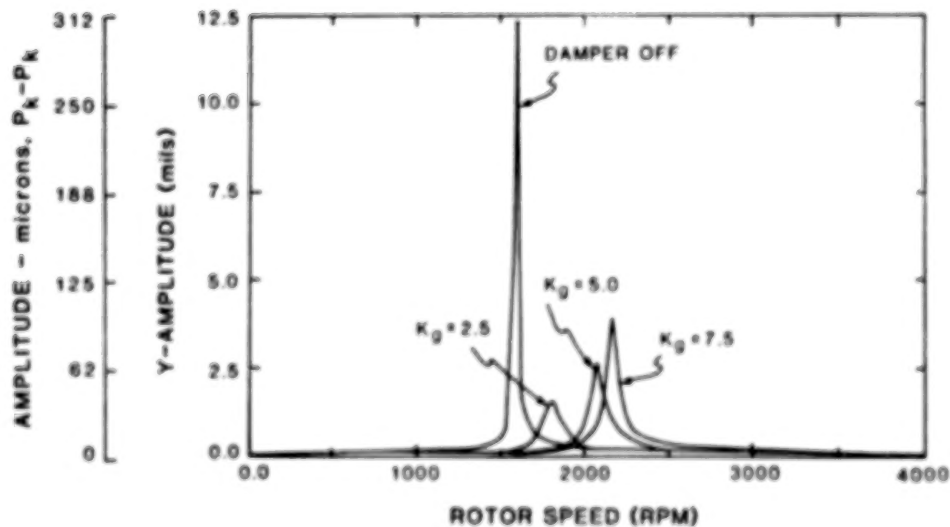


Figure 6 Forced Response Program Predictions for Damper at Midspan (Increasing Proportional Gain (K_g)) at Vertical Midspan Probe - $K_r = 5.0$

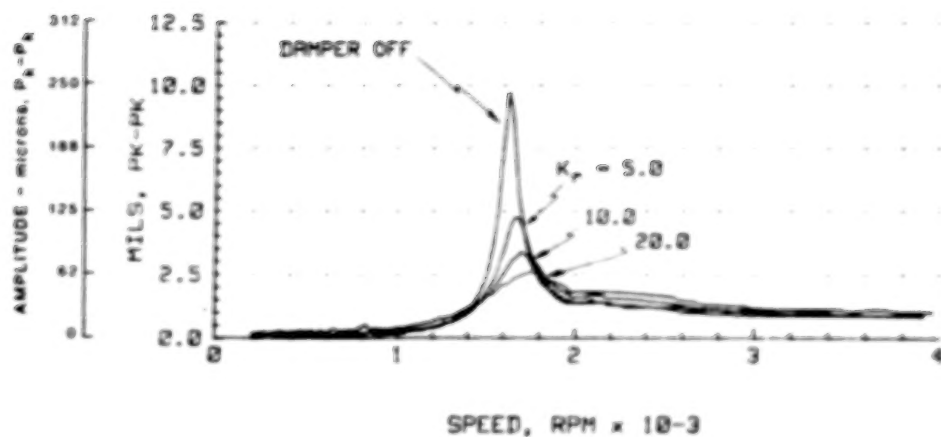


Figure 7 Experimental Results for the Damper at Disk Three (Increasing Rate Gain (K_r)) at the Vertical Midspan Probe - $K_g = 2.5$

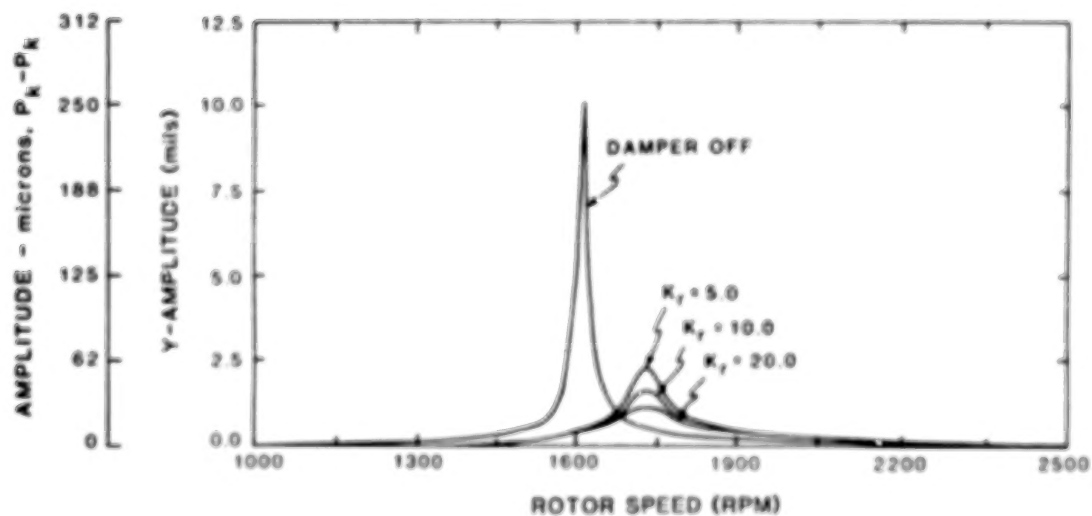


Figure 8 Forced Response Program Predictions for Damper at Disk Three (Increasing Rate Gain (K_r)) at Vertical Midspan Probe - $K_g = 2.5$

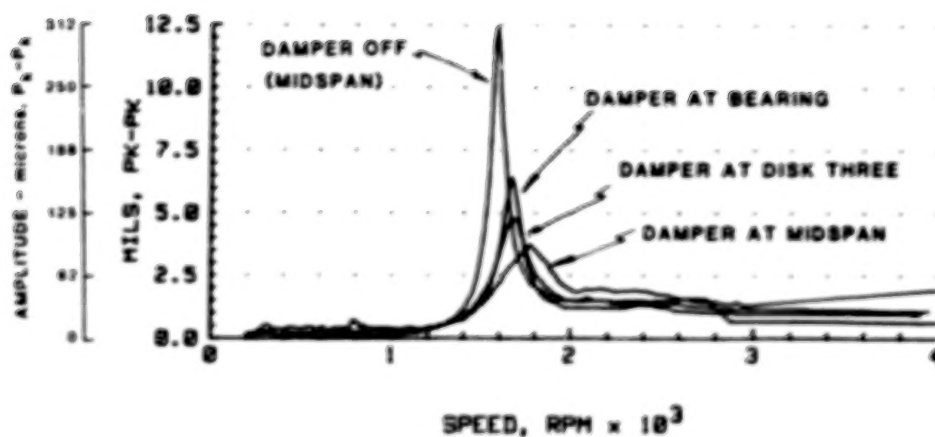


Figure 9 Experimental Results at Vertical Midspan for the Damper at Three Locations (Proportional Gain (k_g) equal to 2.5, Rate Gain (k_r) equal to 5.0)

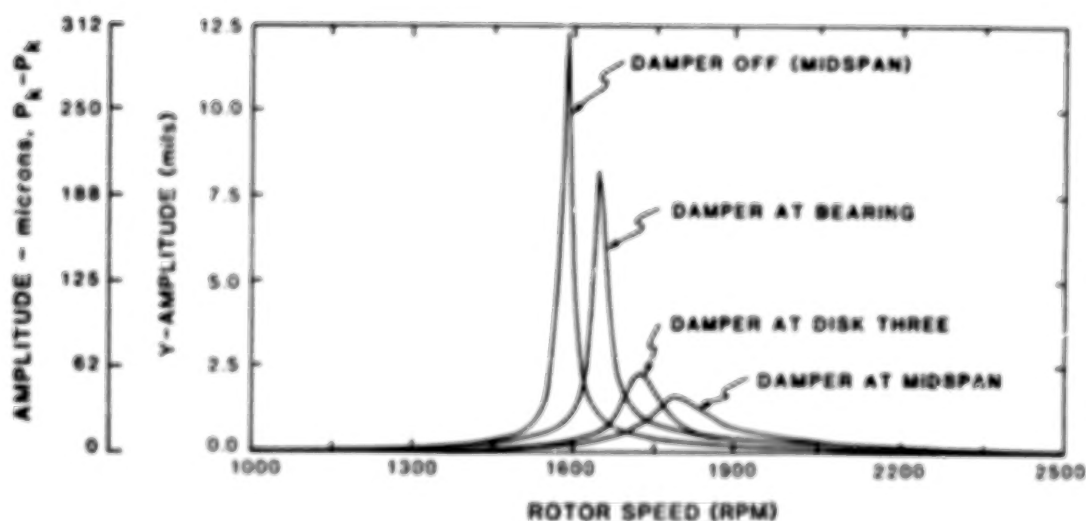


Figure 10 Forced Response Predictions for the Damper at Three Locations (Proportional Gain (k_g) equal to 2.5, Rate Gain (k_r) equal to 5.0)

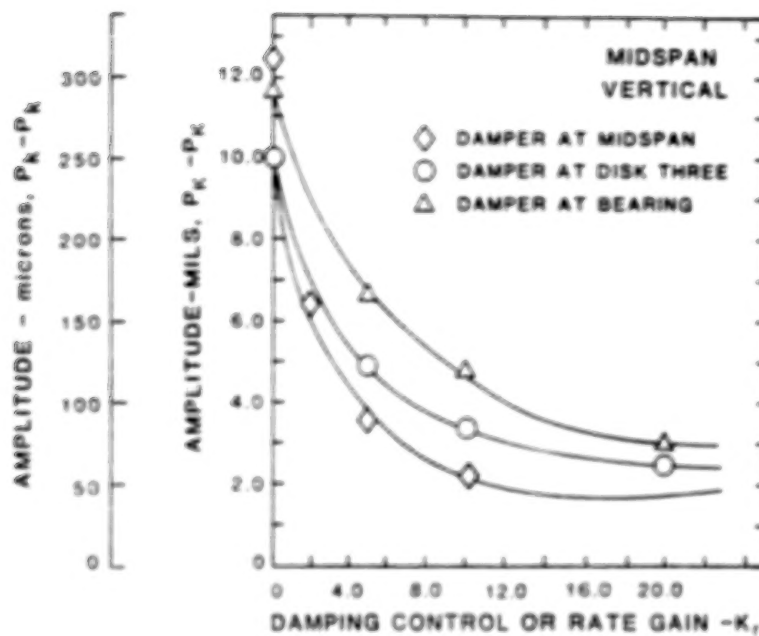


Figure 11 Response Amplitude at First Mode vs. Rate Gain (Damper at Midspan, Disk Three, and Bearing Location)

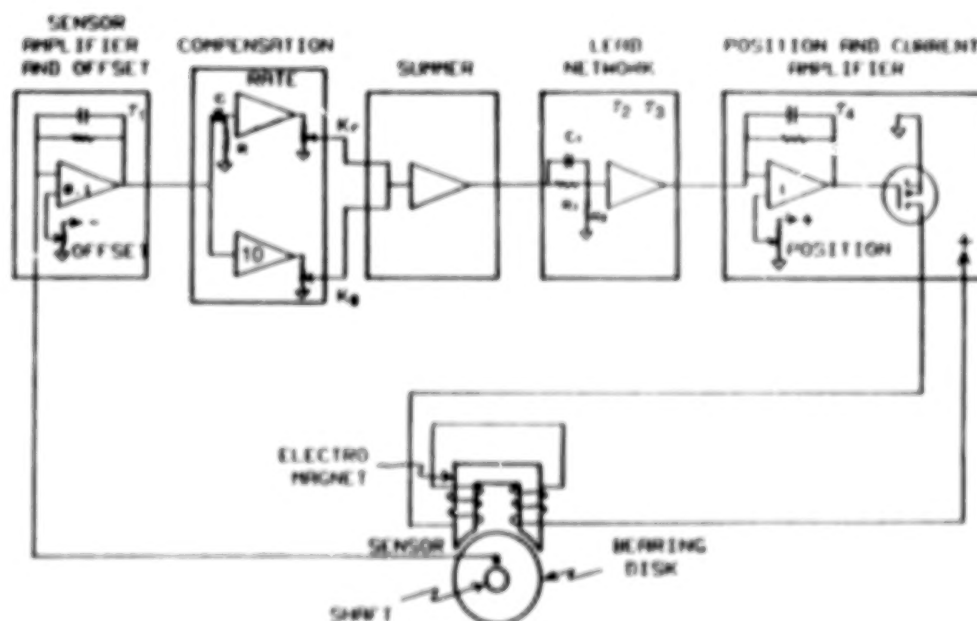


Figure 12 Block Diagram of Control Circuit

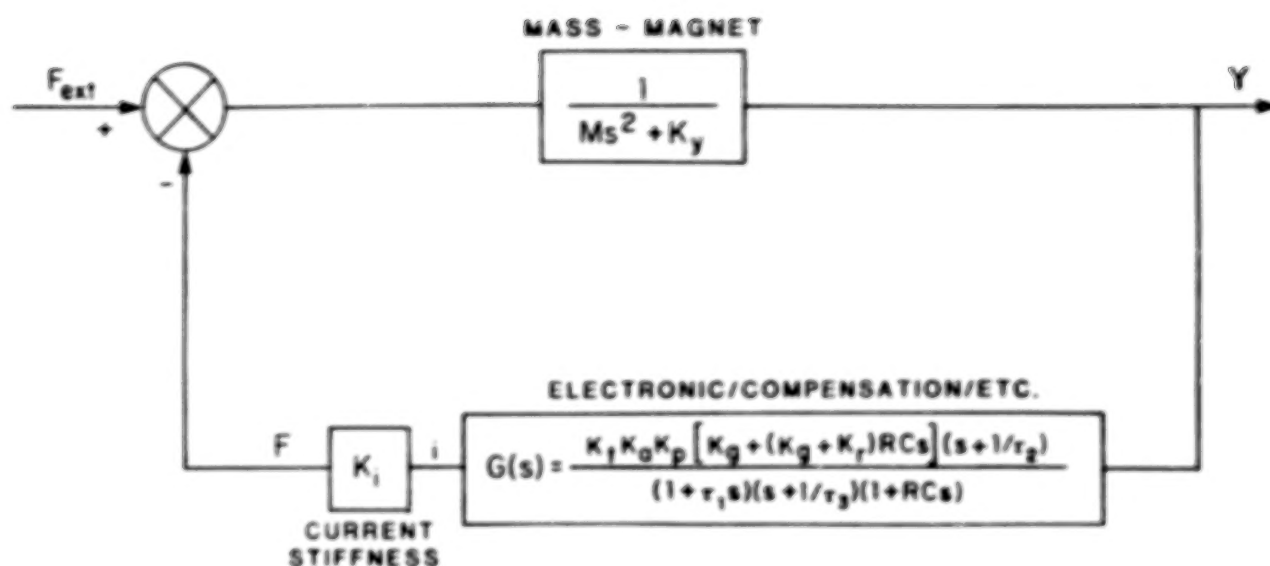


Figure 13 Diagram of Magnetic Damper System for Controller

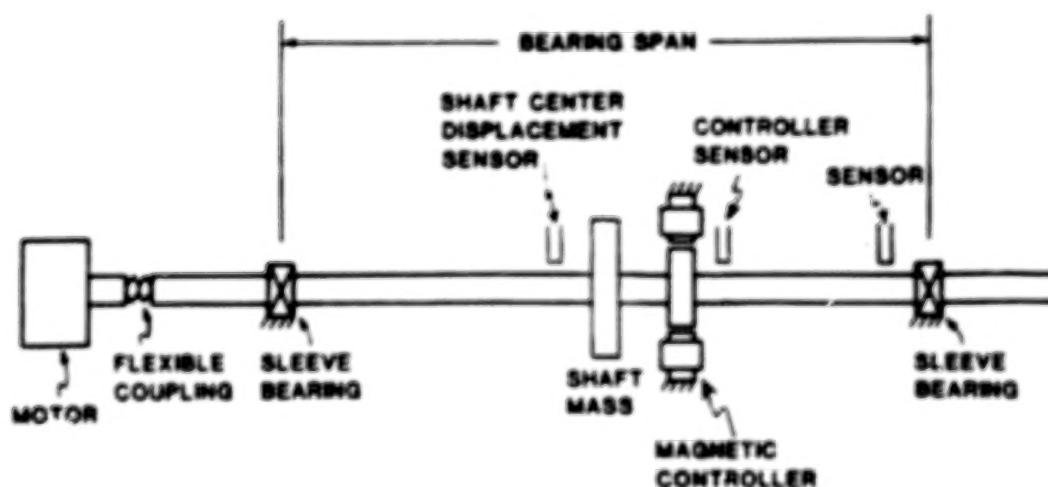


Figure 14 Schematic of Single Mass Rotor with Magnetic Damper (Not to Scale)

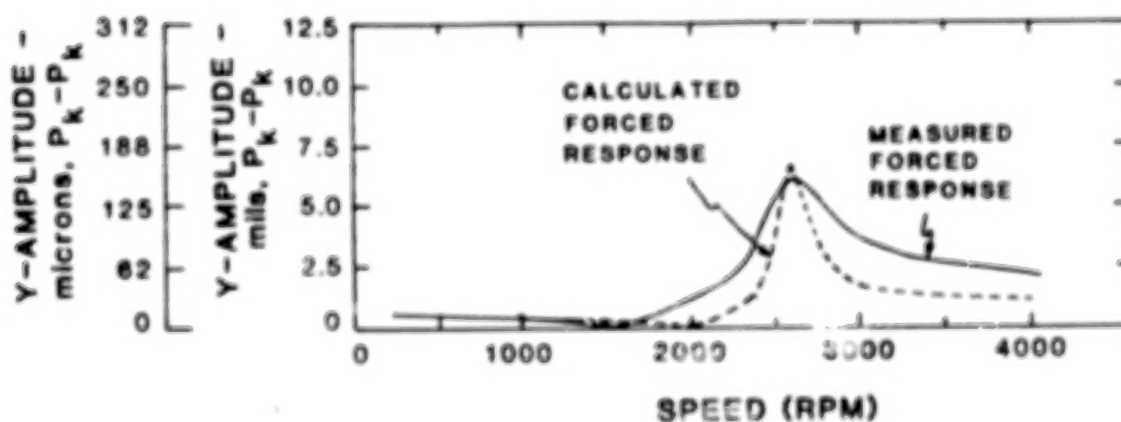


Figure 15 Comparison of Calculated and Experimentally Measured Forced Response

INCORPORATING GENERAL RACE AND HOUSING FLEXIBILITY AND DEADBAND IN ROLLING ELEMENT BEARING ANALYSIS*

R.R. Davis and C.S. Vallance
Aerojet TechSystems Company
P.O. Box 13222
Sacramento, California 95813, U.S.A.

New methods for including the effects of general race and housing compliance and outer race-to-housing deadband (clearance) in rolling element bearing mechanics analysis is presented. It is shown that these effects can cause significant changes in bearing stiffness characteristics, which are of major importance in rotordynamic response of turbomachinery and other rotating systems. Preloading analysis is demonstrated with the new finite element/contact mechanics hybrid method applied to a 45 mm angular contact ball bearing.

INTRODUCTION

Accurate analytical prediction of the rotordynamic performance of turbomachinery has foremost dependence on accurate knowledge of the stiffness of bearings and bearing support components. Classical methods of rolling element bearing loading analysis developed by Jones [1] and Harris [2] have proven quite useful in cases where the inherent race rigidity assumption (except local contact deformation) is reasonable. However, critical speed and rotordynamic stability predictions for turbomachinery using these techniques are often inaccurate. Comparisons with test data usually indicate that the predicted bearing stiffness is too high, sometimes by large factors which have eluded quantitative explanation.

Most conventional turbomachinery using angular contact ball bearings has outer race clearance or deadband to accommodate radial growth and axial movement of the shaft assembly in response to thermal or thrust balance forces. The presence of deadband violates the classical assumption of race rigidity because the outer race is allowed to deform within the clearance annulus when the bearing is loaded. The result is a reduction of bearing stiffness as seen by the rotor, and nonlinearity introduced by the clearance gap.

Despite the possible importance of the aforementioned effects on rotordynamic behavior, they have not received significant attention in the literature. Kleckner, Pirvics, and Castelli [3] have included radial housing and simplified race compliance as influence coefficients in their high capability software CYBEAN and SPHERBEAN, but discussion centered on thermal and other effects pertinent to bearing internal motions only. Childs and Moyer [4], among others, have simulated the bearing deadband effect on rotordynamics and have shown that it can cause resonance frequency shifts and subsynchronous response. However, no one known to the authors has documented in detail the effect of race flexibility. In fact, it is largely ignored even today in very comprehensive turbomachinery bearing investigations such as described in reference [5]. Bearing stiffness testing is often done by back-calculation from shaft critical speeds for lack of confidence in predicted values. For example, see the work of Beatty [6]. These tests may be subject to significant error, as critical speeds depend on other factors that may be difficult to accurately control or model. Furthermore, deadband and bearing stiffness effects are not separable in these tests, leading to questionable results.

This work will expand on the analysis of [3] to describe in detail new methods to incorporate general housing and race flexibility models, including deadband, in the mechanics of rolling element bearing loading. The techniques will be developed in the context of angular contact bearings only in the interest of brevity.

*This work was supported by company IR&D funding at Aerojet TechSystems Company, Sacramento, California, project number NLRDA6, and is approved for public release.

extension to other bearing types is analogous. The objective is to provide straightforward tools to better address the stiffness characteristics of rolling element bearings in rotordynamic analysis. The results are applicable to bearing life evaluation and dynamics as well. Discussion will begin with qualitative description of flexibility and deadband effects. The methods will be developed mathematically, and then demonstrated for bearing preload analysis. General bearing loading examples are extensive and will appear in a separate paper.

NOMENCLATURE

BD	: Unloaded distance between curvature centers, (m)
c	: Radial deadband, (m)
C_{ij}, C_{irj}, C_{izj}	: Inner race component Hertzian contact compliance, (m/N)
C_{oj}, C_{orj}, C_{ozj}	: Outer race component Hertzian contact compliance, (m/N)
C	: Total bearing tangent compliance matrix, (m/N)
C_i, C_o	: Race ball contact tangent compliance matrices, (m/N)
C_{rr} , etc.	: Partitions of race compliance matrix, (m/N)
d_m	: Bearing pitch diameter, (m)
D	: Ball diameter, (m)
f_i, f_o	: Raceway osculations
F_r, F_θ	: External loads on bearing along r, θ , (N)
F_{rk}, F_{zk}	: Radial and axial loads at deadband gap k , (N)
k_r, k_z	: Gap closure stiffnesses, (N/m)
K	: Contact stiffness parameters, (N/m ^{1.5})
K_i, K_o	: Bearing race stiffness matrix, (N/m)
K_{ij}, K_{oj}	: Contact stiffness parameters at ball j , (N/m ^{1.5})
K_{oo} , etc.	: Partitions of race stiffness matrix, (N/m)
KL0, KL1, KL2, KL3	: Configuration labels
l_{1j}, l_{2j}	: Ball load lever arms for inner race, ball j , (m)
Q	: Ball load, (N)
Q_{ij}, Q_{oj}	: Ball loads at ball j , (N)
Q_{irj}, Q_{izj}	: Inner race component ball loads at ball j , (N)
Q_{orj}, Q_{ozj}	: Outer race component ball loads at ball j , (N)
r, θ	: Radial and lateral coordinate directions
r_{hk}, z_{hk}	: Housing deflections at gap k , (m)
r_{ij}, z_{ij}	: Radial and axial inner race deflection at ball j contact, (m)
r_{oj}, z_{oj}	: Radial and axial outer race deflection at ball j contact, (m)
r_{rk}, z_{rk}	: Outer race outer surface deflection at gap k , (m)
R_i, R_o	: Radii to raceway curvature centers, (m)
u_r, u_θ	: Inner race deflections along r, θ , (m)
x, y, z	: Cartesian axes, z axial
\tilde{F}_i	: Inner race axial offset from load application point to curvature center locus, (m)
α°	: Unloaded contact angle, (rad)
α_{ij}, α_{oj}	: Contact angles, (rad)
ΔF_x	: Vector of $\Delta Q_{irj}, \Delta Q_{izj}$
ΔF_δ	: Resultant load error vector
$\Delta Q_{ij}, \Delta Q_{oj}$: Incremental ball loads at ball j , (N)
$\Delta r_{bj}, \Delta z_{bj}$: $\Delta r_j, \Delta z_j$ augmented by race deflection contributions, (m)

$\Delta r_j, \Delta z_j$: Radial and axial ball contact deflections due to inner race rigid body displacements, (m)
$\Delta r_{oj}, \Delta z_{oj}$: Incremental versions of r_{oj}, z_{oj} , (m)
$\Delta \mathbf{x}$: Vector of $\Delta r_j, \Delta z_j$
$\Delta \mathbf{x}_h$: Incremental housing deflection, (m)
$\Delta \mathbf{x}_r$: Incremental outer race outer surface deflection, (m)
ϵ_{oh} , etc.	: Partitions of race stiffness matrix due to gap stiffness, (N/m)
θ_x, θ_y	: Total or incremental rigid body rotations of inner race, (m)
Λ_F	: Resultant load summation matrix
Λ_δ	: Inner race kinematic transformation matrix
δ	: Contact deflection, (m)
δ	: Vector of $\delta_x, \delta_y, \delta_a, \theta_x, \theta_y$
δ_{ij}, δ_{oj}	: Hertzian contact deflections at ball j, (m)
$\delta_{irj}, \delta_{izj}$: Inner race component Hertzian contact deflections at ball j, (m)
$\delta_{orj}, \delta_{ozj}$: Outer race component Hertzian contact deflections at ball j, (m)
$\delta_x, \delta_y, \delta_a$: Total or incremental rigid body translations of inner race, (m)
ψ_j	: Ball azimuth angle from Cartesian x, (rad)
$()^T$: Transpose
$()^{-1}$: Inverse
$()_o$: Outer race
$()_i$: Inner race
$()_j$: Ball index
$()_k$: Gap index
$()_{rk}$: Pertaining to outer race outer surface at gap k
$()_{hk}$: Pertaining to housing at gap k

EFFECTS OF RACE/HOUSING FLEXIBILITY AND DEADBAND

The reduction of bearing stiffness due to outer race freedom has already been mentioned in general terms, and some discussion in the context of roller bearings and simple thin ring assumptions can be found in [2], Chapter 6.11. Outer race bulk deformation can cause redistribution of ball loads within the bearing and change in stiffness characteristics. Besides reduction of bearing axial and radial stiffness, asymmetry of stiffness also results as a by-product of the deadband. Referring to Figure 1, deadband allows the outer race to roll along the housing bore surface in response to load. As a result, the stiffness of the bearing in the direction lateral to contact, θ in Figure 1, may be much smaller than in the contact direction r . In the case of zero contact load, the θ stiffness is in fact zero, while the r stiffness is some finite value in compression. For non-zero load along r , the θ stiffness is greater than zero due to development of a contact area by race bulk deformation that can resist moments. Figure 2 shows the general load-deflection relationships for a given preload system. In rotordynamic analysis, this data would be used in two different ways:

1. **Large Steady Radial Load** - If steady radial loads exist to hold the rotor and bearing against the bore, the slope of the curves for F_r given and $F_\theta = 0$ could be used as linear stiffness for small perturbation modal, imbalance harmonic, or transient analysis. In this case, bearing stiffness is very asymmetric, in fixed directions.
2. **Small Steady Radial Load** - In this case, deadband nonlinearity must be included in transient analysis. Bearing stiffness in conjunction with deadband can be modeled using the radial load-deflection curve only and instantaneous shaft/housing position which can be expressed in r only. The rolling effect is then implicit and bearing stiffness changes in magnitude and direction in proper response to shaft motion.

It is important to note that deadband itself has its own effects on rotordynamics separate from the induced bearing stiffness reduction. Clearance can lead to impact phenomena and complicated response, which will not be discussed in detail here. Clearance has been shown [4] to reduce critical speeds just as a softer bearing would, so the effects are not readily separable unless one carefully quantifies the true stiffness reduction first. The objective is thus to accurately determine the curves of Figure 2 to be used in rotordynamic analysis. Housing/race flexibility and gap closure will determine the shape of the curves, along with the nonlinear Hertzian contact between the rolling elements and the races, described by

$$Q = K\delta^{3/2} \quad (1)$$

NEW FINITE ELEMENT/CONTACT MECHANICS METHOD

Approach

Finite element modeling is readily available and allows general modeling capability, including arbitrary geometry, thermoelastic interaction, and gaps. It is possible to model any inner race, outer race, and housing desired, but accurate calculation of rolling element kinematics is difficult. On the other hand, bearing mechanics software has been well developed for many years, but does not include general race compliance and deadband effects. The logical new approach outlined below augments the bearing mechanics software with a full stiffness representation of the hardware derived from finite element analysis. The existing capability to analyze detailed kinematics, Hertzian contact, and centrifugal loading is used with minor modification.

Modification of Contact Algorithms

The nonlinear equations governing bearing mechanics are commonly solved by Newton-Raphson methods as follows:

1. Guess bearing race rigid body relative deflections.
2. Compute resultant ball deflections and loads by kinematic and Hertzian contact equations.
3. Compare the vector sum of ball loads to given external loads. The difference is error loads.
4. Convert load errors to incremental displacements using an updated linear compliance based on current ball loading (tangent compliance).
5. Return to 2. with new displacements until convergence.

Inclusion of flexibility/deadband effects can be achieved by appropriate modification of step 2, ball load calculation, and step 4, linear compliance calculation. In the new method, the ball loads from step 2, which act equal and opposite on the races, are used to compute race deflections r_{oj} , z_{oj} , r_{ij} , z_{ij} , at the contact points of each ball j (subscripts o , i indicate outer and inner race). These deflections are returned to step 2, along with the updated total relative rigid body deflections δ_x , δ_y (along external radial loads), δ_a (axial), and θ_x , θ_y (angular about external moment axes). The rigid body motions require conversion to individual relative race motions Δr_j , Δz_j , at each ball. Given rigid body radii to raceway curvature centers \mathcal{R}_o and \mathcal{R}_i , and ball j azimuth angle from the x direction ψ_j , the individual ball rigid body motions are, [2],

$$\Delta r_j = \delta_x \cos \psi_j + \delta_y \sin \psi_j \quad (2a)$$

$$\Delta z_j = \delta_a + \mathcal{R}_i \theta_x \sin \psi_j - \mathcal{R}_i \theta_y \cos \psi_j \quad (2b)$$

The actual deflections seen by the ball are less than these values due to race compliance motions,

$$\Delta r_{bj} = \Delta r_j - r_{oj} + r_{ij} \quad (3a)$$

$$\Delta z_{bj} = \Delta z_j - z_{oj} + z_{ij} \quad (3b)$$

Note that cylindrical coordinates are assumed for all race deflections, with positive sense outward for r and in the direction of positive axial loading for z .

As Figure 3 shows for the race flexure case, the variables A_{1j} and A_{2j} used in solving the nonlinear equations, [2], can now be redefined as

$$A_{1j} = BD\sin\alpha^\circ + \Delta z_j - z_{0j} + z_{ij} \quad (4a)$$

$$A_{2j} = BD\cos\alpha^\circ + \Delta r_j - r_{0j} + r_{ij} \quad (4b)$$

while the definitions of X_{1j} , X_{2j} are unchanged by the flexure, [2],

$$X_{1j} = [(f_0 - 0.5)D + \delta_{0j}] \sin\alpha_{0j} \quad (5a)$$

$$X_{2j} = [(f_0 - 0.5)D + \delta_{0j}] \cos\alpha_{0j} \quad (5b)$$

See Harris [2] Chapter 8.3 and 8.6 for details of the subsequent ball load solution using A_{1j} , A_{2j} , X_{1j} , X_{2j} .

Actual computation of the current race flexure r_{0j} , z_{0j} , r_{ij} , z_{ij} is straightforward if bearing race compliance matrices are available for the current ball load levels. Incremental deflections are computed using incremental ball load by

$$\begin{bmatrix} \vdots \\ \Delta r_{0j} \\ \Delta z_{0j} \\ \vdots \end{bmatrix} = \mathbf{C}_0(Q_{0j}) \begin{bmatrix} \vdots \\ \Delta Q_{0j} \cos\alpha_{0j} \\ \Delta Q_{0j} \sin\alpha_{0j} \\ \vdots \end{bmatrix} = \mathbf{C}_0 \Delta \mathbf{F} \quad (6)$$

and added to the deflections from the previous iteration (similarly for the inner race). Generation of the race compliance matrix \mathbf{C}_0 will be discussed later. First, consider step 4 of the solution augmented by this new compliance. The race compliances are in series with the ball compliances, and both vary with ball load. Consider the outer race contact relation, [2],

$$Q_{0j} = K_{0j} \delta_{0j}^{3/2} \quad (7)$$

which can be broken into r and z components by noting

$$Q_{0rj} = Q_{0j} \cos\alpha_{0j} \quad \text{and} \quad \delta_{0rj} = \delta_{0j} \cos\alpha_{0j} \quad (8a)$$

$$Q_{0zj} = Q_{0j} \sin\alpha_{0j} \quad \text{and} \quad \delta_{0zj} = \delta_{0j} \sin\alpha_{0j} \quad (8b)$$

The result in r and z compliance form is

$$\delta_{0rj} = \frac{\cos^{1/3}\alpha_{0j}}{K_{0j}^{2/3}} Q_{0rj}^{2/3} \quad (9a)$$

$$\delta_{0zj} = \frac{\sin^{1/3}\alpha_{0j}}{K_{0j}^{2/3}} Q_{0zj}^{2/3} \quad (9b)$$

Linearized tangent compliance at the current Q_{oj} can be obtained by taking the partials of (9) with respect to Q_{orj} , Q_{ozj} . This is greatly simplified by assuming α_{oj} constant, which is reasonable for small load increments. The compliance is then

$$c_{orj} = \frac{\partial \delta_{orj}}{\partial Q_{orj}} = \frac{2}{3K_{oj}^{2/3} Q_{oj}^{1/3}} = c_{oj} \quad (10a)$$

$$c_{ozj} = \frac{\partial \delta_{ozj}}{\partial Q_{ozj}} = \frac{2}{3K_{oj}^{2/3} Q_{oj}^{1/3}} = c_{oj} \quad (10b)$$

These ball compliances, with similar results for the inner race contact, can be summed with the race compliances to give approximate total bearing tangent compliance in individual ball terms of

$$\mathbf{C} = \mathbf{C}_o(Q_{oj}) + \mathbf{C}_i(Q_{ij}) + \begin{bmatrix} \diagdown c_{oj} \\ c_{oj} \diagup \end{bmatrix} + \begin{bmatrix} \diagdown c_{ij} \\ c_{ij} \diagup \end{bmatrix} \quad (11)$$

\mathbf{C} can then be used to determine the incremental rigid body displacements $\delta_x, \delta_y, \delta_a, \theta_x, \theta_y$, due to load error by using constraint matrices constructed as follows. With multiple applications of equations (2), the conventional (Reference [2]) kinematic relationship can be written in matrix form,

$$\Delta \mathbf{x} = \mathbf{\Lambda}_\delta \delta \quad (12)$$

where

$$\Delta \mathbf{x}^T = [\dots \Delta r_j \Delta z_j \dots] \quad (13a)$$

$$\delta^T = [\delta_x \delta_y \delta_a \theta_x \theta_y] \quad (13b)$$

and $\Delta \mathbf{x}$ and δ are now defined to be incremental quantities for the current external load error, and

$$\mathbf{\Lambda}_\delta = \begin{bmatrix} \vdots & & & & \\ \cos \psi_j & \sin \psi_j & 0 & 0 & 0 \\ 0 & 0 & 1 & R_i \sin \psi_j & -R_i \cos \psi_j \\ \vdots & & & & \\ \vdots & & & & \end{bmatrix} \quad (14)$$

By definition of the compliance matrix \mathbf{C} ,

$$\Delta \mathbf{x} = \mathbf{C} \Delta \mathbf{F}_x \quad (15)$$

where

$$\Delta \mathbf{F}_x^T = [\dots \Delta Q_{irj} \Delta Q_{izj} \dots] \quad (16)$$

are individual ball load errors. The summation of ball load errors gives the external load error, and can be written in matrix form as

$$\Delta \mathbf{F}_\delta = \mathbf{\Lambda}_F^T \Delta \mathbf{F}_x \quad (17)$$

where

$$\Lambda_F = \begin{bmatrix} \cos\psi_j & \sin\psi_j & 0 & -l_{2j}\sin\psi_j & l_{2j}\cos\psi_j \\ 0 & 0 & 1 & l_{1j}\sin\psi_j & -l_{1j}\cos\psi_j \\ \vdots & \vdots & \vdots & \vdots & \vdots \end{bmatrix} \quad (18)$$

l_{1j} and l_{2j} are ball load lever arms about the load application point on the inner race,

$$l_{1j} = R_i - f_i D \cos\alpha_{ij} \quad (19a)$$

$$l_{2j} = \tilde{S}_i - f_i D \sin\alpha_{ij} \quad (19b)$$

where \tilde{S}_i is the constant axial distance from the load point to the plane containing the inner raceway curvature center locus. The effect of inner race deflection on l_{1j} and l_{2j} is negligible.

Inverting (15), and using (12) and (17) yields the compliance relationship in terms of rigid body incremental deflections,

$$\delta = [\Lambda_F^T C^{-1} \Lambda_\delta]^{-1} \Delta F_\delta \quad (20)$$

Note that the matrix computation of Λ_F must be performed in each iteration unless one is willing to neglect the varying terms.

Although some approximations are made in the foregoing (θ_x, θ_y small, for example), the result (20) is of sufficient accuracy to ensure good Newton-Raphson incrementation and convergence. Absolute accuracy is not critical in the Newton-Raphson compliance update steps. The total ball load summation, however, must be accurate to obtain a correct solution, i.e., the load balance must be correct on the inner race. Equation (17) should be used for this purpose. Conventional bearing mechanics programs use $l_{1j} = d_m/2$ and $l_{2j} = 0$ which is convenient because Λ_F becomes constant, but is not strictly correct. Such an approximation neglects moment due to radial ball loads as well as lever arm changes with contact angle.

Bearing Race/Housing Models

The calculation of C_o and C_i required for equations (6) and (11) can be handled as a separate process within each Newton-Raphson iteration. The four types of bearing/housing configurations of interest are the following:

- KL0: flexible inner race.
- KL1: flexible outer race and housing with no deadband.
- KL2: flexible outer race with deadband, and housing assumed rigid.
- KL3: flexible outer race and housing with deadband.

All of these types are amenable to general finite element modeling such as that shown in Figures 4 and 5 with balls omitted. The models need not be symmetric, and can be subjected to thermal loads, interference fits, and so on within the finite element program. The finite element models can be substructured (static condensation) in cylindrical coordinates to only degrees of freedom (DOFs) at nominal ball contact points and gap interfaces. Figure 6 shows the DOFs of interest for each configuration type, and the unloaded reduced stiffness matrix form. The choice of gap interface location and number is left to the analyst.

To ensure invertibility of K_o , it is necessary to add soft springs across enough gaps within the finite element model to restrain rigid body motion (indicated by $\epsilon_{oh}, \epsilon_{rh}$). The springs should be just soft enough to produce negligible load at gap closure. Similarly, invertibility of K_i requires soft springs from several ball

contact points to ground. These springs should be several orders of magnitude softer than the expected bearing stiffness, so that they generate negligible loads. With invertibility assured, the total compliance matrices are

$$KL0: \mathbf{K}_i^{-1} = [\mathbf{C}_i] \quad (21a)$$

$$KL1: \mathbf{K}_0^{-1} = [\mathbf{C}_0] \quad (21b)$$

$$KL2: \mathbf{K}_0^{-1} = \begin{bmatrix} \mathbf{C}_0 & \mathbf{C}_{or} \\ \mathbf{C}_{or} & \mathbf{C}_{rr} \end{bmatrix} \quad (21c)$$

$$KL3: \mathbf{K}_0^{-1} = \begin{bmatrix} \mathbf{C}_0 & \mathbf{C}_{or} & \mathbf{C}_{oh} \\ \mathbf{C}_{or} & \mathbf{C}_{rr} & \mathbf{C}_{rh} \\ \mathbf{C}_{oh} & \mathbf{C}_{rh} & \mathbf{C}_{hh} \end{bmatrix} \quad (21d)$$

where the partitions \mathbf{C}_i and \mathbf{C}_0 are the matrices needed for equations (6) and (11).

During solution iterations, the incremental race deflections are computed using equation (6) with \mathbf{C}_i or \mathbf{C}_0 from above and the current ball incremental loading. First, \mathbf{K}_0^{-1} must be iteratively modified to account for gap closure or opening. The gap interface deflections must be checked by evaluating the increments, which are computed using current ball incremental loading $\Delta \mathbf{F}$

$$\Delta \mathbf{x}_r - \Delta \mathbf{x}_h = (\mathbf{C}_{or} - \mathbf{C}_{oh}) \Delta \mathbf{F} \quad (22)$$

since the ball loads are the only external loads on the race. The increments are then added to the previous gap deflections, and the totals are compared to the specified gap sizes. If a gap has closed, then \mathbf{K}_0 must be augmented by a high stiffness across the gap which can be represented in the matrix form as

$$\begin{bmatrix} F_{rk} \\ F_{zk} \\ -F_{rk} \\ -F_{zk} \end{bmatrix} = \begin{bmatrix} k_r & 0 & -k_r & 0 \\ 0 & k_z & 0 & -k_z \\ -k_r & 0 & k_r & 0 \\ 0 & -k_z & 0 & k_z \end{bmatrix} \begin{bmatrix} r_{rk} \\ z_{rk} \\ r_{hk} \\ z_{hk} \end{bmatrix} \quad (23)$$

Similarly, an opened gap requires augmentation with the negative of above. A new \mathbf{K}_0^{-1} is computed and the gap checking process is repeated until no gaps change. Then the resulting \mathbf{C}_0 can be used in equations (6) and (11). Excessively large values of k_r and k_z can cause solution instability, and should be avoided. A good scheme to determine these values is to find the largest term in the unloaded \mathbf{K}_0 and multiply that by 100 to 1000. It is prudent to check the conditioning of \mathbf{K}_0^{-1} during the analysis and adjust k_r , k_z as required.

Combined Analysis

The overall analysis can now be summarized by the following steps. Steps that are new are highlighted in bold.

1. Supply "rigid" bearing dimensions, parameters and loads, to bearing mechanics program.
2. Read race matrices \mathbf{K}_i and \mathbf{K}_0 into program, along with gap size list.
3. Perform first iteration using race rigidity assumption to obtain ball loads.
4. Compute race deflections by equation (6).

5. Recalculate ball loads using existing code modified by equations (4).
6. Check resultant load errors using the more exact equation (17). If negligible, stop.
7. Update tangent compliance of outer race using K_O and equations (22), (23) in an iterative loop, given incremental ball loads for this iteration.
8. Compute incremental race deflections by equation (6), given incremental ball loads and updated race compliance.
9. Update total tangent compliance C and incremental rigid body motion δ using equations (10), (11), (19), and (20).
10. Return to 5, with all updated displacements (previous + increments), both rigid body and flexural. This allows determination of A_{1j} , A_{2j} .

Note that since steps 7 and 8 use incremental ball loads for the current iteration and not for the total load error in step 6, the compliance corrections and race deflections lag the Newton-Raphson update. Unfortunately, it is not possible to uniquely determine the individual ball load errors due to total load error in step 6. An approximate determination of ΔF_x could be made by using a least squares estimate of equation (17) given ΔF_δ load errors. However, the improvement in Newton-Raphson convergence would be offset by the least squares computations required. For now, the least squares estimation is omitted.

BEARING PRELOADING ANALYSIS

The case of axial loading only at zero speed (preloading) greatly simplifies the computations discussed. All contact angles become equal for a symmetric bearing, radial and moment load resultant are zero, and all balls behave the same given a symmetric race model. The simplified versions of the general equations presented are easily incorporated into existing bearing mechanics software. The sample analysis shown below was performed using an augmented version of the readily available bearing mechanics program developed by A.B. Jones. The new program has been named ROBEAN (Rolling BEaring ANalysis).

The Bearing Model

The bearing described in Table 1 was used for the sample preloading analysis. Figure 4 shows the outer race model. The inner race was assumed rigid. Figure 5 shows a schematic of the gaps at each ball and race restraint used. In addition, very soft springs of 17,520 N/m (100 lb/in) span the gaps in r and z cylindrical directions, and for the KL3 flexible housing case, the housing is represented by 1.75×10^8 N/m (1.0×10^6 lb/in) springs in r and z at each gap. The reduced stiffness matrices for cases KL1, KL2, and KL3 were prepared with ANSYS and read into ROBEAN automatically. Uniform gap values of 0.0050 mm (0.0002 in) were also supplied for KL2 and KL3. Additionally, the usual "rigid" bearing inputs were entered as always.

Results

Preloads of up to 8900 N (2000 lb) were applied to the bearing in ROBEAN, for the three cases KL1, KL2, and KL3. A fourth case where gaps never close was also included for comparison after gap closure of KL2 and KL3. Results from Harris [2], Chapter 6.5, assuming rigid races are presented with the new results in Figures 7 and 8.

The results show the differences in axial deflection and contact angle for the different bearing types studied. In both figures, the nonlinear variations with preload can be seen. Only Hertzian contact at the ball/race interfaces is accounted for in the Harris calculations. Therefore, this bearing model shows the greatest stiffness in Figure 7. The KL1 bearing model adds outer race bulk flexibility, and its effective

stiffness is slightly less. Note that the Hertzian deformations already included in the ball load calculations do not occur in the finite element model because of its mesh coarseness. If they had, KL1 stiffness would be much less.

The KL2 bearing accounts for a radial gap clearance of 0.0050 mm (0.0002 in). A significant decrease in axial stiffness is seen for this bearing before gap closure in comparison to the rigid model. This is due to the unrestrained growth of the outer race. Approximately 5120N (1150 lb) of preload is needed to close the gap. At gap closure, KL2 bearing stiffness is increased, and now essentially matches that of the KL1 case. However, total axial deflection is greater.

The KL3 bearing stiffness is essentially equivalent to KL2 up to the point of gap closure. The extra housing compliance results in a smaller stiffness increase upon gap closure than the KL2 case.

CONCLUSIONS

1. New accurate methods have been developed to include arbitrary race/housing/deadband structures in bearing loading analysis. The flexible structures except balls and Hertzian contact are modeled and substructured using available finite element programs. The effects can be included within existing Newton-Raphson bearing mechanics program iterations with minimal impact.
2. The new methods are shown to be viable for a preloading example. Axial stiffness is significantly affected by outer race clearance.
3. The preloading example results indicate a need to investigate more complex loading cases. The authors will do so and present results in another paper.
4. Although not specifically discussed, the analyst's freedom of gap modeling implicitly allows the new methods to account for general outer race misalignment or "cocking" within the housing bore, including full flexibility and nonuniform geometry effects. This only requires more gaps to be defined, and the formulation is unchanged.
5. The following effects have been neglected in the development presented, and are still under investigation by the authors:
 - contact angle change due to flexure and "cocking" induced local rotation only - likely negligible, because such rotations are much smaller than the contact angle changes.
 - change in R_i , R_o , raceway curvature, and other size parameters due to flexure - likely negligible, because flexural changes are small percentage of nominal.
 - change in race stiffness due to movement of contact point on the race - possibly non-negligible, because movement is significant, proportional to contact angle change.

REFERENCES

1. Jones, A.B., A General Theory of Elastically Constrained Ball and Radial Roller Bearings Under Arbitrary Load and Speed Conditions, *ASME J. of Basic Engineering*, vol. 82, Series D, pp. 309-320, June 1960.
2. Harris, T.A., *Rolling Bearing Analysis*, 2nd Edition, John Wiley & Sons, New York, 1984.
3. Kleckner, R.J., Pirvics, J., and Castelli, V., High Speed Cylindrical Rolling Element Bearing Analysis "CYBEAN" - Analytic Formulation, *ASME J. of Lubrication Technology*, vol. 102, pp. 380-390, July 1980.
4. Childs, D.W. and Moyer, D.S., Vibration Characteristics of the HPOTP (High Pressure Oxygen Turbopump) of the SSME (Space Shuttle Main Engine), ASME paper #84-GT-31, presented at the 29th International Gas Turbine Conference and Exhibit, Amsterdam, 8 pg, June 1984.
5. Cody, J.C. et. al., Bearing Tester Data Compilation, Analysis, and Reporting and Bearing Math Modeling, Final Report, Volume 1, by Spectra Research Systems for NASA/MSFC, contract no. NAS8-34686, NASA CR-171039, 137 pg, May 1984.
6. Beatty, R.F. and Rowan, B.F., Determination of Ball Bearing Dynamic Stiffness, in *Rotordynamic Instability Problems in High-Performance Turbomachinery - 1982*, Proceedings of a Workshop held at College Station, Texas, pp. 98-104, May 10-12, 1982, NASA CR- 2250 .

TABLE 1. Subject bearing specification

Bore	:	45 mm (1.771 in)
Number of Balls	:	14
Ball Diameter	:	8.74 mm (.344 in)
Pitch Diameter	:	59.44 mm (2.34 in)
Unmounted Contact Angle	:	18.24°
Outer Raceway Osculation	:	.523
Inner Raceway Osculation	:	.532

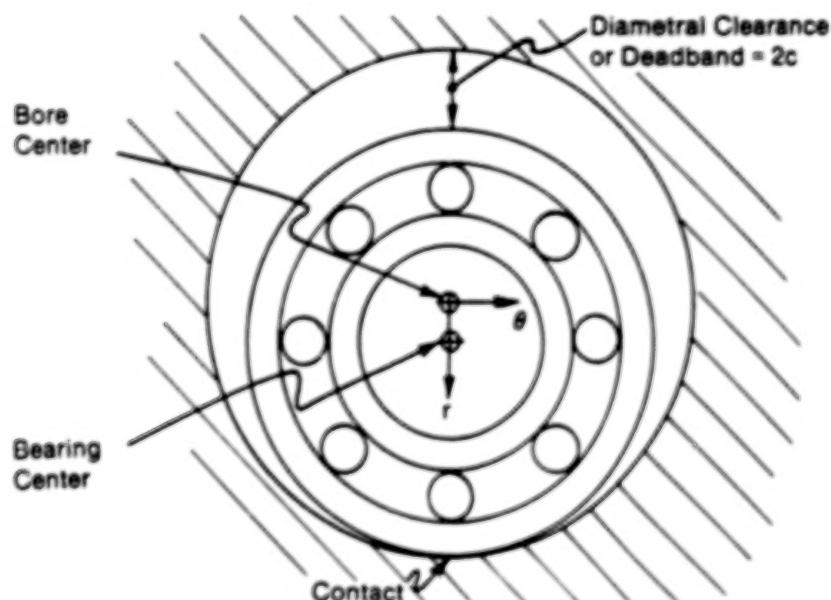


FIGURE 1. A bearing with deadband, unloaded

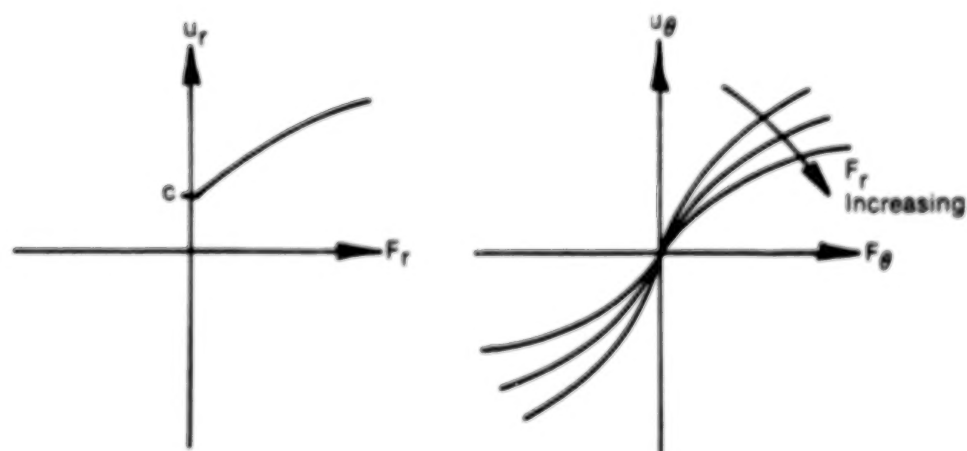


FIGURE 2. General load-deflection relationships for a flexible bearing with deadband

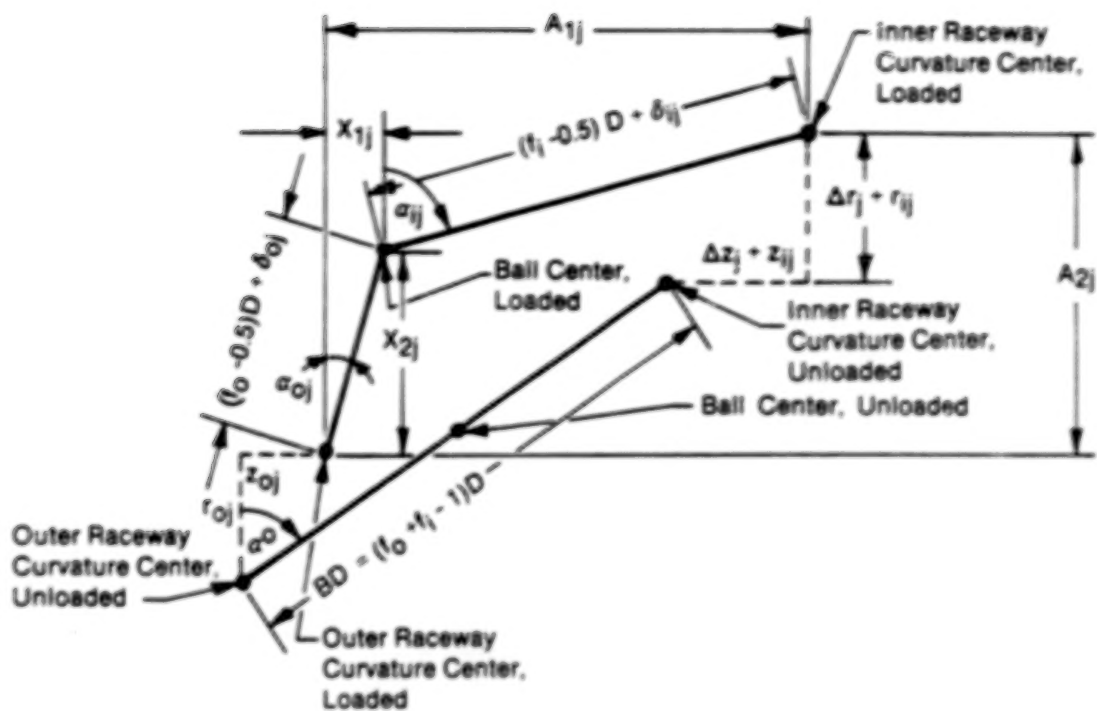


FIGURE 3. Ball bearing kinematics including race flexure

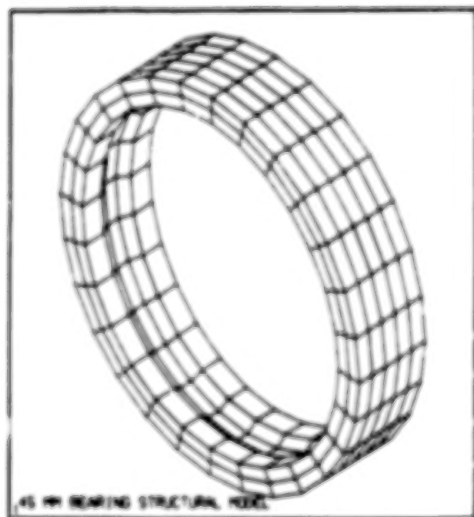


FIGURE 4. Outer race finite element model

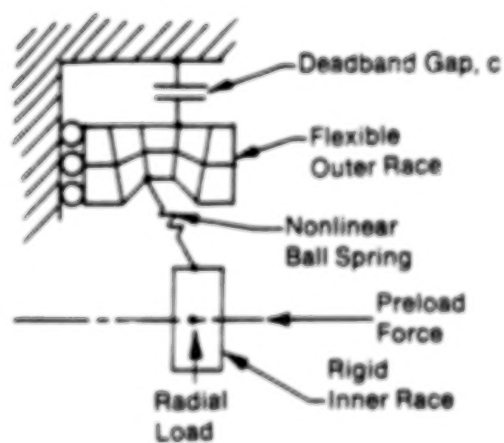


FIGURE 5. Bearing model schematic

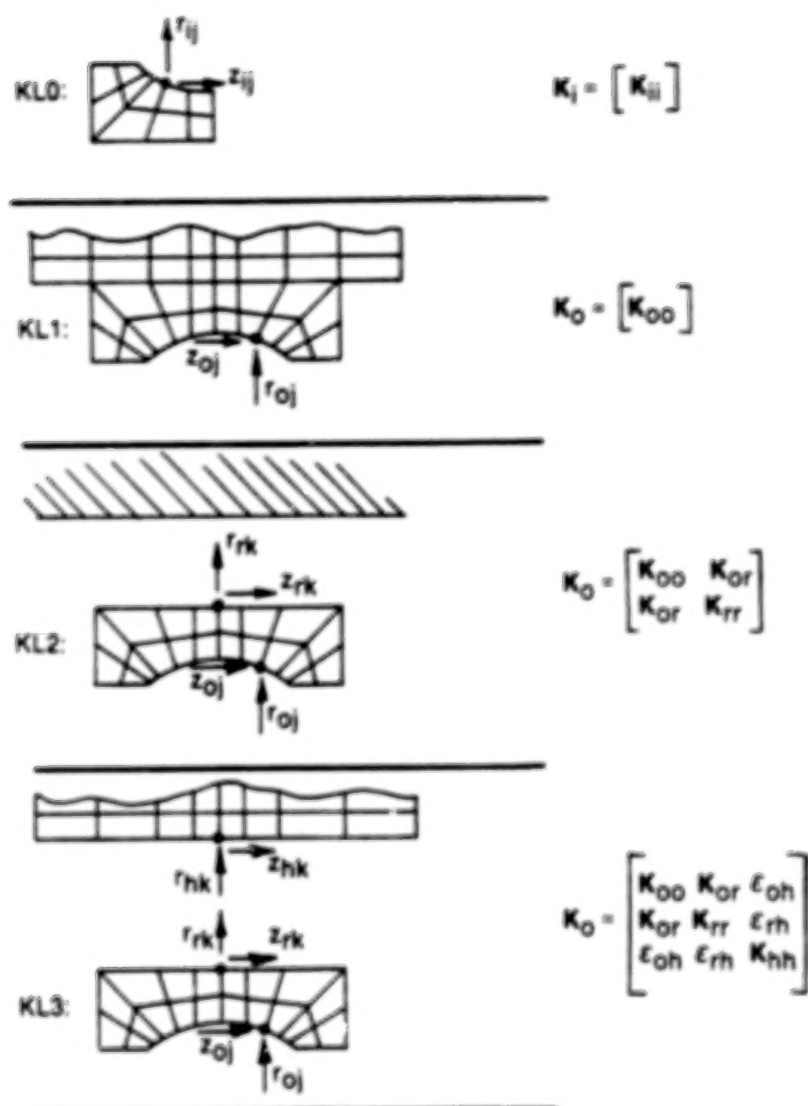


FIGURE 6. DOFs of interest in race/housing models

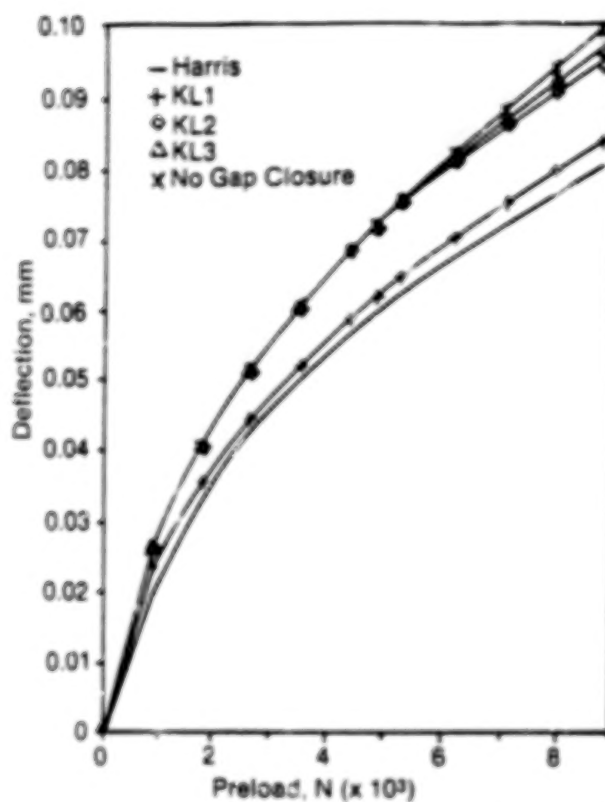


FIGURE 7. Axial deflection vs. preload for the various bearing types

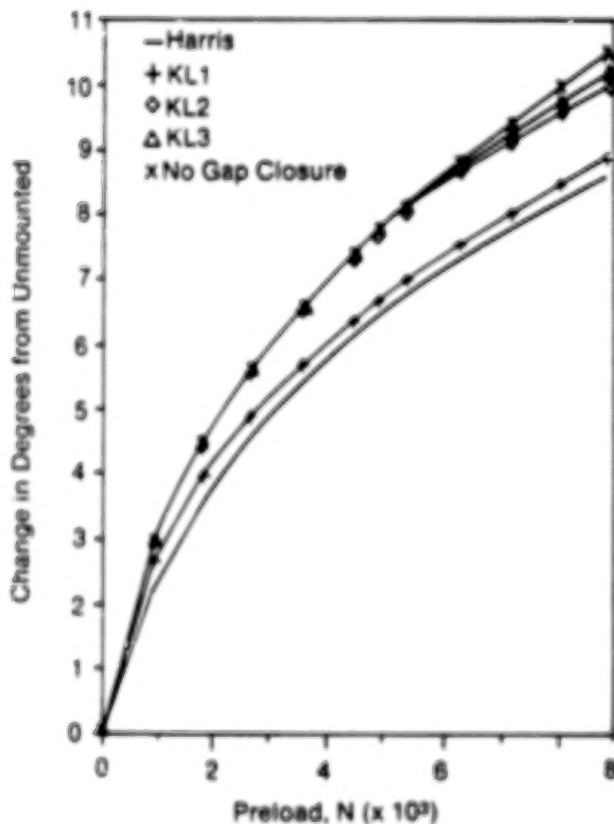


FIGURE 8. Change in contact angle vs. preload for the various bearing types

BLANK PAGE

EXPERIMENTAL VERIFICATION OF AN EDDY-CURRENT BEARING¹

Jorgen L. Nikolajsen
Department of Mechanical Engineering
Texas A&M University
College Station, Texas 77843, U.S.A.

A new type of electromagnetic bearing has been built and tested. It consists of fixed AC-electromagnets in a star formation surrounding a conducting rotor. The bearing works by repulsion due to eddy-currents induced in the rotor. A single bearing is able to fully support a short rotor. The rotor support is inherently stable in all five degrees of freedom. No feedback control is needed. The bearing is also able to accelerate the rotor up to speed and decelerate the rotor back to standstill. This paper describes the bearing design and the experimentation to verify its capabilities.

INTRODUCTION

The Eddy-Current Bearing described here is based on the so-called Electromagnetic River suspension for high speed vehicles which was proposed and demonstrated by Eastham & Laithwaite [1] in 1974. The Magnetic River was turned into a journal bearing by bending it into a circular shape (see Figure 1). The resulting Eddy-Current Bearing was designed and built on the basis of the Magnetic River behavior reported in the literature (see for example references quoted in [2] and [3]). No analytical work has yet been conducted. The objective was to determine whether the bearing would inherit the basic desirable characteristics of the Magnetic River such as inherent stability, support capability in five degrees of freedom, motoring capability, and emergency shutdown capability. This paper reports on the experimental findings to date. Preliminary results were reported in [4]. Additional background can be found in [5]. Work on other types of AC-electromagnetic bearings has been reported in [6] through [9].

THE EXPERIMENTAL APPARATUS

Four U-shaped electromagnets are spaced 90° apart in a star formation to form a 10.16 cm diameter bearing as shown in Figures 1 and 2. The magnets are mounted in a non-magnetic stainless steel housing. The magnet cores are made of grain-oriented 0.356 mm laminations with a saturation flux density of about 2 Tesla. The coils have 58 turns each. They are wound with two parallel flat copper wires with a total cross section of

1. This work was supported by the TAMU Turbomachinery Research Consortium. Rig hardware was donated by IMC Corporation and by Magnetic Bearings, Inc.

approximately 6.35 mm x 4.32 mm. The inductance of two coils mounted on one core was measured to be about 3.2 mH.

Each of the four magnets has an electric circuit as shown in Figure 3. Power is supplied from a 115V 60 Hz single phase outlet. The power is adjusted by means of the variable transformer. The variable capacitor is used to adjust the power factor (or tune the circuit) such that a large current will circulate between the capacitor and the coil while only enough current is drawn from the supply to cover the I²R loss in the coils and in the rotor. The variable capacitor consists of a bank of oil-filled capacitors in parallel which can be switched in and out of the circuit independently. Each capacitor bank consists of 13 100 μ F capacitors and 13 150 μ F capacitors which are connected such that the capacitance can be varied in steps of 100 μ F from zero to 3,250 μ F. Fine-tuning of the power factor is therefore not possible but the reactive power can be reduced sufficiently to permit the experimentation with the available equipment. It was generally found that 11 to 13 capacitors needed to be switched in to minimize the supply current.

Five rotors made of construction aluminum were available for levitation. Three of these were 15.2 cm long with an inner diameter of 7.62 cm and outer diameters of 9.50 cm, 9.73 cm, and 9.91 cm respectively. They were used to study the effect of bearing clearance. A 15.2 cm long solid iron cylinder with 7.62 cm diameter was made to fit snugly inside the aluminum sleeves to provide extra weight. Two additional aluminum sleeves with lengths 12.7 cm and 17.8 cm were used to study the effect of sleeve length. Also, a pure copper sleeve with length 15.2 cm and inner and outer diameters of 7.37 cm and 9.50 cm was made to study the effect of improved conductivity. The masses of the three 15.2 cm aluminum sleeves were 1.038 kg, 1.176 kg, and 1.288 kg. The iron core mass was 4.883 kg and the copper sleeve mass was 3.859 kg.

RESULTS

All three 15.2 cm aluminum sleeves were successfully levitated as shown in Fig. 2 confirming the inherent stability of the bearing and the five degree-of-freedom support capability. Contrary to expectations, slightly larger currents in all four magnets were required to levitate the large diameter sleeve than the medium and small diameter sleeves (75A [82V] versus 60A [65V] in the bottom magnet). The larger current was not required to lift the sleeve but to provide sufficient support stiffness to prevent excitation of radial vibrations of the sleeve by the 60 Hz magnetic flux pulsations. Such excitation otherwise led to rattling of the sleeve against the pole faces.

With the iron cylinder inserted in the aluminum sleeves, there was insufficient power available to energize all four magnets for full levitation. With the bottom magnet excited only, the 6kg sleeve/core combination could be lifted free of the bottom with 130A [128V] and 140A [133V] for the large and medium diameter sleeves respectively while the

small diameter sleeve was unable to fully lift off at 160A [142V] which was the maximum current available. For comparison, 40A [44V] to the bottom magnet was required to lift each of the three sleeves without the iron core.

Although the copper sleeve geometry is almost identical to the small diameter aluminum sleeve, it suffered axial instability and tried to exit the bearing when lifted. The long (17.8 cm) aluminum sleeve behaved similarly suggesting that the copper sleeve could possibly be stabilized by reducing its length. The short (12.7 cm) aluminum sleeve had the largest thrust capability of all the sleeves but inferior radial support capability. This suggests, as expected, that it probably will not be possible to optimize the bearing with respect to all its capabilities simultaneously.

The motoring capability was also confirmed. With single phase current supply, the three 15.2 cm levitated sleeves would rotate in the bearing when the magnet currents were adjusted to position the sleeve eccentrically within the bearing clearance. They would stop rotating when brought back to the concentric position and would rotate in the opposite direction when brought to a diametrically opposite eccentric position. The larger the eccentricity, the higher the speed. The maximum speed recorded with single phase current was about 50 rpm. With 3-phase current, the rotational speed could be increased to about 750 rpm with the sleeves supported mechanically. It was not possible to fully levitate the sleeves with 3-phase current, apparently because the strong torque at zero speed would rotate the sleeves before metal contact could be broken, thus initiating a backward whirl instability.

After a few minutes of operation, the aluminum sleeves got too hot to be hand held whereas the magnets remained cool with only a slight temperature increase to be felt. Also, the copper sleeve did not get as hot as the aluminum sleeves, attesting to its greater conductivity. An increase in supply current to one circuit would result in a similar current in the other circuits, indicating strong mutual inductance between the magnet coils.

The magnetic support stiffnesses, with the three 15.2 cm sleeves levitated, were estimated by impacting the sleeves and counting vibration periods with a stopwatch. The average radial, axial and angular stiffnesses were found to be in the neighborhood of 80 N/m, 60 N/m, and 0.3 Nm/rad. The damping was also very low, as evidenced by the long time taken for any vibrations to die out.

Finally, the effect of power supply frequency was studied using a 60 Hz magnet and a 400 Hz magnet. The 60 Hz magnet was identical to the bearing magnets except that the pole faces were flat. The 400 Hz magnet had identical geometry but was made of 0.1 mm laminations, and the number of turns was 15 per coil to achieve the same magnetic flux density as with the 60 Hz magnet but using a 150V, 400 Hz power supply. According to the analysis of [8], a frequency increase should result in a significant improvement of the lift capacity. This did not occur. The main effect was

that thinner aluminum plates could be lifted with 400 Hz power supply, presumably because the eddy-current penetration depth decreases with increasing frequency.

CONCLUSIONS

The experiments have confirmed that the Eddy-Current Bearing retains the basic advantages and disadvantages of the Magnetic River suspension:

1. A single eddy-current bearing is sufficient to fully support a short rotor in all five degrees of freedom simultaneously.
2. The bearing provides inherently stable rotor support. No feedback control is needed.
3. The bearing will act as a motor and as a support simultaneously.
4. The lift capacity and the stiffness and damping achieved so far are low. Additional damping can be supplied by a simple eddy-current damper and design optimizations may improve the stiffness and the lift capacity but it is unlikely that they will ever exceed those of DC-type magnetic bearings.
5. The efficiency of the bearing is low due to a high I^2R loss in the rotor. This is considered to be the most serious problem which must be overcome before the bearing finds practical application. The current thinking is to move the design closer to a conventional induction motor, thereby further reducing the load carrying capacity but gaining motoring efficiency. The bearing could then be used in space-based applications such as flywheel energy storage systems where it could support the flywheel and also act as the motor/generator.

REFERENCES

1. Eastham, J.F. and Laithwaite, E.R. "Linear Induction Motors as Electromagnetic Rivers", Proc. IEE, Vol. 121, No. 10, pp. 1099-1108, 1974.
2. Jayavant, B.V. "Electromagnetic Levitation and Suspension Techniques," Edward Arnold, London, 1981.
3. Jayavant, B.V. "Electromagnetic suspension and Levitation," IEE Proc., Vol. 129, Pt. A, No. 8, pp. 549-581, 1982.
4. Nikolajsen, J.L. "An AC-Electromagnetic Bearing for Flywheel Energy Storage in Space," To be published in NASA CP, Magnetic

Suspension Workshop, NASA Langley, Feb. 1988.

5. Nikolajsen, J.L. "A Magnetic Bearing Based on Eddy-Current Repulsion," NASA Conference Publication 2443, Rotordyn. Instab. Prob. in Hi-Perform. Turbomach. pp. 460-465, 1986.
6. Bolton, H. "An Electromagnetic Bearing," IEE CP 120, Linear Electr. Machines, London, pp. 45-50, 1974.
7. Iskierka, S. "Influence of Irregularities of Exciting Current Density Distribution on Induction Bearing Work," Acta Technica Csav, No. 5, pp. 572-582, 1984.
8. Iskierka, S. "Analysis of an Induction Bearing by the Finite Element Method," Archiv fur Electrotechnik, Vol. 67, pp. 375-380, 1984.
9. Connor, K.A. and Tichy, J.A. "Analysis of an Eddy-Current Journal Bearing," ASME Pap. 87-Trib-10, 7pp., 1987.

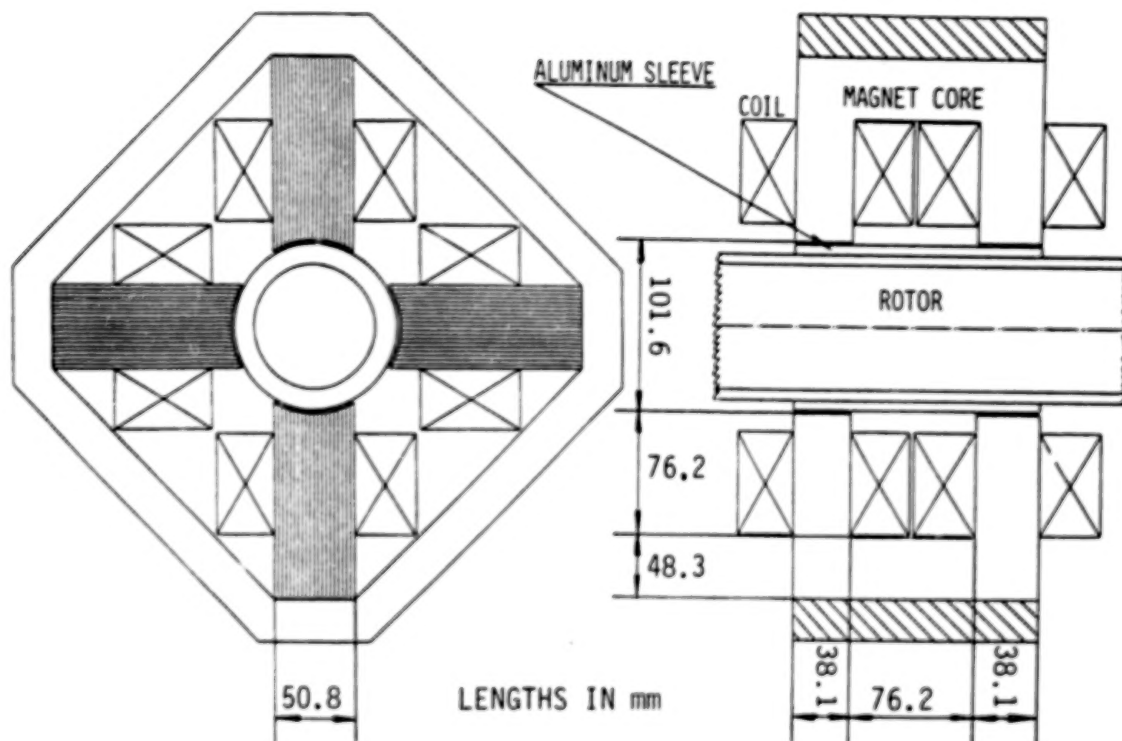


Figure 1 The Eddy-Current Bearing (Schematic)

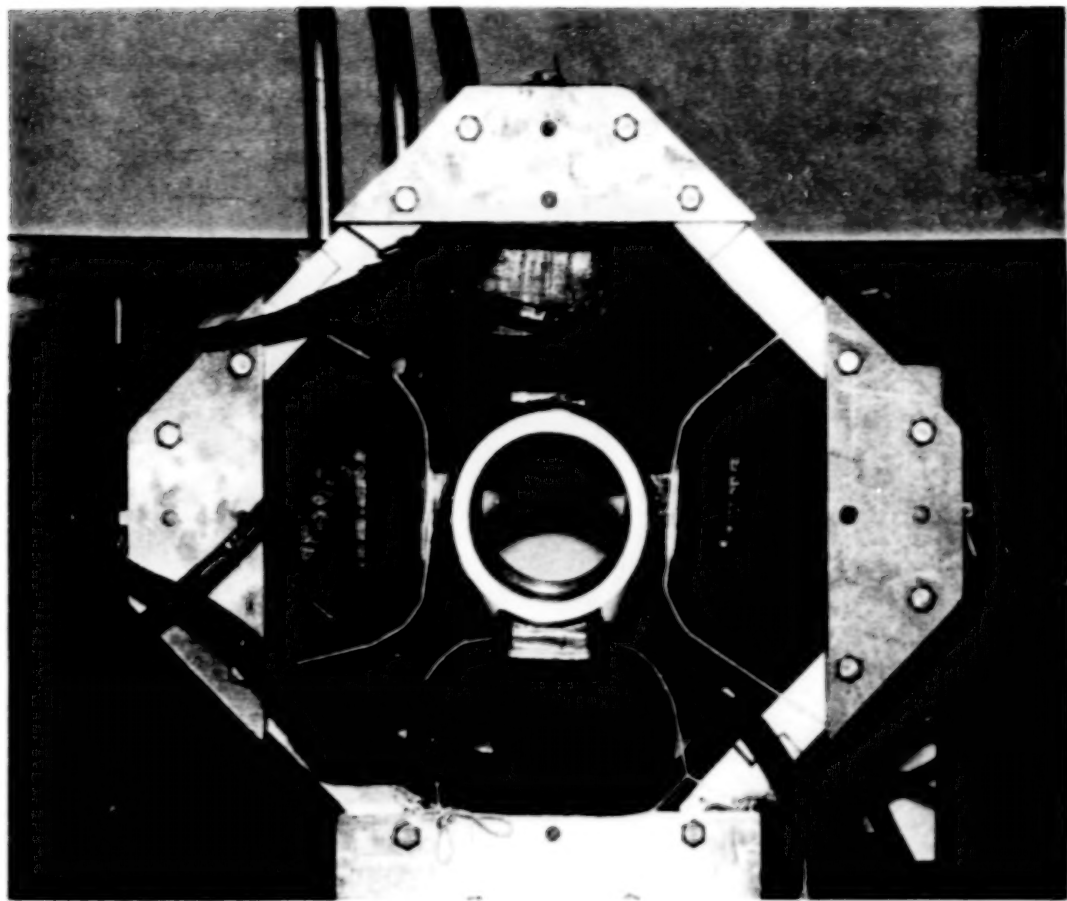


Figure 2 The Eddy-Current Bearing Prototype

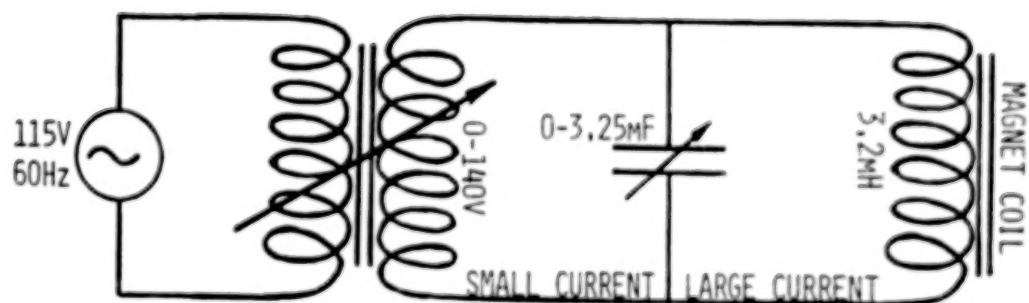


Figure 3 Electric Circuit for Each Magnet

ROTOR DYNAMIC STABILITY PROBLEMS AND SOLUTIONS IN HIGH

PRESSURE TURBOCOMPRESSORS

J. Schmied
Sulzer Escher Wyss, Ltd.
Zurich, Switzerland

The stability of a high pressure compressor is investigated with special regard to the self-exciting effects in oil seals and labyrinths. It is shown how to stabilize a rotor in spite of these effects and even increase its stability with increasing pressure.

Notation

B	width of oil seals
d	damping coefficients of oil seals or labyrinths
D	modal damping factor
	shaft diameter
f	frequency in cps
F_d	displacement dependent oil film force
F_f	friction force
F^*	reference force for oil film forces (see equation (4))
i	imaginary unit, $i = \sqrt{-1}$
k	stiffness coefficient of oil seals or labyrinths
m	mass of oil seal rings
n	rotational speed
p	pressure
r	coordinate in radial direction
R	shaft radius
R_p	radius of the curvature of a pad
So	Sommerfeld number, $So = F_d/F^*$
w_{in}	inlet swirl velocity
w_{rot}	circumferential velocity of the shaft surface
α	real part of an eigenvalue
β	ratio of width to diameter
	dimensionless damping coefficient
γ	angle between displacement and displacement dependent oil film forces
δ	bearing clearance
	seal ring clearance
ϵ	dimensionless radial displacement, $\epsilon = 2r/\delta$
ϕ	circumferential coordinate

λ	eigenvalue, $\lambda = \alpha + i\nu$
ν	imaginary part of eigenvalue
η	oil viscosity
Ψ	relative clearance of oil seal ring
Ψ_b	relative bearing clearance
Ψ_p	relative pad clearance, $\Psi_p = (R_p - R)/R$
Ω	angular velocity of the rotor

Frequently used subscripts

x	subscript for x-direction (vertical)
y	subscript for y-direction (horizontal)
r	subscript for radial direction
ϕ	subscript for circumferential direction
1	subscript for the direction of the displacement dependent oil film force
2	subscript for the direction vertical to 1

1. Introduction

High pressure turbocompressors with a discharge pressure of 600 bar or more are very sensitive to instabilities because of the very high fluid forces in the seals. Often these compressors are used in offshore applications and therefore call for weight saving efforts like less casing per train hence more stages per rotor. This requires longer rotors, which make them even more sensitive to instabilities.

Well known destabilizing effects are

- Internal damping (shrink fit hysteresis, material damping).
- Oil whip in bearings.
- Oil whip in oil seals.
- Self-excitation due to the flow in labyrinths.

Internal damping is a source of self-excitation, if the compressor is run above its first critical speed, as high pressure compressors normally do. This effect, however, is probably the least important one of the above mentioned effects. Problems due to it can be avoided by a proper design (minimization of the friction in shrink fits).

Oil whip in bearings is prevented by using tilting pad bearings and therefore is not a real problem any more.

Oil seals for shaft end sealing are often designed as floating seal rings (fig. 3). The ring is pressed against the casing due to the pressure difference. The friction at the contact surface inhibits the radial floating motion. If the ring is blocked it effects the rotor quite similarly to a plain bearing, hence can cause oil whip at high rotational speeds (often at approximately twice the first critical speed). Special care has to be taken of this problem in case of high pressure differences (200 bar or more), since this calls for long rings causing high oil film forces and also increases the friction enhancing a blocking of the ring. The danger of blocking has to be prevented by pressure balancing the ring and thus reducing the friction force. If the friction, however, is too small the ring can become unstable.

The self-exciting effect of the flow in labyrinths on impeller shrouds, hubs and the balance piston is the most severe destabilizing effect. Without design features to reduce it a high pressure compressor normally can not be run. Swirl brakes for example are such a design feature. Combined with the proper choice of labyrinths they not only prevent an instability but even increase the stability with increasing pressure.

In this paper a high pressure compressor is demonstrated as an example of how to achieve a stable operation of the rotor. The destabilizing effects in the oil seals and labyrinths are handled in detail. It is also shown how to prevent an instability of the oil seal rings. The investigation is mainly carried out theoretically. The most important properties of the labyrinths, however, are checked by measured data.

2. Description of the investigated compressor rotor

The compressor we are dealing with in this paper was designed as a feasibility study for an offshore reinjection application. Figure 1 shows the rotor. It has eight stages with an intercooler after the fourth stage. The basic data are

Suction pressure	198 bar.
Discharge pressure	700 bar.
Molecular weight of the gas	20.05.
Mass flow	47.5 kg/s.
Rotor mass	265 kg.
Bearing distance	1565 mm.
Operating speed	13400 rpm.

The impeller has just a slight shrink fit for centering. The moment is mainly transmitted by dowel pins, which also position the impeller axially. Sleeves are therefore not necessary. This design minimizes the internal friction and allows a large shaft diameter, hence a stiff shaft.

The rotor is supported on two tilting pad bearings with four equal pads. The data of the two bearings are shown in table 1. The damping and stiffness coefficients as well as the oil viscosity are valid for operating conditions. The bearings are isotropic and have no cross coupling coefficients.

Figure 2 shows the modal damping factors D and the frequencies f of the first two bending modes (forward and backward whirl) of the rotor for different rotational speeds. They are determined from the eigenvalues $\lambda = \alpha \pm i\nu$ of a Finite Element model of the rotor as follows:

$$f = \nu / (2\pi) \quad (1)$$

and

$$D = -\alpha / |\lambda|. \quad (2)$$

The eigenvalue extraction was carried out with the program MADYN (ref.1). The oil film viscosity which might change in reality with the rotational speed is assumed to be constant in the calculation. The influence of the seals is not taken into account here. It will be considered later.

The rotational speeds in fig.2 at intersections of the line $f=n/60$ with the frequency curves are critical speeds. The first critical speed is at 3700 rpm. The corresponding damping factor is 15%. The critical speeds with the second bending modes have a very high damping (>30%). Resonances at these speeds therefore will hardly be detectable. The shown eigenvalues are approximately valid for running the rotor up and down, since the pressure in the compressor then is low. Under operating conditions however they change considerably because of the fluid forces in the seals, as we will see later in paragraph 5.

3. Description of the oil seals

Figure 3 shows the floating seal ring of the oil seals. In order to tighten the high pressure against atmospheric pressure the ring is pressed against the casing by an axial force resulting from the pressure difference and the surfaces on which the pressures act. The axial force must not be too small since contact between the ring and the casing must be guaranteed in spite of pressure fluctuations. However it should also not be too large because of the friction force inhibiting the radial motion of the ring.

Two extreme assumptions for the determination of the axial force can be made. The first is, that the outer edge of the contact surface tightens against the atmospheric pressure. This yields a maximum axial and friction force. Assuming that the inner edge tightens yields minimum forces. For our seal these forces are

Maximum axial force:	22267 N.
Minimum axial force:	4517 N.
Maximum friction force:	3565 N.
Minimum friction force:	570 N.

For the friction forces a friction coefficient of 0.16 is assumed.

A Finite Element calculation (results not shown here) considering the thermal deformation of the ring and the deformation due to the pressures showed that the first assumption yielding maximum forces seems to be more realistic.

For the linear rotordynamic calculations (see paragraph 5) we assume either ideally floating or locked up rings. Reality of course is between these two extreme cases.

For the ideally floating case we assume that the rings do not affect the rotor at all; that is, they are not modelled at all.

For the locked up case we assume a centered position of the ring relative to the static position of the shaft. This is realistic, since the compressor is run up with low pressure; hence the friction force is low during running up and the ring can center itself very well. This is in favor of a uniform gap, which prevents the surfaces in the gap to be damaged by small particles transported in the seal oil. The self-excitation, however, then becomes a maximum, if the ring is blocked due to the increased pressure.

For the latter case the oil seals are modelled by linear damping and stiffness coefficients in the same way as journal bearings. More accurately explained, they are considered as short, noncavitating journal bearings.

Our ring with a ratio of width to diameter of 0.35 can be considered as short. This allows us to neglect the pressure gradient in circumferential direction for small disturbances of the centered position. The coefficients then can be calculated analytically from the Reynolds equation (ref.2).

The bearing is considered as noncavitating, since the axial pressure drop normally suppresses any cavitation for small disturbances of the centered position.

The thus determined coefficients are

$$\begin{aligned} k_{xx} &= 0, \\ k_{xy} &= -k_{yx} = \beta^2 \pi F^* / \delta, \end{aligned} \quad (3)$$

$$\begin{aligned} d_{xx} &= d_{yy} = 2 \beta^2 \pi F^* / (\delta \Omega), \\ d_{xy} &= 0, \end{aligned} \quad (4)$$

with

$$\beta = B / D \quad (5)$$

as the ratio of width to diameter and

$$F^* = D B \eta \Omega / \Psi^2 \quad (6)$$

as a reference force.

These coefficients are twice as large as those of a cavitating short bearing (ref.2). The data of the oil seals to determine the reference force are

width	$B = 38.5 \text{ mm},$
shaft diameter	$D = 110.0 \text{ mm},$
oil viscosity	$\eta = 0.015 \text{ Ns/m}^2,$
relative clearance	$\Psi = 1.36 \text{ }^\circ/\text{o}.$

4. Description of the labyrinth seals

The investigation is carried out for the following labyrinth types on the shrouds, hubs and the balance piston.

Balance piston	: Comb grooved labyrinths.
Hub	: Straight-through labyrinths.
Impeller shrouds	: Straight-through, comb grooved labyrinths.

All labyrinths are stator labyrinths. Their geometry is shown in figure 4 a,b,c.

The gas data of each labyrinth are given in table 2. Data of the hub labyrinth of the eighth stage are not given, since the influence of this labyrinth is negligible compared to the influence of the labyrinth on the balance piston just following it.

The inlet swirl velocity of the fluid at each labyrinth is the main cause of the self-excitation of the rotor. It is zero for the hub labyrinths because of the diffuser and return

channel vanes. These labyrinths therefore rather have a damping than an exciting effect. For the other labyrinths the inlet swirl velocity is about 75% of the circumferential velocity of the rotor surface at the labyrinth inlet. When using swirl brakes it is only about 15% of the velocity of the rotor. These values were measured on a real compressor at high pressures at the author's company (ref.3).

The labyrinths are modelled by damping and stiffness coefficients just like the oil seals. These coefficients are calculated according to the theory of Wyssmann et al. (ref.4). Figure 5 shows thus calculated coefficients for the two types of shroud labyrinths of the sixth stage for two different inlet swirl velocities (with and without swirl brakes).

The cross coupling stiffness k_{xy} increases with increasing inlet swirl. The line for the comb grooved labyrinth is shifted to smaller values compared to the straight-through labyrinth. For small inlet swirls, k_{xy} even becomes negative. Therefore care must be taken concerning the excitation of backward whirling modes when using this labyrinth type.

The direct damping coefficient d_{xx} of the comb grooved labyrinth, hence its damping effect, is much smaller than the one of the straight-through labyrinth. For both labyrinths it almost does not depend on the inlet swirl. Due to this property it is possible to increase the stability of a compressor with increasing pressure. The exciting cross coupling stiffness increasing for higher pressures is reduced by swirl brakes, whereas the damping, which also increases for higher pressures, remains unaltered when reducing the swirl.

The ratio of k_{xy} to d_{xx} is considerably larger for the comb grooved labyrinth, except in the small region where k_{xy} is zero or almost zero. Increasing the damping of a rotor by an appropriate inlet swirl therefore seems to be easier when using straight-through labyrinths. When using the comb grooved type one has to realize an inlet swirl, where k_{xy} is almost exactly zero. This is practically impossible.

The direct stiffness k_{xx} for both labyrinth types has considerable negative values for high inlet swirl velocities. For the relative velocity of 0.75 the direct labyrinth stiffness (of one labyrinth!) is about 16% of the stiffness of the rigid supported shaft. The shaft stiffness hereby is defined as a force applied in the middle of the shaft divided by the deflection at the same location due to this force. It can therefore be expected that the direct labyrinth stiffness can significantly reduce the natural frequencies of the rotor.

The cross coupling damping d_{xy} is a conservative term and therefore neither has an exciting nor a damping effect. It influences the rotor in a similar way as gyroscopic terms.

In order to check the theory coefficients of a straight-through and comb grooved labyrinth were measured on the test stand of the Turbomachinery Laboratories at the Texas A & M University. The test stand is described in detail in reference 5. The geometries of the measured labyrinths are shown in fig.6. The tests were carried out with air against atmospheric pressure.

Figure 7 and 8 show measured coefficients for an inlet pressure of 3.08 bar and a rotational speed of 9500 rpm as a function of the inlet swirl velocity. For comparison

calculated coefficients for the test labyrinths are also shown. The measurements confirm the following properties of the calculated coefficients:

- The cross coupling stiffness almost linearly depends on the inlet swirl.
- The cross coupling stiffness of the comb grooved labyrinth is negative for small positive inlet swirls.
- The direct damping almost does not depend on the inlet swirl for the comb grooved labyrinth. For the straight through labyrinths this property is not confirmed as well. It was better confirmed in the measurements presented in reference 3.
- The direct damping for the comb grooved labyrinth is much smaller than for the straight through labyrinth.
- The direct stiffness is negative.

The experimental uncertainty indicated in the figures by the vertical lines is ± 3.5 kN/m for stiffness and ± 60 Ns/m for damping. Hence the coincidence is acceptable. The calculated direct damping values tend to be too small. This however is not so severe, since one is always on the safe side when assessing the stability with calculated damping values. The magnitude of the direct stiffness values also tend to too small values.

5. Stability of the rotor

The stability of the rotor considering the fluid forces in the oil and labyrinth seals is assessed by calculated complex eigenvalues $\lambda = \alpha \pm i\omega$ of the Finite Element model of the rotor, respectively the modal damping factors D (see equation (2)). A positive damping factor means the rotor is stable, whereas it is unstable for negative damping factors.

Figure 9 a and b shows the damping factor and the frequency of the first backward and forward whirling bending mode for ideally floating seal rings. They are shown for the two mentioned labyrinth types at the operating speed of 13400 rpm without labyrinth influence, a condition which is realized in practice for very low pressures, as well as with labyrinth influence for the full discharge pressure of 700 bar. One can recognize the tremendous influence of the labyrinths on the damping as well as on the frequencies.

It can be seen that the forward whirl becomes unstable with increasing pressure for both labyrinth types if no swirl brakes are used. When using swirl brakes and straight-through labyrinths the damping of the rotor is considerably increased with increasing pressure. However when swirl brakes are used in combination with comb grooved labyrinths the backward whirl becomes unstable. This is due to the negative cross coupling stiffness of this labyrinth type for small inlet swirls (fig. 5).

Figure 10 and 11 show results of the rotor with centrally blocked oil seal rings. The modes are quite different from those of the rotor with ideally floating seal rings.

In figure 10 damping factors and natural frequencies of the first four modes are shown as a function of the rotational speed without labyrinth influence ($p = 0$). This figure is shown for a better understanding of the behavior of the rotor with blocked seal rings, although in reality a blocking of the seal rings is not possible for low pressures, that is for rotor speeds below the operating speed.

It can be seen that the frequency of mode 1 and 2 almost linearly depend on the rotor speed. The slopes of the frequency curves hereby are about 0.5. This clearly indicates that these frequencies are determined by the oil whirl in the seals, which approximately has a frequency of half the rotational speed. Mode number 1 becomes unstable at 8000 rpm. This is about twice the critical speed f_{1c} of the rotor without seals (also see figure 2). The oil whirl here turns into the well known oil whip.

Figure 11 shows the influence of labyrinths on the eigenvalues of the four modes in figure 10 at the operating speed. Results are only shown for straight-through labyrinths since comb grooved labyrinths are not recommendable because of the results discussed in figure 9.

It can be seen that the labyrinths make the rotor more stable if swirl brakes are used. The rotor however still is slightly unstable. The seal rings therefore must be balanced at any rate in order to come closer to the behavior in figure 9.

6. Stability of the seal ring

If the friction force between casing and floating seal ring is reduced too much, the ring can become unstable. The corresponding mode can be calculated by modelling the rotor including unbound floating seal rings without friction forces. In this mode the rotor practically does not move and the ring describes a circular orbit around the center of the shaft.

In the following we will calculate limit cycles of this unstable motion taking into account the nonlinear friction forces and also considering the oil film forces as nonlinear, since the expected deflections are in the order of magnitude of the seal ring clearance. Since the rotor practically does not move we consider it as fixed.

The equations of motion of the ring in radial and circumferential direction are (fig.12)

$$m (\ddot{r} - r \dot{\phi}^2) = F_r, \quad (7)$$

$$m (2\dot{r}\dot{\phi} + r\ddot{\phi}) = F_{\phi}, \quad (8)$$

where F_r and F_{ϕ} are the forces on the ring in the radial and circumferential direction. These forces consist of the oil film force and the friction force. They may be written as follows:

$$F_r = F_{dr}(r) - d_{rr}(r)\dot{r} - d_{r\phi}(r)\dot{\phi}r - F_{fr}, \quad (9)$$

$$F_{\phi} = F_{d\phi}(r) - d_{\phi r}(r)\dot{r} - d_{\phi\phi}(r)\dot{\phi}r - F_{f\phi}, \quad (10)$$

where $F_{dr}, F_{d\phi}$ are the displacement dependent oil film forces,
 $d_{rr}\dot{r}, d_{r\phi}\dot{\phi}r, d_{\phi r}\dot{r}, d_{\phi\phi}\dot{\phi}r$ are the velocity dependent oil film forces
 and $F_{fr}, F_{f\phi}$ are the friction forces.

To determine limit cycles (i. e. stationary solutions of equation (7) and (8)) one has

$$\dot{r} = \ddot{r} = \ddot{\phi} = 0, \quad (11)$$

$$F_{fr} = 0, \quad (12)$$

$$F_{f\phi} = F_f. \quad (13)$$

Substituting equation (11), (12), and (13) into equation (7), (8), (9) and (10) yields

$$m r \dot{\phi}^2 = -F_{dr}(r) + d_{r\phi}(r) \dot{\phi} r, \quad (14)$$

$$0 = F_{d\phi}(r) - d_{\phi\phi}(r) \dot{\phi} r - F_f. \quad (15)$$

The solution of $\dot{\phi}$ can be extracted from equation (15):

$$\dot{\phi} = \frac{F_f - F_{d\phi}(r)}{r d_{\phi\phi}(r)}. \quad (16)$$

Equation (16) introduced in equation (14) delivers a quadratic equation for F_f :

$$\frac{m}{r} \left[\frac{F_f - F_{d\phi}(r)}{d_{\phi\phi}(r)} \right]^2 + d_{r\phi}(r) \frac{F_f - F_{d\phi}(r)}{d_{\phi\phi}(r)} + F_{dr}(r) = 0. \quad (17)$$

The solution of this equation is

$$F_f = F_{d\phi}(r) - \frac{d_{r\phi}(r)r \pm \sqrt{(d_{r\phi}(r)r)^2 - 4mF_{dr}(r)r}}{2m} d_{\phi\phi}(r). \quad (18)$$

The second solution of equation (17) with a "-" instead the "+" before the square root in equation (18) physically makes no sense. Since $F_{dr}(r)$ is always negative (eq.(19)), the root is larger than $d_{r\phi}(r)r$. Hence a "-" sign would always yield a friction force larger than the oil film force $F_{d\phi}(r)$ and ϕ would become negative according to equation (16). This means it would have the same direction as the friction force, which is not possible, since the friction force is not the driving force of the motion.

The displacement dependent forces in equation (16) and (18) are (fig. 12)

$$F_{dr}(r) = -F_d(r) \cos \gamma(r), \quad (19)$$

$$F_{d\phi}(r) = F_d(r) \sin \gamma(r), \quad (20)$$

with

$$F_d(r) = F^* S_o(r), \quad (21)$$

where F^* is the reference force according to equation (6) in paragraph 3 and S_o is the Sommerfeld number.

The damping coefficients in equation (16) and (18) are

$$d_{r\phi}(r) = F^*/(\delta\Omega) (b_{22}\sin\gamma\cos\gamma - b_{21}\sin^2\gamma + b_{12}\cos^2\gamma - b_{11}\sin\gamma\cos\gamma) \quad (22)$$

$$d_{\phi\phi}(r) = F^*/(\delta\Omega) (b_{22}\cos^2\gamma - b_{21}\sin\gamma\cos\gamma - b_{12}\sin\gamma\cos\gamma + b_{11}\sin^2\gamma) \quad (23)$$

where β_{22} , β_{21} , β_{12} and β_{11} are dimensionless damping coefficients in the 1,2 coordinate system in figure 12.

The Sommerfeld number and the dimensionless damping coefficients are calculated numerically from the Reynolds equation. A analytical solution by neglecting the pressure gradient in circumferential direction as in paragraph 3 is not possible any more, because the motion of the ring is not only a small disturbance of the centered position.

Figure 13 shows the relative displacement $\epsilon=2r/\delta$ of the ring and the angle γ for different Sommerfeld numbers. Fig 14 shows the dimensionless damping coefficients as a function of ϵ .

Figure 15 a,b show the curves of equilibrium points according to equation (18) and (16) calculated with the values in figure 13 and figure 14 for a mass of the ring of 5.135 kg. It can be seen in figure 15a, that for friction forces below the maximum force of about 2700 N exist two equilibrium points ϵ_1 and ϵ_2 . The first point ϵ_1 is unstable. For the friction force zero this already has been stated at the beginning of this paragraph. For higher friction forces this can be verified by numerically solving equations (7) and (8). The diagram in figure 15a therefore can be understood as follows. If for any reason ϵ becomes equal or larger than ϵ_1 the centrifugal force will make the ring snap through to ϵ_2 , where it describes a circular orbit with the eccentricity ϵ_2 and the frequency according to figure 15b.

If the frequency of this motion is close to a natural frequency of the rotor which is not damped too strong, the rotor vibration is affected by the ring motion. The frequency of the ring motion then can be seen in the spectrum of a rotor vibration probe.

If the friction force is larger than the maximum in figure 15a the ring cannot describe a nondecaying motion on its own, hence it will follow the shafts motion. The ring should therefore be balanced in such a way that the friction force is slightly above the maximum in figure 15a.

It must be mentioned however, that the equilibrium points are very sensitive to the bearing data which are calculated numerically and therefore must not correspond to a real situation. The deduced desired friction force therefore can only be understood as a rough estimation and has to be confirmed experimentally.

7. Conclusions

The stability of a high pressure compressor rotor was investigated with special regard to the self-excitation in the oil and labyrinth seals. The investigations were carried out theoretically. It was shown that both effects can easily destabilize the rotor, if they are not treated properly.

For the labyrinth coefficients, measurements were also considered. A comparison with calculated coefficients showed that a theoretical stability analysis is on the safe side, since

the calculated direct damping coefficients tend to be too low. . Hence the theory is a sound, practical approach.

The self-excitation in the oil seals designed as floating seal rings can be avoided by balancing the ring in order to reduce the friction between casing and ring and guarantee its floating. If the friction, however, is too small, the ring is excited by the oil film force to a circular motion around the center of the shaft. The minimum friction force to prevent this unwanted motion was deduced.

The self-excitation in the labyrinths can be reduced by swirl brakes. Since the swirl brakes practically do not influence the damping but only the exciting cross coupling stiffnesses the rotor can become even more stable with increasing pressure. To achieve this however the properties of the chosen labyrinth type have to be taken into account. It was shown that a comb grooved labyrinth which has only little damping and negative cross coupling stiffnesses for small inlet swirls destabilizes the first backward whirling bending mode when using swirl brakes. An increasing stability with increasing pressure was achieved when using straight-through labyrinths.

References

1. Klement, H.D.: MADYN - ein Programmsystem für die Maschinenberechnung. Unix mail 5 (1987) 1.
2. Cameron, A.: Basic lubrication theory. Longman, London 1970.
3. Wyssmann, H.R.: Rotor Stability of High Pressure Multistage Centrifugal Compressors. Proceedings of the Conference on Rotating Machinery Dynamics, Boston 1987-DE-Vol.2, Editors A. Muszynska and J.C. Simonis (Book No. H0400B).
4. Wyssmann, H.R., Pham, T.C. and R.J. Jenny: Prediction of Stiffness and Damping Coefficients for Centrifugal Compressor Labyrinth Seals. ASME Journal of Engineering for Gas Turbines and Power, Vol. 106, October 1984.
5. Childs, D.W. et. al.: Theory Versus Experiment for the Rotordynamic Coefficients of Annular Gas Seals. Part 1 - Test Facility and Apparatus. ASME Journal of Tribology, Vol. 108, July 1986.

Table 1

Bearing data ($n = 13400$ rpm)

	bearing 1		bearing 2	
Diameter	0.1	m	0.1	m
Width	0.05	m	0.05	m
Relative bearing clearance Ψ_b	0.2	o/o	0.2	o/o
Relative pad clearance Ψ_p	0.4	o/o	0.4	o/o
Oil viscosity	0.01	Ns/m ²	0.01	Ns/m ²
Static load	1251	N	1349	N
Stiffness coefficient	$7.15 \cdot 10^7$	N/m	$7.23 \cdot 10^7$	N/m
Damping coefficient	$5.16 \cdot 10^4$	Ns/m	$5.19 \cdot 10^4$	Ns/m

Table 2

Gas data of the labyrinths

a) Balance piston

mean viscosity [10^{-4} Ns/m ²]	0.47
density before lab. [kg/m ³]	348
pressure before lab. [bar]	682
pressure after lab. [bar]	198

b) Hub

stage	1	2	3	4	5	6	7
mean viscosity [10^{-4} Ns/m ²]	0.26	0.28	0.30	0.32	0.41	0.43	0.45
density before lab. [kg/m ³]	236	250	262	318	325	332	339
pressure before lab. [bar]	253	311	371	429	496	570	639
pressure after lab. [bar]	239	297	356	419	479	551	618

c) Shroud

stage	1	2	3	4	5	6	7	8
mean viscosity [10^{-4} Ns/m ²]	0.26	0.28	0.30	0.32	0.41	0.43	0.45	0.47
density before lab. [kg/m ³]	239	253	264	275	330	337	342	348
pressure before lab. [bar]	239	297	356	419	479	551	618	682
pressure after lab. [bar]	198	253	311	371	429	496	570	633

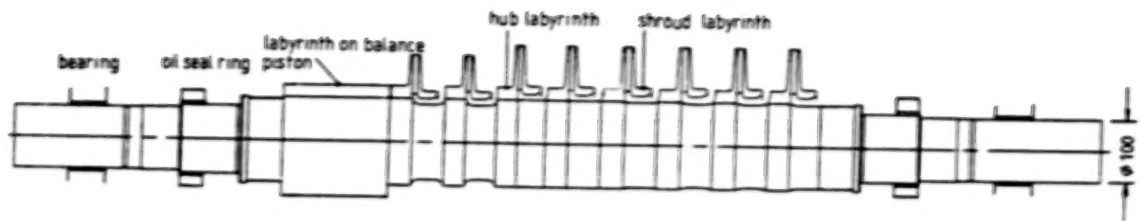


Fig.1 Investigated rotor

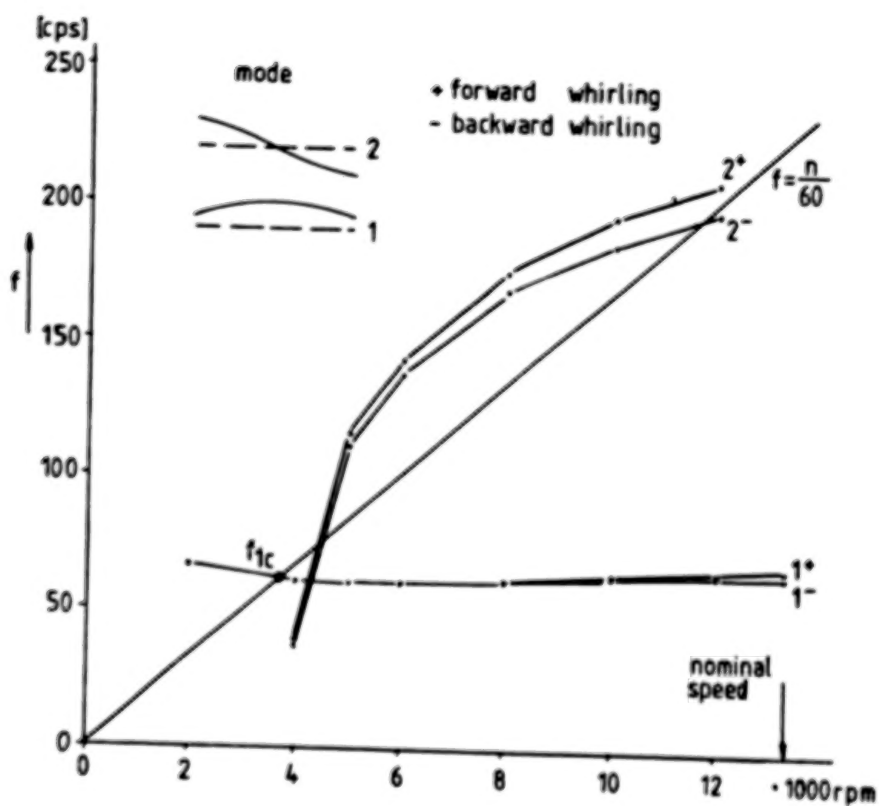
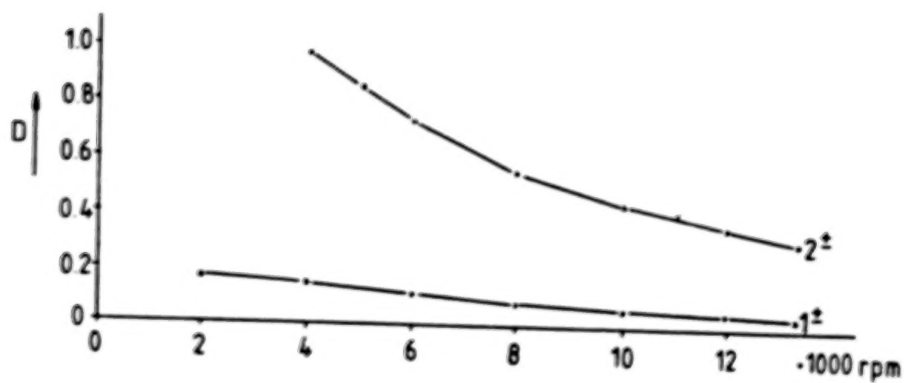


Fig.2 Modal damping factors and natural frequencies of the first two bending modes of the rotor

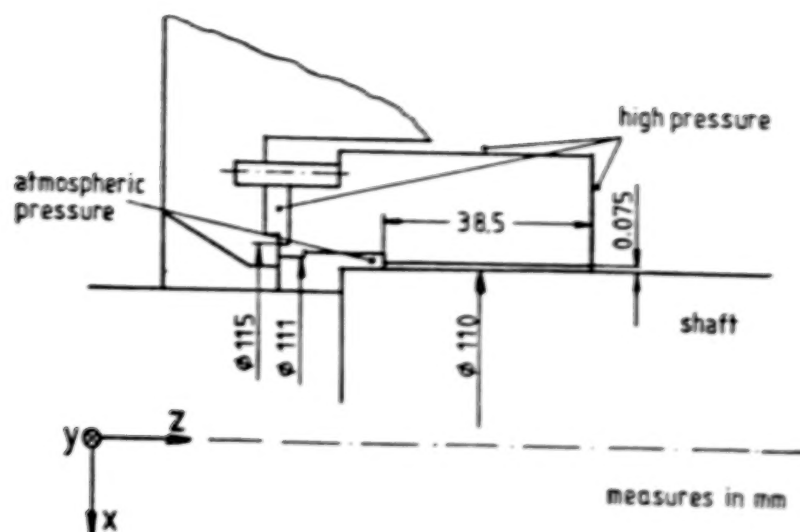
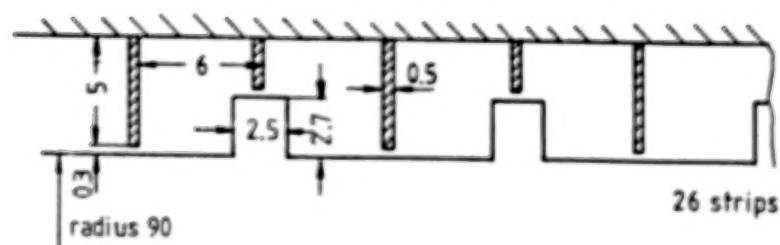
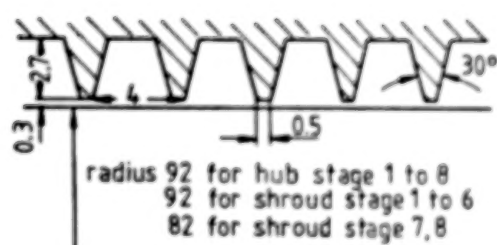


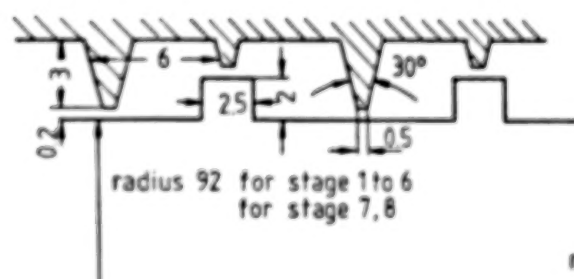
Fig.3 Floating seal ring



a) Balance piston



b) Hub and impeller shroud with straight-through labyrinth



c) Impeller shroud with comb grooved labyrinth

measures in mm

Fig.4 Geometry of labyrinths

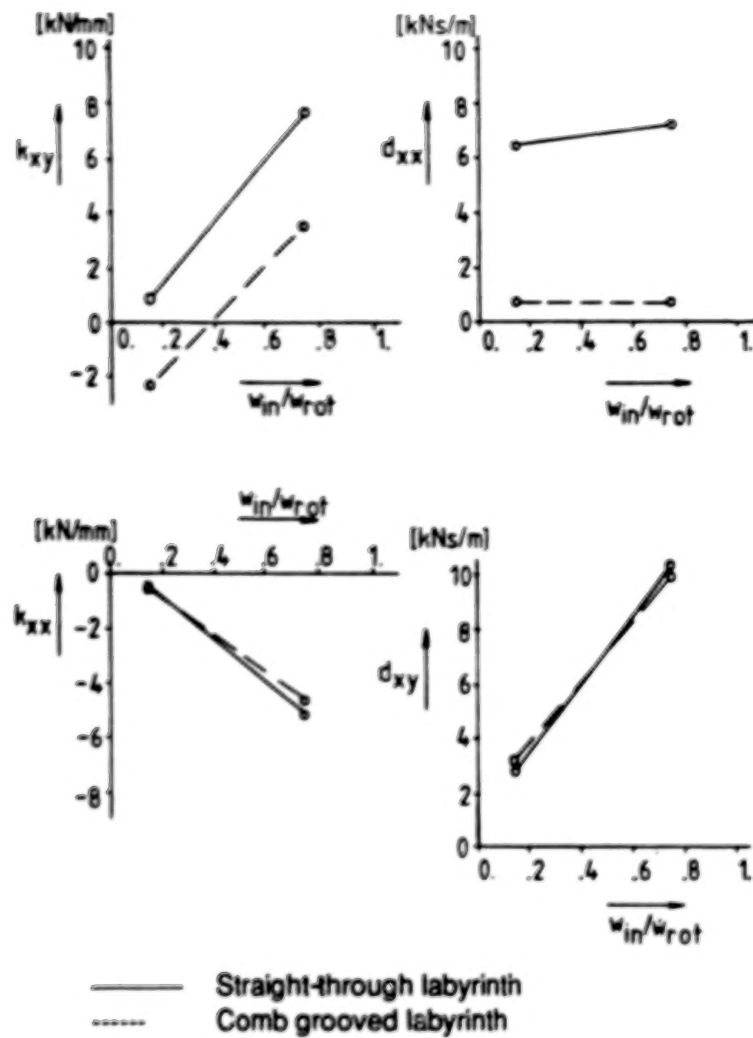


Fig.5

Calculated labyrinth coefficients with swirl brakes ($w_{in}/w_{rot}=0.75$) and without swirl brakes ($w_{in}/w_{rot}=0.15$)

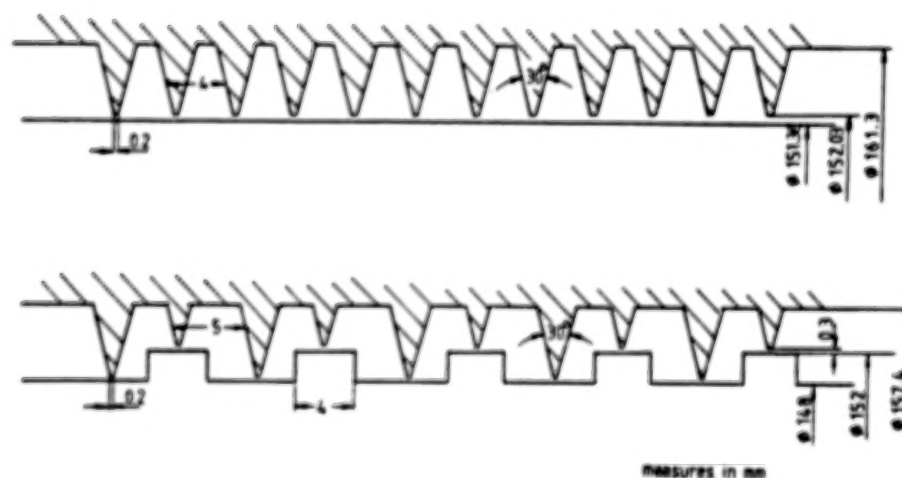


Fig.6

Geometry of measured labyrinths

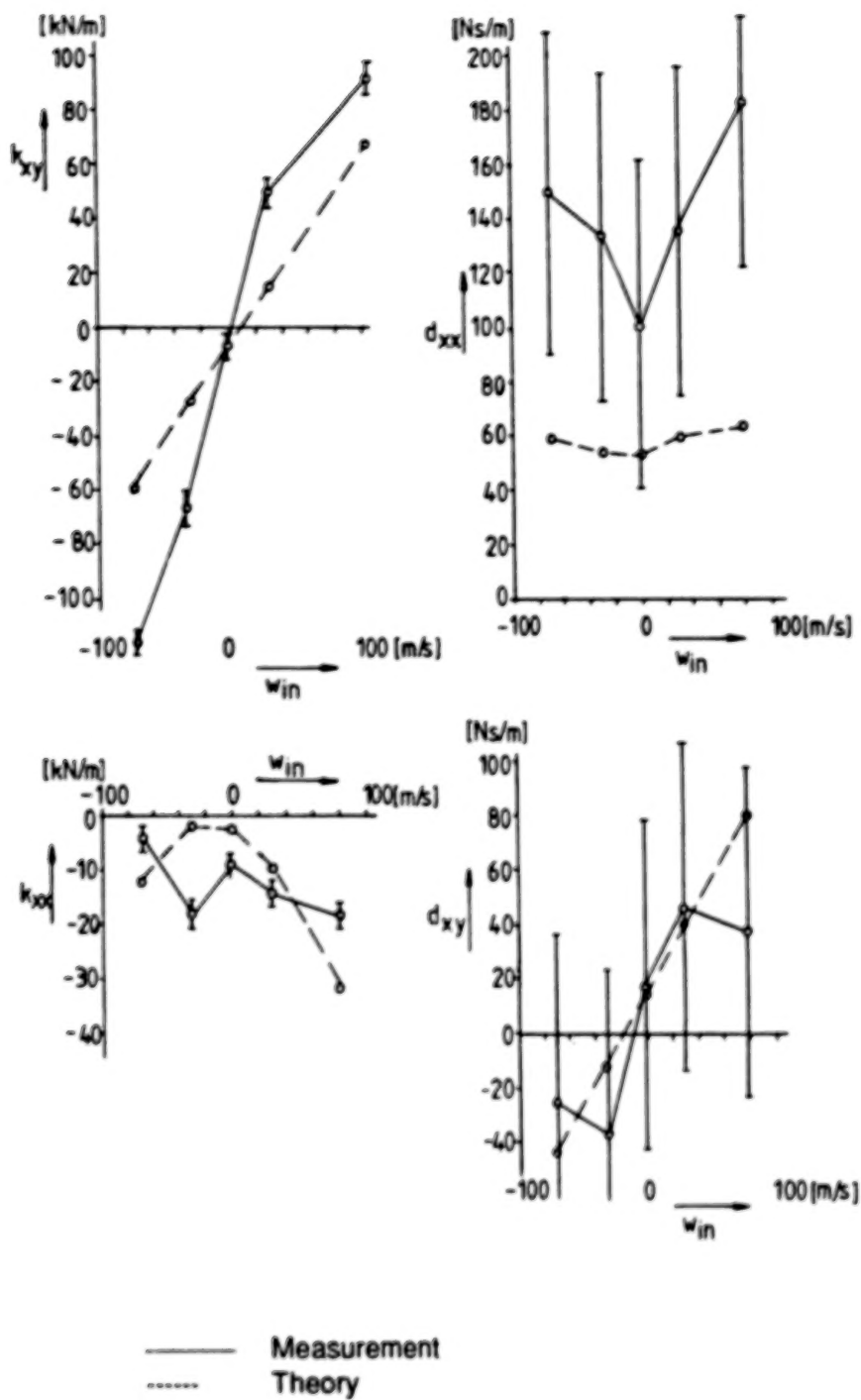


Fig.7

Comparison of measured and calculated coefficients for the straight-through labyrinth

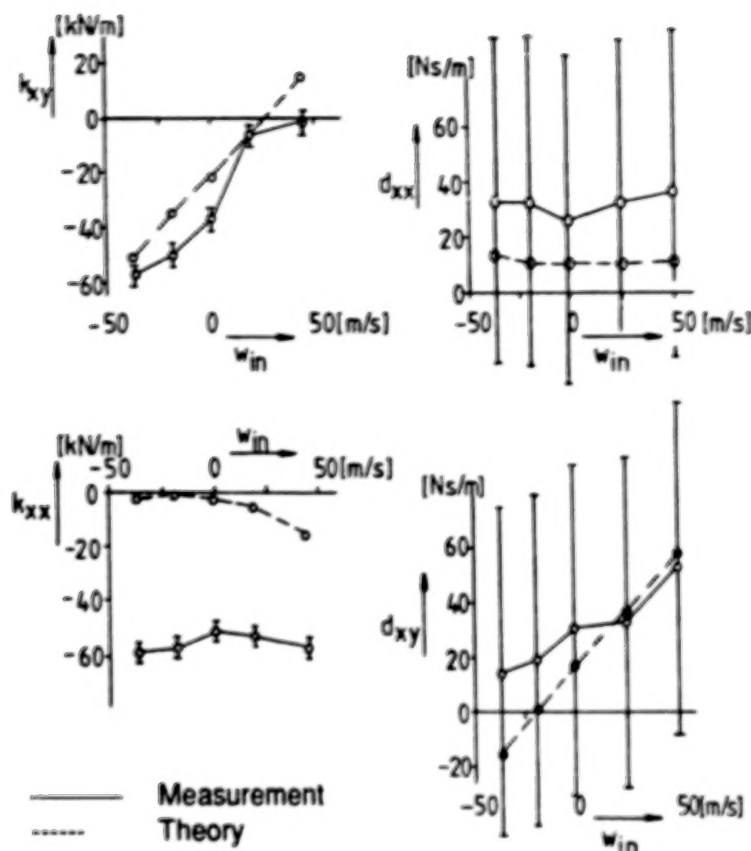


Fig.8 Comparison of measured and calculated coefficients for the comb grooved labyrinth

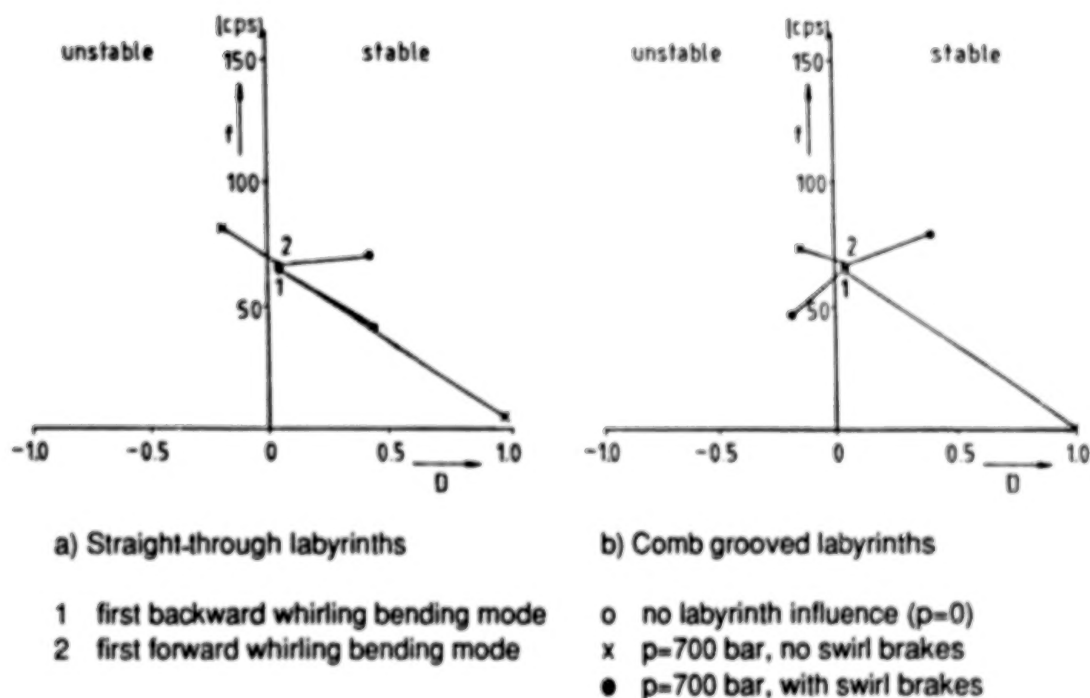


Fig.9 Influence of labyrinths on the damping factors and natural frequencies of the rotor with ideally floating oil seal rings. $n=13400$ rpm

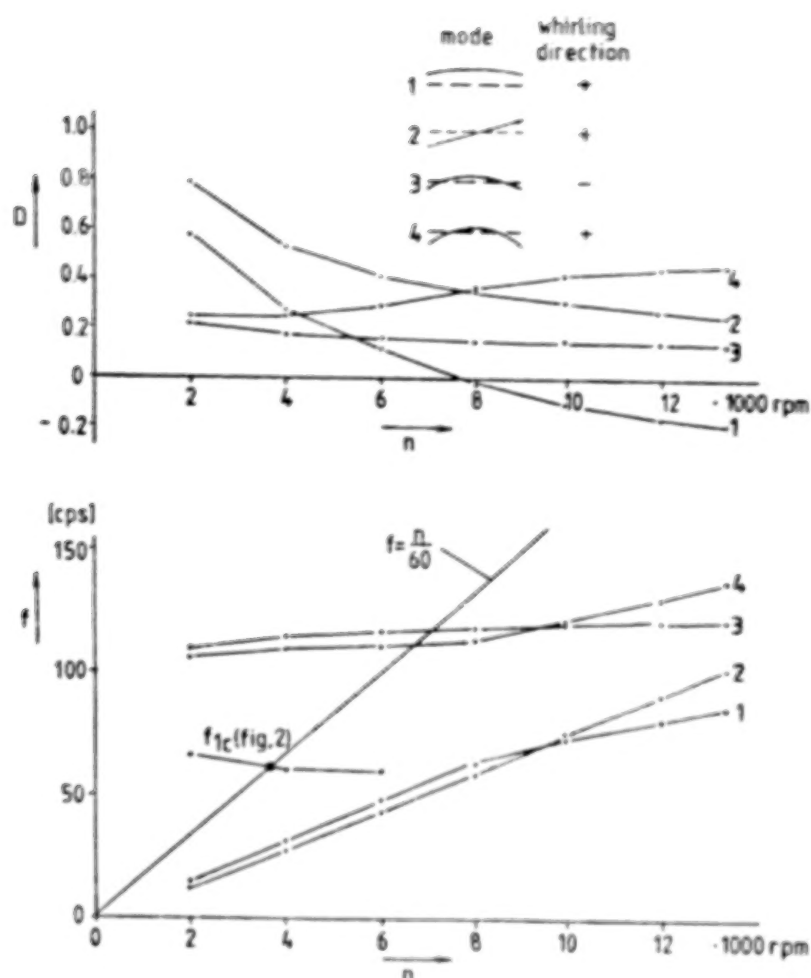


Fig.10 Damping factors and natural frequencies of the rotor for centrally blocked oil seals

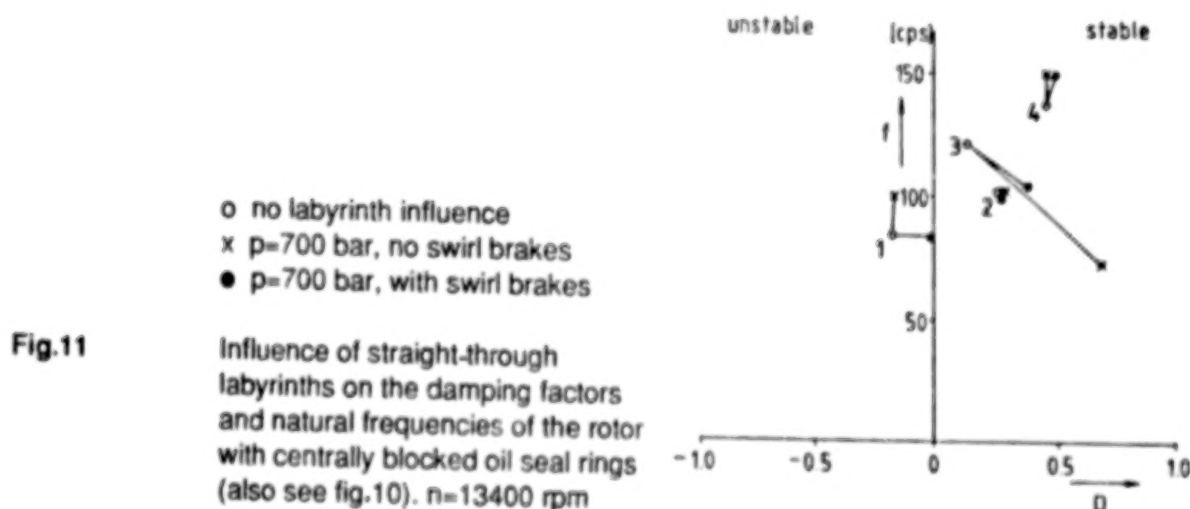


Fig.11 Influence of straight-through labyrinths on the damping factors and natural frequencies of the rotor with centrally blocked oil seal rings (also see fig.10). $n=13400$ rpm

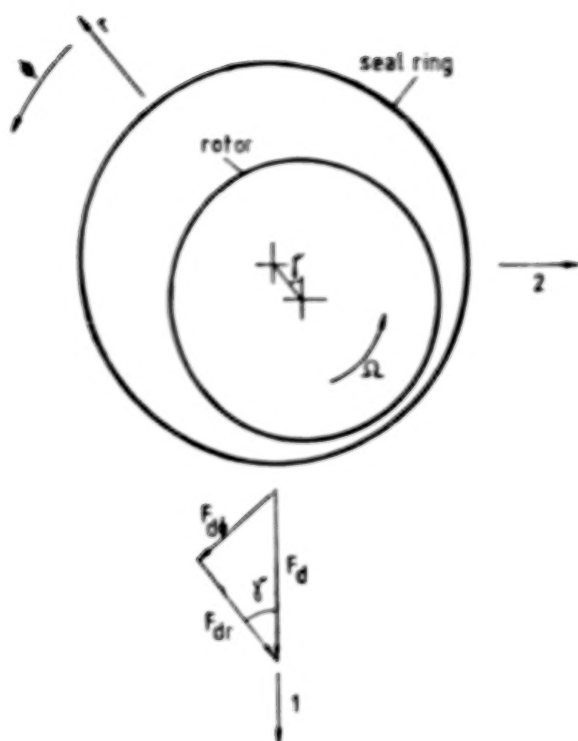


Fig. 12 Coordinates to describe the ring motion and the forces on the ring

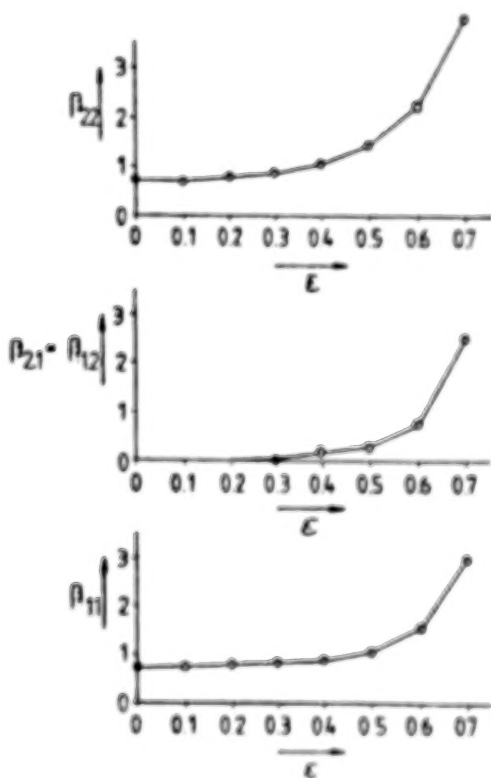


Fig. 14 Dimensionless damping coefficients of the oil seal

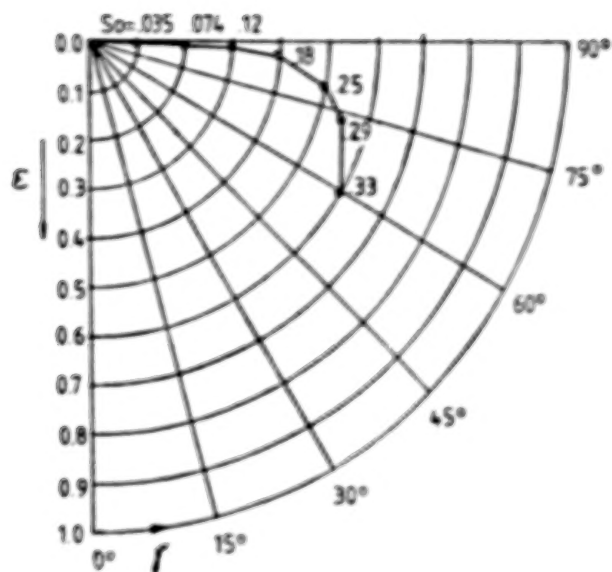
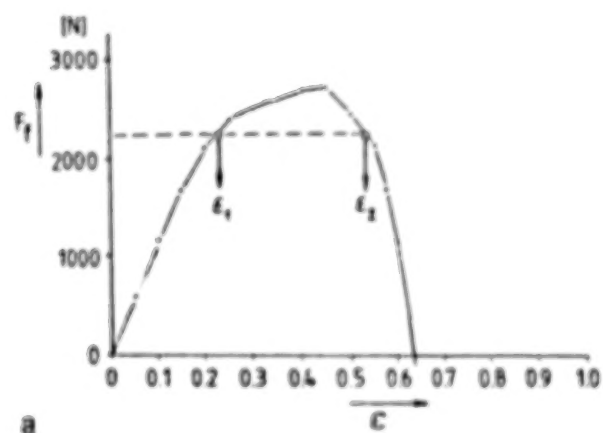
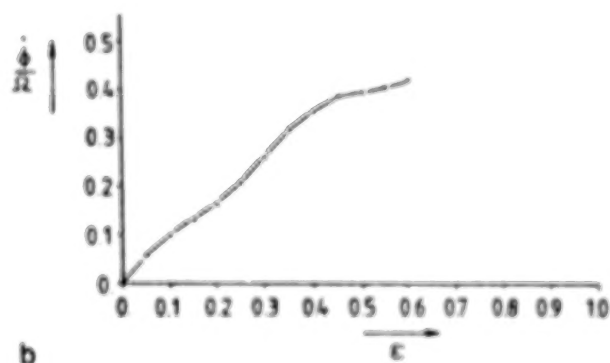


Fig. 13 Relation between $\epsilon = 2r/\delta$, γ and So



a



b

Fig. 15 Curves for the equilibrium of forces in radial and circumferential direction

BLANK PAGE

ROLE OF CIRCUMFERENTIAL FLOW IN THE STABILITY OF FLUID-HANDLING MACHINE ROTORS

D.E. Bently and A. Muszynska
Bently Rotor Dynamics Research Corporation
Minden, Nevada 89423, U.S.A.

The recent studies of the dynamic stiffness properties of fluid lubricated bearings and seals by the authors [Refs. 1-7] have yielded most of the generalized characteristics discussed and used in this paper. They include bearing and seal nonlinear fluid film properties associated with stiffness, damping, and fluid average circumferential velocity ratio. Analytical relationships yield the rotor system's dynamic stiffness characteristics. This paper shows the combination of these data to provide the fluid-induced rotor stability equations.

NOMENCLATURE

C	Bearing or seal radial clearance
D	Fluid film radial damping
D_s	Shaft modal damping coefficient
e	Shaft eccentricity ratio
$\vec{F}_{pert\ z}$	Circular perturbation force vector
j	$\sqrt{-1}$
K, K_1, K_2	Rotor modal stiffnesses
K_B	Fluid film direct (radial) stiffness
K_{Bo}	Fluid film direct (radial) stiffness for concentric shaft
K_D, K_Q	Rotor system direct and quadrature dynamic stiffnesses respectively
M	Rotor modal mass
M_{f1}	Fluidic inertia effect
$\vec{z}=x+jy$	Rotor lateral displacement (x--horizontal, y--vertical)
α	Force/response phase angle for periodic perturbation
η	Fluid viscosity
λ	Fluid circumferential average velocity ratio
λ_0	Fluid circumferential average velocity ratio for concentric shaft
ω	Precession frequency
ω_{ASY}	Asymptotic value at whip precession frequency
ω_{th}	Precession frequency at threshold of stability
Ω	Rotative speed

RESULTS OF PERTURBATION TESTING OF ROTORS IN BEARINGS AND SEALS

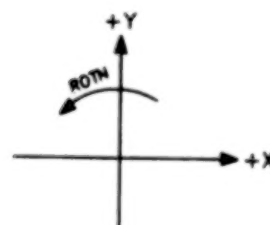
Dynamic stiffness properties of rotor systems are studied by applying a perturbation force of sinusoidal nature to a rotor. The best results are obtained when the force is circular (sinusoidal in two orthogonal lateral directions) and applied in a plane perpendicular to the shaft axis. The rotor is held at a constant speed while the perturbation force frequency is varied from zero to frequencies well above the rotative speed, in either forward (the same direction as shaft rotation) or reverse direction (opposing rotation). The frequency, amplitude, and phase of the perturbation force is accurately documented. The amplitude and phase of the displacement response of the rotor at each perturbation force frequency is then carefully measured. Dividing the perturbation force vectors by the corresponding response vectors yields the dynamic stiffness vectors. Plotting these dynamic stiffness vectors in terms of their direct and quadrature components across wide perturbation frequency ranges allows dissection and evaluation of the dynamic stiffness components [Refs. 1,2,4,5].

In classical rotor dynamics for laterally isotropic systems, the bearing or seal fluid film direct dynamic stiffness terms are referred to as combination of direct (radial) spring, cross damping, and direct mass. The quadrature dynamic stiffness contains cross spring, direct (radial) damping, and cross mass. (Laboratory observations up to this time, however, reveal no cross mass term.)

The authors use the same definitions, but there are the following adjustments: (a) direct spring is shown to be a sum of the fluid film hydrodynamic stiffness plus the hydrostatic (externally pressurized) stiffness minus a component associated with the fluidic inertia effect; (b) cross damping is shown to be a component of the fluidic inertia effect; (c) the direct mass term is a component of the fluidic inertia effect; and (d) cross spring is a product of the direct damping, circumferential average velocity ratio, and rotative speed.

For a particular seal or bearing operated at low eccentricity at a particular rotative speed, with a specific fluid at a known temperature (for knowledge of viscosity), the results of the combination of a forward and reverse perturbation runs typically yield the direct dynamic stiffness and quadrature dynamic stiffness curves as shown in figure 1. Additionally, a steady-state load test can be used to better evaluate the stiffnesses at a zero perturbation (precession) frequency ($\omega=0$) [Ref. 2].

The general expressions of the fluid dynamic force components applied to the rotor with a coordinate system of +Y up and +X right and counterclockwise (X toward Y) rotation are



$$\begin{bmatrix} F_x \\ F_y \end{bmatrix} = \begin{bmatrix} K_{xx} & K_{xy} \\ -K_{yx} & K_{yy} \end{bmatrix} \begin{bmatrix} x \\ y \end{bmatrix} + \begin{bmatrix} D_{xx} & D_{xy} \\ -D_{yx} & D_{yy} \end{bmatrix} \begin{bmatrix} \dot{x} \\ \dot{y} \end{bmatrix} + \begin{bmatrix} M_x & 0 \\ 0 & M_y \end{bmatrix} \begin{bmatrix} \ddot{x} \\ \ddot{y} \end{bmatrix}$$

For sinusoidal isotropic (laterally symmetric) response, due to circular perturbation force \vec{F}_{pert} at frequency ω , the force balance relationship for a concentrically rotating shaft at the bearing or seal is as follows:

$$\bar{F}_{\text{pert } z} = [K_B - (\omega - \lambda\Omega)^2 M_{f1} + jD(\omega - \lambda\Omega) + K - M\omega^2 + jD_s\omega] \bar{z} \quad (1)$$

where:

$\bar{z} = x + jy$ is rotor lateral response vector at frequency ω .

$\bar{F}_{\text{pert } z}$ is the perturbation force vector of the sinusoidal circular nature:

K_B is the sum of the hydrodynamic plus the hydrostatic (externally pressurized) bearing/seal fluid film direct (radial) stiffness (the non-linear character of this term as a function of shaft eccentricity is a vital relationship for the rotor stability solution).

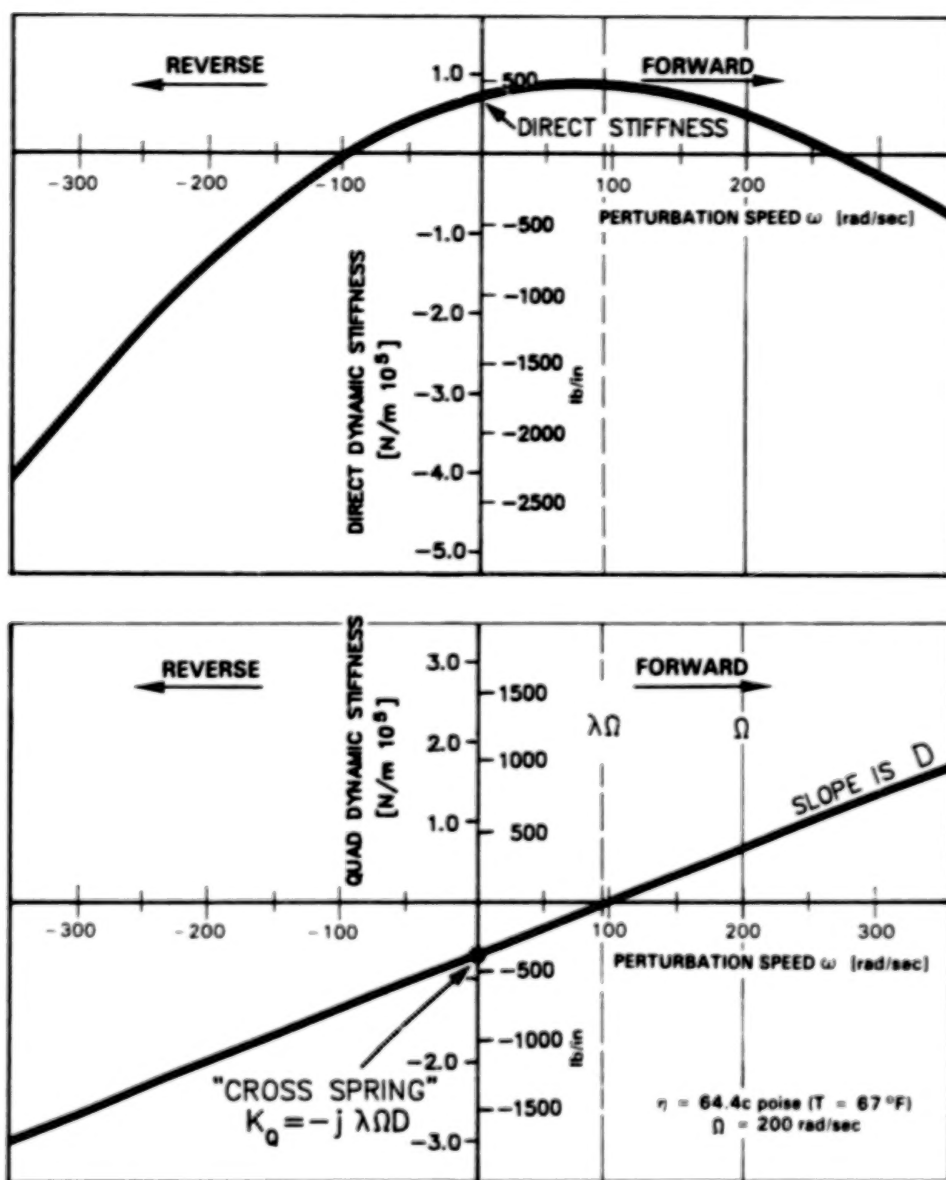


FIGURE 1 TYPICAL SEAL OR BEARING FLUID FILM DYNAMIC STIFFNESS PLOTS VERSUS PERTURBATION FREQUENCY FOR FORWARD AND REVERSE PERTURBATION. DIRECT DYNAMIC STIFFNESS CONTAINS STATIC RADIAL (DIRECT) STIFFNESS AND INERTIA TERMS. QUADRATURE DYNAMIC STIFFNESS CONTAINS RADIAL DAMPING AND "CROSS SPRING" TERMS (SHAFT DAMPING NEGLECTED).

j	is $\sqrt{-1}$.
ω	is sinusoidal perturbation frequency (+ for forward, - for reverse). Later, this same term means <u>also</u> rotor precession rate when instability (stable limit cycle, fluid-induced whirl or whip) occurs.
D	is fluid film direct (radial) damping.
λ	is the average circumferential component of fluid flow ratio to rotative speed in the seal, bearing, or rotor periphery. It is also the rate at which the fluid dynamic force rotates. It has been described in prior publications [Refs. 5-11]. Most authors assume that this rate is $1/2$ [Refs. 14-16]. The major change and improvement documented by the authors is that λ is not constant and, in particular, is a nonlinear, decreasing function of the shaft eccentricity.
Ω	is rotor rotative speed.
M_{f1}	is a synthetic expression with units of mass, called the fluidic inertia effect.
C	is bearing or seal radial clearance.
e	is bearing or seal eccentricity ratio $e= z /C$.
K, M, D_s	are rotor first lateral mode modal (generalized) stiffness, mass, and and external damping respectively.

From (1) the rotor system direct dynamic stiffness is as follows:

$$K_D = (F_{\text{pert}} z / |z|) (\cos \alpha) = K_B - (\omega - \lambda\Omega)^2 M_{f1} + K - M\omega^2$$

The quadrature dynamic stiffness is

$$K_Q = -(F_{\text{pert}} z / |z|) (\sin \alpha) = D(\omega - \lambda\Omega) + D_s \omega$$

where α is angle between the perturbation force and rotor response vectors.

Expanding the binominal terms of the fluidic inertia effect, it may be observed that the fluid-related dynamic stiffness elements are as follows:

(a) $K_{xx} = K_{yy} = K_B - \lambda^2 \Omega^2 M_{f1}$, so that the possibility of a "negative spring" exists, as is noted by the authors in prior reports [Refs. 1-5], and is well known to designers and researchers of squeeze film dampers.

(b) $D_{xy} = D_{yx} = +2\lambda\Omega\omega M_{f1}$. It is important to note that this term is positive in nature, as is being now reported by all researchers. This has been reported as a negative term in the 1950 to 1970 era.

(c) $K_{xy} = K_{yx} = \lambda\Omega D$. The "cross" spring is the stiffness of the fluid wedge support term which, as can be observed, is the product of the fluid average circumferential velocity $\lambda\Omega$, times the fluid direct damping D . It results from the rotative character of the fluid dynamic force [Refs. 5, 11, 14-16]. The term $\lambda\Omega D$ is the key of the rotor stability algorithm.

Two vital characteristics of the fluid inertia effect are

(1) The value of the fluidic inertia effect is zero when the precession speed $\omega = \lambda\Omega$. As most everyone knows, this corresponds, or is near, to one of the conditions of forward fluid-induced instability such as whirl. At the threshold of whirl, the fluidic inertia effect term is, therefore, quite ineffective.

(2) The fluidic inertia effect has the "ghost-like" characteristic because it disappears with increased shaft eccentricity following increasing radial load. Specifically, it is active only as long as circumferential flow is strong and the force from the "cross spring" term is dominant. This occurs at low through medium shaft eccentricities. At high eccentricities the circumferential flow is suppressed, yielding priority to secondary flows (axial and backward [Ref. 10]). At shaft high eccentricities the direct dynamic stiffness terms, mainly the hydrodynamic spring, become dominant and the fluidic inertia effect vanishes.

Due to these characteristics, the fluidic inertia has very little effect on stability threshold or the orbit amplitude and precessional frequency of whirl or whip limit cycles. Therefore, it will be neglected in the following analysis.

NONLINEAR CHARACTERISTICS OF BEARINGS AND SEALS

The next required relationships for determination of rotor stability are nonlinear expressions for the fluid film direct stiffness K_B versus shaft eccentricity, direct damping D versus eccentricity, and the fluid average circumferential flow velocity ratio λ versus eccentricity. It will soon be shown that the only vital nonlinearity affecting the size of whirl or whip limit cycle orbit (rotating eccentricity) is the direct stiffness term. Typical relationships are illustrated in figures 2, 3, and 4. The nonlinear functions of the eccentricity ratio which are taken into consideration are as follows:

$$K_B = \frac{K_{B0}}{(1 - e^2)^3} \quad , \quad K_{B0} = 4000 \text{ lb/in} \quad (2)$$

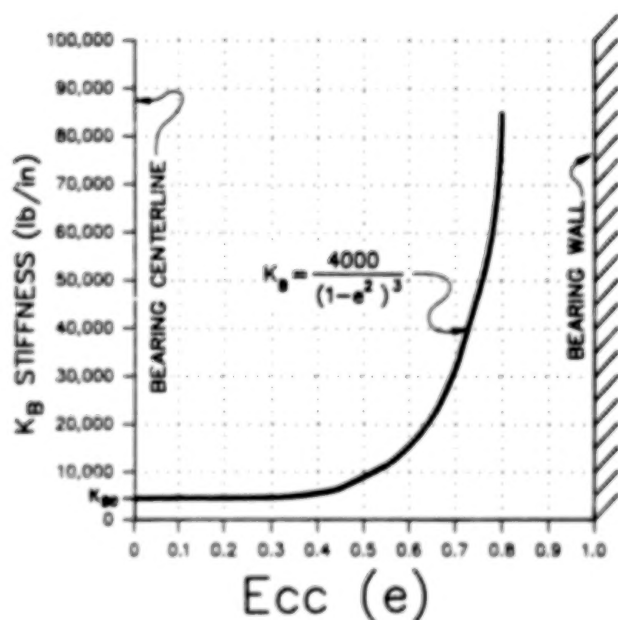


FIGURE 2 TYPICAL FLUID FILM DIRECT (RADIAL) STIFFNESS VERSUS SHAFT ECCENTRICITY RATIO.

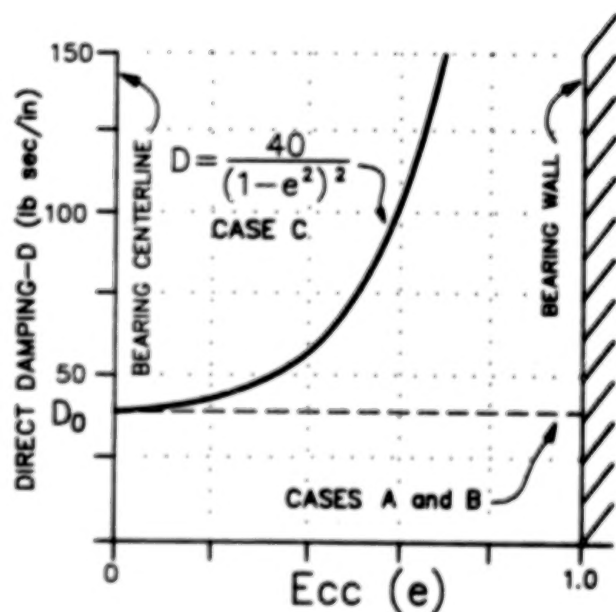


FIGURE 3 TYPICAL FLUID FILM DIRECT (RADIAL) DAMPING VERSUS SHAFT ECCENTRICITY RATIO.

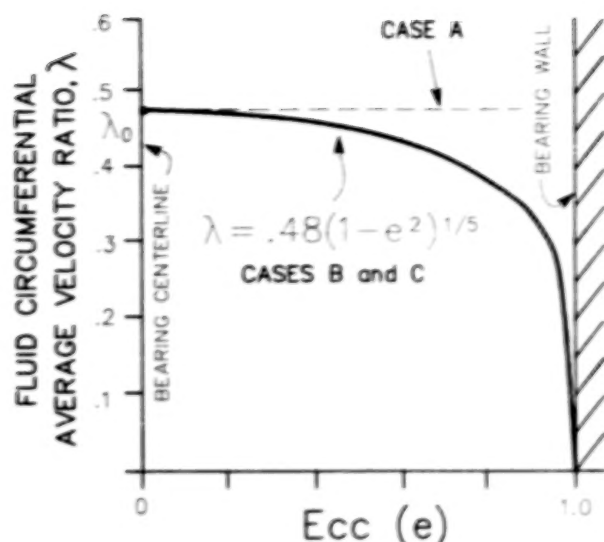


FIGURE 4 TYPICAL FLUID CIRCUMFERENTIAL AVERAGE VELOCITY RATIO VERSUS SHAFT ECCENTRICITY RATIO.

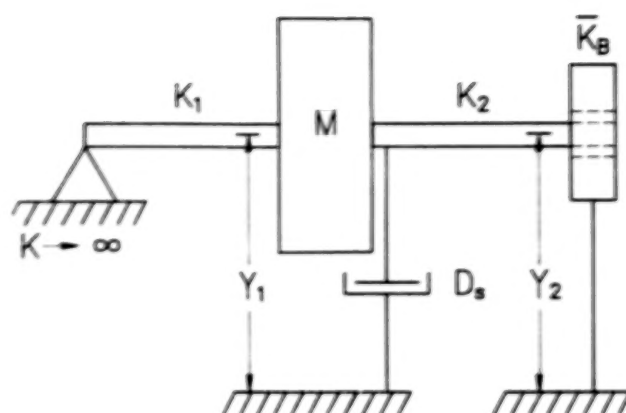


FIGURE 5 ROTOR/BEARING MODEL. THE SIMPLEST SYSTEM DEMONSTRATING WHIRL AND WHIP PHENOMENA.

$$D = \frac{D_0}{(1 - e^2)^2}, \quad D_0 = 40 \text{ lb sec/in} \quad (3)$$

$$\lambda = \lambda_0 (1 - e^2)^{1/5} \quad (4)$$

These functions qualitatively exemplify the bearing/seal parameter behavior. They are not locked into a specific bearing/seal geometry, dimensions, or Sommerfeld number. K_{B_0} , D_0 , and λ_0 are fluid film radial stiffness damping and circumferential velocity ratio at concentric shaft respectively.

The experimentally identified variation of λ with eccentricity ratio is noted in the prior reports [Refs. 7, 9, 11]. No clean laboratory test has been found for observation of λ at this time, but a few indirect measurements have been accomplished. More numerical/analytical calculations, such as in [Ref. 10], will also help to identify the values of λ as function of eccentricity and other parameters.

ROTOR/BEARING SYSTEM

The final set of equations for determination of stability is the equation of the rotor carrying bearing, seal, or other elements which provide the fluid. A simple rotor supported in one rigid and one fluid lubricated bearing is illustrated in figure 5.

The dynamic stiffness, K_{eq} , observed at the mass M of the rotor system in figure 5 is

$$K_{eq} = K_1 - \omega^2 M + j\omega D_s + \frac{\bar{K}_B K_2}{\bar{K}_B + K_2} \quad (5)$$

where \bar{K}_B is fluid film complex stiffness:

$$\bar{K}_B = K_B + jD(\omega - \lambda\Omega) \quad (6)$$

Thus:

$$K_{eq} = \frac{K_2(K_1 - \omega^2 M) + K_B(K_1 + K_2 - \omega^2 M) - D_s D(\omega - \lambda\Omega) + j[\omega D_s (K_2 + K_B) + D(\omega - \lambda\Omega)(K_1 + K_2 - \omega^2 M)]}{K_2 + K_B + jD(\omega - \lambda\Omega)} \quad (7)$$

In Eq. (7) K_1, K_2 are shaft partial modal stiffnesses (first bending mode); M is rotor modal mass; D_s is shaft modal external damping. Fluidic inertia effect is neglected. More formal analysis of this rotor/bearing system is in [Refs. 3 and 13].

ROTOR STABILITY ANALYSIS

From the standpoint of stability, the numerator of K_{eq} represents poles and the denominator represents zeros. Only those poles are of interest for stability. Further, since only a steady level of the instability limit cycle orbit, if it exists, is of interest, the exponentially increasing and the exponentially decreasing orbits (transient processes) are not discussed. This allows the direct and quadrature parts of the numerator of dynamic stiffness K_{eq} (the denominator of dynamic motions) to be separated and set to zero individually to find the stability roots. Another way to state this, is that the roots are evaluated at log decrement of zero. From control theory backgrounds, the root locus shown in figure 6 is solved only when the direct (real) parts of the roots are zero. The corresponding quadrature value is the precession rate, leading the system to the limit cycle of whirl or whip.

Liapounoff contributed strongly to the study of stability. One of his theorems noted in [Ref. 17] is

"Liapounoff's theorem states that under certain conditions which are frequently encountered in physical problems, the information obtained from the linear equations of the first approximation is sufficient to give a correct answer to the question of stability of the nonlinear system."

Restated, the linear portions of the direct and quadrature stiffness K_{eq} solved for their roots yield the answer to the first problem of stability. Once the question of stability is decided, the next step is to evaluate the amplitude of the limit cycle orbit and rotor precession speed as a function of the nonlinear characteristics.

The direct and quadrature components of Eq. (7) are equalized to zero and solved for K_B and Ω so that

$$K_B = \frac{-K_2(K_1 - \omega^2 M)(K_1 + K_2 - \omega^2 M) - \omega^2 D_s^2 K_2}{(K_1 + K_2 - \omega^2 M)^2 + \omega^2 D_s^2} \quad (8)$$

and

$$\Omega = \frac{\omega}{\lambda} \left[1 + \frac{D_s K_2^2}{D[(K_1 + K_2 - \omega^2 M)^2 + \omega^2 D_s^2]} \right] \quad (9)$$

The right-hand side expression of Eq. (8) for various precession rates, omitting the minor terms with D_s , is illustrated in figure 7.

EXAMPLES

In order to plot the precession speed ω against the rotative speed Ω for a particular case, it is necessary to choose values and functional relationships for the various rotor system parameters. The most simple process of solving the problem is to step the eccentricity ratio "e" gradually from 0 to about 0.9. For each eccentricity the values of K_B , D , and λ are calculated from appropriate equations such as Eqs. (2), (3), (4). Eq. (8) is then solved for the precession ω associated with corresponding eccentricity ratio e. Finally, for each rotative speed Ω , the size of the limit cycle whirl/whip orbit eC (where C is bearing or seal radial clearance), and the speed of precession ω , are all established.

As an example, for CASE A the nonlinear terms are stated as follows:

$$K_B = \frac{K_{B0}}{(1-e^2)^3}, \quad K_{B0} = 4000 \text{ lb/in (fluid film radial stiffness at concentric shaft)} \quad (10)$$

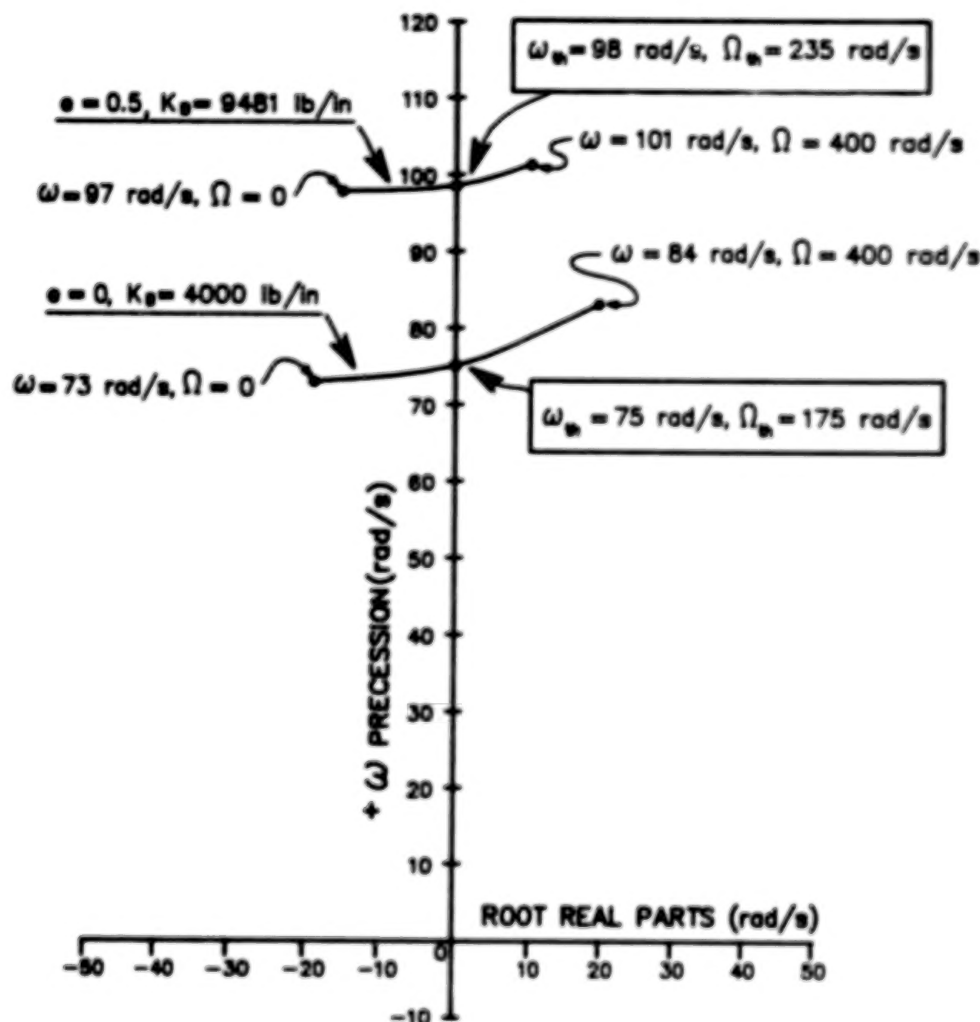


FIGURE 6 EXAMPLE OF ROOT LOCUS OF THE WHIRL/WHIP ROOT (ω_{th} IS THRESHOLD OF STABILITY).

$$D = D_0 = 40 \text{ lb sec/in (constant for this case)} \quad (11)$$

$$\lambda = \lambda_0 = 0.48 \text{ (constant for this case)} \quad (12)$$

The remaining parameters are chosen as

$$\begin{aligned} K_1 &= 2000 \text{ lb/in} & M &= 1.0 \text{ lb sec}^2/\text{in} \\ K_2 &= 38000 \text{ lb/in} & D_s &= 4.0 \text{ lb sec/in} \end{aligned} \quad (13)$$

The graph of the precession frequency of the whirl and whip against the rotative speed is shown in figure 8. This figure also shows the whirl and the whip ranges, and the smooth transition region between whirl and whip. It also shows a few corresponding whirl and whip orbits at the bearing (or seal) with their magnitude and frequency, as well as the stability threshold and asymptotic frequency.

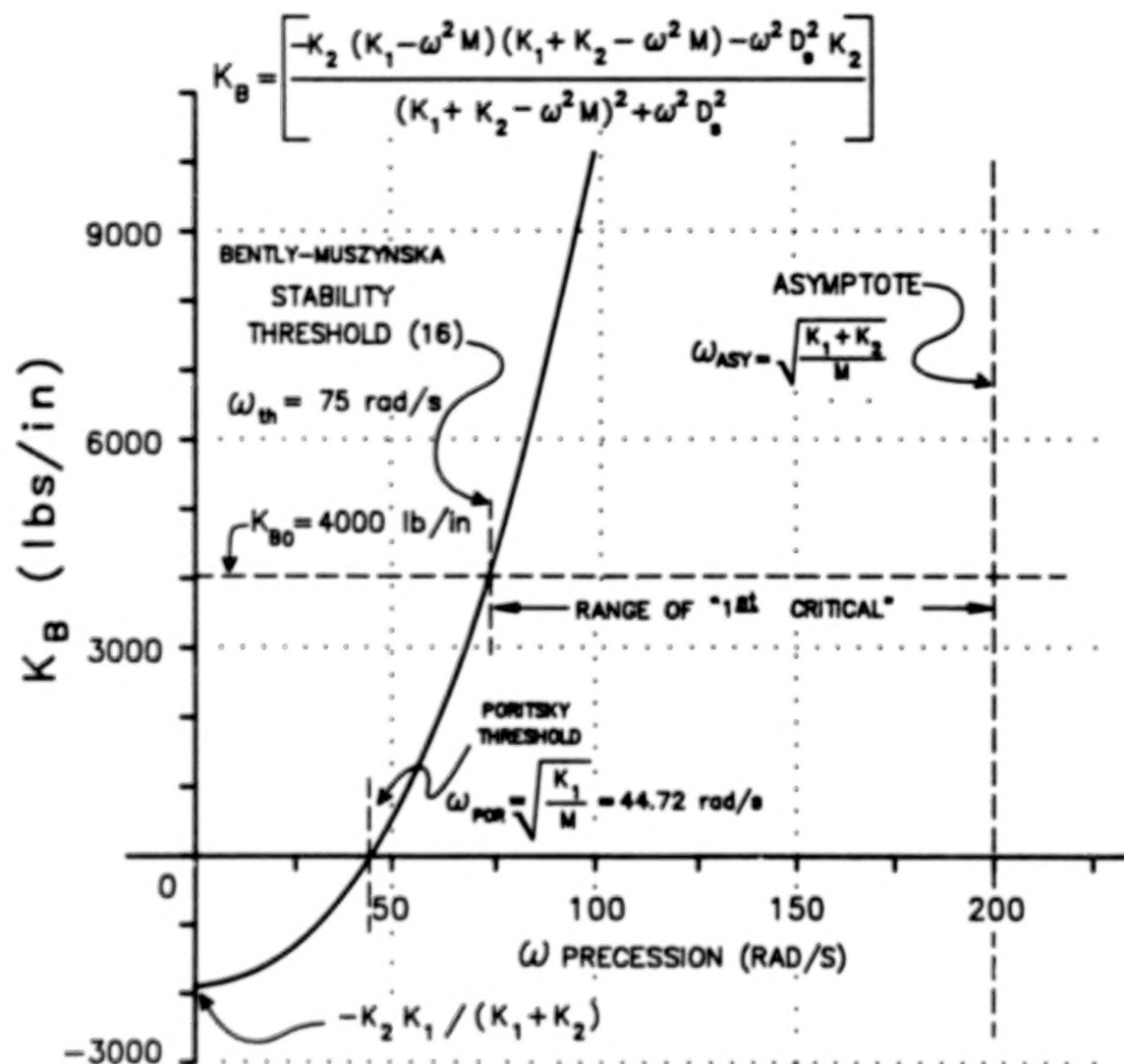


FIGURE 7 RIGHT-HAND SIDE EXPRESSION OF EQUATION (8) VERSUS PRECESSION RATE. EQUATIONS (10) TO (13) INDICATE VALUES OF PARAMETERS USED IN THIS EXAMPLE.

Figure 8 also illustrates the result of CASE B, where λ is no longer considered constant, but $\lambda = 0.48 (1-e^2)^{1/5}$. The result is virtually the same as CASE A, with constant λ .

For CASE C, damping is no longer constant but equals $D = \frac{40}{(1-e^2)^2}$. It may be noted in figure 8 that the whirl/whip frequency of CASE C is much more like practically observed behavior, much closer to the asymptotic frequency, which is natural, because damping is always a nonlinear term.

From Eq. (9) the ratio of the precession rate ω to rotative speed rate Ω is an intrinsic function of ω :

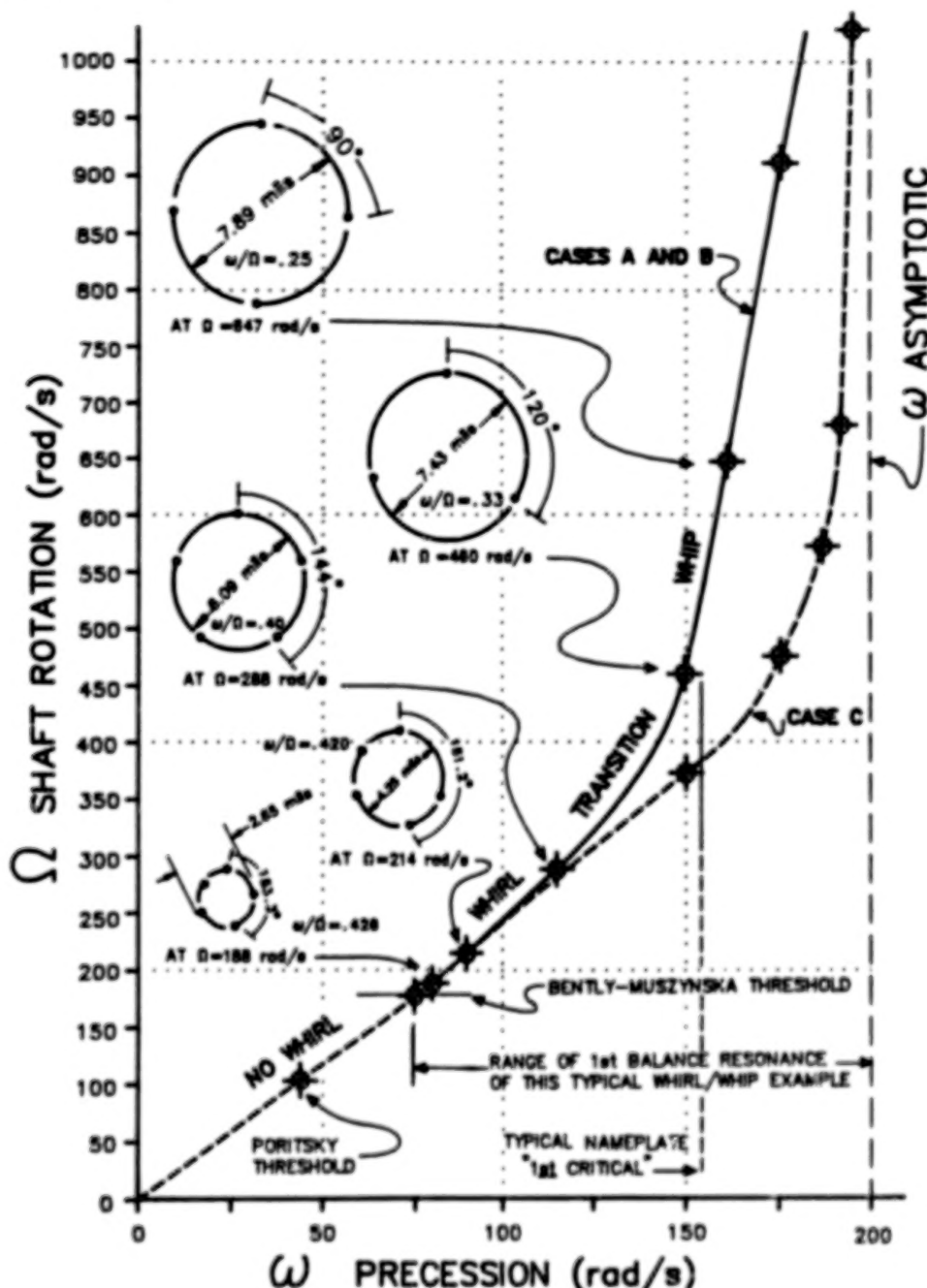


FIGURE 8 ROTATIVE SPEED VERSUS WHIRL/WHIP PRECESSION FREQUENCY FOR THE ROTOR ILLUSTRATED IN FIG. 1 ($C = 5$ MILS, SHAFT CENTERED). WHIRL/WHIP ORBITS.

$$\frac{\omega}{\Omega} = (\lambda) \left[\frac{1}{D_s K_2^2} \right] \left[1 + \frac{D[(K_1 + K_2 - \omega^2 M)^2 + \omega^2 D^2]}{D_s K_2^2} \right] \quad (14)$$

The shaft damping D_s has a fair amount of control over the actual precession frequency ω to rotative speed Ω as shown in Eq. (14), but has very little control over the right-hand side expression in Eq. (8). Therefore, dropping shaft damping D_s from Equation (8) and solving the equation for precession rate ω yields

$$\omega \approx \left[\frac{K_1 K_2 + K_B (K_1 + K_2)}{(K_B + K_2) M} \right]^{1/2} \quad (15)$$

The lowest precession rate ω_{th} that the whirl or whip can have, is at the minimum K_B , which is at K_{B0} for the case of the shaft centered in the seal or bearing considered in this paper. Therefore, in terms of precession frequency ω , the threshold of stability is

$$\omega_{th} \approx \left[\frac{K_1 K_2 + K_{B0} (K_1 + K_2)}{(K_{B0} + K_2) M} \right]^{1/2} \quad (16)$$

Poritsky [Ref. 18] nearly had this threshold more than thirty years ago. He showed the rotative speed whirl threshold at $2\sqrt{K_1/M}$. That is excellent for that time. Note that if bearing stiffness $K_B = 0$, shaft damping $D_s = 0$, and $\lambda_0 = 1/2$ and thus $\Omega = 2\omega$, it would be right on. His paper apparently was subjected to very heavy criticism, so his excellent work was not pursued. The authors privately call the zero bearing stiffness threshold the "Poritsky threshold." It is useful to observe that if the outboard shaft stiffness K_1 (the portion of shaft away from the fluid lubricated bearing) becomes very soft (approaches zero), whirling may occur at extremely low rotative speeds. The authors demonstrated a laboratory model with this phenomenon for several years before fully understanding its rules of behavior.

The asymptotic frequency ω_{ASY} occurs as rotative speed increases so that the shaft orbit takes up most of the clearance, and eccentricity ratio e approaches 1. The limit occurs not with nonlinear terms λ or D , but with bearing stiffness K_B which goes to extremely high values at high eccentricity so that for Eq. (15)

$$\omega_{ASY} = \omega|_{e \rightarrow 1} = \sqrt{(K_1 + K_2)/M} \quad (17)$$

It should be noted that shaft damping D_s was assumed to be 0 for Eq. (15). If shaft damping D_s is high enough, it is possible for the rotor system to escape whipping as shown in [Refs. 12 and 13]. Virtually most documented cases from actual machinery, however, exhibit the asymptotic behavior.

OBSERVATIONS AND CONCLUSIONS

There are numerous straightforward observations available from these stability algorithms.

First, while the "criticals" of machinery are often posted on the nameplate as a fixed frequency, it is obvious that they vary widely due to the nonlinear stiffness of fluid film in bearings and seals. The whirl/whip root of Eq. (8) shows clearly that the resonance ("critical") varies from the threshold to the asymptotic frequency ω_{ASY} as a function of the nonlinear stiffness K_B . In the examples shown, it varies from the threshold of 75 rad/sec (716 rpm) to the asymptotic frequency of 200 rad/sec (1909 rpm) (Figure 8). This fact will probably be met with considerable disbelief, until the nature of the fluid-induced whirl and whip instabilities become more widely understood.

Since both of the quadrature dynamic stiffness elements contain the direct damping term: $K_Q = \omega D - \lambda \Omega D$ the magnitude of the direct damping D has very little effect on stability for rotors operating at low eccentricity. This means that large direct damping D does not create stability.

Direct damping D is well known to be a function of bearing or seal geometry and physical dimensions. It also varies directly with lubricant viscosity η . However, it is not the viscosity in direct damping D which influences stability. It is the influence of viscosity in the hydrodynamic, as well as the hydrostatic (externally pressurized) portions of the bearing or seal stiffness term K_B that exhibits influence on stability.

It is already known that antiscirling mechanisms which suppress the strength of circumferential flow and drive the fluid average circumferential velocity ratio λ as nearly as possible to zero are the proper prevention of fluid-induced whirl and whip [Ref. 6].

Reasonably well known is that forward preswirling of the fluid will drive the precession to rotation ratio to higher values [Ref. 6], sometimes well above half rotative speed. A report on a pump [Ref. 19] with a whirl which tracked about 80% of rotative speed was presented recently. Another verbal report [Ref. 20] on a double volute pump on an offshore platform noted a whirl which tracked 75% of rotative speed. A double driven generator connected by hydraulic clutches with two gas turbines exhibited subsynchronous vibrations with frequency 82.5% to 89.7% of the rotative speed when the clutches were not entirely engaged [Ref. 21]. An "inside-out" bearing with a hollow shaft rotating around a stationary post, will produce λ of slightly over 1/2 [Ref. 22].

The pump with seal whirl [Ref. 19] was most unusual, because nearly all rotor/seal systems exhibit whip only. With good probability, this is because there is a much softer spring K_1 in that pump. Usually when the seal is involved, the stiffness K_1 is much higher. It may be noted in the discussed example that an increase of the magnitude of K_1 leads to the increase of the inception threshold of stability.

It is reasonably well known that any force which moves the rotor to high dynamic eccentricity, thus raising bearing or seal stiffness, can prevent whirl or whip. This action and the stability thresholds due to the unbalance force excitation were previously published [Ref. 3].

It is also well known that steady-state sideload forces, which move the rotor to static high eccentricity in the seal or bearing, are a palliative for fluid-induced instability. Newkirk [Ref. 23] made the first pressure dam bearing for that purpose in 1934. Deliberate sideloads (often by gravity for horizontal rotors) is a very popular "fix" for stability.

Two errors of first magnitude correlated to steady-state sideloads occur. The first is the rule that "the heavier the rotor, the better the stability," which has been published (and apparently believed) for over 30 years. As can be observed from the stability algorithms, the more the rotor mass, the worse the stability for the shaft-centered case. However, since the rule surely was meant to apply to horizontal rotors in the gravity of earth, having more mass means more weight, resulting in higher eccentricity, and thus higher K_B , yielding the better stability. (This assumes no other steady-state sideload forces, such as caused by misalignment, which adds or subtracts from the gravity load.) Two stabilizing and destabilizing factors, namely the weight-related preload and the added mass, are both very effective, so that which factor wins depends upon the particular conditions in each particular case. A formula for stability that utilizes clearance and rotor weight should be carefully avoided, no matter how popular it has been.

The second big problem of a steady-state sideload application occurs when the rotor is stacked (not integral), consisting of shrink-on wheels or, especially, when the rotor is bolted together (known as a shish ke-bab design). The bowing resulting from the steady sideloads strongly activates the hysteretic internal friction. Thus, attempts to sideload the rotor may help reduce the fluid-induced instability by raising K_B , but get the rotor into an even worse problem of hysteretic friction instability, plus possible rotor-to-stator rubs.

There exists another rule which is incorrectly applied by rotating machinery users. It states: "For stability maintain oil pressure low." This rule generally holds true when the bearing has a partial fluid film (180 degrees as opposed to 360 degrees lubrication). As long as the partial film is maintained, a regular circumferential flow pattern is not established so that stability is assured. To maintain partial lubrication, the pressure should be kept low; otherwise the bearing becomes fully lubricated with stronger circumferential flow, which makes the rotor susceptible to instability. The rule, "Keep oil pressure low," became however, universal, and thus often incorrectly applied. Experimental evidences, as well as the conclusions from the stability algorithm discussed in this paper, show clearly that fluid higher pressure, which directly increases the fluid film radial stiffness K_B , improves rotor stability.

An interesting sidelight is that with the discussed stability algorithm it is simple to get some idea of how much torque is developed by the whirl/whip instability action. With a shaft radius R , and whirl or whip orbit radius eC :

Wedge Stiffness	$\lambda \Omega D$	lb in	Whirl/Whip Torque	$\lambda \Omega D e C R$	lb in
Tangential Force	$\lambda \Omega D e C$	lbs	Whirl/Whip Power Loss	$\lambda \Omega D e C R \omega$	lb in/sec

For $\lambda = 0.5$, $\Omega = 250$ rad/sec, $D = 40$ lb sec/in, $e = 0.5$, $C = 0.01$ inch, and $R = 10$ inches, the whirl/whip torque is 250 lb/in, and the power loss at precession frequency 124 rad/s is 31000 lb in/sec.

Finally, the fluid dynamic force relationships discussed in this paper can successfully be used in modelling more complex rotor/bearing/seal systems [Refs. 9,12, 13,22]. The model predicts existence of several whirl/whip regimes and explains

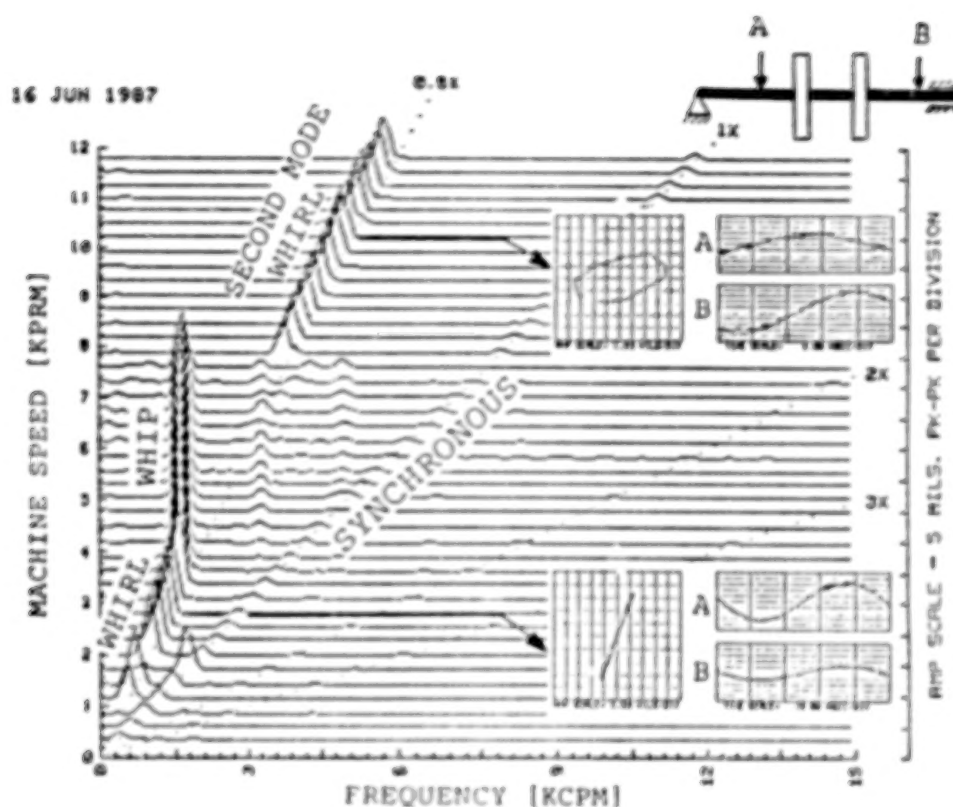


FIGURE 9 SPECTRUM CASCADE OF THE ROTOR VIBRATIONAL RESPONSE DURING START-UP, MEASURED BY THE PROXIMITY TRANSDUCER "B." THE PLOT SHOWS A "JUMP" OF SELF-EXCITED VIBRATIONS FROM WHIP MODE TO THE SECOND MODE WHIRL (JUMP IN AMPLITUDE AND FREQUENCY). THE SKETCH INDICATES TRANSDUCER LOCATIONS. OSCILLOSCOPE IN ORBITAL MODE FOR SIGNALS FROM TRANSDUCERS A AND B DISPLAYS THAT SHAFT AT LOW SPEED WHIRL VIBRATES IN PHASE. AT HIGH SPEED WHIRL SHAFT VIBRATES AT ITS SECOND MODE (RIGHT- AND LEFT-HAND SIDE SHAFT SECTIONS ARE 90 DEGREES OUT OF PHASE).

the "jump" phenomenon observed on laboratory rigs and shown in figure 9, as well as in reported field data (figure 10).

The role of the fluid circumferential flow in rotor stability is emphasized. The fluid average circumferential velocity ratio is the key factor of the "cross spring" term, which, in turn, represents a portion of the quadrature dynamic stiffness: $K_Q = D(\omega - \lambda\Omega)$. The value $\lambda\Omega$ used to be referred to as "bearing resonance" across half a century. While this resonance is hidden in synchronous perturbation tests, it is clearly exposed by nonsynchronous perturbation testing [Ref. 1-5]. An increase of the circumferential flow strength leads to an increase of λ , thus a decrease of the quadrature stiffness of the system. When at the same frequency both K_Q and direct dynamic stiffness K_D equal zero, the instability occurs. This was shown on the root locus of figure 6. The quadrature dynamic stiffness, combined with the nonlinear bearing (or seal) stiffness in the rotor system equation, provides the reliable stability prediction formulas.

REFERENCES

1. Bently, D. E., Muszynska, A., Perturbation Study of Rotor/Bearing System: Identification of the Oil Whirl and Oil Whip Resonances. Tenth Biennial ASME Design Engineering Division Conference on Mechanical Vibration and Noise, 85-DET-142, Cincinnati, Ohio, September 1985.

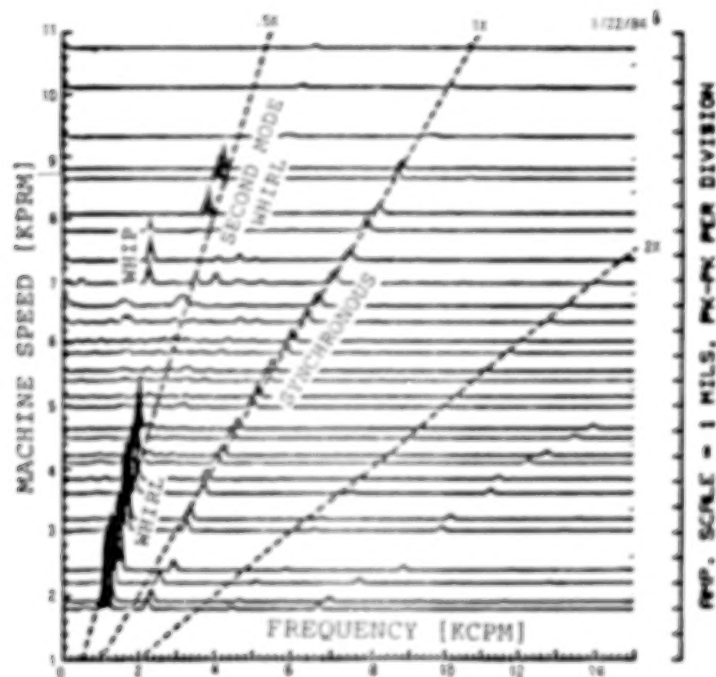


FIGURE 10 SPECTRUM CASCADE OF VIBRATION RESPONSE OF A STEAM TURBINE DRIVEN COMPRESSOR. THE PLOT INDICATES THE WHIRL, WHIP, AND SECOND MODE WHIRL. COURTESY OF C. JACKSON.

2. Bently, D. E., Muszynska, A., Identification of Bearing and Seal Dynamic Stiffness Parameters by Steady-State Load and Squeeze Film Tests. Proc. of BRDRC Symposium on Instability in Rotating Machinery, Carson City, Nevada, NASA Conf. Publ. 2409, 1985.
3. Muszynska, A., Whirl and Whip -- Rotor/Bearing Stability Problems. Journal of Sound and Vibration, Vol. 110, No. 3, 1986.
4. Bently, D. E., Muszynska, A., Modal Testing and Parameter Identification of Rotating Shaft/Fluid Lubricated Bearing System, 4th International Modal Analysis Conference Proceedings, Los Angeles, California, February 1986.
5. Muszynska, A., Modal Testing of Rotor/Bearing Systems, International Journal of Analytical and Experimental Modal Analysis, July 1986.
6. Bently, D. E., Muszynska, A., Anti-Swirl Arrangements Prevent Rotor/Seal Instability. Thermo-Fluid Dynamics of Rotating Machinery. Proc. of 2nd ASME-JSME Thermal Engine Conference. Honolulu, Hawaii, March 1987.
7. Bently, D. E., Fluid Average Circumferential Velocity Ratio a Key Factor in Rotor/Bearing/Seal Models. Orbit, BNC, Vol. 8, No. 1, February 1987.
8. Muszynska, A., Tracking the Mystery of Oil Whirl. Sound and Vibration, February 1987.
9. Muszynska, A., Improvements in Lightly Loaded Rotor/Bearing and Rotor/Seal Models. Rotating Machinery Dynamics. ASME Publ. #H0400A, 11th Biennial ASME

Design Engineering Division Conference on Vibration and Noise, Boston, Massachusetts, September 1987.

10. Tam, L. T., Przekwas, A. J., Muszynska, A., Hendricks, R. C., Braun, M. J., Mullen, R. L., Numerical and Analytical Study of Fluid Dynamic Forces in Seals and Bearings. Rotating Machinery Dynamics, ASME Publ. #H0400B, 11th Biennial ASME Design Engng. Div. Conf. on Vibration and Noise, Boston, Massachusetts, September 1987.
11. Muszynska, A., Fluid-Related Rotor/Bearing/Seal Instability Problems. Bently Rotor Dynamics Research Corporation Report, 1986.
12. Muszynska, A., Multi-Mode Whirl and Whip in Rotor/Bearing Systems. Proc. of the 2nd International Symposium on Transport Phenomena, Dynamics, and Design of Rotating Machinery, Honolulu, Hawaii, April 1988.
13. Muszynska, A., Stability of Whirl and Whip in Rotor/Bearing Systems. Journal of Sound and Vibration, to appear.
14. Bolotin, V. V., Nonconservative Problems in Elastic Stability Theory (in Russian), Gos. Isd. Fiz. Mat. Lit, Moskva, 1961.
15. Black, H. F., Effects of Hydraulic Forces in Annular Pressure Seals on the Vibrations of Centrifugal Pump Rotors. Journal of Mechanical Engineering Science, Vol. II, No. 2, 1969.
16. Black, H. F., Jensen, D. N., Dynamic Hybrid Bearing Characteristics of Annular Controlled Leakage Seals. Proceedings Journal of Mechanical Engineering, Vol. 184, 1970.
17. Minorsky, N., Introduction to Non-Linear Mechanics. Edwards, Y. W., Ann Arbor, 1947.
18. Poritsky, H., Contributions to the Theory of Oil Whip. Trans. ASME, Vol. 75, No. 6, 1953.
19. Massey, I., Subsynchronous Vibration Problems in High-Speed, Multistage Centrifugal Pumps, 14th Texas A&M Turbomachinery Symposium, 1985.
20. Ryan, T., Phillips Petroleum, Private Communications.
21. Franklin, D. E., Van Horne, J. C., Dynamic Analyses of an Over-Running Clutch Vibration Problem on a Gas Turbine Generator Set. Proc. of the Eighth Machinery Dynamics Seminar, NRC Canada, Halifax, Nova Scotia, 1984.
22. Muszynska, A., Bently, D. E., The Role of the Circumferential Flow in Rotor/Bearing/Seal System Stability. Sixth Annual ROMAC Vibration Short Course, 1988.
23. Newkirk, B. L., Grobel, L. P., Oil-Film Whirl--A Non-Whirling Bearing, APM-56-10, 1934.

ENHANCED ROTOR MODELING TAILORED FOR RUB DYNAMIC

STABILITY ANALYSIS AND SIMULATION*

R.R. Davis
Aerojet TechSystems Company
P.O. Box 13222
Sacramento, California 95813, U.S.A.

New methods are presented that allow straightforward application of complex nonlinearities to finite element based rotor dynamic analyses. The key features are 1) the methods can be implemented with existing finite element or dynamic simulation programs, 2) formulation is general for simple application to a wide range of problems, and 3) implementation is simplified because nonlinear aspects are separated from the linear part of the model. The new techniques are illustrated with examples of inertial nonlinearity and torquewhirl which can be important in rubbing turbomachinery. The sample analyses provide new understanding of these nonlinearities which are discussed.

INTRODUCTION

The modeling and simulation of rotordynamic systems with rubbing is generally avoided in the design verification of turbomachinery, but is receiving more attention because rubbing is becoming unavoidable in close tolerance designs. Some understanding of general rub behavior has been developed over the years using simplistic Jeffcot models and various techniques. Ehrich [1] determined stability bounds for full annular rub of a Jeffcot model with a circular but flexibly supported stator using a limit cycle assumption and dynamic equilibrium. A number of analyses such as those by Childs [2] and Muszynska [3] have treated the Jeffcot model with piecewise linear transient analysis or linearized analysis based on harmonic balance methods. The results are enlightening, but cannot be extended to complex systems without significant difficulty.

Much work has been recently done to apply harmonic balance methods to more general systems. The work of Lau, Cheung, and Wu [4] is most notable because it treats aperiodic response by including multiple time scales in the assumed harmonic components. Unfortunately, all harmonic balance and related schemes suffer the debilitating requirement that the response frequency content or some fundamental response ratio be known a priori. Thus, one cannot analyze a given system for general response.

The other remaining option is nonlinear transient simulation. Flexibility in modeling is achieved at the expense of computing time. However, with recent developments in computing power and well known methods of modal synthesis and model reduction, nonlinear transient simulation of real rotor systems is now a reasonable approach. Kascak [5] and Kascak and Tomko [6] have done some of the few analyses documented of transient rubbing with more complex rotors. Padovan and Choy [7] have more recently addressed the Jeffcot model with transient rub simulation, but with the added complexity of turbine blades modeled by static stiffnesses. These analyses have interesting approaches, but their application to general models is not discussed.

General approaches to rotordynamic nonlinear problems are lacking. It is the intent of this work to show how nonlinear effects important in rubbing can be included in analysis of completely general rotor/housing systems with minimal effort, using generally available software augmented by relatively simple user-defined modules. By way of examples, it will be shown that the new techniques can be used to model nonlinearities of high complexity without major reformulation of a problem by exploiting the separability of linear and

*This work was supported by Company IR&D funding at Aerojet TechSystems Company, Sacramento, California, project number NLRDA6, and is approved for public release.

nonlinear parts. The result is highly productive nonlinear analysis that is modular in nature, and thus easier to perform for the average rotor design analyst. Method formulation and examples will address the specific effects of inertial nonlinearity and torque, which invariably occur in rubbing rotordynamic systems. Incorporating general rub laws with flexible rotor blades and disks will be addressed in a later paper.

NOMENCLATURE

A	:	Dynamical matrix
B	:	Load weighting matrix
c_X, c_Y	:	Bearing damping (N sec/m)
C	:	Linear system damping matrix
C_L	:	Load torque coefficient (N m sec/rad)
f	:	System loads (physical and modal)
F	:	System loads (physical only)
F_X, F_Y, F_Z	:	Forces on body in Cartesian system (N)
I	:	Identity matrix
I	:	Polar moment of inertia (kg m ²)
I_0	:	Transverse moment of inertia (kg m ²)
k_X, k_Y	:	Bearing stiffness (N/m)
K	:	Linear system stiffness matrix
K_A	:	Asymmetric effects matrix (physical only)
K'_A	:	Asymmetric effects matrix (physical and modal)
$K(T)$:	Rotor stiffness matrix with steady torque T
K_{TOT}	:	Rotor stiffness matrix, total
L	:	Shaft length (m)
m	:	Disk mass (kg)
M	:	Linear system mass matrix
M_X, M_Y, M_Z	:	Moments on body in Euler system (N m)
M_X, M_Y, M_Z	:	Moments on body in Cartesian system (N m)
0	:	Null matrix
q	:	System displacements (physical and modal)
R	:	Disk radius (m)
s	:	Speed
T	:	Torque vector
T	:	Torque, transient or constant (N m)
T_0	:	Steady torque (N m)
x	:	System displacements (physical only)
x, y, z	:	Body fixed, except spin, coordinates
X, Y, Z	:	Cartesian translations (m)
y	:	First order states
Φ	:	Pseudo-modal matrix
ΔT^+	:	Incremental torque >T (N m)
ΔT^-	:	Incremental torque <T (N m)
$\theta_X, \theta_Y, \theta_Z$:	Cartesian rotations (rad)
ϕ, θ, ψ	:	Euler angles (rad)
K	:	Rotor stiffness gradient matrix
(\cdot)	:	Time derivative
$()^T$:	Transpose

THE GENERAL FINITE ELEMENT BASED APPROACH

Today, every turbomachinery design organization has available to it a finite element analysis software tool. Rotordynamic analysis should exploit this capability to the fullest. Rotor, housing, disk, and blade models can be constructed using powerful solids modelers. The finite element models can be reduced by linear modal analysis or substructuring. Such a reduced matrix model, in the form of linear and symmetric mass, damping, and stiffness matrices, is an excellent base for nonlinear simulation.

To continue with general rotor analysis, one must have complex eigenanalysis and nonlinear transient capability, which is generally available. For some, the finite element program may have this capability, while for others, one may have a dynamic simulation program (ACSL, CSMP, or others) with these options. It is a simple matter to format the matrix data between a finite element program output and a simulation program.

It is assumed that the linear model includes flexibility and mass distribution for rotor, housing, disks, blades or other subcomponents, and possibly linear symmetric bearing or seal models. The entire system is described by the linear equations of motion.

$$\mathbf{M} \ddot{\mathbf{q}} + \mathbf{C} \dot{\mathbf{q}} + \mathbf{K} \mathbf{q} = \mathbf{f} \quad (1)$$

where the subcomponents may or may not be connected. Disconnection results in block diagonal form of the matrices. The displacements \mathbf{q} consist of independent sets of physical or modal degrees of freedom (DOFs) for each unconnected subcomponent. Since physical motions are preferred for applying nonlinearities, any modal coordinates may require conversion to the physical domain using user-prepared pseudo-modal transformations

$$\mathbf{x} = \Phi \mathbf{q} \quad (2)$$

$$\dot{\mathbf{x}} = \Phi \dot{\mathbf{q}} \quad (3)$$

where \mathbf{x} is the full physical degree of freedom set, a different size than \mathbf{q} . Φ contains some identity matrix block diagonals for subcomponents described by physical degrees of freedom, and other block diagonals that are made up of mode shape coefficients. Matrix partitioning is specifically avoided here to maintain generality of the ordering of \mathbf{q} . The physical forces are subject to the pseudo-modal transformation as well,

$$\mathbf{f} = \Phi^T \mathbf{F} \quad (4)$$

The modal transformation can be implemented by the use of linear constraint equations, which are available in most finite element programs, or by manual coding within the nonlinear evaluation routines that will be used later. Note that only the physical DOFs to be used for evaluating or applying nonlinear loads need be treated.

Several simplifications have been made in the foregoing to make preparation of the linear core model straightforward. The assumption of linearity and matrix symmetry along with an assumption of modes computed by undamped analysis ensures real and equal left and right eigenvectors, and thus the same real matrix Φ in all auxiliary equations. This technique is popular and has been used by Noah [8] among others.

Given the linear core model, asymmetric linear effects can now be added directly to \mathbf{M} , \mathbf{C} , and \mathbf{K} matrices. Examples are linear models of Alford forces, gyroscopics, and bearing, seal, or impeller cross-coupling. When modes are used, some physical asymmetric effects may require the modal transformation if they act at physical DOFs that depend on modes. For example, for stiffness,

$$\mathbf{K}'_A = \Phi^T \mathbf{K}_A \Phi \quad (5)$$

where the asymmetric fully physical matrix is \mathbf{K}_A , and the corresponding physical/modal counterpart is \mathbf{K}'_A . \mathbf{K}'_A can then be added directly to the original symmetric stiffness matrix.

In the interest of generality, the linear model can be cast in first order form if required for compatibility with available software such as dynamic simulation packages. This form is

$$\dot{\mathbf{y}} = \mathbf{A} \mathbf{y} + \mathbf{B} \mathbf{f} \quad (6)$$

where

$$\mathbf{y} = \begin{bmatrix} \mathbf{q} \\ \dot{\mathbf{q}} \end{bmatrix}, \quad \mathbf{A} = \begin{bmatrix} \mathbf{0} & \mathbf{I} \\ -\mathbf{M}^{-1}\mathbf{K} & -\mathbf{M}^{-1}\mathbf{C} \end{bmatrix}, \quad \mathbf{B} = \begin{bmatrix} \mathbf{0} \\ \mathbf{M}^{-1} \end{bmatrix} \quad (7)$$

and the auxiliary equations if modal coordinates are used are equations (2), (3) and (4). \mathbf{M}^{-1} will always exist as long as the DOFs of the linear model are independent and the problem is well posed.

Arbitrary nonlinear forces can be applied via the physical loads \mathbf{F} and can be calculated using any state variable in \mathbf{x} , $\dot{\mathbf{x}}$, \mathbf{q} , $\dot{\mathbf{q}}$ or any externally defined variable such as time, rotational speed, temperature, or pressure. The states are directly available from integration of equation (1) or (6) provided by the analysis code used and application of equations (2) and (3). Loads returning to the linear core simulation may need conversion through equation (4).

As a prelude to the development of specific nonlinear force formulations, consider that all linear modeling has been done in an inertial Cartesian coordinate system. Possible DOFs are translations X, Y, Z and right-handed rotations $\theta_X, \theta_Y, \theta_Z$.

INERTIAL NONLINEARITY

The Moment Equations

The general equations of motion of a massive rigid body in space are extremely nonlinear in form. Even for the typical case of a rotor disk, where we may assume axial inertia $I_{ZZ} = I$, transverse inertia $I_{XX} = I_{YY} = I_0$, and all products of inertia are zero, we obtain the moment equations

$$\begin{bmatrix} M_x \\ M_y \\ M_z \end{bmatrix} = \begin{bmatrix} I_0 (\ddot{\theta} - \dot{\phi}^2 \sin\theta \cos\theta) + I\dot{\phi}(\dot{\phi} \cos\phi + \dot{\psi}) \sin\theta \\ I_0 (\ddot{\phi} \sin\theta + 2\dot{\phi}\dot{\theta} \cos\theta) - I\dot{\theta}(\dot{\phi} \cos\theta + \dot{\psi}) \\ I (\ddot{\phi} \cos\theta - \dot{\phi}\dot{\theta} \sin\theta + \ddot{\psi}) \end{bmatrix} \quad (8)$$

which are written using Euler angles precession ϕ , nutation θ , and spin ψ , and the axes x - y - z follow the body except spin as shown in Figure 1. It is desired to cast these equations into the fixed Cartesian system of the linear model. First, the assumption that nutation θ is small ($\sin\theta \sim \theta$, $\cos\theta \sim 1$) will be made. This is a very good assumption for real rotor dynamics problems where shaft excursions are small, and affords great advantages. Given this assumption, the appropriate moment transformation is

$$\begin{bmatrix} M_x \\ M_y \\ M_z \end{bmatrix} = \begin{bmatrix} \cos\phi & -\sin\phi & \theta \sin\phi \\ \sin\phi & \cos\phi & -\theta \cos\phi \\ 0 & \theta & 1 \end{bmatrix} \begin{bmatrix} M_x \\ M_y \\ M_z \end{bmatrix} \quad (9)$$

The small nutation assumption allows the nutation to be vectorially related to the Cartesian rotations θ_X and θ_Y , since they are also small, and small angles can be vectorially combined. Thus,

$$\theta_X = \theta \cos\phi, \quad \text{and} \quad \theta_Y = \theta \sin\phi \quad (10)$$

Inserting equation (8) into (9), collecting terms, and substituting equations (10) and their time derivatives, the moment equations in fixed Cartesian coordinates are

$$\begin{bmatrix} M_X \\ M_Y \end{bmatrix} = \begin{bmatrix} I_0 & 0 \\ 0 & I_0 \end{bmatrix} \begin{bmatrix} \ddot{\theta}_X \\ \ddot{\theta}_Y \end{bmatrix} + \begin{bmatrix} 0 & I_s \\ -I_s & 0 \end{bmatrix} \begin{bmatrix} \dot{\theta}_X \\ \dot{\theta}_Y \end{bmatrix} + \begin{bmatrix} 0 & I\dot{s} \\ -I\dot{s} & 0 \end{bmatrix} \begin{bmatrix} \theta_X \\ \theta_Y \end{bmatrix} + \begin{bmatrix} 0 & -I\theta\dot{\theta}\dot{\phi} \\ I\theta\dot{\theta}\dot{\phi} & 0 \end{bmatrix} \begin{bmatrix} \theta_X \\ \theta_Y \end{bmatrix} \quad (11a)$$

$$M_Z = I\dot{s} - I\theta\dot{\theta}s + (2I_0 - I) \theta\dot{\theta}\dot{\phi} \quad (11b)$$

where s is the total rotational speed, with the small nutation assumption

$$s = \dot{\phi} + \dot{\psi} \quad (12)$$

On the right hand side of equation (11a), only the first term is linear, and should normally be included in the linear model as lumped transverse inertia. For constant speed, the second term is the familiar gyroscopic linear skew-symmetric coupling used by most rotordynamicists, the third term is zero, and the fourth term is nonlinear, depending on nutation angle and rate. The fourth term is only zero for circular precession orbits ($\dot{\theta} = 0$) or planar motion ($\theta = 0$), and in general cannot be assumed small. Although the portion $\theta\theta_X$ is quite small, the portion $\theta\dot{\theta}\dot{\phi}$ could be quite large because both $\dot{\theta}$ and $\dot{\phi}$ are proportional to speed. The approximate order of the whole term is order $\theta^3 s^2$, and should be compared with other cross-coupled stiffness loads in the system model to determine significance when general orbits are expected.

The right hand side of equation (11b) includes the linear angular acceleration term $I\dot{s}$ which may already be included as lumped polar inertia in the linear model. The corresponding DOF already in the linear model, θ_Z , can thus be interpreted as the integral of total local shaft speed. The remaining terms in equation (11b) are clearly nonlinear. They are zero for circular orbits and planar motion and are not necessarily small for other orbits, as both terms are of the order $\theta^2 s^2$.

The Force Equations

The force equation for a rigid body can be written directly in the Cartesian system without resort to the Euler system, thus

$$\begin{bmatrix} F_X \\ F_Y \\ F_Z \end{bmatrix} = \begin{bmatrix} m & 0 & 0 \\ 0 & m & 0 \\ 0 & 0 & m \end{bmatrix} \begin{bmatrix} \ddot{X} \\ \ddot{Y} \\ \ddot{Z} \end{bmatrix} \quad (13)$$

Clearly, these equations are linear and the mass should be lumped in the linear model.

Implementation

The nonlinear inertial effects discussed above could be important in rub analyses because rubs have a complicated effect on the shaft orbit (nutation) and local shaft speed due to the induced impact and torque. The nonlinear terms are relatively straightforward to implement given the equations previously presented and a few more easily derived from them. Figure 2 shows the procedure to be implemented as a user-defined "nonlinear inertia finite element". Note that all required Euler angles and rates are computed from the Cartesian rotations using the small nutation assumption, and singularities are avoided with logic checks. Most importantly, since the nonlinear moments are to be imposed on the model via the load vector \mathbf{F} , the nonlinear terms are flipped in sign from that in equations (11) as if they were moved to the left hand side. Any number of these "finite elements" could be used to model the inertial behavior of multiple turbine disks and impellers in the same system model by multiple calls to a subroutine that implements Figure 2.

Example

To illustrate the effect of inertial nonlinearity, a simple five DOF model was constructed using the techniques described above. The linear core model is shown in Figure 3, and the matrix form is that of equation (1) where the DOFs are

$$\mathbf{q}^T = [X \ Y \ \theta_X \ \theta_Y \ \theta_Z] \quad (14)$$

Note the different X and Y stiffness to induce nutation rate and the offset disk to produce nutation angle under imbalance loading. Note also that the realistic assumption of $I_0 = 0.5I$ will negate the last term in equation (11b). Two cases were run:

1. Linear, constant speed s of 5000 rad/sec, with constant imbalance load of 20 N (linear gyroscopics included).
2. Full nonlinear, initial speed of 5000 rad/sec, constant imbalance load of 20 N modified during simulation to follow the new total rotation angle θ_Z .

Secondary effects on the imbalance load due to slight speed change and disk tilt are neglected here so that they do not obscure the inertial nonlinearities. Damping was included to settle the orbit more quickly, as initial position of the shaft was centered. The speed of 5000 rad/sec is near the third critical speed, which involves mostly nutation.

Figure 4 shows the orbit results for Cartesian translations and rotations. Note that the orbit for rotations is by definition a polar plot of nutation given the small nutation assumption. The nonlinearity slightly increased the translation, and increased nutation by a factor of about three. This is despite fairly heavy rotational damping indicated by the relatively uniform elliptical shape compared to the translation orbits. The net result is a threefold increase in bearing load at this speed due to nonlinearity. A check of the induced speed variation showed miniscule effect. Most of the nonlinear effect is directly from nutation, and total neglect of the \dot{s} terms would have given similar results.

Admittedly, the model was tuned (high speed, ellipticity, nutation) for a severe nonlinear condition, for the sake of illustration. The results do indicate, however, that the nonlinearity of nutation can be important even for very small nutation. The nonlinearity of variable speed can be better evaluated in rub simulations, to be presented in a later paper.

INCLUDING SHAFT TORQUE

Formulation and Implementation

Suppose that the disk in Figure 1 has torque applied to it about the z axis such that it follows the z direction for all time. This is a reasonable assumption for rubbing or for fluid-induced drive or load torques in turbomachinery. Whenever a nutation angle develops, components of the torque occur along the Cartesian X and Y. Using equation (9) and a drive torque vector \mathbf{T} pointing in the +z direction, the resulting fixed Cartesian moments are, for small nutation,

$$\begin{bmatrix} M_X \\ M_Y \\ M_Z \end{bmatrix} = \begin{bmatrix} T\theta\sin\phi \\ -T\theta\cos\phi \\ T \end{bmatrix} = \begin{bmatrix} 0 & T & 0 \\ -T & 0 & 0 \\ 0 & 0 & 0 \end{bmatrix} \begin{bmatrix} \theta_X \\ \theta_Y \\ \theta_Z \end{bmatrix} + \begin{bmatrix} 0 \\ 0 \\ T \end{bmatrix} \quad (15)$$

Thus, following torque acts as a cross-coupled stiffness effect on transverse rotation. Constant torque can, in fact, be included in the system model as a linear cross-coupled stiffness. Since equation (15) is written for load on the system, the cross-coupled terms should be flipped in sign before adding to the system stiffness

matrix. If torque is variable as in rubbing, equation (15) can be used directly to update the system load vector \mathbf{F} .

Example

To show that the small nutation assumption has no significant effect on results, the fully nonlinear model of Vance [9] was exercised using the new method above for constant load torque (linear cross-coupling). The nature of the Vance model assures circular orbit and constant speed, so all inertial nonlinearities vanish and gyroscopics are included as linear cross-coupled damping. Complex eigenanalysis was used to construct root loci of the torquewhirl system as functions of speed. Figure 5 shows a speed dependent root locus for a load torque coefficient of $C_L = +5.625 \text{ N m sec/rad}$ (+50 in lb sec/rad). See reference [9] for all other parameters and definition of terms. The frequency and load torque level (C_L times the speed) at the point where the locus crosses the imaginary axis is the stability boundary.

Upon comparison with the exact solution via Euler's equations, the stability boundary frequency divided by the speed was found to closely match (within a few percent) the exact whirling speed ratio f for nutation angles up to about 10 degrees. This was expected, because f (see Appendix A) does not depend on nutation angle if it is small. The comparison of stability boundary torque computed by both methods also produced a very good match. This correlation forces disagreement with the comment in reference [9] that the inequality

$$\dot{\phi} + \dot{\psi} \neq \dot{\phi} \cos \theta + \dot{\psi} \quad (16)$$

"is central to an understanding of how torquewhirl is produced", because the linearized model assumes $\cos \theta$ is exactly unity. Rather, it is clear from inspection of equation (15) that torquewhirl is produced by a cross-coupled rotational stiffness projected into the transverse plane. It is clearly dependent on the mode shape of the system, which determines the degree of projection achieved. Yim, Noah, and Vance [10] have recently come to the same conclusion. Another conclusion of reference [10], summarized in Table 1, is supported by the current linearized analysis as well.

However, real turbomachinery has both load and drive torques at different shaft locations, so the net effect cannot be determined without specific analysis. The method introduced here makes such analyses particularly easy for constant torques at multiple locations on general rotors, without resort to nonlinear analysis.

Buckling Effects

Yim, Noah, and Vance [10] and Cohen and Porat [11] addressed the effect of shaft torque on the shaft stiffness due to a buckling load effect. This effect is separate from the projection effect treated above, but does lead to similar results in that the previously linear shaft stiffness is modified by symmetric and skew-symmetric changes that have nonlinear dependence on torque level. To model this effect, the entire stiffness matrix related to the rotor requires change as a function of torque. This can be done using the methods presented here, by including the shaft stiffness change and resultant delta internal forces and moments in the system load vector \mathbf{F} .

Since the stiffness change operations essentially require individual shaft element influence coefficients, they can best be done with a finite element program with an enhanced shaft finite element. For torque that can be assumed constant, the torque-modified stiffness can be directly calculated at the outset and incorporated into the system stiffness matrix, which would then be constant and linear but asymmetric. See [10] and [11]. Then substructuring (with care) if desired and all the steps outlined previously could be taken to perform nonlinear analysis.

The case of transient torque requires full reformulation of the rotor stiffness matrix at each time step, which some finite element programs can perform (ANSYS, for example). As an alternative to full reformulation, one

could use a linear fit of the shaft influence coefficients about a nominal operating torque T_0 . Thus the total rotor stiffness could be written

$$K_{TOT} = K(T_0) + (T - T_0) K \quad (17)$$

where $K(T_0)$ embodies the nominal torque effect and is included in the linear model, and

$$K = \left. \frac{dK(T)}{dT} \right|_{T=T_0} \quad (18)$$

The forces on the system due to the delta variation of T with time can then be included in the system load vector F by the term

$$-(T - T_0) K q \quad (19)$$

K can be easily evaluated off-line by computing $K(T)$ at two values of T around T_0 , and then performing the operation

$$K = \frac{K(T_0 + \Delta T^+) - K(T_0 - \Delta T^-)}{\Delta T^+ + \Delta T^-} \quad (20)$$

The method described above is ideal for rubbing problems where rub torques are small compared to steady drive torque.

In many realistic cases shafts operate far below their buckling limit, and the torque buckling effect may not be important compared to the projection effect. Since it is now clear how to separate the two effects, the question deserves further investigation.

CONCLUSIONS

1. Using the power of existing finite element and/or simulation software, quite general nonlinear effects can be applied to rotor/housing models of arbitrary linear complexity.
2. Casting nonlinear rigid body equations of motion into Cartesian form facilitates the understanding of the nonlinearities and simplifies their full implementation in general models. The assumption of small nutation affords great advantages.
3. Inertial nonlinearity can be important in problems with high speed and non-circular orbits, such as found in rubbing phenomena.
4. Casting the effects of projected following torque into Cartesian form using small nutation greatly simplifies torque modeling. Constant torque can even be handled as a linear cross-coupled stiffness.
5. Torques have two separate effects: projection of moments and torque buckling. The relative importance of each depends greatly on rotor design, specifically on mode shape and torque buckling margin, respectively. Torque buckling is amenable to relatively simple modeling in cases where transient torques are small relative to a steady value.
6. The combined effect of the items discussed in rubbing, blade loss, and other rotordynamic situations requires further study. This author will continue investigations, including modeling general bladed disks with rubbing.

APPENDIX A

Stability of an Idealized Rotor with Following Torque

The model of Vance [9], viscous case, was analyzed using Euler's equations with the following results. See [9] for full definitions.

Nonsynchronous Whirling Speed Ratio:

$$f = \frac{\dot{\phi}}{\omega_s} = \frac{l_2 + \sqrt{l_2^2 + \frac{4}{\omega_s^2} (l_1 \cos \theta^* + l_2) (\Omega_g^2 + \Omega_K^2 \frac{\theta^*}{\sin \theta^*})}}{2 (l_1 \cos \theta^* + l_2)} \quad (21)$$

where $\omega_s = \dot{\phi} + \dot{\psi}$ = shaft speed

Stability Boundary Torque

$$T_B = -C_D \ell^2 \omega_s f \cos \theta^* \quad (22)$$

Note that neither quantity depends on θ^* if θ^* is small (small nutation).

REFERENCES

1. Ehrich, F.F., The Dynamic Stability of Rotor/Stator Radial Rubs in Rotating Machinery, *ASME J. of Engineering for Industry*, vol. 91, pp. 1025-1028, November 1969.
2. Childs, D.W., Rub-Induced Parametric Excitation in Rotors, *ASME J. of Mechanical Design*, pp. 640-644, October 1979.
3. Muszynska, A., Partial Lateral Rotor to Stator Rubs, #C281/82 in *Vibrations in Rotating Machinery*, Institution of Mechanical Engineers Conference Publication 1984-10, Mechanical Engineering Publications Limited, London, pp. 327-335, 1984.
4. Lau, S.L., Cheung, Y.K., and Wu, S.Y., Incremental Harmonic Balance Method With Multiple Time Scales for Aperiodic Vibration of Nonlinear Systems, *ASME J. of Applied Mechanics*, vol. 50, no. 4a, pp. 871-876, December 1983.
5. Kascak, A.F., The Response of Turbine Engine Rotors to Interference Rubs, AVRADCOM Technical Report 80-C-14, NASA TM-81518, 1980.
6. Kascak, A.F. and Tomko, J.J., Effects of Different Rub Models on Simulated Rotor Dynamics, AVSCOM Technical Report 83-C-8, NASA TP-2220, 11 pg, February 1984.
7. Padovan, J. and Choy, F.K., Nonlinear Dynamics of Rotor/Blade/Casing Rub Interactions, ASME Paper #86-DE-6, Presented at the *Spring National Design Engineering Conference and Show, Chicago*, 8 pg, March 1986.
8. Noah, S.T., Rotordynamic Analysis of the SSME Turbopumps Using Reduced Models, Texas A&M University for NASA/MSFC, NASA CR-171170, 71 pg, September 1984.
9. Vance, J.M., Torquewhirl - A Theory to Explain Nonsynchronous Whirling Failures of Rotors With High-Load Torque, *ASME J. of Engineering for Power*, vol. 100, pp. 235-240, April 1978.
10. Yim, K.B., Noah, S.T., and Vance, J.M., Effect of Tangential Torque on the Dynamics of Flexible Rotors, ASME paper #86-WA/APM-23, 8 pg, December 1986.
11. Cohen, R. and Porat, I., "Influence of Load Torque on Stability of Rotor Driven by Flexible Shaft, *J. of Sound and Vibration*, vol. 95, pp. 151-160, 1984.

TABLE 1. Following torque stability influence

Torque Sense	Stabilizes Whirl	Destabilizes Whirl
Drive Load	Forward Backward	Backward Forward

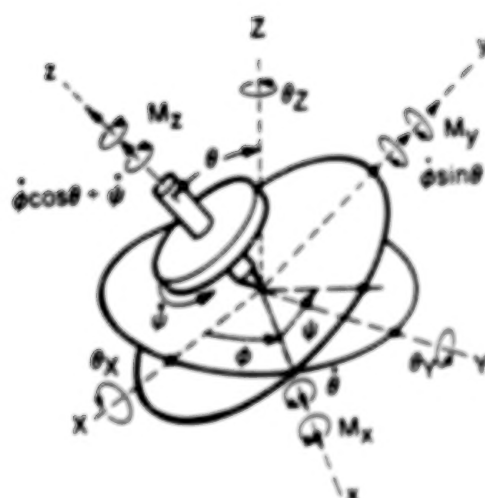


FIGURE 1. Coordinates and Euler angles for a rigid body

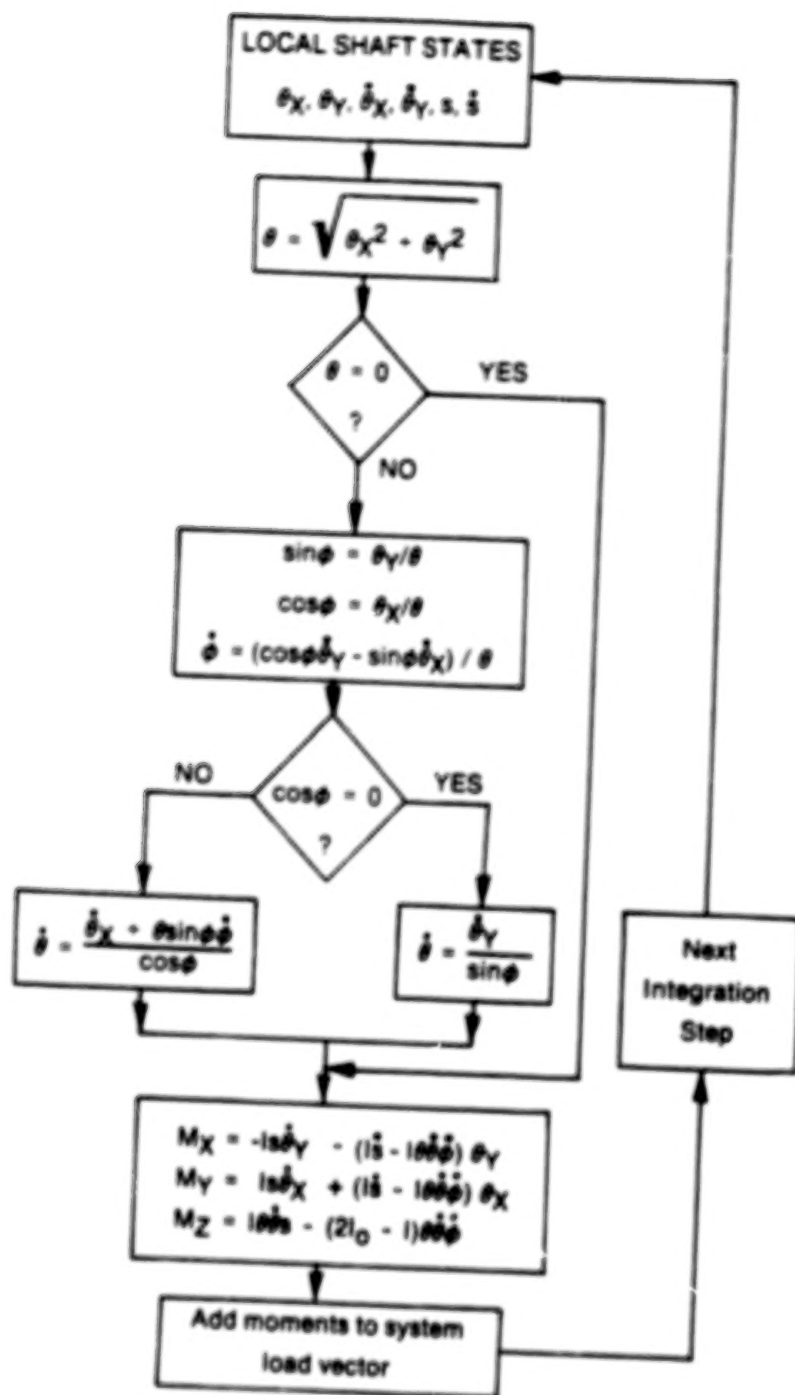


FIGURE 2. Algorithm for inertial nonlinearity finite element

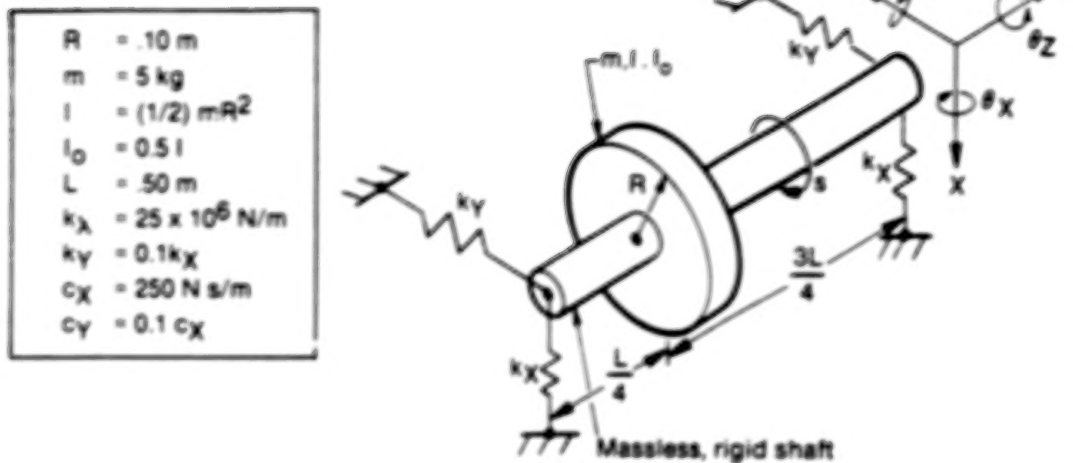


FIGURE 3. Simplified rotor model for inertial nonlinearity example

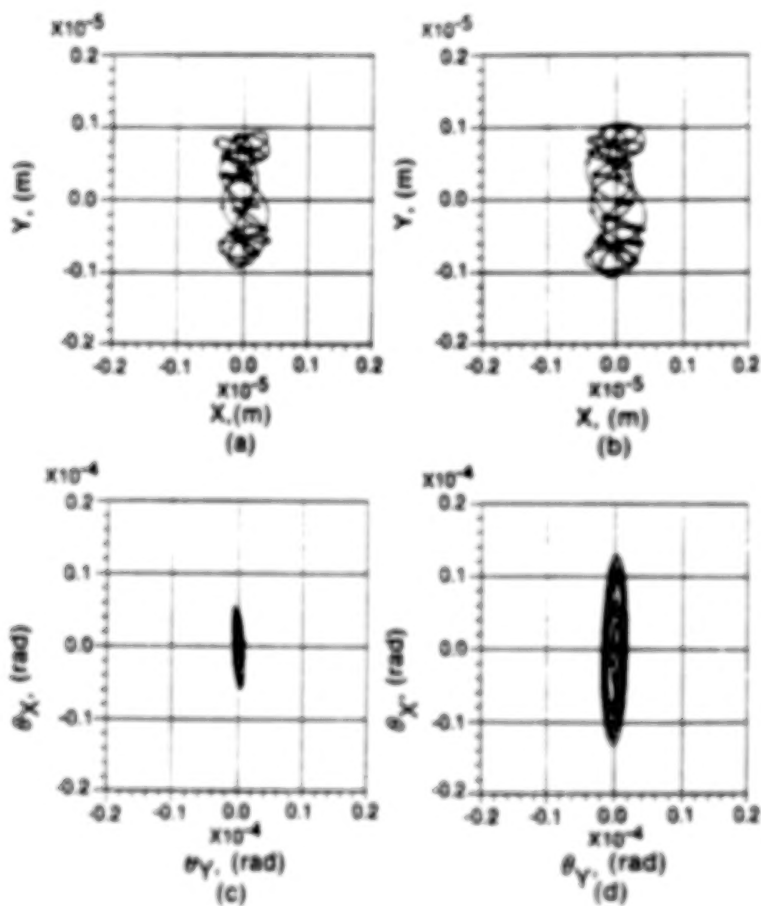


FIGURE 4. Response orbits of the simplified rotor model

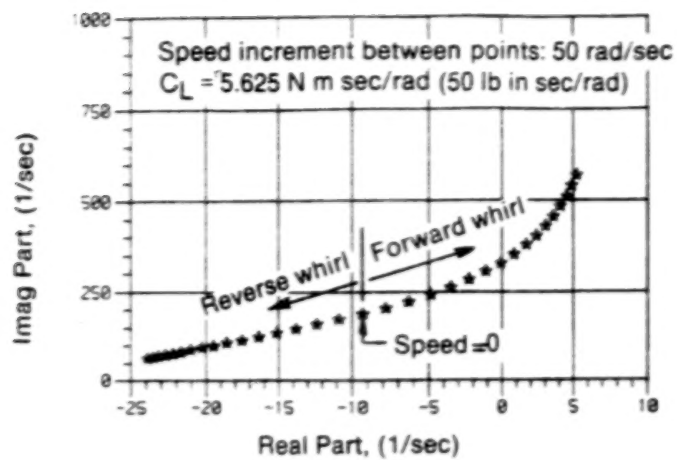


FIGURE 5. Root locus for linearized Vance model

HIGH STABILITY DESIGN FOR NEW CENTRIFUGAL COMPRESSOR

H. Kanki*, K. Katayama†, S. Morii‡, Y. Mouri†,
S. Umemura*, U. Ozawa*, T. Oda*
Mitsubishi Heavy Industries, Ltd.
Takasago, Japan

It is essential that high-performance centrifugal compressors be free of subsynchronous vibrations.

A new high-performance centrifugal compressor has been developed by applying the latest rotordynamics knowledge and design techniques.

- (1) To improve the system damping, a specially designed oil film seal was developed. This seal attained a damping ratio three times that of the conventional design. The oil film seal contains a special damper ring in the seal cartridge.
- (2) To reduce the destabilizing effect of the labyrinth seal, a special swirl canceler (anti-swirl nozzle) was applied to the balance piston seal.
- (3) To confirm the system damping margin, the dynamic simulation rotor model test and the full load test applied the vibration exciting test in actual load conditions.

INTRODUCTION

Performance improvement of centrifugal compressors for chemical plants has been a very important subject because these compressors substantially dominate the cost effectiveness of the plants.

A new high-performance centrifugal compressor has been developed by applying up-to-date techniques in response to these needs [1], and we have succeeded in developing an innovative new type of high-performance compressor and have demonstrated its high performance and reliability in shop tests under actual load conditions.

This paper describes the rotordynamic research undertaken in developing the new compressor.

DESIGN SPECIFICATIONS AND CHARACTERISTICS OF THE NEW COMPRESSOR [1]

The design specifications of the new compressor are shown in Table 1. This compressor was designed for the Ammonia & Methanol Synthesis Process. The specifications are typical for the 1000 T/day ammonia plant where the process gas is a mix of nitrogen and hydrogen.

The total cross section of the compressor is shown in Fig. 1. The low-pressure compressor is a back-to-back type and the high-pressure compressor contains the gas recycling stage.

The distinguishing features of the compressor are as follows, and all these merits are realized by applying the high-speed rotor system.

*Takasago R&D Center

†Takasago Machinery Works

‡Hiroshima R&D Center

- (1) High performance: A comparison of the required power for the conventional and new compressors for the 1000 T/day ammonia synthesis plant is shown in Table 2. The efficiency is significantly improved by applying the 3-dimensional high flow coefficient stages (high-speed impellers) shown in Fig. 2.
- (2) Compactness: A comparison of the new compressor with the conventional type in a similar plant is shown in Fig. 3. The compressor train is simplified and reduced to half size.
- (3) Easy maintenance: As shown in Fig. 3., both the end drive turbine and the cartridge-type internal compressor are applied to the new compressor train. These enable the compressor to be maintained without removing its casing.

The up-to-date techniques shown in Fig. 4 have been applied to the new compressor to realize the features mentioned above.

DEVELOPMENT OF THE COMPRESSOR FROM THE VIEWPOINT OF ROTORDYNAMICS

The new compressor, having up to nine stages, is operated at the highest speed in the world for this class of compressor. In spite of its compact, light-weight rotor, this compressor absorbs relatively high power and handles high-pressure, high-density gas. In similar high-pressure compressors, troubles caused by nonsynchronous vibrations have been reported [2],[3],[4],[8].

Therefore, countermeasures against this kind of vibration were critical in achieving reliable operation of the new compressor.

The forces acting on the compressor are shown in Fig. 5, and vibration stability of the system depends on the balance of the stabilizing force (damping force) and the destabilizing force. Accordingly, increasing the damping force and decreasing the destabilizing force is an essential solution. For the new compressor, with the help of our comprehensive research in this field, the following new techniques have been put into effect through quantitative evaluation of the damping force and destabilizing force.

A flow diagram of rotordynamic research for this compressor is summarized in Fig. 6.

ROTORDYNAMICS ANALYSIS

Rotordynamic characteristics of the high-pressure compressor are related to many components such as the bearings, oil film seals, labyrinth seals, and impellers. A flow diagram of the applied stability analysis method is shown in Fig. 7[8]. The component values are evaluated by using an accumulated data base and analytical tools.

(1) The dynamic coefficients of the oil film bearings are evaluated by the data base accumulated and qualified by the experimental model tests and numerical analysis.

(2) The dynamic coefficients of the oil film seals are estimated by the analytical method for oil film bearings.

(3) The destabilizing coefficients of the impellers are estimated by the following equation (Wachel equation modified to Alford force) [2]:

$$K_c = \frac{9583.2(KW)(MW)}{D \cdot H \cdot (RPM)} \cdot \frac{\rho_d}{\rho_s} \quad (1)$$

where (KW) is the output, (MW) is the molecular weight of the gas, (RPM) is the shaft speed, D is the impeller outside diameter, H is the impeller tip opening at discharge, ρ_d is the density of gas at discharge, and ρ_s is the density of gas in suction. This force estimation must be improved for better accuracy.

(4) The destabilizing coefficients of labyrinth seals are estimated by the theoretical analysis which was recently developed [7] by our research. The stability analysis of the system was done by the modal analysis shown in Fig. 7 or by complex eigenvalue analysis.

DEVELOPMENT OF NEW STABILIZING ELEMENTS

The stability analysis showed that the conventional type rotor bearing system had no margin for unstable vibration when it was applied to this kind of high intensity design. Then the new technology had to be applied to obtain a sufficient margin from the onset of unstable vibration.

The first innovation is a new type of oil film seal with a damper function as shown in Fig. 8. The new seal has a superior damping effect without any sacrifice of space or sealing function.

The mechanism of the damper seal consists of a multilobe bearing and a squeeze film damper. The effectiveness of the new seal system was verified by the model test system shown in Fig. 9.

The newly developed experimental method was used to verify the damping capacity of the rotor-bearing/oil-film-seal system. The method is called "Vibration Exciting Test Method in Working Condition," and it is essential to revealing the phenomena of nonsynchronous vibration.

Fig. 10 is an example of measured frequency response for two typical cases corresponding to the conventional system and the new system with the damper seal.

The speed-dependent vibration characteristics for the first mode are plotted in Fig. 11. As this figure shows, the test method enables the appointed mode to be evaluated for any rotating speed.

A summary of the results of the stability evaluation for the model system is shown in Table 3. The following stability coefficient (modal damping coefficient) is applied to the evaluation.

$$D = 2mw^2 \cdot \zeta \quad (2)$$

where D: stability coefficient
m: model mass of the mode
w: angular frequency of the mode
 ζ : damping ratio of the mode

The results show that the increased rate of the damping capacity is about three times that of the conventional system.

On the other hand, the special swirl canceling mechanism that is illustrated in Fig. 12 is developed and applied to this compressor in order to minimize the destabilizing force generated by the labyrinth seal. The design of the labyrinth seal was based on the recently developed theory and model tests published in a NASA Conference Publication in 1986 [6]. This research confirmed that the gas flow at the labyrinth seal, particularly inlet swirl, is the major cause of the

destabilizing forces. Then, the design of the reliable swirl canceling mechanism was developed. The low destabilizing force with this mechanism was verified by a full load test that is described later.

VERIFICATION TEST IN THE SHOP

To verify the new compressor's performance and mechanical reliability, a four-step testing program has been carried out as shown in Table 4.

In addition to normal tests and inspections for the prototype machine, special rotordynamic tests were performed in the shop to verify vibration stability and smooth operation.

Fig. 13 is a photograph of the shop test setup showing the vibration-exciting test apparatus. The vibration-exciting tests were performed for mechanical run and high-pressure performance conditions. Fig. 14 shows the measured vibration for the high-speed run and actual load tests. Fig. 15 shows the plots of damping vs. load.

These results show a sufficient stability margin even for the full load, full speed condition.

This fact verified the following two points.

- (1) The new oil film seal system gives high system damping for any operating condition, especially for high-speed conditions.
- (2) The destabilizing effect of the compressor, which has not ever be found directly, is verified by the difference value between the high-speed mechanical run and the actual load test.

The results also verified that there would have been marginal instability if the new stabilizing mechanism had not been applied.

The stability evaluation for the compressor is plotted on Fig. 16 with a comparison to the existing unit. This figure shows a sufficient margin of safety against unstable vibration.

EVALUATION OF VIBRATION SENSITIVITY TO THE DISTURBANCE IN NONSTEADY OPERATING CONDITIONS.

Fig. 17 shows the vibration level for all speed ranges. The shaft vibration did not exceed 10 μm p-p including runout. There was no significant critical speed peak for any speed within maximum speed. These phenomena support the fact that the system has a sufficiently large damping ratio [5].

Fig. 18 shows the example of measured data during surge. This figure shows that the vibration, pressure pulsation, and thrust force are all sufficiently small values even in the abnormal condition.

CONCLUSIONS

Rotordynamic research and results for developing a high-speed, high-performance compressor are described.

The newly developed damper seal and swirl canceling mechanism for the labyrinth seal produces a highly stable compressor. The high stability and low

vibration sensitivity of the prototype compressor was verified by many operating tests and special vibration-exciting tests.

Production compressors based on the design of the prototype have been operating smoothly and with high efficiency.

REFERENCES

- (1) Katayama, K., et al., "Development of High-Speed High-Performance Compressor." Mitsubishi Heavy Industries Technical Review, Vol 24, No. 2, 1987.
- (2) Wachel, J.C., "Nonsynchronous Instability of Centrifugal Compressors." ASME paper 75-pet-22, 1975.
- (3) Jenny, R., "Labyrinth as a Cause of Self-Excited Rotor Oscillations in Centrifugal Compressors." Sulzer Technical Review 4, 1980, pp. 149-156.
- (4) Emerick, M.F., "Vibration and Destabilizing Effects of Floating Ring Seals in Compressors." NASA Conference Publication 2250, 1982, pp. 187-204.
- (5) Shiraki, K., & Kanki, H., "A New Vibration Criteria for High Speed Large Capacity Turbo-machinery." Proceedings 8th Turbomachinery Symposium, 1979, pp. 59-70.
- (6) Iwatsubo, T., Motooka, N., & Kawai, R., "Flow Induced Force of Labyrinth Seal." NASA Conference Publication 2250, 1982, pp. 205-222.
- (7) Kanki, H., Morii, S., & Hizume, A., "Theoretical and Experimental Study on the Destabilizing Force by Labyrinth Seal." IFToMM 1986, to be published.
- (8) Morii, S., Nishimoto, K., Kanki, H., & Hirayama, F., On the Sub-Synchronous Whirl in the Centrifugal Compressor, ICVPE Xi'an, 1986-6.
- (9) Kanki, H., Fujii, H., Hizume, A., et al., "Solving Nonsynchronous Vibration Problems of Large Rotating Machineries by Exciting Test in Actual Operating Condition." IFToMM Conference, 1986.
- (10) Umemura S., Mase, M., & Murai, T., Study on the Vibration Analysis of Radial-Flow Impellers, Mitsubishi Juko Giho, Vol. 14, No. 2, 1977.

Table 1 Table of compressor specifications

Item	Unit	Value
Suction flow rate	Am^3/h	5 500 - 6 500
Suction press.	$\text{kgf}/\text{cm}^2 \text{G}$	25
Suction temp.	$^{\circ}\text{C}$	45
Discharge press.	$\text{kgf}/\text{cm}^2 \text{G}$	150 - 220
Max. continuous speed	rpm	15 540

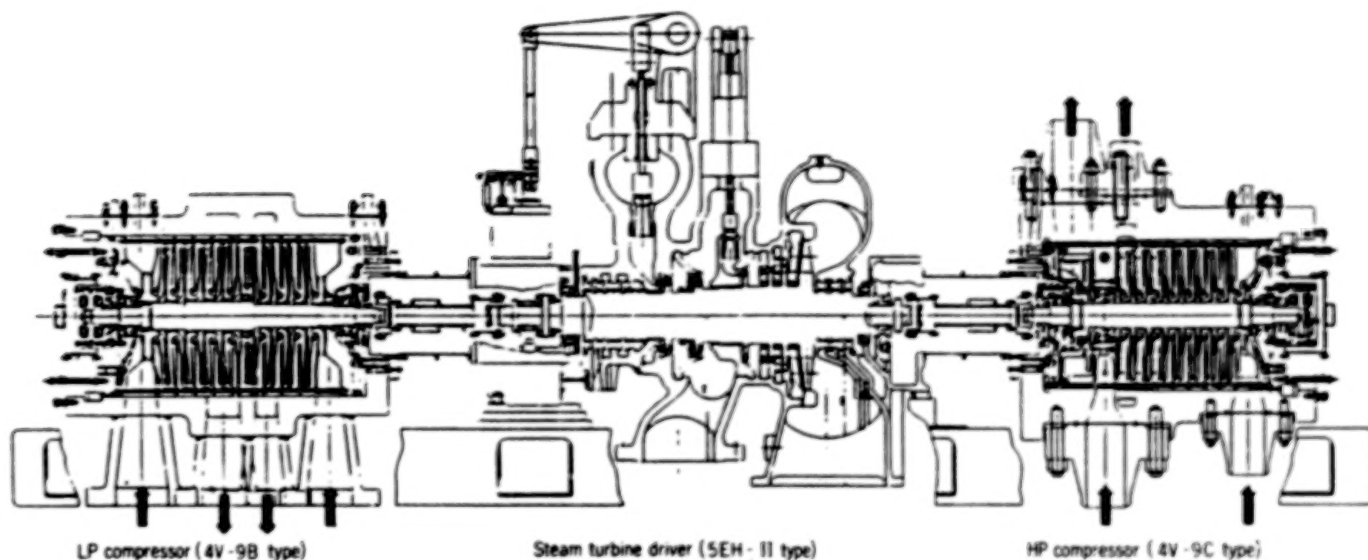


Fig.1 Cross section of the compressor train

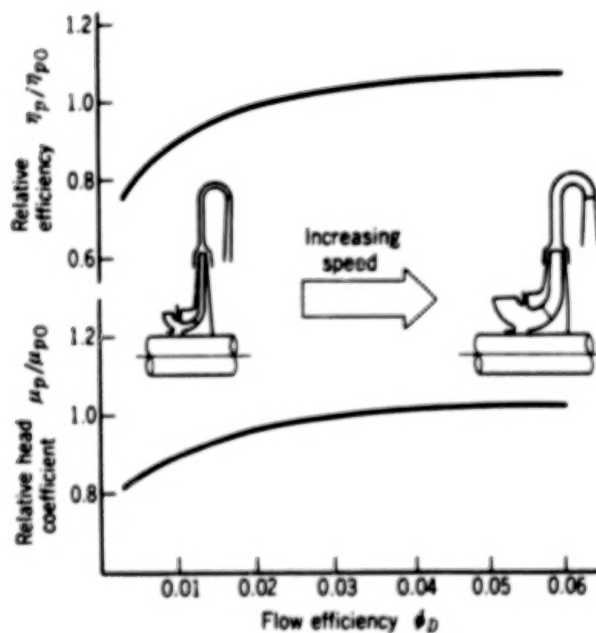


Fig.2 Stage performance vs. flow coefficient

Table 2 Merit of the new compressor (High performance)

Required power of compressor		Reduction in required power (Saving rate)
Conventional unit	New unit	
16 500 kW	14 980 kW	1 520 kW (9%)

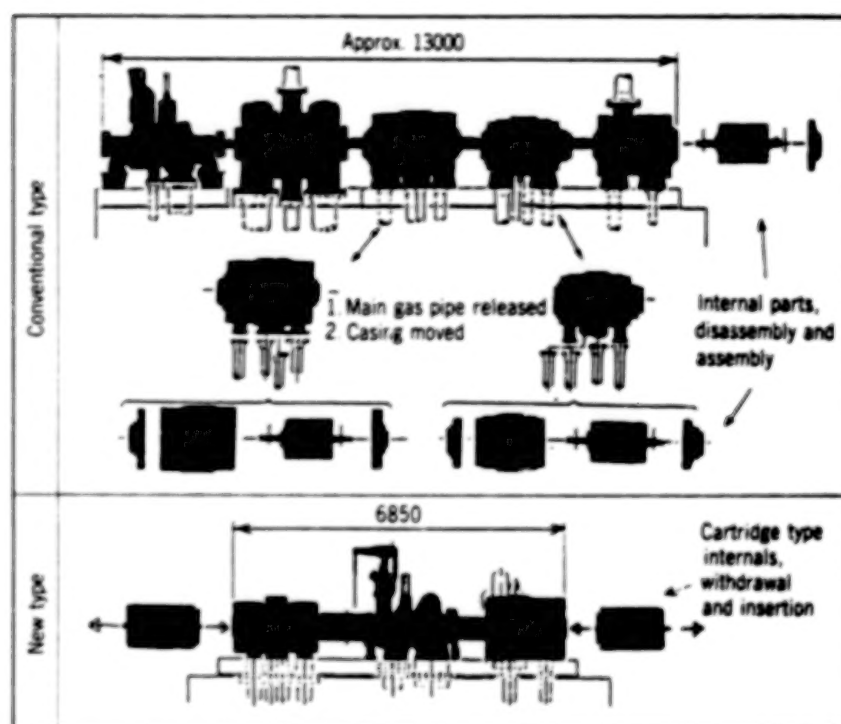


Fig.3 Merit of the new compressor (Compactness, ease of maintenance)

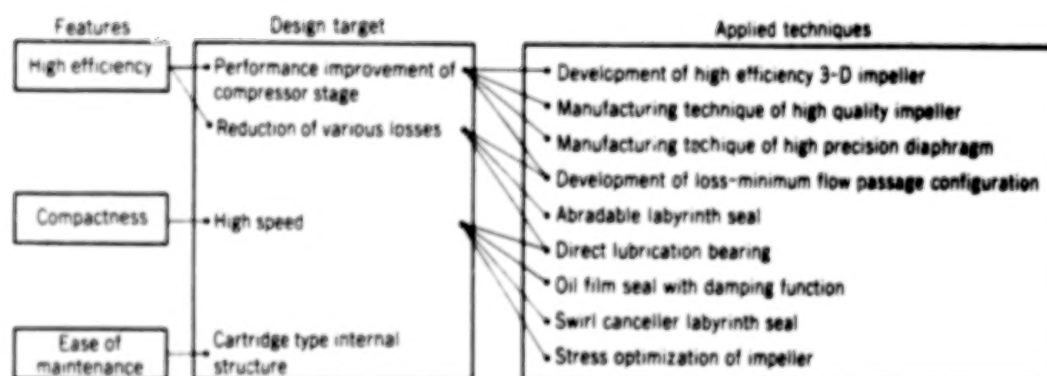


Fig.4 Application of up-to-date techniques

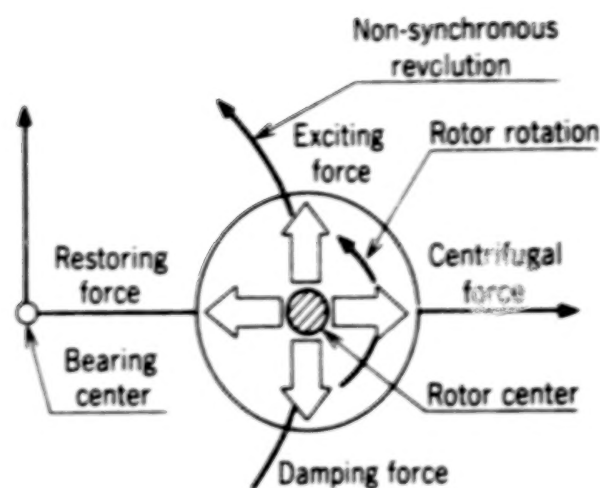


Fig.5 Forces acting on the rotor

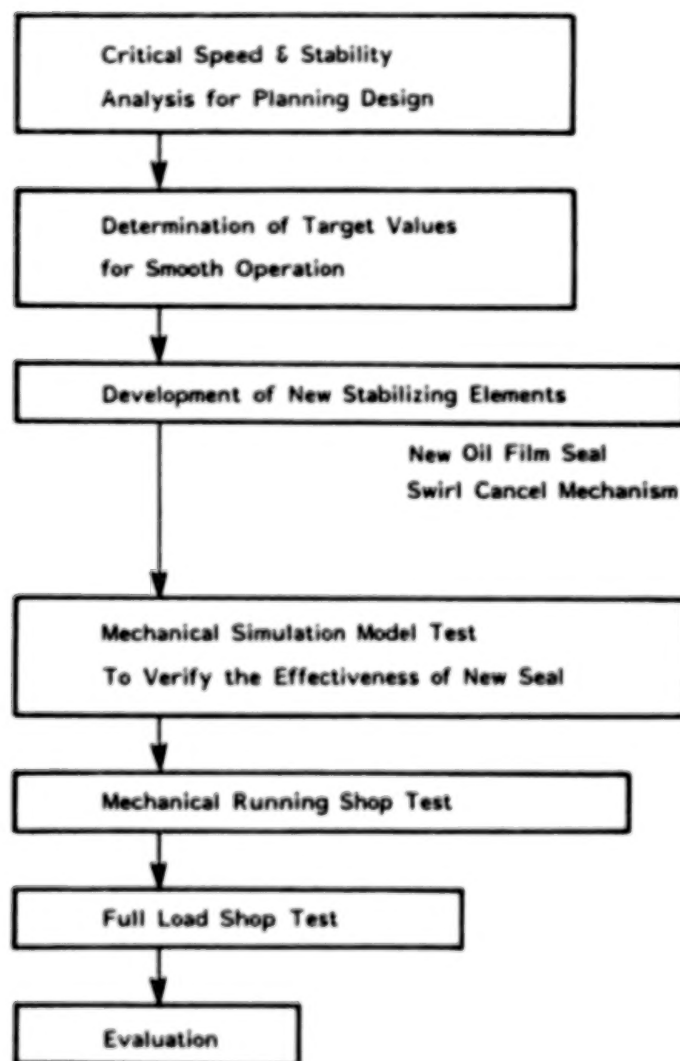


Fig.6 Flow diagram of rotordynamic research for the development of the new compressor

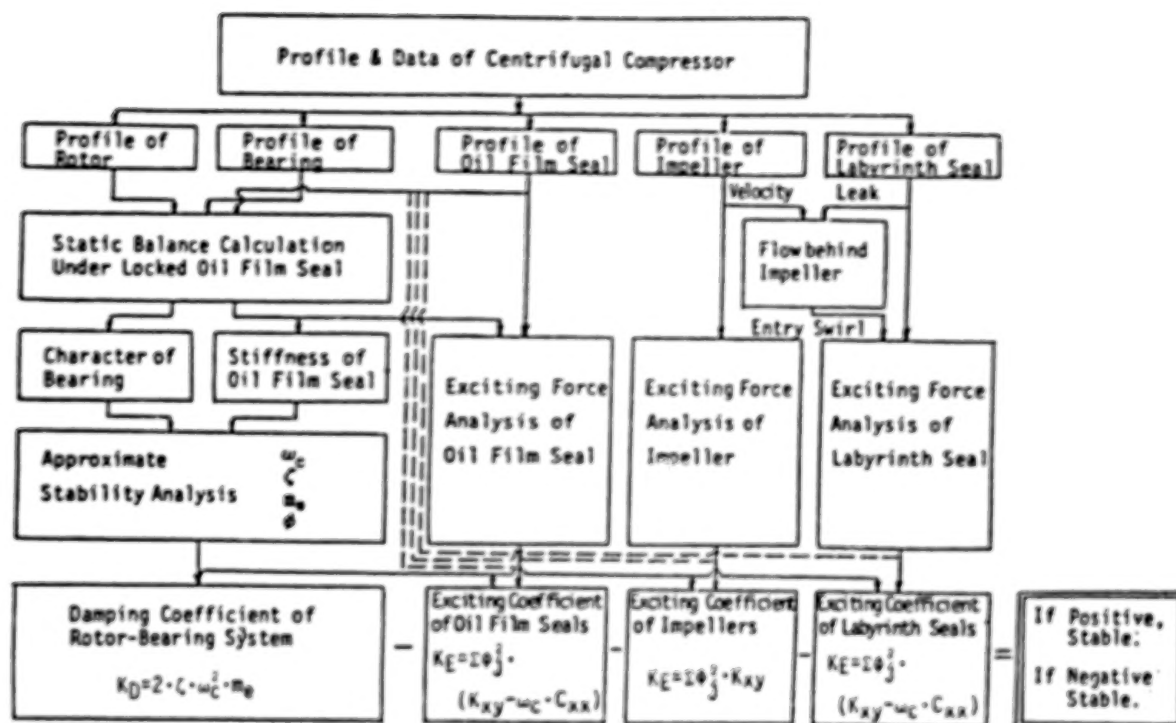


Fig.7 Block diagram of stability analysis method

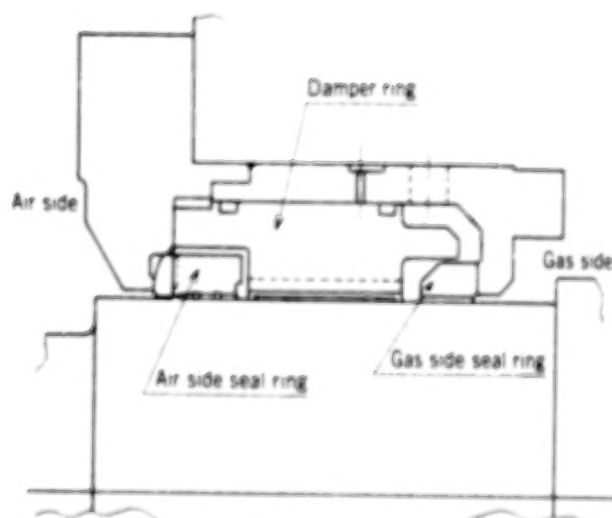


Fig.8 New oil film seal with damping function

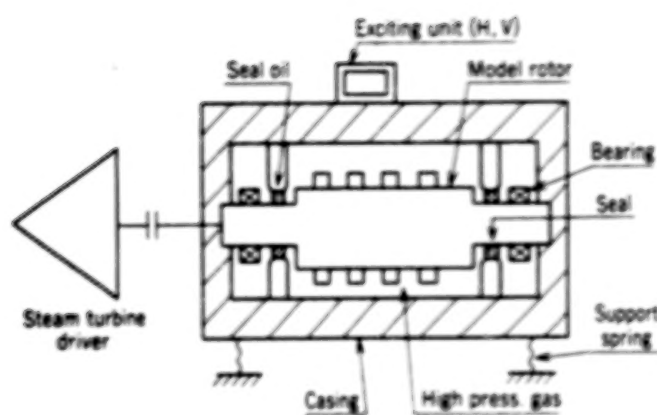


Fig.9 High pressure seal test apparatus

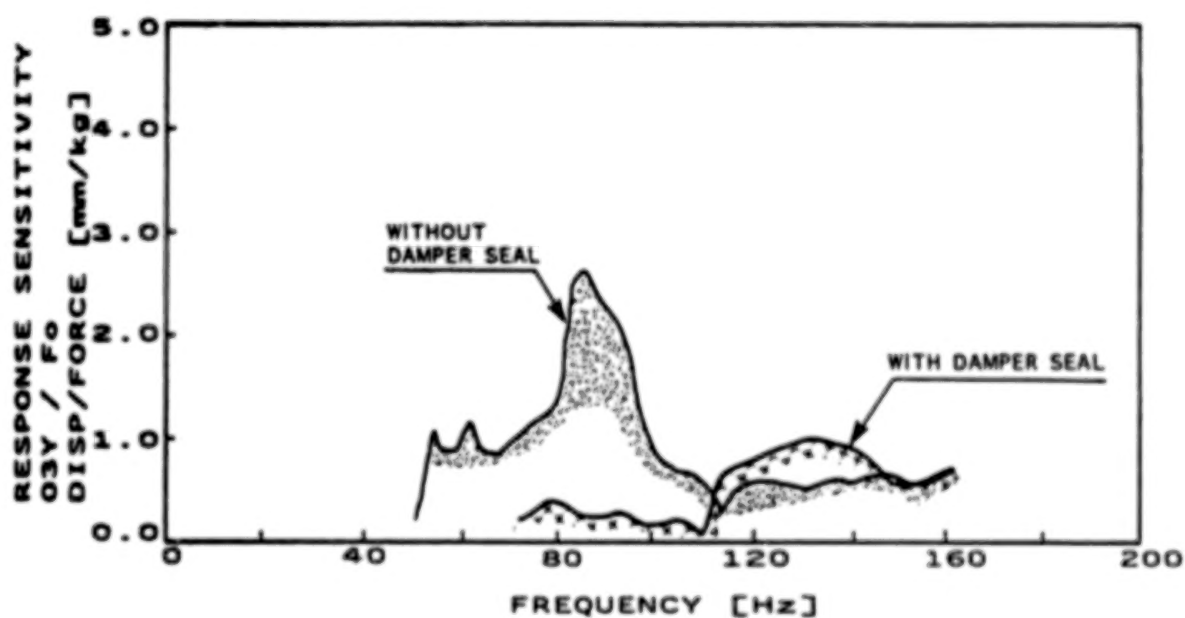


Fig.10 Typical frequency response for seal test

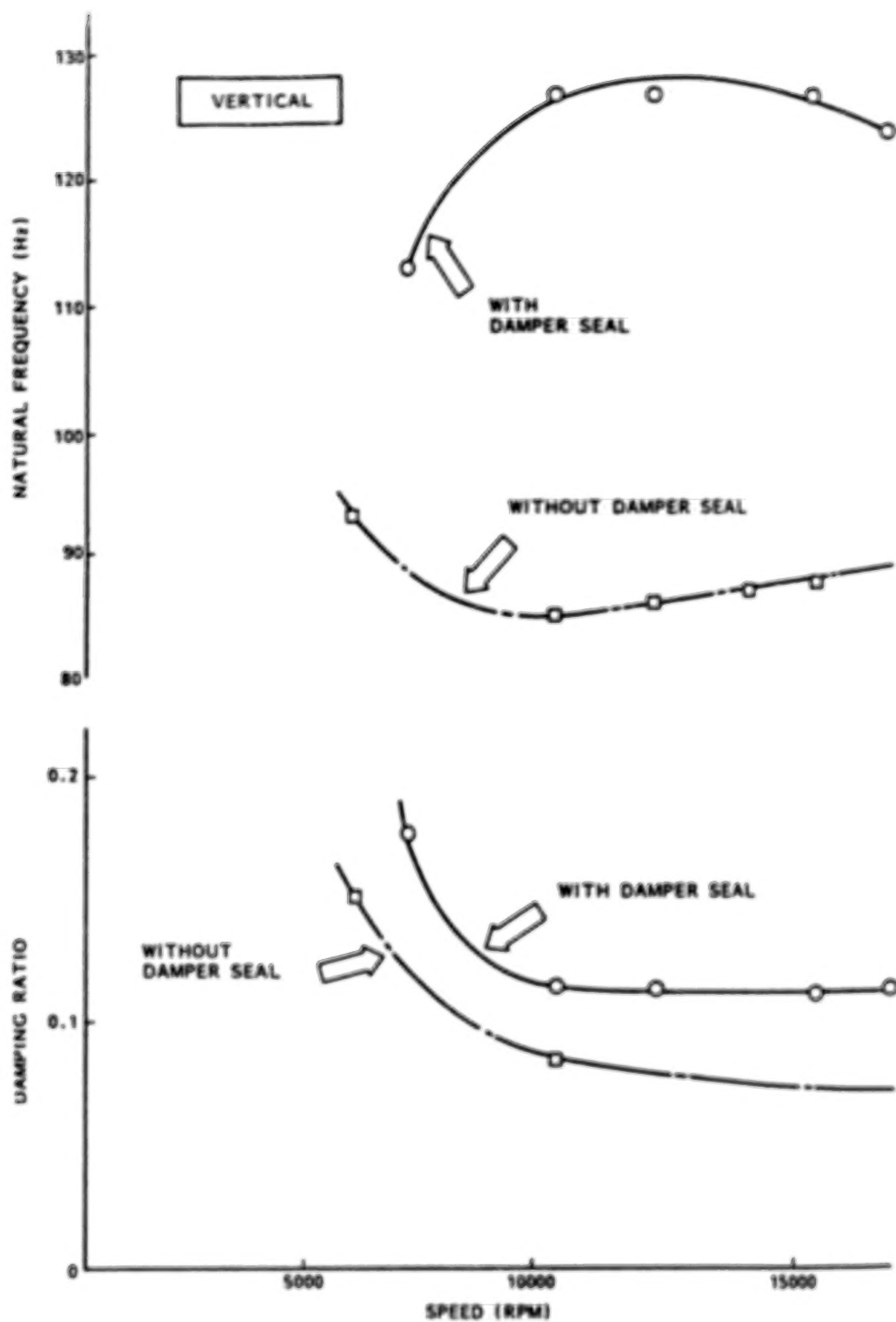
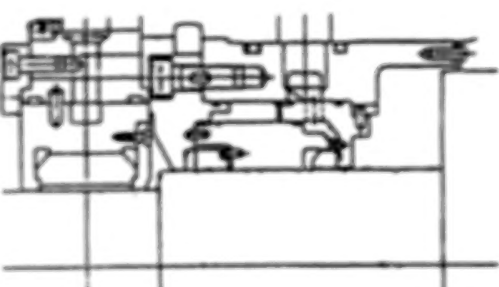
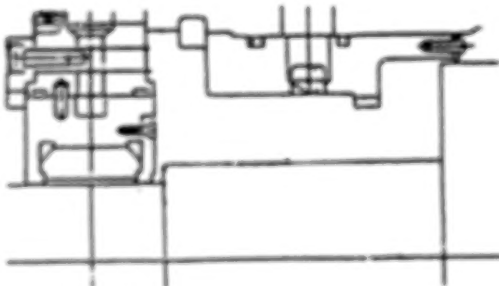


Fig.11 Comparison of vibration characteristics

Table 3 Test results of new oil film seal

	SEAL TEST MODEL	CRITICAL SPEED Q FACTOR FOR UNBALANCE RESPONSE	1ST-MODE		
			FREQUENCY	DAMPING RATIO	EQUIVALENT DAMP. COEF.
WITH DAMPER SEAL		6800 RPM $Q = 2.8$	127.5Hz	0.118	25700 kgf/cm
WITHOUT DAMPER SEAL		5600 RPM $Q = 3.3$	87.2Hz	0.075	7650

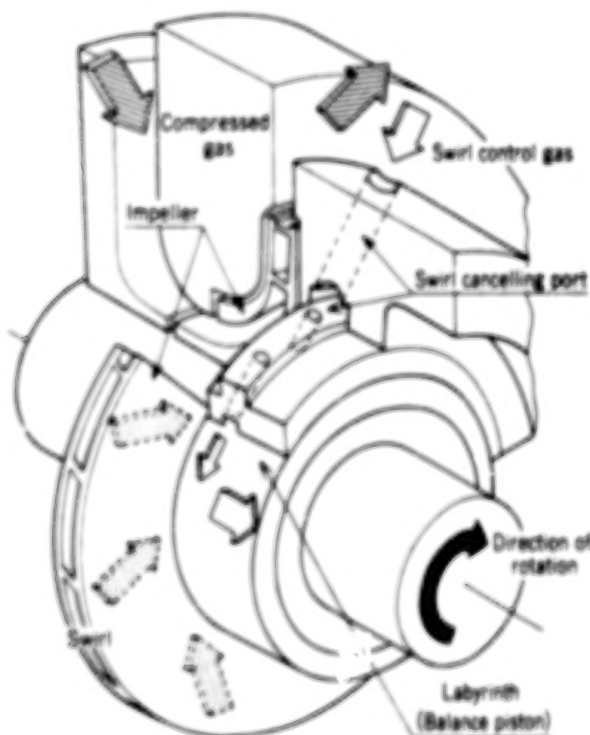


Fig.12 Labyrinth seal with swirl canceler

Table 4 Table of shop test program

Test step	Object
Static seal test	Verification of dynamic behavior of oil film seal and seal oil supply unit
Aerodynamic performance test	Verification of compressor efficiency and required power
High speed mechanical running test	Verification of mechanical stability during high speed running
High press. performance test	Verification of mechanical stability and aerodynamic performance under actual operation conditions

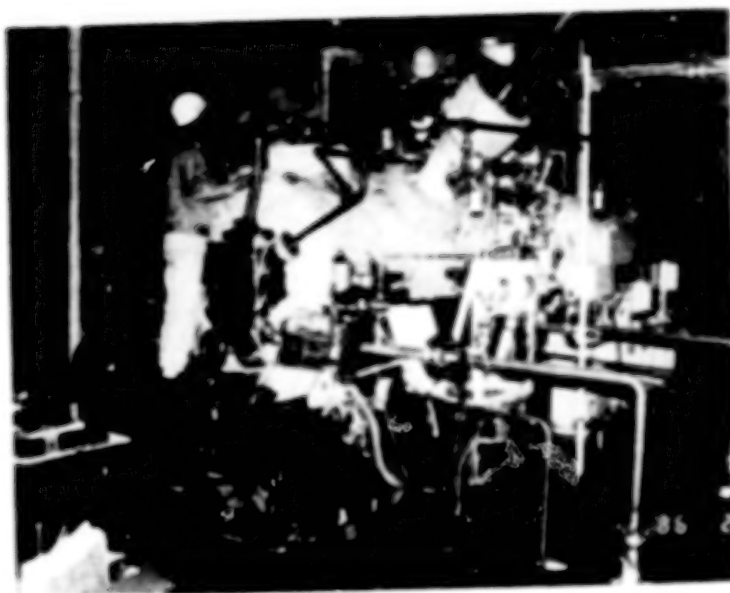


Fig.13 Vibration-exciting test apparatus for shop test

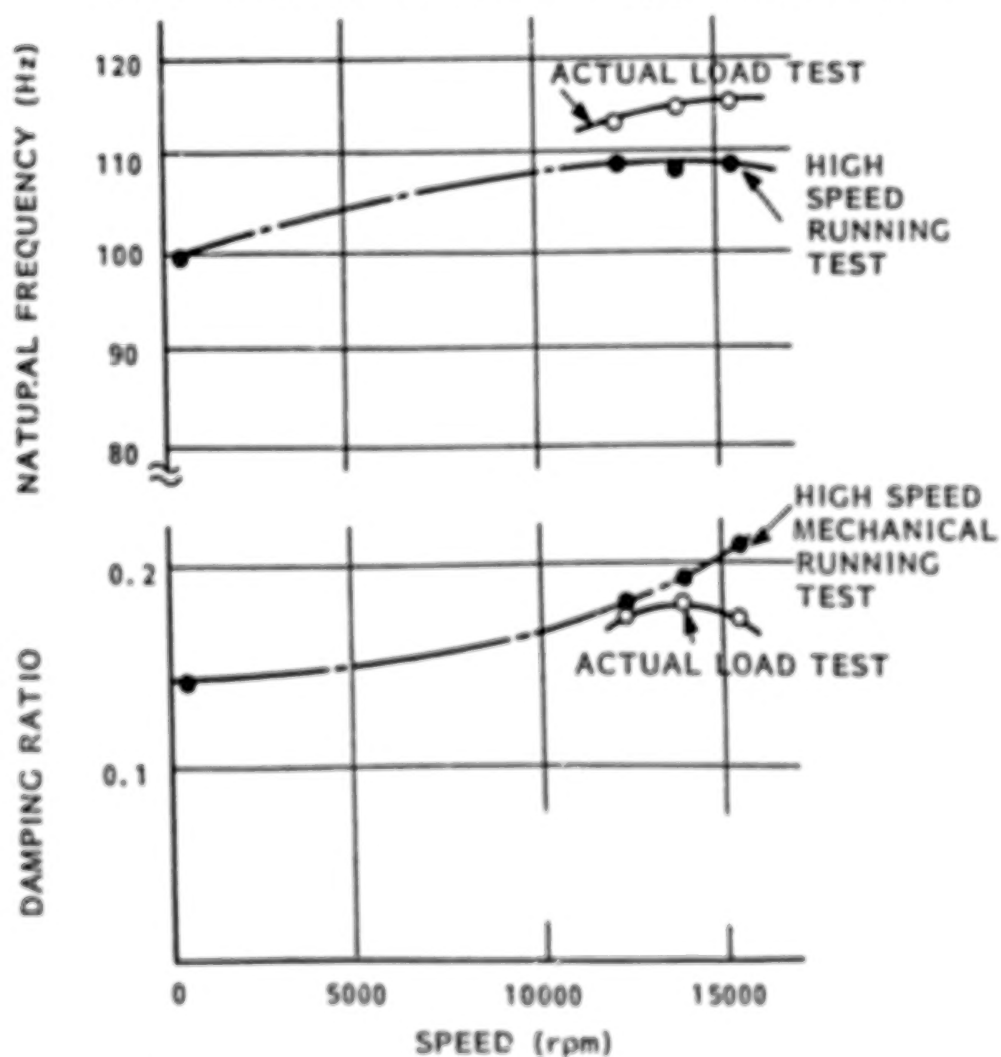


Fig.14 Results of vibration-exciting test (speed vs. natural frequency and damping)

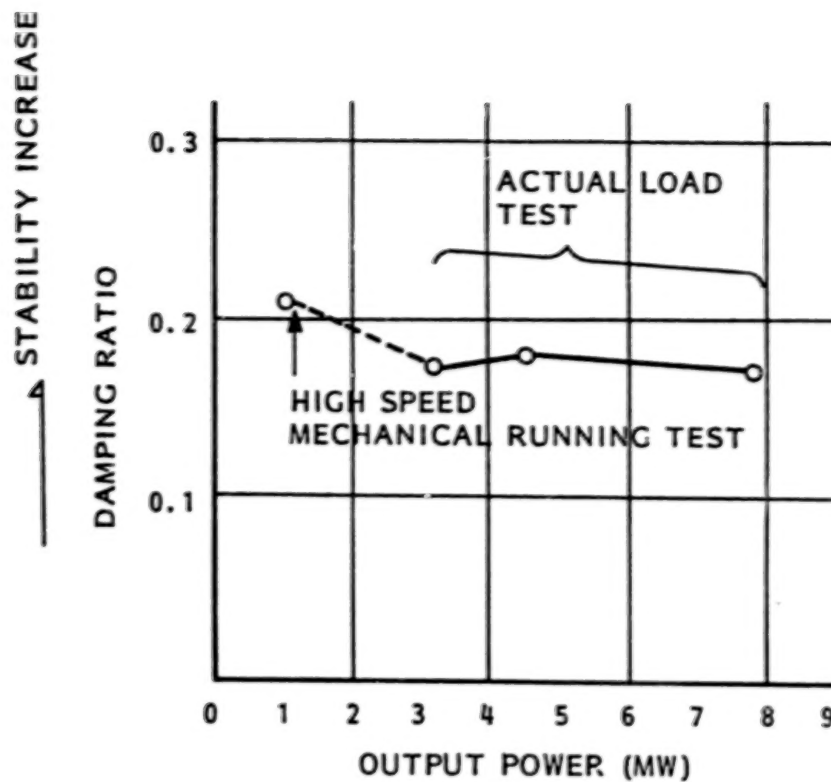


Fig. 15 Results of vibration-exciting test (stability vs. output)

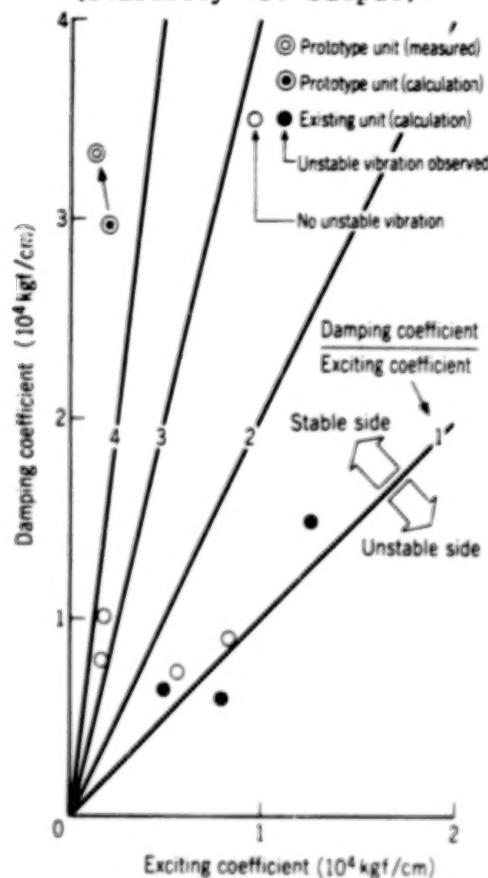


Fig. 16 Measured stability margin for nonsynchronous vibration

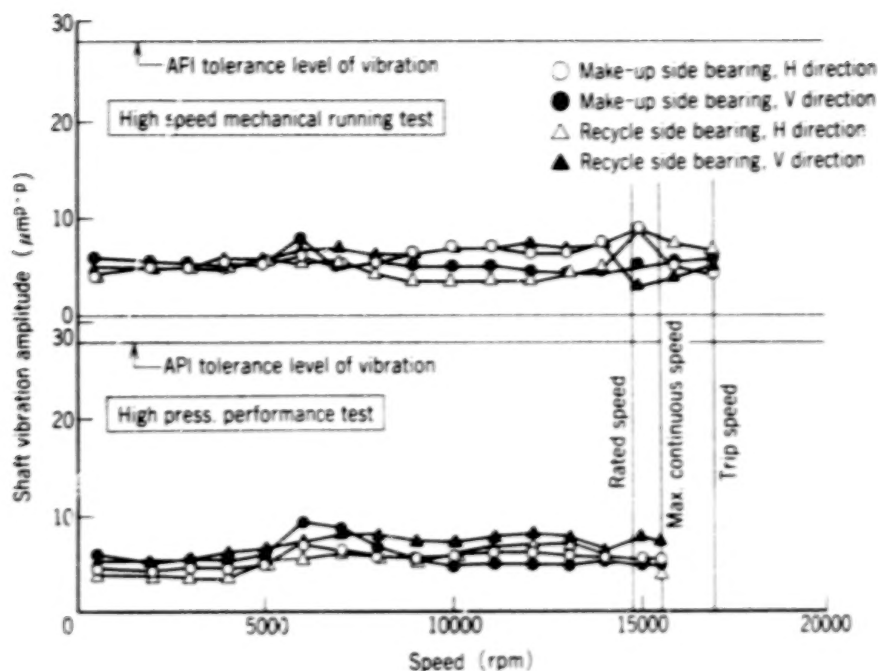


Fig.17 Measured shaft vibration

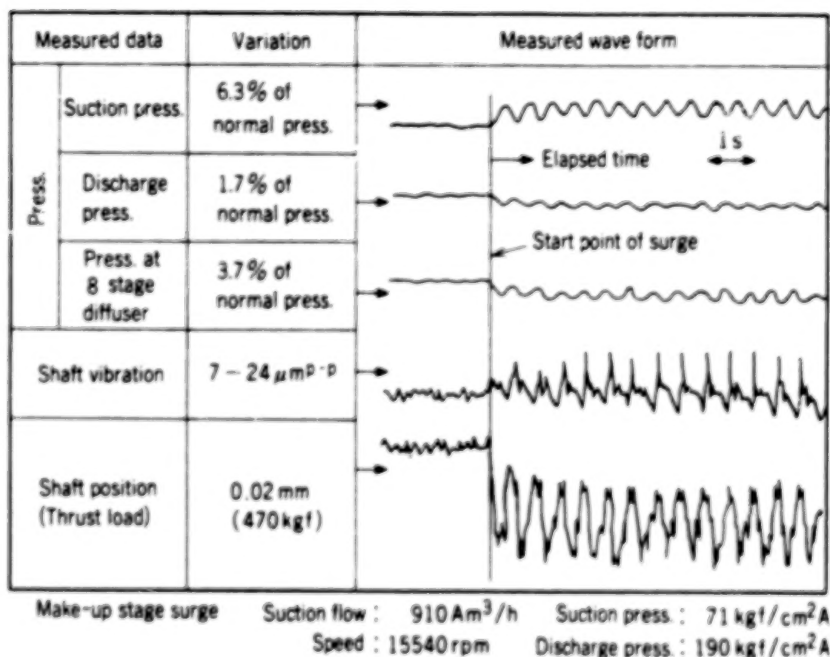


Fig.18 Example of measured data during compressor surge

1. Report No. NASA CP-3026		2. Government Accession No.		3. Recipient's Catalog No.	
4. Title and Subtitle Rotordynamic Instability Problems in High-Performance Turbomachinery—1988				5. Report Date February 1989	
				6. Performing Organization Code 553-13-00	
7. Author(s)				8. Performing Organization Report No. E-4227	
				10. Work Unit No.	
9. Performing Organization Name and Address National Aeronautics and Space Administration Lewis Research Center Cleveland, Ohio 44135-3191				11. Contract or Grant No.	
				13. Type of Report and Period Covered Conference Publication	
12. Sponsoring Agency Name and Address National Aeronautics and Space Administration Washington, D.C. 20546-0001				14. Sponsoring Agency Code	
15. Supplementary Notes The workshop was sponsored by Texas A&M University, College Station, Texas; the U.S. Army Research Office, Durham, North Carolina; the Aeropropulsion Laboratory, Wright-Patterson Air Force Base, Ohio; and NASA Lewis Research Center, and held at Texas A&M University on May 16-18, 1988.					
16. Abstract The first rotordynamics workshop proceedings (NASA CP-2133, 1980) emphasized a feeling of uncertainty in predicting the stability of characteristics of high-performance turbomachinery. In the second workshop proceedings (NASA CP-2250, 1982) these uncertainties were reduced through programs established to systematically resolve problems, with emphasis on experimental validation of the forces that influence rotordynamics. In the third proceedings (NASA CP-2338, 1984) many programs for predicting or measuring forces and force coefficients in high-performance turbomachinery produced results. Data became available for designing new machines with enhanced stability characteristics or for upgrading existing machines. In the fourth proceedings (NASA CP-2443, 1986) there emerged trend toward a more unified view of rotordynamic instability problems and several encouraging new analytical developments. The present workshop supports the continuing trend toward a unified view with several new developments in the design and manufacture of new turbomachineries with enhanced stability characteristics along with new data and associated numerical/theoretical results. The intent of the workshop and this proceedings is to provide a continuing impetus for an understanding and resolution of these problems.					
17. Key Words (Suggested by Author(s)) Rotordynamics Turbomachinery Instability			18. Distribution Statement Unclassified - Unlimited Subject Category 37		
19. Security Classif. (of this report) Unclassified		20. Security Classif. (of this page) Unclassified		21. No of pages 459	
				22. Price* A20	

N 95 / 19391

END

12 - 16-91